

STRATOSPHERIC PROCESSES
AND THEIR ROLE IN CLIMATE
SPARC

A project of the WMO/ICSU/IOC World Climate Research Programme

Assessment of Stratospheric
Aerosol Properties
(ASAP)

Prepared under the auspices of the SPARC Scientific Steering Group

Edited by L. Thomason and Th. Peter

WCRP-124
WMO/TD- No. 1295
SPARC Report No. 4

February 2006

Assessment of Stratospheric Aerosol Properties (ASAP)

Table of Contents

Table of Contents	iii
Foreword	vii
Disclaimer	ix
Executive Summary	xi
Key Findings	xi
Recommendations	xii
Important Findings Per Chapter	xiii
Chapter 1: Stratospheric Aerosol Processes	xiii
Chapter 2: Precursor Gas Measurements	xiv
Chapter 3: Instruments	xv
Chapter 4: Stratospheric Aerosol Record and Climatology	xvi
Chapter 5: Stratospheric Aerosol Trends	xvi
Chapter 6: Modeling of Stratospheric Aerosols	xviii
ASAP Data Archive	xxi
List of Reviewers	xxiii
Chapter 1 - Stratospheric Aerosol Processes	1
1.1 The Importance of Stratospheric Aerosol	3
1.2 The Life Cycle of Stratospheric Aerosol	4
1.3 Sources of Sulfur Gases and Aerosol to the Stratosphere	5
1.4 Stratospheric Aerosol Microphysics and the Particle Size Distribution	6
1.4.1 Global Aerosol	6
1.4.2 Polar Aerosol	12
1.4.3 Non-Aqueous Stratospheric Particles	13
1.5 Volcanic Perturbations to Stratospheric Aerosol	14
1.6 Aerosol in the Tropopause Region	16
1.6.1 Aerosol precursors and nucleation processes	16
1.6.2 Aerosol distribution and composition	18
1.7 Polar Stratospheric Clouds and Sub-visible Cirrus Clouds	20
1.7.1 Polar stratospheric clouds	21
1.7.2 Subvisible Cirrus Clouds	22
1.8 Aviation-produced aerosol	24

Chapter 2 - Precursor Gas Measurements	29
2.1	Introduction 31
2.2	Dynamics and Atmospheric Transport 31
2.3	Sulfur Chemistry 34
2.4	Observations 36
2.4.1	Carbonyl sulfide (OCS) 36
2.4.2	Sulfur Dioxide (SO ₂) 52
2.4.3	Dimethyl sulfide (CH ₃ SCH ₃) 60
2.4.4	Other precursor gases 64
2.5	Fluxes 65
2.5.1	Carbonyl Sulfide Fluxes 66
2.5.2	Sulfur Dioxide Fluxes 67
2.5.3	Dimethyl Sulfide Fluxes 69
2.5.4	Hydrogen Sulfide Fluxes 70
2.5.5	Methyl Mercaptan Fluxes 70
2.5.6	Carbon Disulfide Fluxes 71
2.5.7	Meteors, cosmic radiation, and rocket exhaust 71
2.5.8	Isotopic studies 74
2.6	Summary and open questions 75
2.7	Acknowledgements 76
Chapter 3 - Instruments	77
3.1	Introduction 79
3.2	Global Long-Term Measurements 79
3.2.1	SAM II, SAGE I, and SAGE II: The Occultation Technique 80
3.2.2	HALOE 84
3.2.3	POAM II and POAM III 86
3.3	Global Short-Term Measurements 89
3.3.1	CLAES 89
3.3.2	ORA 91
3.4	Localized Long-Term Measurements 92
3.4.1	Balloon Borne Optical Particle Counter 92
3.4.2	Lidar Systems 94
3.5	Localized Short-Term Measurements 100
3.5.1	The Aircraft-Borne LaRC Aerosol Lidar 100
3.5.2	The Airborne DLR OLEX Lidar 102
3.5.3	Airborne Particle Counters 102
3.5.4	Balloon-borne Backscattersonde 105
Chapter 4 - Stratospheric Aerosol Record and Climatology	107
4.1	Introduction 109
4.2	Primary Measured Aerosol Properties 109
4.2.1	Global Long-term Measurements of Extinction and Optical Depth 110
4.2.2	Global Short-term Measurements 120
4.2.3	Localized Long-term Measurements 123
4.2.4	Short Term Localized Measurements 127
4.3	Retrieved Products 135

4.3.1	Retrieved Products from Global Long-term Measurements	135
4.3.2	Retrieved Products from Localized Long-term Measurements	152
4.4	Relevant Cross-Comparisons Of Averages Or For Coincidences	155
4.4.1	SAGE/HALOE/OPC Comparisons	155
4.4.2	SAGE/POAM Comparisons	168
4.4.3	SAGE/ORA Comparison	169
4.4.4	Comparisons of SAGE Extinctions with Lidar Backscatter	170
4.5	Conclusions	175

Chapter 5 - Stratospheric Aerosol Trends **177**

5.1	Introduction	179
5.2	Fundamental measurements	184
5.2.1	In situ measurements	184
5.2.2	Remote lidar measurements	184
5.2.3	Remote satellite measurements	186
5.3	Measurements	187
5.4	Investigation of trends in the long term aerosol measurement records	194
5.4.1	Comparison of stratospheric aerosol during non volcanic periods	195
5.4.2	Removing the volcanic signal from the long term measurement records	197
5.5	Discussion	207
5.5.1	Aerosol surface area: Differences between satellite and in situ measurements	210
5.5.2	Estimates of global stratospheric aerosol burden during background conditions	213
5.6	Summary and Conclusions	215

Chapter 6 - Modeling of Stratospheric Aerosols **219**

6.1	Summary	221
6.2	Scope and Rationale	222
6.3	Model Descriptions	223
6.4	Model Illustrations of Aerosol Microphysics	226
6.5	Model Simulations of Nonvolcanic Conditions	232
6.5.1	Description of Calculations	232
6.5.2	Comparisons to Precursor Gas Measurements	234
6.5.3	Calculated Aerosol Budgets and Burdens	236
6.5.4	Comparisons to Satellite Extinction Measurements	239
6.5.5	Comparisons to Derived Satellite Products	245
6.6	Sensitivity Studies and Analyses	250
6.6.1	Sensitivity to model formulation	250
6.6.2	Primary aerosol sensitivity	253
6.6.3	Tropopause SO ₂ sensitivity	254
6.6.4	OCS sensitivity	256
6.7	Model Simulations of Volcanic Conditions	256
6.7.1	Description of Calculations	256
6.7.2	Comparisons with Lidar Backscatter Measurements	257
6.7.3	Comparisons with SAGE II Observations	259
6.7.4	Comparisons with OPC Data	260

6.7.5	Aerosol Decay Rates	261
6.8	Discussion	266
6.8.1	Uncertainties	266
6.8.2	Future Trends of Stratospheric Sulfate Aerosols	268
6.8.3	Conclusions	269

References **273**

Appendices

I	WCRP Reports	305
II	Acronyms and Abbreviations	315
III	Authors, Co-authors, and Contributors	319

Foreword

Assessments of stratospheric ozone have been conducted for nearly two decades and have evolved from describing ozone morphology to estimating ozone trends, and then to attribution of those trends. Stratospheric aerosol has only been integrated in assessments in the context of their effects on ozone chemistry and has not been critically evaluated itself. As a result, the Assessment of Stratospheric Aerosol Properties (ASAP) has been carried out by the WCRP project on Stratospheric Process and their Role in Climate (SPARC). The objective of this report is to present a systematic analysis of the state of knowledge of stratospheric aerosols including their precursors. It includes an examination of precursor concentrations and trends, measurements of stratospheric aerosol properties, trends in those properties, and modeling of aerosol formation, transport, and distribution in both background and volcanic conditions. The scope of this report is extensive; however, some aspects of stratospheric aerosol science have been deliberately excluded. For instance, we have not attempted to include an examination of polar stratospheric clouds (PSCs) or other clouds (such as cirrus clouds) occurring at or above the tropopause except in as much as they influence aerosol observations. Polar stratospheric clouds are the subject of a separate SPARC activity. We have produced a gap-free aerosol data base for use beyond this report. This required some new analysis that has not previously appeared in the technical literature. Similarly, the trend analysis required the development of a new analysis technique that is the subject of an article published in the *Journal of Geophysical Research*. New work is clearly identified in the present report.

ASAP began with a general kick-off meeting in November 2001 at CNES in Paris, France. There were also three chapter lead meetings in Nice, France (April 2003), in Frankfurt, Germany (July 2003) and in Lexington, Massachusetts, USA (January 2004). The final report is the result of concerted effort by scientists world-wide who continue to work toward understanding the measurements and processes controlling stratospheric aerosol. Their work was supported by their host institutions and funding agencies that include the WCRP and the SPARC Office (in Paris and Toronto), as well as Atmospheric and Environmental Research, Inc., NASA, the Universities of Frankfurt and Wyoming, and ETH Zurich. An initial overview of ASAP appeared in the SPARC Newsletter No. 23 in July 2004.

We would like to thank and acknowledge our debt to the authors, contributors and reviewers who have helped in the preparation of this assessment. It seems clear that stratospheric aerosol science remains a fruitful area of research and that a sustained effort to draw together this community is necessary. We greatly appreciate the support and patience of the SPARC Science Steering Group as well as the SPARC Chairpersons during this effort Marie-Lise Chanin, Marvin Geller, Alan O'Neil, and A.R. Ravishankara. We are similarly indebted to the Toronto and Paris SPARC Offices including Norm McFarlane, Diane Pendlebury, Victoria De Luca, and Catherine Michaut. Thank you all!

Larry W. Thomason
NASA Langley Research Center
USA

Thomas Peter
ETH Zurich
Switzerland

Assessment Co-Chairs

Disclaimer

What ASAP is about:

This report is composed of six chapters:

- Chapter 1: Stratospheric Aerosol Processes
- Chapter 2: Precursors Gas Measurements
- Chapter 3: Instruments
- Chapter 4: Stratospheric Aerosol Record and Climatology
- Chapter 5: Stratospheric Aerosol Trends
- Chapter 6: Modeling of Stratospheric Aerosols

These chapters describe the stratospheric aerosol's morphology during background (i.e., volcanically quiescent) and volcanically perturbed periods. The precursor gases and microphysical, chemical, and radiative processes that control the structure of the aerosol layer are discussed in detail. Changes in aerosol over the period of the modern observational record, as determined by remote and in situ instruments, are assessed for trends under background conditions.

What ASAP is *not* about:

Although connections are made in Chapters 1 and 6 to clouds in the tropopause region (such as cirrus or cumulonimbus clouds) or in the wintertime polar regions (polar stratospheric clouds, PSCs) this report does *not* treat the microphysical, chemical or radiative properties of these clouds. Work is currently underway to complete a separate report on PSCs under the auspices of SPARC.

Executive Summary

Key Findings

- **The vast bulk of existing aerosol data does not comprise a complete measurement set and, as a result, many parameters required for scientific or intercomparison purposes are derived indirectly from the base measurements.** This is true for space-based measurements where only bulk extinction is measured but also true in degree for most ground-based and in situ systems. Unlike gas species, aerosol cannot be characterized by a single quantity but has a size distribution and variable composition. The fact that each system measures a different set of parameters greatly complicates almost every stage of measurement comparisons, accentuating the need for aerosol models.
- **Disagreements between the various data sets and models indicate that significant questions remain regarding the ability to characterize stratospheric aerosol during volcanically quiescent periods, particularly in the lower stratosphere.** Space-based and in situ measurements of aerosol parameters tend to be consistent following significant volcanic events like El Chichón and Pinatubo. However, during periods of very low aerosol loading, this consistency breaks down and significant differences exist between systems for key parameters including aerosol surface area density and extinction. Comparisons of models and satellite observations of aerosol extinction are generally fairly good at visible wavelengths above 20-25 km altitude region under non-volcanic conditions, but are less satisfactory for infrared wavelengths. Although integrated aerosol quantities such as surface area density and effective radius can be calculated without approximation from a known size distribution, the satellite and in situ observational bases for size distributions are controlled by a priori assumptions regarding the distribution itself or by having coarse size resolution, respectively. During volcanically quiescent periods, models and observations disagree significantly mainly due to the fraction of the surface area density produced by models residing in particles too small to be measured, especially near nucleation regions. While there are some model short-comings relative to observations, particularly in the lower stratosphere, it seems likely that space-based data sets underestimate, perhaps significantly, aerosol surface area density in the lower stratosphere.
- **The analysis of non-volcanic stratospheric aerosol, although hampered by very limited periods without volcanic influence since systematic measurements began, indicates no long term trend.** Since the beginning of systematic stratospheric aerosol measurements in the early 1970s there have been three periods with little or no volcanic perturbation, although only the period from 1999 onwards can be confidently identified as free of volcanic aerosols. The other periods (late 1970s and late 1980s) are difficult to evaluate, given their brevity and the complex variability observed. In particular the period in the late 1980s seems likely to have not reached a stable non-volcanic level. Trends derived from six long term data sets for the late 1970s to the current period are not significantly different from zero.
- **The dominant stratospheric aerosol precursor gases are OCS and SO₂ and, through SO₂, human-related activities may influence the observed background stratospheric aerosol.** There is general agreement between measured and modeled OCS in the tropical stratosphere. However, there is a significant dearth of SO₂ measurements, and the role of

tropospheric SO₂ in the stratospheric aerosol budget – while significant – remains a matter of some guesswork. In addition, it is not well understood whether decreasing global human-derived SO₂ emissions, or increasing emissions in low latitude developing countries, such as China, dominate the human component of SO₂ transport across the tropical tropopause.

Recommendations

- **The importance of stratospheric aerosol in climate and atmospheric chemistry strongly supports a commitment to continuing both space-based and in situ observations of aerosols into the foreseeable future.** Both types of measurements are necessary because neither approach seems likely to independently produce a robust depiction of global, stratospheric aerosol properties.
- **Observations of SO₂ in the upper troposphere and lower stratosphere and of H₂SO₄ and SO₂ in the middle and upper stratosphere would be extremely valuable to improve our modeling and predictive capabilities of stratospheric aerosol.** Currently, there is a general scarcity of measurements of key sulfur-bearing gases during their transport from the upper troposphere into the upper stratosphere.
- **A more complete understanding of the detailed structure of the underlying aerosol size distribution is required to facilitate improvement in the closure between measurement data sets and confidence in derived properties like surface area density.** This is becoming increasingly important as measurement systems change and robust conversion between data sets is required to maintain data sets amenable to trend analysis. It is also important to improve aerosol size distribution and composition knowledge in the vicinity of the tropical tropopause where such information is crucial input to microphysical models of stratospheric aerosol. In addition, aerosols in the upper troposphere are not composed purely of H₂SO₄/H₂O but include organics (up to 50 % by mass), mineral dust, soot, and other compounds. Organics are also found in stratospheric aerosols in small quantities. Since the role of non-sulfate aerosols in serving as sites for chemical reactions and as condensation nuclei with concomitant effects on the stratospheric aerosol is not well known, measurements focused on these aerosols are desirable.
- **The upper troposphere and lower stratosphere, particularly in the tropics, is a crucial region for understanding stratospheric aerosol and warrants detailed scientific investigation.** Sensitivity studies in this report show that the lower stratospheric aerosol layer is strongly dependent on input from the tropical upper troposphere.
- **Future modeling studies should strive to include important but as yet missing or poorly treated elements, such as upper tropospheric and meteoritic particles, and various relevant chemical and dynamical processes.** The stratospheric aerosol could be quite sensitive to aerosol input through the tropical tropopause, as suggested in the present report. Also, meteoritic material descending into the stratosphere from the mesosphere may be important to the morphology of stratospheric aerosols, particularly in polar air and perhaps globally. Chemically the photolysis of sulfuric acid affecting the upper edge of the aerosol layer especially in the polar regions should be included in the models.

In addition, a more robust 3-D representation of transport and cloud processes is required to reproduce aerosol observations in the troposphere-stratosphere transition region, as well as to face the challenge of reproducing the seasonal variability of aerosols.

Important Findings per Chapter

Chapter 1: Stratospheric Aerosol Processes

- **The past two decades with enhanced observational capabilities have led to a generally high level of understanding of microscale and synoptic scale aerosol processes, which determine the lifecycle of the stratospheric aerosol.** Most microphysical processes, such as nucleation, coagulation, condensational growth and evaporation, and sedimentation, are thought to be well understood. Of these processes, nucleation still is least understood, and this limits our description of non-volcanic aerosol formation through binary homogeneous nucleation of sulfuric acid and water in rising air masses close to the tropical tropopause. However, these uncertainties are unlikely to be of importance for global stratospheric aerosol. On the synoptic scale, transport and transformation of aerosol within the Brewer-Dobson circulation, and removal of aerosol in air traversing the extra-tropical tropopause are thought to be well understood. A fundamental weakness is the poor understanding of mesoscale processes, such as deep convection, which transport precursor gas and aerosol into the stratosphere through the tropical tropopause.
- **Aerosol in the tropical regions is rapidly transported zonally with mean stratospheric winds, while transport is restricted meridionally by the transport barrier of the tropical pipe in the 15-30° latitude range.** This reduced transport is most effective at altitudes between about 21 and 30 km; poleward transport at lower altitudes is more rapid. After a volcanic eruption the transport barrier of the “leaky tropical pipe” leads to build-up of a tropical reservoir of aerosol mass, an observation which has led to a general improvement of our understanding of stratospheric dynamics.
- **Aerosol in air masses transported into the mid and high latitudes continues to evolve through microphysical processes.** These processes include evaporation at the upper edge of the aerosol layer and nucleation/re-condensation during descent, as well as condensation and coagulation. Air which descends diabatically to the lowermost stratosphere can be removed from the stratosphere through quasi-isentropic transport of the air in tropopause folds. This is the dominant removal mechanism for stratospheric aerosol. Additional removal occurs over the poles when the sulfuric acid particles serve as sites for polar stratospheric cloud (PSC) particle formation.
- **Sedimentation is an important aspect of the aerosol lifecycle.** Throughout the lifetime of the aerosol, gravitational settling adds substantially to the altitude distribution and removal of the particles despite their small size. Due to the long lifetime of the particles, their sedimentation velocities (~ 100 m/month for particles with $0.1 \mu\text{m}$ radius and strongly growing for larger ones) cannot be neglected.
- **The contribution of primary tropospheric particles and material of extraterrestrial origin remains very uncertain.** Observations in the lower stratosphere suggest that me-

teoritic material is present in a significant fraction of stratospheric particles. Observations at and just above the tropopause also show the presence of a peak in the aerosol mass distribution that may indicate the presence of tropospheric particles in the lower stratosphere. The effect of insoluble extraterrestrial and tropospheric particles on hydrate and ice formation needs to be determined.

Chapter 2: Precursor Gas Measurements

- **SO₂ and OCS are the dominant source gases of background stratospheric sulfate aerosol based on lifetime, abundance, and flux.** Overall, the contribution of OCS is well known, however, the contribution of SO₂ remains uncertain. By emission rate into the troposphere, the key gases in the sulfur budget are, in order, SO₂, OCS, CS₂, DMS, H₂S, CH₃SH. However, due to differences in their lifetime, their rank by flux into the tropical tropopause layer (TTL) is OCS, SO₂, CS₂ and DMS.
- **The TTL is the main entry region of the tropospheric source gases into the stratosphere.** The estimate for the sulfur mass flux reaching the TTL is 1.5×10^{11} kg/s. In contrast, tropopause folds and quasi-adiabatic transport between the upper troposphere and the subtropical stratosphere associated with monsoon circulations, synoptic systems and planetary wave breaking do not affect the stratospheric composition above 100 hPa.
- **The flux of sulfur through the TTL is not well known due to uncertainty in the transport from the surface to the TTL.** In addition, the changing pattern of anthropogenic SO₂ emissions (decreasing in the US and Europe, increasing in many parts of Asia) makes the trend in TTL sulfur uncertain. Aircraft emissions do not play a significant role. Emissions from major volcanic eruptions can effect the SO₂ concentrations for up to a few months.
- **There is now a consistent picture of the seasonal and latitudinal variability of OCS in surface air and its relation to major terrestrial and marine sources and sinks.** Measurements over land show minimum OCS mixing ratios during the summer due to the uptake by land vegetation. The data suggest a strong, land-based, seasonally-varying uptake of OCS, the effect of which propagates to high altitudes and away from mid-latitudes with some time delay. The measured seasonal variabilities are between 3 and 30%, depending on the location, with higher variability in the northern hemisphere.
- **The pre-industrial OCS concentrations were about 330-370 pptv in the 17th century, roughly 30-40% lower than today's values.** The atmospheric OCS total column and surface air mixing ratios have been decreasing by 0.5-1 % / yr over recent decades.
- **Meteoritic material contributes a significant fraction to the total stratospheric aerosol mass.** Recent investigations suggest that the flux of meteoritic material amounts to between 44 and 260 tons/day with an uncertainty as large as a factor of six. These mass fluxes compare to about 820 tons/day for the overall net mass flux from the troposphere to the stratosphere of all material that is eventually transformed into aerosols during volcanically quiescent times.

- **Meteors, cosmic radiation, and rocket exhaust make a small contribution to the sulfur budget in the lower stratosphere.** In terms of the element sulfur, the extraterrestrial input represents 0.2 to 2.9% of the terrestrial input to the lower stratosphere. This sulfur flux is insignificant in the lower stratosphere; however, it may dominate in the upper stratosphere, above the stratospheric aerosol layer where most of the sulfur of terrestrial origin resides.
- **The consistency between the mass burden of stratospheric sulfate aerosol, its lifetime, transport and oxidation of precursors into the aerosol reservoir, and removal of aerosol needs to be better established.** At present, the best estimate is that only 9 % of the OCS transported into the stratosphere is photolyzed, and that the remaining source of sulfur, of similar magnitude, required to explain the aerosol layer stems from SO₂ transported by deep convection into the stratosphere. These numbers remain uncertain, in particular the mesoscale transport path of SO₂ across the tropopause.

Chapter 3: Instruments

- **Various techniques have been established for investigations of the stratospheric aerosol layer.** These include solar occultation, limb emission, lidar, in situ optical particle counters, each having its own strengths and weaknesses, so that only a mix of these techniques will ensure the future monitoring and detection of global stratospheric change.
- **Information on stratospheric aerosols is derived from a number of remote and in situ instruments, some with global coverage (satellite instruments) and some which make only localized observations (lidars, particle counters). Long term data records from the SAGE satellite series, four long term lidar records, and balloon-borne in situ measurements at Laramie provide for the characterization of the stratospheric aerosol layer over decadal time scales.** The instruments may be categorized as
 - global long term measurements (e.g. SAGE, HALOE, POAM);
 - global short term measurements (e.g. CLAES, ORA);
 - local long term measurements (e.g. lidars, balloon-borne particle counters);
 - local short term measurements (e.g. airborne lidars and particle counters).
- **Various primary aerosol properties are now available with very low uncertainties.** These primary aerosol properties are
 - aerosol extinction from the solar occultation satellite instruments;
 - backscatter coefficients from the lidar systems;
 - cumulative size distributions from the particle counters.
- **Aerosol information obtained from the various instruments may differ significantly due to the differences in the applied measurement techniques, in particular when secondary (derived) aerosol properties are concerned.** For example, surface area densities derived from remote and in situ measurements may differ considerably, though both pieces of information need not be contradictory. Furthermore, occultation measurements give averaged information over a relatively large region while in situ instruments yield highly localized information.

Chapter 4: Stratospheric Aerosol Record and Climatology

- **Time series of aerosol extinction coefficients have been archived from various instruments, in particular cloud-free SAM, SAGE, HALOE and POAM data (when available) for 1971-2002.** Both tropospheric and polar stratospheric clouds have been removed. These data sets are available online.
- **Comparisons between SAGE/HALOE/OPC, SAGE/POAM, SAGE/ORA, SAGE/lidar generally show good agreement.** To carry out such comparisons, modeling has been necessary since the primary products differ for the various instruments, so that direct comparisons are not generally possible. For example, comparison of SAGE extinction coefficients at visible and near infrared wavelengths and HALOE extinctions in the infrared requires assumptions on size distributions and particle composition. Comparisons between SAGE and the number densities obtained with the optical particle counters require an evaluation of the extinctions based on assumptions of the aerosol properties, especially index of refraction.
- **Derived products from SAGE, HALOE, OPC and Lidar, such as the effective radius, surface area density, volume density, and size distributions agree quite well during periods of heavy aerosol loading, but significant differences arise during “background” aerosol periods.** In general these comparisons rely on a small number of coincident measurements. Discrepancies between surface area densities made by the various measuring techniques are a consequence of various assumptions made in the comparisons, such as filling of particle size gaps or indices of refraction, but may also result from differences in the volume of air sampled.
- **A SAGE data set without gaps due to optically dense conditions or due to instrument failure or absence has been generated, which will be most beneficial for future modeling work.** Gaps within the SAGE data exist during the period between SAGE and SAGE II and shortly after the Pinatubo eruption (due to “saturation” effects). These have been filled by using data from other instruments, including SAM II and lidar systems, and a nearly continuous global dataset has been generated.
- **The presentation of the SAGE II extinctions in an equivalent latitude/potential temperature coordinate system reduces the dynamically induced short term atmospheric variability.** This provides a more physically based way of presenting the data, resulting in a smoother aerosol distribution.

Chapter 5: Stratospheric Aerosol Trends

- **Based on two different analyses of six long term data sets we conclude that background (non-volcanic) stratospheric aerosol has not significantly changed over the past thirty years.** The analyses are based on: four lidar records of integrated backscatter (São José dos Campos, Brazil, 23°S; Mauna Loa, Hawaii, USA, 20°N; Hampton, Virginia, USA, 37°N; Garmisch-Partenkirchen, Germany, 48°N); in situ concentrations for radii >0.15 and

>0.25 μm (Laramie, Wyoming, USA, 41°N), and on SAGE II altitude latitude dependent optical depths at 1020 nm.

- **The stratospheric aerosol measurements which can be reliably used to assess trends in the non-volcanic component of stratospheric aerosol began in the early 1970s.** Earlier assessments of trends in non-volcanic stratospheric aerosol included Junge's initial stratospheric aerosol measurements, 1959 - 1960. Based on the stability of measurements following the decay of Pinatubo volcanic aerosol, we conclude that there is not significant confidence in the size range or number concentration of Junge's initial in situ measurements to reliably compare them with the in situ record begun in 1971 and continued to the present.
- **The period following the decay of aerosol from the eruption of Pinatubo provides our best opportunity to observe a stratosphere unperturbed by volcanic activity since long-term stratospheric aerosol measurements began.** There have been fewer small volcanic eruptions following Pinatubo than during the two previous volcanically quiescent periods. The pre-Pinatubo period was elevated compared to the present and pre-El Chichón periods. Stratospheric aerosol loading is not expected to fall significantly below current levels, although longer-term variations cannot be ruled out.
- **Volcanic aerosol from Pinatubo disappeared from the long-term measurement records between 4.5 and 7.5 years following the eruption, dependent on latitude and measurement platform.** The earliest returns to background aerosol levels were observed by lidar at Mauna Loa (19°N), while volcanic aerosol may still be present in late 1998 in SAGE II extinction measurements between 18 and 23 km.
- **A comparison of measurements during the three volcanically quiescent periods in the long term records is controlled by measurements prior to the eruption of El Chichón and after the eruption of Pinatubo, and indicates no long term trend.** Only the one in situ and four lidar records capture the three volcanically quiescent periods, pre El Chichón, pre Pinatubo, and post Pinatubo. Investigations of these records suggest that the first two periods may not have reached background, particularly prior to Pinatubo. Problems with a simple linear regression of the data arise because of the high degree of autocorrelation, and problems with time series regression occur because of irregular time intervals and nonlinearities. The subset of measurements which suggest changes in background aerosol without accounting for autocorrelation, do not suggest any trend when autocorrelation is included. Although estimates of growth/decay rates change little when incorporating autocorrelations, standard errors typically about triple. Four of the six data sets analyzed (2 in situ aerosol sizes and 4 lidar records) suggest no long term trend in background aerosol. Mauna Loa and Laramie 0.25 μm measurements indicate a trend on the order of $-1.0\% \text{ yr}^{-1}$, but with uncertainties which include zero.
- **An empirical model to remove the volcanic signal from the local thirty-year in situ and remote stratospheric aerosol records, and the global twenty-year satellite record also indicates no trend in background aerosol.** The model was applied to the 4 lidar data sets, 2 in situ data sets (two aerosol sizes) and 33 SAGE II data sets (optical depths at 1.02 μm at three altitude and eleven latitude intervals). These analyses (excepting SAGE II) allowed for first order autocorrelation and used a one-dimensional spatial representation to account for the temporally disparate sampling intervals. For 31 of the 33

SAGE II data sets, 3 of 4 lidar records, and the in situ measurements at 0.15 μm , the analyses suggest no long term trend in stratospheric aerosol. For one lidar site (Hampton) and the 0.25 μm in situ measurements the results suggest a negative trend, on the order of $-2\% \text{ yr}^{-1}$. Both these estimates suffer from difficulties introduced by the eruption of Mt. St. Helens, and a comparison of the model with the data suggests problems in representing properly the measurements prior to El Chichón. In contrast to these two estimates of a negative trend, two SAGE II data sets (30-35 km, 30° and 40°N) suggest a positive trend of the same magnitude, $2\% \text{ yr}^{-1}$.

- **The statistical analyses were completed on altitude/latitude integrals of the measurements, precluding establishing, or ruling out, long term changes in microphysical properties of background stratospheric aerosol.** The focus on integral properties, an inherent limitation of this investigation, is dictated by the fact that all but the in situ instruments make measurements on ensembles of particles and thus inherently integrate over the size distribution. Thus the in situ record was also integrated to provide a relatively homogenous data set for comparison with the other long term records. Some information concerning the long term tendency of aerosol size distributions is available by comparing altitude integrals of the two sizes measured, $r > 0.15$ and 0.25 μm . Some differences were observed, but were not statistically significant.

Chapter 6: Modeling of Stratospheric Aerosols

- **Models provide a way to synthesize our knowledge of stratospheric aerosol processes and quantitatively test our understanding against observations.** However, model uncertainties, especially transport rates, limit our confidence.
- **Sedimentation is a crucial process determining the vertical distribution of aerosol mass and sulfur in the stratosphere.** Sedimentation is a strong function of altitude as well as particle size, and reduces sulfur in the upper model stratospheres by over 75 %.
- **Nucleation of new particles is important near the tropopause, particularly in the tropics, and at polar latitudes in the middle stratosphere in winter.** Particle size is determined by nucleation, and subsequently by coagulation, condensation and evaporation, as well as transport and mixing.
- **OCS, SO₂, and particles transported across the tropopause are the primary precursors to stratospheric aerosol.** Analysis of sulfur budgets in the models shows that transport of SO₂ and particles, for which SO₂ is the precursor, across the tropical tropopause are potentially large contributors to the stratospheric aerosol burden. Large uncertainties remain in our ability to quantify the relative contributions, but the models show OCS to be the main contributor above 25 km and SO₂ and particles to play a larger role below.
- **OCS mixing ratios in the tropics are well represented by the models.** However, the models do not all match observations of OCS in mid and high latitudes, reflecting the variability of transport between models. Since this gas represents the main sulfur source in the mid-stratosphere, confidence in the rate of OCS oxidation and aerosol formation in the tropics is gained.

- **SO₂ mixing ratios in the tropics show large variability between models.** Model differences are probably due to the short lifetime of SO₂ in the tropics along with differences in the OH concentrations and transport differences.
- **More SO₂ measurements would be valuable.** Better knowledge of SO₂ concentrations in the upper troposphere would be required to obtain a correct description of the transport of sulfur into the stratosphere. Knowing SO₂ in the lower-mid stratosphere helps verify the OCS chemical destruction rate and the SO₂ to H₂SO₄ conversion rate, along with transport rates. Above 35 km, observations show an increase in SO₂ which can only be reproduced by models that include a photolytic conversion of gaseous H₂SO₄ into SO₂.
- **Comparisons between models and satellite observations of aerosol extinction are generally fairly good at visible wavelengths but are less satisfactory for infrared wavelengths.** Aerosol extinction measurements from SAGE II at 525 and 1020 nm are matched by models above 20-25 km altitude under non-volcanic conditions. Tropical observations show a sharp vertical gradient in extinction at 17-20 km which varies with season and is not reproduced by the models. Models are also less successful at reproducing extinction observations from the HALOE instrument at 3.46 and 5.26 μm.
- **Models predict aerosol size distributions which can be approximated by a lognormal function except near regions of nucleation or evaporation.** Integrated aerosol quantities such as surface area density and effective radius can in principle be calculated without approximation from model size distributions, whereas satellite observations and in situ measurements by optical particle counters used to derive these quantities are either controlled by a priori assumptions regarding the size distribution or have coarse resolution at the small size bins. Comparisons of these quantities during volcanically quiescent periods are problematic because much of the aerosol density may reside in particles too small to be observed, especially near nucleation regions.
- **Simulations of the Mt. Pinatubo period are generally good but dependent on the assumed initial vertical distribution of volcanic sulfur.** For instance, model results show very good agreement with column integrated lidar backscatter at both tropical and mid latitude sites, including the magnitude and timing of the aerosol maximum and the rate of decay. Comparisons with SAGE II extinctions show that models may under- or over predict extinction at different altitudes, depending on the applied model, and the assumed vertical distribution of volcanic sulfur at the beginning of the event.
- **The modeled rate of recovery from the Pinatubo eruption depends on the quantity considered (extinction, number density, surface area density) and the latitude and altitude of interest.** Recovery time constants (e-folding times) show decay rates lengthening with time past the eruption, in agreement with observations. Different models exhibit different recovery time constants, but with a scatter not larger than that of the observations.

ASAP Data Archive

Data sets that comprise the basis for the data analysis are archived at the SPARC Data Center (<http://www.sparc.sunysb.edu/>) including altitude/latitude gridded fields of aerosol extinction and derived quantities for the SAGE time series. Data sets used in the trend analysis are either available at this location, or links provided to the Network for the Detection of Stratospheric Change (<http://www.ndsc.ws/>) and other data sources. In addition, links to other sources of aerosol data that appear within this report are included. The SAGE data sets are also available remapped to equivalent latitude and potential temperature.

A final product that is made available is a ‘gap-filled’ data set for the period 1979 through 2004 based on the SAGE record. Gaps exist between the June 1991 eruption of Mount Pinatubo and the end of 1993 due to instrument saturation and between November 1981 and October 1984, when global space-based aerosol extinction measurements were not available. To fill the missing values, we have used aerosol backscatter profile measurements from sites at Camaguey (Cuba), Mauna Loa, Hawaii (USA), and Hampton, Virginia (USA) and backscatter sonde measurements from Lauder, New Zealand. This period encompasses the El Chichón eruption and the onset of the Antarctic ozone hole and is, therefore, of particular interest. Beginning in April 1982 and through the beginning of SAGE II observations in 1984, we have used a composite of data consisting of SAM II, the NASA Langley 48-inch lidar system, and lidar data from the NASA Langley Airborne Lidar System. Data from this latter data set has only been partially recovered for the 1982 to 1984 period. If more lidar data from past aircraft missions or a revised Solar Mesospheric Explorer (1981-1986) aerosol product become available, additional work on the El Chichón period would be profitable.

List of Reviewers

The editors express their gratitude to the following colleagues who reviewed one or two of the report chapters or served as overall reviewers for the entire report:

Tim Bates
NOAA/Pacific Marine Environmental Lab
Seattle, WA, USA

Steve Massie
NCAR/Atmospheric Chemistry Division
Boulder, CO, USA

Chuck Brock
NOAA Aeronomy Laboratory
Boulder, CO, USA

Roland Neuber
Alfred-Wegener-Institut
Potsdam, Germany

David Considine
NASA Langley Research Center
Hampton, VA, USA

Irina Petropavlovskikh
NOAA/SRRB
Boulder, USA

Derek Cunnold
Georgia Institute of Technology
Atlanta, GA, USA

Andreas Petzold
Dt. Zentrum für Luft- und Raumfahrt,
DLR, Oberpfaffenhofen, Germany

Katja Drdla
NASA Ames Research Center
Moffett Field, CA, USA

Lamont Poole
NASA Langley Research Center
Hampton, VA, USA

Dave Fahey
NOAA Earth System Research Laboratory
Boulder, CO, USA

Bob Portmann
NOAA Earth System Research Laboratory
Boulder, CO, USA

Hans Graf
University of Cambridge
Cambridge, UK

Cora Randall
University of Colorado
Boulder, CO, USA

Matt Hitchman
University of Wisconsin
Madison, WI, USA

Bill Randel
NCAR/Atmospheric Chemistry Division
Boulder, CO, USA

Jens Hjorth
The EC Joint Research Centre
Ispra (VA), Italy

Donald Thornton
Drexel University
Philadelphia, PA, USA

Ben Liley
Natl.Inst.of Water & Atmos. Res.(NIWA)
Lauder, Central Otago, New Zealand

Rich Turco
University of California, Los Angeles
Los Angeles, CA, USA

Rob MacKenzie
Lancaster University
Lancaster, UK

Rudy Zander
University of Liege
Liege, Belgium

CHAPTER 1

Stratospheric Aerosol Processes

Lead Authors:

Kenneth S. Carslaw

Bernd Kärcher

1.1 The Importance of Stratospheric Aerosol

Stratospheric aerosol is important for a number of processes that affect the chemical and radiation balance of the atmosphere [McCormick et al., 1995; Solomon, 1999]. During periods of high volcanic aerosol load there is evidence for heterogeneous chemistry on the sulfate aerosol reducing ozone [Angell et al., 1985; Hofmann and Solomon, 1989; Jäger and Wege, 1990; Gleason et al., 1993; Deshler et al., 1996], for stratospheric warming [Labitzke and McCormick, 1992; Angell, 1993; Russell et al., 1993], and for tropospheric cooling [Manabe and Wetherald, 1967; Pollack et al., 1976; Dutton and Christy, 1992; Hansen et al., 1992]. Stratospheric aerosol plays a role in the budget of several trace gases, in particular NO_x . These chemical effects are enhanced when the aerosol surface area is increased after volcanic eruptions: for example, NO_2 columns were reduced after both El Chichón and Pinatubo [Johnston and McKenzie, 1989; Johnston et al., 1992] from the hydrolysis of N_2O_5 [Rowland et al., 1986; Tolbert et al., 1988; Mozurkewicz and Calvert, 1988]. At low aerosol loading NO_x increases and induces ozone loss from the nitrogen catalytic cycle [Crutzen, 1970]. Fahey et al. [1993] provided direct measurements of the anticorrelation of aerosol surface area and the NO_x/NO_y ratio. The hydrolysis of N_2O_5 saturates as aerosol surface area increases above $5\text{-}10 \mu\text{m}^2 \text{cm}^{-3}$, thus the role aerosol plays in controlling NO_x is primarily important during periods of low aerosol loading [Prather, 1992]. Changes in NO_x also affect the abundance of ClO_x and HO_x , both of which also react with ozone [Wennberg et al., 1994; Solomon et al., 1996]. The importance of aerosol in stratospheric chemistry first became apparent with the suggestion of its role in polar ozone loss [Solomon et al., 1986]. Long term stratospheric aerosol measurements had their beginnings about fifteen years prior to this realization.

During volcanically quiescent periods, when the stratospheric aerosol is in a "background" state unperturbed by volcanism, radiative effects of the aerosol are negligible. However, following a major eruption the increased aerosol loading can have a transient but significant radiative impact [McCormick et al., 1995]. Radiative heating can lead to significant warming of the middle stratosphere [Labitzke and McCormick, 1992]. It also increases the albedo of the Earth [Brogniez et al., 1999; Stenchikov et al., 1998], leading to changes in surface temperature, although changes are not evenly distributed [e.g., Hansen et al., 2002].

Volcanic aerosols may also have indirect effects on the troposphere. For example, aerosol transported into the upper troposphere may affect the microphysical structure of deep convective clouds [Minnis et al., 1993].

The distribution of stratospheric aerosol can also be used to understand the circulation of the stratosphere. Examples include the meridional circulation changes associated with the Quasi-Biennial Oscillation [Treppe and Hitchman, 1992] and seasonal changes in the Brewer-Dobson circulation [Hitchman et al., 1994]. In addition, observed interleaving of high and low aerosol loadings in subtropical jets implies extensive two-way stratosphere-troposphere exchange of aerosol [Wilson et al., 1992]. These and other examples of using stratospheric aerosol to understand stratospheric circulation are reviewed in Hitchman et al. [1994].

1.2 The Life Cycle of Stratospheric Aerosol

The life cycle of stratospheric aerosol (Figure 1.1) involves processes of gaseous precursor species and aerosol particles entering the stratosphere through the tropical tropopause, the transport and transformation of the aerosol within the Brewer-Dobson circulation, and the removal of aerosol in air traversing the extra-tropical tropopause and through gravitational sedimentation.

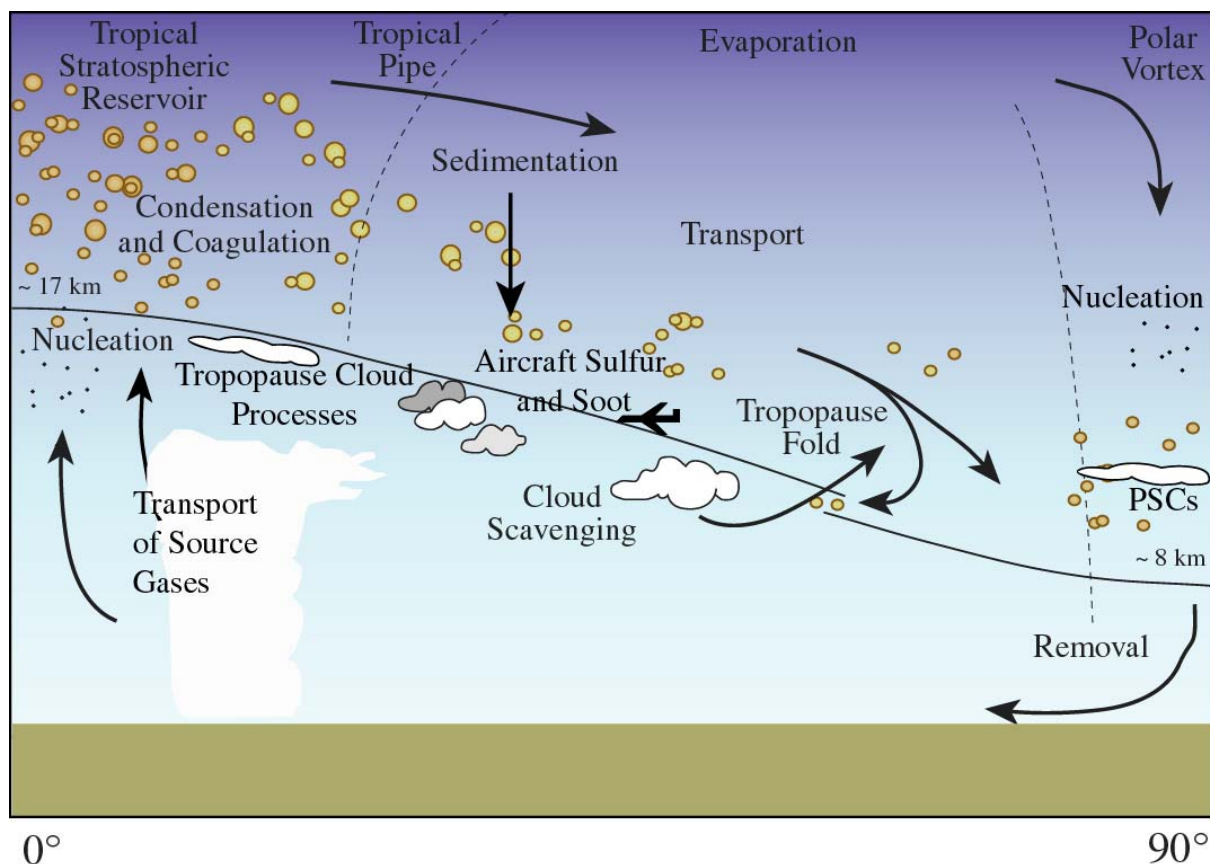


Figure 1.1. Schematic of the stratospheric aerosol life cycle [from Hamill et al., 1997].

Non-volcanic stratospheric aerosol particles are formed primarily through binary homogeneous nucleation of sulfuric acid and water in rising air masses close to the tropical tropopause [Goodman et al., 1982; Yue and Deepak, 1984; Brock et al., 1995]. These particles grow by condensation of H_2SO_4 and water vapor and undergo coagulation, both with other newly formed particles and with larger aged particles mixed into the same atmospheric region. The aerosol in the tropical regions is rapidly transported zonally with the mean stratospheric winds, while the transport meridionally is determined by large-scale stirring and mixing, with an air mass boundary existing in the 15-30° latitude range [Plumb, 1996]. The existence of such a “leaky tropical pipe” reduces the rate of dilution of tropical aerosol mass into the extra-tropics [Trepte and Hitchman, 1992]. Poleward transport of aerosol becomes effective during the westerly phase of the quasi-biennial oscillation but is restricted during the easterly phase.

Aerosol transported into the mid and high latitudes evolves in several ways. Firstly, particle growth by condensation of H_2SO_4 continues as OCS and SO_2 are oxidised. The particle size distribution evolves through processes of growth, coagulation and sedimentation (see Section

1.4). In addition, the aerosol descends diabatically to the mid-latitude lowermost stratosphere where it can eventually be removed in the troposphere through quasi-isentropic transport of the air in tropopause folds. Such transport in air moving into the troposphere is the dominant removal mechanisms for stratospheric aerosol, although the aerosol mass towards the top of the aerosol layer is around 50% lower than at the bottom of the layer because of vertical redistribution of the particles by gravitational sedimentation. Particles transported into the polar vortex are also removed in diabatically descending air during winter and spring. Additional removal occurs over the poles when the sulfuric acid particles serve as sites for polar stratospheric cloud (PSC) particle formation. Some PSC particles composed of nitric acid hydrate or ice can grow to several microns in diameter and sediment rapidly to the tropopause, taking included sulfuric acid particles with them. Similar removal processes occur within cirrus clouds forming at tropopause altitudes.

The large-scale poleward transport and isentropic mixing of aerosol, coupled with the processes of particle condensational growth, coagulation and sedimentation leads to the generation of a quasi-steady aerosol layer (Junge layer). At the bottom of the layer, particles are removed at the tropopause. The top of the layer (typically >35 km altitude) is set by the thermodynamic stability of the sulfuric acid particles. Higher temperatures and lower partial pressures of H_2SO_4 and H_2O at high altitudes are such that the acidic particles evaporate completely. The model calculations in Chapter 6 show that the total sulfur above the aerosol layer ($= \text{SO}_2 + \text{OCS} + \text{H}_2\text{SO}_4$) is very strongly controlled by the sedimentation of particulate sulfur throughout the aerosol layer, being approximately one-third of the total abundance that would result if sedimentation were not effective.

Global 2-D and 3-D models have been developed that couple the gas phase chemistry of sulfur species with the large-scale dynamical transport and aerosol microphysics (see Chapter 6). These models have been quite successful in reproducing observed particle surface area densities, mass loadings and size distributions. The models are also useful in diagnosing the relative contribution of the different source gases to the eventual aerosol loading.

1.3 Sources of Sulfur Gases and Aerosol to the Stratosphere

Sulfur gases enter the stratosphere along with freshly nucleated aerosol primarily at the tropical tropopause. The global distribution of the gases OCS, SO_2 , and H_2SO_4 is then determined by the large-scale circulation, gas-phase chemical reactions, and eventual removal of H_2SO_4 by condensation on to the aerosol.

The non-volcanic “background” stratospheric aerosol loading (see the Introduction) is a critical quantity because, in comparison with models that simulate the aerosol loading, it provides a baseline quantification of the non-volcanic sulfur flux from the troposphere to the stratosphere (see Chapter 2).

The accurate quantification of gas concentrations at the tropopause, where air enters the stratosphere, requires precise knowledge of geographical distributions of sources, emission strengths of individual sources, and non-chemical sinks (e.g., uptake of OCS on vegetation in the NH introducing a seasonal signature in net OCS input to the free troposphere, see Chapter 2). The total sulfur emission at the Earth’s surface lies between 89 and 102 Tg/year, with SO_2 emissions during the industrial period dominating this source. Although OCS emissions make up only a small fraction of the total sulfur emitted, the long atmospheric lifetime of OCS means that it is a significant source of sulfur to the stratosphere (Chapter 2).

Even when tropospheric source strengths of sulfur gases are known, there remains the difficulty of quantifying gas concentrations at the tropical tropopause. A particular problem in models has been to estimate the input of SO₂ to the stratosphere because of its complex chemistry and interaction with clouds as it is transported to the tropical tropopause. Deep extratropical thunderstorms may also transport gases directly and irreversibly into the lowermost stratosphere, aided by breaking gravity waves at cloud top [Wang, 2004]. Pitari et al. (personal communication, 2002) have estimated that 70% of stratospheric sulfuric acid is derived from tropospheric SO₂ and 30% from OCS and Pitari et al. [2002] have shown that tropospheric convective transport of SO₂ to the tropical upper troposphere is required in order to generate stratospheric aerosol loadings that agree with those derived from SAGE II observations. However, as this assessment shows, there remains considerable uncertainty in these numbers and much inter-model variability in SO₂ concentrations in the tropics (Chapters 2 and 6). At present, the lack of SO₂ observations during volcanically quiescent periods makes it difficult to improve these uncertainties. A particularly uncertain process in model is the efficiency with which SO₂ is removed by precipitation in the cloud column.

It is important to note that SO₂ input to the stratosphere has an immediate impact on the aerosol properties near the tropical source region, as it becomes quickly oxidized to condensable sulfuric acid. In contrast, the comparatively slow chemical conversion of OCS into sulfuric acid means that it has widespread impact on the global stratosphere. Thus, uncertainties in quantifying the net stratospheric input of OCS will directly affect a large fraction of the aerosol mass in the middle and upper stratosphere globally, while uncertainties in SO₂ input tend to influence lower stratospheric aerosol properties, where the bulk of the aerosol mass resides. As SO₂ derived from combustion sources has a different isotopic mass than SO₂ derived from oxidation of OCS, isotopic fractionation of sulfur species in aerosol particles could in principle be used to determine the origin of particulate sulfur.

Another difficulty in quantifying the background stratospheric aerosol loading is the poor quantification of the particles entering through the tropical tropopause. Particle concentrations in the tropical UT are poorly quantified from measurements and difficult to estimate from models. Only recently, in situ measurements of particle size distributions in the accumulation mode size range have become available in this region (see Chapter 6). In Chapter 6 the sensitivity of stratospheric aerosol to the assumed tropospheric source of particles is investigated. Overall, the model simulations conducted as part of this assessment suggest that OCS dominates as a source of sulfuric acid above about 25 km, with SO₂ becoming significant at lower altitudes. Sulfate particles transported from the upper troposphere is also a significant source below 25 km.

1.4 Stratospheric Aerosol Microphysics and the Particle Size Distribution

1.4.1 Global Aerosol

The microphysical processes of nucleation, condensational growth, coagulation, sedimentation and evaporation determine the particle number concentration and size distribution. Figure 1.2 shows size distributions from in situ optical particle counter measurements at 21 km altitude above Laramie, Wyoming during non-volcanic and volcanic conditions. The observations have been fit to a bimodal lognormal distribution. A single mode lognormal distribution has the form

$$\frac{dN(r)}{dr} = N_0 \frac{\exp\left(-\frac{1}{2} \left[\frac{\ln^2(r/r_m)}{\ln^2 \sigma} \right] \right)}{r \ln \sigma (2\pi)^{1/2}},$$

where N is the number concentration, N_0 is the total particle concentration in the mode, r is radius, r_m is the median radius, and σ is the width of the distribution. Lognormal distributions have been used to fit the stratospheric aerosol sizes for some time [Jäger and Hofmann, 1991; Hofmann and Deshler, 1991], although other distributions have been tested [Rosen and Hofmann, 1986]. Lognormal distributions are commonly used because they typically fit the data very well. In addition, in a simple evolving aerosol there are physical reasons to expect a lognormal-like particle size distribution to develop, although the processes that shape the natural distribution in the stratosphere include also mixing of young and aged aerosol and gravitational settling, so lognormal distributions are likely to be only an approximation in most cases. Typical parameters of the distribution under volcanically quiescent periods are $N_0 = 5\text{-}10 \text{ cm}^{-3}$, $r_m = 0.07 \text{ }\mu\text{m}$ and $\sigma = 1.6\text{-}1.8$.

The observations in Figure 1.2 show that the background particle number and volume distribution is clearly bimodal during both volcanic and non-volcanic conditions, with one mode at typically $<0.1 \text{ }\mu\text{m}$ radius and a larger mode at $\sim 0.3\text{-}0.4 \text{ }\mu\text{m}$. The larger mode tends to be more pronounced in aerosol perturbed by the Pinatubo eruption. The particle number and surface area are dominated by the small mode, while the larger mode may contribute significantly to the total particle mass in some regions. Bauman et al. [2000; 2003] discuss the importance of bimodality for the retrieval of particle properties from satellite extinction measurements under background and volcanically perturbed conditions.

Figure 1.3 shows how the size distribution changes with altitude during volcanic and non-volcanic conditions. The number concentration in the small mode remains constant at between $5\text{-}10 \text{ cm}^{-3}$ up to altitudes of $30\text{-}35 \text{ km}$ during volcanic and non-volcanic conditions. In contrast, the number of particles in the larger mode falls sharply in the vertical during non-volcanic conditions, from around 0.1 cm^{-3} at $19\text{-}20 \text{ km}$ altitude to 0.01 cm^{-3} above 25 km . The fraction of observed distributions with a detectable large mode also falls with altitude; almost all distributions are observed to be bimodal below 25 km but the fraction falls to zero at 35 km . The most obvious change in the vertical aerosol profile during volcanic conditions is the number of particles in the larger mode – typically around 1 cm^{-3} in the lower stratosphere, which is a factor 10 greater than during non-volcanic conditions. In contrast, the size of the particles in the large mode remains approximately constant at $\sim 0.3\text{-}0.5 \text{ }\mu\text{m}$ radius.

Global stratospheric aerosol microphysics models do not capture the observed bimodality above $0.1 \text{ }\mu\text{m}$ radius (Chapter 6). Typical model size distributions have a mode at about $0.01 \text{ }\mu\text{m}$ and a second mode at $0.1 \text{ }\mu\text{m}$. The small model mode is too small to be measured by optical particle counters, while the larger model mode agrees well with that observed. The observed large particle mode at $0.3\text{-}0.4 \text{ }\mu\text{m}$ may be related to sources of primary particles at the tropopause. The observed decrease in the occurrence frequency and number of particles in this mode is consistent with such a tropospheric source. The observed large particle mode could also be generated from aerosol recycled within the stratosphere via the Brewer-Dobson circulation followed by transport back into the tropical updraft, but the importance of this pathway relative to a tropospheric source is difficult to assess. It is possible that such particles could

act as heterogeneous ice nuclei forming ice at low supersaturations and perhaps affect ozone chemistry [Meilinger et al., 2001].

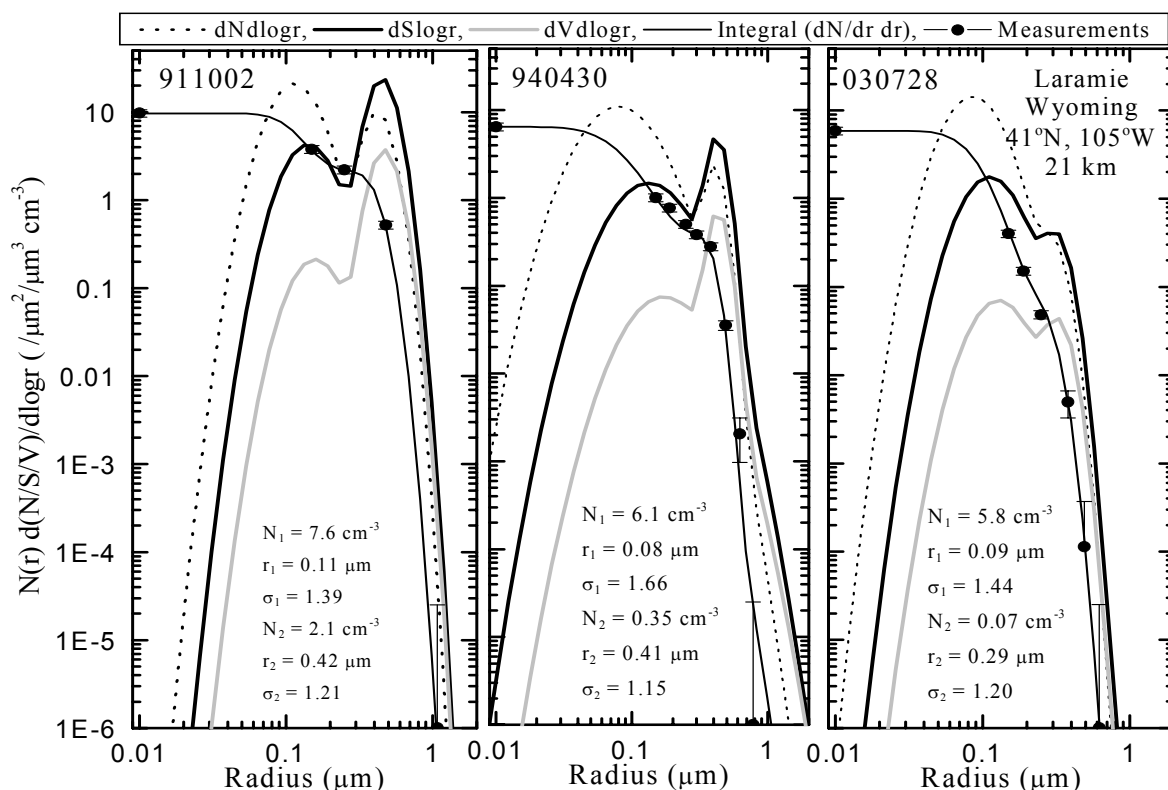


Figure 1.2. Differential number (cm^{-3}), surface area ($\mu\text{m}^2 \text{cm}^{-3}$), and volume ($(\mu\text{m}^3 \text{cm}^{-3})$) distributions, as a function of $\text{dlog}_{10}(r)$ derived from fitting bimodal lognormal size distributions to in situ optical particle counter measurements above Laramie, Wyoming. The measurements are shown as data points with Poisson error bars. The solid lines passing near the data points are the cumulative number distributions obtained from integrating the size distributions fit to the data. The measurements are all 1.0 km averages centered on 21 km, and are representative of mid stratospheric aerosol for cases of large volcanic loading (5 October 1991 - 911005), moderate loading (30 April 1994 - 940430) and background (28 July 2003 - 030728). Note that there is a second mode to the distribution even in

Observations and model calculations (see Chapter 6) show that sulfuric acid particle nucleation occurs only in the coldest regions of the stratosphere – close to the tropical tropopause (Figure 1.4) and in the polar winter stratosphere (Section 1.4.2), while nucleation rates at the mid-latitude tropopause are considerably lower. Goodman et al. [1982] noted that size distributions observed over Panama (80°E , 10°N) by the ER-2 were consistent with newly formed particles. This observation was supported by the first SAGE observations of aerosol extinction [Yue and Deepak, 1984], and later by more recent tropical aircraft measurements and theoretical considerations [Brock et al., 1995]. The Brock et al. observations show aerosol particle concentrations just below the tropical tropopause of up to $10^4 \text{ mg}^{-1} \text{ air}$ ($\sim 2 \times 10^3 \text{ cm}^{-3}$ at 100 hPa and 200 K), which is considerably higher than typical condensation nucleus (CN) concentrations of $\sim 10 \text{ cm}^{-3}$ observed at mid-latitudes (see Figure 1.3). Aerosol processes in the tropopause region are discussed further in Section 1.6. Observations outside the tropical regions also show an enhanced mode of small aerosol near the tropopause [Wilson et al., 1992].

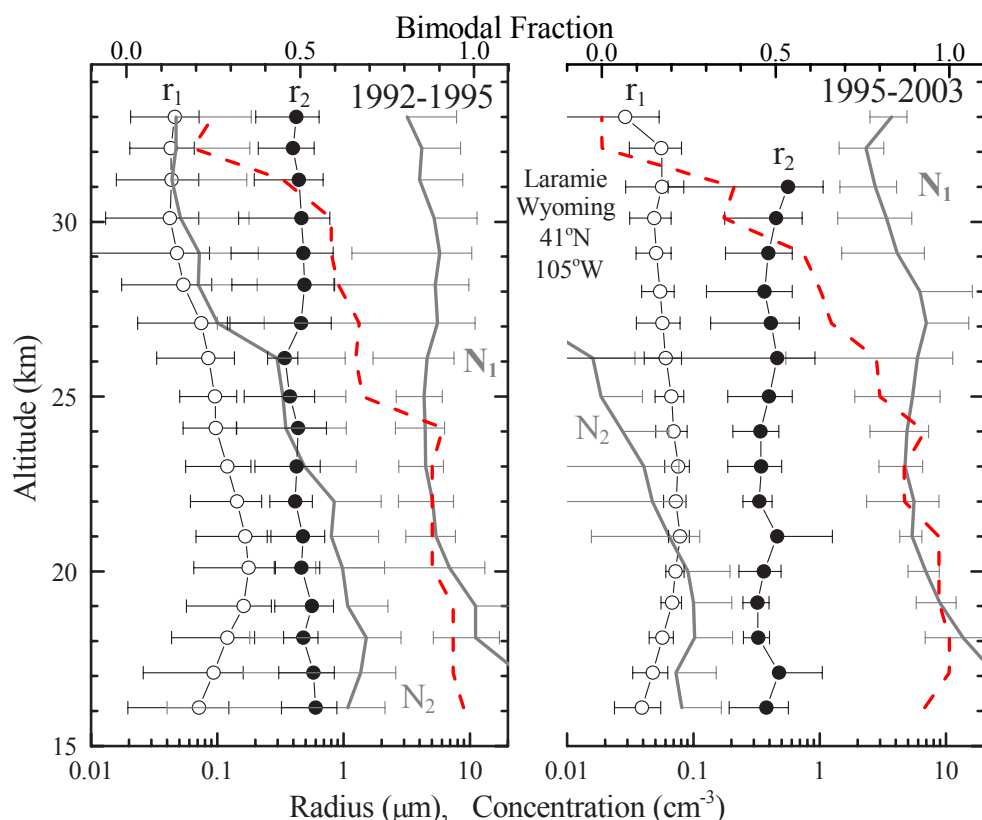


Figure 1.3. Vertical profiles of integral number concentration (cm^{-3}) and median radii (μm) from unimodal/bimodal lognormal parameters fit to balloonborne in situ optical particle measurements [Deshler et al., 2003]. Averages and standard deviations for modal number concentration, N_1 , N_2 (gray lines with error bars), and median radii, r_1 , r_2 (dark lines with data points and error bars), and fraction of measurements which were bimodal (red dashed lines, with scale at the top) are shown. The fitting parameters from two time periods are shown, 1992-1995, encompassing the Pinatubo aerosol and its decay, and 1995-2003, representing the current stratospheric background. Both time periods include about 30 individual profiles.

Coagulation and condensation of H_2SO_4 vapor as the aerosol is transported to higher latitudes leads to the development of the typical mid-latitude distribution containing ~ 10 particles cm^{-3} , although as Hamill et al. [1997] have shown, the mixing of young and aged aerosol and the vertical redistribution of the largest particles likely play an important role in shaping the canonical distribution. Although a full microphysical model that couples these processes is required to generate observed distributions, some approximate time constants for the individual processes can be estimated. For example, using a simple box model Hamill et al. [1997] have shown that although coagulation and mixing is important in controlling the width of the particle size distribution, it is condensation of H_2SO_4 that accounts for most of the growth. They were able to broadly reproduce an observed size distribution by artificially mixing distributions that had evolved in the model over a period of 2 years. The very rapid initial coagulation

of high number densities of particles at the tropical tropopause, the long lifetimes of the aerosol in the stratosphere, and the rapid decrease in coagulation rate with decreasing particle concentration all ensure that the aged mid-latitude size distribution is relatively insensitive to the initial nucleation rate (Chapter 6). In fact, conditions at the tropical tropopause are such that the nucleation rate is often close to the kinetic limit, rendering the stratospheric aerosol population fundamentally insensitive to the assumed nucleation rate. This also implies that ion-assisted nucleation is of little importance in the tropical UT, because the number of ion pairs is typically much smaller (by two orders of magnitude) than the number of nuclei mode particles.

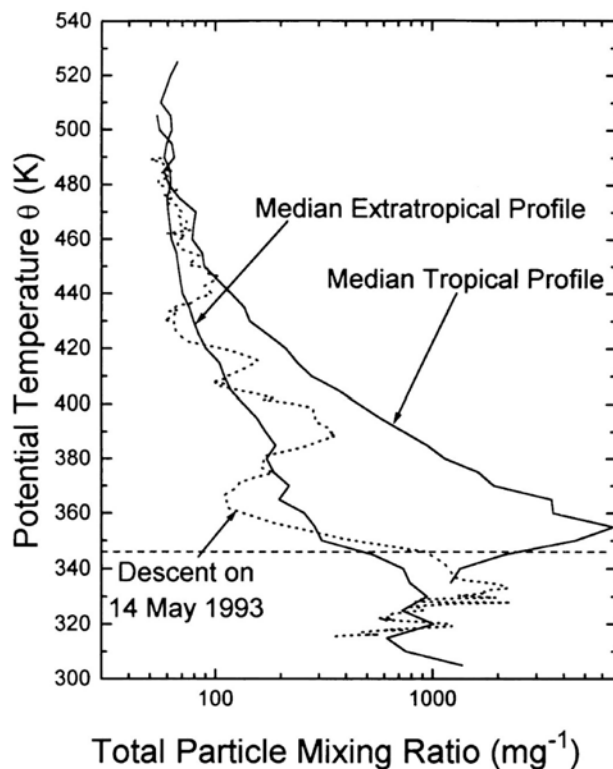


Figure 1.4. Tropical upper troposphere/lower stratosphere condensation nucleus (CN) concentrations measured by Brock et al. (1995). The horizontal dashed line marks the approximate height of the tropopause.

To first order, the composition of the stratospheric aerosol outside the polar regions ($T > 200$ K) can be considered as a mixture of sulfuric acid and water. The H_2SO_4 concentration in the aerosol particles depends on the water partial pressure and temperature, and the particles can be assumed to be in equilibrium with the ambient water on the timescale of seconds or less. Early calculations of the acid concentration [Steele and Hamill, 1981] over the full range of stratospheric conditions have been updated by more sophisticated thermodynamic model calculations [for a review, see Carslaw et al., 1997], although the changes relative to earlier calculations for binary $\text{H}_2\text{SO}_4/\text{H}_2\text{O}$ aerosol under most stratospheric conditions are small. Temperatures are low enough in the polar regions during winter to allow appreciable partitioning of other soluble gases such as HCl, HBr and HNO_3 into the sulfuric acid [Carslaw et al., 1994; Tabazadeh et al., 1994; Carslaw et al., 1997]. Figure 1.5 shows model calculations of the change in particle composition (and hence also size) with temperature.

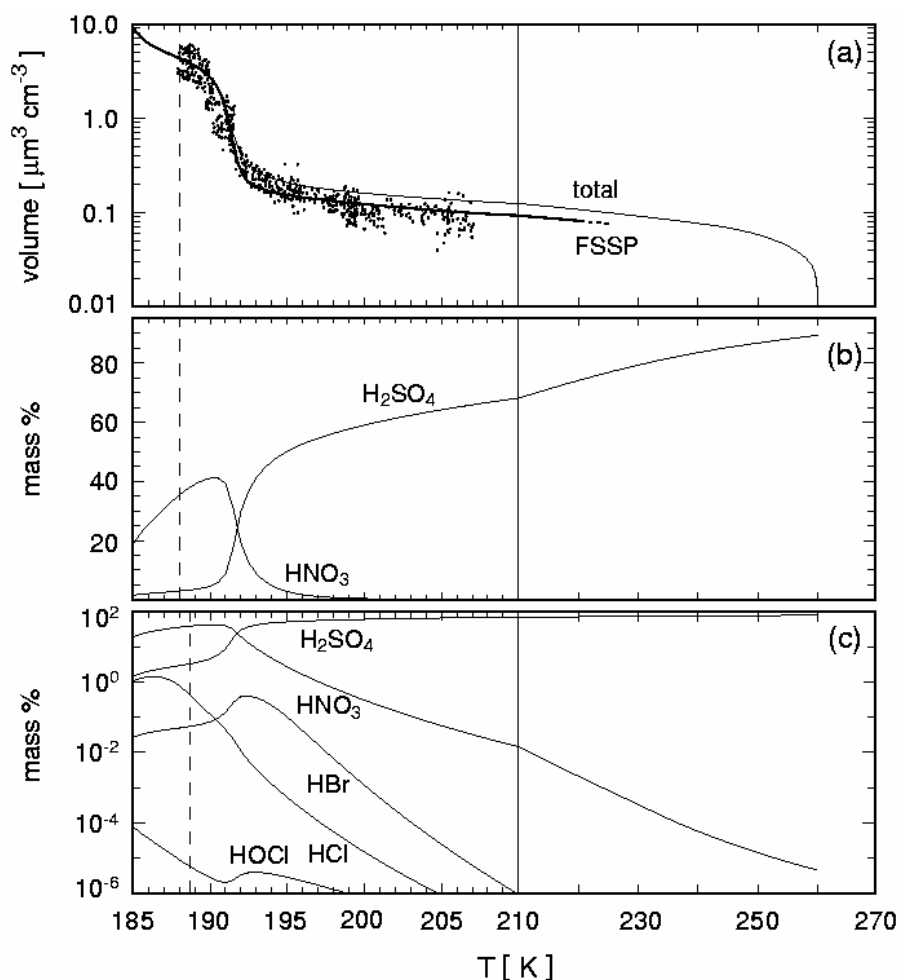


Figure 1.5. Model calculations of (a) specific particle volume and (b), (c) composition of stratospheric particles as a function of temperature, including uptake of soluble gases under polar winter conditions. The nitric acid trihydrate (NAT) and ice equilibrium temperatures are marked. In panel (a) the volume as measured by the Forward Scattering Spectrometer Probe (FSSP) during a flight of the ER-2 into the Arctic vortex in 1988 is shown as data points along with the equivalent model calculation. From WMO [1998].

The change in the equilibrium composition and water content of stratospheric particles in response to changes in temperature and humidity lead to seasonal changes in particle size that need to be taken into account when examining variations in aerosol extinction observed by satellite instruments (refractive indices also change with composition, but are of secondary importance to changes in particle size). For a change in temperature from 215 to 220 K the extinction ratio for a typical mid-latitude sulfuric acid size distribution (number = 10 cm^{-3} , radius = $0.1 \mu\text{m}$) changes by approximately 10%. Away from regions of new particle formation in the tropics, the stratospheric condensed sulfur amount is a rather slowly evolving quantity, although the aerosol physical and chemical properties can react essentially instantly to changes in temperature and humidity.

1.4.2 Polar Aerosol

Aerosol properties can be strongly perturbed in the polar regions due to several factors: (1) the strong diabatic descent of the vortex air and the dynamical barrier of the vortex edge; (2) the sedimentation of PSC particles carrying with them the background aerosol, leading to reductions in particle surface area; (3) very low temperatures, which are conducive for nucleation of new particles. The formation and properties of PSC particles is described in Section 1.7. Here, we briefly summarise the special properties of polar aerosol.

Measurements over Antarctica have revealed the presence of an enhanced CN layer with particle concentrations greater than 100 cm^{-3} at around 26 km altitude [Hofmann and Rosen, 1985; Wilson et al., 1992]. The CN layer occurs at the same time as the ozone depletion (between September and November). Aerosol extinction observed by satellite is also observed to decrease in this region, indicating a reduction in aerosol with sizes that are efficient for visible light scattering ($\sim 0.1\text{-}0.2 \mu\text{m}$).

Several possible explanations for the enhanced CN have been proposed. Rosen and Hofmann [1983] suggested that photodissociation of OCS in Antarctic spring could release a large amount of H_2SO_4 vapor that subsequently forms new particles through homogeneous nucleation. However, later calculations suggested OCS photodissociation is too slow a process to produce H_2SO_4 vapor concentrations sufficient to grow the new particles to observable sizes [Zhao et al., 1995a]. Although only modest concentrations of H_2SO_4 are required to initiate nucleation in the cold conditions of the Antarctic stratosphere [Hamill et al., 1990], model calculations suggest that condensation of the vapor on to existing aerosol suppresses H_2SO_4 concentrations to levels that are insufficient to explain the growth of new particles to observable sizes [Zhao et al., 1995a]. Rosen and Hofmann [1983] also suggested that evaporation of sulfate aerosol in a warming event followed by cooling would lead to nucleation of new aerosol, although there is no evidence for rapid significant decreases in existing particles preceding the CN events. Zhao et al. [1995a] postulated that SO_2 , derived from high altitude photolysis of H_2SO_4 , could bring sufficient sulfur into the lower spring stratosphere, where it would subsequently be converted to H_2SO_4 through reactions initiated by OH in sunlight. This source of H_2SO_4 vapor is much more rapid than from OCS photolysis and is sufficient to explain the observed CN bursts with as little as 100 ppt of SO_2 at 25-30 km. In the form of SO_2 , the sulfur source for particle formation is not scavenged by existing aerosol, as is the case for H_2SO_4 vapor, so high concentrations of H_2SO_4 can become available as SO_2 reacts with OH when sunlight returns. Mills et al. [1999] used a 2-D model to estimate that a photolytic cross section of H_2SO_4 greater than 10^{-21} cm^2 in the UV region would be required to produce a sufficient reservoir of SO_2 just above the aerosol layer. They based this cross section on upper limits set by Burkholder et al. [2000], although more recent measurements and calculations suggest no appreciable UV electronic absorption [Wrenn et al., 1999; Hintze et al., 2003]. More recently, Vaida et al. [2003] have estimated photolysis rates of H_2SO_4 vapor by visible solar radiation. The estimated J values are sufficiently large to explain upper stratospheric and mesospheric SO_2 concentrations and the subsequent availability of sulfur in the lower Antarctic vortex. The explanation for CN bursts in the lower polar stratosphere therefore appears to be downward transport of SO_2 from the mesosphere and upper stratosphere followed by production of H_2SO_4 vapour locally in the lower stratosphere through reaction of SO_2 with OH.

1.4.3 Non-Aqueous Stratospheric Particles

In terms of mass, stratospheric particles are normally considered to be composed primarily of aqueous solutions of sulfuric acid and water, with increasing aqueous concentrations of HNO_3 and HCl in the polar winter stratosphere. However, non-aqueous components of extra-terrestrial and tropospheric origin are known to be present in some particles [Murphy et al., 1998; Cziczo et al., 2001]. Based on estimated fluxes of non-sulfur aerosol components into the stratosphere it is possible that these non-aqueous components comprise a significant fraction of the particle mass, at least in some parts of the stratosphere. For example, the total sulfur mass cycled through stratospheric aerosol (the mass of sulfur as H_2SO_4 vapor condensed, equal to the mass lost through the tropopause) is approximately 355 ton day^{-1} , while the estimated flux of meteoritic material is 44 ton day^{-1} (Chapter 6). The magnitude of these fluxes suggest that meteoritic material may comprise over 10% by mass of stratospheric aerosol. Single particle aerosol mass spectrometer instruments have detected a wide range of elements in lower stratospheric aerosols up to 19 km altitude [Murphy et al., 1998]. Among these have been elements indicative of meteoritic material, brought down from the mesosphere [Cziczo et al., 2001] (Section 1.4.2).

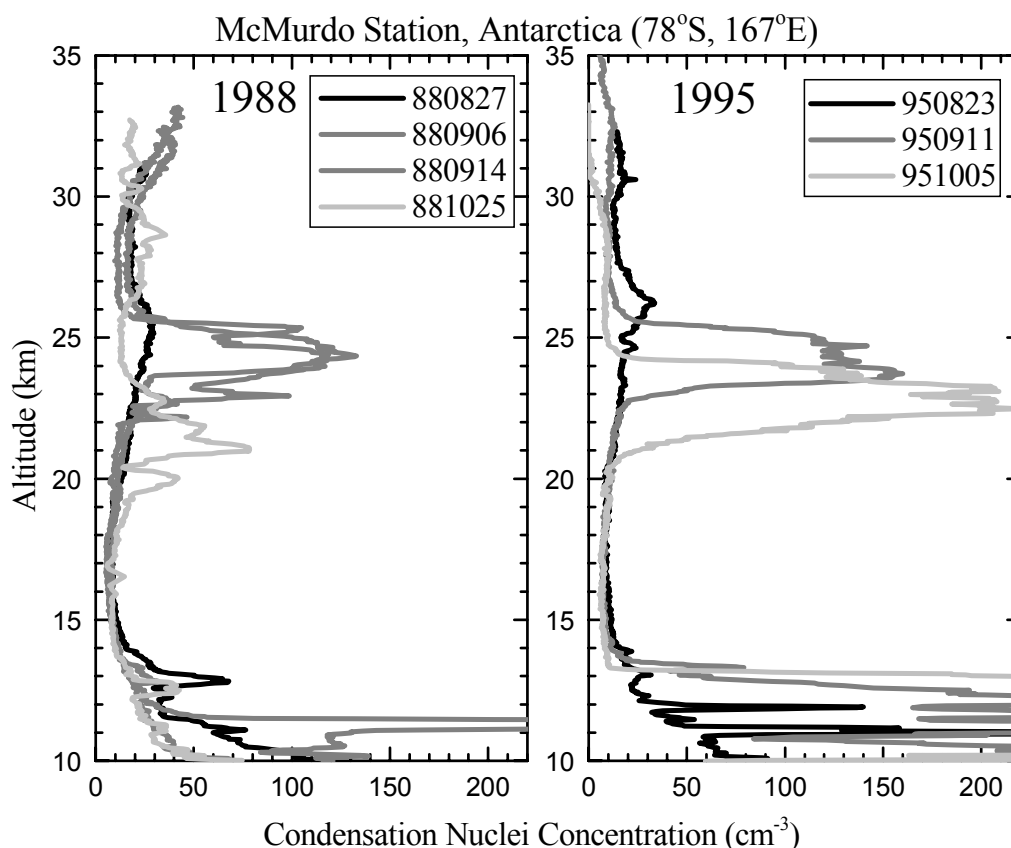


Figure 1.6. Vertical profiles of condensation nuclei (CN) concentration from McMurdo Station, Antarctica, during the late winter and early spring. The development of a CN layer near 25 km and its subsequent descent is a repeatable observation of the springtime austral stratosphere. The example profiles shown are from 4 measurements in 1988 and three in 1995. Similar layers have been observed in the Arctic, but much less frequently.

Black carbon particles (soot) have been observed on few occasions in the lower stratosphere [Pueschel et al., 1997; Strawa et al., 1999; Fromm et al., 2000]. The contribution of soot particles to the total particle number concentration has been estimated at about 1%, although the contribution to surface area in some locations may be as high as 10% [Strawa et al., 1999] (see also Section 1.6.2). Satellite and lidar observations revealed that aerosol from boreal forest fires over Canada and eastern Russia during the fire season in 1998 (August through October) led to substantial increases of the stratospheric aerosol extinction and optical depth at lower stratospheric altitudes (13-16 km) for a period of up to 3 months [Fromm et al., 2000]. The troposphere-to-stratosphere transport mechanisms favoring such intrusions are not well understood, but it is likely that this stratospheric pollution event was caused by widespread severe convective activity during the wildfire season. Pueschel et al. [2000] have also speculated that soot aggregates emitted by aircraft in conventional flight corridors (10-12 km altitude) can be transported into the mesosphere due to gravito-photophoresis (a sunlight-induced force acting on particles that are geometrically asymmetric and which have uneven surface distribution of thermal accommodation coefficients).

Although non-aqueous particulate components do not dominate the total stratospheric aerosol mass, they may still affect important number-based physical processes. As two examples, we note that the presence of such particles could provide a link to the formation of large PSC particles [Fahey et al., 2001] by heterogeneous nucleation [Drdla et al., 2002; Voigt et al., 2005] or they may modify the optical extinction of the lower stratospheric aerosol, in particular when they are strong light absorbers, such as black carbon. The efficacy of these particles as heterogeneous nuclei for solid phase formation in the stratosphere may depend upon whether they are present as inclusions in sulfuric acid particles or as separate particles.

1.5 Volcanic Perturbations to Stratospheric Aerosol

The most profound influence on stratospheric aerosol levels comes from the periodic injections of SO_2 and ash directly into the stratosphere by volcanic eruptions. Sulfur dioxide output by volcanic eruptions has been observed since the late 1970s by the Total Ozone Monitoring System (TOMS) and, later, by the Global Ozone Monitoring Experiment (GOME). During this time, approximately 50 events emitted more than 0.1 Tg of SO_2 [Carn et al., 2003] but only a handful of these events were observed to even transiently perturb stratospheric aerosol levels and much of the SO_2 emitted by volcanic events remains in the troposphere or is introduced into the stratosphere only by dynamically driven transport. About 10 events since 1979 were observed to produce in excess of 1 Tg of SO_2 though, from stratospheric aerosol measurements, we know that only three of these (El Chichon (~7 Tg), Mt. Pinatubo (~20 Tg), and Cerro Hudson (~3 Tg)) were primarily stratospheric events.

Once in the stratosphere, volcanic SO_2 is transformed to gaseous H_2SO_4 that then condenses to form high number concentrations of small $\text{H}_2\text{SO}_4/\text{H}_2\text{O}$ particles by binary homogeneous nucleation in the first few weeks after the eruption. These particles subsequently coagulate to form a stable bimodal aerosol size distribution (Figures 1.2 and 1.3). The most pronounced change in the background distribution after a volcanic eruption is a significant increase in the number of particles in the mode centred on 0.4 μm radius. The decay of measured aerosol extinction and lidar backscatter ratio after an eruption (Chapter 5) shows that the additional particles have a residence time in the stratosphere on the order of one year [McCormick et al., 1995].

Despite their rarity, large events in the past 3 decades have dwarfed the background aerosol level such that much of the historical data record is a chronicle of the relaxation toward a non-volcanic background. It is also worth noting that, while Mt. Pinatubo is by far the largest stratospheric event in recent volcanic history, inferences from ancient eruptions such as that of Toba in approximately 75,000 B.P. (~1000 Tg) [Pinto et al., 1989] clearly demonstrates that 1991 Mt. Pinatubo eruption is not exceptional in its modification of the stratospheric aerosol loading.

The 1982 El Chichon eruption (Mexico) and the 1991 Mt. Pinatubo eruption (Philippines) dominate the history of stratospheric aerosol in the last quarter of the twentieth century. Both of these low latitude eruptions followed a similar pattern in which much of the injected material found its way into the tropical stratosphere where it effectively formed a tropical ‘reservoir’ of aerosol. The reservoir occurs in a region (above ~20 km) with strong meridional gradients of wind shear, which effectively shield the tropics from mid-latitude disturbances and suppress meridional transport (the so-called tropical pipe). At altitudes where westerlies reside over the equator, particularly below 20 km, the subtropical wind shear is diminished or absent and greater meridional mixing is able to take place. The aerosol reservoir charged by Mt. Pinatubo and El Chichon, and smaller eruptions such as Nevada del Ruiz (Colombia in 1985), is a persistent feature in the global aerosol morphology shown in Chapter 3.

In the past three decades, mid and high latitude eruptions have had a considerably smaller impact on stratospheric aerosol levels than tropical eruptions. This is in part an accident of geography since the largest volcanic injections of SO₂ at the highest altitudes in this period have occurred at low latitudes. In fact, the largest non-tropical eruption since 1979 was Cerro Hudson (Chile) in 1991 whose aerosol signal was overwhelmed within a few months by nearly simultaneous Mt. Pinatubo eruption [Pitts and Thomason, 1993]. Transient plumes from several eruptions including Spur (USA, 1992), Lascar (Argentina, 1993), and Shishaldin (USA, 1999) [Rizzi et al., 2000] have been noted by a few instruments though Mt. St. Helens (USA, 1980) was the only other event of note (stratospherically) among the mid and high latitude eruptions. It is also not uncommon to observe apparently volcanically derived aerosol plumes without attribution to a particular eruption [Yue et al., 1994]. Historically, aerosol from mid and high latitude eruptions tends to be transported to high latitudes where subsidence and other dynamical processes can efficiently remove them from the stratosphere. As a result, non-tropical eruptions have had a far more transient effect on aerosol levels than tropical eruptions though it is worth noting that we have no observational experience to judge how a Pinatubo-sized event in Alaska or Antarctica would evolve. Tropical eruptions in which the effects are confined below 20 km tend to behave in a manner similar to that observed in mid and high latitudes. For example, the aerosol associated with the 1990 eruption of Kelut (Indonesia) was confined to this altitude range and was transported primarily to high southern latitudes within several months of the eruption.

Stratospheric aerosol can have a transient but significant radiative impact following a major eruption [McCormick et al., 1995]. For instance, radiative heating resulting from both the El Chichon and the Pinatubo aerosol increases was associated with significant warming in the middle stratosphere [Labitzke and McCormick, 1992] that may have played a role in ozone decreases observed in this region [Kinne et al., 1992] and the lofting of aerosol above 30 km in January 1992. Stratospheric aerosol also increases the albedo of the Earth system and can exert a significant climate forcing [Brogniez et al, 1999; Stenchikov et al., 1998]. However, observations and modeling [e.g., Hansen et al., 2002] demonstrate that the effects on surface temperatures are not evenly distributed around the globe. For instance, a typical pattern in winter shows warming over

North America and Europe with cooling over northern North America and the Middle East. Volcanic aerosols may also produce an indirect radiative effect because aerosol transported into the upper troposphere can be incorporated into deeper convective clouds, alter their microphysical structure and produce albedo changes [Minnis et al., 1993].

Model simulations [e.g., Tie et al., 1994; Zhao et al., 1995b; Koziol and Pudykiewicz, 1998; Timmreck and Graf, 2000] have been quite successful in capturing the spatial and temporal development of volcanic aerosol with results that in general agree well with in situ [Deshler et al., 1993] and satellite observations [McCormick et al., 1995]. The comparison of models with observations of volcanic aerosol is addressed in Chapter 6.

1.6 Aerosol in the Tropopause Region

Transport of trace gases and particles across the tropopause (TP) couples a plethora of tropospheric processes controlling emissions and transformations of aerosol and their gaseous precursors to the lower stratosphere. As a result, it influences the total mass and other properties of the stratospheric aerosol. Liquid particles with or without crystalline or insoluble inclusions are the precursors of ice crystals in cirrus clouds and polar stratospheric clouds.

1.6.1 Aerosol precursors and nucleation processes

Transport and subsequent accumulation of aerosol precursor gases from the boundary layer into the TP region occurs in deep convective clouds within time scales of a few hours or less [Chatfield and Crutzen, 1984] and by lifting of air masses in warm conveyor belts on longer time scales (~ 2 days) [Eckhardt et al., 2003]. The efficiency of gas transport in a given mixed phase convective cloud is controlled by the gas solubility, the retention coefficient, and the trapping efficiency [Yin et al., 2002], the former describing the fraction of a dissolved gas that is retained in an ice particle upon freezing, the latter describing the amount of a gas trapped in growing ice particles. Neither coefficient is well characterised for most gases of interest.

In situ measurements [Laaksonen et al., 2000; Twohy et al., 2002] show enhanced levels of upper tropospheric SO_2 (~ 1 ppbV), suggesting that this gas can efficiently be transported to the TP region, leading to photochemical production of H_2SO_4 . Enhanced levels of acetone, an important source of OH radicals, have been detected in the TP region [Arnold et al., 1997] possibly stimulating rapid in situ photochemical production of nucleating gases and subsequent gas-to-particle conversion. Besides the photochemical source, dynamical processes initiating the formation of aerosol particles from the vapor phase include: atmospheric waves; turbulence; mixing across the tropopause; and outflow of (deep) convective clouds. There is experimental evidence for all of these forcing mechanisms.

Most studies on nucleation of aerosol particles from the vapor phase in the atmosphere concentrated on the homogeneous binary $\text{H}_2\text{SO}_4/\text{H}_2\text{O}$ system. Sulfuric acid resulting from gas phase oxidation of SO_2 is probably the most important aerosol-forming species in the TP region. According to global model calculations, it is unlikely that ammonia (NH_3) is present there in concentrations relevant to nucleation, but it is difficult to predict ammonia and ammonium concentrations in the UT accurately due to uncertainties in the emission inventories and the parameterization of wet removal processes [Kärcher et al., 2004]. Concentrations of condensable organic vapors in this region of the atmosphere are not well known but could be

comparable to those of H_2SO_4 [Murphy et al., 1998, Talbot et al., 1998; Kärcher and Solomon, 1999]. In regions closer to the Earth's surface other nucleation mechanisms may be of greater relevance [Turco et al., 1998; Korhonen et al., 1999; Napari et al., 2002; Hanson and Eisele, 2002].

The various formulations of the binary nucleation rates of H_2SO_4 and H_2O have not been directly validated and their accuracy is actually not known under TP conditions. Predictions of these rates based on the classical liquid drop model are suspect and should be applied with caution [Lovejoy et al., 2004]. However, in regions (such as the TP region, in particular in the tropics) where binary homogeneous nucleation occurs in the form of bursts, a type of nucleation which is almost barrierless, much of the uncertainty of the classical theory is damped out [Clement and Ford, 1999].

However, it must be kept in mind that in most observations the conclusions regarding the importance of $\text{H}_2\text{SO}_4/\text{H}_2\text{O}$ nucleation are not fully decisive, often owing to missing experimental information. One case study suggests that vapors other than H_2SO_4 and H_2O must have contributed either to nucleation or particle growth in the upper troposphere [de Reus et al., 2000]. Recently Lee et al. [2003] reported strong observational evidence for ion-assisted $\text{H}_2\text{SO}_4/\text{H}_2\text{O}$ nucleation in different regions of the upper troposphere and lower stratosphere under typical conditions of relatively low pre-existing aerosol surface area and sufficient sunlight. Numerical model results constrained by measured ion cluster thermodynamics [Lovejoy et al., 2004] and atmospheric species could explain the observations. Ion-induced nucleation thus appears to be a globally important source of aerosol particles, warranting more detailed research in the future.

Many organic vapors (in particular alkenes, alkynes, and aldehydes) have a large proton affinity and high solubility in aqueous acid solutions [Solomons, 1996] and may thereby increase the dry aerosol mass by condensation on pre-existing particles. However, the knowledge about speciation, chemical properties, and nucleation potential of organic atmospheric aerosols is very limited [Jacobson et al., 2000]. Particulate organic matter is subject to oxidation and may decrease over time in the absence of sources, but little is known about the time scales involved in this process.

While transport of tropical air across the subtropical jet may inject particles into the midlatitude lowermost stratosphere, it is recognized that the upper troposphere near the TP is an effective source of new particles. In winter, concentrations of condensation nuclei (CN) are larger than in summer. Observed high concentrations of new particles below 20 nm in diameter in the upper troposphere and TP region appear to be regulated by the relatively low levels of larger (optically active) particles in the accumulation mode (above 300 nm) that make up most of the available surface area. This is seen on a climatological basis at one midlatitude continental site [Hofmann, 1993], and in field studies [de Reus et al., 1998]. In addition to climatological data, all available short-term tropospheric field measurements focusing on aerosol nucleation have been analysed [Kulmala et al., 2004].

Atmospheric measurements obtained in the tropical and midlatitude regions of both hemispheres were analyzed in order to investigate the role of the upper tropical troposphere as a source of new particles for the stratospheric aerosol during times which were not strongly influenced by volcanic eruptions [Brock et al., 1995]. The measurements and numerical calculations indicate that binary homogeneous nucleation of H_2SO_4 and H_2O occurs in this region. The nuclei coagulate and are transported upwards in the rising tropical air masses. Oxidized

sulfur gases condense onto the resulting $\text{H}_2\text{SO}_4/\text{H}_2\text{O}$ droplets. The observed vertical profiles of total particle mixing ratios exhibit a maximum in both the tropical (see Figure 1.4) and extratropical TP regions, the latter consistent with midlatitude data [Schröder et al., 2002; Minikin et al., 2003]. Particle mixing ratios decrease smoothly with increasing altitude above the tropical TP due to coagulation. The maximum in particle number in the tropics is ~ 7 times larger than in the extratropics, suggesting that new particles are preferentially formed near the tropical TP [Brock et al., 1995].

Additional factors triggering nucleation besides photochemical production of nucleating gases include dynamically induced mixing of air masses with different temperatures and relative humidities [Bigg, 1997] and turbulent fluctuations of temperature and gas concentrations [Easter and Peters, 1994]. In fact, airborne particle measurements indicate that such processes could sometimes serve as trigger events for new particle formation [Schröder and Ström, 1997]. Particle formation in the mid-latitude lowermost stratosphere may be induced by convective lifting of the tropopause and associated adiabatic cooling [de Reus et al., 1999]. Turbulent mixing and atmospheric waves as triggers of nucleation have also been emphasized in model studies [Nilsson and Kulmala, 1998; Nilsson et al., 2000].

The low temperatures of the upper troposphere, low pre-existing particle surface areas, high concentrations of aerosol precursor species vented aloft, high actinic fluxes accelerating photochemistry, high relative humidities by detrainment of water from the cloud interior, all associated with turbulent regions of cloud outflow, are likewise known to create ideal conditions for aerosol nucleation.

While most observations of cloud-induced aerosol formation have been reported for low level, marine boundary layer clouds [Perry and Hobbs, 1994], some experiments demonstrate that such processes do occur in the free troposphere and result in the production of new particles in accord with classical theory of $\text{H}_2\text{SO}_4/\text{H}_2\text{O}$ aerosol formation when applied to the conditions prevailing near evaporating cloud edges [Clarke et al., 1999]. Volatile aerosol has been observed in the outflow of a huge (many 100 km^2 horizontal extension) mesoscale convective system in the upper troposphere [Twohy et al., 2002], with photochemical production of H_2SO_4 from convected SO_2 being the driving factor of the nucleation event [Clement et al., 2002]. It is estimated that a substantial fraction ($\sim 20\%$) of the global upper tropospheric small particle budget can be produced in the outflow regions of such storms. The question whether evaporating cirrus clouds can trigger aerosol formation has not been investigated. On the other hand, cirrus ice crystals nucleate on sulfuric acid-containing particles and the large surface area of these clouds should efficiently scavenge nuclei mode particles, both acting as a sink for the upper tropospheric aerosol.

First attempts to explicitly simulate tropospheric sulfate size distributions in a 3D general circulation model confirm the important role of binary aerosol nucleation in the TP region [Adams and Seinfeld, 2002; Spracklen et al., 2005]. Importantly, simulated mid-latitude cloud condensation nuclei (CCN) concentrations exhibit a sensible dependence on assumptions for $\text{H}_2\text{SO}_4/\text{H}_2\text{O}$ nucleation rates, highlighting the need for a better understanding of such microphysical processes.

1.6.2 Aerosol distribution and composition

Mass spectrometric, single particle analyses of particles above $\sim 200 \text{ nm}$ in diameter reveal a tremendous variety in aerosol composition and shed light on the complexity of aerosol

sources and chemistry, and on the interaction of aerosol transformation processes with atmospheric transport [Murphy et al., 1998]. Stratospheric aerosol particles primarily consist of H_2SO_4 and H_2O , but many (up to ~50%) of the probed particles analysed also contain light-absorbing meteoritic material and small amounts of organics. The influence of aerosol originating in the troposphere is seen in mass spectrometric data at up to 5 km above the tropopause in some locations (D.M. Murphy, personal communications, 2005). Below the TP, organic components were often more abundant than sulfates. Organics and sulfates were usually internally mixed. Airborne filter measurements over the North Atlantic [Dibb et al., 2000] detected primarily acidic aerosol, but a significant number of collected samples contained enough ammonium to fully neutralize the strong acids. There exist contamination issues due to manual handling of aerosol probes in flight, so the actual ammonium concentrations at altitude remain uncertain. Traces of magnesium and calcium have also been detected.

The measurements of Brock et al. [1995] show a greater proportion of nonvolatile particles at extratropical locations as compared to the mostly volatile, tropical particles. The weaker, extratropical maximum of the upper tropospheric particle mixing ratios may be due to in situ nucleation and/or transport of particles and aerosol precursors by convective pumping and frontal transport [Brock et al., 1995]. As the authors conjecture, a possible cause for the reduced volatility is the incorporation of ammonia over the time of quasi-horizontal transport from the tropics toward midlatitudes. Quasi-horizontal transport from the tropics is likely not a significant source for particles at and below the extratropical TP due to inefficient mixing between the tropics and the extratropics, in contrast to regions in the lowermost stratosphere.

A decade of in situ aerosol observations performed during the 1990s around the Pacific basin is available [Clarke and Kapustin, 2002]. The TP portions of vertical aerosol profiles taken in the tropics show signatures of particle formation as discussed above. Highest condensation nuclei (CN) concentrations are found in regions over the equatorial zone of deep convection, emphasizing the role of deep convection in removing high aerosol mass by scavenging and creating new and small CN after cloud evaporation. The data also demonstrate that nonvolatile particles originating from the Earth's surface are mixed up into upper tropospheric air, either by convection or long-range transport. Nonvolatile particles include dust, black/organic carbon, and sea salt. Metallic compounds, mineral dust particles, and insoluble meteoritic material of stratospheric origin have been found enriched in tropical cirrus ice crystal residues [DeMott et al., 2003a; Cziczo et al., 2004]. Deep convection contributes to the TP aerosol budget also at midlatitudes [Huntrieser et al., 2002].

In situ observations of gases and aerosol in the TP region in both hemispheres over the Atlantic and across the tropics confirm the significance of convection for the formation of new particles and the presence of nonvolatile particles there [Minikin et al., 2003]. Aitken particles exhibit much less variability in the southern than in the midlatitude northern hemisphere, suggesting less frequent and less intense particle formation events at southern midlatitudes. A substantial fraction of the particles is nonvolatile ($\sim 10\text{-}40 \text{ cm}^{-3}$).

Meridional and seasonal probability distributions of submicrometer particles in the TP region along an international civil flight route from Munich to Colombo are available from three years of continuous measurements [Hermann et al., 2003]. The observations suggest that the main processes regulating the concentrations of CN must act on spatial scales of $\sim 10 \text{ km}$, stressing the importance of atmospheric waves as a trigger of aerosol nucleation as has been found for ice nucleation in cirrus clouds [Kärcher and Ström, 2003].

Model studies emphasise the role of letovicite ($(\text{NH}_4)_3\text{H}(\text{SO}_4)_2$) as a possibly widespread constituent of the tropospheric aerosol [Colberg et al., 2002]. A thermodynamic model for multi-component aerosols coupled to a chemistry-transport model predicts monthly mean (August 1997) aerosol nitrate and sulfate mixing ratios at 6°E and 200 hPa of 20-100 pptV and 10-100 pptV, respectively [Metzger et al., 2002]. Particulate nitrate and sulfate exhibit distinct meridional patterns and take their peak values in the tropical region and at midlatitudes, respectively. Available global model results describing the TP aerosol composition have to be scrutinized as accurate measurements of the size partitioning of ammonium and other species there are not available.

Black carbon (BC) particles containing sulfuric and organic impurities (soot) are produced during incomplete fossil fuel combustion, wildfires, or biomass burning. The global BC cycle was recently re-analyzed with a general circulation model [Hendricks et al., 2004]. At 250 hPa, the mass concentrations of BC from surface sources still reveal the emission regions (mainly Europe and Asia for fossil fuel BC and Africa for biomass burning), with plumes zonally dispersing the particles transported aloft. Simulated BC concentrations are in the range 0.1-10 ng/m^3 . BC number concentrations from surface sources ranges between 0.1-5/ cm^3 , well exceeding 1/ cm^3 at northern hemisphere midlatitudes (see also Chapter 1.7). The authors point out that comparison with the few available soot observations are difficult owing to the lack of accurate measurements and uncertainties in emission inventories. More robust model evaluations will become possible when future in situ observations better quantify mass, number, and size partitioning of BC particles, both in their source regions and at altitude.

In summary, there is ample experimental evidence for H_2SO_4 and H_2O to play an important role in producing new particles from the gas phase in the TP region. Ion-assisted nucleation seems to be crucial, especially in threshold formation conditions. In some, but not all cases H_2SO_4 can also explain particle growth. The role of organics in particle formation and growth is unknown due to the lack of appropriate measurements. Detailed knowledge of the underlying nucleation mechanism may not significantly influence the predicted number of particles formed in vigorous nucleation bursts, but is essential for a robust determination of frequency and location of atmospheric nucleation events. Further improvements in measuring ultrafine particles, in bridging the gap between molecular cluster kinetics and bulk phase properties in nucleation theory, and in the parameterization of nucleation in large-scale models are needed to accurately quantify the role of aerosol formation processes at the entry to the stratosphere. More experimental data on the distribution and chemical composition of atmospheric ion clusters and aerosol particles and a better understanding of gas/aerosol processes in deep convective clouds and warm conveyor belts are required to calculate the amount of SO_2 present in the tropical TP region and to accurately predict the future evolution of the stratospheric aerosol.

1.7 Polar Stratospheric Clouds and Sub-visible Cirrus Clouds

The occurrence of low temperatures in the polar winter stratosphere and in the tropical TP region can lead to the formation of hydrates containing HNO_3 , ice, and substantial increases in aerosol volume due to condensation of HNO_3 and H_2O into the liquid aerosol. Subvisible cirrus clouds mainly consist of water ice crystals and occur almost globally in the TP region. Particles in polar stratospheric and subvisible cirrus clouds and other particle types need to be distinguished from aerosol in any climatology.

1.7.1 Polar stratospheric clouds

Polar stratospheric clouds (PSCs) occur between about December and March in the Arctic at altitudes from 16-26 km typically north of 60°N and over the Antarctic between May and September [Poole and Pitts, 1994; Fromm et al., 2003]. Our understanding of PSCs has improved greatly over the last 10 years as a result of extensive in situ and remote measurements. They are composed either of solutions of HNO_3 , H_2SO_4 and H_2O (liquid ternary aerosol, LTA), nitric acid hydrates, or water ice. The HNO_3 abundance in the lower stratosphere (~ 10 ppb) normally exceeds the condensed H_2SO_4 (equivalent to ~ 0.1 ppb) by a large margin, so nitric acid-containing PSCs will normally have specific volumes much larger than background aerosol. However, under volcanically perturbed conditions when H_2SO_4 abundances are enhanced or when HNO_3 is depleted by denitrification, the differences between PSC volumes and aerosol volumes may be small.

Nitric acid hydrates and ice are distinct phases with unique phase transition temperatures for given abundances of HNO_3 and H_2O . LTA, in contrast, is simply stratospheric H_2SO_4 aerosol containing dissolved HNO_3 and the change in volume with decreasing temperature occurs over a 2-3 K range (Figure 1.5). A ‘transition’ temperature at which aerosol becomes LTA therefore needs to be defined in terms of a specified fractional change in volume or aerosol composition. Figure 1.7 shows how the LTA transition temperature varies with HNO_3 and H_2O abundances in the lower stratosphere, defined as when the HNO_3 and H_2SO_4 concentrations in solution are equal. Note that the LTA transition temperature is higher than the ice frost point except for HNO_3 abundances below about 1 ppb. The nitric acid trihydrate (NAT) condensation temperature is typically 4-5 K higher than the LTA transition temperature and about 8 K higher than the ice frost point.

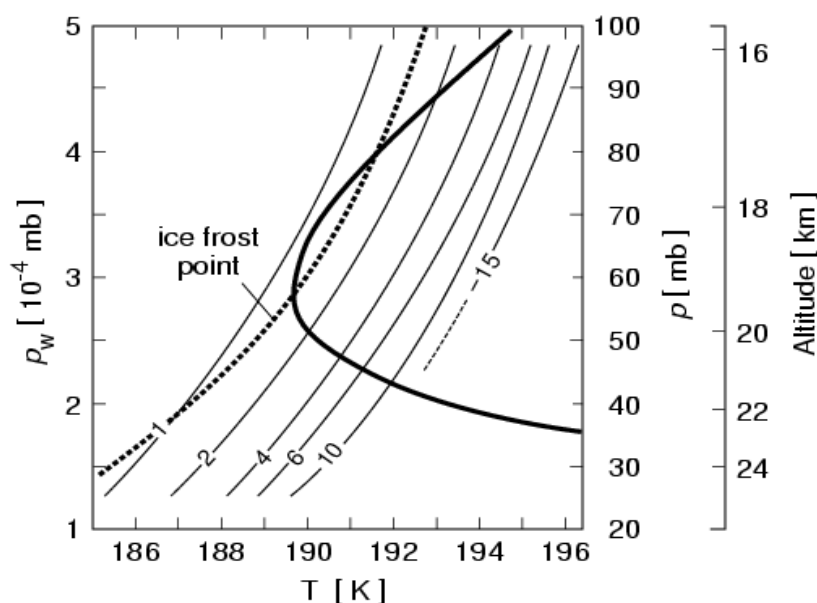


Figure 1.7. Liquid ternary aerosol (LTA) ‘transition’ temperatures: conditions for which the mass fractions of HNO_3 and H_2SO_4 are equal in solution for different initial HNO_3 partial pressures (in 10^{-7} mb marked on each contour). To the right of each contour (higher temperatures), droplets are composed mainly of H_2SO_4 and H_2O , while at lower temperatures they are HNO_3 -rich. For example, for a water partial pressure (p_w) = 2.5×10^{-4} mb and an HNO_3 partial pressure of 5×10^{-7} mb (5 ppm H_2O and 10 ppb HNO_3 at 50 mb total pressure) LTA forms at 191.5 K. The axes on the right give the atmospheric pressure and approximate altitude for which the given water partial pressures are expected assuming 5 ppm H_2O . The thick line shows typical Antarctic mid-winter conditions. From Carslaw et al. [1997].

In order to set a threshold temperature for excluding PSCs from an aerosol climatology, it is sufficient in the stratosphere to use the NAT condensation temperature, which can be derived analytically from the equations given by Hanson and Mauersberger [1988].

1.7.2 Subvisible Cirrus Clouds

Cirrus clouds form in the upper troposphere and in the tropopause region. The temperatures in the formation regions are typically below the spontaneous freezing point of pure water (~ 235 K), for which reason these clouds predominantly consist of ice crystals. The main cloud formation mechanism is believed to be homogeneous freezing of liquid aerosol particles. There is mounting evidence for heterogeneous freezing involving more efficient ice nuclei, but the impact of ice nuclei on cirrus microphysical and optical properties remains largely unexplored [DeMott et al., 2003b; Haag and Kärcher, 2004].

Cirrus clouds forming in the vicinity of the tropopause are optically and geometrically thin (visible optical depth < 0.03 and vertical thickness \sim few 100 m). Such thin cirrus are invisible to a ground-based observer and are therefore referred to as subvisible cirrus (SVC). A small number of heterogeneous ice nuclei could control the formation and properties of SVCs, although homogeneous freezing nuclei are far more abundant [Kärcher, 2002].

The SAGE instrument is particularly sensitive to the presence of SVCs and provides a global picture of their frequency of occurrence (Figure 1.8).

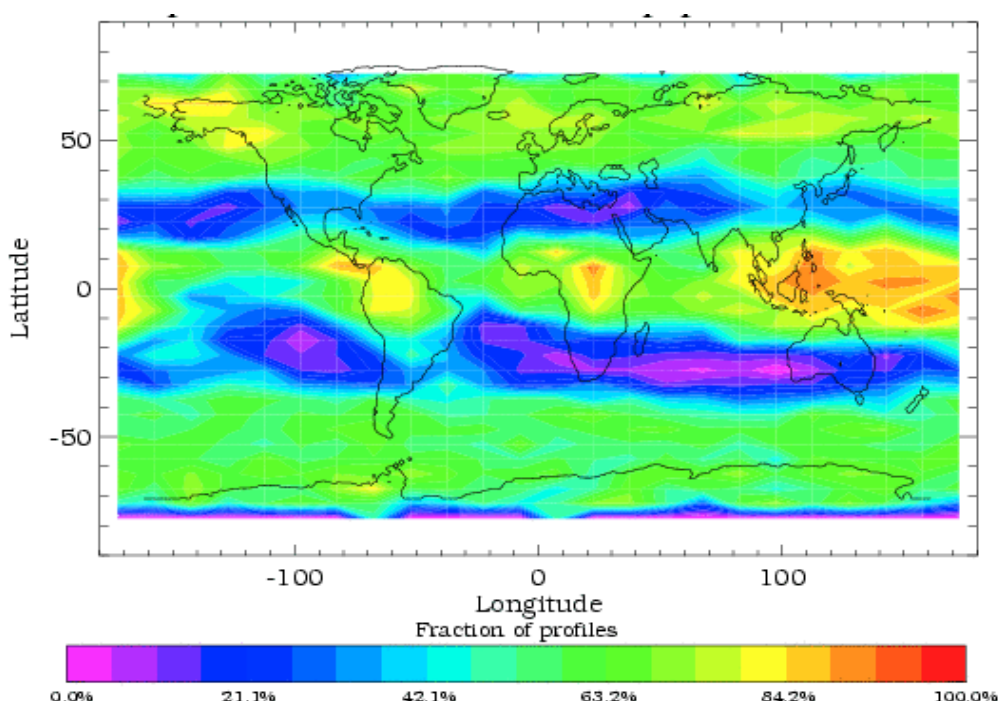


Figure 1.8. Fraction of profiles with subvisible cirrus clouds above the tropopause-3km from SAGE II measurements in the period 1994-1999.

Figure 1.8 shows that SVCs occur globally, with very high frequencies in the tropics and very small frequencies in the subtropical regions of subsidence. A common notion is that the high SVC cover in the tropics is a result of the low temperatures just below the TP. In the polar winter lowermost stratosphere, cirrus also form frequently in cold and humid conditions. Here, a sharp transition between SVCs and PSCs may not always exist. SVCs also appear to be surprisingly widespread at midlatitudes, with a more pronounced seasonal cycle (not shown) despite much higher temperatures. Dynamical factors also play a role in generating SVCs. There appears to be a link between SVC occurrence, deep convection, and synoptic weather systems [Bregman et al., 2002].

Thin cirrus clouds in the tropics are thought to freeze-dry air entering the stratosphere and influence the radiative balance. In regulating the global stratospheric moisture content, they indirectly influence the chemical source of OH radicals and heterogeneous chemical processes. Radiative effects of SVCs have impacts on the stratospheric circulation and the distribution of ozone. At middle and high latitudes, ice particles in SVCs might be directly involved in halogen activation or might indirectly affect ozone by denitrifying the upper troposphere. None of these effects seems to be well understood to date.

It is important to consider SVCs because they can complicate the retrieval of aerosol properties in the tropopause region. We present two examples below.

The abundance of HNO_3 at the tropical tropopause is much lower than in the polar lower stratosphere (typically < 0.3 ppb). Under these conditions, the temperatures below which LTA and NAT can exist tend to be much closer to the ice frost point, or even below it. In situ measurements of NO_y , NO_x , and temperature [Jensen and Drdla, 2002] show that NAT particles could form at the tropical tropopause at HNO_3 mixing ratios of 0.2-0.3 ppb, resulting in a NAT mass of $\sim 0.3 \mu\text{g m}^{-3}$. Jensen and Drdla point out that much larger NAT condensed masses are required to explain enhanced aerosol extinctions around the tropopause, but also note that localized regions of enhanced HNO_3 produced by oxidation of lightning-generated NO might exist. With condensed NAT mass of $\sim 0.2 \mu\text{g m}^{-3}$ NAT layers would be identified as clouds by SAGE II only if the particle diameters were in the optimum range of about 0.6 to 2 μm . The SAGE II extinction ratio measurements (0.5 $\mu\text{m}/1.0 \mu\text{m}$) cannot distinguish NAT clouds from mixtures of optically thin ice clouds and background aerosols.

Measurements of aerosol properties under high relative humidity conditions in the absence of ice clouds are very scarce. Aircraft observations of tropopause aerosols above ice saturation at polar latitudes are available [Petzold et al., 2000]. These data show that the background aerosol develops into a pronounced haze mode at relative humidities over ice between 100-117% at temperatures 201-203 K and H_2O mixing ratios of 12 ppm. Haze mode particles have diameters in the range 0.75-10 μm (mean value 1.2 μm) and number densities 1.7 cm^{-3} . A deliquescence transition in rising air parcels near ice saturation and evaporation without recrystallization in sinking air parcels is evident in the data. Model studies suggest that letovicite along with dissolved HNO_3 might have played a vital role in the haze-mode formation process [Romakkaniemi et al., 2004]. Interestingly, the SAGE II sensors would have classified these liquid haze mode droplets as SVCs, based on their visible extinction coefficients estimated from the in situ data.

1.8 Aviation-produced aerosol

Aircraft jet engines are responsible for the formation of aerosols and condensation trails (contrails) at subsonic (in the TP region between 9-13 km) and supersonic (in the lower stratosphere above 16 km) flight levels. The effects of aviation upon the atmosphere have been reviewed in detail [IPCC, 1999; Lee et al., 2000; Schumann and Ström, 2001]. Here we assess how aviation-produced aerosols may change the background particle concentrations and composition.

Chemical reactions including the production of chemi-ions in the jet engines set the stage for the subsequent evolution of the exhaust in the atmosphere. They determine which fractions of the primary emissions of sulfur (S) and nitrogen oxides are transformed into aerosol-forming species such as H_2SO_4 and HNO_3 . In situ observations and numerical simulations show the presence of molecular cluster ions nucleating a stabilized mode of liquid $\text{H}_2\text{SO}_4/\text{H}_2\text{O}$ particles in young (age < 10 s) aircraft plumes [Yu and Turco, 1997; Schröder et al., 1998; Anderson et al., 1998; Kärcher et al., 1998; Yu et al., 1999; Wohlfrom et al., 2000]. Low-volatile unburned hydrocarbons contribute to the liquid particle mass [Yu et al., 1999], but the organic fraction becomes dominant only for low sulfur fuel (< 50-100 mg S per kg of fuel).

A key parameter controlling the perturbation of atmospheric aerosols by aircraft is the conversion fraction η of fuel S into H_2SO_4 at emission. Figures in the range 0.5-10% are consistent with most observations, with values at the high end in that range perhaps being more likely for modern jet engines [Schumann et al., 2002].

The wide observational variance of aircraft ultrafine particle concentrations seen in measurements taken in the field could be fully ascribed to variations of plume age, particulate organic matter (when low S fuel has been used), and the detection threshold size of condensation nuclei counters (CNCs), using a parameterization scheme that incorporates the key microphysical processes involved in aerosol formation and growth [Kärcher et al., 2000]. The parameterization is able to forecast the complex evolution of liquid aircraft aerosols and can consistently explain most of the field data, increasing the confidence in the current understanding of the physical processes that control the formation of aircraft aerosols. Recent measurements have support the basic features of the above-mentioned ion and sulfur chemistry [Kiendler and Arnold, 2002; Miller et al., 2005]. To better quantify and predict concentrations and composition of chemi-ions that ultimately form new, stable aerosol particles, further research is needed on organic vapors and ion production and recombination processes in the combustor and turbine flow of jet engines.

In the absence of contrails or cirrus clouds, the newly formed aerosols grow by coagulation and are scavenged by larger background aerosols. Condensation of H_2SO_4 and perhaps other material may accelerate the growth rates and thereby reduce scavenging rates. Because it is not yet clear which organic species from the exhaust are involved in new particle formation and growth, the fate of the organic aerosol fraction in the atmosphere is unclear.

Numerical simulations indicate that during the winter season and in regions with low background aerosol surface area density (SAD, < $5 \mu\text{m}^2/\text{cm}^3$), a significant portion (up to several 10%) of the liquid aircraft particles may evolve into potential cloud condensation nuclei (CCN), with diameters larger than 80 nm after 10 days past emission [Yu and Turco, 1999]. However, detailed observations of the microphysical and chemical evolution of these particles

from the plume to the global scale are lacking, representing an important uncertainty in assessing their global impact on perturbing the background CCN population.

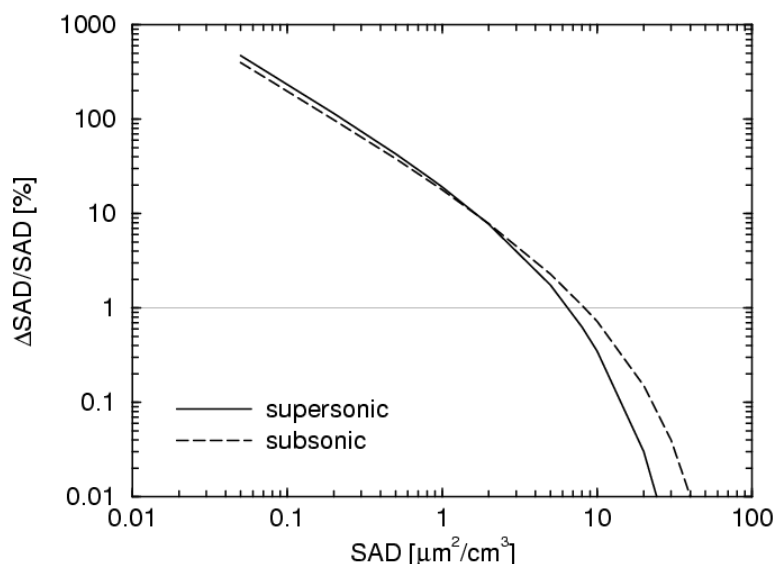


Figure 1.9. Perturbation $\Delta\text{SAD}/\text{SAD}$ of the background aerosol layer versus background aerosol surface area density SAD obtained by a parameterization for subsonic (solid line) and supersonic (dashed line) aircraft. From Kärcher and Meilinger [1998] with changes.

Kärcher and Meilinger [1998] estimated regional-scale, steady-state perturbations of the background sulfate aerosol SAD caused by the actual subsonic or hypothetical supersonic aircraft fleets (Figure 1.9). The aircraft-induced SAD becomes a significant portion ($> 10\%$) for background SAD values below $\sim 2 \mu\text{m}^2/\text{cm}^3$. The relative perturbations ($\Delta\text{SAD}/\text{SAD}$) become insignificant ($< 1\%$, below the horizontal line) whenever the background SAD exceeds $\sim 8\text{-}10 \mu\text{m}^2/\text{cm}^3$, as increasing SAD values enhance scavenging losses of the new liquid particles. Compared to the lower stratosphere ($\text{SAD} = 0.5\text{-}1 \mu\text{m}^2/\text{cm}^3$), aerosol SAD in the tropopause region is much more variable ($0.8\text{-}20 \mu\text{m}^2/\text{cm}^3$), so perturbations from the subsonic fleet may or may not become relevant, depending on the seasonal and regional variations of ambient particles. Background tropopause SAD values below $\sim 2 \mu\text{m}^2/\text{cm}^3$ are observed in regions cleared from aerosols via scavenging by cloud particles [Schröder et al., 2002]. If the upper troposphere/lower stratosphere is perturbed by a strong volcanic eruption ($\text{SAD} = 5\text{-}50 \mu\text{m}^2/\text{cm}^3$), the aircraft impact becomes negligible.

It was also found that aircraft-induced SAD changes increase with the sulfur conversion fractions η at emission (not shown). The increase in SAD is small for $\eta < 2\%$ because the new particles stay small (mean diameters $< 4 \text{ nm}$) and are efficiently scavenged by preexisting particles, but ΔSAD increases rapidly for η values in the range 2-10%. For higher conversion fractions, the mean diameters take on values $> 10 \text{ nm}$ which reduces their effectiveness to increase SAD. Dependences on plume dilution rates and soot emissions are small.

The above estimates of $\Delta\text{SAD}/\text{SAD}$ roughly agree with a statistical analysis of balloon-borne CN data [Hofmann et al., 1998], yielding regional CN enhancements of 5-13% caused by subsonic aircraft, although a direct comparison with the calculations is not possible. CNCs with lower cut-off radii of 10 nm or larger (Chapter 4) as well as instruments measuring optical extinction such as SAGE (Chapter 3) may not be able to detect the full enhancement as the

bulk of the ultrafine particles may not grow past these sizes. A significant impact of subsonic aviation emissions on the atmospheric sulfur mass as suggested previously [Hofmann, 1991] could not be confirmed [Kjellström et al., 1999].

For supersonic aircraft, global simulations including plume effects are available. By coupling the parameterization for the formation of ultrafine plume aerosols from chemi-ions discussed above with the AER far wake and 2D global tracer models (for the latter see Chapter 5), previous simulations of the stratospheric aerosol SAD changes induced by a hypothetical (2015) fleet of supersonic aircraft ignoring subgrid-scale aerosol processing [IPCC, 1999] have been re-evaluated [Kärcher et al., 2000]. The updated simulations include the microphysical transformations on the scale of the plume and reveal comparable changes of SAD, but the range of uncertainty of the previous simulations has been considerably reduced. Further, the impact of particulate organic emissions and S conversion efficiency on SAD can now be studied in global models.

Simulations show that the $\text{H}_2\text{SO}_4/\text{H}_2\text{O}$ particles may also take up HNO_3 at emission or may possibly form NAT-layered ice particles if temperatures are sufficiently cold to induce a contrail [Kärcher, 1996]. While the dissolved HNO_3 may persist in sufficiently cold and HNO_3 -rich stratospheric air (that is, in PSC formation conditions), it is only short-lived (< 1 min) under typical upper tropospheric conditions. The possible increase in PSC occurrence along polar flight routes that are caused by such processes has not yet been investigated. Such contrail-induced PSC formation adds to the increase in PSC occurrence caused by emissions of nitrogen oxides and subsequent enhancements of NAT formation [Peter et al., 1991].

Aircraft engines also emit black carbon (soot) particles. Soot formation and oxidation in jet engines burning kerosene is a very complex issue. It is not yet possible to predict the soot properties as a function of engine parameters. Possibly as a result of rapid coagulation and surface oxidation processes, soot particles acquire a bimodal size distribution. Observations typically show a primary mode with mean diameters (assuming sphericity) of 30-40 nm and a total number concentration of $2\text{-}3 \times 10^7$ per cm^3 of air at the engine exit; a second, more variable mode may exist with mean diameters 150 nm and concentrations $1\text{-}10 \times 10^4 \text{ cm}^{-3}$ [Petzold et al., 1999]. The total number emission index ranges between $2\text{-}20 \times 10^{14}$ particles per kg of fuel (lower figures more representative for modern aircraft), almost independent of the fuel sulfur content [Schumann et al., 2002].

Soot particles become electrically charged by interacting with chemi-ions and free electrons [Sorokin et al., 2003] and quickly acquire an aqueous sulfate/organic-coating because they scavenge part of the smaller liquid exhaust aerosols or trigger binary ($\text{H}_2\text{SO}_4/\text{H}_2\text{O}$) heterogeneous nucleation [Kärcher et al., 1996]. Coagulation between exhaust soot particles is slow owing to the relatively small number densities which are successively reduced by plume dilution effects. Soot particles will be scavenged by ambient aerosol particles on the time scale of days (exact rates depending on the ambient aerosol loading), constituting an important sink of exhaust soot. However, the fraction of exhaust soot remaining externally mixed on the scale of the plume has not been quantified experimentally.

Global models suggest that aviation may be a significant source of soot in the tropopause region [Rahmes et al., 1998; Danilin et al., 1998], but these studies did not include all sources of black carbon. The global distribution and cycling of soot particles from all known sources has been reevaluated using a climate model using a mass-based aerosol module including the key tropospheric aerosol species (black/organic carbon, sulfate, mineral dust, and sea salt) and a

cloud module solving prognostic equations for liquid/ice water content and droplet/ice crystal number concentration [Hendricks et al., 2004]. Surface-derived and aircraft-emitted soot number concentrations are tracked separately and subgrid-scale scavenging of aircraft soot by

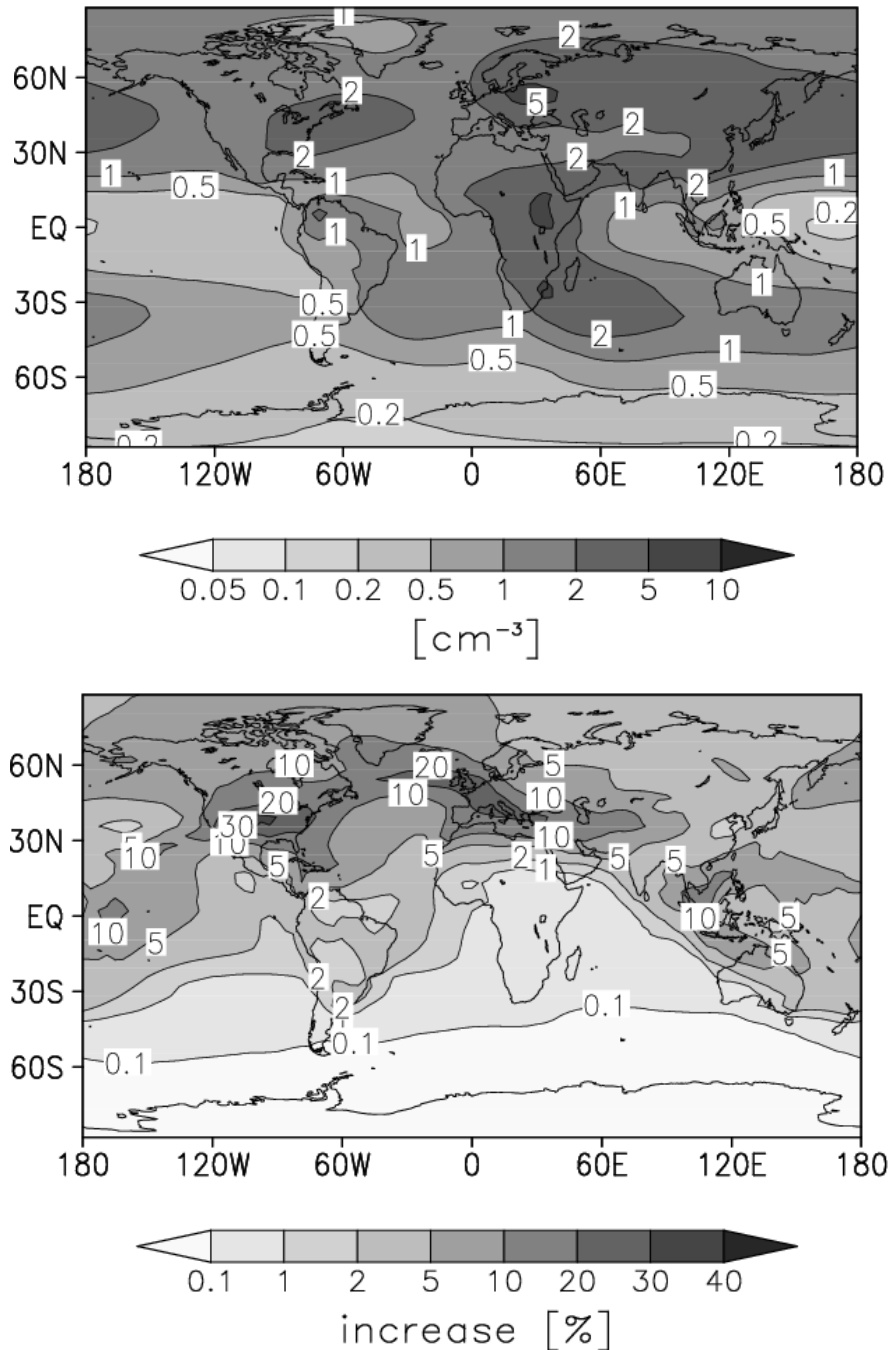


Figure 1.10. Calculated annual and zonal mean soot number concentrations at 250 hPa. Particles from surface sources (left) and from aircraft emissions (relative increase, right). The aircraft contribution shown here is a lower limit estimate and may reach up to 40% when using minimised losses for aircraft BC particles. Adapted from Hendricks et al. (2004).

background aerosols on the plume scale is parameterized.

Aircraft emissions contribute little ($< 1\%$) to the total soot mass, even though these particles are directly injected into the tropopause region. Figure 1.10 shows the corresponding number concentrations. Soot concentrations originating from surface sources range between $0.1\text{--}5/\text{cm}^3$ and thus well exceed $1/\text{cm}^3$ at northern hemisphere midlatitudes. Contrary to mass, the aircraft contribution is significant in terms of particle number and ranges between 10–40% over much of the northern hemisphere. This may have hitherto unknown implications for cirrus cloud formation [Hendricks et al., 2005].

Aircraft emissions into the lowermost stratosphere or mixing of upper tropospheric soot particles from aircraft and other sources over the tropopause in folds may lead to detectable changes in aerosol chemical composition and perhaps size distributions. Mass spectrometric measurements confirm the presence of carbonaceous compounds in stratospheric aerosol (see Section 1.4.3), but it is not clear whether this would lead to changes of aerosol number and size detectable with CNCs. The predicted soot number concentrations (in particular from surface sources) are uncertain owing to a lack of observations to compare with and to various assumptions related to soot properties and wet removal processes.

CHAPTER 2

Precursor Gas Measurements

Lead Authors:

Justus Notholt
Heinz Bingemer

Authors:

Harald Berresheim
James Holton
Anthony Kettle
Emmanuel Mahieu
Stephen Montzka

Contributors:

David Griffith
Nicholas Deutscher
Peter V. Hobbs
Nicola Blake

2.1 Introduction

The stratospheric aerosol layer is formed from sulfur containing trace gases originating in the troposphere, which after oxidation to sulfuric acid cocondense with water as tiny $\text{H}_2\text{SO}_4\text{-H}_2\text{O}$ droplets. The goal of this chapter is to discuss the most important precursor gases that contribute sulfur to this aerosol layer and to assess their atmospheric burdens, distributions, trends, and fluxes.

Sulfur containing trace gases enter the stratosphere mainly through the upper tropical troposphere. Therefore, the physical state of the tropical tropopause layer (TTL) plays an important role in regulating the amount of sulfur that reaches the stratosphere. The relevant aspects of atmospheric dynamics and transport are discussed in Section 2.2. Besides providing a qualitative description of tropical deep convection, this Section also includes some quantitative estimates of exchange rates for transport of air masses between the boundary layer and the TTL. The atmospheric chemistry of relevant sulfur containing species is covered in Section 2.3. The chemistry of these gases depends to a great extent on the radical concentration in the TTL, which is highly variable and not fully understood. Section 2.4 compiles the observations of sulphur containing gases, such as SO_2 , DMS, H_2S , CH_3SH , CS_2 and OCS, with some focus on the latitudinal, vertical and seasonal variability, and long term trends of the two most important ones, namely OCS and SO_2 . Section 2.5 considers the biogeochemical cycles and fluxes of the main compounds, including extraterrestrial sources of stratospheric sulfur. Section 2.6 summarizes and addresses some open questions.

2.2 Dynamics and Atmospheric Transport

An understanding of the dynamical processes responsible for transport into and through the stratosphere requires distinguishing between the *stratospheric overworld* and the *lowermost stratosphere* (Figure 2.1, see Holton et al. [1995]). The stratospheric overworld is the region above ~ 17 km (~ 380 K potential temperature or 110 hPa) in which the isentropic surfaces lie entirely in the stratosphere. Transport into this region from below requires that air parcels undergo radiative heating; transport from this region to lower levels requires radiative cooling. The lowermost stratosphere is the region between the tropopause and the lower boundary of the stratospheric overworld in which isentropic surfaces cross the tropopause so that adiabatic transport and mixing can result in transfers between the upper tropical troposphere and the lowermost stratosphere. The stratospheric aerosol layer lies primarily in the overworld, so that it is transported to and from the overworld that is of most interest for this assessment. It has been known since the work of Brewer [1949] that the primary pathway for transport of trace constituents into the stratospheric overworld is through the tropical tropopause. The global scale meridional circulation responsible for transport into the overworld (commonly called the Brewer-Dobson circulation) is now known to be driven primarily by westward directed wave drag in the extratropical and subtropical stratosphere, caused by atmospheric disturbances propagating upward from the troposphere. Through the Coriolis force such wave drag causes air parcels to drift poleward and thus by mass continuity forces upward motion (accompanied by radiative heating) in the tropics and downward motion (accompanied by radiative cooling) in the extratropics [e.g., Holton et al., 1995].

Although the above simple picture of a stratospherically driven global-scale overturning circulation has been fairly successful in explaining the exchange of long-lived tracer constituents between the troposphere and the stratosphere, the mean Brewer-Dobson circulation cannot provide quantitative understanding of the water vapor budget of the stratosphere [Kley et al., 2000]. Nor can it satisfactorily explain the stratospheric budget of short-lived constituents that

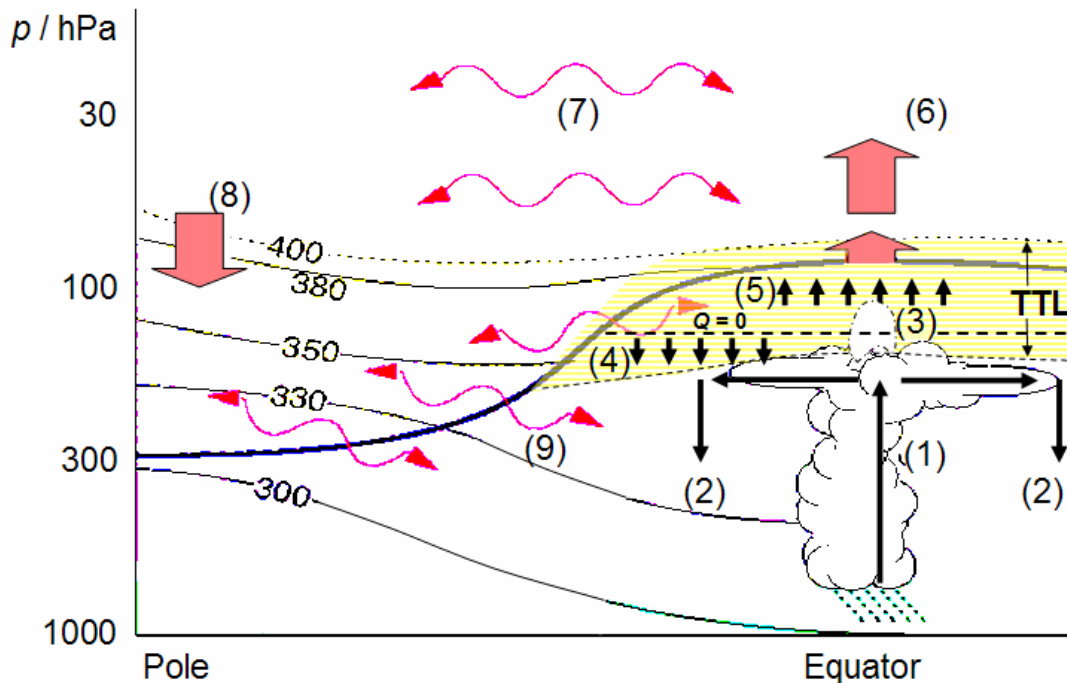


Figure 2.1 Illustration of major transport processes in the troposphere/stratosphere system. The Tropical Tropopause Layer (TTL) is given in yellow. Black solid line: (cold-point) tropopause. Thin dashed line: zero net radiative heating level ($Q = 0$). Numbers at contours: potential temperature levels. The TTL is between approximately 340–400 K potential temperature. Bracketed numbers: (1) Deep convection lifting low level air into the upper troposphere, horizontal arrows indicating main detrainment. (2) Downward branches of tropospheric Hadley circulation. (3) High cloud tops penetrating TTL. (4) Descent in TTL below $Q = 0$. (5) Radiatively driven ascent in TTL above $Q = 0$. (6) Upward branch of Brewer-Dobson circulation (tropical pipe). (7) Stratospheric stirring and meridional transport by breaking waves. (8) Large scale subsidence. (9) Quasi-adiabatic exchange across tropopause. (Th. Peter, personal communication, modified after Holton et al. [1995].)

undergo chemical or physical transformations during passage through the tropical troposphere [Prather and Jacob, 1997; Sherwood and Dessler, 2003; Notholt et al., 2005].

The transport of short-lived constituents from the tropical boundary layer to the stratosphere is complicated by the requirement that such constituents must pass through the layer of the tropical atmosphere between about 12 km (~ 200 hPa, $\theta \sim 350$ K) and the cold point tropopause (16–17 km, 100–90 hPa, $\theta \sim 380$ K). This layer, which has mixed characteristics intermediate between those of the troposphere and stratosphere [e. g. Highwood and Hoskins, 1998; Thuburn and Craig, 2002] was referred to as the *substratosphere* by Thuburn and Craig. Although the cold point tropopause is important for the dehydration of the air entering the stratosphere; the cold point has no special significance for transport of other constituents. In fact, some tropospheric circulations (such as overshooting convection, monsoon circulations, and equatorial waves) can extend for some distance above the cold point tropopause. Thus, it seems appropriate to extend the definition of the tropical transition layer to include the first few kilometers above the cold-point. For this reason, we refer to this region as the Tropical Tropopause Layer (TTL) rather than the substratosphere. The TTL as defined here includes the entire region between the level at which the temperature profile begins to depart from the moist adiabatic profile enforced by tropospheric convection (~ 10 km in undisturbed regions to ~ 12 km in disturbed regions [Gettelman and Forster, 2002] to the level in the stratospheric overworld beyond which the influence of tropospheric circulations becomes insignificant (~ 50 hPa, ~ 20 km, $\theta \sim 470$ K).

Within the TTL as defined above, a number of parameters undergo rapid change in the vertical: in the lower portion of the TTL (~12–14 km) convective mass fluxes decrease rapidly with height, corresponding with the main convective outflow, and clear sky radiative cooling rates also decrease rapidly with height. Above about 14 km (but well below the cold-point) ozone mixing ratios generally begin to increase substantially with height and the mass flux owing to the stratospherically driven Brewer-Dobson circulation begins to dominate over the convective mass flux. The cold-point tropopause, which generally occurs between 16 and 17.5 km is crucial in dehydrating air to stratospheric mixing ratios, and to the formation of subvisible cirrus. Above 14 km, where convective transport and mixing are small, large-scale horizontal transport processes become increasingly important for meridional transport and mixing of trace constituents. Horizontal transport may also be important for dehydration, through its role in transporting air through regions where the cold-point temperatures are anomalously low, such as the “cold trap” of the Western Pacific [Gettelman et al., 2002b; Holton and Gettelman, 2001].

At the bottom of the TTL the net vertical transport in the tropics is determined by the difference between the upward mass flux in deep convection and the subsidence in the radiatively cooling clear air. The observed annual mean mass flux in the Hadley circulation between 15°N and 15°S is about 10^{11} kg/s [Hartmann, 1994]. The clear sky radiative cooling rate in the tropical troposphere is ~1.6 K/day [e.g., Hartmann et al., 2001], leading to a downward mass flux of about 2.0×10^{11} kg/s between 15°N and 15°S. The estimation is based on the assumption of a dry adiabatic descent and that the convective disturbances cover less than 10 % of the tropics, as confirmed by satellites. Thus the upward flux from the boundary layer in convection must be about 3.0×10^{11} kg/s. It can be assumed that about 50 % of the mass flux from the boundary layer reaches the base of the TTL, with the rest detraining into the lower and middle troposphere [Gettelman et al., 2002a]. Since virtually all of the upward mass flux from the boundary layer to the upper tropical troposphere must be in convective ascent, and about 50 % of the convective mass flux appears to reach the TTL, then the estimate for mass flux reaching the TTL is 1.5×10^{11} kg/s.

Tropopause foldings at midlatitudes also transport tropospheric air into the stratosphere and vice versa. However, none of the air exchanged in tropopause folding get above the lowest portion of the midlatitude stratosphere so that this is not a viable mechanism to get air into the stratospheric overworld. There is some quasi-adiabatic exchange between the deep tropical upper troposphere and the subtropical stratosphere associated with monsoon circulations, synoptic systems and planetary wave breaking but this does not affect the stratosphere above the 100 hPa level.

The air in the TTL gets “trapped” in the subtropical anticyclones of the West Pacific and spirals around these anticyclones while gradually ascending [Hatsushika and Yamazaki, 2003]. Since the mass of the tropical boundary layer and mass of the TTL are each about 1.3×10^{17} kg, the average replacement time for air in the TTL by boundary layer air is about 10 days. In the lower portion of the TTL, the replacement time will be shorter, whereas in the upper portion it can be as long as several months [Gettelman et al., 2002a, b]. Furthermore, according to Rosenlof and Holton [1993] the annual flux across the 100 hPa surface (near the coldpoint) in the 15°N and 15°S latitude range is 8.5×10^9 kg/s, which is only ~3% of the flux of air out of the tropical boundary layer.

Thus, although the above estimates are rather uncertain, it is clear that only a small fraction of the air leaving the tropical boundary layer actually crosses into the tropical stratosphere. It is also clear that time-scales for transport through the TTL can be sufficiently long so that short-

lived chemical precursors may undergo substantial chemical transformations. Furthermore, the very large ratio of horizontal to vertical transport in the upper part of the TTL suggests that a significant fraction of air in the TTL may be processed through cold trap regions such as the tropical West Pacific, where the tropical tropopause temperatures are colder than average, and subvisible cirrus clouds are ubiquitous [Wang et al., 1996].

2.3 Sulfur Chemistry

The gaseous precursor for the stratospheric aerosol sulfate is sulfuric acid (H_2SO_4). In the troposphere gaseous H_2SO_4 has a lifetime on the order of minutes and is efficiently removed by wet and dry deposition to the Earth's surface, deposition to pre-existing aerosol particles and by gas-to-particle conversion forming new sulfate particles. Therefore, with the exception of sporadic direct injections from volcanic eruptions, stratospheric H_2SO_4 is thought to originate from OCS photolysis [Crutzen, 1976] and from in situ oxidation of SO_2 , OCS and (possibly) reduced sulfur gases reaching the stratosphere. The dominant reactions contributing to

Table 2.1. Important gas phase reactions and rate constants in stratospheric sulfur chemistry

Initial Reaction	λ	phot, s^{-1} ; k , $\text{cm}^3 \text{molec}^{-1} \text{s}^{-1}$	Ref.
$\text{OCS} + h\nu \rightarrow \text{CO} + \text{S}$	$\leq 388 \text{ nm}$	1×10^{-9} ($z = 20 \text{ km}$)	1
$\text{OCS} + \text{O} \rightarrow \text{CO} + \text{SO}$		$2.1 \times 10^{-11} \exp(-2200/T)$	2
$\text{OCS} + \text{OH} \rightarrow \text{CO}_2 + \text{HS}$		$1.1 \times 10^{-13} \exp(-1200/T)$	2
$\text{SO}_2 + \text{OH} + \text{M} \rightarrow \text{HOSO}_2 + \text{M}$		$(k_0/1+(k_0/k_\infty)) \times 0.6^B$ $B = 1/(1+(\log_{10}(k_0/k_\infty))^2)$ $k_0 = 3 \times 10^{-31} (T/300)^{-3.3} [\text{M}]$ $k_\infty = 1.5 \times 10^{-12}$	2
$\text{CH}_3\text{SCH}_3 + \text{OH} \rightarrow \text{SO}_2, \text{OCS}, \text{other products}$		$k_{\text{abs}} = 1.2 \times 10^{-11} \times \exp(-260/T)$ $k_{\text{add}} = 10^{-39} [\text{O}_2] \exp(5820/T) / \{1+5 \times 10^{-30} [\text{O}_2] \exp(6280/T)\}$	2; see text
$\text{CH}_3\text{SCH}_3 + \text{O} \rightarrow \text{CH}_3\text{SO} + \text{CH}_3$		$1.3 \times 10^{-11} \exp(410/T)$	2
$\text{CS}_2 + \text{OH} + 2\text{O}_2 \rightarrow \text{OCS} + \text{HO}_2 + \text{SO}_2$		$\{1.25 \times 10^{-16} \exp(4550/T)\} / \{T + 1.81 \times 10^{-3} \times \exp(3400/T)\}$	2, 3
$\text{CS}_2 + \text{O} \rightarrow \text{CS} + \text{SO}$		$3.2 \times 10^{-11} \exp(-650/T)$	2
$\text{H}_2\text{S} + \text{OH} \rightarrow \text{SH} + \text{H}_2\text{O}$		$6.0 \times 10^{-12} \exp(-75/T)$	2
$\text{CH}_3\text{SH} + \text{OH} \rightarrow \text{CH}_3\text{S} + \text{H}_2\text{O}$		$9.9 \times 10^{-12} \exp(360/T)$	2
$\text{SO}_2 + h\nu \rightarrow \text{SO} + \text{O}$	200-230 nm		4a
	$< 218 \text{ nm}$		4b
$\text{SO}_3 + h\nu \rightarrow \text{SO}_2 + \text{products}$	190-230 nm	2×10^{-7} ($z = 20 \text{ km}$)	5
$\text{H}_2\text{SO}_4 + h\nu \rightarrow \text{SO}_2 + \text{products}$	195-330 nm	1×10^{-11} ($z = 25 \text{ km}$)	6
$\text{H}_2\text{SO}_4 + h\nu \rightarrow \text{SO}_3 + \text{H}_2\text{O}$	Vis & NIR		7

phot = photolysis rate constant at altitude z ; $\text{M} = \text{O}_2, \text{N}_2$. Ref.: 1: Chin and Davis [1995]; 2: Sander et al. [2003], Atkinson et al., [2004]; 3: Hynes et al. [1988]; 4a: Brasseur and Solomon [1984]; 4b: Finlayson-Pitts and Pitts [1986]; 5: Burkholder and McKeen [1997]; 6: Burkholder et al. [2000]; 7: Vaida et al. [2003].

stratospheric H_2SO_4 are listed in Table 2.1 (by estimated degree of importance). The table also shows recent estimates for the photolytic sinks of SO_2 , SO_3 , and H_2SO_4 which are likely to be important in the middle and upper stratosphere [Burkholder et al., 2000; Burkholder and McKeen, 1997; Rinsland et al., 1995; Reiner and Arnold, 1997]. The intermediate products of the photolysis and oxidation reactions listed in Table 2.1 are short-lived (e.g., S, SO, HS) and rapidly converted by further oxidation with O, O_2 , O_3 , OH, and/or HO_2 .

Most of these mechanisms contributing to the stratospheric H_2SO_4 budget have already been considered by Crutzen [1976] and Turco et al. [1980] and were re-evaluated by Chin and Davis [1995]. Since these earlier studies an additional mechanism has been proposed to be of potential importance as a source of stratospheric H_2SO_4 especially over tropical marine regions, namely rapid upward transport in deep convection of dimethylsulfide (DMS; CH_3SCH_3) to the UT/LS [e.g., Chatfield and Crutzen, 1984; Thornton et al., 1997].

In addition to previously known products of DMS oxidation [e.g., Berresheim et al., 1995] OCS may also have to be taken into account [Kettle et al., 2002a]. The latter compound has been identified in laboratory studies as a product of the DMS oxidation by OH with a yield of 0.7% S at 1000 hPa at low NO_x concentrations [Barnes et al., 1994; 1996; Arsene et al., 2001]. This result suggests a significant re-evaluation of current model predictions of the stratospheric OCS burden and its contribution to stratospheric H_2SO_4 . However, based on the uncertainties in the literature data we recommend that these laboratory results should be further substantiated.

Moreover, better estimates of the global flux of DMS into the UT/LS must first be established to evaluate the importance of this potential source of stratospheric OCS. At these altitudes DMS is oxidized, not only by OH but also by $\text{O}(^3\text{P})$, the latter reaction becoming dominant approximately above 10 km. Similar considerations apply to the potential contributions from CS_2 oxidation by OH and $\text{O}(^3\text{P})$. Significant intrusions of CS_2 and H_2S into the UT/LS may only be important during sporadic volcanic eruptions and/or strong convective transport over corresponding source regions (see the section on flux estimates which also includes methyl mercaptan, CH_3SH). Considering H_2S and CH_3SH the corresponding rate constants with respect to OH are well known. However, the rate constant with respect to reaction with $\text{O}(^3\text{P})$ is reported only for H_2S [Sander et al., 2003]. Nevertheless, in the UT/LS regime the latter reaction is negligible compared to the oxidation of H_2S by OH. Reactions of DMS, CS_2 , H_2S , and CH_3SH with O_3 have either not yet been studied or only rate constants for 298 K have been reported (for DMS and H_2S ; see Sander et al., [2003]). Here we consider stratospheric sulfate production from these compounds via O_3 reaction to be negligible. Also direct photolysis of DMS, CS_2 , H_2S , dimethyl disulfide (DMDS), or CH_3SH in the UT/LS should be negligible compared to the rate of reaction of these compounds with OH.

Recently it has been suggested, based on ab initio calculations of absorption cross sections that excitation of vibrational overtones of H_2SO_4 in the near-infrared and visible may lead to photolysis, forming sulfur trioxide (SO_3) and water [Vaida et al., 2003]. This may help reducing discrepancies between observations and models at high altitudes above the stratospheric aerosol layer. This mechanism still needs to be verified experimentally.

Using reactions from Table 2.1 and vertical profiles of the photodissociation rates of OCS [Chin and Davis, 1995], concentrations of O and OH [Spivakovsky et al., 2000; Brasseur et al., 1999; DeMore et al., 1997; Brasseur and Solomon, 1984], pressure and temperature (U.S. Standard Atmosphere, U.S. Government Printing Office, Washington, D.C., 1976) the chemical lifetimes of OCS, SO_2 , DMS, and CS_2 have been calculated. The results are shown in Figure 2.2. For DMS, CS_2 , H_2S , and CH_3SH the calculations extend only up to 25 km since intru-

sions of these compounds higher up than that altitude are expected to be negligible. The results show that the contributions of OCS to H_2SO_4 are dominated by photolysis followed by reaction with O and OH (compare with modelling results in Chapter 6).

The lifetimes of most precursor gases depend on the OH concentrations. Recent observations reveal that the HO_x levels in the upper tropical troposphere were frequently higher by a factor of 2-4 compared to simulations based on the primary source of HO_x, the photolysis of O₃ [Jaeglé, 2001, Jaeglé et al., 2001; Arnold et al., 1997; Folkins et al., 1997; Jaeglé et al., 1997]. This will influence the lifetime of SO₂ to a great extent and can have a direct influence on the aerosol formation efficiency.

2.4 Observations

2.4.1 Carbonyl sulfide (OCS)

OCS is the most abundant and longest chemically-lived sulfur-bearing gas in the unpolluted troposphere. These characteristics combined with a low solubility allow a significant fraction

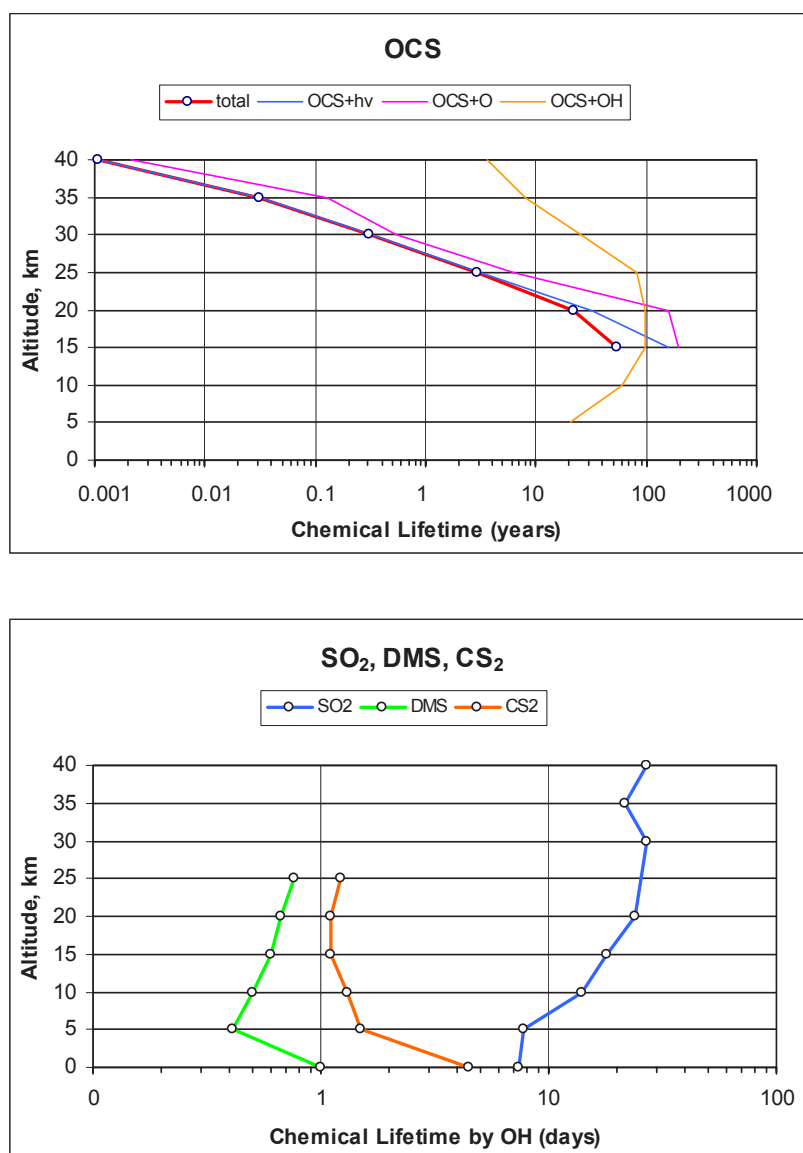


Figure 2.2 Chemical lifetimes of OCS with respect to photolysis, reaction with O and OH, and the sum of all three processes (top) and of SO₂, DMS, and CS₂ wrt reaction with OH (bottom).

of this compound to reach the stratosphere. There, a fraction of OCS is oxidized to SO_2 and subsequently to H_2SO_4 , thus contributing to the global stratospheric aerosol layer, while the rest is carried back into the troposphere by the general circulation. This was described first by Crutzen in 1976.

The main sources of atmospheric OCS appear to be (in order of their importance, Kettle et al. [2002a]): the atmospheric oxidation of (1) DMS from marine planktonic origin, of CS_2 from (2) industrial and (3) from marine natural origin, and (4) the gas exchange of OCS between the oceans and the atmosphere. The main sinks are identified as (1) assimilatory uptake by land plants, (2) uptake by oxic soils, and (3) atmospheric oxidation by hydroxyl radicals [Kettle et al., 2002a].

Significant seasonality with maxima in summer may be expected for those source and sink processes that are triggered by sunlight, like the atmospheric photochemical production and destruction of OCS, the marine photochemical production of dissolved OCS from planktonic precursors, and the assimilatory uptake of OCS by land plants. Bearing in mind the high biogeographical variability of marine and terrestrial species and biomass, of oceanographic and climatological factors affecting fluxes (e.g. wind-driven air/sea exchange, nutrition, assimilation rates, etc.), a complex geographical and seasonal pattern of sources and sinks of OCS may be expected. This chapter discusses observations of atmospheric OCS in the light of present knowledge of its biogeochemical fluxes, whose main features are (a) a strong continental sink by assimilation during summer, and (b) a marine photochemical source during summer.

A major breakthrough was recently achieved from measurements in a global surface monitoring network [Montzka et al., 2001] and from analysis of ice and firn cores [Sturges et al., 2001; Montzka et al., 2004]. The new OCS surface data [Montzka et al., 2001] explain much of the previously unexplained variability, in accordance with the main source and sink characteristics, i.e. a continental sink and a marine source during summer. The recent firn and ice core data [Montzka et al., 2004] however revealed a substantial, yet unexplained variability of preindustrial atmospheric OCS, pointing to major gaps in our understanding of the natural OCS cycle and its relation to climate.

The observations of OCS reported here were performed by different measurement techniques. In-situ measurements have been performed by gas chromatography (GC) with flame photometric detectors (FPD), electron capture detectors (ECD) or mass spectrometers (MS). Remote sensing techniques measure the absorption of OCS in the infrared by using the sun as light source. These different techniques measure different atmospheric quantities. While current remote sensing instruments are sensitive to the total column density of OCS at a given location or through a slice of the atmosphere, the chromatography-based instruments detect local concentrations. Provided the shape of the vertical profile of the trace gas mixing ratio is realistic total column densities from the former instruments can be converted to volume mixing ratios (vmr), but with limited confidence. In the case of OCS, a constant tropospheric vmr with decreasing vmr in the stratosphere is often assumed, based upon measurements from balloons and from space. In addition to the OCS total column measurements, the analysis of the pressure broadened spectral line shape of OCS absorption lines observed in solar spectra allows the retrieval of concentration profiles from the remote sensing observations with an altitude resolution of about 4-8 km [Notholt et al., 2003], see also Figure 2.11.

Annual and hemispheric mean mixing ratio of tropospheric OCS

In the Northern Hemisphere a wide range of annual mean mixing ratios has been reported (Figure 2.3). The highest annual means have been measured in the free troposphere remotely

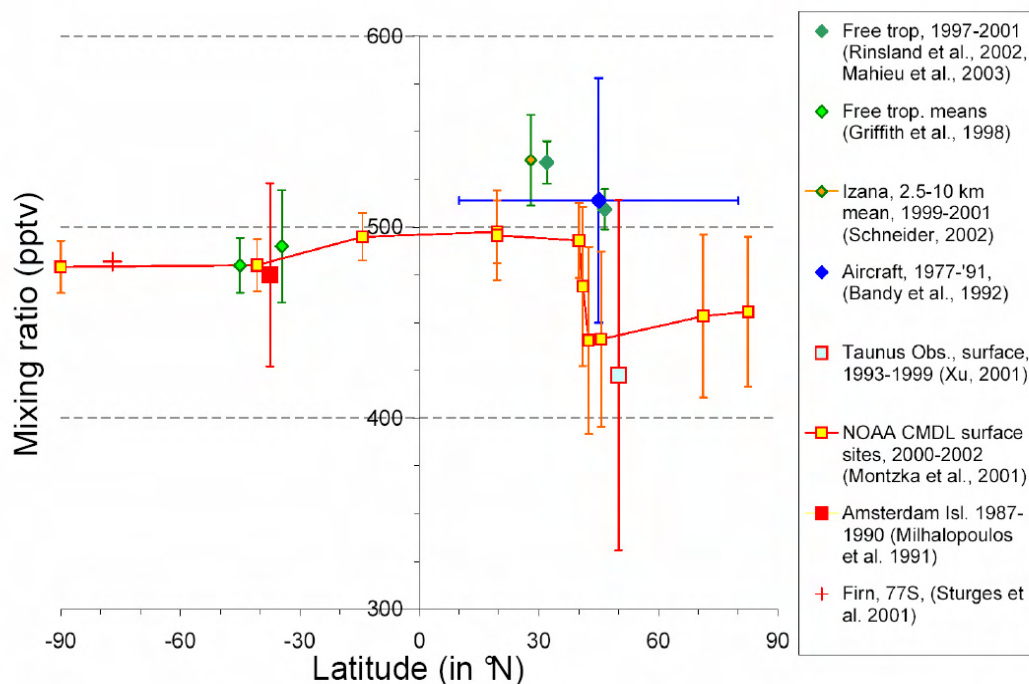


Figure 2.3 Annual means of atmospheric OCS measured at different locations across the globe. Error bars shown indicate ± 1 s.d. of the results obtained at each location and also include variability associated with seasonal changes (see Section 1.3). Results shown are free tropospheric means from long-path absorbance measurements for recent years, when available. Green filled diamonds: 1997-2001 [Mahieu et al., 2003]; 1997-2002 [Rinsland et al., 2002]; green diamonds filled with light green: 1993-1997 at 45°S and 1996 only at 34°S [Griffith et al., 1998]; green diamond filled with orange: 1999-2002 [Schneider, 2002]. Also shown are the mean from a variety of aircraft campaigns during 1977-1991 (blue diamond [Bandy et al., 1992]), from a marine surface site during 2 years in the late 1980s (red square [Milhalopoulos et al., 1991]), from a continental site during 1993-2000 (red square filled with light blue [Xu, 2001]), from a range of marine and continental sites, two of which are at high altitude, during 2000-2002 (red squares filled with yellow [Montzka et al., 2001]), and as inferred from firn measurements in 1998 (red cross [Sturges et al., 2001]).

by long path absorption and in situ on aircraft. Lower mixing ratios have been observed at selected surface sites, and the lowest mixing ratios have been measured at rural forested continental sites at mid-latitudes. From remote sensing instrumentation, a free tropospheric annual mean of 534 pptv was estimated for 1997-2001 above Kitt Peak (31.9°N, 111.6°W, 2090 m) [Rinsland et al., 2002] and 509 ppt were extracted from the data of Mahieu et al., [2003] for the free tropospheric mean above the high Alpine station on the Jungfrauoch (46.5°N, 8.0°E, 3580 m) during 1997-2001. A recently published record of long-path absorbance measurements above Izaña (28.3°N, 16.5°W, 2367 m) suggested an annual mean tropospheric mixing ratio of 530 ppt during 1999-2000 [Schneider, 2002; T. Blumenstock, personal communication, 2002]. A mean mixing ratio of 514 ppt was reported by Bandy et al. [1992] during multiple aircraft campaigns over a wide region in the Northern Hemisphere from 1977-1991 (10°N to 80° N latitude, and 52°E to 155°W longitude, at various flight levels).

Annual mean OCS mixing ratios of 490 to 500 ppt have been measured at Hawaii within the marine boundary layer (Kumukahi, 19.5°N, 154.8°W, 3 m) and atop the Mauna Loa volcano (19.5°N, 155.6°W, 3397 m). A similar annual mean was found at the high altitude continental site Niwot Ridge, USA (40°N, 105°W, 3475 m), see Figure 2.3 [Montzka et al., 2001]. Substantially lower annual means have been reported for low-altitude, continental sites in Europe (422 ppt during 1993-1999 at the Taunus Observatory, 50°N, 8°E, 815 m a.s.l., sampling inlet

is 2 m above ground [Xu, 2001]), and North America (444 ppt during 2000-2002 at Harvard Forest, 42.5°N, 72.2°W, 340 m a.s.l., inlet is 29 m above ground; and 446 ppt during 2000-2002 on a tall tower in Wisconsin, 45.6°N, 90.2°W, inlet is 868 m a.s.l., which is 396 m above ground [Montzka et al. 2001]). Results from surface sites in the Arctic in recent years also suggest low OCS mixing ratios; annual means at Barrow, USA (71.3°N, 157°W, 8 m) and Alert, Canada (82.5°N, 62.3°W, 210 m) during 2000-2002 were found equal to 455 and 460 ppt, respectively [Montzka et al., 2001].

In the Southern Hemisphere, a much narrower range of annual mean mixing ratios have been reported at Earth's surface and in the free troposphere (Figure 2.3). Griffith et al. [1998] report annual means for the free troposphere above Lauder, NZ (45.0°S, 169.7°E, 370 m) and Wollongong, Australia (34.4°S, 150.9°E, 30 m) during the 1990s of 480 and 490 ppt. An annual, ambient air mean of 482 ppt is suggested by firn-air measurements for recent years at Dronning Maud Land, Antarctica (77°S, 10°W, 2300 m [Sturges et al., 2001]). Furthermore, results from Amsterdam Island (37.8°S, 77.5°E, ~25 m) in the late 1980s suggest an annual mean OCS mixing ratio of 475 ppt for that time [Milhalopoulous et al., 1991]. In measurements from flasks collected at South Pole (90°S, 2837 m) and Tasmania (40.7°S, 144.7°E, 94 m), annual mean mixing ratios of 480 and 483 ppt are estimated for the period 2000-2002 [Montzka et al., 2001]. A slightly higher annual mean of 495 ppt was measured at American Samoa (14.3°S, 170.6°W, 77 m) by the same investigators.

Given our understanding of OCS sources and sinks, the wide range of annual mean mixing ratios reported for the Northern Hemisphere may reflect strong mixing ratio gradients across latitudes, longitudes, altitude and season. Such gradients would make estimates of hemispheric means and mean hemispheric differences dependent upon the timing and location of OCS measurements. This may explain the wide disparity among past estimates of mean hemispheric differences for OCS (i.e., the inter-hemispheric ratio, or IHR). For example, the IHR (NH/SH) estimated from free tropospheric annual mean mixing ratios at 2 sites in each hemisphere has been estimated at 1.15 [Griffith et al., 1998]. Given the slow decline observed for OCS in the NH [Rinsland et al., 2002], an updated estimate from data collected at these sites suggests an IHR of only 1.08 during the late 1990s. When estimated with annual mean data solely from *surface* sites (land and ocean), however, an IHR for OCS in recent years of approximately 0.97 is obtained [Montzka et al., 2001]. The true IHR of OCS at present likely lies somewhere between 1.08 and 0.97. Results from the analysis of firn air at a single site in each hemisphere [Sturges et al., 2001] also point to the possibility that the IHR of OCS has changed in recent years, although this conclusion may be affected to some degree by relative seasonal mixing ratio variations at either of the two sites involved.

Estimates of the IHR for OCS have also been derived from short-duration measurement campaigns onboard ships and aircraft [Torres et al., 1980; Bingemer et al., 1990; Johnson et al., 1993; Weiss et al., 1995; Notholt et al., 2000; Xu et al., 2001]. Such estimates, however, are likely influenced by seasonal and local effects on OCS mixing ratios (see section below). Accordingly, more accurate estimates of the IHR for OCS will have to await more comprehensive sampling programs and ultimately may be best derived from an assimilation of available measurement data by models.

Latitudinal distribution of tropospheric OCS

The existing observational data base of the latitudinal distribution of OCS (Figures 2.4 and 2.5) at first glance appears as an unruly scatter plot. However, it can be qualitatively understood, based on recent knowledge of the seasonality and distribution of OCS sources and

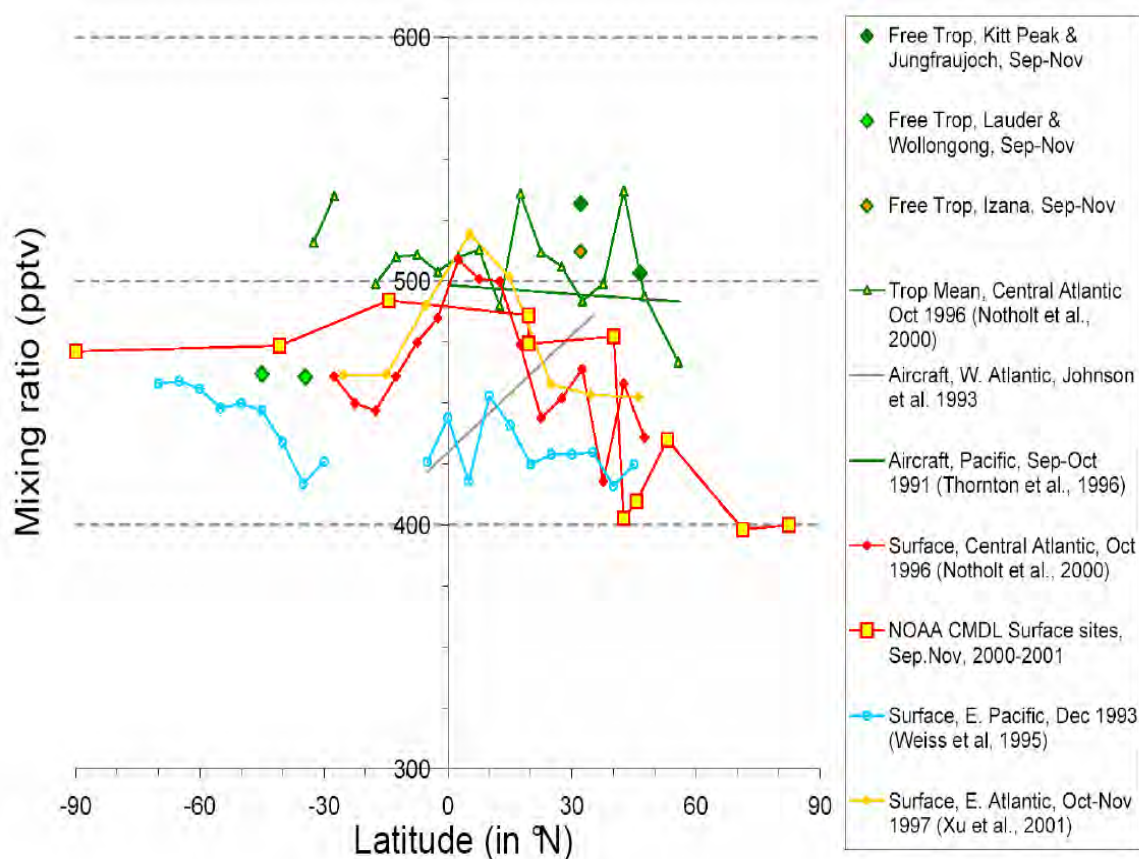


Figure 2.4 Mean mixing ratios of OCS as a function of latitude during September-December of different years. Free tropospheric means: Green filled diamonds: Mahieu et al. [1997] and Rinsland et al. [2002]; green triangles filled with light green: Griffith et al. [1998]; green diamond orange filled: Schneider [2002]; green triangles yellow filled: Central Atlantic, Notholt et al. [2000]; straight green line: aircraft measurements in Pacific, Thornton et al. [1996]; and a fit to aircraft results in the Western Atlantic: grey line, Johnson et al. [1993]. Also shown are surface means from ocean cruises in the Atlantic (gold diamonds and line [Xu et al., 2001]; red diamonds and line [Notholt et al., 2000]) and the Pacific (light-blue circles and line [Weiss et al., 1995]), and surface means from a variety of surface sites during 2000-2002 (yellow-filled red squares and line [Montzka et al., 2001]).

sinks [Kettle et al., 2002a] and the broad scale seasonality detected from measurements by the surface monitoring network of NOAA [Montzka et al., 2001; Dutton et al., 2001]. For clarity of presentation the cases of Northern Hemisphere fall (September through November, Figure 2.4) and spring (April through June, Figure 2.5) are distinguished.

Consideration of results from ocean cruises, aircraft, long-path absorbance, and long-term land-based measurements suggests the presence of seasonally varying gradients across longitudes and altitude for OCS in the troposphere. For example, similar mixing ratios (~500 ppt) have been observed in the Northern Hemisphere free troposphere above both the Atlantic and Pacific Basins during September through December in different measurement campaigns over 10 years apart, see Figure 2.4 [Thornton et al., 1996; Notholt et al., 2000; Schneider, 2002]. Near the equator (up to ~20°N), these free tropospheric means are very similar to surface data obtained in the Atlantic [Notholt et al., 2000; Xu et al., 2001], and in the Pacific after Kumukahi [Montzka et al., 2001], suggesting only small vertical gradients within the troposphere during this time of year. However, north of 20° a comparison of free-tropospheric means to surface data suggests the presence of strong vertical gradients in OCS mixing ratios. Surface

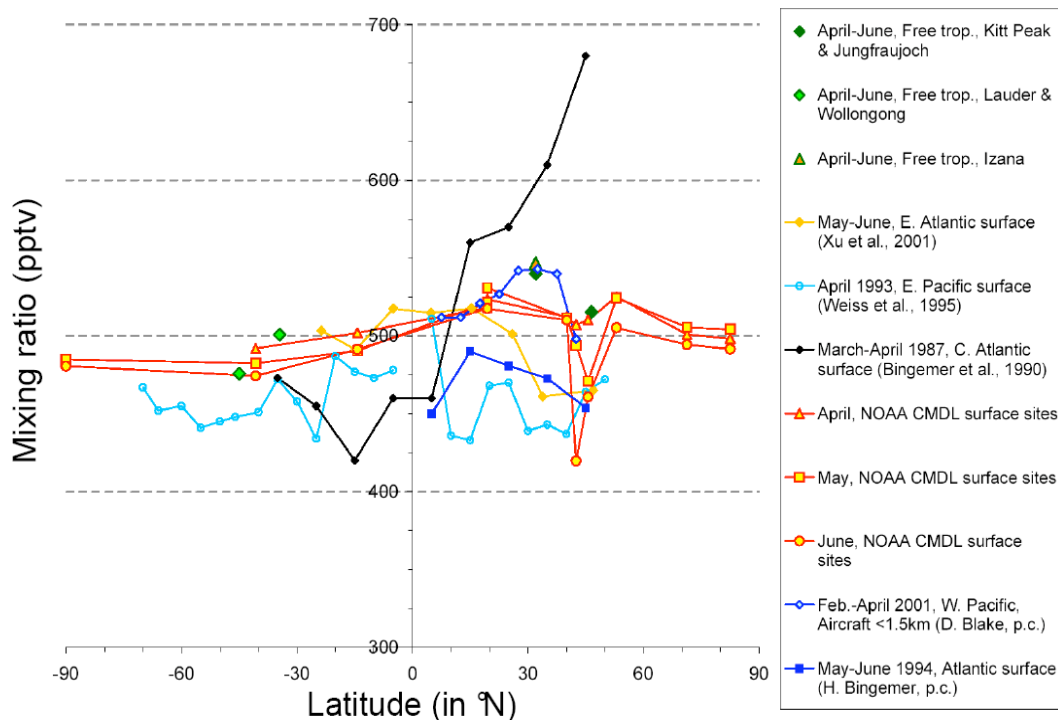


Figure 2.5 Mean mixing ratios of OCS as a function of latitude during April-June for different years. Free tropospheric means: Green filled diamonds: Mahieu et al. [1997] and Rinsland et al. [2002]; green triangles filled with light green: Griffith et al. [1998]; green triangle orange filled: Schneider [2002]. Also shown are surface means from ocean cruises in the Atlantic (black diamonds and line [Bingemer et al., 1990]; dark blue squares and line, H. Bingemer, unpublished data, 1994; gold diamonds and line [Xu et al., 2001]) and the Pacific (light-blue circles and line [Weiss et al., 1995]), and surface means from a variety of surface sites during 2000-2002 (orange symbols and lines, squares=April, triangles=May, circles=June [Montzka et al., 2001]). Results from aircraft over the west Pacific Ocean during February-April 2001 (TRACE-P; D. Blake of UCI, unpublished data, 2001; dark blue lines and points) are medians for 5 degree latitude bins for samples collected below 2 km altitude.

mixing ratios both over land (Niwt Ridge, Wisconsin, Harvard Forest [Montzka et al., 2001] and sea (cruise results from Xu et al. [2001] and Notholt et al. [2000]; coastal results from Mace Head (53°N), and Trinidad Head (41°N) [Montzka et al., 2001]) are between 25 and 100 ppt lower than free-tropospheric means [Thornton et al., 1996; Mahieu et al., 2003; Notholt et al., 2000; Rinsland et al., 2002; Schneider, 2002], see Figure 2.4. In the Northern Hemisphere OCS mixing ratios at the surface reach a minimum during these months [Xu et al., 2001; Montzka et al., 2001; Dutton et al., 2001] and vertical gradients arising from rapid terrestrial uptake might be largest then.

Measurements onboard aircraft along the eastern coast of both North and South America during August and September of 1989 [Johnson et al., 1993] showed lower mixing ratios in the tropics and higher mixing ratios towards mid-latitudes. Such differences may suggest strong gradients across longitude in this region that are not typical of other regions. Such a gradient would be consistent with a strong land-based source over the eastern USA. Weiss et al. [1995] also obtained unusual results during a December cruise in the Pacific Ocean. Although instrument problems during this mission may explain some of the differences (see text below), the observed OCS levels in this case may have been dominated by regional effects.

During April (Figure 2.5), latitudinal gradients measured at land-based surface sites and within the free troposphere show fairly good consistency and they suggest slightly higher

mixing ratios in the Northern- compared to the Southern Hemisphere. As the months progress from April to June, however, sharply lower mixing ratios are noted at the continental, mid-latitude sites, presumably because of vegetative losses for OCS at this time of year. Over the oceans a much wider range of results have been obtained. Although Bingemer et al. [1990] observed much higher mixing ratios in the Northern Hemisphere compared to the Southern Hemisphere during a 1987 cruise in the Central Atlantic, a gradient of opposite sign (lower mixing ratios in Northern Hemisphere mid-latitudes compared to near the equator) was measured in the Eastern Atlantic during 1998 [Xu et al., 2001]. Lower mixing ratios in the Central Atlantic were also noted in a 1994 cruise (H. Bingemer, unpublished data, 1994). Across the Pacific during this season in 1993, Weiss et al. [1995] suggest mixing ratios that are slightly elevated in the tropics compared to both hemispheres. Results from TRACE-P appear to demonstrate that OCS mixing ratios over the West Pacific Ocean basin can be influenced strongly by land-based, anthropogenic sources during this time of year; the highest mixing ratios of OCS (600-1200 ppt) were observed in air transported from the Asian continent that contained elevated levels of gases associated with anthropogenic pollution [Blake et al., 2004].

Seasonal variability of tropospheric OCS

Until recently much of the available data suggested that hemispheric OCS mixing ratios varied little with season. In earlier reports, free tropospheric means for OCS above Kitt Peak and the Jungfraujoch showed only small seasonal variations [Mahieu et al., 1997; Rinsland et al., 1992]. Reanalyses of extended databases now suggest peak-to-peak seasonal changes in tropospheric mean mixing ratios of about 15 ppt at Kitt Peak and 20 ppt at the Jungfraujoch [Rinsland et al., 2002; Mahieu et al., 2003], which remain relatively low, i.e., about 3 and 4% of the mean concentrations, respectively. These low seasonal variations are not contradicted by Bandy et al. [1992] who found no clear seasonal signal in a less extensive, aggregated set of OCS mixing ratios.

Although substantial seasonal variations have been reported for the lower free troposphere (Figure 2.6a,b) above Wollongong [Griffith et al., 1998] and Izaña [Schneider, 2002] these results have not been interpreted to suggest that OCS mixing ratios vary seasonally on broad scales. Griffith et al. [1998] proposed that the seasonal variations measured above Wollongong arised from seasonal changes in regional ocean temperature, OCS flux, and the direction of prevailing winds to the site. The seasonal variations observed above Izaña during 1999-2002 exhibited a peak-to-peak amplitude of about 10 % (with a large interannual variability), similar to that observed above Wollongong in 1996 (~ 12 %) after tropopause height variations were accounted for. Schneider [2002] suggested that the variation above Izaña may have resulted in part from CO₂ spectroscopic interferences. Minimum OCS mixing ratios at Izaña are measured in November, thus commensurate with the timing of the small seasonal signal reported above Kitt Peak (14 ppt peak-to-peak amplitude; December minimum at 32° N; Rinsland et al. [2002]) and above the Jungfraujoch (~ 20 ppt peak-to-peak amplitude; December-January minimum; updates of Mahieu et al. [2003]). Mixing ratios measured 2 m above ground at the German Taunus Observatory, a rural forested site, exhibited a large seasonal variability, with minima in Sept-Oct. This variability was interpreted as being consistent with a strong summertime vegetative sink of atmospheric OCS [Xu, 2001]. In marine air during September-October, Thornton et al. [1996] noted substantially reduced and highly correlated levels of OCS and CO₂ in air that originated from remote land areas, consistent with the uptake of OCS by vegetation. Others have suggested that a strong vegetative sink could result in a substantial seasonal variation for atmospheric mixing ratios of OCS [Bingemer et al., 1990; Johnson et al., 1993], although Kettle et al. [2002a] have pointed out that compensating high summertime fluxes from the ocean would act to offset this influence.

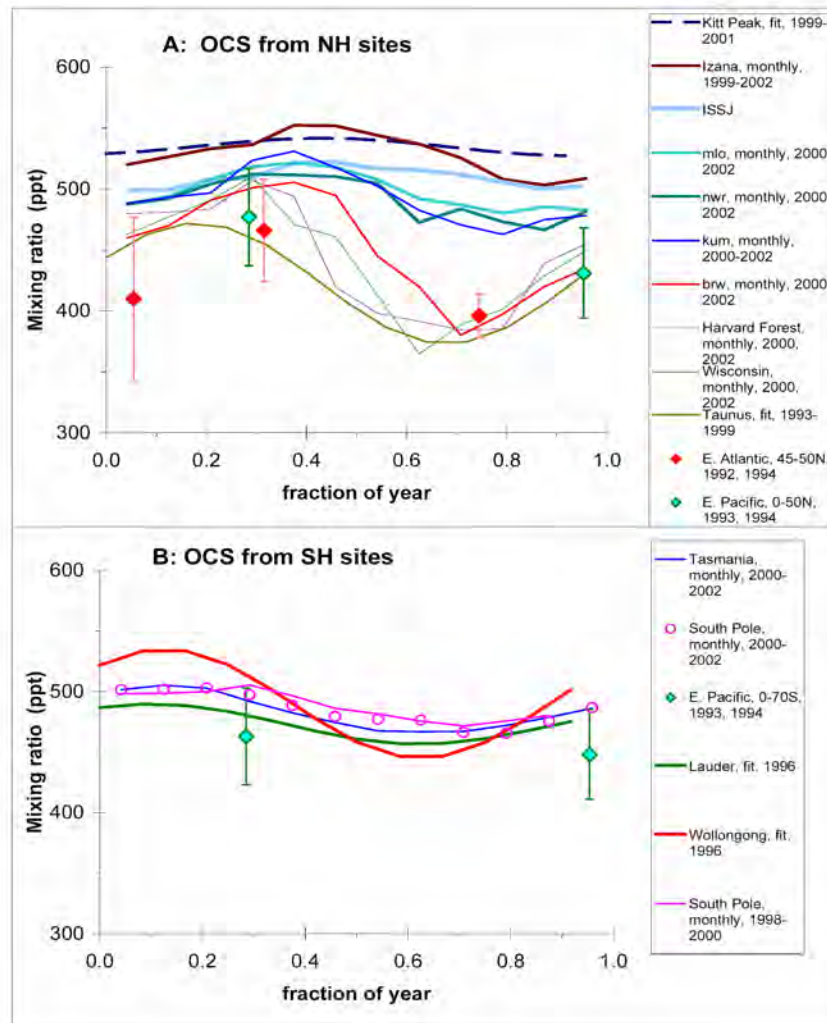


Figure 2.6 Seasonal changes in OCS mixing ratios at different sites. Results at most sites are an average of monthly means during multiple years, thick lines are free-tropospheric (FT) means or means from high-altitude (HA) sites (> 3000 m a.s.l.); results from Kitt Peak and Taunus are fits to the data. (A) For the Northern Hemisphere [Rinsland et al., 2002; Schneider, 2002; Mahieu et al., 2003; Montzka et al., 2001; Ulshofer et al., 1995; Weiss et al., 1995]. (B) For the Southern Hemisphere [Griffith et al., 1998; Weiss et al., 1995; Montzka et al., 2001; Dutton et al., 2001].

New results from more than two years of data at 10-12 remote sites across the globe (see Figure 2.7) suggest that strong seasonal variations are common at many surface sites in both hemispheres [Montzka et al., 2001; Dutton et al., 2001]. At mid-latitude, low altitude, continental sites in the Northern Hemisphere (Harvard Forest at 42.5°N and Wisconsin at 45.6°N), and at sites in the Arctic (Barrow at 71°N and Alert at 82.5°N), large seasonal variations are observed with peak-to-peak amplitudes of 25 to 30 % ((high-low)/mean). These variations are similar in phase and magnitude to the mean seasonality observed during 1993-1999 at the Taunus Observatory in rural Germany [Xu, 2001], and indicate that these large seasonal swings can be observed at many sites in the mid- to high-latitude Northern Hemisphere (Figure 2.7). At these sites, maximum mixing ratios are observed in March-May, and minima are measured in August-October.

Seasonal variations with a slightly delayed phase and smaller amplitude (April-May peak, August-September minima; 7 to 12 % peak-to-peak amplitude) have been observed at Niwot

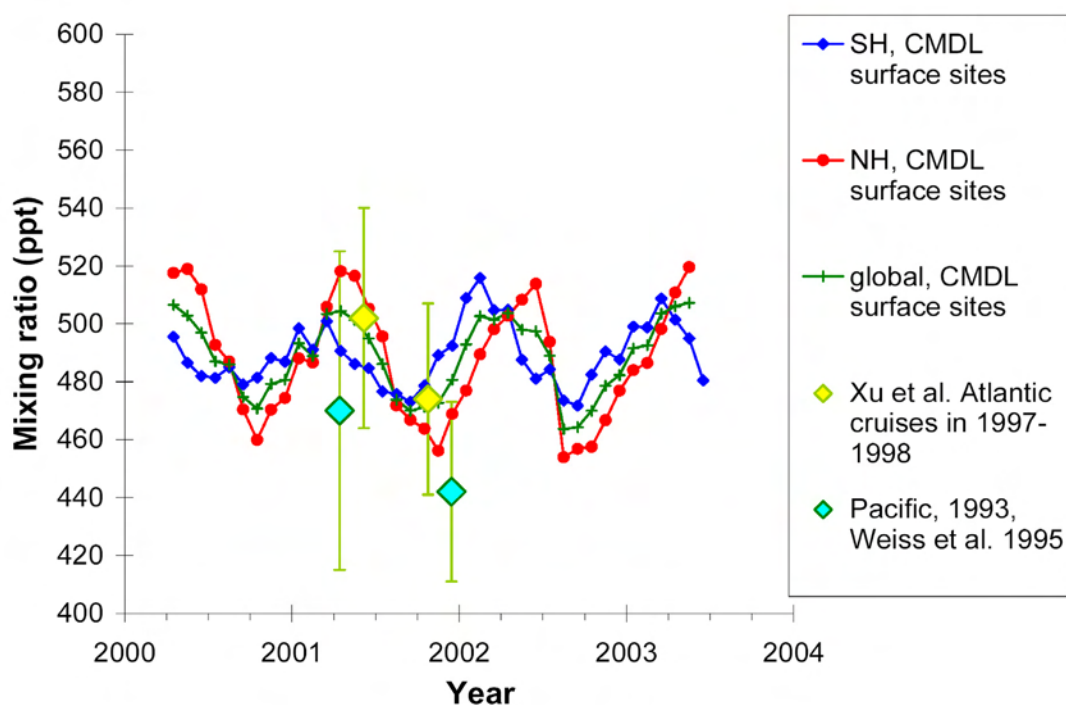


Figure 2.7 Global surface OCS mixing ratios as estimated from a range of surface sites (data from South Pole, Tasmania, Samoa, Kumukahi, Mauna Loa, Niwot Ridge, Barrow, and Alert were used to calculate hemispheric means [Montzka et al., 2001]). Also shown are global means estimated from short-duration cruises in the Atlantic [Xu et al., 2001] and Pacific [Weiss et al., 1995] Ocean.

Ridge, a high-altitude continental site, and at high and low altitude sites at lower latitudes in the Pacific Ocean basin of the Northern Hemisphere (Kumukahi and Mauna Loa, both at 19.5°N, [Montzka et al., 2001]), see Figure 2.6a.

The results from Kumukahi and from past cruises suggest that seasonal variations of OCS are substantial even within the marine boundary layer of the Northern Hemisphere. For example, the ranges reported for OCS mixing ratios by Weiss et al. [1995] and Ulshofer et al. [1995] in different seasons are quite consistent with the seasonal changes measured at the ground-based sites (Figure 2.6a and 2.6b). Furthermore, the range of surface means reported from short-duration cruises in both the Pacific [Weiss et al., 1995] and Atlantic [Xu et al., 2001] Oceans may be explained in part by a seasonal variation that is apparent in the land-based surface results (Figure 2.7). The apparent differences between the results from Weiss et al. [1995] compared to those of Montzka et al. [2001] and Xu et al. [2001] may be related to differences in standardization, although the exact cause is not currently known.

Combining all northern hemispheric data, most of the distributions and seasonal variations measured suggest a coherent seasonal change for mixing ratios of OCS in the lower atmosphere. The results appear to be consistent with a strong, land-based, seasonally-varying uptake of OCS, the effect of which propagates to high altitudes and away from mid-latitudes with some time delay. Some published data, such as the unusual latitudinal gradients observed in the Atlantic at different times in the past [Johnson et al., 1993; Bingemer et al., 1990], are less consistent with this overall picture, however, and may suggest that a good deal of uncertainty remains regarding our understanding of OCS distributions and seasonality in the Northern Hemisphere.

In the Southern Hemisphere, a consistent and substantial seasonal variation is observed in non-polluted air at both Tasmania and at South Pole [Montzka et al., 2001; Dutton et al., 2001] see Figure 2.6 b. The phase and amplitude (8 % peak-to-peak) of the variation are closely matched at these sites. Peak mixing ratios are observed at both sites during the months of January through March while minimum mixing ratios are observed in August through October. These seasonal variations are similar in phase but slightly smaller in amplitude than those measured in the lower free troposphere above Wollongong. The consistent seasonality observed at the Australian sites and at the remote South Pole suggests instead that OCS may undergo a coherent seasonal change throughout the mid-to high latitudes of the Southern Hemisphere.

Seasonal variations in free tropospheric OCS above Lauder were reported to be on the order of 6 % peak-to-peak [Griffith et al., 1998], but the authors suggested that most of this variability arises from seasonal tropopause height variations. The timing of the seasonal variations above Lauder is very similar to that observed above Wollongong and at the surface at Tasmania and South Pole.

Clear seasonal variations for OCS have not been observed at Amsterdam Island, 37°S [Mihalopoulos et al., 1991] or Samoa, 14°S [Montzka et al., 2001; Dutton et al., 2001]. The sample-to-sample variations observed at these sites are comparable to or larger than the amplitude of seasonal variations observed in recent years at South Pole, Tasmania, and Wollongong (Figure 2.6b). Enhanced sample-to-sample variability may suggest the influence of local processes at Amsterdam Island and Samoa.

Unlike many other trace gases that exhibit seasonal variations at Earth's surface, the seasonality observed for OCS in the Southern Hemisphere is not out-of-phase by 180 days with that observed in the Northern Hemisphere. Instead, peak OCS mixing ratios are observed in the Southern Hemisphere during Austral summer (January-March) about three months before the peak is observed in the Northern Hemisphere. This suggests that very different processes are affecting the seasonal changes observed for OCS in the different hemispheres. Whereas seasonality in the north appears to be driven by a strong summertime loss associated with land, seasonality in the south may be influenced more strongly by the ocean source of OCS. Ocean processes favor an enhanced production of OCS during summer [Weiss et al., 1995; Ulshöfer et al., 1995]. Results of a 3-D model calculation [Kjellstrom, 1998; Kjellstrom, personal communication, 2001] suggest seasonally varying mixing ratios in the middle to high-latitude Southern Hemisphere with a phase similar to that observed at South Pole, Tasmania, and Wollongong. The calculated peak-to-peak amplitude, however, is only 2 %, or about 4 times less than suggested by the surface measurements at these sites.

Vertical variability of OCS throughout the troposphere

Strong vertical gradients were not observed in some earlier aircraft sampling campaigns [Bandy et al., 1992; Johnson et al., 1993], but such gradients may vary with longitude and with season (see *Section annual means*). Measurements during TRACE-P over the west Pacific Ocean [Blake et al., 2004] show a gradual decrease for OCS of about 10 % from the surface to 10 km during February through April of 2001. The highest OCS levels (600-1200 ppt, means around 560 pptv) were observed below 2 km near the coast of Asia, presumably because of the influence of land-based sources in this region. A slightly negative gradient with altitude (-5 %, FT vs. BL) was also noted over the central/eastern Pacific south of 25°N, while north of 25°N OCS was found to be enhanced in the 5-10 km altitude range, likely originating from biomass burning emissions [Blake et al., 2004].

Given that the largest losses of OCS are thought to be uptake by vegetation, vertical gradients that vary with season and latitude might be expected to arise, and can be deduced from differences between surface in situ measurements and tropospheric mean mixing ratio observations shown in Figures 2.4 and 2.5. The free troposphere and surface VMR of OCS agree rather well between $20^{\circ}\text{S} - 20^{\circ}\text{N}$ during boreal fall as well as north of 20°N during boreal spring (the time of maximum surface OCS), suggesting only small vertical gradients. North of 20°N during boreal fall (the time of minimum surface OCS) however, the surface mixing ratios are lower than the free troposphere mixing ratios by 25-100 ppt.

Despite the consistency between surface-based and free tropospheric measurements between 20°N and 20°S during boreal fall (Figure 2.4), substantial enhancements have been noted recently for OCS in the upper tropical troposphere [Notholt et al., 2003]. Observations onboard a ship using infrared solar absorption spectrometry yielded the vertical distribution of OCS between 80°N and 70°S above the middle of the Atlantic Ocean (Figure 2.8). Mixing ratios of up to 600 pptv were observed between 20°N and 20°S at 12-16 km altitude in October 1996

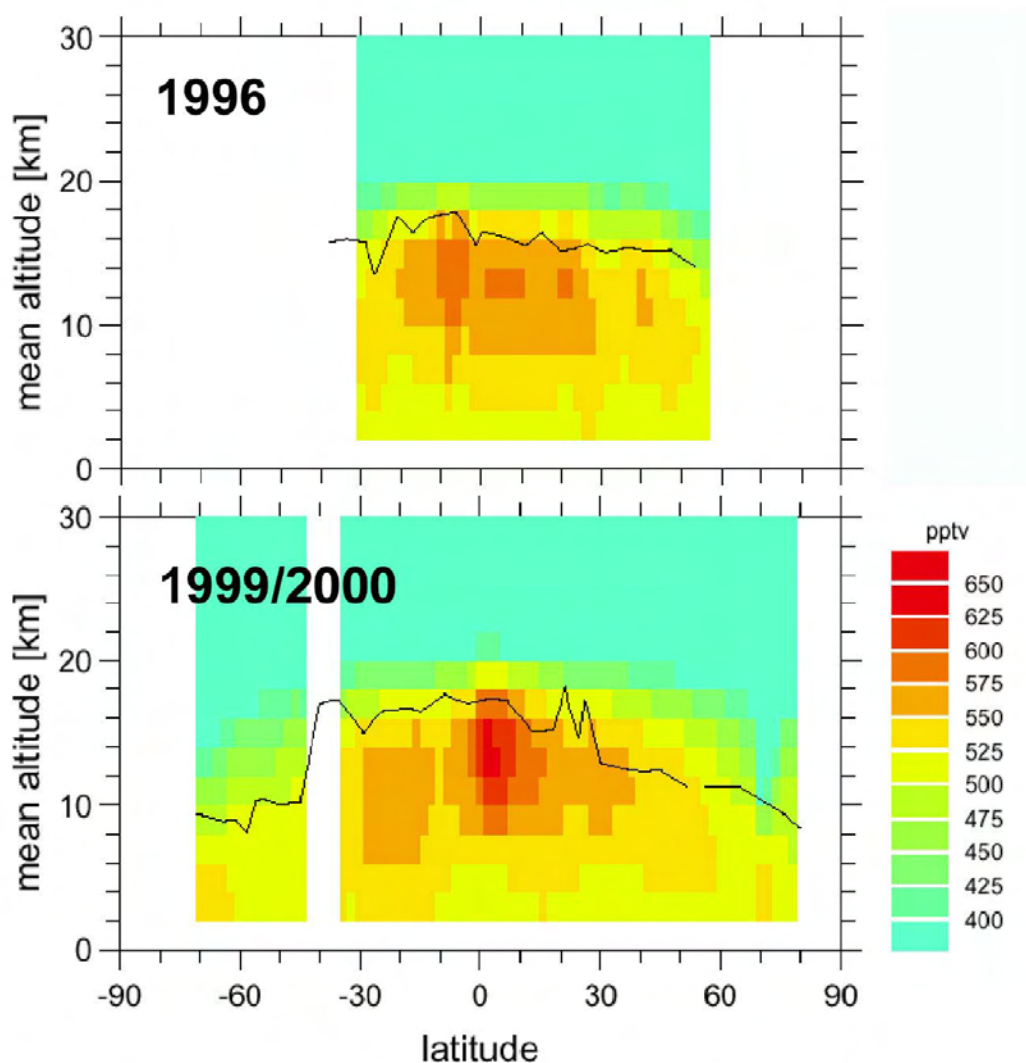


Figure 2.8 Latitude transects of OCS VMR measured by FTIR [Notholt et al., 2003] during ship cruises in the Atlantic. Black line gives thermal tropopause altitude as measured from balloon measurements during cruise.

and December 1999. OCS at these altitudes and tropical latitudes had not been studied by balloons and previous aircraft observations were limited to 12 km altitude. The enhanced mixing ratios in the TTL were independently confirmed by ATMOS space shuttle observations from November 1994. The enhanced levels were attributed to biomass burning emissions on the continents, followed by deep convection and effective horizontal transport within the TTL.

Stratospheric and upper tropospheric observations from space

Measurements of the vertical distribution of OCS have been performed by the ATMOS infrared remote sensing Fourier transform spectrometer onboard the space shuttle during four missions, from 1985 to 1994. Two papers have reported on related results [Zander et al., 1988; Rinsland et al., 1996]. Since then, a complete reanalysis of all available ATMOS observations has been performed, leading to the production of the “Version 3” dataset for over 30 atmospheric species¹ [Iriou et al., 2002]. This dataset has been used to determine the stratospheric and upper tropospheric zonal mean vertical distributions of OCS in the Northern Hemisphere, considering solar occultations recorded between 8 and 49° during the ATMOS/ATLAS-3 mission in November 1994. Figure 2.9 shows these 10° binning averages, with error bars corresponding to standard deviations around the zonal means. The latitudinal variation of OCS in the stratosphere is significant, with mixing ratios ranging from about 75 to 280 pptv at 25 km, between 40-49 and 8-20°N, respectively. Furthermore, these measurements imply mixing ratios of 460-480 pptv in the upper troposphere between 8 and 49°N, or somewhat less than suggested by Figure 2.4 for the free troposphere during this time of year.

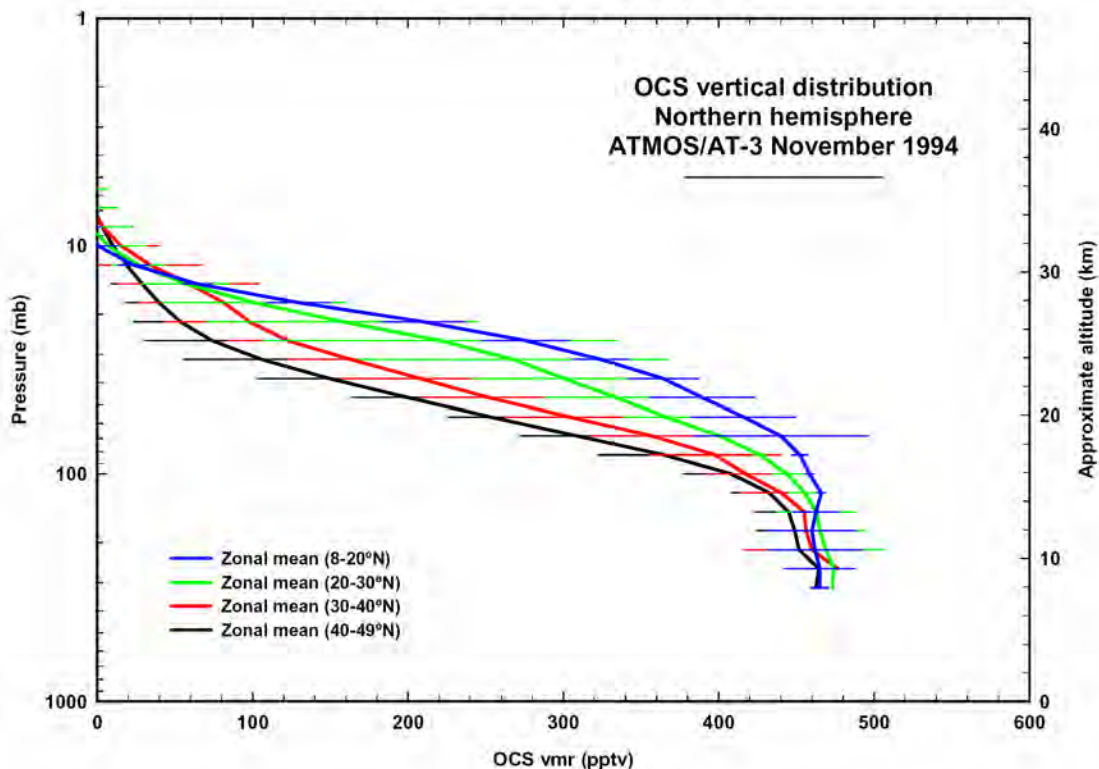


Figure 2.9 OCS vertical distributions on the basis of the FTIR observations from the Space Shuttle during the ATMOS/ATLAS mission in November 1994.

¹ <http://remus.jpl.nasa.gov/atmosversion3/atmosversion3.html>

Long-term trend

Several papers have dealt with trends of carbonyl sulfide in the atmosphere over the last decades. These studies relied on ground-based measurements of total vertical column abundances of OCS deduced from the analysis of high-resolution IR solar spectra, and on firn air analysis by gas chromatography.

A recent study considered remote sensing observations performed at Kitt Peak (Arizona, 31.9°N) between 1978 and 2002 [Rinsland et al., 2002]. The time series of daily averaged tropospheric mixing ratios indicates that the OCS burden has remained nearly constant over the 24-year period under investigation with a slow but statistically significant trend of $(-0.25 \pm 0.04) \text{ %/yr}$, see Figure 2.10. This mean trend is consistent with results obtained by the same technique at other sites, i.e. at the Northern hemisphere Jungfraujoch station (Swiss Alps, 46.5°N) between 1988 and 2002 [(Mahieu et al., 2003)], and at two sites in the Southern hemisphere (Wollongong, Australia, 34.5°S, and Lauder, New Zealand, 45°S) [Griffith et al., 1998] which all indicate decreases of less than 1 %/yr.

Figure 2.11 displays the monthly mean time series for the total, as well as the partial tropospheric and the stratospheric columns of OCS derived above the Jungfraujoch station at 46°N and 3.58 km altitude [Mahieu et al., 2003]. The partial columns have been separately calculated for the altitudes 3.5-11 km and above 11 km. The 11 km limit was adopted because the mean tropopause height above this mid-latitude site is about 11.35 km over the last decade. The error bars in Figure 2.11 correspond to the standard deviations around the monthly mean total or partial columns. Seasonal variations and long-term trends have been determined using a function which combines a sinusoidal and a second order polynomial component. This function suggests a significant mean trend close to $-(0.50 \pm 0.05) \text{ %/yr}$ for the tropospheric and total column data sets displayed in Figure 2.11. Figures 2.12 and 2.13 show the time series for Lauder (45°S) and Wollongong (34°S) for the total, and the partial tropospheric and stratospheric columns. The total column trends above Lauder for the years of 1992 – 2003 and

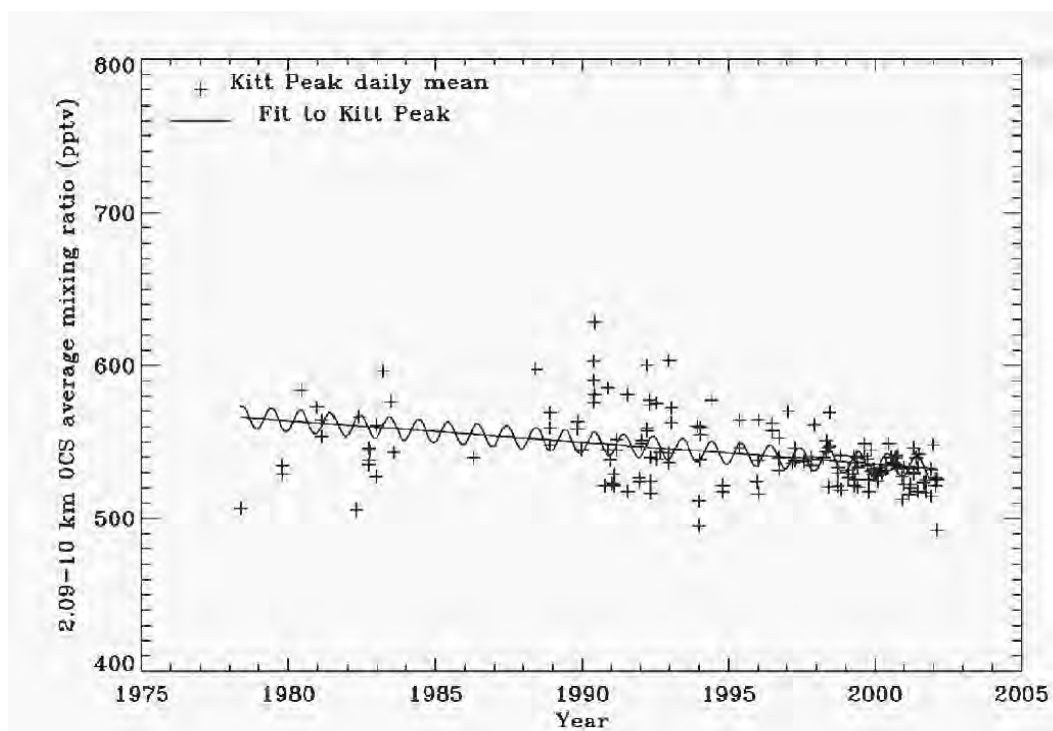


Figure 2.10 Total column long-term trend of OCS at Kitt-Peak (31.9°N, 111.6°W) measured by Rinsland et al. [2002].

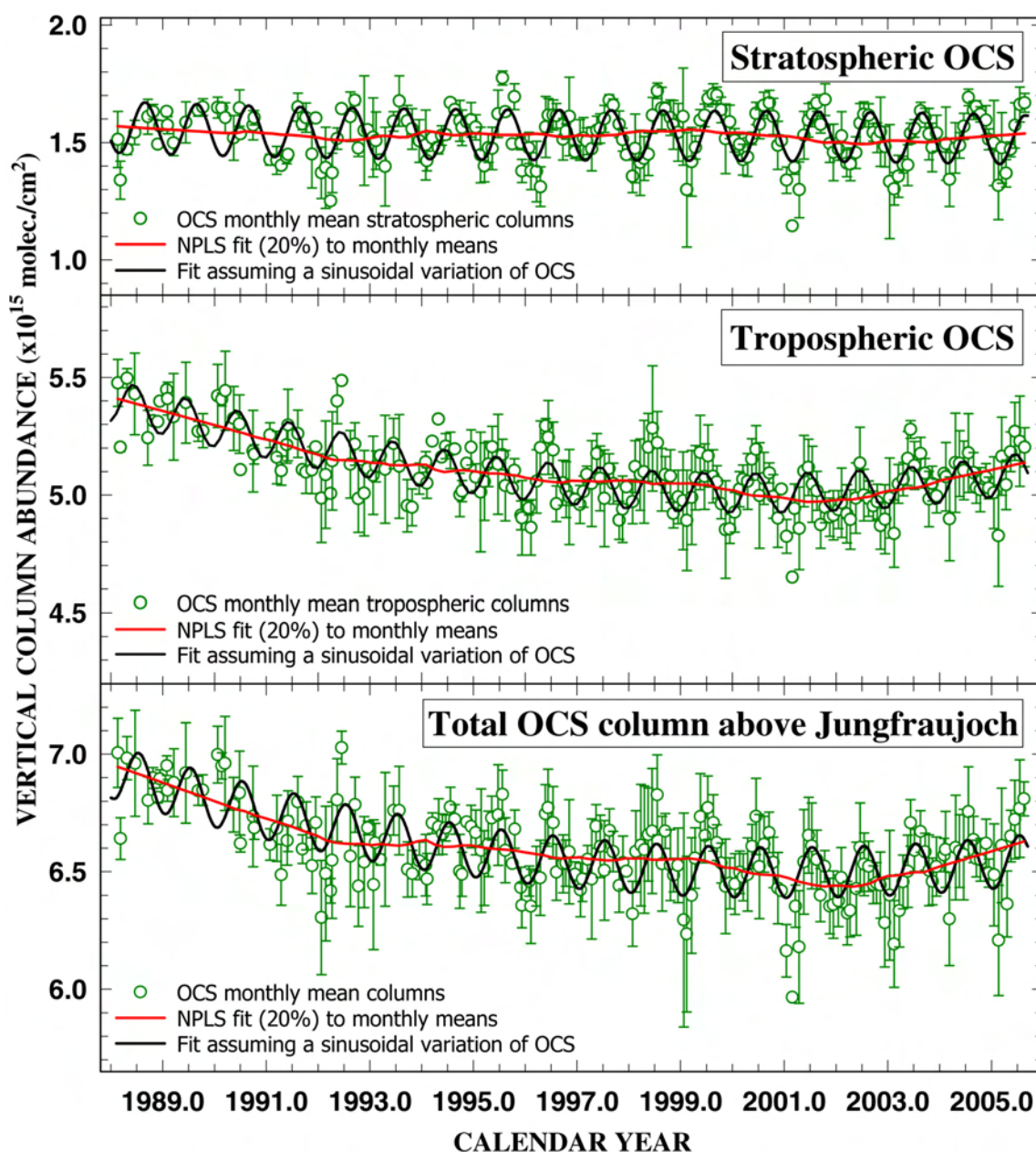


Figure 2.11 Monthly mean total- and partial columns of OCS above the Jungfraujoch Station (Switzerland) from 1988 to 2002, based on Mahieu et al. [2003].

above Wollongong for the years 1996 – 2003 are (-0.69 ± 0.28) %/yr and (-0.35 ± 0.12) %/yr, respectively [Deutscher and Jones, unpublished data]. Figure 2.14 gives the long-term trend of the stratospheric, the tropospheric and total column of OCS in the high Arctic in Ny-Ålesund (79°N , 11°E). Due to the high latitude the solar absorption measurements can only be performed between March and September. For the total columns the observations yield a trend of -0.2 ± 0.2 %/yr.

Recent decreases in northern hemispheric OCS mixing ratios are also suggested from an analysis of firn air collected in the Arctic and Antarctic [Sturges et al., 2001]. These firn-air results also suggest that mixing ratios in the Southern Hemisphere have not changed appreciably during the past 30-50 years. Mean air sample ages extended from the middle to the end of the 20th century. Results show a considerable scatter, however, suggesting constant burdens in the South and a decline of (8 ± 5) % over the last 10 years in the Arctic. The latter was at-

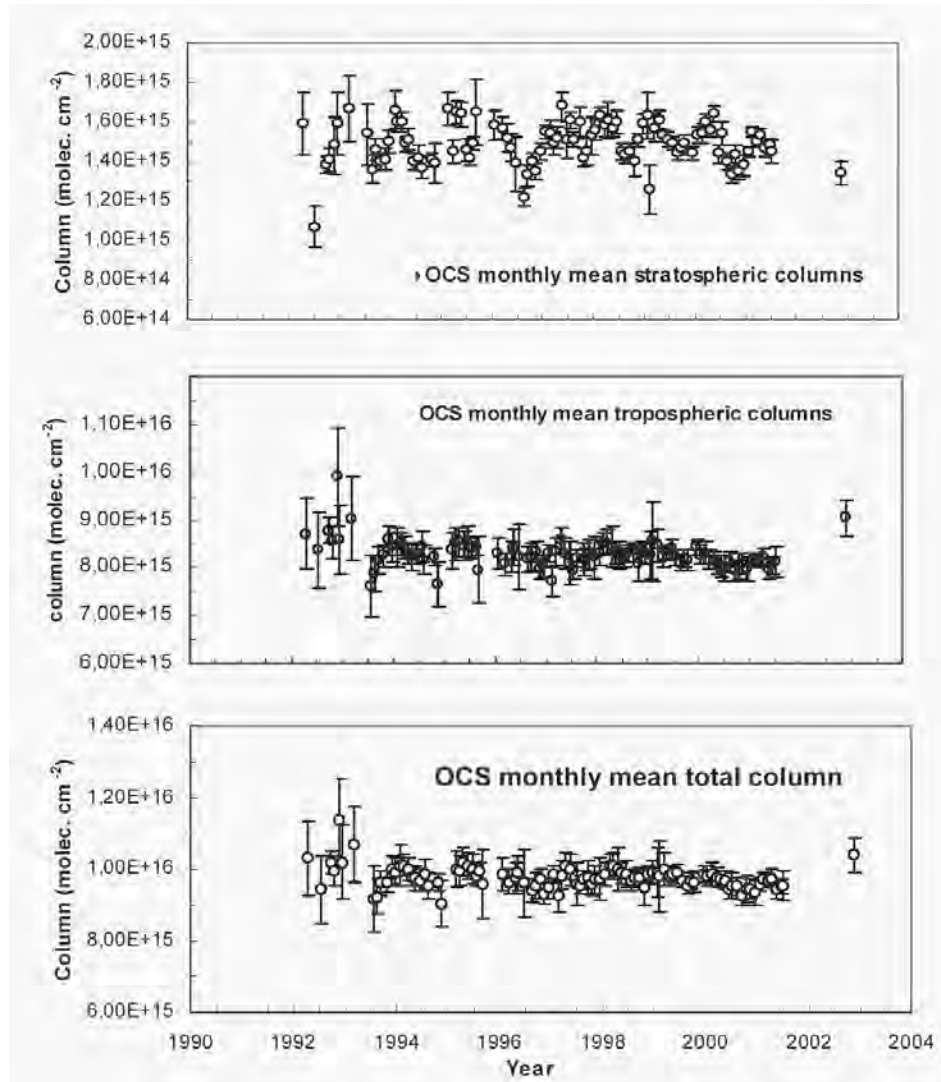


Figure 2.12 Time series of monthly mean total, tropospheric and stratospheric columns of OCS above Lauder, New Zealand, from 1992 – 2003 by FTIR measurements of Deutscher and Jones (unpublished results). The tropospheric column was assumed to be from ground level to 12 km, the average tropopause height, and the stratospheric column from 12 km upward.

tributed to the decline of anthropogenic CS₂ emission from viscose-rayon production, a potential source of OCS.

A history of atmospheric OCS over the last 350 years has been established recently by Aydin et al. [2002] and Montzka et al. [2004]. In air from the Antarctic Siple Dome ice core the 17th century atmospheric OCS level was analyzed to be (373.8 ± 37.2) pptv [Aydin et al., 2002], roughly 25% lower than at present. Measurements of younger portions of the same ice core [Montzka et al., 2004] revealed even lower atmospheric OCS of around 330 pptv for the period of 1700-1850 (Figure 2.15), or 33-43% lower than today. Provided that these results are not compromised by any slow production or destruction of OCS within snow and ice, the data prior to 1850 present the first evidence for a substantial long-term natural variability of atmospheric OCS, and its biogeochemical cycle. The cause of this variability is unknown. As potential mechanisms, the authors point to components of the biogeochemical OCS cycle that are related to climate, terrestrial and marine vegetation and land use, which need to be investigated. The analysis of firn air from South Pole [Montzka et al., 2004] revealed the rise of atmospheric OCS during the 20th century to a maximum around the mid-1980s, and a subsequent 60-90 pptv decline during the past 10-15 years. The authors found a close correlation

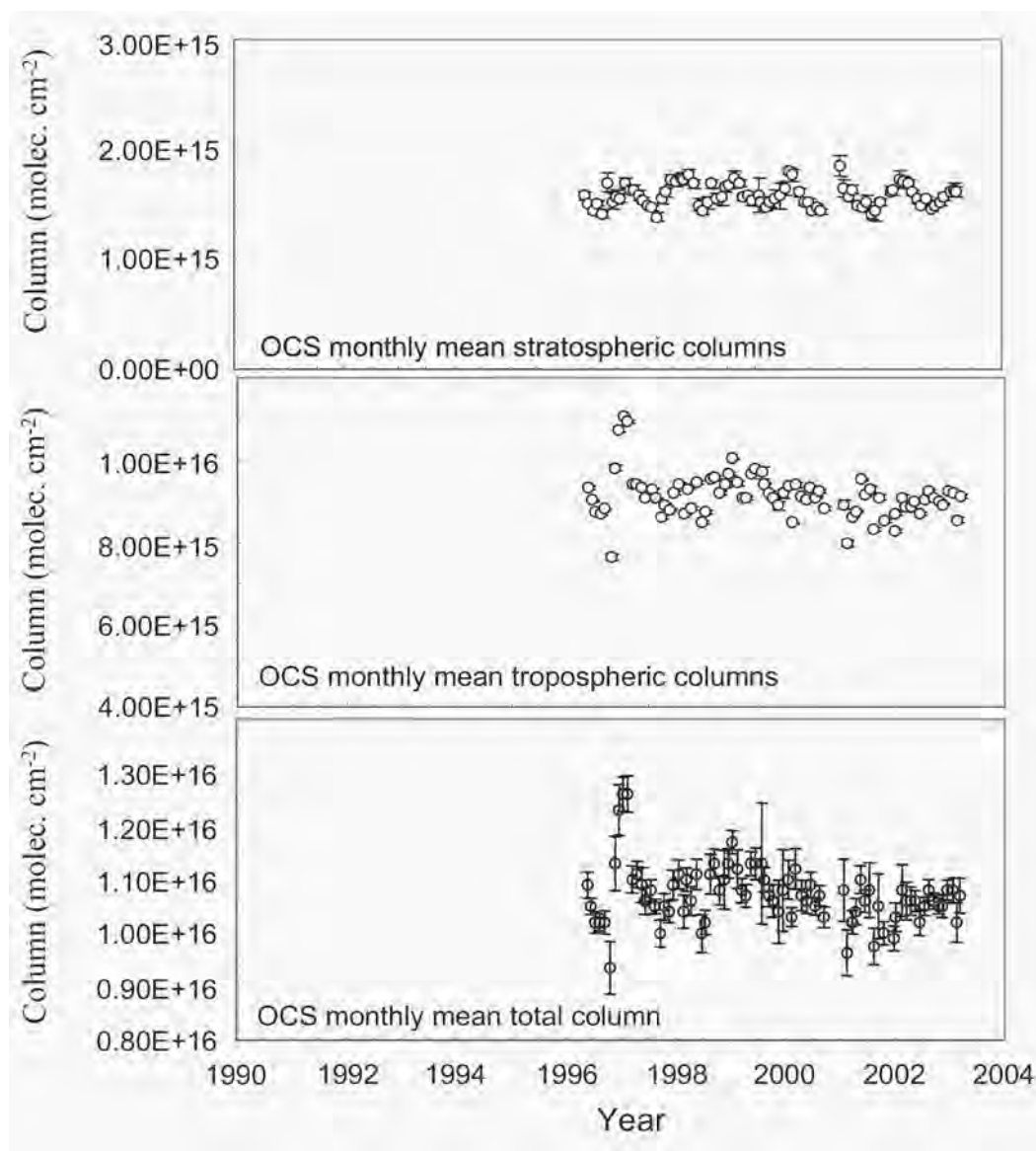


Figure 2.13 Time series of monthly mean total, tropospheric and stratospheric columns of OCS above Wollongong, Australia, from 1996 – 2003 by FTIR measurements of Deutscher and Jones (unpublished results). The tropospheric column was assumed to be from ground level to 12 km, the average tropopause height, and the stratospheric column from 12 km upward.

between the histories of atmospheric OCS and anthropogenic sulfur emission since ~1850, and noted that this similarity could be explained if a small fraction (0.3-0.6 %) of anthropogenic sulfur emissions were released (directly or indirectly) as OCS. This would be consistent with the results of Blake et al. [2004] from TRACE-P over the western Pacific, who noted remarkably similar altitude/latitude distributions of OCS to gases with strong fossil fuel combustion sources like CO, SO₂ and ethene.

However, observational evidence on both the natural biogeochemical processes which are responsible for the preindustrial variability of atmospheric OCS and on the anthropogenic processes that caused its variation during modern time is currently lacking.

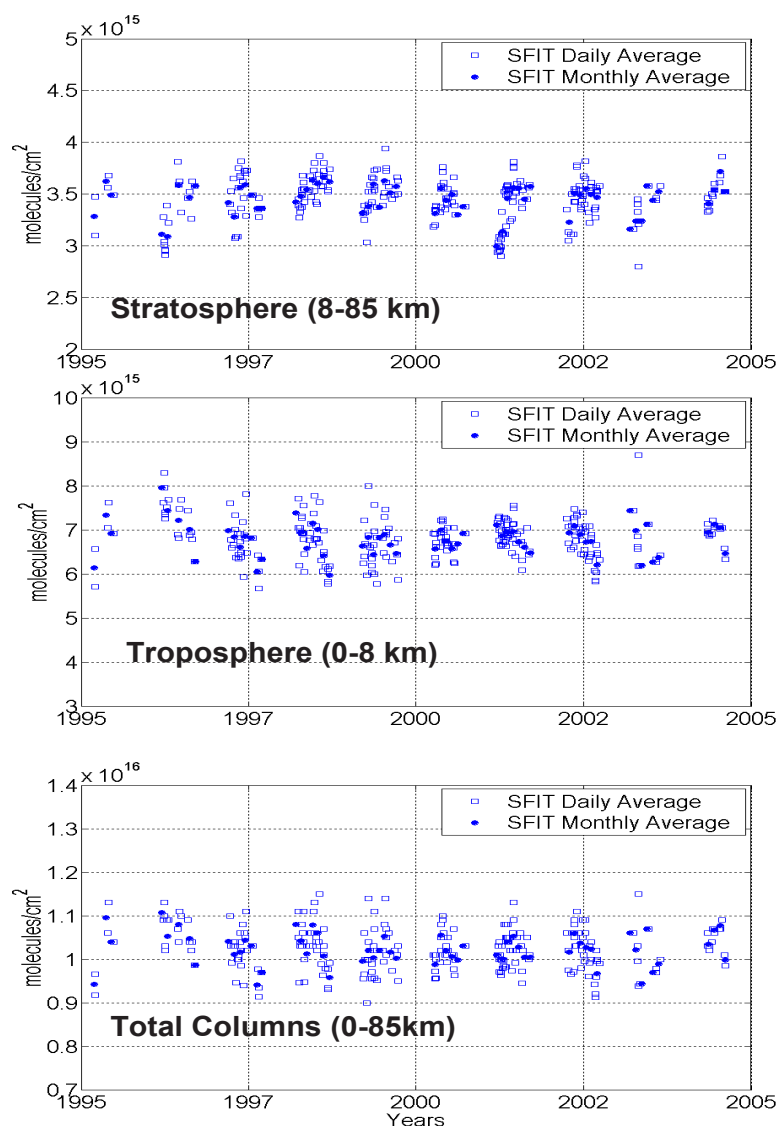


Figure 2.14 Total and partial columns of OCS measured in the high Arctic in Ny-Ålesund (79°N, 11°E). Due to the high latitude the solar absorption measurements can only be performed between March and September. The altitude of 8 km corresponds to the mean tropopause altitude at this site.

2.4.2 Sulfur Dioxide (SO₂)

Sulfur dioxide, a classical air pollutant, has been widely measured in surface air by pollution monitoring stations for approximately 50 years. Background monitoring networks in North America and Europe measure SO₂ since the late seventies [Hicks et al., 2002; Loevblad et al., 2004]. The continental background levels of SO₂ and sulfate aerosol in surface air over North America and Europe reached a maximum in the 1980s, and since then steadily declined, as a consequence of emission control measures. For the East of the U.S.A., the overall trend is – 2.8 %/yr [Hicks et al., 2002], exceeding the trend for the emissions of sulfur (–1.3 %/yr) typically by a factor of 2. From the measurements within the EMEP network during 1980 - 2000, a similar trend in the levels of airborne SO₂ and sulfate is observed over many parts of Europe [Loevblad et al., 2004], i.e. reductions of 85 – 90% for SO₂ and of 50 – 75% for sulfate.

SO₂ in the free troposphere

Since SO₂ has a short and highly variable lifetime and sources that are both intense yet regionally limited, the SO₂ mixing ratios in the free troposphere vary by several orders of mag-

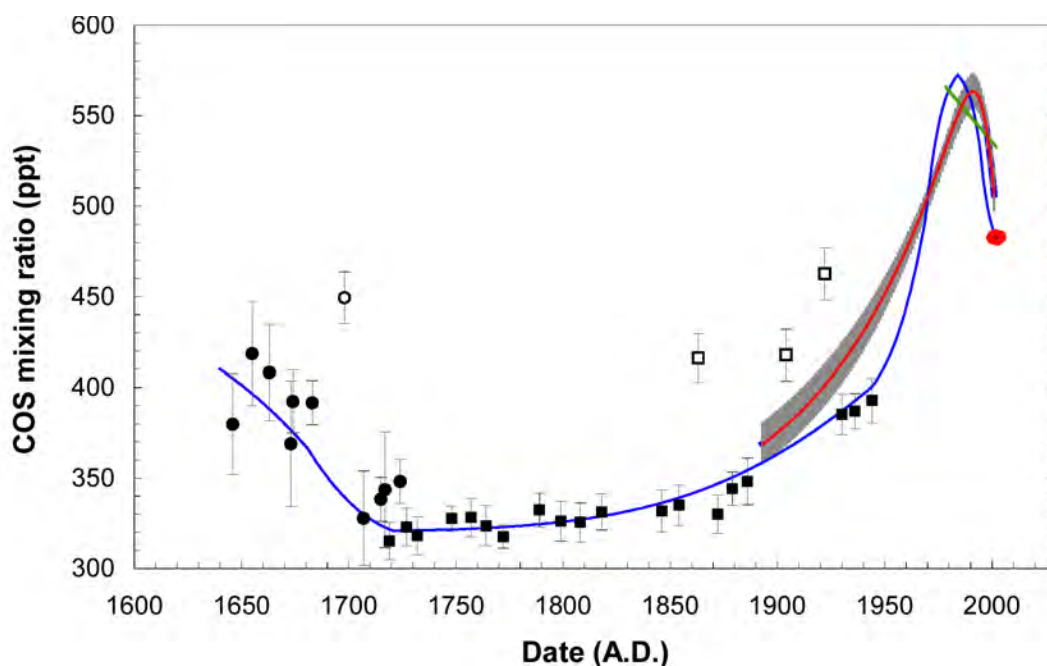


Figure 2.15 Atmospheric history for COS [Montzka et al., 2004] from Antarctic firn air measurements (red line with 68.3% uncertainty bound) and from a combination of ice core, firn air, and ambient air (blue line). Dated ice core results (solid black circles [Aydin et al., 2002]; solid black squares: [Montzka et al., 2004]; unfilled black squares and circles not considered) represent a mean vmr over a range of years. Annual means from flask measurements at South Pole since 2000 are shown as red circles. The green line represents a fit to the long-term decline reported by Rinsland et al. [2002] for the Northern Hemisphere.

nitude from peak vmr of several ppbv in layers of polluted air (above the centers of pollution and in continental outflow) to values of less than 10 pptv or less in the upper troposphere above the remote southern Pacific Ocean. Despite this variability, some characteristic features of the global distribution of SO_2 among specific atmospheric environments, as well as zonal, meridional and vertical profiles may be distilled from existing data (see Tables 2.2 and 2.3).

The continental outflow of pollutants into the marine troposphere has been investigated for the pathways from North America to the western North Atlantic by the projects WATOX [Galloway et al., 1990], NARE [Banic et al., 1996], and TARFOX [Hobbs, 1999], from India into the Indian Ocean during INDOEX [Lelieveld et al., 2001], and from Asia into the Pacific Ocean during the NASA PEM- and TRACE-P missions [Thornton et al., 1999; Tu et al., 2003; 2004].

Along the eastern seaboard of North America and above the Western North Atlantic SO_2 peak values of several ppb were found in the lowest kilometers close to the coast, and little transport seen above 3 km [Banic et al 1996; Hobbs 2002, private communication]. 900-1500 pptv of SO_2 were sampled during INDOEX at 500 km south of India in pollution layers (1.5-2.5 km altitude) of the monsoonal outflow [Reiner et al., 2001, Lelieveld et al., 2001]. These data agree with those of Thornton et al. [1999] from the PEM missions, who sampled between several hundred pptv up to 2 ppbv SO_2 at < 0.5 – 4 km altitude over the western Pacific Ocean, noting that horizontal transport may extend to substantially longer distances, if efficient vertical transport uplifts the pollutants and allows for advection in the mid- and upper troposphere.

The long-range transport of East Asian SO_2 in the lower troposphere has been further substantiated recently by fast time resolution mass spectrometric SO_2 measurements (Thornton et al.,

2002) in a series of flights over the Yellow Sea and the North Pacific Ocean during the NASA TRACE-P field experiment. A significant transport of continental SO₂ across the Yellow Sea at altitudes between 0.5 and 2 km was found, with SO₂ plume mixing ratios up to several ppbv [Tu et al., 2004]. The origins and transport routes of SO₂ across the northern Pacific Ocean were identified from trajectory and model studies and the chemical signatures of the air [Tu et al., 2004]. The major transport occurred in the midlatitudes (30°-60°N) and in the lower troposphere in layers that were effectively isolated from the ocean surface. In these layers between the top of the convective marine boundary layer and 5 km altitude, low water vapour limited liquid and gas phase SO₂ oxidation, and low turbulence maintained the integrity of the layers. While both anthropogenic and volcanic (see below) sources in east Asia had direct influence on SO₂ in the central Pacific, the effects of the more widely distributed anthropogenic sources were diminished as compared to their impact near the Asian coasts.

For the upper troposphere up to the tropopause level less data are available. Episodic transport of pollution may occur at these levels as well, as noted by Arnold et al. [1997], who encountered a heavily polluted airmass of up to 3 ppbv SO₂ at 9 km above the Eastern North Atlantic. Chemical tracers and trajectory analysis indicated an origin from surface sources in the north eastern U.S.A., 4-5 days prior to the measurement. However, mean vmr of SO₂ in the range of several tens to several hundreds of pptv are more commonly reported for this altitude range both over the continents and oceans. Over central Europe, at the tropopause level, mean mixing ratios of 200 pptv were found at 8 km and 40-55 pptv at around 10 km [Meixner, 1984; Reiner et al., 1998]. Above the Canary Islands in airmasses that predominantly had travelled across the North Atlantic Ocean < 200 pptv SO₂ in the lower troposphere and typically between 10 to 60 pptv at 6 to 13 km were measured by Curtius et al. [2001], using CIMS. In the continental remote troposphere (6 km) over western North America 160 pptv were sampled during the 1980ies [Maroulis et al., 1980]. For the free troposphere above the humid tropical rainforest of the Amazon, significantly lower mixing ratios of 15-30 pptv are reported during both the dry and wet seasons [Andreae and Andreae, 1988; Andreae et al., 1990]. In the Arctic, considerably higher VMR of 200 – 1200 pptv SO₂ in polluted layers and 10 – 100 pptv during background conditions were measured by Jaeschke et al. [1999], similar to Möhler and Arnold [1992], who found 100 – 350 pptv at 0 – 2 km below the Arctic tropopause and 15 – 100 pptv at 0 – 2 km above.

Most experiments study episodes of transport and only a few address the distribution of SO₂ on the large scale. Current remote sensing techniques however cannot detect background levels of SO₂, but only enhanced levels near large emissions sources. As an example, Figure 2.16 shows enhanced SO₂ levels caused by industrial emissions in Europe and China (A. Richter, University of Bremen, unpublished results) and by volcano eruptions. The aircraft experiment TROPOZ II attempted to measure the large scale meridional and vertical distribution of SO₂ over the continental rim of the Atlantic Ocean and along the west coast of South America [Wolz and Georgii, 1996]. In both hemispheres the measured vertical profiles decrease out of polluted coastal boundary layers of several hundred pptv SO₂ to less than 20 pptv at 6 to 11 km altitude. In the free troposphere south of 40°S, vmr of 10 – 20 pptv SO₂ were measured, similar to the data of Thornton et al. [1999] over the south Pacific.

From a synopsis of their broad data base obtained during the NASA PEM- and ACE 1-missions over the Pacific Ocean (4679 GC/MS/ILS samples from 60°N to 72°S) Thornton et al. [1999] established a background pollution signal on the interhemispheric scale. For the troposphere below the flight altitude of 12 km over the central and eastern Pacific this signal of multiple continental sources (Asia and upwind) displays as a marked N-S-gradient of SO₂ (Figure 2.17). From 40°N to 40°S, the SO₂ VMR (altitude range 4 – 12 km) decreased by about an order of magnitude from around 100 – 200 pptv to 10 – 20 pptv. The southern hemi-

spheric troposphere below 4 km generally had SO_2 VMR < 30 pptv in the mid and high latitudes. Above 4 km SO_2 was < 30 ppt throughout the southern hemisphere, showing the smallest variability of all environments investigated.

Vertical columns of SO_2 (in Dobson Units)

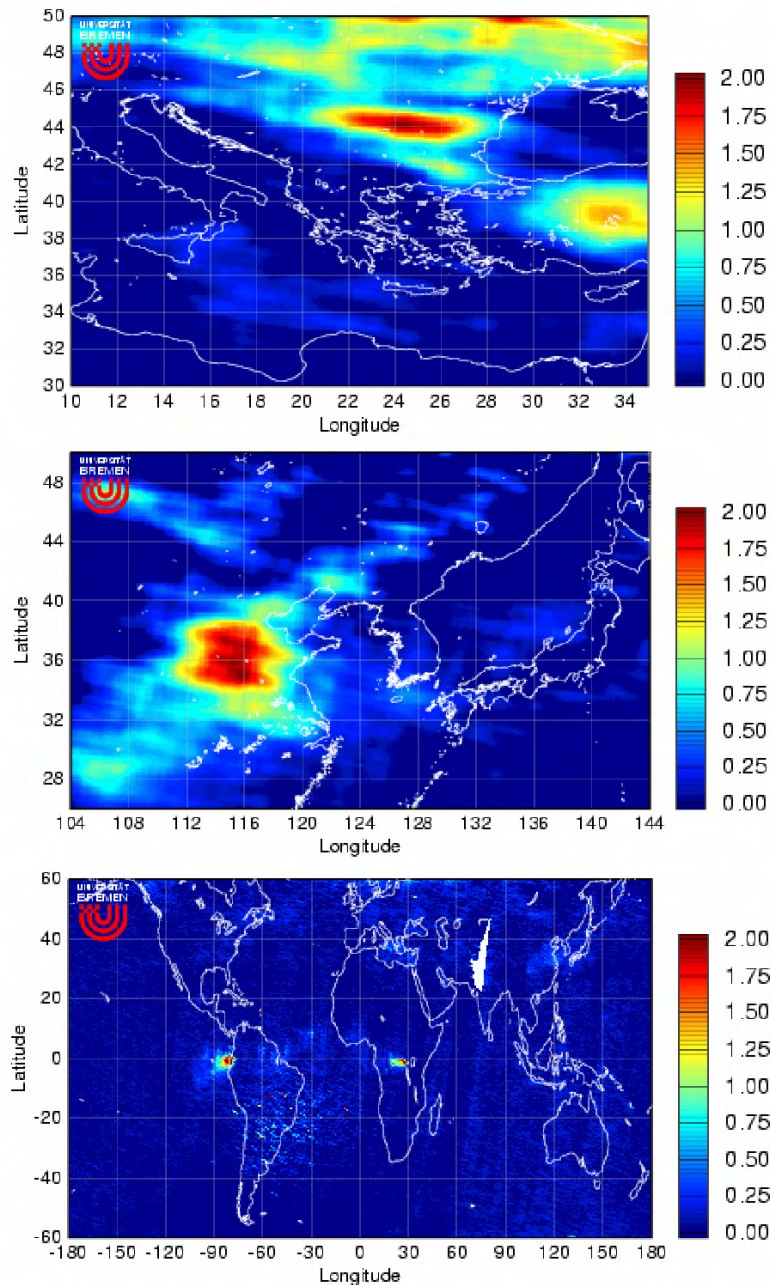


Figure 2.16 GOME satellite pictures of SO_2 (A. Richter, University of Bremen, unpublished results). Top panel: Global map retrieved in November 2002. Large amounts of SO_2 are emitted from volcanic eruptions (El Reventador, Nyamuragira, Mt. Etna) but some elevated SO_2 is also observed above China. For this image, airmass factors appropriate for a volcanic eruption have been used, underestimating SO_2 in the boundary layer where it is located in polluted regions. Middle panel: SO_2 columns from January 2000 above China. Large amounts of SO_2 are observed each winter in China, probably as a result of the use of sulphur rich coal for domestic heating and also in power plants. Lower panel: SO_2 columns from January 2000 above Eastern Europe. Most of the SO_2 observed probably is emitted by coal fired power plants.

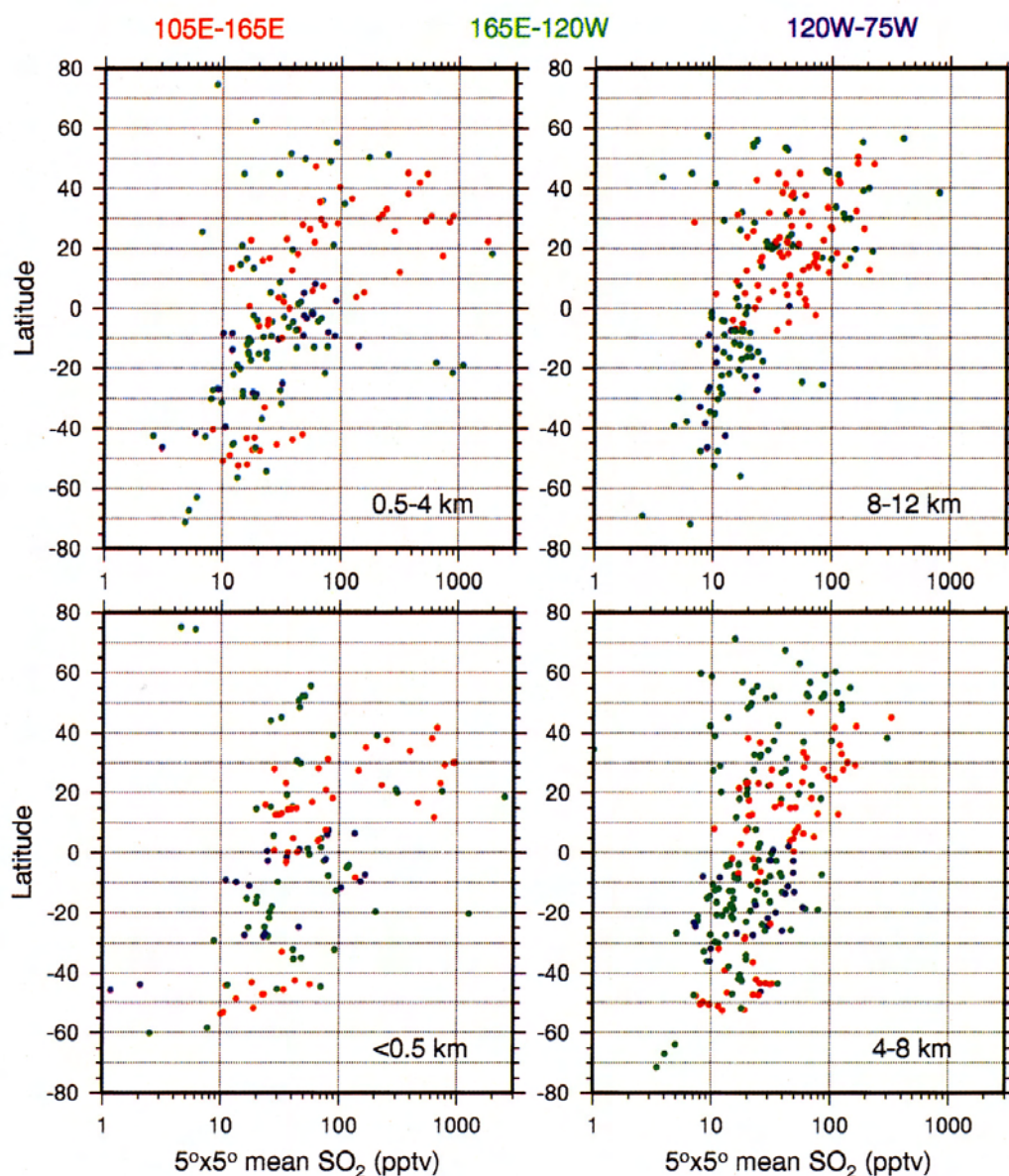


Figure 2.17 SO_2 above the Pacific Ocean from airborne GC/MS measurements by Thornton et al. (1999) during the NASA Pacific Exploratory Missions (PEM) and the First Aerosol Characterization Experiment (ACE 1) in 1991-1996. Data (arithmetic mean VMR) are binned in 5° longitude by 5° latitude boxes as function of altitude, latitude, and region.

SO₂ from volcanos

Besides anthropogenic sources, volcanos are the other principal source of the SO_2 in the remote troposphere. In June 1991 the Mt Pinatubo eruption injected SO_2 directly into the lower stratosphere. Three months later, the mixing of stratospheric and tropospheric air was reflected by relatively high mixing ratios of several hundred pptv in the UTLS above the northwestern Pacific. These values are quite similar to the 460 – 515 pptv reported by Meixner et al. [1981] from the plume of Mt. St. Helens at 11 km altitude above the North Sea. From their PEM and ACE 1 data, Thornton et al. [1999] conclude that, even in the absence of major volcanic activities, volcanos along the western Pacific ring of fire have a significant effect on SO_2 in the UTLS of the northern hemisphere and may contribute to most of the SO_2 found in

the middle and upper troposphere of the southern hemisphere, especially in the tropics with its enhanced convection. These findings have been substantiated further by recent results from TRACE-P [Tu et al., 2004]. Above the central North Pacific around Midway Island layers of SO₂ enhancement of several hundred pptv and up to 1.3 ppbv were detected, mainly in the 1 to 4.5 km altitude range. Applying several different trajectory- and chemistry transport models to the situations encountered and considering the emissions of the major east Asian anthropogenic SO₂ sources as well as the Mijake-jima volcano (Japan) the authors conclude that emissions from the volcano dominated the SO₂ distribution in the central Pacific during the spring 2001. This result is consistent with Chemistry-Transport-Model calculations by Graf et al. [1997, 1998] on the effect of quiescent and small eruptive global volcanism on the distributions and burden of SO₂ and sulfate. Although volcanic degassing contributes only 14 % to the total global SO₂ emissions, its impact on the global burden of SO₂ and sulfate was calculated to be 35 % and 36 %, respectively, with a most pronounced effect on concentrations and vertical profiles in tropical latitudes. The efficiency of volcanic emissions on the total atmospheric SO₂ burden (i.e. the relative contribution of volcanos to the atmospheric burden related to their share in the total source strength) was thus found to be about a factor of 5 higher than the respective figure for anthropogenic SO₂ emissions. The geographical distribution and height of volcanic emissions, which favours a longer lifetime of SO₂, are the main reasons [Graf et al., 1998].

SO₂ from aircraft

The impact of air traffic emissions in the North Atlantic flight corridor on upper tropospheric SO₂ and other species was investigated by the projects POLINAT [Schumann et al., 2000] and SONEX [Singh et al., 1999]. SO₂ abundances varied between 10 pptv and 1.5 ppbv, with maxima occurring at the levels of major air traffic from 10.5 to 11.5 km. The authors concluded that, although air traffic emissions are clearly measurable in terms of increased SO₂ within individual aircraft exhaust plumes, they have a small impact on the composition of the flight corridor region and were not detectable in the measurements at corridor scales. Using trajectories and chemical tracers, high VMR at major air traffic levels were interpreted as signals from surface emissions in the U.S.A. [Arnold et al., 1997].

Table 2.2: In situ aircraft measurements of SO₂ in the troposphere and tropopause region.

Environment	Experiment	Altitude range^a km	Mixing ratio^b ppt	Number of Obs.	Reference
1. Continental Troposphere					
(a) N.H., polluted					
US east coast	WATOX-86	BL	1830±2070	60	Thornton et al., 1987
		FT	140±210	4	
US east coast	TARFOX	0-4.5	0-20,000 ^c		Hobbs 2002
Canada, east coast	NARE	0-2	1000 ^d		Banic et al. 1996
Central Europe		FT(6-10)	19-57	12	Meixner 1984
		LS(9-14)	8-115	24	
Germany		8	200 ^e		Reiner et al. 1998
		>10	40-55	>50	

(b) Remote continental					
Western North America	GAME-TAG	BL FT(6)	112 160	20 59	Maroulis et al. 1980
(c) Tropical					
Amazon, dry season	ABLE-2A	BL FT HL	27 \pm 10 18 \pm 16 42 \pm 24	24 15	Andreae & Andreae 1988
Amazon, wet season	ABLE-2B	BL FT	24 \pm 14 15 \pm 8	13 12	Andreae et al. 1990
2. Marine Troposphere					
(a) continental influence					
Indian Ocean, Indian monsoonal outflow	INDOEX	0-5	900-1500 ^k		Lelieveld et al. 2001, Reiner et al. 2001
Yellow Sea, Asian continental outflow	TRACE-P	0.1-3	30-12,000 ⁿ		Tu et al. 2003
Central Pacific, Midway Isl.	TRACE-P	1-4.5	540-1300 ^o		Tu et al. 2004
Western Pacific, 110E-165E	PEM-West A/B, ACE 1	<0.5 0.5-4 4-8 8-12	87 162 36 60	548 580 522 551	Thornton et al. 1999
NW-Atlantic, US coast	WATOX	FT	85 ⁱ	6	Galloway et al. 1990
Bermuda		FT	29 ⁱ	10	
North Atlantic (Flight Corridor)	POLINAT	9 10 11 9	560 \pm 520 ^f 190 \pm 220 290 \pm 1480 40-200 ^g ;	921 1403 4658 >150	Schumann et al. 2000,
Northeast Atlantic		9	1000-3000 ^h		Arnold et al. 1997
North Atlantic continental rim	STRATOZ III	FT (4-12) FT (3-12)	30-350 20-260	ca. 45 ca. 40	Ockelmann and Georgii 1989
South American Pacific & Atlantic coast					
North Atlantic continental rim	TROPOZ II	FT (3-12) FT (3-12)	<20-100 <20-100 ^j	50 53	Wolz and Georgii 1996
South American Pacific & Atlantic coast					
NW-Atlantic, off U.S. coast	CITE-3	BL (1.5) FT (5)	456 \pm 804 89 \pm 41	158 24	Thornton et al. 1993
Northeast Atlantic, Tenerife	ACE-2	BL FT (1-7)	36 \pm 30 15 \pm 10	9 19	Andreae et al. 2000

North Atlantic, Azores	ASTEX	BL+FT (0.1-5)	146±179	312	Blomquist et al. 1996
b) Remote Marine					
Central Pacific	GAMTAG	BL, FT(6)	54, 85		Maroulis et al. 1980
SW-Atlantic, off Na- tal, Brazil	CITE-3	BL (1.5) FT (5)	100±142 101±77	48 18	Thornton et al 1993
Central Pacific	EMEX	BL FT	<10-43 <10-64		Thornton and Bandy 1993
Central Pacific, 165E- 120W	PEM- Tropics, PEM- West, ACE 1	<0.5 0.5-4 4-8 8-12	455 ¹ 434 ¹ 36 56	403 442 788 389	Thornton et al. 1999
Eastern Pacific, 75W- 120W	PEM- Tropics	<0.5 0.5-4 4-8 8-12	60 51 37 15	92 96 217 51	Thornton et al. 1999
3. Polar Troposphere					
North American Arc- tic	AGASP II	BL & FT	890±2130	160	Thornton et al. 1989
Arctic, circumpolar		0-8	bg: 10-100 ^m p. 200-1200		Jaeschke et al. 1999
Arctic, Northern Scandinavia		0-2 above TP 0-2 below TP	15-100 100-350	16 5	Möhler and Arnold 1992
4. Special conditions					
(a) Volcanically perturbed					
Mt. St.Helens plume, North Sea		10-11	460-515	2	Meixner et al. 1981
Western Pacific, 3 month after Pinatubo	PEM-W-A	7-12	121	35	Talbot et al. 1996
Central Pacific, plume of Miyake-jima	TRACE-P	1.3-3	300		Tu et al. 2004

^a FT = free troposphere, LS = lower stratosphere, BL = boundary layer, HL = haze layer, TP = tropopause, alt. mean or range given in brackets; ^b arithmetic mean ± s.d. or range, unless stated otherwise; ^c range of values for 18 flights supplied by Hobbs 2002; ^d estimated average peak vmr in BL from 15 flights; ^e mean and range of means given by authors; ^f data taken from (specify web source); ^g range of background vmr; ^h range of peak vmr; ⁱ median; ^j local pollution over Chile excluded; ^k peak vmr in polluted layers; ^l influenced by volcanos; ^m bg = background conditions, p = pollution; ⁿ range between continental background and peak vmr in plumes; ^o peak vmr in layers of volcanic and anthropogenic SO₂ transported above the convective BL over long distances.

Table 2.3: Overview of SO₂ mixing ratios observed from aircraft in characteristic tropospheric environments.

	continental		marine		
	remote		polluted	Continental outflow	remote
	tropical	temperate			
Upper troposphere				40-560	10 - 40
Free troposphere	15-20	100 - 150		500-1300	
Boundary layer	25 - 30		100 - 20000	30 - 12000	30 - 60

2.4.3 Dimethyl sulfide (CH₃SCH₃)

Dimethylsulfide (DMS) is the product of marine algae. Its marine and atmospheric abundance and flux from the ocean to the atmosphere varies considerably both geographically [Andreae and Raemdonck, 1983; Bates et al., 1987, 1992; Kettle and Andreae, 2000] and seasonally [Nguyen et al., 1990; Berresheim et al., 1991; Ayers et al., 1995; Turner et al., 1996], as well as interannually [Sciare et al., 2000].

In the marine atmosphere, the vertical profile as determined by the surface source, the atmospheric turbulent diffusion and a chemical lifetime of around a day in the lower troposphere (see Section 2.2 and Figure 2.2) decays exponentially with altitude throughout the free troposphere. This is generally observed both in the marine and continental free troposphere [Gregory et al., 1996; Davis et al., 1999; Bingemer et al., 1992] above the planetary boundary layer, where accumulation due to capping by inversions may occur. Significant deviations from this situation are found during vigorous convection and in storm systems.

Table 2.4 compiles some DMS mixing ratios observed at various altitude regimes of the marine troposphere. In the surface layer (0-30 m) of the atmosphere over the remote open ocean, DMS characteristically varies in a diurnal cycle between about 50 and 200 pptv, induced by the OH sink reaction [Andreae et al., 1985; Saltzmann and Cooper, 1988; Bandy et al., 1996; Davis et al., 1999]. From in situ aircraft sampling of the marine boundary layer atmosphere, mean mixing ratios of DMS ranged mostly between 10 and 80 pptv [Thornton and Bandy, 1993; Blomquist et al., 1996, Gregory et al., 1996; Talbot et al., 1997; Davis et al., 1999; Cubukcu et al., 2003]. The kinetics, products and local budgets of DMS are still not fully understood. While Blomquist et al., [1996] and Andreae et al., 2000] from Lagrangian-type aircraft experiments in the marine BL revealed that the kinetics and local budget of DMS and its major products are quantitatively well understood, Davis et al. [1999] conclude from their study that both sulphate and methanesulphonate from DMS are predominantly formed from complex and still poorly characterized heterogeneous processes. SO₂ and gaseous H₂SO₄ were identified as the major products of DMS, and both displayed regular diurnal cycles that were anti-correlated to DMS [Davis et al., 1999]. Measurements in the tropical boundary marine layer during PEM-Tropics B indicated that the intermediate DMS oxidation product DMSO is not correctly predicted or that an unidentified direct source of this compound may exist [Nowak et al, 2001].

Table 2.4: Mixing ratio of DMS observed in the marine troposphere.

Environment	Altitude	ppt DMS	No. of samples	Comment	Reference
Surface layer					
Pacific Ocean, Atlantic Oc.	≤ 30 m	100 – 200	~ 900	ship, approx. between dayt. Min and nightt. Max	Andreae et al., 1985
Pacific Ocean, Christmas Island	20 m	100 - 300	hundreds	Range between dayt. Min and nightt. Max	Bandy et al. 1996
Boundary layer					
Central Pacific, typical trade wind regime	BL	56	32	median	Thornton and Bandy 1993
Atlantic (Azores)	BL	46	188	Mean	Blomquist et al., 1996
Tropical Pacific, aged marine air	< 0.5 km	54; 47		Median of 2 data sets	Gregory et al., 1996
South of Tasmania	30-150m 900-1200m	80-120 20-50	~40 ~30		Russel et al. 1998; Mari et al. 1998
Free troposphere					
Central Pacific					
Tropical Pacific, aged marine air	3-13 km	6, 5		Median of 2 data sets	Gregory et al., 1996

In the mid- and upper troposphere above the oceans for conditions that are not disturbed by strong convection, the volume mixing ratio of DMS is generally only several pptv [Andreae et al., 1993; Cooper and Saltzmann, 1993; Johnson and Bates, 1993; Ferek and Hegg, 1993; Blomquist et al., 1996; Gregory et al., 1996]. Figure 2.18 shows a vertical profile of DMS from the BL to 13 km altitude, which is considered representative for aged Pacific marine air [Gregory et al., 1996]. The vertical transport of DMS and its products through deep tropical convection over the oceans receives special interest, as it might be a significant source of precursor gases at the tropopause level. The PEM-Tropics database reports mid-tropospheric DMS mixing ratios at 8-9 km of 4-5 pptv for convective situations and 1-2 pptv for non-convective situations [Fenn et al., 1999; Cubukcu et al., 2003].

Thornton et al. [1997] estimated the contribution of DMS to upper tropospheric SO₂ under conditions of deep convection from their DMS and SO₂ measurements in the boundary layer and free troposphere (> 8.5 km alt.) above the Pacific. They found that sufficient DMS was available at > 8.5 km only 1 % of the time during PEM-West A and 7% during PEM-West B, to maintain the steady state condition with SO₂, while during 92 % and 81 % of time, respectively, DMS could explain less than 25% of the SO₂ observed. The rare cases when upward transport of DMS could sustain the SO₂ levels present in the free troposphere were sampled near the top of typhoon „Mireille“. During this situation, 80 pptv of DMS were encountered at 12 km altitude in the eye wall cloud convection region, indicating a substantial entrainment of boundary layer air (90 pptv DMS). Mass flux considerations [Newell et al., 1996] lead to an estimated DMS-sulfur flux to the upper free troposphere of nearly half the mean DMS-input from the ocean into the boundary layer for this particular case. An assessment of the relevance

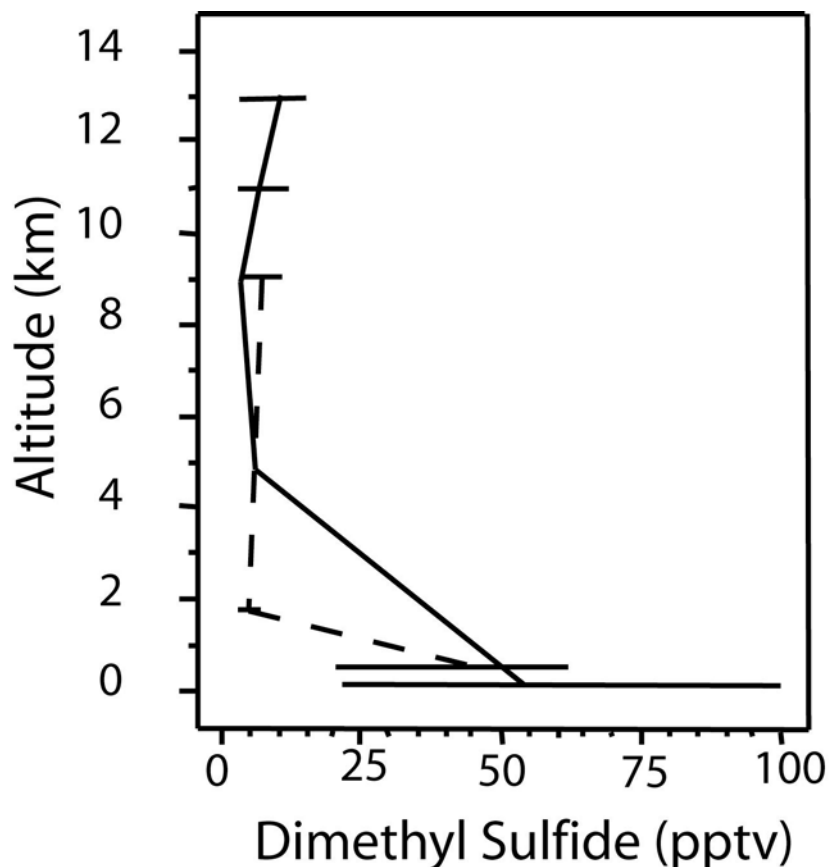


Figure 2.18 Vertical distribution of DMS measured by GC from DC-8 aircraft in aged (more than 10 days above ocean) Pacific marine air during NASA PEM-West Experiment in 1991 [Gregory et al., 1996]. The solid line connects median values in air of the northwestern tropical Pacific, the broken line connects median values in air of the eastern equatorial Pacific.

of such extraordinary conditions in the global sulfur budget requires more data to be incorporated into a global model.

The emission of DMS (and probably CH_3SH) from continental biogenic surface sources to the atmosphere and thus their abundance in the continental free troposphere is mostly even lower than in the marine case. In the FT below 6 km above the equatorial rainforests of the Amazon and of Africa, mixing ratios of 1-5 pptv DMS and <0.5 pptv CH_3SH are found [Andreae and Andreae, 1988; Andreae et al., 1990; Bingemer et al., 1992].

Regarding the role of DMS for the stratospheric aerosol layer, the major questions are: Does marine DMS play a significant role as *global* source of upper tropospheric SO_2 that may enter the stratosphere? Are the mixing ratios of DMS high enough to be of significance for the stratospheric sulfur budget? Based on the observations, the latter can be ruled out, and the first is unlikely. Only during strong convection and exceptional updraft events, such as in tropical cyclones, significant contributions of DMS to SO_2 in the upper tropical troposphere are possible. In a climatological sense quantitative aspects of this issue remain currently unresolved.

Table 2.5: H₂S mixing ratios (in pptv) sampled from ship or aircraft in the marine and continental boundary layer and free troposphere (below 5 km altitude; mean \pm s.d. or range, (*n*) = number of samples, BL = boundary layer, FT = free troposphere)

Marine Troposphere		Continental Troposphere	Reference
Continental influence	Marine conditions		
South Florida, aircraft, BL + FT, 58 \pm 34, (32)			Slatt et al., 1978
Abidjan, Ivory Coast, aircraft, monsoon layer ~130			Delmas and Servant, 1983
Bahamas, ship 82 \pm 56, (38)	Caribbean, ship 8.5 \pm 5.3, (36)		Saltzman and Cooper, 1988
Gulf of Mexico, ship 45 \pm 30, (21)			
West. North Atlantic, ship 10 – 40, (~20)	West. North Atlantic, ship 5 – 11, (7)		Andreae et al., 1991
	Equat. Pacific, ship 3.6 \pm 2.3, (72)		Yvon et al., 1992
West. North Atlantic, aircraft BL: 8 – 600, (27) FT: \leq 1 – 60, (15)	Tropical South Atlantic, aircraft BL: \leq 1 – 12, (12) FT: \leq 1 – 10, (7)		Andreae et al., 1993
West. North Atlantic, aircraft BL: 117 \pm 139, (14) FT: 20.5 \pm 14.7 (6)	West. North Atlantic, aircraft BL: 8.4 \pm 1.2 (2) FT: 3.0 \pm 3.2 (4)		Cooper and Saltzman, 1993
	Tropical South Atlantic, aircraft BL: 2.9 \pm 1.4, (13) FT: 1.0 \pm 2.2, (9)		
		Amazon rainforest, aircraft BL: 47 \pm 21, (6) FT: 7 \pm 7, (3)	Andreae et al., 1990
		Congo rainforest, aircraft BL: 25 \pm 16, (~9) FT: 7 – 13, (3)	Bingemer et al., 1992

2.4.4 Other precursor gases

Carbon disulfide (CS₂)

The large-scale tropospheric distribution of the relatively short-lived CS₂ as observed in situ from aircraft shows mixing ratios to drop in general with distance from the continents (Figure 2.19), suggesting that anthropogenic sources dominate over marine sources. Relatively high and variable mixing ratios were obtained over land (6.8+4.4 pptv at 6 km above the central U.S., [Tucker et al., 1985]), over coastal or continentally influenced areas (26+14 pptv at 7.3-7.9 km above Caribbean and western North Atlantic; [Carroll, 1985]; 5-27.7 pptv (range of flight means) along the western shores of South America [Tucker et al., 1985]), and in particular in continental outflow (0.5-30 pptv along the eastern seaboard of the U.S. [Bandy et al., 1993; Cooper and Saltzman, 1993]). Above the northeastern Pacific Ocean in continental outflow of Asia, Blake et al. [2004] observed as much as 90 pptv CS₂ in plumes transported from northern China, with a strong correlation to CO and other pollution markers. Remote

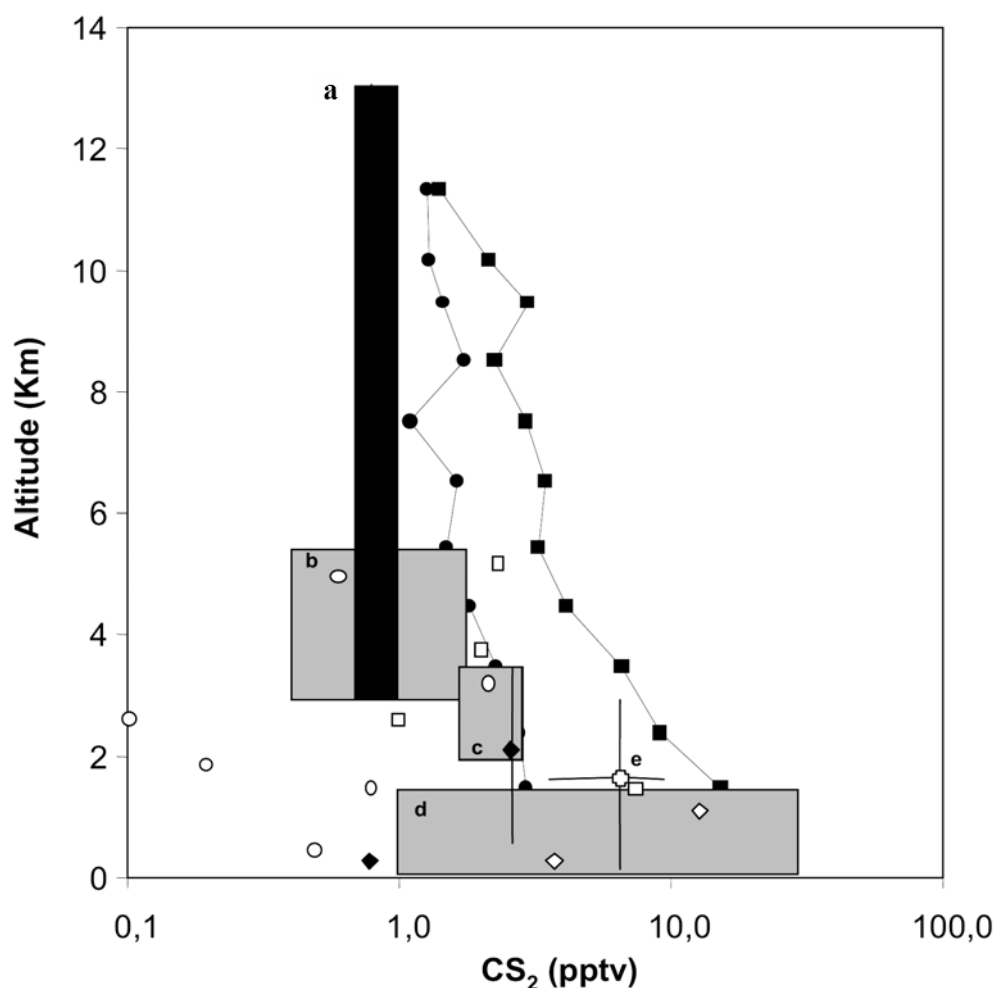


Figure 2.19 CS₂ mixing ratios in the marine troposphere observed by various investigators from in situ measurements on board aircraft, arithmetic mean values unless stated otherwise, ● = Central Pacific at < 25°N, Blake et al. (2004); ■ = Western Pacific at > 25°N, Asian continental outflow, Blake et al. (2004); □ = Northwest Atlantic, Cooper and Saltzmann (1993); ○ = Tropical Southwest Atlantic, Cooper and Saltzmann (1993); ◇ = Northwest Atlantic, Johnson and Bates [1993]; ◆ = Tropical Southwest Atlantic, Johnson and Bates (1993); a = aged South Pacific marine air, median, lower and upper quartiles for 3-13 km, Gregory et al. [1996]; b = Western Tropical Atlantic, range of values, Bandy et al. [1993]; c = Tropical Southwest Atlantic, range of values, Bandy et al. [1993]; d = Northwest Atlantic, continental outflow, range of values, Bandy et al. [1993]; e = Eastern North Atlantic (Azores), horizontal bars give standard deviation, Blomquist et al. [1996].

from the continents or in aged marine airmasses, the free troposphere in general contains less than 5 pptv of CS₂. The mean vmr of CS₂ reported by various authors for such conditions mostly fall in the range of 0.5 to 2pptv, in particular for altitudes above 5 km [Bandy et al., 1993; Cooper and Saltzman, 1993; Johnson and Bates, 1993; Gregory et al., 1996; Blake et al., 2004].

Hydrogen sulfide (H₂S)

Mixing ratios of atmospheric H₂S are reported for various atmospheric environments, and fluxes between the atmosphere and several biogeochemical compartments (e.g. ocean, shelf, estuaries, salt marshes, mud flats, soils, volcanoes etc.) were investigated. For a thorough discussion of these data, which show an enormous range of variability and dependence on environmental conditions (e.g. productivity and type of vegetation, tide, temperature, light, soil humidity, pH, etc.), the reader is referred to the reviews of Shooter [1999] and Watts [2000], which also cover analytical and methodological caveats against some of these data. There are however only few measurements of H₂S from aircraft or ship cruises that may be regarded representative for the troposphere above the oceans or continents. Overall, H₂S mixing ratios are mostly found to be higher in the continental than in the marine troposphere, higher in the northern than in the southern hemisphere (Table 2.5), and to decrease with altitude, thus displaying the effects of its continental (and anthropogenic) ground based sources and the tropospheric sink (reaction with OH, see Section 2.2). In the northern hemisphere marine boundary layer under coastal and continental influence, ship measurements show mean \pm s.d. = 57 \pm 29 pptv [Saltzman and Cooper, 1988;] and 25 \pm 10 pptv [Andreae et al., 1991]. A series of flights along the eastern seaboard of the U.S. showed 10-200 pptv [Andreae et al., 1993] and 117 \pm 139 pptv [Cooper and Saltzman, 1993]. In marine airmasses the mean H₂S mixing ratios fall into the narrow range of 1-15 pptv in both hemispheres and throughout the boundary layer and free troposphere below 6 km altitude, see Table 2.5 [Slatt et al., 1978; Delmas and Servant, 1983; Saltzman and Cooper, 1988; Andreae et al., 1991; Cooper and Saltzman, 1993; Yvon et al., 1993; Andreae et al., 1993]. Above the equatorial rainforest of the Amazon [Andreae et al., 1990] and Congo [Bingemer et al., 1992] 47 \pm 21 pptv and 25 \pm 16 pptv H₂S, respectively, were found in the boundary layer, and 7 \pm 7 pptv and 7-13 pptv above. Much higher values of around 130 pptv H₂S were reported by Delmas and Servant [1983] for the monsoon layer above Ivory Coast during January and March.

2.5 Fluxes

Sulfur-containing gases are emitted into the atmosphere from anthropogenic and biological sources, as well as from geological (volcanic) sources. The estimated total annual emissions of gaseous sulfur to the atmosphere from all sources range between 89 – 102 Tg S/yr for the years 1980 to 1990 [Spiro et al., 1992; Benkovitz et al., 1996; Rodhe 1999]. Anthropogenic SO₂ contributes about 70-80 % of this flux.

Biogenic reduced sulfur compounds in the atmosphere originate both from the land surface and from the upper ocean. A large number of reduced sulfur compounds have been measured in the atmosphere and in natural waters. However, in terms of global integrated fluxes and atmospheric lifetimes (Figures 2.2 and 2.20), only a few compounds need to be considered: OCS, CS₂, DMS, CH₃SH, H₂S, and SO₂. Based on atmospheric lifetimes, these compounds may be separated into two families: OCS (and its precursor CS₂) with a multi-year lifetime and the rest of the sulfur species with lifetimes in the order of hours to days. The task of understanding the stratospheric aerosol source from OCS is simplified by its long atmospheric lifetime and its relative constant mixing ratio throughout the whole troposphere. In contrast, the most important source of tropospheric aerosols is the rapid oxidation of the shorter-lived

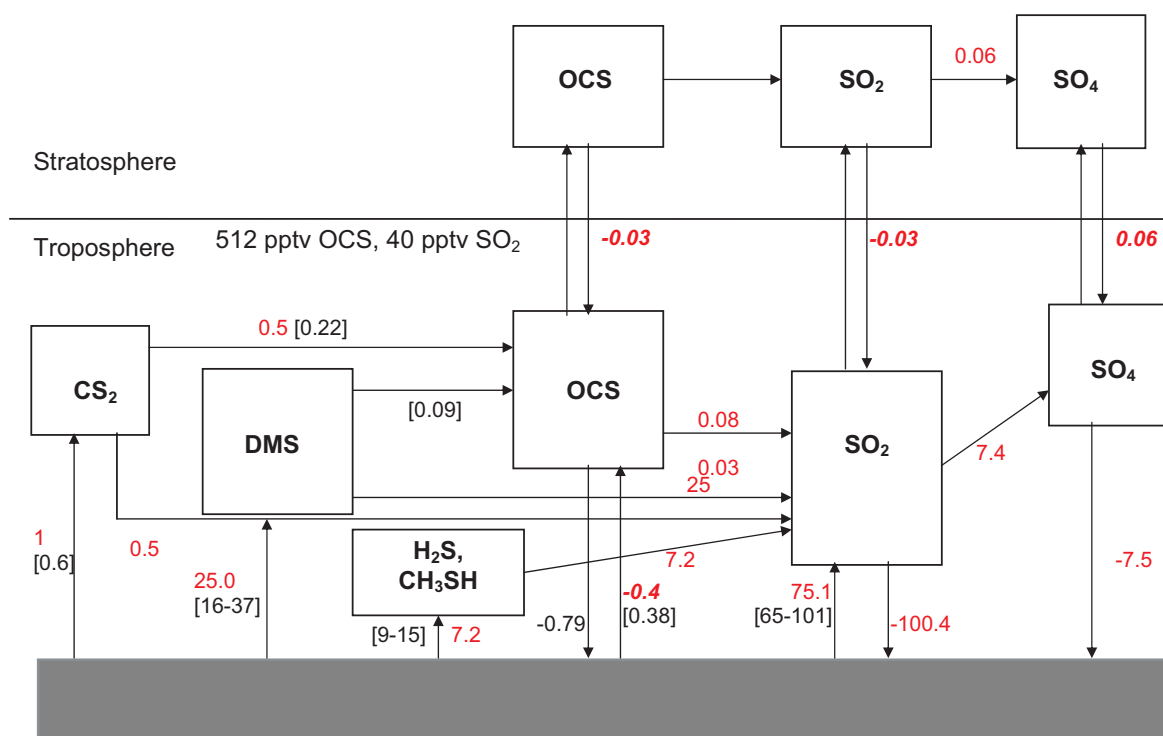


Figure 2.20 Fluxes (Tg S yr^{-1}) of major sulfur-containing precursor gases and their products in the atmosphere. Black numbers in square brackets are derived from observations as discussed in section 2.4, red numbers are based on the AER 2D-model calculations presented in Chapter 6 under the assumptions of 40 pptv of SO_2 , 512 pptv of OCS, and no aerosol imposed in the TTL. At some bidirectional fluxes the net model-fluxes are given as bold italic characters. A loss from the troposphere is denoted negative.

sulfur species near the source regions. Hence, in order to understand the global distribution of sulfate aerosol it is important to know the regional variability of fluxes of the short-lived sulfur species [Simó and Dachs, 2002]. The global fluxes of reduced sulfur compounds have been assessed in previous work [e.g., Chin and Davis, 1993; Berresheim et al., 1995; Watts, 2000]. This section collects more recent results to understand global fluxes at higher spatial and temporal resolution. Figure 2.20 displays the fluxes in the system based on current knowledge from modeling and field work. While the troposphere/stratosphere fluxes of OCS, SO_2 and SO_4 based on modeling are balanced, there is a 23 % (0.21 Tg S/yr) imbalance between the tropospheric sources and sinks of OCS.

2.5.1 Carbonyl Sulfide Fluxes

The global OCS emission of around 0.7 Tg S yr^{-1} is smaller than that of the other reduced sulfur gases [Chin and Davis, 1993; Watts, 2000], but due to its long lifetime, OCS is, besides SO_2 , the most important precursor of the sulfate aerosol in the stratosphere [Crutzen, 1976]. An imbalance in the globally integrated sources and sinks of OCS was noted by Chin and Davis [1993] and indicated that not all terms in the global budget were adequately well characterized. Experimental errors in the methods used to assess the OCS uptake by soils were subsequently identified, and the updated budget of Watts [2000] replaced the significant soil source by a significant soil sink. The main sources in this budget were identified as CS_2 oxidation, sea-air flux, and DMS oxidation, and the main sinks were identified as uptake by oxic soils, vegetation, and chemical reactions taking place mostly in the stratosphere [Watts, 2000].

OCS produced from biomass burning was assumed not to be significant on the global scale, but as discussed by Berresheim et al. [1995] and more recently measured by Notholt et al. [2003], biomass burning might be the most important OCS source to the atmosphere in tropical latitudes during the burning season. Since the tropospheric air has to pass the upper tropical troposphere before entering the stratosphere [Holton et al., 1995] the impact of biomass burning emissions on the OCS fluxes needs to be recalculated.

Kettle et al. (2002a) used a series of databases and models to calculate the monthly mean and spatial distribution of the dominant sources and sinks of OCS and produced updated global, annually integrated estimates. The work suggested a temporal variation in the integrated OCS loading with a similar phase for both the Northern and Southern Hemispheres. The observations were corroborated in an inverse approach by Kettle et al. [2002b] who used available time series of OCS total columns from several stations to infer seasonal variations of hemisphere-integrated loading. Important differences were noted in the forward and inverse approaches used to deduce global OCS fluxes, and future investigations might resolve these discrepancies.

2.5.2 Sulfur Dioxide Fluxes

Anthropogenic SO₂ emissions from fossil fuel combustion and the industry contribute to about 70-80 % of the total flux of sulfur gases into the global atmosphere (Table 2.6), mainly in the northern hemisphere. The SO₂ emissions (Figure 2.21) have been reduced between 1982 – 2001 by 52 % in the U.S.A. [EPA, 2003] and by more than 60 % in Europe between 1980 – 2000 [Loevblad et al., 2004]. This reduction is partially compensated by the rapidly growing SO₂ emissions from countries in east and southeast Asia, see Figure 2.22 [Streets et al., 2000]. Emission projections predict a further shift of the global emission patterns towards tropical latitudes [Carmichael et al., 2002], where deep convection favours upward transport into the TTL. While the emission changes are reflected by the doubling of the anthropogenic sulfate aerosol component at Midway Island in the Pacific during 1981-1995 [Prospero et al., 2003], the fraction of SO₂ that actually reaches the TTL is highly uncertain, partly due to the liquid phase chemistry during the ascent, which is not fully understood.

Volcanos and biomass burning further contribute to the atmospheric SO₂. The rare large direct injections of SO₂ deeply into the stratosphere by single volcanic eruptions is evident from historical [Stoiber et al., 1987; Halmer et al., 2002] and TOMS data [Bluth et al., 1993], as

Table 2.6: Annual sulfur emissions to the atmosphere, excluding sea salt and soil dust, based on Rodhe [1999], Watts [2000] and Kettle and Andreae [2000]. The SO₂-flux is for the year 1990, fluxes of reduced gases with a dominant natural source do not refer to a specific year.

Sulfur gas	Source	Global flux (range) Tg S yr ⁻¹
SO ₂	fossil fuel combustion	70 (60-80)
	volcanos	8 (4-16)
	biomass burning	3 (1-5)
DMS	ocean	24 (15-33)
	soils, terrestrial vegetation	2 (1-4)
H ₂ S	anthropogenic, soils	7 (6-8)
CH ₃ SH	ocean	5 (3-7)
CS ₂	anthropogenic, ocean	0.56 (0.4-0.72)
OCS	ocean, anthropogenic	0.7 (0.59-0.85)

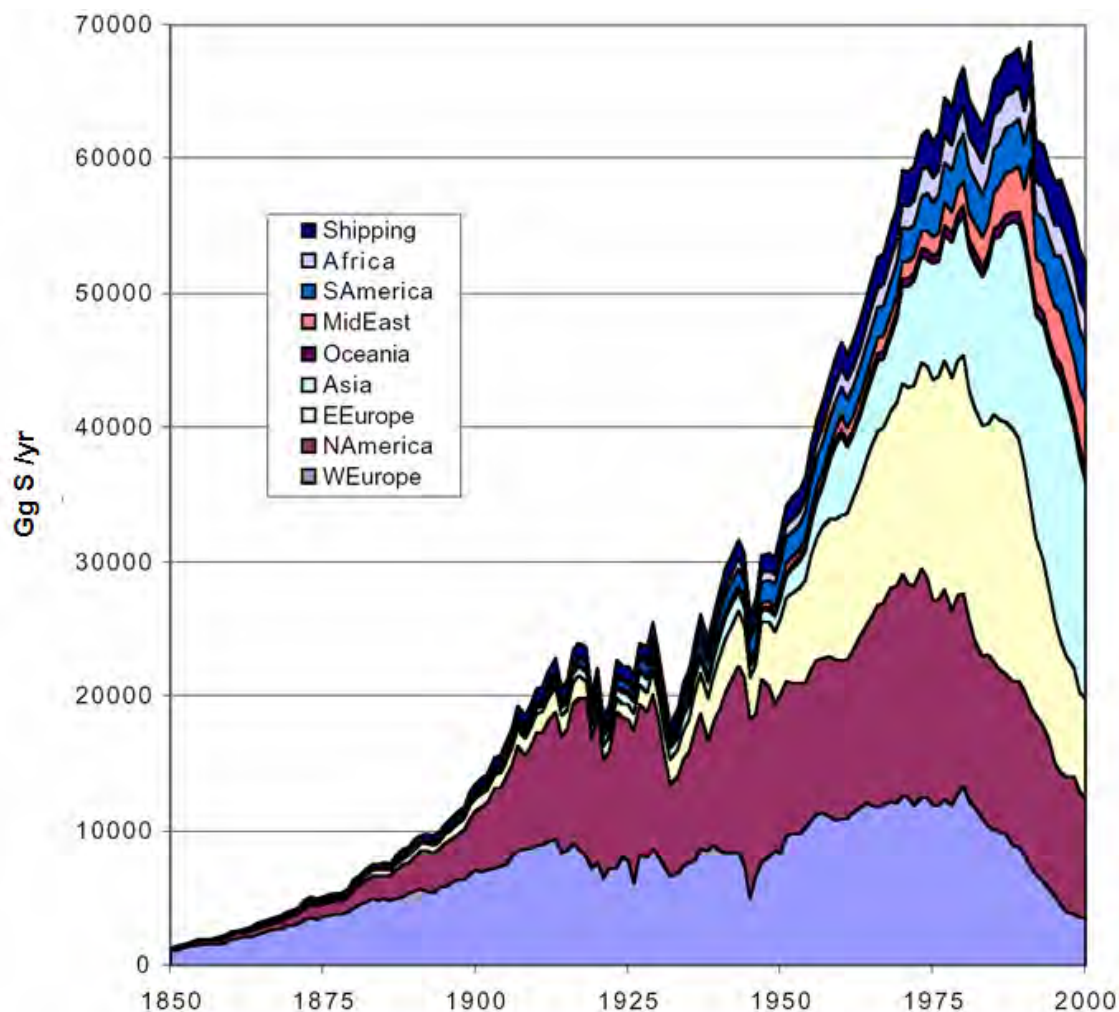


Figure 2.21 History of anthropogenic Sulfur emissions in geographical regions from 1850 – 2000. From Stern [2003].

well as from ATMOS observations [Rinsland et al., 1995]. Quiescent volcanic degassing and small eruptions contribute to the tropospheric SO_2 background, but the estimated fluxes are considered highly uncertain [Penner et al., 2001; and references therein]. Model calculations by Graf et al. [1998] indicate that the flux of sulfur gases from volcanoes (14 ± 6 Tg S/yr), dominated by quiescent and small eruptive emissions (10 Tg S/yr), leads to an effect on the sulfate burden of the free troposphere that is comparable to that of anthropogenic SO_2 sources, although its source strength is less than 20 % of the latter. This is caused by the altitude-latitude distribution of volcanic emissions, and is most pronounced in tropical latitudes.

In addition to surface sources, potential contributions from aircraft emissions to the atmospheric sulfur fluxes have to be considered. Model calculations by Kjellström et al. [1999] indicate, that the relative contribution of aircraft emissions to the atmospheric sulfate burden is larger than the ratio between aircraft emissions and surface emissions, due to the relatively long lifetime of SO_2 emitted at high cruising altitudes. However, in terms of sulfate mass balance, the overall impact of aircraft emissions is small.

The greatest single uncertainty in the overall sulfur flux to the stratosphere is presently the SO₂ flux within tropical convection, especially with regard to actual and predicted shifts of the global emission patterns towards tropical latitudes. Since the lifetime of SO₂ in the TTL is increased with respect to its lifetime at lower altitudes due to both the altitude dependence of its sink reaction with OH (see Figure 2.2) and the low washout/snowout capability of this uppermost tropospheric layer, the overall uncertainty is mainly given by that of the estimate of the vertical SO₂ flux at the bottom of the TTL. It seems that there are several ways to estimate

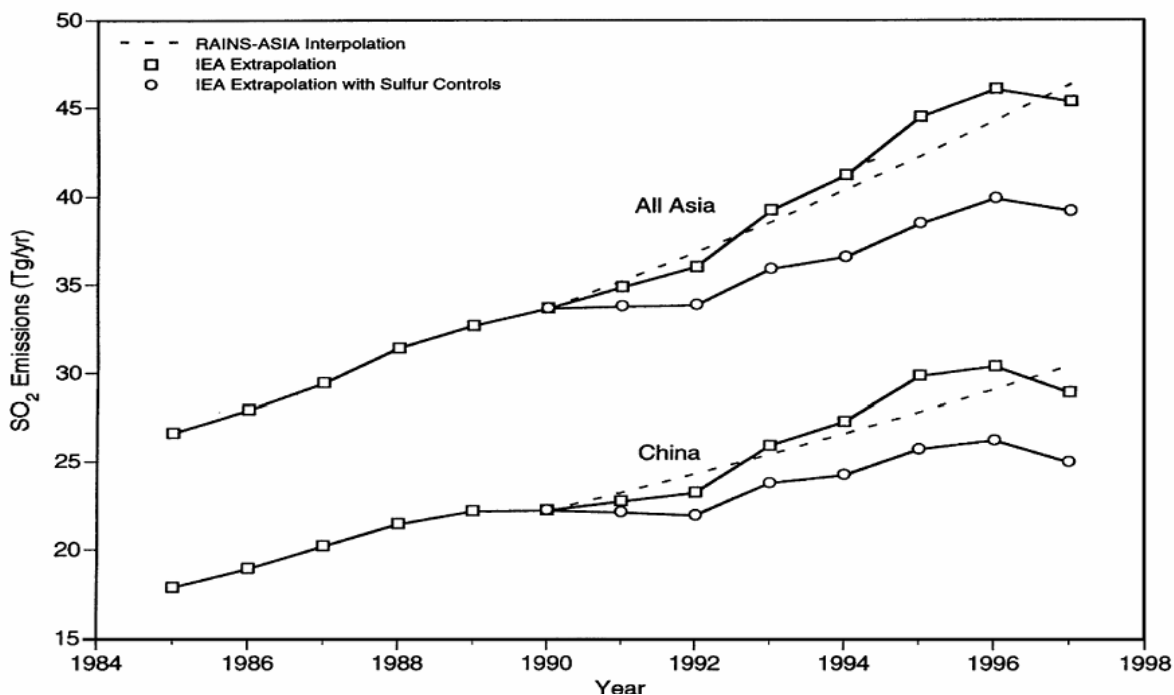


Figure 2.22 History of Asian anthropogenic SO₂ emissions from 1985–1997. From Streets et al. [2000].

the average SO₂ concentration at the lower boundary of the TTL, but they are all back of the envelope calculations. 10 % of the continents between ± 15 degrees latitude are covered with deep convective clouds. 50 % of the input from the boundary layer is detrained into the troposphere and does not make it to the TTL. Therefore, using these numbers as multipliers and the current SO₂ emissions inventories, a rough estimate can be made of the fraction of emissions entering the TTL. The mass input into the TTL is about 1.5×10^{11} kg/s. If we assume a pipe from the boundary layer to the TTL and that the average mixing ratio in the boundary layer is known, then the rate of SO₂ pumping into the TTL can be calculated. This would give an independent SO₂ flux estimate possibly very different from what has been estimated above. Knowing the fluxes at any altitude, the steady state concentrations will depend on all the sinks and oxidizers/scavengers. That will depend on OH radical concentration and liquid water droplet concentration. The OH concentrations show a large variability. Furthermore, observations suggest, that HO_x levels were frequently 2-4 times higher previously calculated assuming only the primary source, the photolysis of O₃ [Jaeglé, 2001 and references therein].

2.5.3 Dimethyl Sulfide Fluxes

DMS is the second largest source of gaseous sulfur to the troposphere after SO₂. Most of the DMS in the atmosphere originates in the upper ocean and is produced by phytoplankton either as an osmolyte [Kirst et al., 1991], a cryoprotectant [Karsten et al., 1992], or as a sink of free radicals [Sunda et al., 2002]. Other minor sources include salt marshes and possibly vegeta-

tion [Watts, 2000]. The importance of oceanic DMS as a source of sulfur to the atmosphere was recognized in an early study by Lovelock et al. [1972], but the biological nature of the source made it difficult to gain an understanding of the spatial and temporal distribution of the air-sea fluxes until enough information was available to establish surveys over larger regions. Early work on establishing the temporal and spatial variation of DMS concentration was performed for the Pacific Ocean [Bates et al., 1987], the Southern Ocean [Turner et al., 1995], and the North Sea [Turner et al., 1996]. Kettle et al. [1999] drew together data of most of the available measurements and were able to determine the spatial and seasonal distribution of DMS sea surface concentrations over most of the oceans. The largest concentrations are observed at high latitudes with a seasonal peak in springtime that does not coincide with the chlorophyll maximum associated with the spring bloom. The temporal and spatial pattern of fluxes follows the same general trend than the sea surface concentrations, and the annual average DMS flux from the ocean probably lies in the range 15-33 Tg S yr⁻¹ [Kettle and Andreae, 2000] with earlier estimates ranging up to 54 Tg S yr⁻¹ (see the review of Watts [2000]). The more recent literature uses the same data set of in-situ sea surface DMS measurements to calculate global, monthly mean DMS fields by considering separately regions of high and low biological activity [e.g., Anderson et al., 2001; Simó and Dachs, 2002]. The latest update of the in-situ DMS measurements has been made available by the Pacific Marine Environmental Laboratory at <http://saga.pmel.noaa.gov/dms/> (Jim Johnson, private communication, 2003). Global mapping procedures would be facilitated by mechanistic models that explain and predict DMS concentrations in terms of biological interactions, chemical sources and sinks, and ocean circulation processes. Progress has been made in ecosystem box models [e.g., Gabric et al., 1993], one-dimensional models [e.g., Lefèvre et al., 2002], and regional coupled biological/physical models [e.g., van den Berg et al., 1996] that incorporate DMS production and destruction terms within a larger web of biological trophic interactions. Aumont et al. [2002] have developed a global coupled ecosystem model incorporating DMS, and they note that one set of model rate constants describing the DMS budget may not be adequate to describe the temporal and spatial variation of DMS for all oceans. Extrapolation of upper ocean DMS concentrations to actual fluxes across the sea-air interface is further limited by large uncertainties in gas flux parameterizations [e.g., Zemmeling et al., 2002]. Considerable progress in the direct measurement of DMS fluxes above the sea surface and of the air/sea transfer coefficients has recently been achieved by employing eddy correlation techniques [Stevens et al., 2003a, b; Huebert et al., 2004].

2.5.4 Hydrogen Sulfide Fluxes

Other reduced compounds represent minor sources of sulfur to the atmosphere in comparison to oceanic DMS [Watts, 2000]. The flux of H₂S may be the second most important source of reduced sulfur to the atmosphere with an estimated source strength of about 7 Tg S yr⁻¹ [Watts, 2000]. H₂S originates from a variety of sources, and the most important may be anthropogenic followed by volcanism [Watts, 2000]. The open ocean H₂S source quoted by Watts [2000] is uncertain because H₂S should exist mostly in dissociated, ionised form at seawater pH [Andreae et al., 1991]. Shooter [1999] concluded that there is probably not a significant flux of H₂S from the ocean to the atmosphere.

2.5.5 Methyl Mercaptan Fluxes

CH₃SH from the oceans may be the next most important source of reduced sulfur to the atmosphere. Sea surface CH₃SH and DMS data collected during a meridional transect of the Atlantic Ocean have revealed that CH₃SH concentrations and fluxes are approximately 20 % those of DMS [Kettle et al., 2001]. Scaling the results of this one cruise with the previous work for the global oceanic DMS flux suggests that the global CH₃SH flux is in the range 3-7

Tg S yr^{-1} and may therefore be comparable to the H_2S flux. However, the distribution of the sources of H_2S and CH_3SH is very different with H_2S being possibly the most important reduced sulfur outgassed from land surfaces. In contrast, the high flux regions for CH_3SH appear to be approximately coincident with DMS so that there may be few regions where CH_3SH is the most important source of reduced sulfur to the atmosphere. Future studies will have to shed more light on the spatial and temporal distribution of CH_3SH and this may lead to the development of process models incorporating the mechanisms of formation and destruction on a global scale.

2.5.6 Carbon Disulfide Fluxes

As a source of reduced sulfur to the atmosphere, CS_2 ranks after DMS, H_2S , CH_3SH and OCS with an estimated annual flux of 0.6 Tg S yr^{-1} [Watts, 2000]. Watts [2000] ranks the most important sources of CS_2 anthropogenic, followed by the outgassing from the sea surface, and emission from anoxic soils. The spatial and temporal variation of the dominant sources and sinks of CS_2 are perhaps better understood than the variability of DMS, H_2S , and CH_3SH . The spatial and temporal distribution of the anthropogenic sources can be estimated by scaling the integrated estimate with other fields of human activity that are better understood, such as the anthropogenic SO_2 emission [e.g., Kettle et al., 2002a]. An emission inventory for CS_2 (and OCS) emissions of Asia, which covers the major industrial and agricultural processes relevant for these gases, has been recently established by Blake et al. [2004]. A total Asian CS_2 emission of $99 \pm 65 \text{ Gg yr}^{-1}$ was derived, with the industrial manufacture and use of CS_2 itself being the largest (91 %) single contributing source. These CS_2 emissions agree well with independent estimates by the same authors, which were derived from in situ aircraft measurements of CS_2/CO and CS_2/CO_2 ratios made in Asian continental outflow over the Pacific Ocean during the TRACE-P missions [Blake et al., 2004] in relation to regional CO and CO_2 emissions. The oceanic source of CS_2 to the atmosphere was estimated from measurements by Chin and Davis [1993], updated by Watts [2000]. More recently, Kettle [2000] and Kettle et al. [2002a] have determined the spatial and temporal distribution of the global oceanic CS_2 flux based on the observation that the species is photochemically produced in the upper ocean [Xie et al., 1998] and has a chemical lifetime in seawater [Kim and Andreae, 1987] that exceeds the residence time with respect to surface outgassing. The model results for the CS_2 fluxes are highest in the equatorial regions with lowest solar zenith angles [Kettle et al., 2002a].

2.5.7 Meteors, cosmic radiation, and rocket exhaust

Meteors

The meteoric debris mass influx has been surveyed by various authors. Hunten et al. [1980] state that the different results agree to within 50 % and they suggest a value of 44 metric tons per day or $1.0 \times 10^{-16} \text{ g cm}^{-2} \text{ s}^{-1}$ for the whole Earth [Hughes, 1978]. Most of the material ablates in the 80 – 100 km altitude region, leading to a meteoric aerosol number density profile that peaks at 84 km. Figure 2.23 shows the effects in terms of particle number and mass for the stratosphere [Hunten et al., 1980]. The elemental composition of interplanetary dust, meteors and chondritic meteorites are alike and correspond closely to that of the sun. According to Turco et al. [1981] the sulfur component of meteors is $\leq 10 \%$ of the total meteoritic mass, resulting in a sulfur flux to the earth of 4 tons per day.

Hunten et al. [1980] and Turco et al. [1981] calculate $2 \times 10^{-15} \text{ g cm}^{-2} \text{ s}^{-1}$ (~ 820 tons per day) for the overall net mass flux from the troposphere to the stratosphere of all material that is transformed into aerosol particles during volcanically quiescent times. Comparing this with the total meteoric mass influx of about $1 \times 10^{-16} \text{ g cm}^{-2} \text{ s}^{-1}$ (~ 44 tons per day) suggests that the

meteoric mass flux should constitute about 5 % of the total aerosol mass flux during volcanically quiescent times.

Turco et al. [1981] and Hunten et al. [1980] conclude from their model studies that micrometeorites contribute at large sizes and recondensed meteor ‘smoke’ at small sizes. Meteoric debris is an important natural aerosol constituent for particles larger than 1 μm throughout the stratosphere, and may be dominant for particles less than 0.01 μm above 20 km. For other sizes and altitudes, meteoric material generally comprises less than 10 % of the total aerosol mass. Meteoric dust is likely to be the dominant aerosol in the upper stratosphere, where the prevailing high temperatures cause the aqueous sulfuric acid solution droplets to fully evaporate (see Figure 2.23b). Very few meteoritic particles reach the upper troposphere in their natural state as most of them coagulate with the stratospheric $\text{H}_2\text{SO}_4\text{-H}_2\text{O}$ droplets. However, Turco et al. [1981] point out that because of a lack of detailed observational data, these model

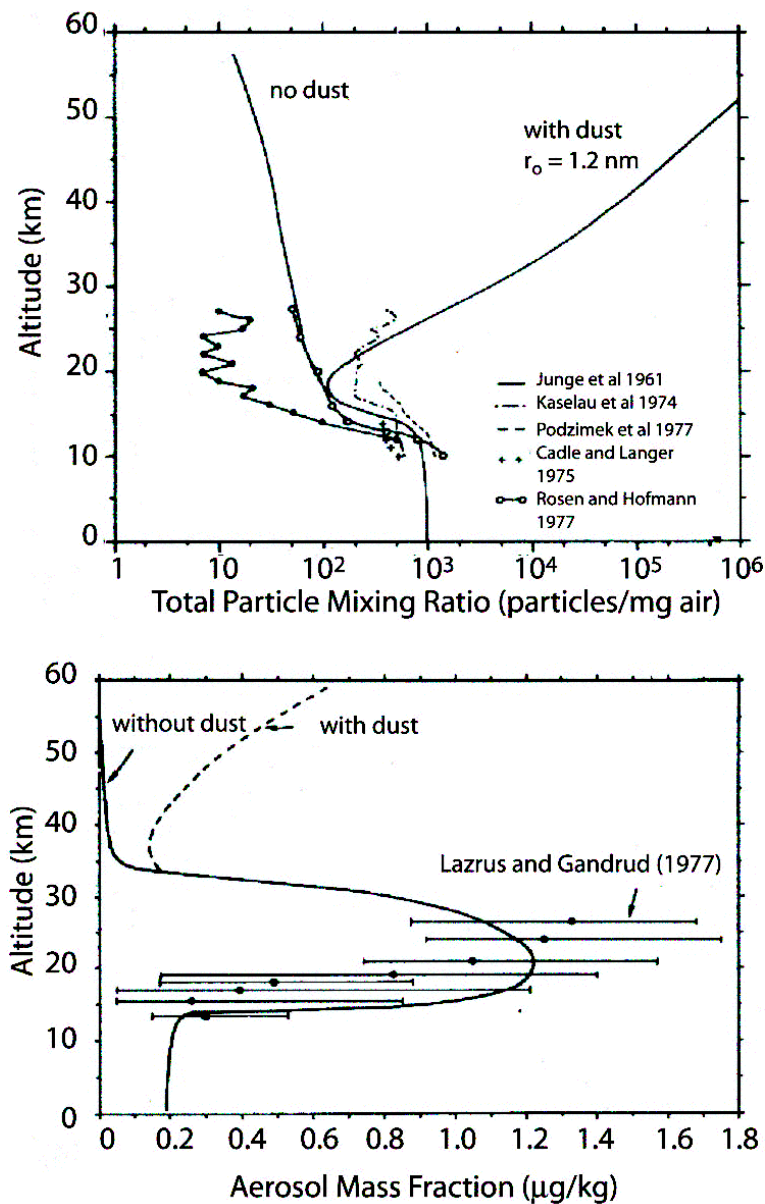


Figure 2.23 Total number of particles and mass mixing ratios, calculated with a stratospheric aerosol model that includes the meteoric dust assuming 1.3 nm smoke particles. Observations of stratospheric aerosol mass and number are also shown. From Hunten et al. [1980].

calculations cannot be rigorously checked, a statement that still holds true today. Meteoric Na may be an important participant in the positive ion chemistry [Liu and Reid, 1979]. Furthermore, Turco et al. [1981] speculate that metal ions of meteoric origin can neutralize sulfuric acid aerosols in the upper stratosphere, which could lead to a reduction in ambient H₂SO₄ abundances.

A more recent study by Bland et al. [1996] summarizes observational results yielding a higher total mass flux of extraterrestrial particles of 130-260 tons per day. These authors also provide arguments that the flux of meteoritic particles to the Earth should have remained roughly constant over the past 50,000 years. A direct measurement of the mass accretion rate of cosmic dust for the mass range 10⁻⁹ to 10⁻⁴ g was made by Love and Brownlee [1993], yielding ~100±50 tons per day. The meteoric mass distribution peaks near 1.5 × 10⁻⁵ g (200 μm in diameter). For the interval 10 to 10⁶ g. Bland et al. [1996] give a small contribution of 0.15 tons per day.

Nielsen et al. [1991] state that, based on Keil [1969] typical sulfur concentrations for iron and stone meteorites lie between 3 and 50 g per kg, and therefore an estimate of 10 g per kg for the mean sulfur content of the Earth seems realistic. Assuming an overall meteoric mass flux between ~200 tons per day [Bland et al., 1996] and 40 tons per day [Hunten et al., 1980] results in a meteoric sulfur input between 2.0 and 0.4 tons per day, respectively.

Murphy et al. [1998] have performed mass-spectrometric single particle analysis of atmospheric aerosols larger than 0.2 μm sampled between 5 km and 19 km altitude. The mass-spectrometric measurements yield chemical, or due to the ionization and photolytic decomposition of molecular species, elemental information. They conclude that most of the iron in stratospheric aerosols originates from meteoric material, based on their observations that (i) the ion mass spectra with large iron peaks were much more common in the stratosphere than in the troposphere, and (ii) the iron-containing stratospheric aerosol particles also contained other elements in composition ratios typical of meteoric material. Although their measurements took place in middle and low latitudes, Murphy et al. [1998] suggest that many of the polar stratospheric particles may contain meteoric material, since a large fraction of the air descending from the mesosphere into the stratosphere is concentrated in the winter polar regions. They further conclude, that the stratospheric aerosol layer should contain between 0.3 and 9 % of meteoric material by mass, assuming that the stratospheric residence times of meteoric material and of sulfuric acid are similar. Surprisingly, many of the analyzed particles up to 20 km altitude contained mercury, most abundant just above the tropical tropopause at 19 km, which they assign to emissions from the Earth surface.

Recently, the same group performed more single-particle analysis of stratospheric aerosols [Cziczo et al., 2001]. They conclude that about half of the particles contain 0.5 to 1.0 weight percent meteoric iron by mass, requiring a total extraterrestrial influx of 20 to 100 tons per day. Based on the sulfur content of meteorites they estimate that this extraterrestrial flux corresponds to 1.4 to 4.7 tons per day sulfur injected into the high atmosphere. They assume that about 60 % of the incoming extraterrestrial flux is vaporized at about 100 km altitude, where atmospheric heating is the maximum for small entry bodies. This material, about 10 to 50 tons per day, recondenses, coagulates and subsides, forming the “meteoritic smoke as described by Hunten et al. [1980], which is eventually incorporated in the H₂SO₄-H₂O droplets in the stratospheric aerosol layer. Other larger bodies (micro-meteorites, spherules, and large dust grains) are not significantly heated and fall rapidly to the surface. Cziczo et al. [2001] conclude that the extraterrestrial flux represents 0.3 to 1.7 % of the total stratospheric sulfur budget. Although this flux is insignificant in the lower stratosphere, it may dominate in the

upper stratosphere above the stratospheric aerosol layer wherein most of the sulfur of terrestrial origin resides [Cziczo et al., 2001].

The studies cited above give an overall extraterrestrial sulfur flux spanning a range of 0.4 [Keil, 1969; Hunten et al., 1980] to 4.7 [Cziczo et al., 2001] tons S per day. The net flux of aerosol mass from the troposphere is approximately 60 kilotons S per year (see Chapter 6) or about 164 tons S per day. Thus, the extraterrestrial input represents 0.2 to 2.9 % of the terrestrial sulfur input to the lower stratosphere.

Solid-fueled rocket motors

Solid-fueled rocket motors deposit Al_2O_3 particles as a dominant component among other exhaust products into the stratosphere. The total stratospheric Al_2O_3 emission was estimated by Danilin et al. [2001] to be 1780 t/yr for an assumed scenario of space shuttle, Titan IV, Ariane 5, Atlas II and Delta II annual launch frequencies. Considering coagulation, sedimentation and washout of the particles they calculate a global stratospheric burden of 311 tons and a stratospheric lifetime of 0.28 years for this aerosol. The annually and zonally averaged maximum values of alumina surface area- and mass-densities at around 20 km in the Northern Hemisphere are at least a 1000 times less than those of background sulfate aerosol [Danilin et al., 2001].

Cosmic radiation

Radioactive ^{35}S is produced in the atmosphere by bombardment of ^{40}Ar by cosmic rays. It decays to ^{35}Cl with a half-life of 87 days, which is significantly longer than the typical tropospheric residence time of SO_2 of 1-10 days. The production rate of this radionuclide increases exponentially with increasing altitude and attains a maximum at 12-15 km at midlatitudes [Lal and Peters, 1967]. After its production ^{35}S is rapidly oxidized and becomes gaseous $^{35}\text{SO}_2$. Tanaka and Turekian [1991] report on the use of cosmogenic ^{35}S as a way of determining the time constants for oxidation, in-cloud scavenging and aerosol deposition by measuring the ^{35}S levels in gaseous SO_2 , aerosol sulfate and precipitation. Lal and Peters [1967] give a production rate of 1.4×10^{-3} atoms $\text{cm}^{-2} \text{s}^{-1}$ in the total atmosphere. Assuming a total mass flux of 8.5×10^9 kg/s (~ 700 G tons per day) across the 100 hPa level and an average mixing ratio of 40 pptv SO_2 gives a stratospheric input of about 3×10^{24} molecules $\text{SO}_2 \text{s}^{-1}$. Distributing this over the whole globe gives a 'production' of 6×10^5 sulfur atoms $\text{cm}^{-2} \text{s}^{-1}$. Thus, the upward flux from the troposphere is larger by eight to nine orders of magnitude than the production of $^{35}\text{SO}_2$ by cosmic radiation, which can therefore be neglected in the overall budget.

2.5.8 Isotopic studies

Isotopic studies are a tool to assess the contribution of individual precursor gases to the stratospheric sulfate aerosol. Goldman et al. [2000] performed the first atmospheric OCS isotopic studies using balloon borne and ground-based infrared spectra. Leung et al. [2002] examined the stratospheric OC^{34}S and OC^{32}S concentration profiles in solar occultation balloon spectra. Because of the relatively large natural abundance of ^{34}S (4.2 %) compared to those of the heavier isotopes of carbon and oxygen, OC^{34}S and OC^{32}S are the only relevant isotopologues. Isotope fractionation will result during the photolysis of OCS if the ratio of actinic light absorbances differed from the relative isotopologue concentrations:



They found that OC^{34}S is preferentially depleted by solar photolysis. The derived ^{34}S enrichment factor $\varepsilon = +73.8 \pm 8.6\%$, in conjunction with literature values of $d^{34}\text{S} \sim +11\%$ for tropospheric OCS [Krouse and Grinenko, 1991], and a 10% net processing of the OCS transported upwardly into the stratosphere, suggests that aerosol sulfate originating from OCS should be highly enriched in $d^{34}\text{S} \sim 80\%$. Comparing their prediction with reports of $d^{34}\text{S} \sim +2.6\%$ for background SSA [Castleman et al., 1974], they infer that either OCS is a minor contributor to SSA or that current views about its ^{34}S abundance and atmospheric circulation are seriously flawed.

2.6 Summary and open questions

The gaseous precursor for the stratospheric aerosol sulfate is sulfuric acid (H_2SO_4). With the exception of sporadic direct injections from volcanic eruptions, stratospheric H_2SO_4 is thought to originate from a handful of sulfur bearing compounds, mainly from SO_2 and OCS.

All precursor gases must reach the lower part of the tropical tropopause layer (TTL) in order to permanently enter the stratosphere, generally through deep convection above the continents. The estimate for the mass flux reaching the TTL is 1.5×10^{11} kg/s. Tropopause foldings and the quasi-adiabatic exchange processes do not affect the stratospheric composition above 100 hPa.

Among the precursors, SO_2 has the largest source of gaseous sulfur in the atmosphere followed by DMS, H_2S , CH_3SH and OCS and CS_2 . Based on emission strengths and lifetime, OCS and SO_2 are believed to be the main precursor gases for the formation of the stratospheric aerosol layer. While the emissions of OCS are much smaller than those of SO_2 and DMS, it possesses a very long lifetime in the troposphere and this permits it to be one of the dominant sources of sulfur to the stratosphere. On the other hand, despite a very short lifetime, some SO_2 reaches the TTL through rapid transport by deep convection. In volcanically quiescent periods, OCS and SO_2 are believed to contribute about equally to the stratospheric sulfur budget.

There is now a consistent picture of the seasonal and latitudinal variability of OCS in surface air and its relation to major terrestrial and marine sources and sinks. Throughout the last 15-20 years atmospheric OCS decreased at a rate of between $-0.25\% \text{ yr}^{-1}$ (FTIR total column measurements) to around $-1.2\% \text{ yr}^{-1}$ (firn air analysis). A substantial, yet unexplained historical variability of atmospheric OCS over the last 350 years has been established from ice core the analyses.

There are only few and sporadic measurements of SO_2 available in the TTL, which is critical to understand transport into the stratosphere. The emission patterns of SO_2 have changed throughout the last decades. While the anthropogenic emissions in the northern hemisphere have decreased, emissions in Asia, China and the entire tropical belt with biomass burning have increased. It is not clear to what extent these changes will compensate each other. Another complicating factor is that the oxidation capacity (OH and HO_x concentrations) in the upper tropical troposphere. Observations indicate that the HO_x levels within the TTL might be a factor 2-4 higher than previously assumed. Since the main sink of SO_2 is its reaction with OH, variability in the OH-concentration will have a strong impact on the SO_2 burden. In general, knowledge of the seasonal and longitudinal variability of SO_2 and HO_x (as well as other sulfur bearing compounds) in the TTL is very limited. As a result, it is not currently possible to infer the SO_2 trend in the TTL.

Meteors, cosmic radiation, and rocket exhaust contribute to a small extent to the sulphur budget in the lower stratosphere. The extraterrestrial input represents 0.2 to 2.9% of the terrestrial sulfur input to the lower stratosphere. However in the upper stratosphere above the stratospheric aerosol layer the extraterrestrial input may dominate in the sulfur budget.

2.7 Acknowledgements

We gratefully acknowledge Dave Griffith and Nicholas Deutscher from the University of Wollongong/Australia for unpublished OCS data, Peter V. Hobbs (University of Washington) for supplying his SO₂ data from TARFOX, and Nicola Blake (University of California, Irvine) for the CS₂ data from TRACE-P. Furthermore, financial support by the European network of excellence ACCENT is acknowledged. We are also indebted to Andreas Richter from University of Bremen for permitting us to use previously unpublished satellite SO₂ data.

CHAPTER 3

Instrument Descriptions

Lead Authors:

Patrick Hamill
Colette Brogniez
Larry Thomason
Terry Deshler

Authors:

Juan Carlos Antuña
Darrel Baumgardner
Richard Bevilacqua
Charles A. Brock
Christine David
Michael Fromm
Didier Fussen
Mark Hervig
Chris A. Hostettler
Shan-Hu Lee
John Mergenthaler
Mary T. Osborn
Graciela B. Raga
J. Michael Reeves
James Rosen
James C. Wilson

Contributors:

Sharon P. Burton
Nina Iyer

3.1 Introduction

The properties of stratospheric aerosol particles are measured with various types of instrument. Each instrument measures a particular subset of aerosol properties. None provides a complete depiction of aerosol composition and size distribution. Consequently, measurements from different instruments are often not directly comparable and the values of aerosol properties indirectly inferred from the base measurements may not always be consistent. In this chapter we provide brief descriptions of the instruments to assist the reader in interpreting the measured values and the inferred aerosol properties, as well as to understand instrument characteristics and limitations. The results obtained and the aerosol properties inferred from these measurements are presented in Chapter 4.

Measurements of the stratospheric aerosol can be characterized in the following manner:

- “global long term measurements” (Section 3.2),
- “global short term measurements” (Section 3.3),
- “localized long term measurements” (Section 3.4), and
- “localized short term measurements” (Section 3.5).

The term “global” is used loosely and is intended to convey the idea that the measurements cover a large geographic region. Therefore the POAM measurements are classified as “global” even though they only cover the Arctic and Antarctic regions. The CLAES data cover a much larger region of the Earth, but the experiment had a (planned) lifetime of only 19 months, so it is classified as “global short term.” Measurements made from a fixed location, such as lidar measurements, which have been carried out routinely for a long period of time are classified as “localized long term measurements.” Measurements made with instruments mounted on aircraft are classified as “localized short term measurements.” While this document is primarily focused on long-term global measurements, shorter term and more spatially isolated data sets are relevant because they also contribute significantly to the body of information on the stratospheric aerosol. In addition, they provide key validation for the other data sets, and they are useful for filling in the gaps in the global long-term data sets.

The data presented in this assessment are representative but not comprehensive. There are a number of very valuable data sets that for one reason or another were not included in this report. Among them are the stratospheric aerosol data sets obtained by the Solar Mesosphere Explorer (SME) satellite [Rusch et al., 1994; Eparvier et al., 1994], ILAS and ILAS II, the Improved Limb Atmospheric Spectrometer [Sasano, 2002], the Improved Stratospheric and Mesospheric Sounder (ISAMS) on the Upper Atmosphere Research Satellite [Lambert et al., 1993], the balloon-borne mass spectrometer of the Max Planck Institute [Weisser, et al., 2005] and data from several lidar stations.

3.2 Global Long-Term Measurements

The measurement systems discussed below have dissimilar coverage both in space and time. In Table 3.1 we present the coverage for instruments having global or large geographic area coverage. See the appropriate sections for the coverage of instruments with limited geographic coverage.

Table 3.1: Geographic and Temporal Coverage by “Global Scale” Instruments

Instrument	Geographic Coverage	Time Frame
SAM II	64-83 S and 64-83 N	Oct 1978-Dec 1993
SAGE I	80 S - 80 N	Feb 1979 - Nov 1981
SAGE II	80 S - 80 N	Oct 1984 - present
HALOE	80 S to 80 N	October 1991 - present
POAM II	63-88 S and 54-71 N	Sept 1993 - Nov 1996
POAM III	63-88 S and 54-71 N	March 1998 - present
CLAES	34N to 80S or 34S to 80N	Oct 1991 - May 1993
ORA	40 S – 40 N	Aug 1992 – May 1993

3.2.1 SAM II, SAGE I, and SAGE II: The Occultation Technique

The Stratospheric Aerosol and Gas Experiment (SAGE) is a series of NASA instruments that have produced global measurements of stratospheric aerosol extinction in the visible and near infrared since 1978. This series consists of the Stratospheric Aerosol Measurement (SAM II) (1978-1993), SAGE (1979-1981), SAGE II (1984-present), and the more recently launched SAGE III. Although SAGE could be considered “short term” we have included it here as it is one of a series of similar instruments. These instruments provide from one to nine wavelengths of aerosol extinction measurements, and yield an unbroken record of aerosol extinction at 1000 nm that extends from 1978 through the present. Data from these instruments have been extensively used in international assessments of changes to stratospheric ozone and water vapor [WMO, 2003, SPARC, 2000] as well as being previously used in the evaluation of stratospheric aerosol trends [Thomason et al., 1997a; Bauman et al., 2003a,b; Bingen et al., 2004a,b] and the creation of aerosol products useful in models of chemical/dynamical processes such as aerosol surface area density [Thomason et al., 1997b].

The SAGE series of instruments use the solar occultation technique to measure atmospheric transmission along the line of sight between the spacecraft and the Sun along paths passing through the atmosphere. Consequently, the Sun, relative to the instrument, is being occulted or obscured by the atmosphere and the solid Earth. The geometry is shown in Figure 3.1. This is a common measurement strategy for space-based instruments focused primarily on the stratosphere and is used by the Halogen Occultation Experiment (HALOE) and the Polar Ozone and Aerosol Measurement (POAM). It is well suited for situations in which horizontal inhomogeneity is not a significant concern and where the optical depth is relatively low: features that are generally characteristic of the stratosphere. In applying the technique, each spherical layer of the atmosphere is assumed to be homogeneous. For layers 1 km thick, an onion peeling technique extending from 10 km to 40 km, would require horizontal homogeneity over a line of sight of about 1200 km. For a smaller altitude range or thicker layers, the homogeneity requirement is less restrictive, but it should be kept in mind that this is an inherent assumption in the technique.

An event, defined as a set of the measurement of line-of-sight transmission at different tangential altitudes, occurs during each sunrise or sunset encountered by the spacecraft. This

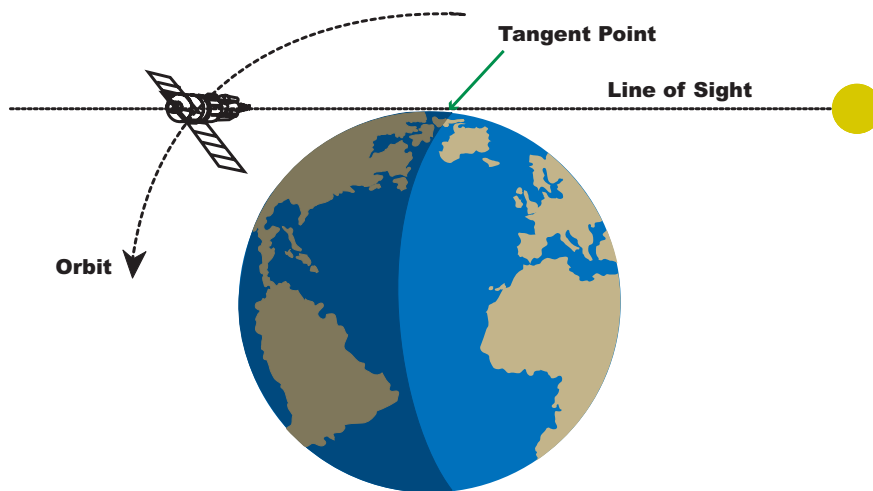


Figure 3.1: An illustration of solar occultation geometry

limits solar occultation to about 28-30 events per day. The latitudinal coverage of measurements is dependent on the orbital characteristics of the platform and generally varies quite slowly. Events obtained during the course of one day in a given hemisphere are all at nearly the same latitude. Instruments aboard platforms in sun-synchronous orbits, such as SAM II and POAM II and III, are limited to observations at high northern and southern latitudes whereas instruments in mid-inclination orbits such as HALOE and SAGE II carry out measurements over a broad range of latitudes, albeit requiring from 25 to 40 days to sweep out a full range of latitude. Since these instruments measure direct, unattenuated sunlight before or after each series of measurements, they are effectively calibrated at each measurement opportunity. Consequently, solar occultation instruments are not highly sensitive to changes in instrument performance and are, therefore, well-suited to the detection of long-term trends in measured quantities.

SAGE aerosol products are reported at altitudes between 0.5 and 40.0 km although extinction is often too low to measure above 30 km and the presence of clouds often terminate profiles in the mid and upper troposphere. Termination occurs when the line-of-sight transmission is less than approximately 0.002 which corresponds to nadir optical depths around 0.08 depending on wavelength and the vertical distribution. Typically, the cutoff occurs in the troposphere and is due either to clouds or the solid Earth. However, during the first several years following the 1991 eruption of Mt. Pinatubo, SAGE II events terminated as high as 27 km (in the tropics in late 1991). The loss of data in this period is a significant problem for modeling the climate and chemical changes that occurred as a result of the Pinatubo eruption. The method used to fill this data gap, and the results obtained, are presented in Chapter 4.

Figure 3.2 shows that the 1020 nm aerosol extinction profiles frequently extended to 3 km below the tropopause between 1985 and 1989 (the tropopause altitude is provided as a part of the National Center for Environmental Prediction (NCEP) data products). During this relatively quiet period between 80 and 90 % of all profiles extended down to 3 km below the tropopause. This is typical of the entire SAGE data set except for a few years following the Pinatubo eruption.

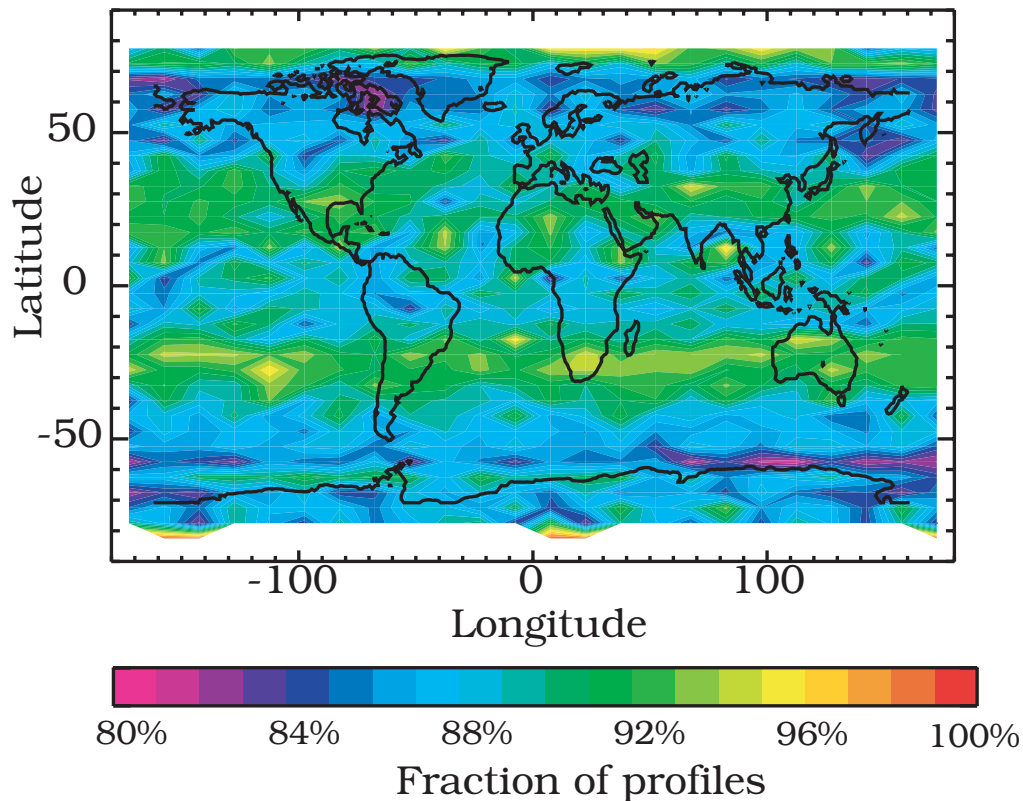


Figure 3.2: Mean likelihood of a SAGE II 1020-nm aerosol extinction profile reaching 3 km below the tropopause during the period 1985-1989.

SAM II

The SAM II instrument was a single-channel (1000 nm) sun photometer measuring profiles of aerosol extinction between 10 and 30 km. It flew aboard the Nimbus-7 spacecraft in a sun-synchronous orbit making measurements in both the Arctic and Antarctic. The SAM II data coverage began on 29 October 1978 and extended through 18 December 1993 with a gap between mid-January 1993 and October 1993. From 1978 through 1987 the latitude of the measurement location slowly varied between the lowest latitude (64 degrees at the solstices) and the highest latitude (83 degrees at the equinoxes). However, after 1987, changes in orbit and platform attitude degradation caused the measurement locations to migrate toward the equator.

SAGE

The first SAGE (Stratospheric Aerosol and Gas Experiment) sensor was launched in February 1979 on an Application Explorer Mission satellite and was operational until November 1981. The instrument carried out measurements of solar intensity at four different wavelengths, two of which (450 and 1000 nm) were intended for aerosol extinction determination. SAGE was in a mid-inclination orbit of 56 degrees yielding latitudinal coverage of 80°S to 80°N. During much of its lifetime, a battery problem limited operations to sunset events. The algorithm for the archived version is given in Chu and McCormick [1979].

SAGE II

The SAGE II (Stratospheric Aerosol and Gas Experiment II) sensor was launched into a 57-degree inclination orbit aboard the Earth Radiation Budget Satellite (ERBS) in October 1984 and continues to operate more than 20 years later. This instrument has seven channels nominally at 386, 448, 452, 525, 600, 935, and 1020 nm from which vertical profiles of ozone, nitrogen dioxide, water vapor, and aerosol extinction (at 386, 452, 525, and 1020 nm) are derived. In version 6.1 and later, the base data files also contain aerosol surface area density and effective radius derived using the method described in Thomason et al. [1997b]. Orbital coverage is a function of season and extends from 80°S to 80°N. Following a mechanical fault in July 2000, no data were obtained until December 2000 whereupon operations were resumed at a 50% duty cycle though not restricted by event type. The original algorithm for SAGE II is described in Chu et al. [1989]. Descriptions of the algorithm changes that occurred with the release of 6.0 in June 2000 and 6.1 in October 2001 are described in Thomason et al. [2001].

SAGE III

The SAGE III instrument, launched in December 2001, is a sophisticated descendent of the earlier instruments. The detector is a CCD array (rather than a single wavelength photometer) plus a photodiode at 1545 nm. Aerosol and gas data are obtained at 9 wavelengths (386, 449, 521, 601, 676, 755, 868, 1022, and 1545 nm). We are not using the SAGE III data in this assessment because at the time of writing the data have not been fully validated [Thomason and Taha, 2003].

SAGE Processing Procedure

Measurements by all members of the SAGE series follow the same procedure. When the satellite is about to pass into (or emerge from) the shadow of the Earth, the instrument is activated a few minutes before the platform sunset (sunrise). A detector is used to center the field-of-view (FOV) of the instrument on the azimuthal center of brightness. The instrument then uses a mirror to scan the spectrometer across the Sun vertically relative to the Earth, sampling spectra at 64 Hz (“a packet”). The detection of the edges of the Sun is a key element in locating packets in the atmosphere and on the solar disk. These two elements are, in turn, crucial to the production of all higher-level data products including aerosol extinction as they directly affect altitude registration, measurement noise, and normalization of the data. The scanning process continues throughout the event lasting between 2 and 4 minutes. Events are limited in altitude range to paths that pass within 300 km of the Earth’s surface and by the solid Earth, clouds, or dense aerosol at lower altitudes.

The process of going from measurement to data product is essentially the same for all the instruments in the SAGE series. In fact, future data releases planned for SAGE and SAM II make almost exclusive use of SAGE II processing software. During any sunrise or sunset encountered by the instrument, the instrument FOV is scanned in elevation (altitude) by a mirror at a rate of ~15 arc minutes per second and the spectral channels are sampled at 64 Hz. This results in a series of samples, each spatially overlapping its predecessor by 50 %. The total range of motion of the FOV allows the solar disk to be seen from the Earth's limb to heights greater than 250 km. During a sunrise or sunset event, the FOV tracks the center of brightness of the solar disk in azimuth and is scanned vertically across it in a repetitive up and down pattern. The result of this scanning motion is that a particular altitude in the Earth's

atmosphere is sampled several (typically four or more) times using different portions of the solar disk during an event.

The initial task of the processing is to determine where a particular channel sample was taken in the Earth's atmosphere and what point on the sun was in view. Knowing where each point was taken and which part of the solar limb darkening curve to use in calculating transmission is all that is required to build a line-of-sight transmission profile. To determine the location of each measurement point in the atmosphere and the location of the source point on the solar disk requires knowing the time a scan crosses the edge of the Sun, the location of the spacecraft and the scan rate, as well as accounting for atmospheric refraction. The merit of these quantities directly impacts the accuracy of altitude registration and solar irradiance outside the atmosphere and, ultimately, the quality of the data products. The effect of refraction is a function of altitude, the shape of the Earth, and the density profile of the atmosphere. The spacecraft location is monitored as a part of routine spacecraft operations. The density profile is derived from NCEP reanalysis profiles and the Global Reference Atmospheric Model (GRAM 95) above 55 km.

Once transmission profiles are produced for each instrument channel, profiles of gas species are derived along the line-of-sight using an instrument specific algorithm. For SAM II, which has a single aerosol channel, the algorithm simply subtracts the effects of molecular scatter to produce an aerosol extinction profile. The SAGE I analysis uses a four channel algorithm [Chu and McCormick, 1979] that derives aerosol at 450 and 1000 nm, ozone, and NO₂. The current SAGE II algorithm [Thomason et al. 2000] uses a revision of the SAGE II version 5.96 species separation processing algorithm that was developed for the Stratospheric Processes and their Role in Climate (SPARC) and United Nations Environmental Programme (UNEP) ozone assessments [SPARC, 1998] and is similar to earlier versions that followed the method described in Chu et al. [1989].

3.2.2 HALOE

The Halogen Occultation Experiment (HALOE) is on board the Upper Atmosphere Research Satellite (UARS) and has operated without flaw since its activation on 11 October 1991. The UARS mission is to investigate the global photochemistry, energy balance, and dynamics of the Earth's upper atmosphere. HALOE uses the principle of solar occultation to measure profiles of solar attenuation through the atmosphere's limb, as the sun rises or sets relative to the spacecraft. Measurements in eight infrared bands are used to retrieve the profiles of seven gas mixing ratios (HF, HCl, CH₄, NO, NO₂, H₂O, and O₃) temperature, and aerosol extinction $\beta(\lambda)$ at four wavelengths ($\lambda = 2.45, 3.40, 3.46, \text{ and } 5.26 \mu\text{m}$) [Russell et al., 1993]. HALOE measurements cover two longitude sweeps each day (15 profiles each), one at the latitude of sunsets and one at the latitude of sunrises. The progression of measurement latitude with time provides near global coverage over periods of 3-4 weeks, as demonstrated in Figure 3.3. The instrument field of view projected at the limb is 1.6 km vertically by 6 km horizontally. Optical effects and electronic smoothing yield an effective vertical resolution of ~ 2 km, corresponding to a tangent point path length of ~ 320 km.

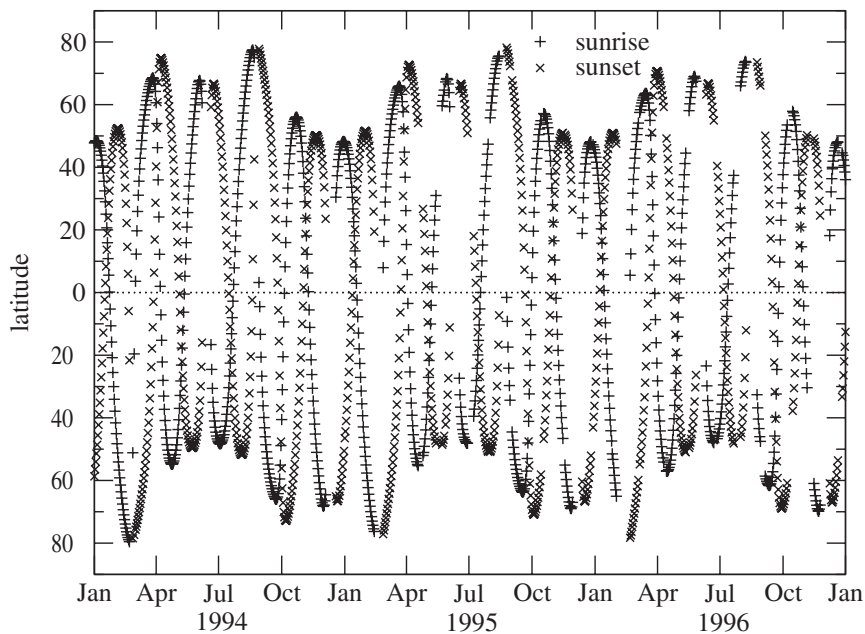


Figure 3.3: HALOE latitude coverage versus time for the period from 1994 to 1996. Symbols represent daily average latitude for either sunrise or sunset measurements.

HALOE aerosol extinction retrievals are accomplished using measurements from four gas correlation channels [Hervig et al., 1995]. For these measurements, the incoming radiation for each channel is split into two paths. One path passes through a cell containing a sample of the gas to be measured (e.g., HCl) and the other passes through vacuum. The difference of these two signals is insensitive to aerosols, and allows accurate retrieval of the target gas abundance. Once the target gas mixing ratio profile is retrieved, it is then used to subtract the gaseous signal from the vacuum path measurement. The remaining vacuum path signal is due only to aerosols, and is then used to retrieve profiles of aerosol extinction. Aerosol extinctions are retrieved at the over-sampled vertical spacing of 0.3 km, and have uncertainties on the order of $\pm 10\text{-}15\%$ [Hervig et al., 1996]. Because gaseous interference must be removed to retrieve aerosol extinction, errors in HALOE aerosol extinctions are lowest when the aerosol signal is large compared to the gaseous contribution. Within the HALOE time-frame, the lowest extinction uncertainties are associated with the early 1990s when Pinatubo aerosols were present. Extinction uncertainties increase with dissipation of the Pinatubo aerosols. HALOE aerosol retrievals extend in altitude from the upper troposphere to about 90 km. Above the stratospheric aerosol layer (roughly 35 km), aerosol retrievals serve primarily to characterize polar mesospheric clouds. The lower limit for measurable extinction is determined by the signal digitization where one bit corresponds to an aerosol extinction of $2 \times 10^{-6} \text{ km}^{-1}$. Measurement noise inherent to the electro/optical system raises the extinction noise floor to about $5 \times 10^{-6} \text{ km}^{-1}$. The limb view becomes completely opaque for aerosol extinctions greater than about 10^{-2} km^{-1} .

HALOE measurements have been used to characterize a variety of atmospheric particles including stratospheric sulfate aerosols, cirrus clouds, polar stratospheric clouds (PSCs), and polar mesospheric clouds (PMCs). Since this assessment is concerned with stratospheric aerosols, clearing measurements of other particle types within HALOE data is necessary. Tropospheric cloud tops were identified in HALOE profiles using two indicators described

by Hervig and McHugh [1999]. In one approach, the rapid increase in extinction associated with cloud tops was found to be a reliable cloud top indicator. In a second approach, uniformity among the four HALOE extinctions provides another reliable cloud indicator, because the large particles associated with cirrus produce relatively flat extinction spectra when compared to aerosol extinction. These two cloud identifiers were not confused by the presence of volcanic aerosols. Stratospheric cloud identification was accomplished using the vertical extinction gradient for results presented in this report. An example of the cloud top frequency distribution determined from HALOE measurements during 1998 is shown in Figure 3.4. A record of cloud tops identified in HALOE profiles is available on the HALOE web site: <http://haloedata.larc.nasa.gov/Haloe/home.html>.

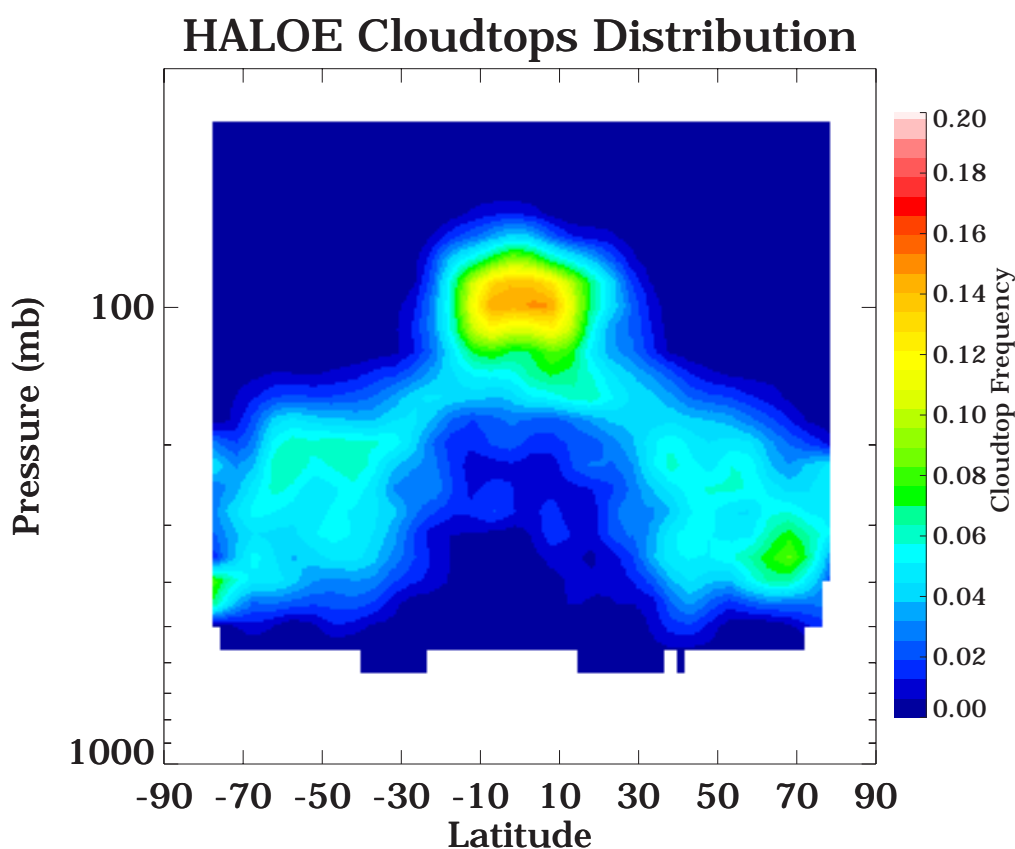


Figure 3.4: The cloud top frequency distribution determined from HALOE measurements during 1998.

3.2.3 POAM II and POAM III

The Naval Research Laboratory's Polar Ozone and Aerosol Measurement II (POAM II) was a satellite-based visible/near infrared photometer for making measurements of constituents in the polar stratosphere. POAM II measured atmospheric slant optical depth in nine narrow band channels from 0.352 to 1.060 μm . These measurements were used to retrieve ozone, water vapor, nitrogen dioxide, and aerosol extinction at five wavelengths (0.353, 0.442, 0.780, 0.920, and 1.060 μm). POAM II was launched aboard the French SPOT-3 satellite in September 1993 into a Sun synchronous polar orbit, and made measurements until the host satellite failed in November 1996. As seen from the satellite, the Sun rose in the Northern

Hemisphere and set in the Southern Hemisphere roughly 14 times per day, providing 14 measurements daily in each hemisphere around a circle of latitude. Sunrise measurements were made in a latitude band from 54-71°N, while sunsets occurred between 63-88°S. The POAM II instrument and mission is described in detail by Glaccum et al. [1996]. The POAM II measurements have been applied to studies of ozone, aerosols and PSCs in the Antarctic and the Arctic (see, e.g., Bevilacqua [1997] and references therein).

The POAM II version 5 retrieval algorithm is described and characterized (including a detailed error analysis) by Lumpe et al. [1997]. For the purposes of this report, the most important aspect of the POAM II retrieval algorithm is that, in the separation of the total measured optical depth into its specific components, the aerosol component is not determined separately in each spectral channel. Rather, the wavelength dependence of the aerosol slant optical depth, $\delta_{i(\text{aerosol})}$, at each tangent altitude is constrained by the following parameterization:

$$\ln(\delta_{i(\text{aerosol})}) = \mu_0 + \mu_1 \kappa_i + \mu_2 \kappa_i^2 ,$$

where the μ_j are the effective aerosol coefficients retrieved in the algorithm, and $\kappa_i \equiv \ln(\lambda_i)$, with λ_i being the central wavelength of channel i . This functional form provides a smooth spectral dependence of aerosol optical depth that has been found to fit a large range of stratospheric aerosol models [Lumpe et al., 1997].

The final, archived POAM II retrieval version is version 6. The main differences between the version 5 and 6 algorithms can be summarized as follows: (1) the version 6 retrievals use temperature/pressure profiles obtained from the United Kingdom Met Office (UKMO) analysis instead of the NCEP analysis used in version 5 for the specification and removal of Rayleigh scattering from the measured slant optical depths, and (2) in version 6, NO_2 is retrieved simultaneously with ozone and aerosol extinction whereas in version 5, NO_2 was fixed at climatological values. The aerosol parameterization and retrieval methodology employed in the version 6 algorithm are identical to that used in version 5 described briefly above and in detail by Lumpe et al. [1997].

The vertical resolution of the POAM II aerosol extinction retrieval, defined as the full-width-half-maximum of the retrieval averaging kernels, is about 1.2 km at 20 km with resolution values increasing at lower altitudes to about 2 km at 10 km, and at higher altitudes to about 2.5 km at 25 km. The precision of the 1.060 μm aerosol extinction retrieval is estimated to be about 10 %, roughly independent of altitude below 25 km. At 0.442 μm the random error is about 12 % at 18 km, increasing with both increasing and decreasing altitude to near 30 % at 12 km and 20 % at 25 km [Randall et al., 2000]. The POAM II aerosol extinction measurements have been validated by comparison with balloon-borne polarimeter and lidar measurements by Brogniez et al. [1996], and with SAGE II measurements by Randall et al. [1996, 2000]. POAM II measurements of the seasonal variation of stratospheric aerosol extinction at polar latitudes, and the decrease of volcanic aerosol over the period November 1993 through February 1996, from the Mt. Pinatubo eruption, are presented by Randall et al. [1996].

The POAM II mission was terminated by a satellite failure in November of 1996. A follow-on instrument, POAM III, was subsequently launched in March 1998 aboard SPOT-4, and is still operational at the time of this writing. The orbit is identical to that of POAM II, providing a direct extension of the POAM II data record in time. The POAM III instrument is similar to POAM II, but includes several design improvements. Many of the measurement channels (especially the 0.354 μm channel) have much higher signal-to-noise ratios than that ob-

tained in POAM II. The sun sensor is also more sensitive, enabling POAM III to routinely measure lower into the atmosphere. Also, the wavelengths and bandwidths of the science channels differ slightly from those in POAM II. The POAM III aerosol channels are 0.354, 0.442, 0.779, 0.922, and 1.020 μm . In this regard, the only significant difference is that the red channel has been moved from 1.060 in POAM II to 1.020 μm (i.e., identical to SAGE II) for POAM III. The POAM III interference filters were manufactured using an ion assisted deposition process. Both the center wavelength and bandpass of these filters have been shown to be very stable in extensive testing under extreme environmental conditions [Heath et al., 1997, 1998]. The POAM III instrument is described in detail by Lucke et al. [1999].

In August 2004, the operational POAM III retrieval algorithm was upgraded from version 3 to version 4, and the entire data set was reprocessed. The version 3 retrieval algorithm is described and characterized in detail by Lumpe et al. [2002]. (It might be noted that version 3 for POAM III is similar to version 6 for POAM II.) The most significant changes between the version 3 and 4 algorithms are:

1. As in version 3, altitude registration at higher altitudes is determined by maintaining the expected slant optical depth ratios between channels that are dominated by Rayleigh scattering, and at lower altitudes by using the instrument potentiometer (which gives the instrument pointing angle with respect to the spacecraft). As explained by Lumpe et al. [2002], in version 3 the transition between these two approaches for determining the pointing occurred at about 34 km, whereas in version 4 it has been pushed down to about 26 km.
2. The calibration of the instrument potentiometer, used for altitude registration below 26 km, has been improved in version 4, and is less susceptible to errors resulting from small variations in the non-linearity of the potentiometer.
3. The parameterization of the spectral dependence of the aerosol slant optical depth (optical depth versus wavelength) used in the aerosol extinction retrieval has been changed from the quadratic in the log of the slant optical, used in the version 3 retrievals (and the POAM II retrieval algorithm), to a quadratic in the optical depth directly. This simple, linear parameterization leads to a faster and more robust gas species retrieval without loss of accuracy in the aerosol extinction retrieval.

Estimated random errors in the POAM III aerosol extinction profiles at 1.02 μm are 10-15 % below 23 km, increasing to 30 % at 25 km. At 0.442 μm they range from 10 % above 15 km, increasing to about 20 % at 12 km. These estimates are roughly similar to the POAM II values at 1.02 μm , but are somewhat smaller than the POAM II values at 0.442 μm . The vertical resolution of the POAM III aerosol extinction retrievals is 1-1.5 km (that is, somewhat higher than the POAM II aerosol extinction retrieval both near the tropopause and at 25 km) for all aerosol channels up to 25 km. The POAM III (version 3) aerosol extinction measurements have been validated by Randall et al. [2001] through extensive comparisons with both SAGE II and HALOE.

3.3 Global Short-Term Measurements

3.3.1 CLAES

The CLAES Instrument and the Measurement Process

The Cryogenic Limb Array Etalon Spectrometer (CLAES) was one of ten complementary experiments launched on the Upper Atmosphere Research Satellite (UARS) in 1991. CLAES measured concentrations of ozone, methane, water vapor, nitrogen oxides, CFCs, temperature, and aerosol absorption at multiple wavelengths. These measurements were analyzed to develop a better understanding of the photochemical, radiative, and dynamical processes taking place in the ozone layer.

CLAES analysis inferred concentrations of stratospheric constituents from the measurement of infrared emission features associated with each gas. To separate the often very weak signatures of trace gases such as CFCs from the background radiation requires both high spectral resolution and high sensitivity. This was done by combining a telescope with an infrared spectrometer and solid state detectors, and cryogenically cooling the whole instrument to prevent its own thermal infrared emissions from interfering with the measurement of weak atmospheric signals. The spectrometer had a resolving power of about 4000 and operated over the wavelength range 3.5 to 12.9 μm .

The instrument consisted of a front-end sensor, made up of the telescope, spectrometer, and detectors, and the back-end cryogenic cooler, made up of an inner tank of solid neon (at -257°C) and a surrounding tank of solid carbon dioxide (at -150°C). The entire instrument was kept under vacuum during ground test and launch, and then exposed to the vacuum of space when the telescope door was opened in orbit. The cryogenics, which slowly evaporated as they cooled the instrument, were designed to last about 19 months in orbit. CLAES made scientific measurements from 1 October 1991 through 5 May 1993, when the cryogenics had fully evaporated and the instrument warmed up. CLAES was approximately 2.7 m long and 1.2 m in diameter, used an average of about 25 watts of power in orbit, and had a mass of about 1200 kg when loaded with cryogen.

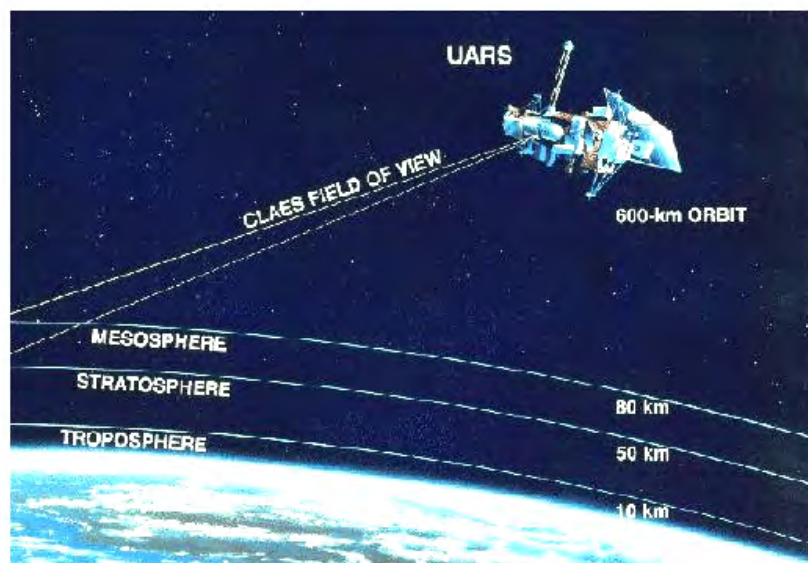


Figure 3.5: CLAES limb viewing geometry

CLAES looked out from one side of the UARS spacecraft at a fixed 90° angle to the velocity vector and was mostly pointed above the earth horizon (or “limb”) to observe the upper atmosphere between about 10 and 60 km above the surface, as shown Figure 3.5. This is the region encompassing the stratosphere and the lower mesosphere.

The instrument used an array of detectors providing 20 “footprints” at the earth limb between the 10 and 60 km altitude levels, each one separated by 2.5 km to provide vertical profiles of each gas with this vertical resolution. The UARS orbit had a 57° inclination and this allowed CLAES to view to 80° latitude in one hemisphere, and to 34° in the other. This orbit precessed 180° in about 36 days relative to the Sun. Because of this, UARS was rotated 180° in yaw approximately every 36 days such that one side of the spacecraft was kept facing away from the sun and instruments on this side, including CLAES, would stay cool. This meant that CLAES alternately viewed from 34°N to 80°S or 34°S to 80°N in 36 day periods. For a more detailed instrument description see Roche et al. [1993].

Figure 3.6 shows the latitude/longitude tracks of the center of the CLAES field of view at the earth limb for one day for a north-looking case. A south-looking case would look essentially the same, with the latitude limits changed to 34°N and 80°S . There are 15 orbits per day, and since CLAES took about 65 seconds for a complete measurement cycle it acquired about 1300 measurement sets per day. As the figure shows, measurement tracks are particularly dense near the polar regions, allowing for good coverage of ozone-related chemistry and dynamics over the Arctic and Antarctic.

CLAES produced a 19-month global database of stratospheric gases and aerosol and their variation with time of day, season, latitude, and longitude.

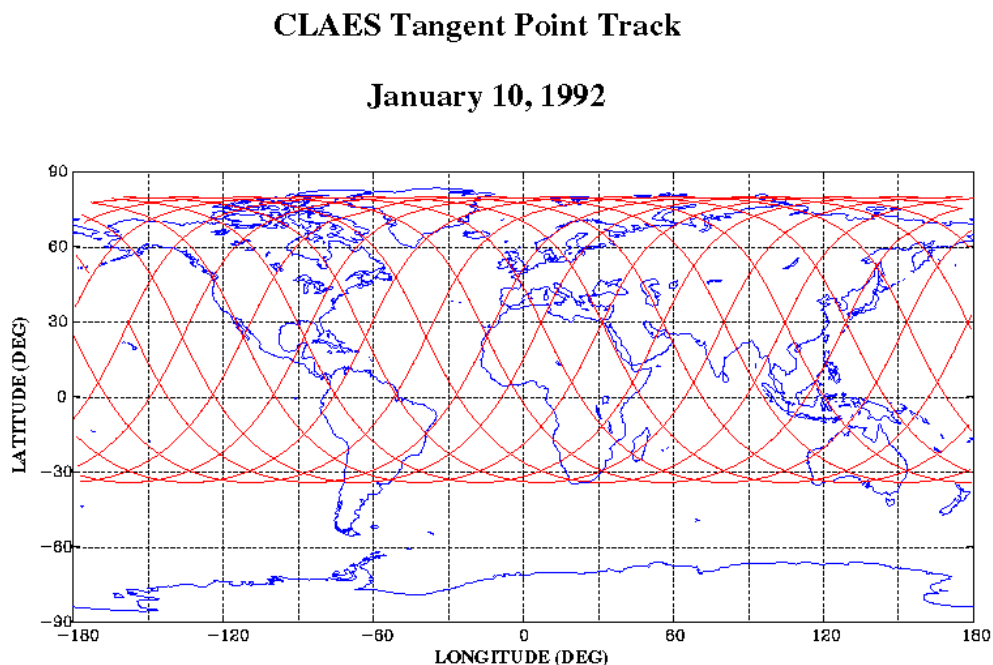


Figure 3.6: CLAES sampling for a “northern look” (34°S to 78°N). Coverage alternated between this and the “southern look” (34°N to 78°S) about every 36 days.

CLAES aerosol measurements and data

CLAES acquired medium resolution spectra of infrared thermal emission from the Earth's limb in nine channels ranging from 3.5 to 12.8 μm and over an altitude range of approximately 10-60 km. Vertical profiles of temperature, several gaseous species (NO, NO₂, H₂O, CH₄, N₂O, N₂O₅, CFC-11, CFC-12, HNO₂, ClONO₂ and O₂) and aerosol volume absorption coefficient for each channel (7 channels, 5.3 to 12.8 μm) were inferred from the limb radiance measurements. During the CLAES lifetime, stratospheric aerosol levels were quite elevated due to the 15 June 1991 eruption of the Mt. Pinatubo volcano in the Philippines. Because the infrared channels did not saturate, and thermal emissions provide relatively high density coverage, the CLAES data set is the most comprehensive limb view of the decay of the Pinatubo aerosol. The spectral micro-windows were chosen to contain emission features of a target gas, but they also contain information in the continuum emission which can be used to estimate aerosol loading. This requires knowledge of pressure and temperature; these were determined from a multi-emitter multi-channel onion-peeling retrieval applied to the micro-window targeting the 790.2 cm^{-1} CO₂ Q-branch. Given this temperature/pressure knowledge, the continuum emission in each of the other channels was processed to yield aerosol volume absorption coefficients in the remaining micro-windows. The retrieval process is based on the development of Rodgers [1976] and is described by Kumer et al. [1996]. There were three releases of the CLAES processing software (versions 7, 8, and 9) with incremental improvements in each data set. The aerosol validation paper, Massie et al. [1996], was written using V7 data. Differences between V7 and later versions including the current V9 data are available on the Goddard Distributed Active Archive Center (DAAC).

CLAES products include "Level 1" or calibrated limb radiance data, "Level 2" retrieved products on their native 2.5 km vertical grid, and "Level 3 Along Track" (L3AT) aerosol volume absorption coefficients. These retrieval products are interpolated in time along the tangent point observation path to the center of the 65.3 second sampling interval, and in pressure to the standard UARS surfaces defined by $p = 10^{3-N/6}$ hPa where N is the layer index. Aerosol data are recorded for levels from 346 hPa to about 0.1 hPa. The primary validation paper for these data [Massie et al., 1996] focuses on the region from 100 hPa to about 10 hPa. The layers centered at 215, 146, 100 and 68 hPa ($N = 4, 5, 6$ & 7) cover the region where tropical cirrus clouds are likely to be seen in CLAES data. Cirrus and PSCs are included in the aerosol data and must be separated from the sulfate aerosol with some process such as the threshold method developed in Mergenthaler et al. [1999].

3.3.2 ORA

The Occultation Radiometer (ORA) instrument on the European Retrievable Carrier (EURECA) satellite was launched in August 1992 and placed in a low inclination orbit. The instrument was equipped with eight broadband channels in the 0.259-1.013 μm range [Arijs et al., 1995]. It measured ozone [Fussen et al., 2000], nitrogen dioxide, water vapor and aerosol extinction profiles from August 1992 up to May 1993 in the 40°S-40°N latitude range and therefore provided a unique opportunity to observe the Mt. Pinatubo aerosol [Fussen et al., 2001b, 2001c]. About 7000 orbital sunsets and sunrises were measured during this period.

Although the apparent vertical resolution is poor (about 25 km, defined to be the solar size at the tangent point) due to the simplicity of the optical design, the very large signal-to-noise ratio allowed a final vertical resolution of 2-3 km to be obtained. Also, aerosol extinction profiles could be retrieved for altitudes lower than possible with more sophisticated

instruments such as SAGE II. This required, however, the use of complex inversion algorithms [Fussen et al., 1997, 2001a]. The comparison of data with other experiments showed fairly good agreement for aerosol extinction [Fussen et al., 1998] and optical thickness [Vanhellemont et al., 2000] and for derived aerosol parameters [Bingen et al., 2002].

3.4 Localized Long-Term Measurements

3.4.1 Balloon Borne Optical Particle Counter

Stratospheric aerosol measurements at Laramie, Wyoming, began in 1971 using an optical particle counter (OPC) initially developed by Rosen [1964]. The instrument, a white light counter measuring aerosol scattering at 25° from the forward direction, is a single particle counter. Mie theory is used to determine aerosol size [Mie, 1908]. An incandescent lamp, optics, and light controller supply a stable image of the incandescent lamp filament in the scattering region that is larger than the aerosol sample stream, thus edge effects are not a problem in defining sample volume. Light scattered from single particles passing through the beam is collected over a solid angle of ~ 0.17 steradian and focused onto a photomultiplier tube (PMT) for pulse height detection. Two symmetrical independent photon paths use coincidence to limit noise, Rayleigh scatter, and the influence of cosmic rays. Single coincident PMT pulses exceeding preset voltage levels are counted, determining size and number concentration. Prior to each flight the instruments are calibrated with polystyrene latex (PSL) spheres and the pump flow rate measured. Periodically the stability of the pumps throughout flight range pressures is checked, and the theoretical counter response function checked against PSL and monodispersed diethyl hexal sebacate at several sizes. See Deshler et al. [2003] for additional details.

Initial measurements in the 1970s consisted of measurements of particles $r > 0.15$ and $> 0.25 \mu\text{m}$ at a sample flow rate of 1 liter min^{-1} [Pinnick and Hofmann, 1973; Hofmann et al., 1975]. In 1989 the OPC was modified to make measurements for particles $> 0.4 \mu\text{m}$, to increase the number of sizes measured, and to decrease the minimum concentration measurable. This was done to use the instrument to measure PSC particles $> 0.4 \mu\text{m}$ because of the importance of these particles in polar ozone loss [Solomon et al., 1986]. The scattering angle of the detector axis was increased from 25 to 40° and the air sample flow rate increased from 1 to $10 \text{ liter min}^{-1}$, with appropriate changes in inlet design to maintain roughly isokinetic sampling. This new scattering angle allowed unambiguous detection of particles throughout the size range 0.15-10.0 μm in twelve size bins. Minimum detectable concentrations for this improved OPC are $6 \times 10^{-4} \text{ cm}^{-3}$ as opposed to $6 \times 10^{-3} \text{ cm}^{-3}$ for the initial OPC. The improved OPCs were first used in Antarctica in September 1989 [Hofmann and Deshler, 1991]. After calibration flights in Laramie to insure that the measurements at 0.15 and 0.25 μm radius are the same, within measurement limits, for the OPC with scattering angle at 25 and at 40°, the 40° OPC has replaced the original OPC also for the flights from Laramie [Deshler et al., 1993; Deshler et al., 2003]. Measurements with the 40° OPC from Laramie began in 1991. Tests with both OPCs continued until 1994 comprising 22 comparison flights. Current measurement capabilities consist of condensation nuclei (CN, $r > 0.01 \mu\text{m}$) and optically detectable aerosol, $r \geq 0.15$ -2.0 or 10.0 μm in twelve size ranges, from the surface to 30 km. The strength of these in situ measurements is in providing measurements easily converted into size distributions, from which other quantities of interest, e. g. aerosol surface area, or extinction, can be calculated. Additional details concerning the instrument function and laboratory tests are provided by Deshler et al. [2003].

Before each flight an OPC is calibrated by adjusting instrument gain until measured instrument response is consistent with theoretical instrument response for measurements on well characterized monodisperse aerosol. Instruments are calibrated using commercially available PSL spheres near 0.5 μm radius, a standard aerosol which has been used since the 1970s. It is sufficient to calibrate the instrument using only one particle size; however, the theoretical counter response curve has been checked a number of times using monodisperse particles of several sizes and different refractive indices [Pinnick and Hofmann, 1973; Zhao, 1996; Miao, 2001; Deshler et al., 2003].

Aerosol sizing errors result primarily from pulse width broadening of the PMT response for a constant optical input. Variations in intensity of the light beam, and variations in aerosol paths through the beam play secondary roles. These errors lead to sizing errors which are a function of index of refraction since the shape of the counter response curve varies with index of refraction. For temperatures above -65°C and water vapor concentrations near 5 ppmv, the real part of refractive index for sulfuric acid aerosol varies from 1.43 to 1.45, with no absorption [Steele and Hamill, 1981; Russell and Hamill, 1984]. Variations of index of refraction in this range lead to sizing errors well below those associated with the pulse width broadening discussed above, and do not contribute significantly. Counter response curves from Pinnick and Hofmann [1973] and Deshler et al. [2003], and the measured pulse width broadening from the phototubes leads to a sizing error of $\pm 10\%$ at 0.15 and 0.25 μm for a nominal index of refraction of 1.45.

Errors in concentrations measured by these instruments depend on variations in air sample flow rate, the reproducibility of a measurement from two identical instruments, and Poisson counting statistics. The pumps used for these instruments are constant volume gear displacement pumps. In laboratory tests pump flow rates are found to decrease by 3 % at ambient pressures of 30 hPa and by 13 % at 5 hPa [Miao, 2001]. These variations are, however, less than other uncertainties, and concentration measurements are not corrected for measurements at low pressures. Laboratory tests with two identical counters on several samples of differently sized monodisperse aerosol indicate a measurement precision of $\pm 10\%$ for relatively high concentrations of aerosol when Poisson counting statistics are not a factor.

Poisson counting statistics define the fractional uncertainty of a count as its inverse square root, $C^{-0.5}$ for C counts in one sample, becoming important at low concentrations. The aerosol concentration, $N = C \times S / F$ for sample frequency S and flow rate F . Thus the Poisson error fraction, in terms of concentration, is $(N \times F / S)^{-0.5}$. For these instruments: $S = 0.1$ Hz, $F = 16.7 \text{ cm}^3 \text{ s}^{-1}$ for the 25° OPC, and $F = 167 \text{ cm}^3 \text{ s}^{-1}$ for the 40° OPC. In the stratosphere these ambient air flow rates are reduced to about 80 % of these values by temperature differences between outside air and pump. This leads to uncertainties of 85, 25, and 8 % for concentrations of 0.01, 0.1, 1.0 cm^{-3} at the low flow rate and concentrations of 0.001, 0.01, 0.1 cm^{-3} at the high flow rate. Poisson counting errors dominate at concentrations below 0.1 (0.01) cm^{-3} for the low (high) flow rate instrument. At concentrations higher than these a concentration error of $\pm 10\%$ reflects measurement precision.

3.4.2 Lidar Systems

Lidars are active remote sensing instruments analogous to radar, but using optical wavelengths. (“Lidar” is the acronym for “LIght Detection And Ranging.”) Lidars came about with the development of very short single pulses of laser energy, capable of illuminating a narrow atmospheric column. The return signal is collected and the time between the emitted laser pulse and the scattered return signal is proportional to the altitude at which the scattering occurred. Properties accessible to a lidar are linked to the interaction between radiation and matter, which in turn depends on the nature of the particles and on the type of scattering/absorption being studied [Measures, 1984]. Specifically, with a lidar, one can measure Rayleigh scattering, Mie scattering, Raman scattering, resonance scattering, fluorescence, and absorption. Multi-wavelength lidars can measure differential absorption and scattering. The earliest lidar experimental applications were devoted to atmospheric dust and aerosol layer observations [Fiocco and Smullin, 1963; Fiocco and Grams, 1964; McCormick et al., 1966].

Spectral properties of the elastic scattering of light by particles of radii ranging from about 0.05 to 100 μm are described by Mie theory, under the assumption of particle sphericity and homogeneity. The optical properties of particles measured by lidar are determined by their composition (refractive index), by their phase (liquid/solid) and by their size distribution. In principle, these parameters can be retrieved through lidar signal inversion, but in reality, there are too many unknowns for a single equation. Indeed, in the basic lidar equation, optical properties at each range are determined by the elastic backscatter at that range and attenuation along the two-way path, which contains both a molecular contribution (Rayleigh scattering) and a particulate contribution (Mie scattering). The molecular atmosphere is accounted for by using correlative atmospheric density profiles from either radiosonde profiles, atmospheric models or temperature Raman lidar profiles [Keckhut et al., 1990]. A critical assumption is the relationship between the backscatter cross-section and the extinction cross-section. Klett [1981] showed that such relationships are highly variable as they require an *a priori* knowledge of particle shape and chemical composition.

Particular lidar applications allow one to derive aerosol extinction coefficients independent of the aerosol backscatter. In the High Spectral Resolution Lidar (HSRL) approach, the aerosol and molecular scattering contributions are separated on the basis of the much wider Doppler broadening of molecular scattering [Shipley et al., 1983]. Vertical profiles of aerosol extinction and backscatter coefficients can be independently determined simultaneously using elastic (Rayleigh-Mie) and inelastic (Raman) backscatter lidar signals [Ferrare et al., 1998].

Considerably more information is available in the received wave by considering its polarization characteristics. Indeed, for single scattering, Rayleigh backscatter from atmospheric gases and Mie backscatter from spherically symmetric particles retain the incident polarization to within 2%. Consequently, the most likely sources of any observed depolarization would be the irregular shape and multiple scattering.

Most lidar measurements of stratospheric aerosols are made using single wavelength systems. The choice of the wavelength is not critical for an aerosol lidar, but there are two points considered by researchers in selecting the operating wavelength: first, to avoid atmospheric gaseous spectral absorption regions (i.e., $\lambda \leq 1000$ nm approximately), and second, to pick a wavelength long enough so that the aerosol scattering signal is not too small compared to the molecular Rayleigh scattering (i.e. $\lambda \geq 300$ nm). Typically, the range goes from near UV to near IR. Most aerosol lidars use the 532 nm wavelength, which is the second harmonic of

Nd:YAG lasers. The fundamental (1064 nm) and third (355 nm) harmonics are also used. Traditionally, the relative particulate contribution to backscatter is represented at each range by the backscatter ratio, defined as the ratio of the total to molecular backscatter coefficient. A backscatter ratio greater than 1 indicates the presence of scatterers distinct from the molecular atmosphere.

The strength of an aerosol lidar is its ability to yield information on the morphology and structure of the aerosol layers, with very high vertical and temporal resolutions, and the prospect of obtaining long-term series. The direct products are optical properties so aerosol lidars are not instruments of "remote spectroscopy" and the retrieval of the physical properties of the particles requires a priori knowledge and assumptions. Meanwhile, indirect retrieval of particle properties is made possible by the combination of lidar observations together with in situ instruments (optical counters, for instance), other optical sensors (giving a multispectral approach) or using model constraints.

Integrated Backscatter from Various Lidar Systems

Less than one decade after the first lidar atmospheric applications were developed, the applicability of this technique to long-term monitoring of stratospheric aerosols became apparent [Fiocco and Grams, 1964]. The first operational routine measurements were carried out in the early 70's with instruments using a sodium laser at 589 nm (as in Saõ José Dos Campos, Brazil) or a ruby laser at 694 nm (as in Hampton, USA, Garmisch-Partenkirchen, Germany and Mauna Loa, USA). Since the end of the 1980s, most of the instruments have used Nd:YAG lasers at 1064 nm, frequency doubled to emit at 532 nm or frequency tripled at 355 nm.

Today, lidar systems are operated routinely all over the world, at all latitude bands, but with the majority located in the Northern Hemisphere. Table 3.2 gives a list of the various stratospheric aerosol lidars operated in the past or still running today, from Arctic to Antarctic latitudes. The geographical locations, the time frames and the operating wavelength are given, together with the updated names of investigators.

Some lidar stations, often included in national or international long-term stratospheric monitoring programs, provide quasi-continuous long-term records, with a high operation rate. In general, operations are only interrupted for technical reasons or during the summer periods (daytime) in the polar regions. These lidar stations can provide suitable datasets for establishing a stratospheric aerosol climatology. Their location is shown on Figure 3.7 and their characteristics and integrated backscatter records are given below.

Ny-Alesund – Arctic

Stratospheric aerosol and PSC observations are performed at Ny-Alesund, Spitsbergen (78.92°N, 11.93° E) using a multi-wavelength and polarization backscatter lidar instrument [Beyerle et al., 1994; Biele et al. 1997; Biele et al., 2001]. The station is the Primary Arctic Station of the Network for the Detection of Stratospheric Change (NDSC).



Figure 3.7: Map showing the locations of the lidar stations providing long-term continuous series of stratospheric observations.

Measurements shown in Chapter 4 use the second harmonic of a Nd:YAG laser at a wavelength of 532 nm operating with a pulse repetition frequency at 30 Hz. Laser pulse energy is typically 180 mJ. The backscattered signals are collected by a 60 cm telescope (field of view 0.8 mrad), separated according to wavelength and perpendicular/parallel polarization and detected by sensitive photomultipliers in photocounting mode. A mechanical chopper prevents saturation of the photodetectors by signals from low altitudes. The vertical resolution varies over different years from 15 to 200 m. The instrument was refined and improved several times during the period. The atmospheric density profile is calculated from pressure and temperature profiles measured daily by the local meteorological radiosonde. The lidar signal inversion is based on the Klett [1981, 1985] method.

Garmisch-Partenkirchen – Northern Middle Latitude

Measurements at Garmisch-Partenkirchen, Germany (47.48°N, 11.06°E) began in 1976 and are focused, among other parameters, on the stratospheric aerosol [Reiter et al., 1979; Jäger, 1991, Jäger, 2005]. The station is part of the northern mid-latitude primary station of NDSC, (Alpine Station).

Early observations were obtained with a ruby lidar system at 694 nm. Between 1990 and 1991, observations were interrupted to rebuild the lidar system. Measurements starting in 1991 use the 532 nm second harmonic of the Nd:YAG laser, emitting, at this wavelength, about 600 mJ at a 10 Hz repetition rate. Lidar signals are received on a 52 cm diameter Cassegrain telescope. Vertical resolution was typically 600 m with the ruby system, and is typically 75 m with the Nd:YAG system. All 532 nm aerosol optical parameters are converted into 694 nm values to easily compare them with earlier measurements obtained with the ruby laser. Molecular density is derived from radiosonde profiles made at Munich, 100 km north of the lidar location.

Backscatter integrations cover the altitude range from the tropopause + 1 km to profile top (around 30 km). Error estimates range from 10 to 50 %, depending on stratospheric aerosol load, for the ruby measurements. These errors are reduced by about half for the 532 nm measurements.

Observatoire de Haute-Provence – Northern Middle Latitude

The Observatory of Haute-Provence (OHP, 43.94°N, 5.71°E), located in the South-East of France, is one of the four French Atmospheric Observatories (with Dumont d'Urville, Alomar and La Réunion Island). The OHP station is part of the mid-latitude primary station of NDSC in the Northern Hemisphere (Alpine Station). OHP is equipped with the complete set of NDSC instruments, including a stratospheric aerosol lidar [Chazette et al., 1995].

The stratospheric aerosol lidar is a 532 nm backscatter lidar, without depolarization, including a Raman N₂ channel. The instrument has operated on a routine basis since March 1991 although observations exist sporadically since 1986. Clear-sky weather conditions, which prevail mostly at OHP, allow for high frequency lidar operations. The lidar system, except the perpendicular polarization detection and the inversion methodology, are similar to those described below for the Dumont d'Urville lidar. The atmospheric density profiles are derived from daily meteorological radiosondes from Nîmes (about 150 km west of OHP). Daily integrated aerosol backscatter values are obtained between the tropopause and 30 km, with an uncertainty of 10 to 30 %, depending on the aerosol loading.

Hampton – Northern Middle Latitude

Routine ground-based lidar measurements have been taken at Hampton, Virginia, U.S.A. (37.1°N, 76.3°W) since May 1974 [Fuller et al., 1988; Woods et al., 1994; Osborn et al., 1995]. The instrument consists of a ruby laser that nominally emits 1 joule per pulse at a wavelength of 694 nm at a repetition rate of 0.15 Hz and a 122-cm (48 inch) Cassegrain telescope (field of view 4.0 mrad). The data are collected at 15-m vertical resolution but are software averaged to a 150-m vertical resolution before retrieving and archiving aerosol backscatter and scattering ratio. Splitting of the optical return signal between 3 photomultiplier tubes in the receiver (1 %, 9 %, and 90 %) enables accurate measurements over a large dynamic range. Although there have been incremental improvements in the system, the fundamental operating wavelength and measurement principles have not changed since the 1970s.

Measurements are obtained weekly, weather permitting. Molecular density is calculated from temperature-pressure profiles obtained from the radiosonde station at Wallops Island (120 km northeast of the lidar system). The retrieval procedure for aerosol optical parameters relies on an iterative method. For this mid-latitude station, the integration interval for integrated backscatter is from the tropopause to 30 km. Errors range from 15 to 50 % under low (background) stratospheric loading conditions, decreasing to 5 % for measurements following large eruptions.

Mauna Loa – Northern Tropic

In Mauna Loa, Hawaii (19.54°N, 155.58°W), lidar observations began in 1974, with a main focus on the stratospheric aerosol [DeFoor and Robinson, 1987; DeFoor et al., 1992; Barnes and Hofmann, 1997; 2001]. The initial system used a ruby laser, emitting at 694 nm. In 1994, a new lidar was built using a Nd:YAG laser operating at 30 Hz, measuring backscatter

at both the 532 nm harmonic and the 1064 nm fundamental. Backscattered light is received by a 61 cm telescope, with an altitude resolution of 300 m (for both systems). Mauna Loa is part of the tropical primary site of the NDSC (Hawaii Station).

As in Garmisch, for data continuity, the 532 nm data are converted to 694 nm to be easily compared with the early measurements. Errors in the integrated backscatter range from 15 % to more than 30 % for the ruby measurements, depending on aerosol load. These errors are reduced to approximately 6 % for the 532 nm measurements. Since the station is located in the tropics, tropopause fluctuations are minor. Thus, the altitude interval for backscatter calculations can be fixed: in this case, 15.8 to 33 km. Molecular density was obtained from a model for the Ruby lidar analysis and from the nearest radiosonde site (Hilo, HI) for the Nd:YAG lidar. There was an overlapping period of about a year (40 observations) during which the ruby lidar backscatter and the Nd:YAG lidar backscatter at both wavelengths were measured. The average absolute backscatter of the ruby lidar agreed to within 2 % of the Nd:YAG backscatter interpolated from the two wavelengths.

São José dos Campos – Southern Tropic

A sodium lidar operating at 589 nm has been used since 1972 at São José dos Campos (23.12°S, 45.51°W), Brazil, for monitoring the vertical distribution of stratospheric aerosols [Clemesha and Simonich, 1978; Simonich and Clemesha, 1997]. Most of the measurements were made as an offshoot of work on atmospheric sodium. The receiving telescope of the lidar was improved and the electronics were recently modified to measure the Doppler temperature of the sodium atoms and Raman scattering from the stratosphere. However, the wavelength used for the measurements has not changed since the start of operations. Early data, up to about 1980, had a height resolution of 2 km, subsequent measurements have a resolution of either 1 km or 250 m.

The aerosol profiles are determined by fitting the lidar backscatter profiles to an atmospheric model at altitudes above 30 km. A single model atmosphere is used for all seasons because the seasonal variation in the atmospheric density profile is small at tropical latitudes. Molecular density profiles are obtained from a standard atmosphere. Because the main purpose of the lidar measurements has normally been to study the 80–110 km region, the signal is sometimes saturated in the lower stratosphere. For this reason the lower limit of the scattering ratio profiles varies between 10 and 20 km. For most monthly averages, however, this limit is less than 15 km. Hence, monthly averages of integrated aerosol backscatter are obtained between 17 and 35 km. Since the site is located in the tropics, the tropopause is high and its fluctuations are minor. Error estimates on the integrated profiles are 5 %.

Dumont d'Urville – Antarctica

The lidar experiment in Dumont d'Urville (66.67°S, 140.01°E) is a French-Italian cooperation that has provided stratospheric aerosol and PSC optical parameter profiles since 1989. Dumont d'Urville is the French Antarctic Station, part of the Antarctic NDSC primary station. The present set of instruments includes a stratospheric aerosol and PSC lidar.

The 532 nm lidar, with depolarization, has operated routinely since June 1989. The frequency doubled Nd:YAG laser emits 450 mJ at a 10 Hz repetition rate. The backscatter signal is collected on an 80 cm diameter Cassegrain telescope and split into two components polarized respectively parallel and perpendicular to the laser emission. Both components are detected by photomultipliers, gain switched to prevent saturation by the stronger returns from

the lower altitudes. The signals are then time resolved with a 30 m vertical resolution and averaged over 5 min. The range and background corrected signal is inverted using the Klett method. The quantities derived from the combined Mie and Rayleigh components of the lidar signal include backscatter ratio and depolarization ratio. The atmospheric density profiles are derived from local daily meteorological radiosondes. Daily integrated aerosol backscatter values are obtained between the tropopause and 28 km, with uncertainties between 15 and 40 %, depending on stratospheric particle loading [David et al., 1998].

Table 3.2: List of various aerosol lidars which have run or are still running, from northern polar to southern polar latitudes, together with their location, time frame and investigators' names. In blue are the active lidar stations that provide almost continuous long-term series.

Aerosol Lidar	Location	Time Frame	λ	PI
Eureka (NDSC)	80.05°N - 86.42°W	February 1993 → 2002	1064 nm 532 nm	T. Nagai O. Uchino
Ny-Alesund (NDSC)	78.92°N – 11.93°E	Winter 1991 → now	532 nm	R. Neuber, M. Müller
Thule (NDSC)	76.53°N - 68.74°W	November 1990 → now	532 nm	G. Fiocco
Andoya (NDSC compl.)	69.3°N - 16.00°E	1995 → now	532 nm	A. Hauchecorne
Garmisch-Partenkirchen (NDSC)	47.48°N - 11.06°E	1976 → now	694 nm 532 nm	H. Jäger, T. Trickl
Obs. de Haute-Provence (NDSC)	43.94°N - 5.71°E	June 1991 → now	532 nm	C. David, P. Keckhut
Toronto (NDSC compl.)	43.66°N - 79.4°W	late 1989 → April 2001	532 nm	S. Pal, A. Carswell
Suwon (NDSC compl.)	37.2°N - 127.6°E	November 1995 → now	355 nm	C. H. Lee
Hampton	37.1°N – 76.3°W	May 1974 → now	694 nm	C. Hostetler, P. Lucker
Table Mountain (NDSC compl.)	34.4°N – 117.7°W	February 1988 → now	532 nm	S. McDermid, T. Leblanc
Mauna Loa (NDSC)	19.54°N - 155.58°W	1974 → now July 1993 → now	694 nm 532 nm	J. Barnes, S. McDermid, T. Leblanc
Saõ José dos Campos	23.2°S – 45.9°W	March 1972 → now	589 nm	D. Simonich
Lauder (NDSC)	45.04°S - 169.68°E	1994 → 1997 1993 → 1999	532 nm	L. Stefanutti T. Nagui
Dumont d'Urville (NDSC)	66.67°S - 140.01°E	March 1989 → now	532 nm	G. Di Donfranceso, C. David
McMurdo (NDSC)	77.9°S – 166.76°E	1990 → now	532 nm	M. Snells

McMurdo Station - Antarctica

The lidar experiment at McMurdo Station (77.85°S, 166.67°E), an Italian-American cooperation, has operated routinely since August 1990, with measurements including the early winter beginning in 1994 [Adriani et al., 1995, 2004]. McMurdo, the American Antarctic station, is one of the Antarctic NDSC primary stations. The frequency-doubled Nd:YAG laser emits a 532 nm polarized signal at 150 mJ and 10 Hz. The backscattered signal is collected with a 40 cm diameter Cassegrain telescope, split into parallel and perpendicular polarizations, and detected with photomultiplier tubes. A mechanical chopper blocks the strong lower altitude signal. The signals are time resolved with a 30 m vertical resolution and averaged over 5 min. The range and background-corrected signal is inverted using the Klett method. The quantities derived from the combined Mie and Rayleigh components of the lidar signal in-

clude backscatter ratio and depolarization ratio. Atmospheric density profiles are derived from local daily meteorological radiosondes. Daily integrated aerosol backscatter coefficients are obtained between the tropopause and 28 km, with uncertainties between 15 and 40 %, depending on stratospheric particle loading [David et al., 1998, Adriani et al., 2004]. In 2004 the lidar system was replaced with a Nd:YAG laser emitting at 1064 nm (100 mJ) and 532 nm (190 mJ), with a 10 Hz repetition rate. The new receiver, a 36.5 cm diameter Schmidt Cassegrain telescope coupled to 5 detectors, is operated in photon counting mode. Three photomultipliers detect at 532 nm parallel polarized light (low and high altitude) and perpendicular polarized light. A fourth photomultiplier tube detects 607.3 nm Raman scattering of 532 nm by molecular nitrogen, and serves for calibration purposes. The fifth detector, an avalanche photodiode, detects the 1064 nm scattering. The 532 to 1064 nm scattering ratio might provide information on aerosol particle size.

3.5 Localized Short-Term Measurements

3.5.1 The Aircraft-Borne LaRC Aerosol Lidar

Between July 1982 and February 1984, NASA Langley Research Center (LaRC) deployed an airborne lidar system aboard an Electra aircraft for five missions that reached as far north as 76°N and as far south as 56°S (summarized in Table 3.3). The system consisted of a ruby laser nominally emitting 1 J/pulse at 0.5 Hz at a wavelength of 694.3 nm and a 35.6 cm Cassegrainian-configured receiving telescope. Two photomultipliers, electronically switched on at specific times after the laser firing, are used to enhance dynamic range. The transmitted output divergence is 1.0 mrad and the receiver field of view is 0.2 mrad. Two 40.6 cm quartz windows separated by 1 m were used in the top of the aircraft fuselage. One window was used for the laser transmitter and the other for the receiver. The signal becomes usable at 3 to 4 km above the aircraft flight altitude. A detailed error analysis for this system is described in Russell et al. [1979]. Details of the flight paths and data analysis are available in a series of five NASA Reference Publications by McCormick and Osborn [1985a, 1985b, 1986a, 1986b, and 1987] and summarized in McCormick et al. [1984]. Unfortunately, the digital records of these missions are no longer available and only the tabulated data in the Reference Publications still exist. For the purposes of this report only 3 profiles close to the equator have been included in the analysis though clearly a more ambitious use of this data set would be desirable. Currently, the entire data is in the process of being recovered from paper and it will eventually be archived at the NASA Langley Research Center Atmospheric Science Data Center (<http://eosweb.larc.nasa.gov/>).

Table 3.3: NASA Langley Airborne Lidar System Flights between 1982 and 1984.

Dates	Latitude Range
July 1982	42°N to 12°N
October-November 1982	46°N to 46°S
January-February 1983	27°N to 76°N
May 1983	72°N to 56°S
January 1984	38°N to 77°N

The more recently developed NASA LaRC Aerosol Lidar measures profiles of aerosol and/or cloud backscatter at 532 and 1064 nm and aerosol/cloud depolarization at 532 nm. This lidar is a piggy-back instrument on NASA Goddard Space Flight Center's Airborne Raman Ozone,

Temperature, and Aerosol Lidar (AROTAL) lidar. The light source for the aerosol measurements is a Continuum 9050 Nd:YAG laser operating at 50 shots per second. The laser nominally transmits 475 mJ at 1064 nm, 300 mJ at 532 nm, and 225 mJ at 355 nm. AROTAL also employs an excimer laser transmitting at 308 nm and uses the molecular and Raman backscatter from the 355 and 308 beams to measure ozone and temperature. Backscattered light at all wavelengths is collected by a 400 mm diameter Newtonian telescope with a selectable field stop. Directly behind the field stop is a rotating shutter wheel which blocks the near-range (0-4 km) backscatter from the receiver to eliminate the distortions in the relatively weak far-range signals due to transients induced by the very strong near-range signals. In the aft optics assembly following the telescope and field stop, the UV signals are separated from the 532 and 1064 nm signals by a dichroic beam splitter. The UV signals are directed to the AROTAL receiver assembly and the 532 and 1064 nm signals are directed to the LaRC Aerosol Lidar receiver assembly. The 532 and 1064 nm signals are separated by a dichroic beam splitter and the 532 nm signal is further separated into orthogonal polarization components using a polarizing beam cube. A computer-controlled half-wave plate in front of the polarizing beam cube is rotated so that the polarization of the 532 nm signal is measured in components that are parallel and perpendicular to the polarization of the transmitted laser pulse. The signals at both wavelengths and both 532 nm polarizations are transmitted to detectors at the Aerosol Lidar data acquisition rack via fiber optic cables. Each optical signal, the 1064 nm total backscatter and the 532 nm parallel and perpendicularly polarized backscatter, is further split between two detectors, with 10% going to one detector and 90% to the other, in order to more accurately measure the signals over their full dynamic range. In addition to the main channels described above, a “mini-receiver” with a 75 mm aperture measures the 532 and 1064 nm backscatter in the 1-4 km range (i.e., corresponding to that part of the range blocked by the chopper in the main receiver). The 532-nm returns are measured with photo-multiplier tubes and the 1064 nm returns are measured with avalanche photo-diodes. Because of the high optical signal levels, all data are acquired in analog mode, using 12-bit analog-to-digital converters. The instrument operates under both daytime and nighttime lighting conditions, with some degradation in data quality during the daytime due to noise from solar background light.

The signals measured by the instrument are composed of backscatter from both air molecules and aerosol/cloud particles. The aerosol/cloud component of the signal is estimated using density profiles derived from assimilation model results using the technique of Russell et al. [1979]. Data products retrieved from the measurements include: total scattering ratio at 532 nm, total scattering ratio at 1064 nm, aerosol backscatter coefficient at 532 nm, aerosol backscatter coefficient at 1064 nm and aerosol depolarization ratio at 532 nm.

The LaRC Aerosol Lidar participated in the SAGE III and Ozone Loss Validation Experiment (SOLVE) campaign, conducted in the winter of 1999-2000, and the SOLVE-II campaign, conducted in January 2003. For the SOLVE mission, 22 flights were conducted over the course of three deployments, and for the SOLVE-II campaign, 11 flights were conducted over the course of a single deployment. Archived products from the LaRC Aerosol Lidar were generally produced over an altitude range extending from approximately 4 km to 25 km above the aircraft for SOLVE and 1 km to 25 km above the aircraft for SOLVE-II. The difference in coverage was due to the fact that the mini-receiver which captures the near-range signal were not yet installed for the SOLVE mission. Data are acquired at sampling resolutions of 15 m vertical and 500 m horizontal (2 s integration). The archived products are averaged to lower resolutions, generally 75 m vertically and 8 km horizontally, although the data may be averaged to higher resolutions as required by the application.

3.5.2 The Airborne DLR OLEX Lidar

The four wavelength aerosol-ozone lidar (OLEX) of the DLR can be operated in upward and downward looking modes. It makes use of a flashlamp-pumped Nd:YAG laser with a fundamental wavelength of 1064 nm. Frequency doubling and tripling provides simultaneous output at 532 nm and 355 nm. The instrument emits the laser beams in an off axis mode via an extra window in the aircraft fuselage. Complete overlap of the laser beams and the receiver FOV is achieved after a distance of 1-1.5 km. The receiver is a 35 cm Cassegrain telescope with 1 mrad field of view. Narrow band filters are positioned in front of the detectors to minimize the contributions of the atmospheric background illumination and the surface. The received 532 nm signal is split into two perpendicularly polarized portions which allow one to calculate the depolarization of the light.

With a repetition rate of 10 Hz and a typical aircraft speed of 150 m/s the raw data resolution is 15 m horizontally. Vertically the 10 MHz analog-to-digital converter (ADC) sampling rate results in a resolution of 15 m. However, depending on the specific demand, a trade-off between signal noise and spatial resolution is performed. In order to qualitatively investigate small scale structures in an inhomogeneous environment (e.g. for comparison of cloud boundaries obtained from ground based radar and airborne lidar) only a few shots (< 1 s) are averaged, degrading the horizontal resolution to about 100 m. For the derivation of quantitative optical parameters like optical depth or the multiple scattering contribution the signal is typically averaged over 10-20 s and slightly smoothed vertically which leads to a resolution of 1-3 km horizontally and 30 m vertically.

The attenuation of the laser beam in the atmosphere is treated by employing a numerical Klett-type inversion of the lidar equation in which an extinction/backscatter coefficient ratio (lidar ratio) and a starting value at some distance from the receiver have to be assumed to iteratively derive the profiles. With the inferred lidar ratio the extinction coefficient and its integral, the optical depth, can be estimated from the backscatter signal. The depolarization of the 532 nm signal by the scattering particles contains information about their shape. A volume depolarization of 0.014 (or 1.4 %) occurs if only the asymmetric air molecules contribute to the depolarization. If the sampled volume contains depolarizing (non-spherical, solid) particles, the volume depolarization is between 0.014 and 1 depending on the concentration and shape of the scattering particles. Clouds with *only* spherical (liquid) particles may cause volume depolarization below 1.4 % since they increase only the intensity in the parallel channel.

3.5.3 Airborne Particle Counters

NMASS, FCAS and Passive, Near-Isokinetic Inlet

The University of Denver Focused Cavity Aerosol Spectrometer, FCAS, is a single particle, optical aerosol spectrometer that detects particles in the 90 to 1000 nm diameter range [Jonsson et al., 1995]. Stratospheric aerosol is dominated by sulfuric acid and water. The measured size distributions essentially correspond to those for dry aerosol particles because the sample is heated prior to measurement. Water vapor and temperature measurements made by other investigators are used to determine the ambient size distributions from measured dry distributions. FCAS has been an element of a number of field campaigns (summarized in Table 3.4) that has produced measurements that span, in the Northern Hemisphere, the equator to the pole and 7 km to 21 km in altitude. The ambient integral parameters are available to the public at the NASA ESPO website

(www.espoarchive.nasa.gov).

The response matrix of the FCAS II was determined from numerous calibrations and is used in a Twomey inversion [Markowski, 1988] to determine the measured size distribution from FCAS output. Over the last seven years, the FCAS II has been tested with more than 350 monodisperse aerosols at pressures that covered the range experienced by the instrument in flight. On average, the absolute value of the discrepancy between the particle diameters determined from the FCAS response and that determined from the differential mobility analyzer settings used to obtain the test aerosols is less than 3 % of the diameter. Calibrations for concentration were done using a dual-channel, low-pressure condensation nucleus counter, CNC, and show an uncertainty of around 15 % [Wilson et al., 1983]. The FCAS data provide accurate measurements of stratospheric aerosol surface and volume except from October 1992 through April 1993 when some particles were larger than its upper detection limit due to the eruption of Mt. Pinatubo. Data combining FCAS and FSSP measurements from this period are available from J. C. Wilson at the University of Denver. The FCAS data from 1994 do not meet the standards of accuracy described in this report.

Prior to 1998, knowledge of smaller particles was limited to number concentration and resulted from measurements with a low-pressure condensation nucleus counter. Since 1998, the Nuclei-Mode, Aerosol Size Spectrometer (NMASS) has been flown on 6 missions [Brock et al., 2000]. The NMASS consists of 5 condensation nucleus counters. Each CNC has a different threshold for detecting particles due to different temperature differences between the saturator and condenser. The 50 % detection sizes for the five CNCs are set to approximately 4, 8, 16, 32, 60 nm. These characteristics remain constant with altitude because the NMASS is run at a constant pressure. The full response matrix and the Twomey inversion are used when retrieving size distributions from the CNCs outputs. The combined dry NMASS and FCAS size distributions are archived at the NASA ESPO website.

The passive, near-isokinetic inlet employs two diffusers to slow the sample flow from the true air speed of the aircraft to appropriate instrument speeds [Jonsson et al., 1995]. The inlet is instrumented and the size distribution data are corrected for deviations from isokinetic sampling.

FSSP and MASP

FSSP (Forward Scattering Spectrometer Probe) and MASP (Multiangle Aerosol Spectrometer Probe) at NCAR (National Center for Atmospheric Research) are two instruments that measure the intensity of light scattered by individual particles that pass through a focused laser beam. The FSSP-300 collects the light that is forward scattered over angles between 4° and 12°. The MASP uses a different light collection geometry and collects light from 30°-60° and 120°-150°. The size of particles (in the radius size range from 0.2 to 20 µm) are derived from both instruments with Mie theory that relates the intensity of light scattering to particle size, refractive index, angle of light collection, and laser wavelength. The number concentration is derived by dividing the number of particles detected by the known volume of the air sampled by each instrument. The surface area and volume is derived from the integrals of the size distributions, weighting the concentration at each size category by either the area or volume of a sphere for that size. This assumes that the particles are spherical.

Table 3.4: Missions in the NASA ESPO archive with FCAS and CNC or NMASS Data.

Mission Identifier	Aircraft Identifier (ext)	Year
AASE2	ER2	1991-1992
SPADE	ER2	1993
STRAT	ER2	1995-1996
POLARIS	ER2	1997
WAM	WB57	1998
ACCENT	WB57	1999
SOLVE	ER2, DC8	2000
CRYSTALF	WB57	2002
SOLVE2	DC8	2003
Pre-AVE	WB57	2004

Table 3.5: Chronological summary of aircraft missions with stratospheric aerosol measurements using the FSSP-300 or the MASP.

<i>Aircraft Mission</i>	<i>Aircraft</i>	<i>No. of Flights</i>	<i>Dates</i>	<i>Latitude Range</i>	<i>Particle Probe</i>
AASE I	ER-2	18	12/88 – 2/89	30°N – 90°N	FSSP-300
AASE II	ER-2	29	10/91 – 3/92	22°N – 90°N	FSSP-300
SPADE	ER-2	12	10/92 – 5/93	15°N – 60°N	FSSP-300
APE-POLECAT	Geophysica	9	12/96 – 1/97	42°N – 78°N	FSSP-300
ASHOE/MAESA	ER-2	25	3/94 – 11/94	70°S – 60°N	MASP
POLARIS	ER-2	22	4/97 – 9/97	3°S – 90°N	MASP
WAM	WB-57F	4	5/98	9°N – 45°N	MASP
APE-THESEO	Geophysica	4	2/99 – 3/99	42°N – 9°S	FSSP-300
ACCENT	WB-57F	6	9/99	5°N – 40°N	MASP
SOLVE I	ER-2	14	1/00 – 3/00	35°N – 90°N	MASP
EUPLEX/Envisat	Geophysica	18	1/03 – 3/03	42°N – 78°N	FSSP-300

In situ measurements were made with these optical particle spectrometers on three airborne platforms, the NASA ER-2 and WB-57F from 1989 to the present day, and the Russian Geophysica from 1996 to present. The measurements on the ER-2 were from 136 flights carried out during six missions, on the WB-57F they were from 10 flights made during two missions, and on the Geophysica they come from 31 flights during 3 missions. Table 3.5 lists the project information.

The operating principles, measurement limitations and uncertainties of the FSSP-300 are discussed by Baumgardner et al. [1992]. The primary uncertainty is in the determination of particle size as a result of the dependency of light scattering on refractive index that is sensitive to composition. As the composition is generally not known with any great accuracy, the Mie function can vary from 5-50 %, depending on size and composition. Thus, the estimated, average uncertainty in sizing from the FSSP-300 is approximately 20 % over the 0.2-20 μm size range of this instrument. The uncertainty in measuring concentration, ~ 15 %, is primarily a result of how well the sample volume can be determined. These uncertainties in concentration and size are propagated when calculating surface area and volume, since these depend on the square and cube of the diameter, respectively. The estimated accuracies in derived surface area and volume are 25 % and 35 %, respectively.

The operating principles of the MASP are discussed by Baumgardner et al. [1995]. The uncertainties are similar to the FSSP-300 since the measurement principle is similar. The major difference in the two instruments is the optical geometry. Additional information about the particle composition can be derived from the MASP since two intensity measurements are made from each particle, a forward scattering component and a backward scattering component. The ratio between the forward and backward scattering components is a function of size and refractive index. This allows an estimate of the particle refractive index and hence a lowering of the uncertainties in sizing [Baumgardner et al., 1996].

3.5.4 Balloon-borne Backscattersonde

The backscattersonde, developed between 1987 and 1989, measures the locally backscattered light at two wavelengths in the red and blue range. The measurements are representative of the ambient aerosol scattering properties within about 10 m of the instrument. The sampled volume is on the order of 1 m³. The instrument, designed to be carried about 50 m below a balloon, also measures ambient pressure and temperature and is sensitive to both tropospheric and stratospheric aerosol. The light source is a quasi-collimated beam from a 10 J xenon flash lamp. The returned signal is detected with two silicon photodiodes using filters to limit the wavelengths sensed. The distribution of wavelengths and backscatter angles associated with the backscattersonde is taken into account in modeling the instrument response. The results of the modeling show only a small difference between the response for 180 degree backscatter and the backscattersonde for stratospheric aerosols. The uncertainty associated with the distribution of wavelengths passing each filter can be essentially eliminated for natural aerosols by selecting 921 and 495 nm as the effective wavelengths. Changes in lamp intensity from flash to flash and over the course of a flight are accounted for with two separate reference photometers which are used to correct the measured backscatter signals in each color channel.

Calibrating the instrument requires, similar to a lidar, determining the Rayleigh (molecular scattering) signal at a known pressure and temperature. In principle this can be done in aerosol free air; however, at the surface, it is not possible to achieve completely aerosol free air without introducing additional complications such as scattering from the walls of an aerosol free chamber. Thus, somewhat indirect methods have been developed. One method consists of maintaining a ground standard (consisting of 4 separate instruments) against which all backscattersondes are compared prior to flight. The Rayleigh signal can then be determined from the flight instrument if it encounters an aerosol free region at high altitude. In practice this has only been achieved in the winter polar regions. There, on a number of flights, the instrument response has apparently approached the theoretical Rayleigh limit above 20 km. The results from these flights can then be used to calibrate the ground standard and in effect all flights which have been compared with the ground standard. In 1999, another more reliable method of calibration was developed which consisted of comparing a “mini-backscattersonde” that could be calibrated in an aerosol free chamber with the flight backscattersonde (Rosen, 2000, unpublished manuscript). This resulted in a slight change in the absolute calibration of all backscattersonde data. All of the soundings reported to the NDSC reflect the 1999 absolute calibration effort.

The accuracy of measured backscatter is nominally 1-3%, with an effective resolution of .5-1% at altitudes below 20 km. Above 20 km statistical fluctuations in backscatter due to low signal become noticeable and may dominate other uncertainties at the highest altitudes. These fluctuations can be reduced by averaging with a corresponding loss in altitude resolution. To represent an aerosol measurement the backscattered signal is divided by the theoretical molecular scattering determined by ambient pressure and temperature and the ground calibra-

tion. This gives the backscattering ratio = (aerosol scattering + molecular scattering)/molecular scattering.

A more complete description of the backscattersonde, its calibration, and the comparison with other instruments can be found in Rosen and Kjome [1991b] and Rosen [2000, unpublished manuscript]. Methodologies and formulas for converting backscattersonde measurements to equivalent measurements from lidar, satellite extinction and mass mixing ratios can be found in Rosen [2000, unpublished manuscript].

The first backscattersonde measurements began in Laramie, Wyoming, in May 1989. Since then the instrument has been flown in the Arctic [e.g. Rosen et al., 1989; 1994a; Larsen et al., 1996], in the Antarctic [Rosen et al., 1991; 1993], in volcanic aerosol [Rosen et al., 1992; 1994b], in the mid latitudes [McKenzie et al., 1994], in the tropics [Rosen et al., 2004], and has been used to analyze tropospheric aerosol profiles [Rosen et al., 1997; 2000]. Table 3.6 summarizes the backscattersonde flight history.

Table 3.6: Flight history, as of March 2005, of the backscattersonde. These data are publicly available on the NDSC web site, <http://www.ndsc.ws/>.

<i>Location</i>	<i>Latitude</i>	<i>Longitude</i>	<i>Altitude</i>	<i>Number of flights</i>	<i>Dates</i>
Laramie WY	41.3 N	105.6 W	2160	93	5/89- 9/00
Lauder New Zealand	45.0 S	169.6 E	370	77	2/92- 3/00
Natal Brazil	6.1 S	35.3 W	50	42	11/95-10/04
Cuiaba Brazil	15.0 S	56.0 W	225	3	8/9/95
Mildura Australia	34.2 S	142.1 E	52	4	9/10/98
South Pole Station	90.0 S	0.0 E	2835	11	winters 90&91
Table Mountain CA	34.4 N	117.7 W	2260	4	Mar-97
Boulder CO	40.0 N	105.1 W	1743	3	7/89- 5/90
Alamogordo NM	33.3 N	105.0 W	1280	2	Jun-90
Vanscoy Canada	52.1 N	106.6 W	50	4	8/91- 9/00
Air sur l'Adour France	43.7 N	00.3 W	79	2	Mar-94
Gap France	44.5 N	06.0 E	550	1	Jun-93
Rylsk Russia	51.6 N	34.7 W	200	5	8/89-10,92
Moscow Russia	56.0 N	41.0 E	190	2	Jun-94
Kiruna Sweden	67.9 N	21.1 E	327	17	11/91- 1/00
Sodankyla Finland	67.4 N	26.6 E	179	54	9/94- 3/05
Thule Greenland	76.5 N	68.8 W	60	32	1/92-12/97
Scorebysund Greenland	70.5 N	21.5 W	60	5	10/94- 2/96
Sondre Stromfjord	67.0 N	50.9 W	50	2	3/95- 1/96
Ny Alesund	78.9 N	11.9 E	10	16	1/96- 2/05
Heiss Is. Russia	80.6 N	58.1 E	10	12	1/89- 3/92
Alert NWT Canada	82.5 N	62.3 W	66	35	1/89- 1/93
Resolute Canada	74.2 N	95.0 W	40	1	Oct-91
Arkhangel'sk Russia	64.6 N	40.5 E	4	3	1/93- 1/94
Dixon Is. Russia	73.5 N	80.2 E	42	5	1/91- 3/92
Salekhard Russia	66.5 N	67.5 E	160	2	2/99- 1/00
Yakutsk Russia	62.0 N	130.9 E	106	10	1/95- 3/98

CHAPTER 4

Stratospheric Aerosol Record and Climatology

Lead Authors:

Patrick Hamill
Colette Brogniez

Authors:

Juan Carlos Antuña
Darrel Baumgardner
Rich Bevilacqua
Christine Bingen
Greg Bodeker
Christine David
Terry Deshler
Didier Fussen
Mark Hervig
Chris A. Hostettler
John Mergenthaler
Thomas Peter
Graciela B. Raga
Larry Thomason
James C. Wilson

4.1 Introduction

In this chapter we present the stratospheric aerosol record obtained during the first three decades of quantitative measurements of its properties, and present a climatology of the stratospheric aerosol. The most intensely monitored property of the stratospheric aerosol layer is the extinction of solar radiation by the aerosol particles. This quantity has been measured by different satellite borne sensors for twenty-five years. Therefore, the principal parameter considered in this record is the aerosol extinction as a function of time, latitude, altitude, and wavelength.

The large amount of data obtained from satellite observations during the past quarter century forces us to limit ourselves to a few representative samples of the numerous plots and tables that have been generated for this report. A full set of the plots, tables and data sets that are described here are available at the SPARC Data Center web site <http://www.sparc.sunysb.edu> or at other web sites referenced below.

In Section 4.2 we present samples of the *primary* measured aerosol properties obtained by the various instruments: extinction, backscatter, absorption, and number density. The various measurements are characterized as follows:

- (1) Global long term measurements of aerosol extinction and aerosol optical depth as obtained from the satellite systems SAM II, SAGE and SAGE II, HALOE, POAM II and POAM III.
- (2) Global short term measurements of aerosol extinction from CLAES and ORA.
- (3) Localized long term measurements of number density from the University of Wyoming balloon borne optical particle counter (OPC), and measurements of aerosol backscatter from a number of different lidar systems.
- (4) Localized short term measurements from aerosol sensors on aircraft.

In Section 4.3 we present *derived* products from several of the data sets, specifically: aerosol surface area per unit volume of air (surface area density), aerosol volume (per unit volume of air), and particle effective radius, as derived from the SAGE II, HALOE and POAM II and III global long term measurements. We also discuss surface areas and effective radius from the University of Wyoming Optical Particle Counter (OPC), a localized long term measurement.

In Section 4.4 we *compare* primary and derived products as determined by various instruments. In particular, we present extinction comparisons for SAGE/HALOE, for SAGE/POAM and for SAGE/ORA. All of these instruments yield extinction as a primary product, although generally at different wavelengths. Extinction comparisons are also made for SAGE/OPC and SAGE/lidar. In these cases the extinctions for the OPC and the lidar systems are derived quantities. Furthermore, we present in that section comparisons of SAGE/HALOE/OPC derived values of surface area density, volume density, and effective radius.

Finally, some general conclusions are presented in section 4.6.

4.2 Primary Measured Aerosol Properties

Section 4.2.1 presents long term global measurements, that is extinction and optical depth measurements from the SAGE series of satellite instruments, the HALOE instrument, and the POAM satellite instruments. This is followed in Section 4.2.2 by aerosol extinction and optical depth from the global short term satellite instruments, namely CLAES and ORA. Section 4.2.3

gives localized long term measurements, specifically, the measurements of aerosol number density made with the University of Wyoming balloon borne optical particle counter (OPC), and measurements of aerosol backscatter from various lidar systems. Finally, Section 4.2.4 presents a number of short term measurements made by instruments mounted on aircraft, specifically lidars and particle counters.

4.2.1 Global Long-term Measurements of Extinction and Optical Depth

SAGE Series Aerosol Extinction and Optical Depth Measurements

The SAGE public release data is available on the NASA Langley Research Center's Atmospheric Sciences Data Center (<http://eosweb.larc.nasa.gov/>). With a few exceptions, as noted, this report is based on the release versions 6.1 for SAGE II and unnumbered versions for SAM II and SAGE. The recently released version 6.2 has an improved water vapor product but the aerosol products are essentially unchanged.

The dynamic range of extinction measurements (uncertainties < 100%) is instrument dependent. SAM II, SAGE, and SAGE II all have upper limits for extinction of around 0.02 km^{-1} , above which the line of sight optical depth is large enough for the atmosphere to be effectively opaque to the instruments. At 1000 nm wavelength, the lower extinction limits (due to instrument noise and limits on the digitizer) are $2 \times 10^{-6} \text{ km}^{-1}$ for SAGE and SAGE II but only about $5 \times 10^{-5} \text{ km}^{-1}$ for SAM II. At the shorter wavelengths the lower limit is $2\text{-}4 \times 10^{-5} \text{ km}^{-1}$. The absolute precision of the measurements is relatively constant, thus the relative uncertainty decreases with increasing extinction. The precision is also dependent on the contribution of gas species to the total measured optical depth in the aerosol channels. For channels around 1000 nm, aerosol is by far the largest contributor except well above the tropopause where molecular scatter is important. On the other hand, molecular scatter and absorption by ozone strongly contribute in the shorter wavelength channels. As a result the precision in these channels is not as good as in the longer wavelength channels despite the short wavelength extinction being greater than the long wavelength extinction. In addition, since the magnitude of these effects is spatially and temporally variable, the precision has seasonal and latitudinal dependence. Figure 4.1 (a-d) shows the aerosol extinction measured vs. the relative uncertainty for the four SAGE II aerosol extinction channels in May of 1994. As this figure shows, the relative uncertainty at the upper end of the dynamic range is on the order of a few percent but increases significantly at the lower extinctions. The three shorter wavelength channels show a bifurcated structure in the relative error plots. The left wings of these plots correspond to data in the tropics where the Rayleigh contribution is smaller than for equivalent extinctions at mid and high latitudes since they occur at lower pressures. Due to the strong spectral dependence of the molecular scatter cross section ($\propto \lambda^{-4}$), molecular scatter at 386 nm is almost twice as large as it is at 452 nm and almost 50 times larger than it is at 1020 nm.

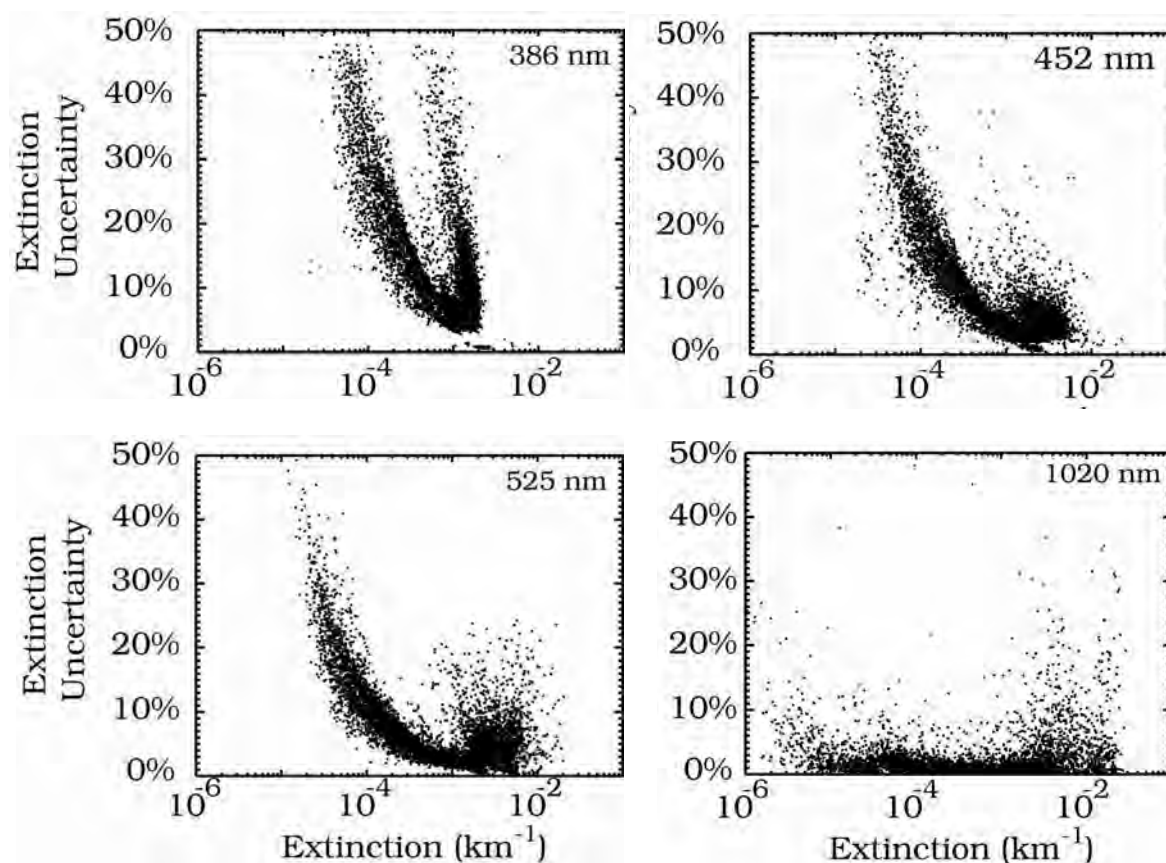


Figure 4.1 (a-d): Precision of SAGE II aerosol extinction in May 1994 as a function of extinction for 386, 452, 525, and 1020 nm, respectively.

Unlike measurements of most gas species, there is no standard measurement by which to assess systematic errors in the aerosol extinction measurements and efforts to evaluate this aspect of the measurements has been limited to comparisons with other satellite data sets [e.g., Burton et al., 1999; Randall et al., 2000, 2001]. These comparisons, and those later in this chapter, can establish the level of systematic bias between data sets but cannot establish an independent level of bias. For instance, comparisons of SAGE II and SAGE III extinction data in Thomason and Taha [2003], show mean differences less than 5% at the 3 short wavelength SAGE II channels, but nearly 15% at the 1020 nm channels which are generally considered to be the most robust measurements for both instruments. As of this writing, it is not clear what produces this difference. The optical depth measurements have a range of 0.0006 to 0.08 with precisions running from approximately 10% at the lower range to around 1% at the upper limit.

Figures 4.2a-d show the aerosol extinction as a function of latitude and altitude during January 1994 for 386, 452, 525, and 1020 nm, respectively. These figures were produced using 5-degree latitude bins and the native 0.5 km altitude bins and require at least 5 points per bin in order to create a value. The average tropopause altitude is calculated by NCEP, which also supplies the SAGE project with temperature profiles at measurement locations. The presence of cloud in individual profiles has been identified using the method of Kent et al. [1997a] and data determined to be clouds have been excluded from the archive and from the aerosol data sets discussed in the rest of this section. A brief discussion of the cloud clearing process and the statistics of cloud occurrences in the SAGE data sets is given in Section 4.3.1. All these figures show similar and familiar details [e.g., Trepte and Hitchman, 1993]. Aerosol extinction above 20 km has a maximum in the tropics where aerosol trapped within the tropical “pipe”

from the Pinatubo June 1991 eruption remains. (The tropical pipe model assumes the lower tropical stratosphere is isolated with respect to mixing from higher latitudes [Plumb, 1996].) Generally, away from low latitudes, lines of constant aerosol extinction gradually descend in altitude and, in fact, tend to be fairly homogeneous on surfaces of constant potential temperature (not shown). The exception is that within the winter/spring polar vortices (particularly in the Antarctic) aerosol extinction in the absence of polar stratospheric clouds (PSCs) is substantially less than outside the vortex as a result of diabatic subsidence and irreversible removal of aerosols through PSC formation [Thomason and Poole, 1993].

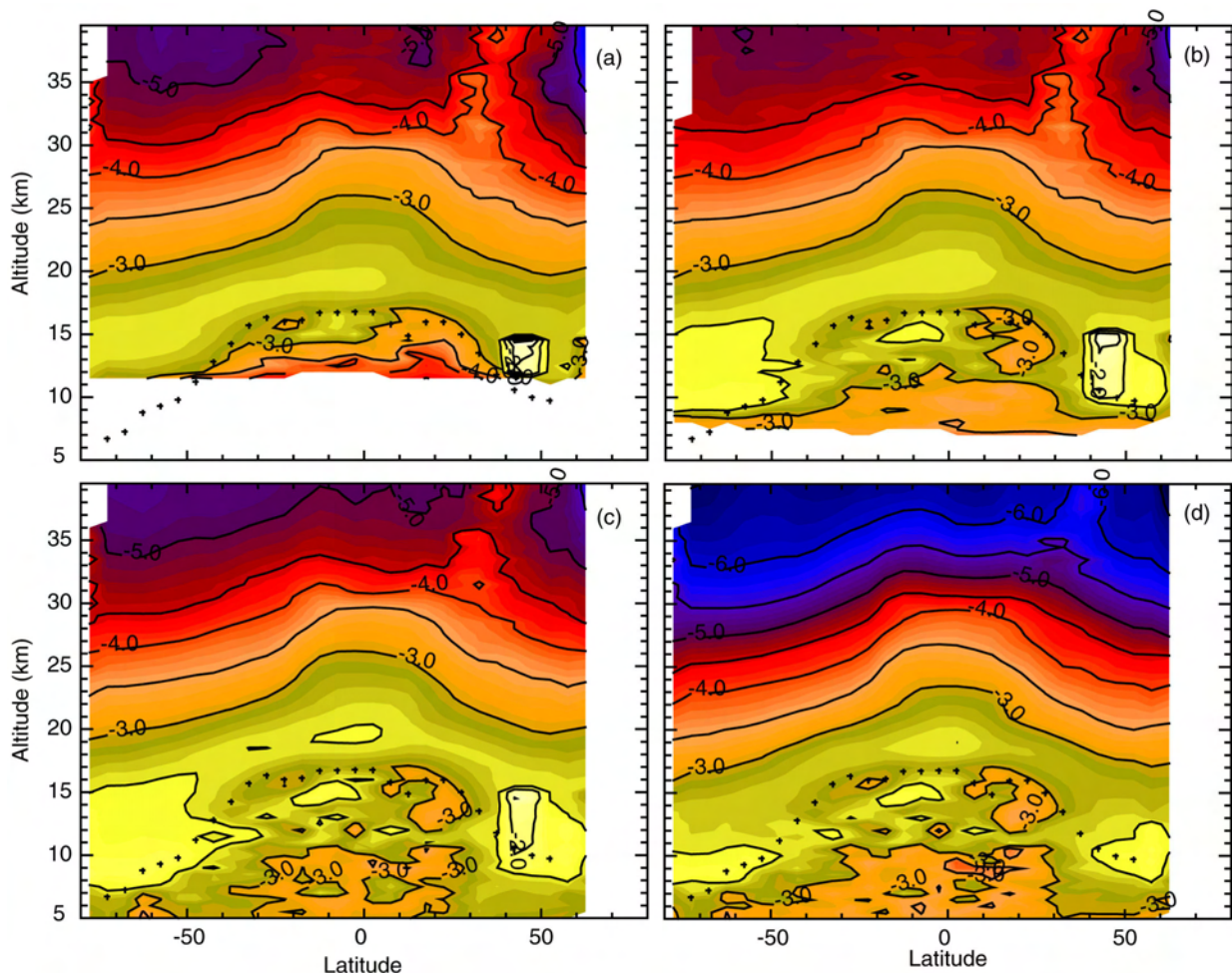


Figure 4.2: Zonal depictions of \log_{10} aerosol extinction at (a) 386, (b) 452, (c) 525, and (d) 1020 nm measured by SAGE II during January 1994. The crosses represent the average tropopause altitude.

The two panels of Figures 4.3 show analyses typical of the data included in the ASAP (Assessment of Stratospheric Aerosol Properties) data archive. In these figures, 1020 nm aerosol extinction from SAGE II is shown as a function of altitude and time for 40–45°N and 0–5°N. The data are shown at one month increments with a 3 month running median and requiring at least 5 points to produce a value in the data grid. In these figures, the effects of the eruptions of Nevado del Ruiz (Nov 1985), Kelut (Feb 1990), and Pinatubo (Jun 1991) can be seen. For the archive, data are produced for all four channels at 5 degree bins from 80°S to 80°N with both one and three month windows (called non-interpolated and interpolated, respectively). These analyses leave seasonally-based gaps at high latitudes as well as gaps at all latitudes during the period following the Pinatubo eruption and between the end of the SAGE mission in November 1981 and the beginning of the SAGE II mission in October 1984. SAM II, SAGE, and SAGE II data files are archived separately.

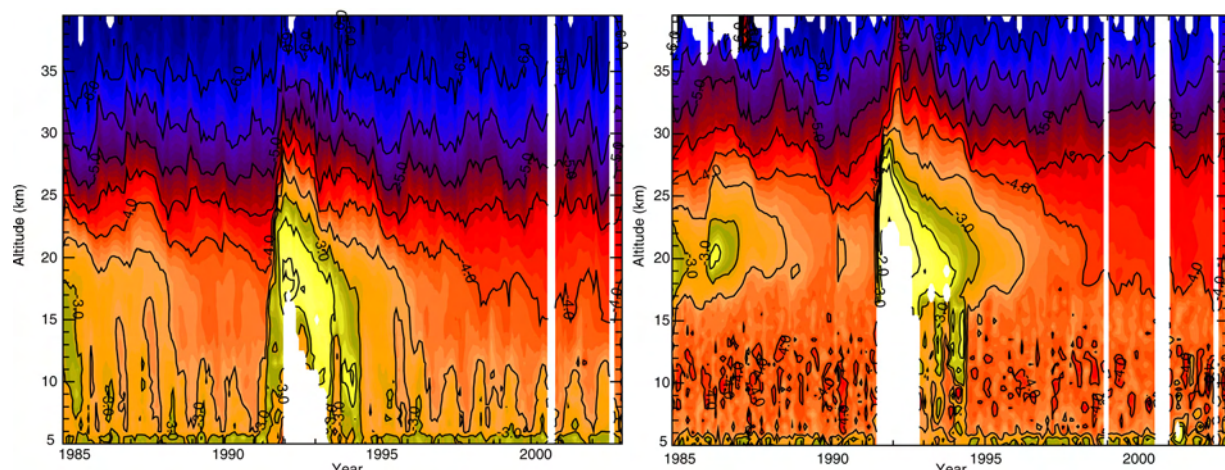


Figure 4.3: The SAGE II 1020 nm aerosol extinction (as \log_{10}) between 1984 and 2002 as a function of altitude for 40-45°N (left) and 0 to 5°N (right).

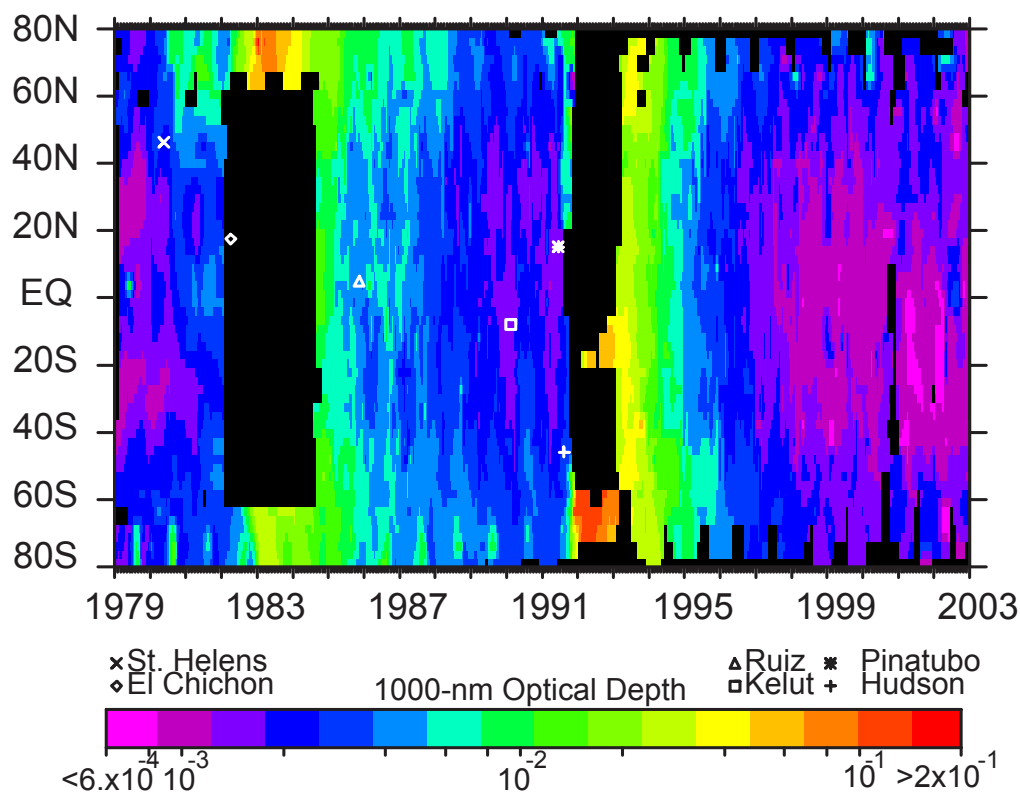


Figure 4.4: SAM II, SAGE, and SAGE II stratospheric aerosol optical depth at 1000 nm from 1979 through 2002. Profiles that do not extend to the tropopause are excluded from the analysis leading to a significant region of missing data following the eruption of Mt. Pinatubo in 1991. The earlier gap (1982-1984) was the period between SAGE and SAGE II.

Optical depth is so closely and simply related to extinction that we treat it as a primary product rather than a derived quantity. The optical depth data archived in the ASAP aerosol data set includes 1000-nm data from SAM II, SAGE, and SAGE II. Like the profile data, it is produced using a 3 month running median filter and 5-degree latitude bins. Aerosol optical depth at 1000 nm for 1979 through 2002 is shown in Figure 4.4 where all profiles that do not extend

down to the tropopause (due to the presence of cloud or high aerosol loading) are excluded. The persistent maximum in the tropical region is a result of the injection of aerosol (or its gaseous precursors) into the so-called tropical pipe by the powerful low latitude eruptions of El Chichón and Pinatubo. There are small wavelength differences between the instruments (1000 nm for SAM II and SAGE; 1020 nm for SAGE II) that can cause systematic differences in aerosol optical depth. Given the observed wavelength dependence of stratospheric aerosol optical depth, the differences should be less than 4%. The creation of a continuous, gap-free 1000 nm stratospheric optical depth data set is discussed in later sections.

HALOE Extinctions and Optical Depths

The current public release of HALOE data (V19) is available on the internet at <http://haloedata.larc.nasa.gov/Haloe/home.html>. Aerosol measurements are reported as extinction (units of km^{-1}) profiles at four wavelengths (2.45, 3.40, 3.46, and 5.26 μm). Optical depths are not reported as a standard product but can be easily computed from the profiles as the vertical integral of extinction. Periodic measurement gaps are a result of variations in latitude coverage related to the UARS orbit, normal operational concerns, and (in some cases) spacecraft anomalies. For example, during normal operations HALOE measurements are paused if the instrument temperature is elevated due to increased sun exposure. During normal orbit progression, the angle between the orbit plane and earth-sun vector (“beta angle”) oscillates between roughly -65° and $+65^\circ$, and the greatest solar exposure (and therefore heating) occurs at large beta angles. Data gaps increased after the late 1990’s due to spacecraft anomalies. Degradation of the UARS power and data systems has required duty cycling of the UARS instruments resulting in reduced operation time for HALOE.

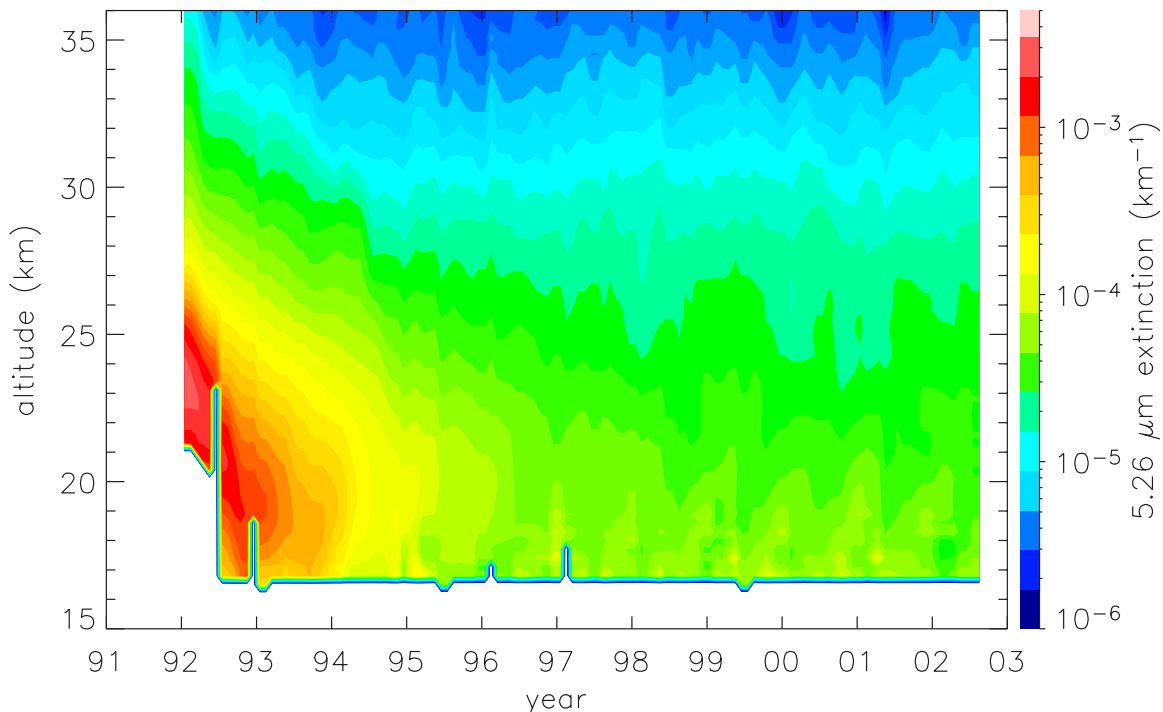


Figure 4.5: Time-height cross section of 5.26 μm HALOE aerosol extinction. The data are an average for latitudes from 2.5°S–2.5°N. White areas represent absent data. Measurements identified as affected by cirrus clouds were removed, resulting in the absence of data below 16 km altitude.

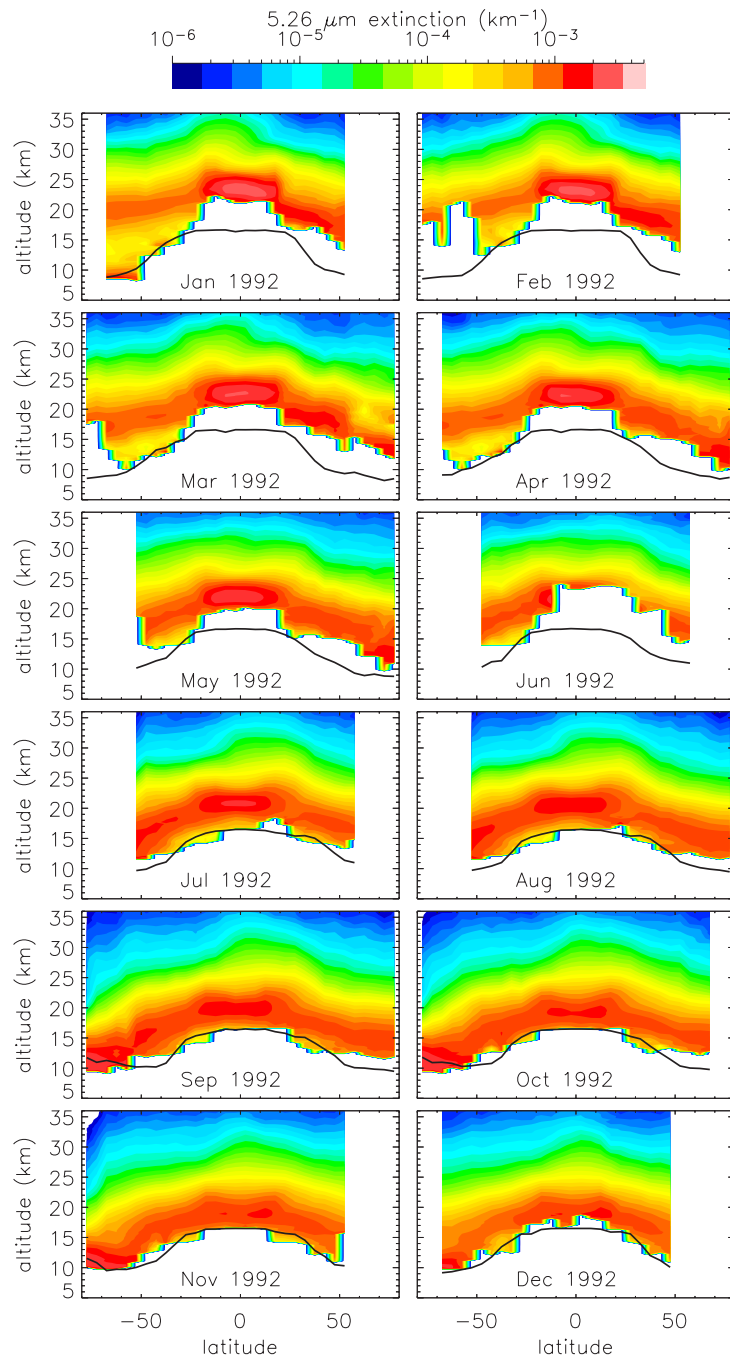


Figure 4.6: HALOE 5.26 μm aerosol extinctions as a function of altitude and latitude for each month in 1992, the year after the Pinatubo eruption. White areas represent missing data, and lines indicate average tropopause height. Measurements identified as cirrus were removed, resulting in the absence of data below the tropopause.

This section presents examples of stratospheric HALOE aerosol extinction and aerosol optical depths. The altitude history of 5.26 μm aerosol extinction near the equator is shown in Figure 4.5. Pinatubo aerosols are evident as enhanced extinctions at altitudes from the tropopause to over 35 km during the early 1990's. The enhanced aerosol loading decays rapidly until a near steady state is apparent after roughly 1997. During early 1992 the optical depth of the stratosphere was sufficient to cause complete opacity along the limb. The resulting saturation of the measurements accounts for data gaps in the lower stratosphere during early 1992. Latitude-

height cross sections of zonally averaged extinctions in 5 degree latitude bands are shown in Figures 4.6 and 4.7. Figure 4.6 shows 5.26 μm wavelength extinctions for each month in 1992. Pinatubo aerosols were concentrated at tropical latitudes during the early part of 1992, and spread towards polar latitudes as time progressed. Extinctions during the month of July for years from 1992 to 2002 are presented in Figure 4.7. The overall decrease in extinction from 1992 onward is due to decay of the Pinatubo aerosol cloud. Increasing data gaps after 1998 are due to duty cycling of the HALOE instrument.

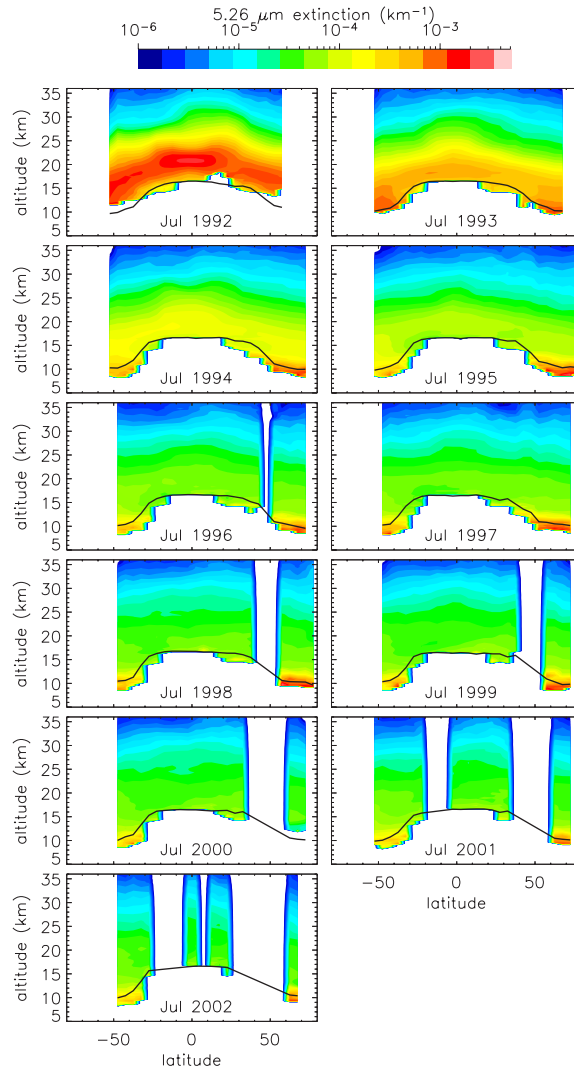


Figure 4.7: HALOE 5.26 μm aerosol extinctions as a function of latitude and altitude for the month of July during each year from 1992 to 2002. White areas represent missing data and lines indicate average tropopause height. Measurements identified as cirrus were removed, resulting in the absence of data below the tropopause.

HALOE optical depths at 5.25 μm are shown in Figure 4.8 as functions of latitude and time. Optical depths were calculated by integrating the extinction profiles from 2 km above the tropopause to 36 km and are presented as monthly averages. The steady removal of Pinatubo aerosols is observed in the early 1990s until an apparent steady state is reached after 1997.

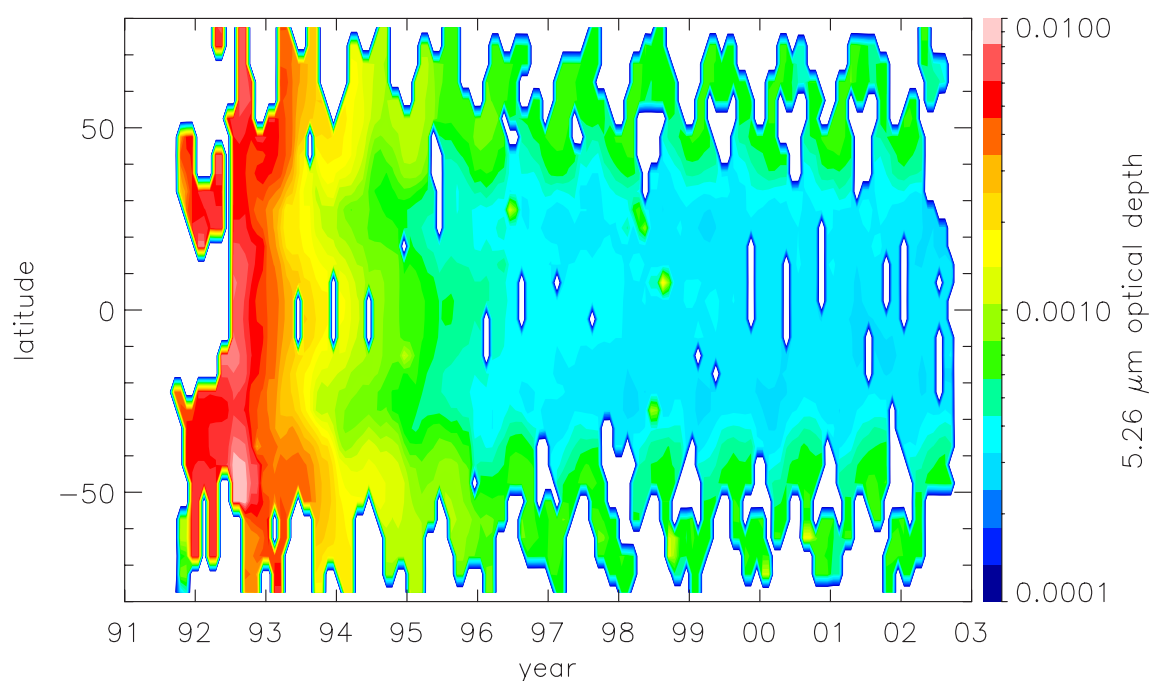


Figure 4.8: HALOE aerosol optical depth at $5.25 \mu\text{m}$ wavelength as a function of latitude and time for the period from 1991 to 2002. Optical depth was computed for altitudes from 2 km above the local tropopause ($z_{\text{trop}} + 2 \text{ km}$) to 36 km. White areas represent missing data.

POAM II, POAM III Extinctions

As described in Chapter 3, as a consequence of satellite orbital properties, POAM II and POAM III only make measurements at high latitudes, The latitudinal variation of the POAM II and POAM III measurements is (exactly) annually periodic, as shown in Figure 4.9a (the POAM II and POAM III measurement coverage is identical).

In this section we present monthly averaged extinctions from the POAM instruments for the northern hemisphere (Figure 4.9b) and the southern hemisphere (Figure 4.9c). Extinction enhancements caused by PSCs were identified [e.g., Fromm et al., 1997, and 1999] and removed from the data to produce cloud free averages. PSCs occur intermittently in the POAM NH winter measurements, but are ubiquitous in the SH winter measurements. Data voids in the SH plots indicate periods where there were insufficient cloud free measurements to calculate a cloud free average. There are slight differences in the channel wavelengths of the POAM II and POAM III instruments. The extinction data shown for the first part of the time period 1994-1996 (POAM II) were obtained at wavelengths of 0.780 and $1.06 \mu\text{m}$. The data during 1998-2004 (POAM III) were obtained at 0.779 and $1.02 \mu\text{m}$.

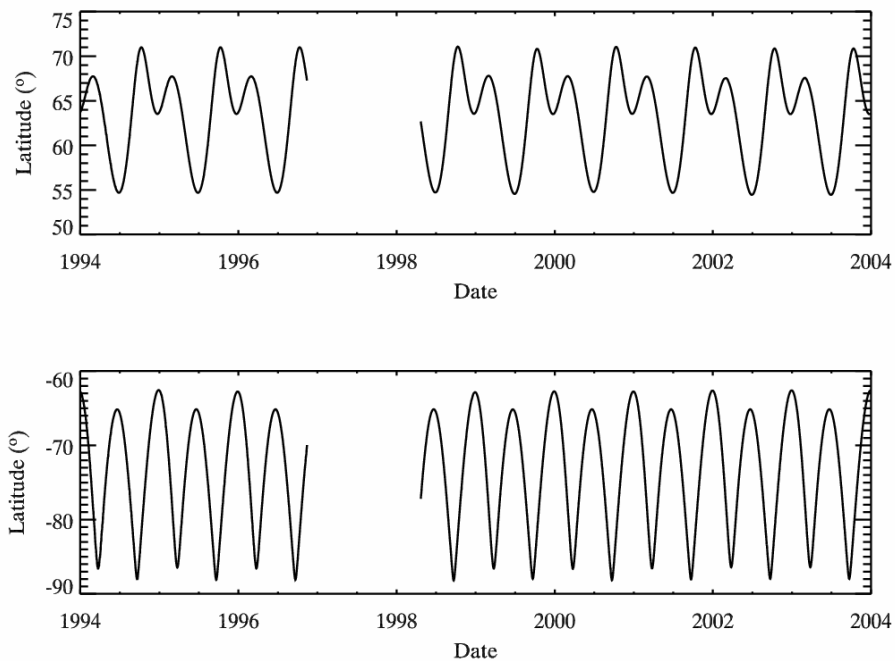


Figure 4.9a: POAM II and POAM III measurement coverage. For both instruments, the southern hemisphere measurements are obtained in spacecraft sunset, and the northern hemisphere measurements in spacecraft sunrise.

The northern hemispheric extinctions clearly show the residual effect of the Mt. Pinatubo eruption that caused elevated extinctions up to at least 23 km until late 1996. The periodic increases observed in the 10-13 km altitude region are most probably the result of enhanced horizontal transport during the summer of high aerosol extinction upper troposphere air from lower latitudes. Similar features were observed in the POAM water vapor and ozone mixing ratios as reported by Nedoluha et al. [2002] and Prados et al. [2003].

The POAM latitude variation is greater in the SH than the NH, and impacts the seasonal variation observed in the SH. The extinction maxima observed mainly in the late winter at low altitudes is probably the result of incomplete removal of PSC extinction enhancements (which extend down nearly to the tropopause late in the winter [Fromm et al., 1997]) from the data record.

The monthly averaged POAM extinction profiles were integrated vertically to calculate the total stratospheric optical depth, as shown in Figure 4.10. The vertical range of integration begins at 3 km above the tropopause and extends to 30 km altitude, using a tropopause defined by the 3 pvu potential vorticity level. The near constant aerosol optical depth after the decay of the residual Mt. Pinatubo aerosol suggests that background aerosol levels were reached in the polar regions in the measurement gap between 1996 and 1998.

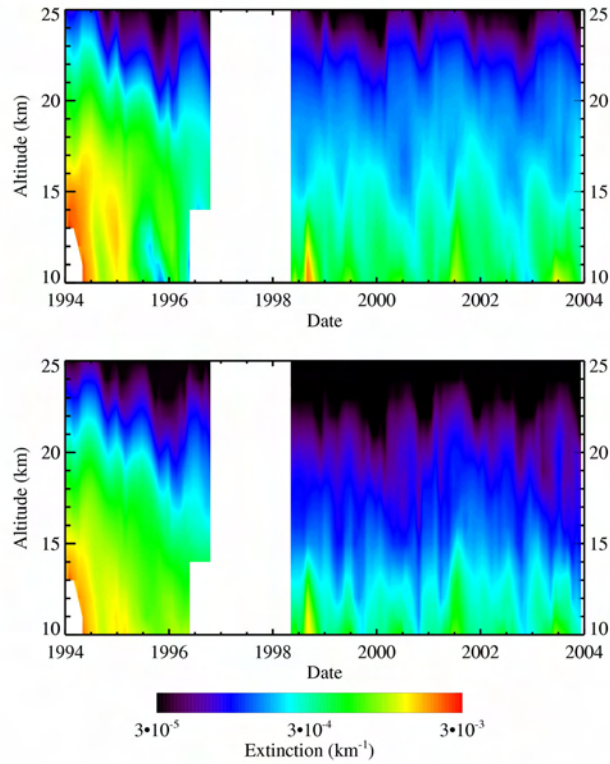


Figure 4.9b: POAM northern hemisphere aerosol extinction measurements for 1994 to 2003. (a) Extinction at 0.781 μm before gap and 0.779 μm after gap. (b) Extinction at 1.06 μm before gap and 1.02 μm after gap. Year labels denote the beginning (Jan 1) of each year.

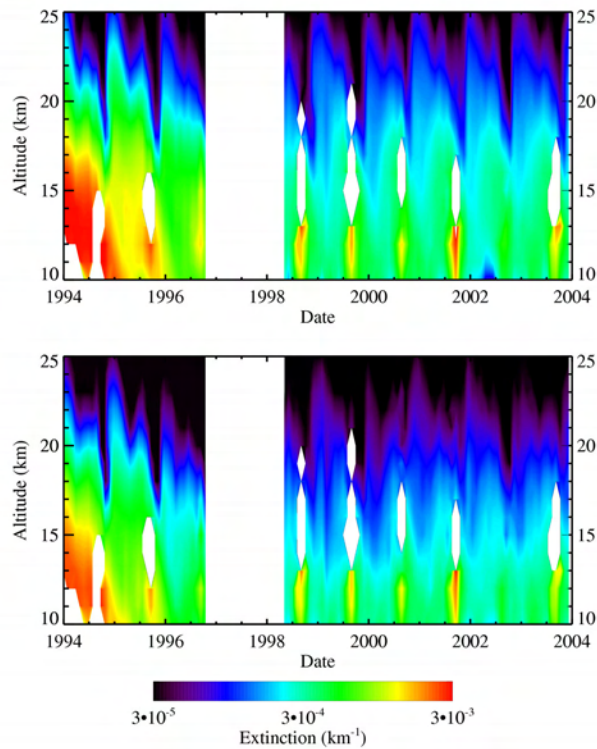


Figure 4.9c: POAM southern hemisphere aerosol extinction measurements for 1994 to 2003. (a) Extinction at 0.781 μm before gap and 0.779 μm after gap. (b) Extinction at 1.060 μm before gap and 1.020 μm after gap. Year labels denote the beginning (Jan 1) of each year.

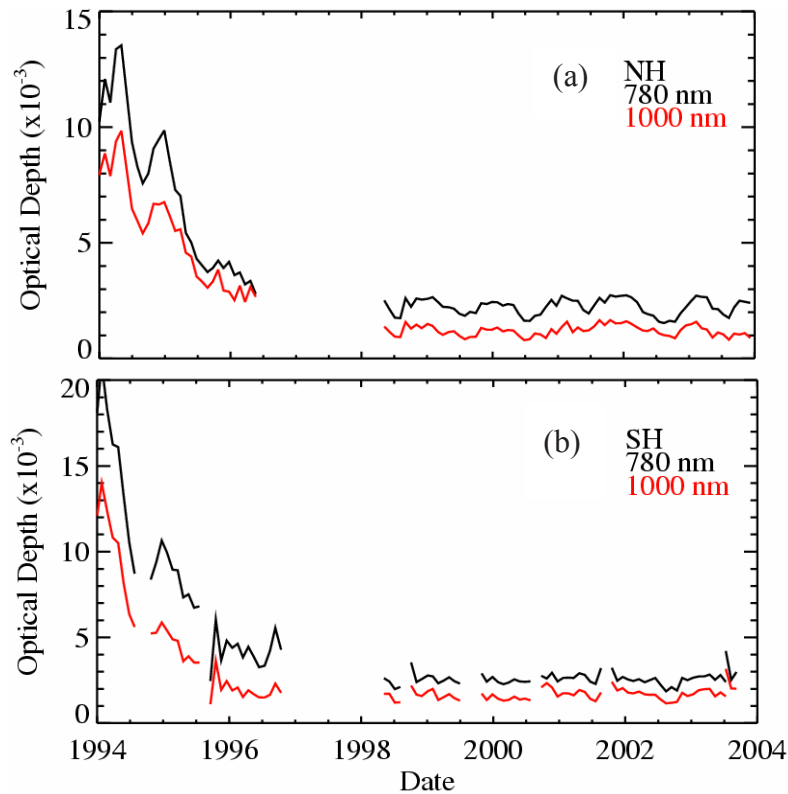


Figure 4.10: POAM stratospheric aerosol optical depth for the (a) northern hemisphere and (b) southern hemisphere. The optical depth was calculated by integrating the extinction profiles from 3 km above the tropopause to 30 km in altitude. The optical depth at 0.78 μm (black) and 1.0 μm (red) are shown.

4.2.2 Global Short-term Measurements

ORA

An overview of the ORA extinction profiles at 1013 nm is given in Figure 4.11 for the month of February 1993. The extinction profiles are defined at 26 altitude levels, with an increment of 1 km up to 25 km, and 2.5 km from 25 to 50 km. All profiles have been binned in latitude intervals of 5°, and cover most of the ORA latitudinal range (40°S to 40°N). Similar data are available over the whole duration of the ORA mission (August 1992 – May 1993) and for 6 spectral channels at 340, 385, 435, 442, 600 and 1013 nm. These data are available on the SPARC Data Center website.

CLAES

In this section we present plots of extinction *vs.* altitude and latitude as obtained from the CLAES data set. Figures 4.12 – 4.14 are examples of higher level aerosol products constructed from individual aerosol volume extinction coefficient profiles. Extinction and absorption coefficients are used interchangeably in discussions of CLAES aerosol data since they are essentially equal for the infrared wavelengths of interest here.

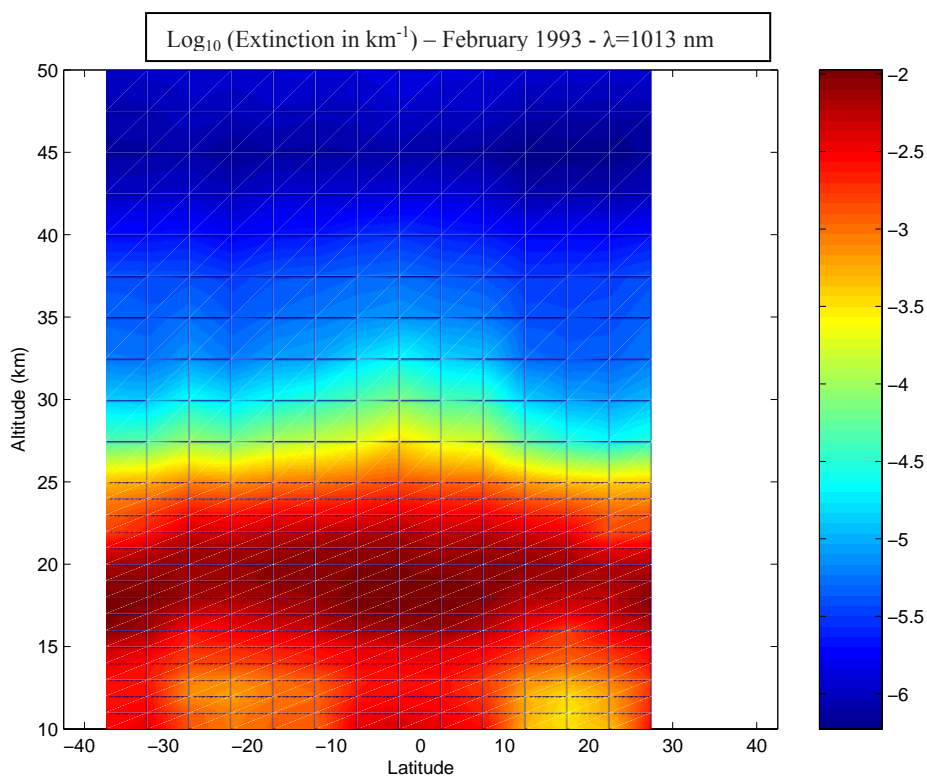


Figure 4.11: Dependence in latitude and altitude of the aerosol extinction (at 1013 nm) measured by the ORA instrument during February 1993. The color bar corresponds to the base 10 logarithm of the extinction measured in km^{-1} .

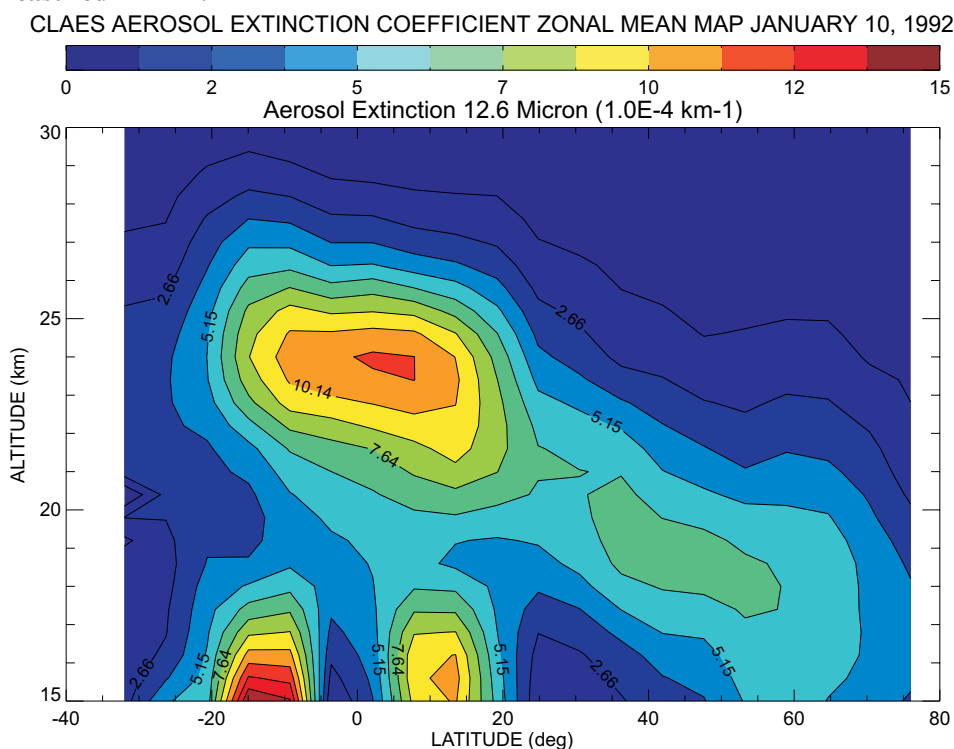


Figure 4.12: Extinction vs. latitude and altitude for one day (January 10, 1992) from the CLAES 12.6 μm measurements.

Figure 4.12 shows the zonal mean of aerosol extinction at 12.6 μm for January 10, 1992 (early winter NH). The tropical stratospheric “reservoir” region shows high aerosol extinction from

the Mt. Pinatubo eruption of June 15, 1991. Clearly, a significant amount of aerosol has been transported into the winter hemisphere at this time; nevertheless the stratosphere at very high northern latitude is relatively clean due to the barrier presented by the polar vortex. At low altitudes in the tropics, the high extinction patches are due to tropical cirrus near the tropopause (~16 km).

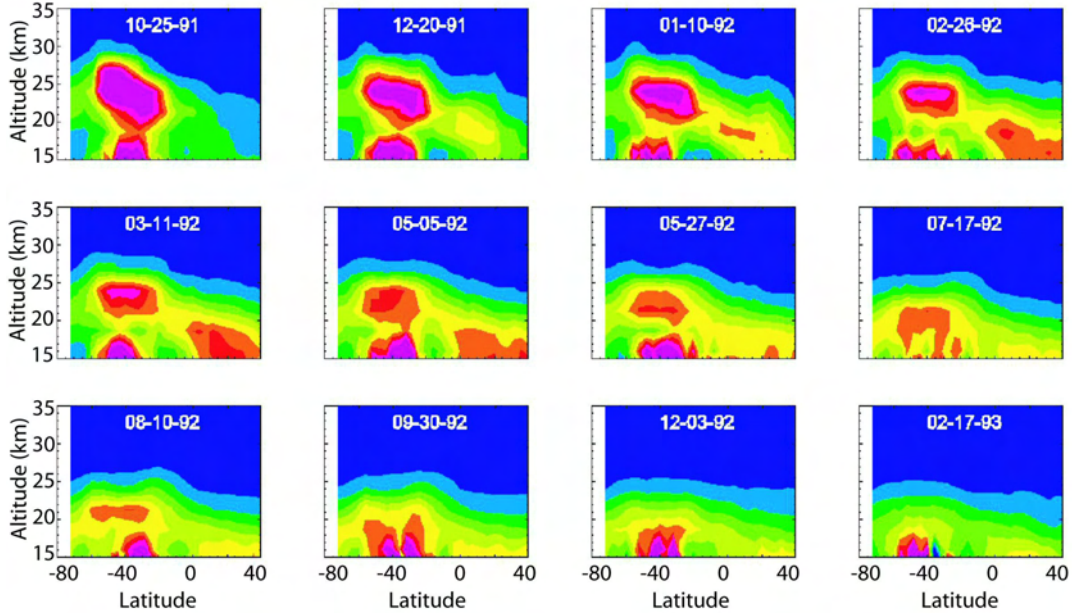


Figure 4.13a: CLAES zonal mean aerosol absorption as function of altitude (15-35 km). The orientation of the satellite yields this northward view, so the coverage is from 34°S to 80°N.

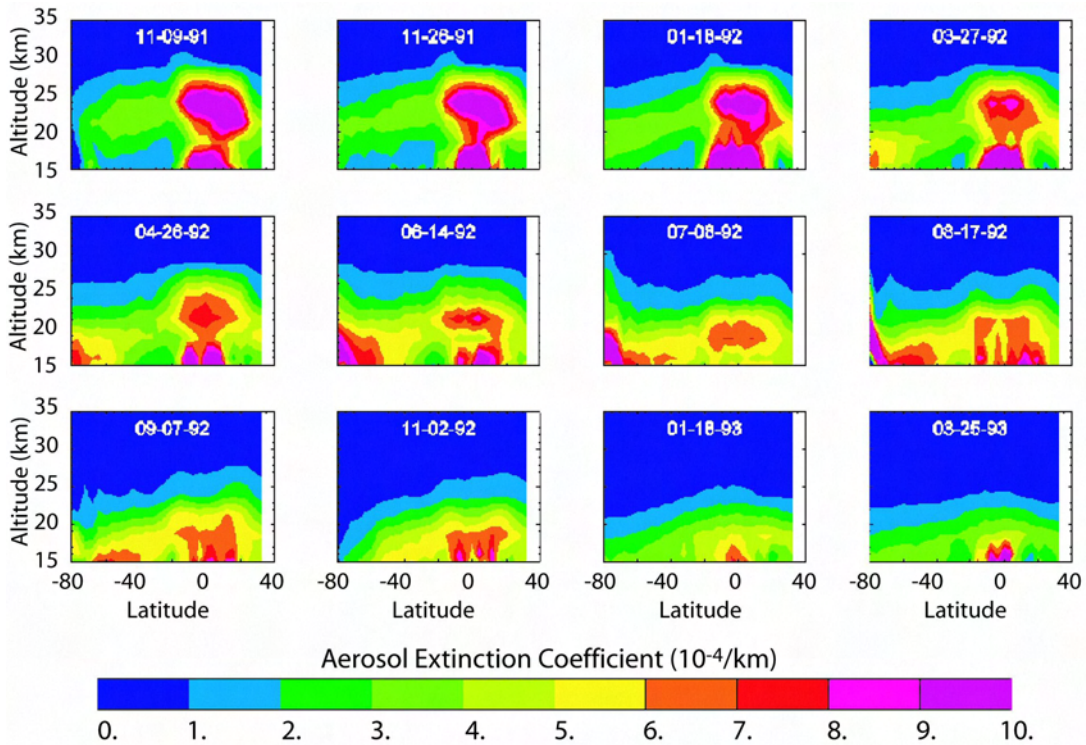


Figure 4.13b: CLAES zonal mean aerosol absorption as function of altitude (15-35 km). The orientation of the satellite yields this southward view, so the coverage is from 80°S to 34°N.

Figures 4.13a and 4.13b are a series of zonal mean aerosol extinction snapshots at $12.6 \mu\text{m}$ for north and south viewing, respectively. Taken together they reveal the evolution of the Mt. Pinatubo aerosol as observed over the entire CLAES lifetime. Polar stratospheric clouds are prominent as high extinction regions particularly in the SH winter. The parameter Z^* is pressure equivalent altitude, given by

$$Z^* = 16.0 \times (3 - \log_{10}(p)),$$

with p in hPa and Z^* in km.

Figure 4.14 shows the mean aerosol optical depth at $12.8 \mu\text{m}$ as constructed from the mission-long set of zonal mean averages. This composite was constructed by integrating mean aerosol extinction upward from 68 hPa in the tropics (20°S to 20°N) and upward from 100 hPa in the extratropics.

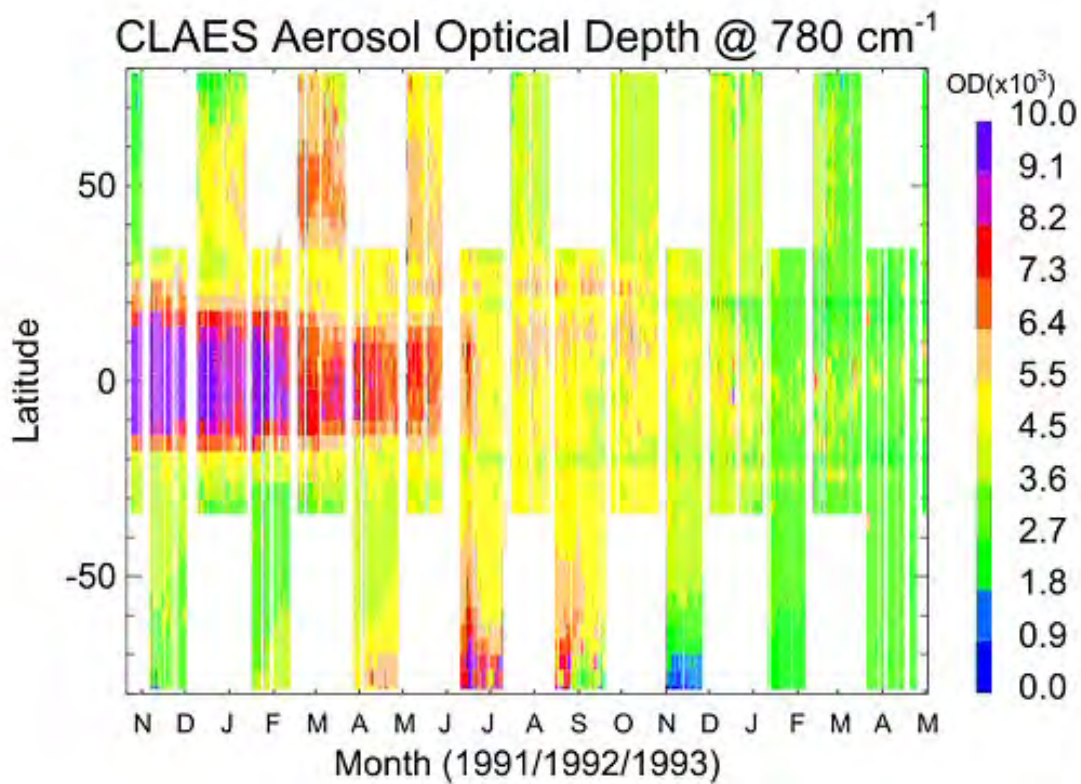


Figure 4.14: CLAES zonal mean optical depths at $12.8 \mu\text{m}$ for the entire mission.

4.2.3 Localized Long-term Measurements

University of Wyoming balloon borne in situ measurements

Balloon borne optical particle counters have been used by the University of Wyoming to measure stratospheric aerosol size and number density since 1970. Although the balloon borne sensors have been launched from many locations, regular long term flights have only been conducted from Laramie Wyoming. These have captured the major eruptions of Fuego, El Chichón and Pinatubo as well as a number of smaller eruptions. Example aerosol profiles for volcanically perturbed and quiescent periods are shown in Figure 4.15.

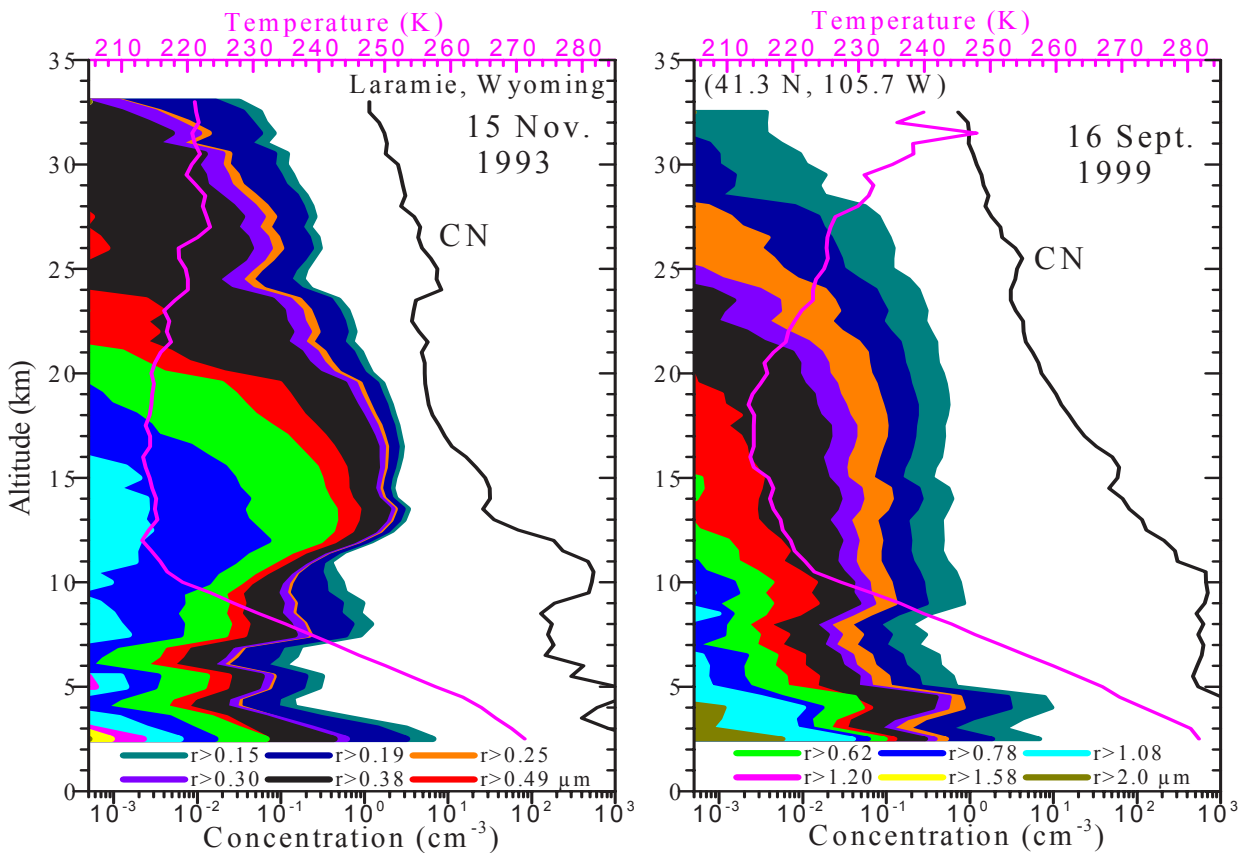


Figure 4.15: Vertical profiles of aerosol concentration above Laramie, Wyoming, for particles in twelve size classes ranging from radius $r > 0.15$ to $r > 2.0 \mu\text{m}$ (in color), and condensation nuclei ($r > 0.01 \mu\text{m}$, black line). Temperature profile is also shown (pink line). The left hand panel was obtained 18 months after the eruption of Pinatubo when the stratosphere was still highly disturbed. The right hand panel is a typical profile during a volcanically quiescent period. The color codes for the twelve size ranges are presented at the base of the two panels.

The temporal history of the Laramie measurements is shown in Figure 4.16. The figure presents the history of the two fundamental sizes measured since the program began. Error bars represent the counting error, and are at times smaller than the data symbols. The Laramie measurements represent about 340 individual profiles. Also included in the figure are 12 measurements from Lauder, New Zealand using the same instrumentation. Eruption times for the nine stratospherically important volcanic eruptions occurring during the period are indicated.

Integrated Backscatter from Various Lidar Systems

Table 3.2 (in Chapter 3), gives a list of the various stratospheric aerosol lidars operated in the past or still running today, from Arctic to Antarctic latitudes. These lidar stations can provide suitable datasets for establishing a stratospheric aerosol climatology. Their location is shown in Figure 3.7 and their characteristics and integrated backscatter records are given below.

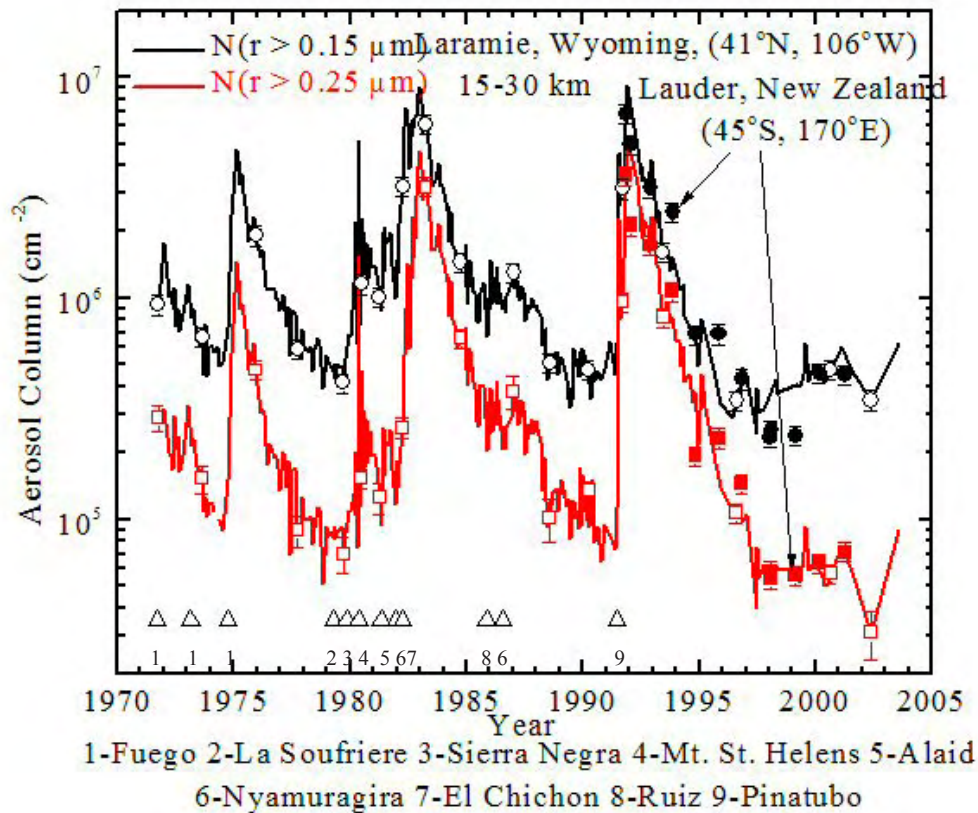


Figure 4.16. History of 15-30 km column integrals, above Laramie, Wyoming, of aerosol number for particles > 0.15 (black line) and $0.25 \mu\text{m}$ (red line) radius. Example error bars are shown on the occasional data point. Twelve measurements from Lauder, New Zealand are included (filled symbols with error bars).

Formulation of a Lidar-Based Stratospheric Aerosol Climatology

Establishing a reliable stratospheric aerosol climatology from ground-based lidar observations is difficult because of the inhomogeneous geographical distribution of the lidar stations throughout the world, in latitude and longitude. Most lidar sites are located in industrial countries in the northern hemisphere, as shown in Figure 3.7, between 20°N and 50°N , and between 160°W and 15°E . Only three datasets are available in the southern hemisphere. Of these, two are polar and one is tropical so limited measurements are available from the southern mid-latitudes. Consequently, lidar observations do not give a complete picture of the zonal distribution of stratospheric aerosol properties.

Long-term time series of lidar aerosol measurements from selected sites are presented in Figure 4.17. They are presented as time evolution of the integrated backscatter coefficient. The various datasets are not readily compared due to the differences between experimental procedures, particularly operating wavelengths and processing methodologies used in each location, as well as different altitude ranges used for evaluation. Additionally, polar locations provide measurements only during winter, and their focus is polar stratospheric cloud observations. The dif-

ferences in aerosol content (background or volcanic) also induce a high variability of total uncertainties for each data set.

Ny-Alesund, Spitzbergen

78.92° N, 11.93° E
532 nm
trop+ 2 km → 30 km

**Garmisch-Partenkirchen,
Germany**

47.48° N, 11.06° E
694 nm
trop + 1 km → 30 km

Hampton, U.S.A.

37.1° N, 76.3° W
694 nm
trop → 30 km

Mauna Loa, U.S.A

19.54° N, 155.58° W
694 nm
15.8 km → 33 km

**Saõ José dos Campos,
Brazil**

23.2° S, 45.9° W
589 nm
17 km → 35 km

**Dumont d'Urville,
Antarctica**

66.67° S, 140.01° E
532 nm
trop → 30 km

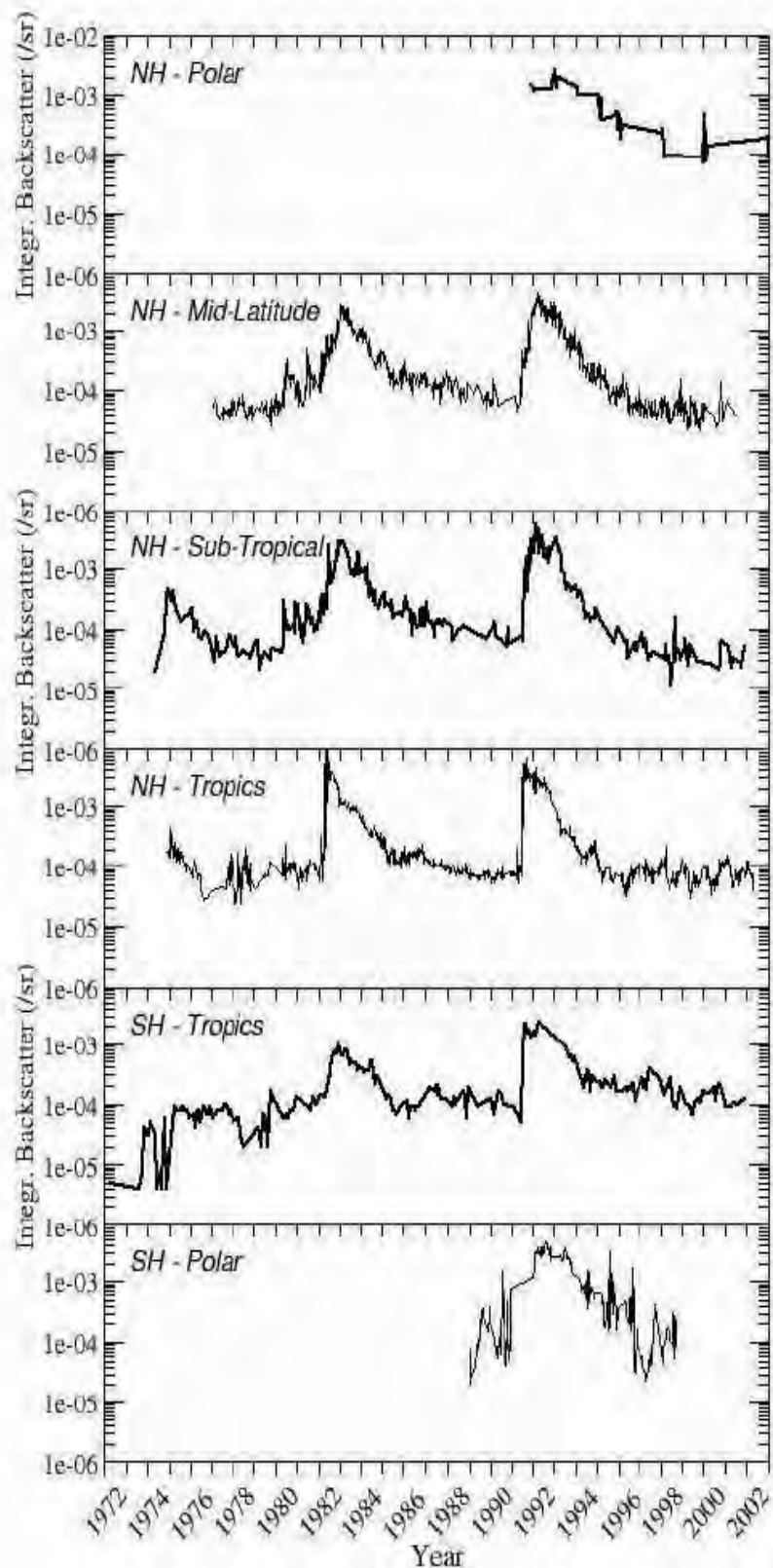


Figure 4.17: Time evolution of integrated backscatter coefficient from aerosol lidar measurements in different latitude bands, from north to south, between 1972 and 2003. The altitude integration interval is given for each station as last entry in the left column (trop. = tropopause height).

Polar Stratospheric Clouds are visible in the data sets from both Polar Regions. The impacts of various volcanic eruptions also appear, depending on the location of the eruption with respect to the measurement station. Most of the data sets clearly show the decay of the volcanic loading and an apparent return to background conditions.

4.2.4 Short Term Localized Measurements

NASA Langley Airborne Aerosol Lidar

Airborne lidars offer distinct advantages over ground-based systems in that they can characterize the horizontal as well as the vertical distribution of aerosol and can be deployed to locations of interest around the globe. They also offer advantages over satellite instruments in terms of far greater vertical and horizontal resolutions and the ability to focus the observations on a particular target at a specified time (e.g., a volcanic plume or the formation of PSCs in the Arctic cold pool). The disadvantage, of course, is that such systems are deployed only occasionally and do not provide wide geographic coverage. Nonetheless, occasional airborne lidar measurement campaigns have provided otherwise unobtainable information on the distribution of aerosols and insight into sampling issues associated with satellite instruments that rely on occultation or other geometries which have much lower horizontal and vertical resolution.

Below we present observations acquired by the NASA Langley Aerosol Lidar while deployed on the NASA DC-8 aircraft during the SOLVE-II/Vintersol campaign. This lidar is a piggy-back instrument on the NASA Goddard Airborne Raman Ozone Temperature and Aerosol Lidar (AROTAL), which measures ozone and temperature profiles in a zenith viewing geometry.

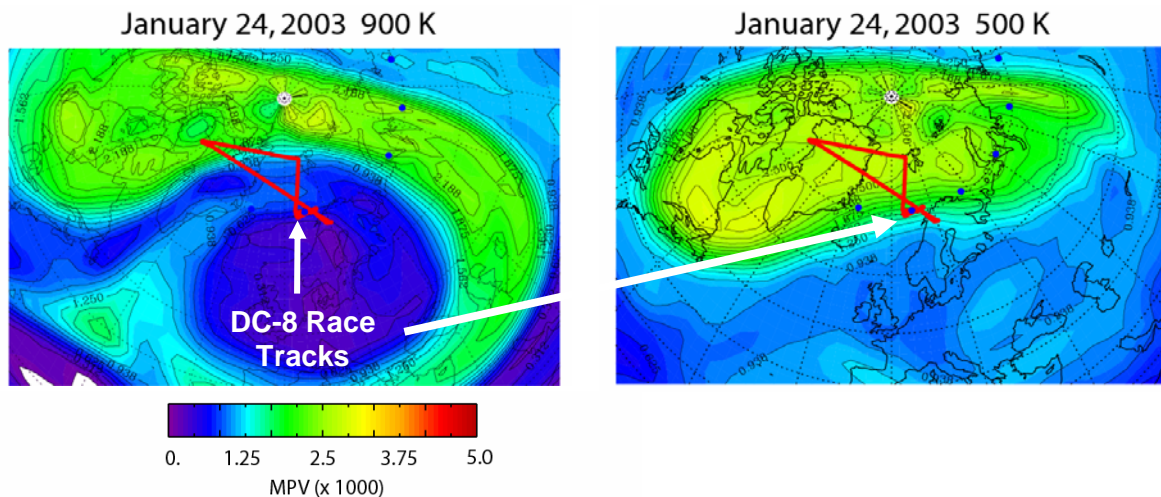


Figure 4.18. Potential vorticity contours for the 500K and 900K potential temperature surfaces and the flight track (red lines) of the NASA DC-8 for the 24 January 2003 flight of the SOLVE-II/Vintersol campaign.

On 24 January 2003, the polar vortex was transitioning from a two-lobe structure to an elongated elliptical circulation pattern. Figure 4.18 shows potential vorticity contours at the 500 K and 900 K levels and the flight track of the DC-8. As can be seen from the difference between the potential vorticity contours, the vortex boundary sloped to the northwest with altitude along the flight track of the DC-8. Figure 4.19 shows the lidar data and the contours of potential vorticity as a function of altitude and distance along the DC-8 flight track. The lidar profiles acquired along most of the flight track penetrated two regimes, with the lower altitude region being generally within the vortex and the higher region being generally outside the vortex. The

thin filamentary layers above 20 km are similar in structure to the potential vorticity contours. It is clear that these filaments were external to the polar vortex while the lower mass of stratospheric aerosol located toward the middle of the plot (~12:50 – 17:32 UT) was largely within the vortex. Seven-day back trajectories confirm that the filaments originated at lower latitudes.

From 10:30 to 12:00 UT, the DC-8 was flown in a series of nearly closed circuits at varying altitudes (racetrack pattern) in the vicinity of a SAGE III occultation point. Figure 4.20 presents a comparison between the SAGE III extinction profile and that computed from the lidar data acquired near the occultation point. The lidar backscatter data were converted to extinction using extinction-to-backscatter ratios derived from mid-latitude balloon-borne optical particle counter measurements of stratospheric aerosol size distributions [Jäger and Deshler, 2002]. The thin aerosol layers above 20 km appearing in the lidar data in Figures 4.19 and 4.20 are also apparent in the SAGE III data.

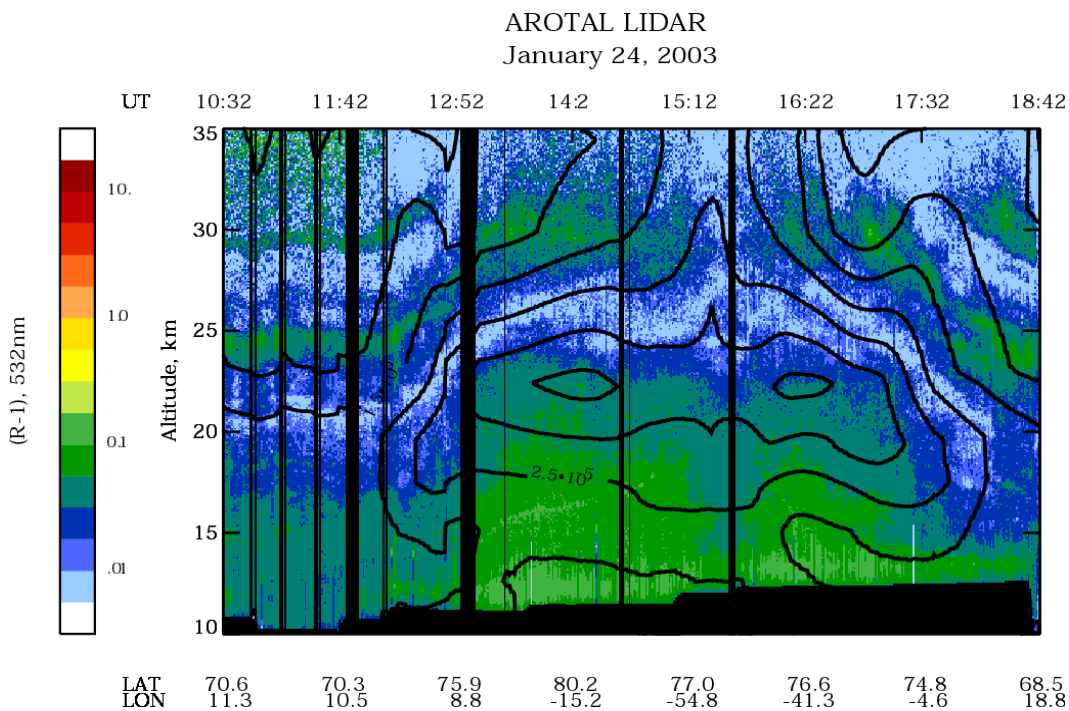


Figure 4.19. AROTAL/LaRC Aerosol Lidar data from the 24 January 2003 flight on SOLVE-II/Vintersol. The color contours show the 532 nm aerosol scattering ratio (ratio of aerosol backscatter to molecular backscatter) and the black lines show contours of potential vorticity.

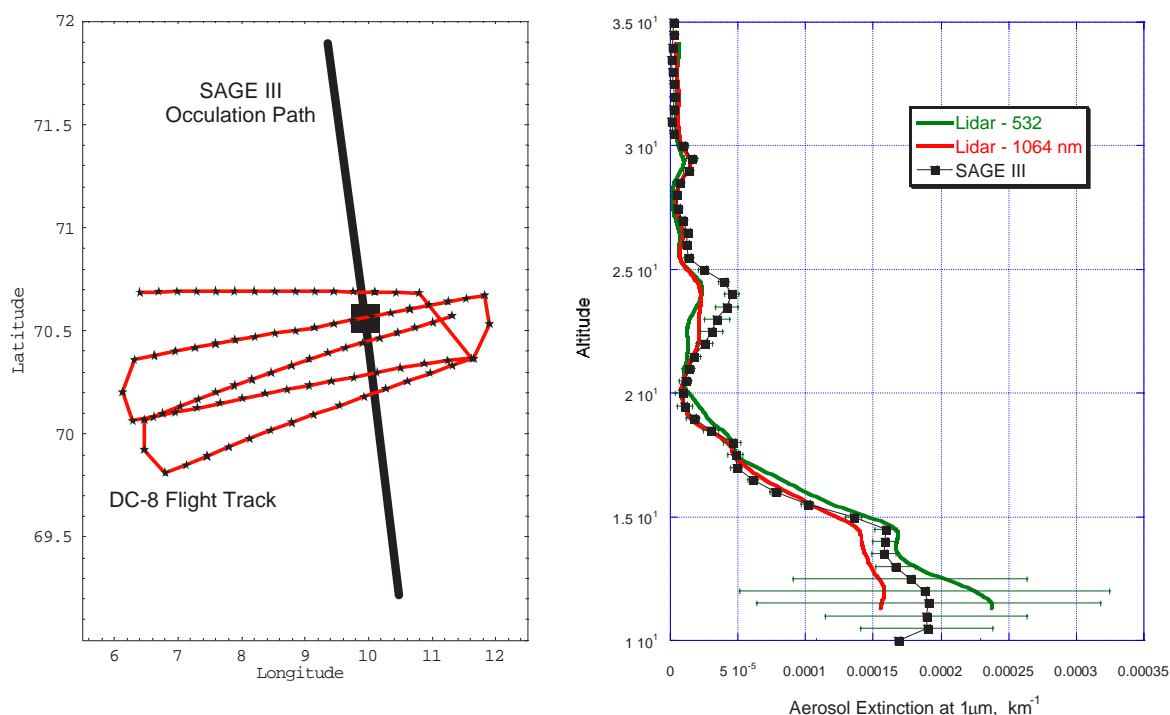


Figure 4.20. The left panel shows the DC-8 flight tracks and SAGE III occultation path for the 24 January 2003 validation coincidence from the SOLVE II mission. The DC-8 flight track is in red with locations of archived lidar profiles marked with stars. The SAGE III occultation path is shown in black. The right panel shows a comparison of SAGE III extinction at 1020 nm with extinction at 1064 nm computed from the lidar 532 nm (green) and 1064 nm (red) aerosol backscatter data averaged in the vicinity of the SAGE III ray path. The lidar aerosol backscatter data were scaled to extinction at 1064 nm using conversion parameters from Jäger and Deshler [2002].

The lidar data provide a useful validation of both SAGE III extinction values and altitude registration. The vertical structure observed in the SAGE III data is reproduced in the lidar data, and through much of the profile the lidar extinction values are nearly identical. Differences between the SAGE III and lidar extinction values (such as at 24 km in Figure 4.20) are likely due to several causes. First, the microphysical models used to convert aerosol backscatter to extinction were based on mid-latitude measurements of size distribution which can be quite different in the polar region. Second, the DC-8 did not fly its racetrack pattern along the direction of the SAGE III occultation path: the SAGE III occultation path was nearly perpendicular to the vortex boundary viewing across the largest gradients in aerosol distribution, while the DC-8 flight tracks were approximately parallel to the boundary. Third, differences may also be caused by subtle instrument nonlinearities (a very small nonlinearity can create a relatively large error in the aerosol retrieval when aerosol loading is very low, as it is for this case). Regardless of these differences, variation of the vertical and horizontal structure of the aerosol as shown by the lidar data in Figure 4.19 provides insight on sampling issues for satellite-based occultation instruments, in particular, the potential for vertical smearing of complex structures due to the long occultation path (e.g., ~175 km). For those situations where detailed information on the small scale vertical and horizontal structure of the aerosol distribution is required, airborne lidar remains the best technique currently available.

DLR Airborne Lidar

Figure 4.21 shows another example of a 2-D aerosol curtain as observed by an aircraft-borne lidar, the aerosol and ozone lidar (OLEX), onboard the DLR Falcon. The data were taken during a flight from Kiruna to Munich on 8 February 1999. This flight took place below the Arctic vortex, which was elongated towards central Europe and interleaved with layers of mid-latitude air. The air in the Arctic vortex is older than stratospheric air at mid-latitudes [Waugh and Hall, 2002] and is subjected to the general subsidence that takes place in the vortex. Therefore, the sulfate aerosol backscatter observed in the vortex differs from that observed outside the vortex, as is evident from Figure 4.21. Note that within the vortex, as outside it, the stratospheric aerosol is strongly stratified. During January 1999, there were intrusions of mid-latitude air into the vortex and a peeling of filaments from the vortex edge, followed by intensive stirring. The filament boundary layers typically extend over 100 m vertically and a few kilometers in the horizontal. Under typical stratospheric conditions, it takes about two weeks until 3-D turbulence takes over and effectively mixes air masses at these scales [Flentje and Kiemle, 2003].

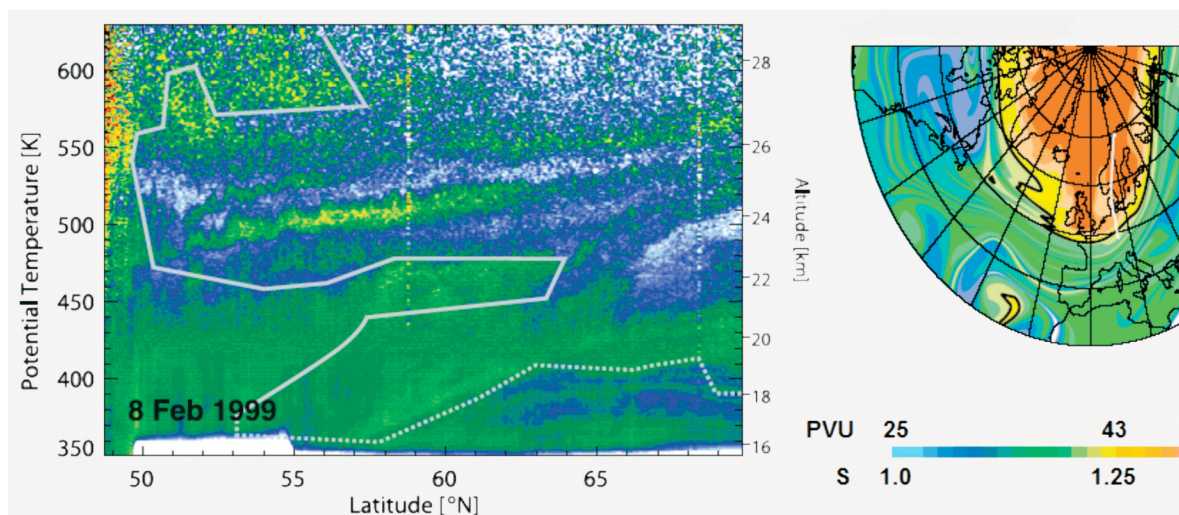


Figure 4.21: Left panel: Profile of aerosol backscatter ratio (S) at 1064 nm ranging between 1.0 and 1.5 along the aircraft flight path from Kiruna to Munich on 8 February 1999, not corrected for extinction. The altitude scale is accurate at the right border of the section. The superimposed bright contour marks the vortex edge derived from contour advection calculations; the dotted contour indicates the lower boundary of the vortex, which is not well defined. Right panel: Polar stereographic projection of the potential vorticity (PV) at 525 K calculated by contour advection. Colors correspond to PV-units (PVU) ranging from 26 to 61 $\text{K m}^2 \text{kg}^{-1} \text{s}^{-1}$. The white line indicates the flight path. Adapted from Flentje and Kiemle [2003].

*Airborne particle counters: FSSP-300 and MASP**FSSP-300 and MASP*

The FSSP-300 (Forward Scattering Spectrometer Probe, Model 300) has been flown on the ER-2 aircraft since the late 1980s [Baumgardner et al., 1992] and on the Geophysica since the mid-1990s [Borrmann et al., 2000]. As discussed in Section 3.5.3, this instrument measures particles in the 0.2–20 μm radius range, i.e. the FSSP-300 sees only the large size tail of the distribution. Given this property, the instrument has been used for cloud measurements, in particular concerning PSCs and cirrus, whereas the instrument's capabilities to

completely depict stratospheric aerosol especially in volcanically quiescent times is limited. Nonetheless, the FSSP can provide valuable data about aerosol. For instance, Figure 4.22 depicts examples of particle size distributions in the 1996/97 winter from measurements inside (solid curve) and outside (dotted curve) of the polar vortex on similar levels of potential temperature, as well as close to the vortex boundary (dashed curve). These measurements were taken at a time when most of the Pinatubo aerosol had already disappeared from the stratosphere. The measurements corroborate the lidar observations presented in the previous section: Inside the vortex the smaller particles ($r \sim 0.2 \mu\text{m}$) are suppressed about a factor of 5 when compared to the out-of-vortex size distribution, whereas the larger particles ($r \sim 0.4 \mu\text{m}$) are suppressed about a factor of 40.

Figure 4.23 shows the measured particle number density for radii between 0.2 and $11.5 \mu\text{m}$ as function of flight time for flights conducted with the ER-2 and the Geophysica at various northern hemispheric latitudes [from Borrmann et al., 2000]. The time scale on the abscissa has been normalized with respect to the duration of the flight between takeoff and landing (usually between 4 and 8 h). On the left and right sides of the figure the concentration increases because these are the measurements from the takeoff and landing. The center region of the graph presents measurements by both aircraft at altitudes between 18 and 21 km pressure altitude. The uppermost line indicates the aerosol levels encountered by the ER-2 during flights between January and March 1992 [Borrmann et al., 1993]. The solid single thick line in the middle of the figure shows the levels measured by the ER-2 during a flight from Wallops Island, USA, to Stavanger, Norway, on 31 December 1988, mostly outside of the polar vortex. This flight took place in a period of relative volcanic quiescence and represents what were thought to be background conditions at that time. However, Thomason et al. [1997] pointed out that 1989 may not have been at true background level, due primarily to Nevado del Ruiz in 1985 and Nyamuragira in 1986. The group of 3 dotted lines underneath the ER-2 flight on 31 December 1988 are the measurements onboard the Geophysica during flights from Pratica di Mare (near Rome, Italy) in November and early December 1996. These represent outside vortex, mid-latitude data from similar latitudes as the ER-2 flight in late 1988. The lowermost 3 dashed lines are the Geophysica flights during the APE-POLECAT campaign [Stefanutti et al., 1999] from January 1997 from Rovaniemi, Finland, mostly inside the polar vortex. The lowermost solid curve shows another flight into the polar vortex from this campaign, however following a subtropical inversion, and showing distinctly less aged air with higher aerosol number densities.

This figure illustrates the atmospheric changes of the aerosol number densities from before until long after the Mount Pinatubo eruption. In particular, the decrease of the atmospheric particle concentrations in the winter 1996/97 compared to the previous apparent background aerosol of 31 December 1988 suggests that 1989 may not have been at true background level [Thomason et al., 1997]. However, questions of comparability must be asked in view of using separate flight series, separate aircraft, and especially different instruments. Particle number density for $r > 0.2 \mu\text{m}$ is sensitive to the detector cutoff. As outlined in Section 3.5.3 the average uncertainty in sizing from the FSSP-300 is approximately 20 % over the range of this instrument. However, the question of comparability is a generic one applying basically to all measurements. While the 20-% uncertainty limits the accuracy of the FSSP-300 measurements, its precision and comparability may be expected to be better since the FSSP-300 underwent no changes in its design during the years of these measurements.

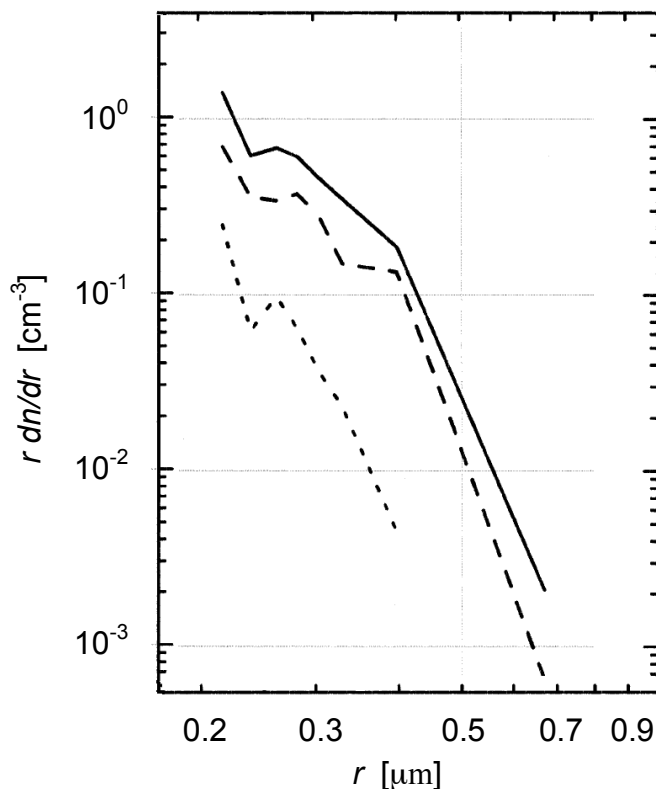


Figure 4.22: Size distribution measurements of the FSSP-300 system on Geophysica on the potential temperature surface ~ 480 K in December 1996. Solid curve: outside of the vortex (over Italy). Dashed curve: close to the edge of the polar vortex (over Scandinavia). Dotted curve: in the vortex (over Scandinavia). The averaging periods for these size distributions are between 300 and 1000 s of flight time depending on the counting statistics [adapted from Borrmann et al., 2000].

Whereas the FSSP-300 samples the light scattered by the particles in the near forward direction upon illumination, the MASP is a Multiangle Aerosol Spectrometer Probe which can obtain a higher size resolution and information on the index of refraction of the scattering particles. A summary of all quality-assured measurements made with the FSSP-300 and MASP, from December 28, 1988 to March 12, 2000, in the altitude range from 17 – 20 km is shown in Figure 4.24. Here the concentration has been averaged as a function of latitude, in 5° intervals (solid lines) and all encounters with possible cirrus clouds have been excluded from the analysis. The measurements in the southern hemisphere were only made from March to November, 1994. There is a distinct minimum at tropical latitudes, in contrast to the aerosol optical depths that are derived from various satellite products. This is because the aerosol particles at these latitudes are dominated by those with radii smaller than $0.2 \mu\text{m}$ and they are not detected by either the FSSP-300 or MASP whose size range is nominally 0.2 to $10 \mu\text{m}$. The maxima occur at the mid-latitudes, more so in the northern than southern hemisphere. Most of the northern measurements at high latitudes were made in the winter months. This is most likely the reason for the rapid decrease in concentrations since the flights were mostly in the polar vortex where the majority of particles are smaller than the lower size thresholds of either spectrometer.

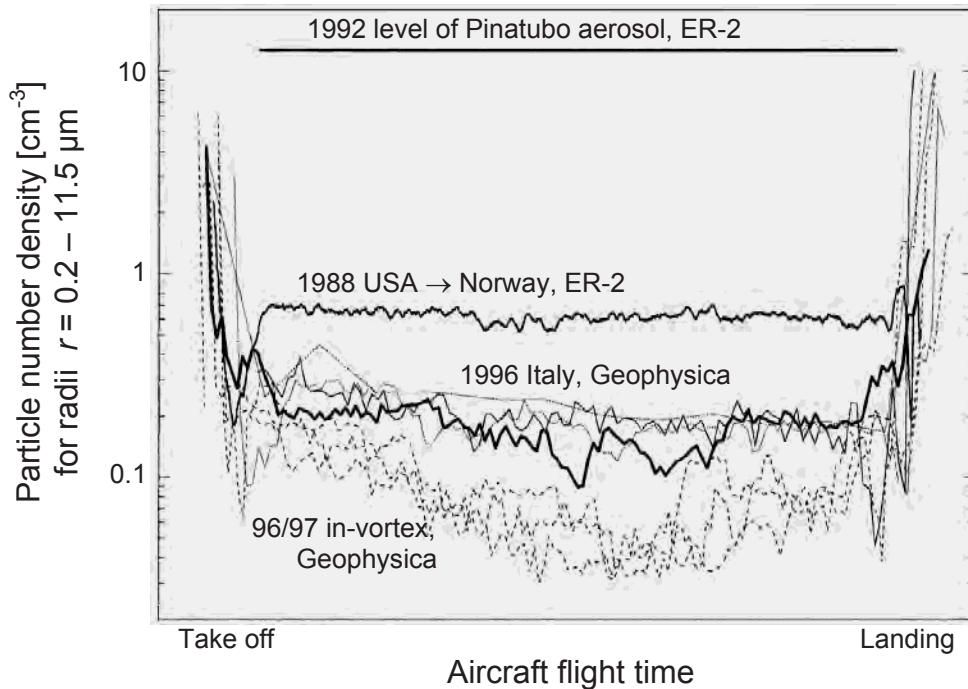


Figure 4.23: Particle number densities from FSSP-300 measurements on the ER-2 and Geophysica from northern hemispheric locations for the pre-Pinatubo background period, the Pinatubo volcanic aerosol period, and the 1996/97 winter, see text for details [Borrmann et al., 2000].

December 1988 - March 2000

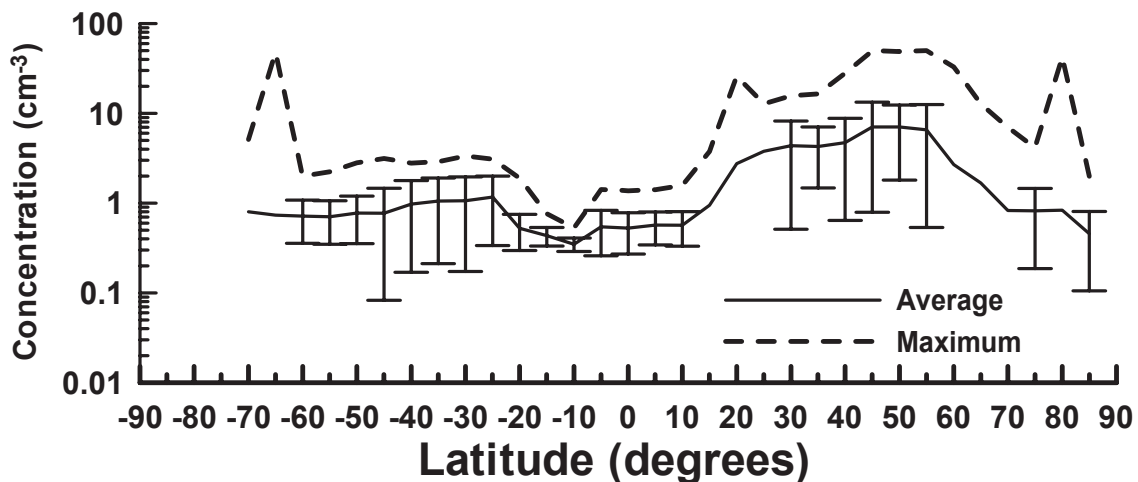


Figure 4.24: Particle number density measurements made with the FSSP-300 and MASP in the altitude range from 17 – 20 km averaged in 5° intervals of latitude. The vertical bars are standard deviations about the average (solid line) and the dashed lines are the maxima.

FCAS and N-Mass

The Focused Cavity Aerosol Spectrometer (FCAS), the Condensation Nucleus Counter (CNC), and the Nucleation-Mode Aerosol Sizing Spectrometer (N-MASS) measurements have been carried out in the upper troposphere and lower stratosphere during a number of recent missions, as shown in Table 4.1. The data set consists of 57,700, 30-second size dis-

tributions from 96 flights excluding the influence from 1991 Mt Pinatubo volcano eruption, rocket plumes and clouds.

Table 4.1 Mission Information (total flights: 96)

<i>Mission</i>	<i>Period</i>	<i>Latitudes</i>	<i>Pressure Altitudes (Km)</i>
STRAT	May, Oct 1995 & Jan, Feb Jun- Sep, Dec, 1996	2.2S - 60.2N	7.2 – 21.0
POLARIS	Apr – July 1997	3.4S – 89.9N	7.2 – 21.2
WAM	Apr, May 1998	9.5N – 45.9N	7.8 – 19.7
ACCENT	Apr, Sep, Oct 1999	5.0N – 39.2N	7.8 – 19.3
SOLVE	Jan – May 2000	42.4N – 89.1N	2.1 – 20.9

The FCAS heats particles to nearly 30 °C prior to measurement and drives much of the water off of sulfuric acid-water particles. The dry aerosol volume is calculated from these measurements and expressed as mass mixing ratio of sulfate in air. Sulfate dominates the composition of particles ($d > 200$ nm) at more than ~ 10 K (potential temperature) above the tropopause [Murphy et al., 1998]. The mass mixing ratio of sulfate increases with altitude above the tropopause. As air ascends in this region, sulfur precursor gases are converted to sulfuric acid that deposits on the preexisting aerosol. Values for sulfate mixing ratios range from 0.5 to 3 ppbm above (but near) the tropopause.

At high latitudes, two different particle sources were observed: new particles formed in the troposphere, and in aged, descending air. During the SOLVE mission, a few thousand particles/mg air were observed in the diameter range from 4-8 nm at 10-13 km altitude (Figure 4.25). This new particle formation may be due to the Hekla eruption that occurred during the mission and other pollution sources which enhanced background SO₂ concentrations. Also, during SOLVE, particles of similar size in the mid-latitude troposphere at higher number concentrations were observed (not shown).

Mixing ratios of particles having diameters less than 180 nm were clearly enhanced in descending air having low N₂O (Figure 4.26). (The air with the lowest N₂O mixing ratio is assumed to have descended from the highest altitude.) Previous CNC measurements in Antarctica during AAOE showed that descending air in the polar region is the source of particles. The present measurements show that by the time the air reached ER-2 altitudes (~ 20 km and below), most of the added particles were in the 30 to 180 nm diameter range (Figure 4.26).

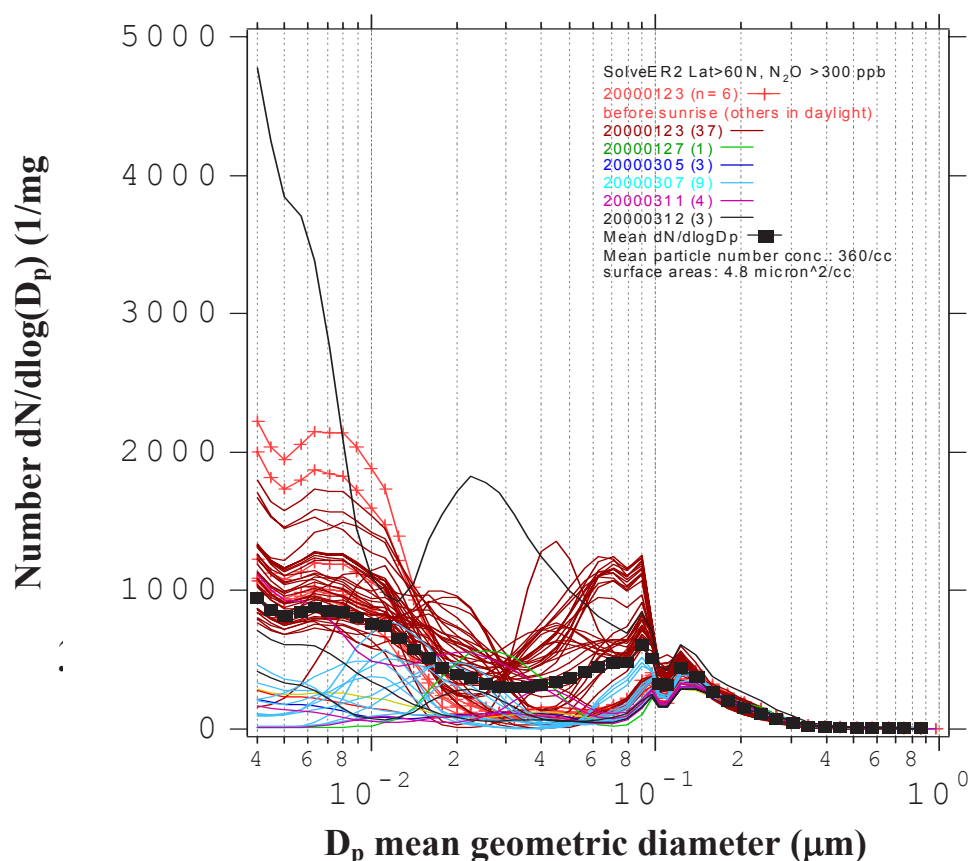


Figure 4.25 Number size distribution in the high latitude troposphere ($N_2O > 0.3$ ppmv). Fewer particles in diameter range from 4-8 nm were seen at high latitudes than at mid and low latitudes. The new particle formation might have been promoted by the Hekla volcanic plume or other pollution sources.

4.3 Retrieved Products

In this section we present some retrieved (or derived) products from the various measurements described above. These are generally the products of interest to modelers, namely, number density, surface area and effective radius of the aerosol particles.

4.3.1 Retrieved Products from Global Long-term Measurements

Retrieved products from SAM II, SAGE, and SAGE II

Routinely retrieved aerosol products for the SAGE series of instruments are limited in scope. Currently, no products beyond aerosol extinction are stored in the SAM II or SAGE data files. Operational SAGE II products report estimates of aerosol surface area density (SAD) and effective radius (r_{eff} , defined as three times the ratio of volume density to surface area density). The calculation of r_{eff} was first based on the method of Thomason et al. [1997b], using principal component analysis to derive SAD and total aerosol volume density from a linear combination of the four aerosol extinction measurements where the coefficients are selected to move the weight of the retrieval to the more reliable long wavelength channels. This relationship for SAD has been simplified for implementation in the operational software using an empirical fit based on the 525 to 1020-nm extinction ratio, r ,

and the absolute 1020-nm aerosol extinction that captures approximately 90% of the variance of the original. It is given as

$$SAD = k_{1020} \left(\frac{1854.97 + 90.137 * r + 66.97 * r * r}{1. - 0.1745 * r + 0.00858 * r * r} \right) \quad (4.1)$$

This has the advantage of being a considerably faster calculation and avoids the use of the shortest wavelength channels that are much noisier than the two channels retained in the calculation.

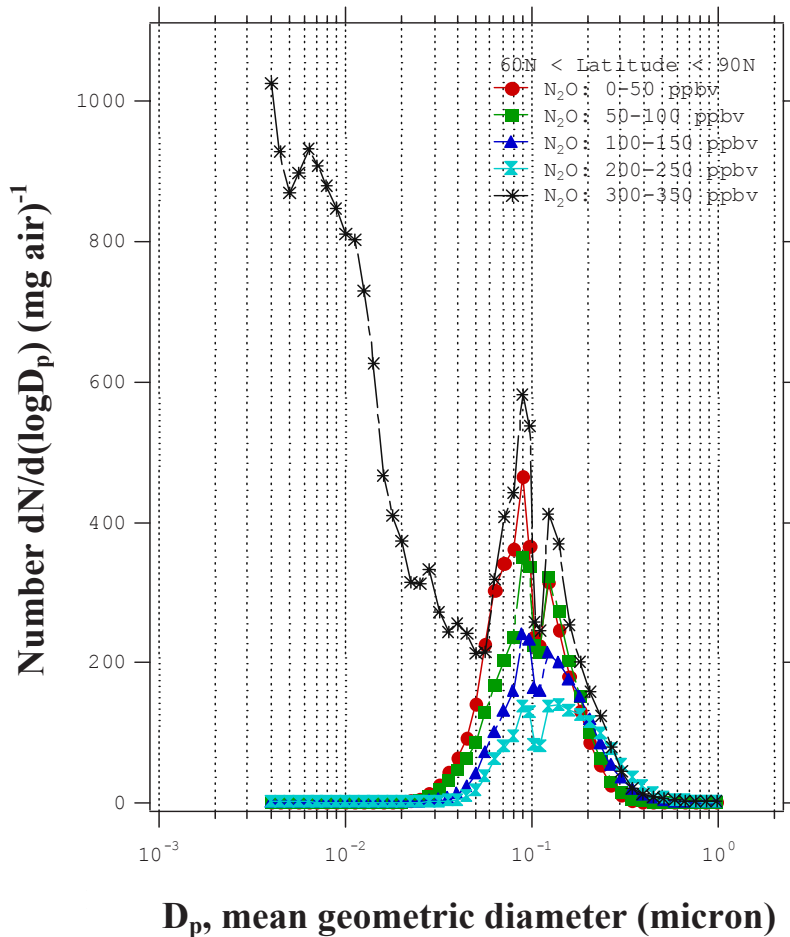


Figure 4.26 Particle number distribution at high latitude as a function of N_2O mixing ratios. The smallest particles ($<0.01 \mu m$) are seen in the tropospheric measurements. The air with lowest N_2O has descended most and has the most added particles amongst the stratospheric air parcels. They appear in the 0.03 to $0.18 \mu m$ diameter range.

The SAGE II SAD data product for January 1994 is shown in Figure 4.27. A number of techniques including fitting to model size distributions like the log-normal, constrained linear inversion, and linear error minimization have been employed to infer either the aerosol size distribution or aerosol bulk properties [e.g., Wang et al., 1989; Lin et al., 1992; Steele and Turco, 1997; Yue, 1999]. While these techniques can be quite different in mathematical expression, they tend to yield values for higher moments (such as SAD) that are within realistic uncertainty bounds of the retrievals (15-30%).

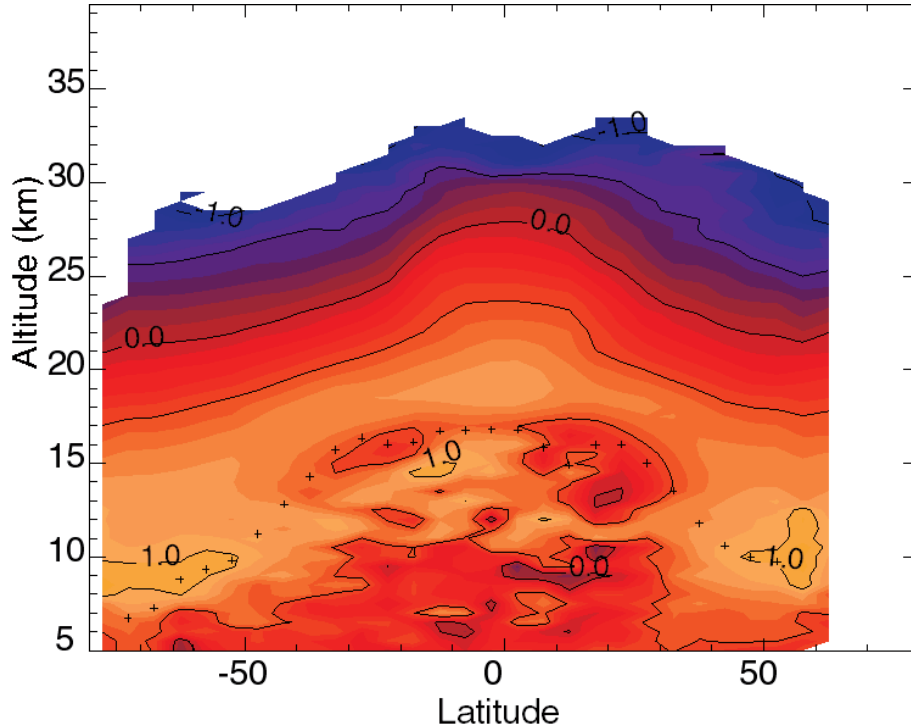


Figure 4.27: Aerosol surface area density in units of $\mu\text{m}^2\text{cm}^{-3}$ (shown as \log_{10} SAD) estimated from SAGE II aerosol extinction measurements for January 1994. Crosses indicate the average tropopause.

The efficacy of any technique for retrieving aerosol attributes is limited by the kernels of the integral equation from which extinction is derived. The Mie expression for the computation of the extinction by a distribution of spherical aerosol particles is given by

$$k_{\lambda} = \int \frac{3Q_{\lambda}(r)}{4r} \frac{d\nu(r)}{dr} dr \quad (4.2)$$

where λ is wavelength, r is radius, $Q_{\lambda}(r)$ is the Mie extinction efficiency factor at this wavelength, and $d\nu(r)/dr$ is the differential volume density of aerosol between r and $r + dr$. For SAGE II, these kernels are shown in Figure 4.28. The refractive indices used were from Palmer and Williams [1975]. The plots demonstrate several important features of any effort to extract either the underlying aerosol distribution or bulk properties thereof. The four channels provide some coarse size discrimination capabilities for aerosol between 0.1 and 0.6 μm , but little sensitivity to aerosol below 0.05 μm and little size discrimination for aerosol larger than 0.8 μm . As a result, for properties such as total particle number or mean radius that are highly dependent on the number of small particles, retrievals are very sensitive to the model used in the retrieval algorithm. Even higher order moments like surface area density or volume density (or mass) can be significantly dependent on model assumptions regarding effectively invisible small aerosol particles during low aerosol loading periods (when the aerosol particles are fewer and also typically smaller than during higher loading periods). Since the operational retrieval model puts little material in this ‘blind spot’, it is possible that values reported in these conditions significantly underestimate SAD, slightly underestimate the volume density, and concomitantly overestimate the value of r_{eff} . The scope of the problem remains unclear. Because of the difficulty in deriving physically

meaningful values for low order moments, aerosol number density and mean radius are not a part of the SAGE II operational product. These quantities have, however, been estimated by other investigators, including Bingen et al. [2004a, 2004b] and Bauman et al. [2003a, 2003b].

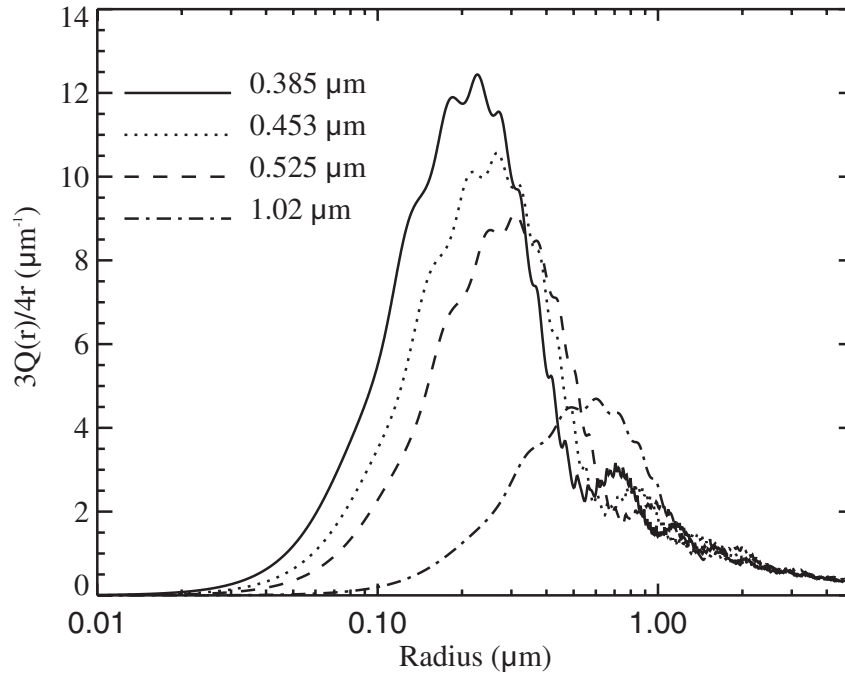


Figure 4.28: Mie scattering kernels for the four SAGE II aerosol extinction channels.

Since SAM II is a single channel instrument at 1000 nm and SAGE has its most reliable aerosol channel also at 1000 nm, no operational version of SAD or r_{eff} is routinely produced from either data set. However, Thomason et al. [1997b] presented a simple relationship for converting from 1000-nm aerosol extinction to SAD. The standard deviation of SAD using this relationship relative to the four channel method (applied to SAGE) is about 30% for extinctions larger than 10^{-4} km^{-1} . Solomon et al. [1996] found good agreement between this relationship and SAD from the University of Wyoming Optical Particle Counter. The technique is based on a regression between the two parameters that is allowed under most circumstances by the well-behaved relationship between SAGE II 1020-nm aerosol extinction and the SAD derived using four channels. This relationship is expressed as

$$SAD = s = \begin{cases} 425 \times k^{0.68} & k < 4 \times 10^{-3} \\ 1223 \times k^{0.875} & 4 \times 10^{-3} < k < 2 \times 10^{-2} \\ 2000 \times k & 2 \times 10^{-2} < k \end{cases} \quad (4.3)$$

where k is the 1000-nm aerosol extinction in units of km^{-1} and surface area density is produced in units of $\mu\text{m}^2 \text{cm}^{-3}$. This relationship is based upon the observation that under most circumstances the wavelength dependence of aerosol extinction (as expressed in the 525 to 1020-nm aerosol extinction ratio) is nearly constant for a given aerosol extinction [Thomason and Osborn, 1992]. The only significant deviation from a tidy relationship was ob-

served in the lower stratosphere in the northern hemisphere in the first few months following the eruption of Mt. Pinatubo in 1991. This deviation was the result of injection of large amounts of small aerosol that created an unusual situation where large extinction occurred in conjunction with small aerosol size. As a result, it is possible that the use of this model during similar periods (e.g., Mt. St. Helens or El Chichón) may result in a similar transient period with large errors in the estimation of SAD.

For the purposes of this assessment and the creation of the most complete possible long-term aerosol climatology, an additional function has been derived for the computation of aerosol effective radius from 1000-nm aerosol extinction using the same procedure used to derive Equation 4.2. Four-channel retrieved values for r_{eff} versus 1020-nm aerosol extinction are shown in Figure 4.29 for January 1994 to June 1994. As with SAD, this relationship varies little with time and can be expressed in analytic form as

$$r_{\text{eff}} = \begin{cases} 0.0303 \times [\ln(k) + 11.513] + 0.16 & 1 \times 10^{-5} < k < 3.0 \times 10^{-4} \\ 0.15 \times \exp(0.04916 \times [\ln(k) + 11.513]^2) & 3.0 \times 10^{-4} < k < 1.8 \times 10^{-3} \\ 0.55 & 1.8 \times 10^{-3} < k \end{cases} \quad (4.4)$$

where k is the 1000-nm aerosol extinction in units of km^{-1} and the effective radius is produced in units of μm . The standard deviation from this relationship is about $0.05 \mu\text{m}$ but, unlike SAD, there are substantial outliers during all periods and, as a result, this relationship should be viewed and applied cautiously. The use of these equations with the SAM II and SAGE data sets yields estimates of SAD and r_{eff} that are generally consistent with those data sets, but they also inherit the limitations associated with the data.

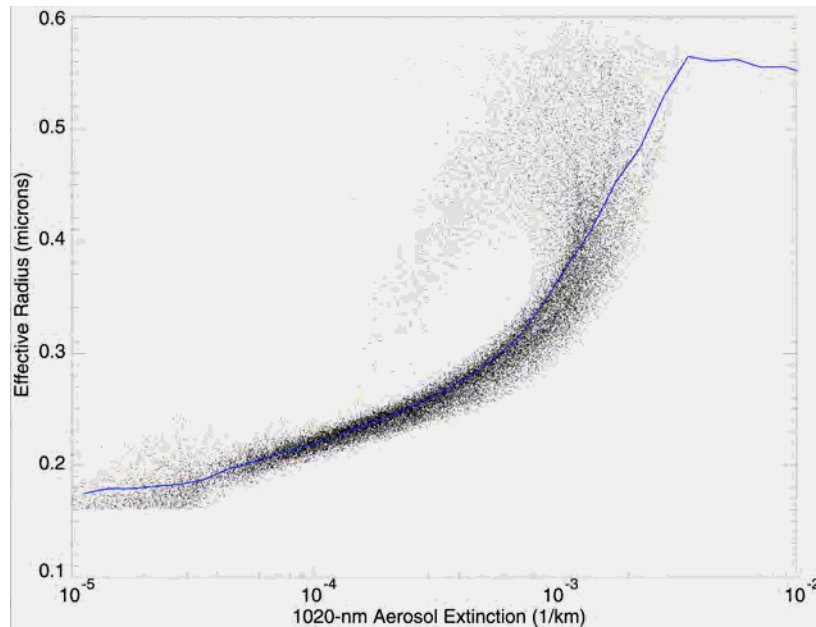


Figure 4.29: A depiction of the correlation of SAGE II 1020-nm aerosol extinction and aerosol effective radius derived from the multi-wavelength aerosol extinction measurements. The blue line shows the median fit through these data.

Figure 4.29 demonstrates that in general there is a good correlation between the two parameters but that there is also a substantial spread in the relationship. The median is used

rather than the mean because the mean or average value can be biased towards outliers (that is, the clouds). The median filter used is applied in steps of $1/10^{\text{th}}$ of a log cycle and eliminates the effects of clouds missed by the cloud filter.

Cloud Clearing with SAGE data. Clouds are a ubiquitous feature of SAGE and solar occultation data. They are observed most often in the troposphere where they often are responsible for terminating an occultation measurement, but are also seen in the stratosphere both as polar stratospheric clouds (PSCs) and possibly as thin cirrus clouds occurring near the tropopause. Clouds can simply terminate a specific observational event (extinction going off scale) or appear in the data as non-opaque features with cloud-like spectral features. These clouds are sometimes referred to as sub-visual clouds with the expectation that they are thin sheet-like cirrus clouds invisible to nadir-viewing instruments. However, this interpretation has not been rigorously tested and the geometry of occultation measurements is sufficiently complex that this interpretation is arguable [Kent et al., 1997b]. For the purposes of this aerosol assessment in which cloud contaminated data were removed, clouds in the SAGE II data set were identified using the technique developed by Kent et al. [1997a] in which aerosols and clouds are distinguished by the ratio of extinction at 525 and 1020 nm. Under most circumstances, the 525 to 1020-nm aerosol extinction ratio for aerosols is greater than two, indicating that stratospheric aerosol extinction is dominated by particles less than 0.3 or 0.4 μm . Cloud particles, with the exception of Type I PSCs, are considerably larger and exhibit an extinction ratio close to one. Thus, the technique identifies clouds based on the magnitude of extinction and the extinction ratio. An example of the partitioning between cloud and aerosol is shown in Figure 4.30 for March through May 1999. For most of the record, this technique works well and there is little obvious leakage of clouds into the aerosol data set. However, during the few years following the Pinatubo eruption, aerosol extinction ratios were close to one and cloud identification is not possible between June 1991 and the end of 1993. Toward the end of this period there is evidence that some cloud events (seen as enhanced extinction) remain in the aerosol data set. These events are relatively rare and their impact was to a great extent mitigated by the use of median filters in the creation of the ASAP SAGE data files. Figure 4.31 shows the frequency of clouds within 3 km below the tropopause between 1985 and 1989. Not surprisingly this figure is very similar to Figure 3.2 (penetration frequency) with a noteworthy maximum in the tropics and minima in the subtropics. Generally, there is no strong longitudinal dependency in cloud occurrences except in the tropics where there is a maximum over the Indonesian warm pool. It is probably worth noting that the zonal parameters in the SAGE data files are, as a result, weighted to longitudes away from this region.

Base Data Files and Filling Data Gaps. While the SAGE series of instruments have produced almost 300,000 solar occultation events over the previous 25 years, there are substantial and climatically important periods in which the data are either incomplete (due to saturation by volcanic aerosols) or missing entirely. Unfortunately a major volcanic event (El Chichón) occurred during the SAGE-SAGE II gap, and a gap in data occurred following the second major volcanic event (Pinatubo). To facilitate long-term climate modeling, we have produced a complete, nearly gap free, data set using SAM II data and a variety of lidar data sets to fill gaps in the El Chichón period (1982-1984) and post-Pinatubo period (1991-1993). Discrepancies of up to 4% resulting from wavelength differences between SAM II (1000 nm) and SAGE II (1020 nm) extinctions are ignored. The sources of data used to fill the Mt. Pinatubo and El Chichón data gaps are presented in Table 4.2.

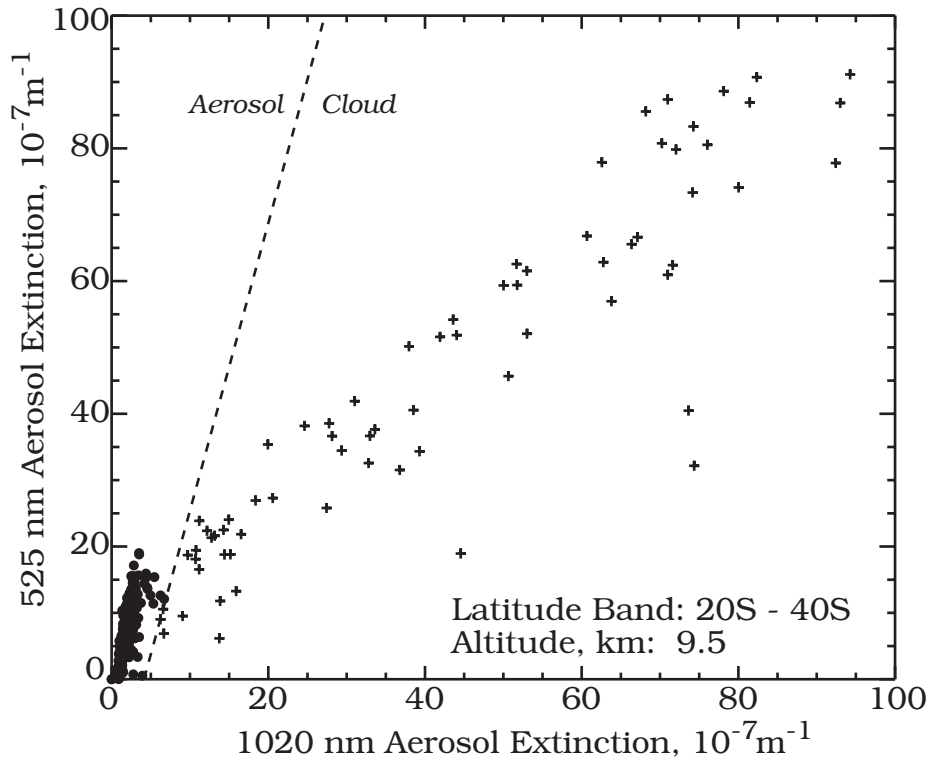


Figure 4.30: A demonstration of the two-wavelength cloud identification method of Kent et al. [1997b]. High extinction but small extinction ratio pairs (right of the dashed line) are considered cloud and, for this application, excluded from the analysis.

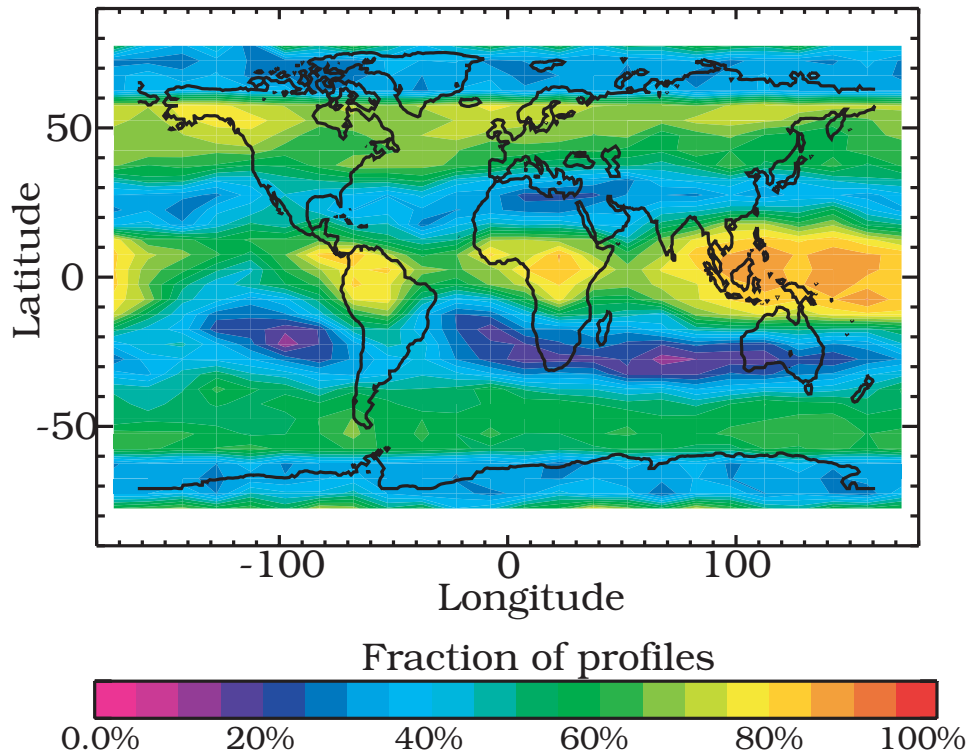


Figure 4.31: The fraction of events for which a cloud has been identified at or above the tropopause - 3km for 1985 through 1989.

Table 4.2: Sources of data used to fill the El Chichón and Mt. Pinatubo data gaps.

<i>Time Period</i>	<i>Zone</i>	<i>Fill Source</i>
1982-1984	North polar	SAM II
	North mid-latitudes	Langley 48-inch lidar
	Tropics	NASA airborne lidar
	South mid-latitudes	SAM II
	South high latitudes	SAM II
1991-1994	North mid and high latitudes	Langley 48-inch lidar
	Tropics	Composite of the Mauna Loa and Camaguey lidars
	South mid and high latitudes	Backscatter sondes (Lauder, New Zealand)

The data analyses produces the aerosol extinction at one or more wavelengths, as well as SAD and r_{eff} in 0.5 km (SAGE II) or 1-km (SAGE) monthly 5-degree latitude bins. Since the latitude for SAM II observations changes slowly with time, SAM II is reported at a mean latitude for each event type (sunrise and sunset) in 1-km, monthly bins. The base data files, referred to as non-interpolated, contained values only in months in which observations occur. These files are most suitable for comparing with other data sets such as the HALOE data. Individual values are not true monthly medians but rather are median values for observations occurring within that month. The observations may occur over several days anytime within the month including non-contiguous periods. The mean day of observations is included in the data files.

Due to the sampling characteristic of solar occultation, for any given month many latitudes are not sampled during the month. To fill these ubiquitous data gaps, a second set of files is created where the sampling window has been increased to 10 degrees of latitude (still reported every 5 degrees) and fit temporally with a spline (but not in altitude or latitude). The resulting fit is used to fill missing values whenever observations occur within 1.5 months. This eliminates almost all sampling related gaps except at high latitudes in winter, during the mechanical downtime episode (July-December 2000), at low altitudes during post Pinatubo saturation, and in the gap between SAGE and SAGE II (1982-1984). Interpolated values in these files are denoted with uncertainties of -1.

Pinatubo Gap Filling. Between the June 1991 eruption of Mount Pinatubo and the end of 1993 substantial parts of the SAGE II interpolated files are missing due to the saturation effect. Aerosol backscatter profile measurements from lidar sites at Camaguey (Cuba), Mauna Loa, Hawaii (USA), and Hampton, Virginia (USA) and backscatter sonde measurements from Lauder, New Zealand were used to fill the missing values. The most critical area to fill is the tropics between 15°S and 15°N. Unfortunately, only a few scattered lidar observations are available in these latitudes. The stations in Cuba and Hawaii, while close to the tropics, are best considered sub-tropical stations and their individual records show that they periodically underlie both the tropical pipe (where the Pinatubo aerosol was concentrated) and air more typical of the mid-latitudes. To synthesize a tropical record from these two data sets, a 3-month window was used from which the maximum value at each altitude was selected assuming that the largest values were most representative of the aerosol within the tropical pipe. The backscatter was converted to 1020-nm aerosol extinction using the method of Antuña et al. [2003]. A comparison of this composite data file with SAGE II observations between 0 and 5°N is shown in Figure 4.32. In regions where the

two records overlap, the comparison, while not perfect, is generally favorable and gives at least modest confidence that the composite lidar record can be used to fill missing tropical SAGE II data.

For northern latitudes, the NASA Langley 48-inch lidar record converted to 1020 nm aerosol extinction was used (as in Antuña et al. [2003]). The comparison of SAGE II and this record is shown in Figure 4.33 and is also favorable though perhaps not as good as the tropical comparison. Particularly after the eruption, the mid-latitudes are not zonally homogeneous and it is not surprising that this comparison is less robust. It is possible that averaging data from a number of sites would improve this model. In southern latitudes, the backscatter sonde data from Lauder, New Zealand was used after conversion to 1020 nm aerosol extinction following the method recommended by the instrument principal investigator (James Rosen, personal communication). Like the northern hemisphere, the comparison of the data (not shown) is broadly favorable though with a broader scatter than is found for the tropical data record.

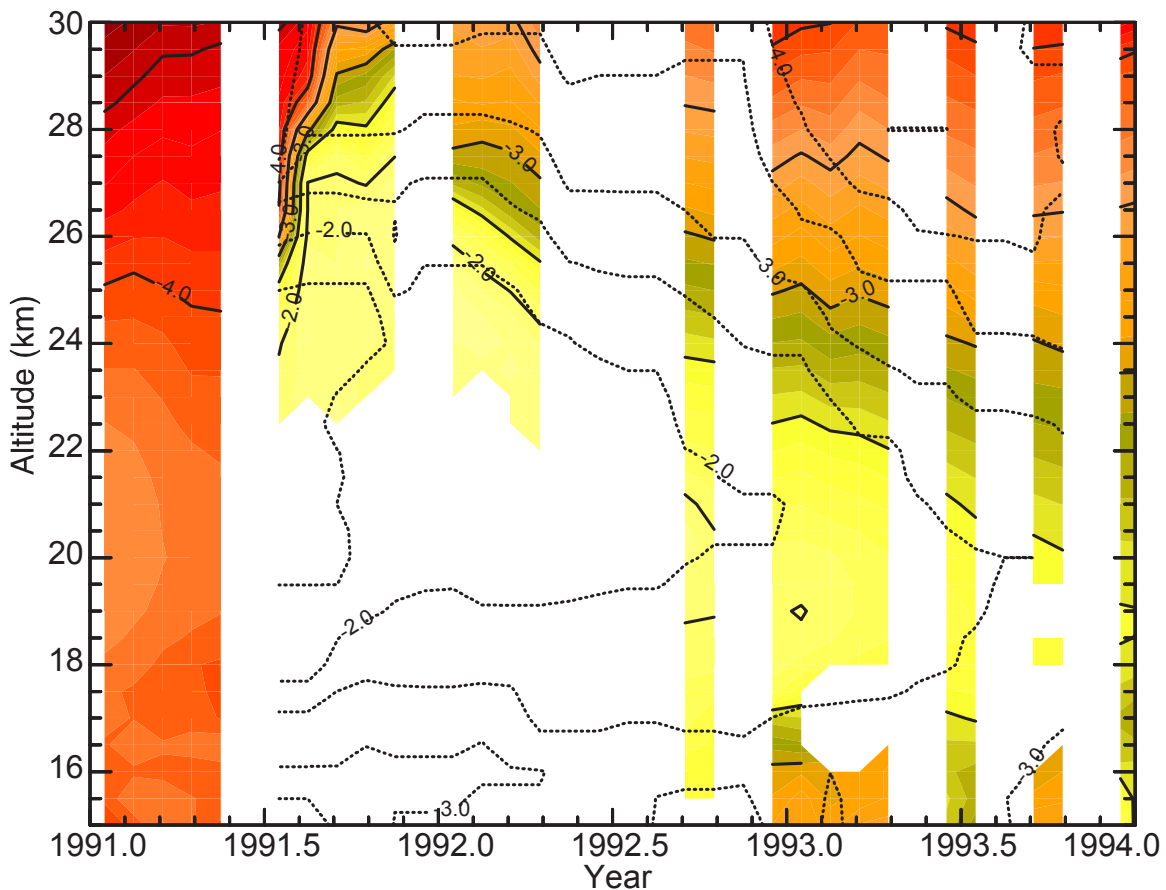


Figure 4.32: A comparison of the SAGE II aerosol extinction between 0 and 5°N (color contours and solid lines) and the composite Camaguey/Mauna Loa lidar based record (dotted lines), which has been used for filling the observational gaps in the SAGE II record in the tropics. Contour labels give \log_{10} extinction (in km^{-1}).

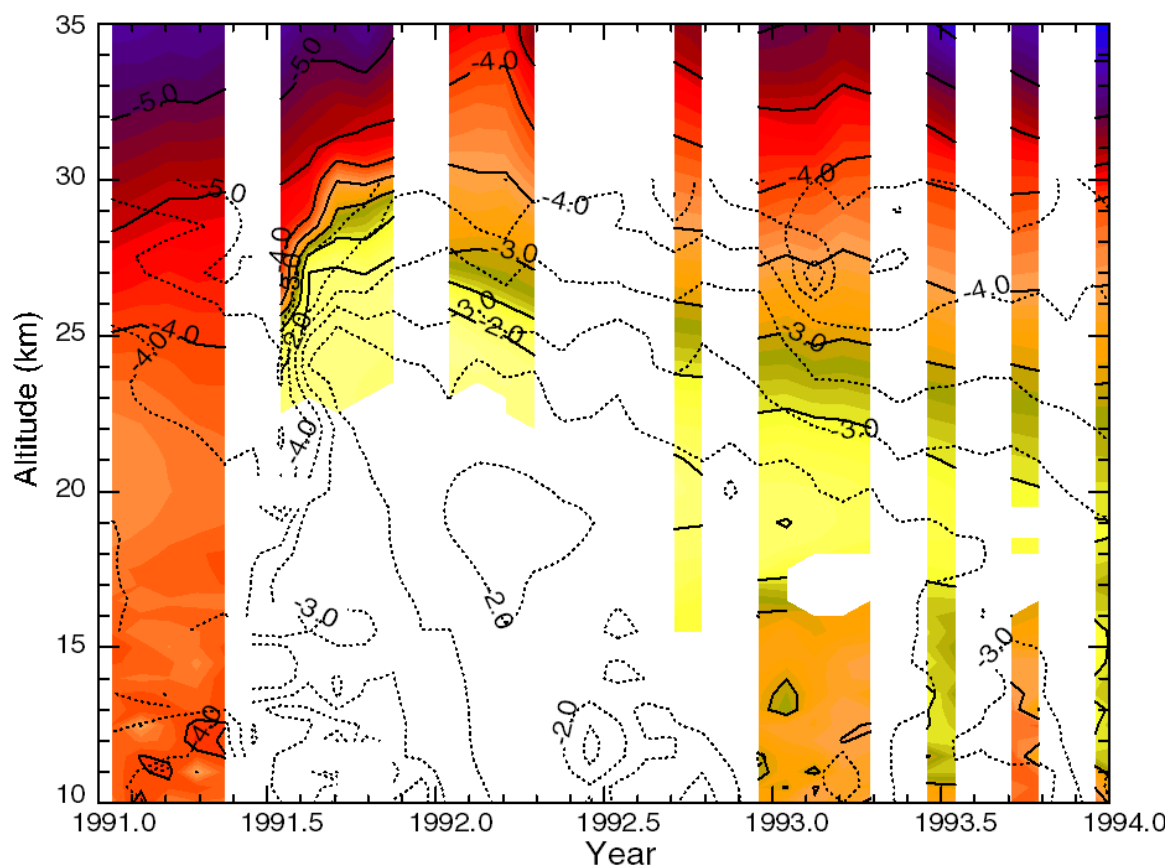


Figure 4.33: A comparison of the SAGE II aerosol extinction between 35 and 40°N (color contours and solid lines) and the NASA Langley 48-inch lidar based record (dotted lines) which has been used for filling the observational gaps in the SAGE II record in the northern mid-latitudes.

These three temporal records are used to fill missing values in the SAGE II interpolated record for 1020-nm aerosol extinction, the tropical record for latitudes between 15°S and 15°N, the northern record for 25°N to 80°N, and the southern record for 25°S to 80°S. The subtropics are filled using a linear interpolation of the mid-latitude and tropical records. The mid-latitude records are shifted in altitude as a function of latitude following zonally-averaged potential temperature surfaces. Estimates for SAD and r_{eff} are produced using Equations 4.3 and 4.4. In the archived ‘filled’ versions of these data files interpolated and filled values are denoted by the use of -1 in the measurement uncertainty values.

El Chichón Gap Filling. Between November 1981 and October 1984, global space-based aerosol extinction profile measurements were not available. This period encompassed the El Chichón eruption and the onset of the Antarctic ozone hole and is, therefore, of particular interest. The last full month of SAGE data (November 1981) was used for December through March 1982. Beginning in April 1982 and through the beginning of SAGE II observations in 1984, a composite of data consisting of SAM II, the NASA Langley 48-inch lidar system, and lidar data from the NASA Langley Airborne Lidar System was used to produce a complete 1-km by 5-degree by month grid. The NASA Langley Airborne Lidar System made five flights between July 1982 and January 1984 of which three flights entered the tropics and two extended into the southern hemisphere; a description is given in Chapter 3 (The NASA Langley Airborne Lidar System). In this case, only SAM II events that have been tagged as outside the polar vortices using the method developed by M. Fromm were used [e.g., Bevilacqua et al., 2002].

In the northern hemisphere, the 1000-nm extinction record is filled with SAM II data between 80°N and 65°N. From 65°N to 40°N, a linear interpolation in latitude of the logarithm of extinction between the SAM II data and 1000-nm aerosol extinction derived from the NASA Langley 48-inch lidar system were used. From 40°N to 25°N, the 48-inch lidar is used. From 25°S to 80°S, the entire record is filled (by hemisphere) using SAM II data shifted in altitude as a function of latitude following zonally averaged potential temperature surfaces. From April 1982 to September 1984, a composite of profiles is used to create an effective tropical El Chichón record. For April through July, the southernmost (13°N) airborne lidar profile July 1982 was used. Following that period a linear interpolation in time of the logarithm of 1000-nm aerosol extinction estimated from lidar profiles (using a ruby backscatter to 1000-nm extinction ratio of 30) in July 1982 (4.1°S) and May 1983 (0°) and the SAGE II tropical data in October 1984 was used. This synthetic record is shown in Figure 4.34. As with the Pinatubo gap filling process, the subtropics (25 to 15°) are filled using a linear interpolation of the mid-latitude and tropical records. Estimates for SAD and r_{eff} are produced using Equations 4.3 and 4.4.

As an example of the end result of the gap-filling process, Figure 4.35 depicts the 1000-nm stratospheric aerosol optical depth (shown unfilled in Figure 4.4) in which the procedures described above have been used to produce a gapless record. In generating Figures 4.34 and 4.35 no correction was applied for differences between 1020 nm and 1000 nm extinctions.

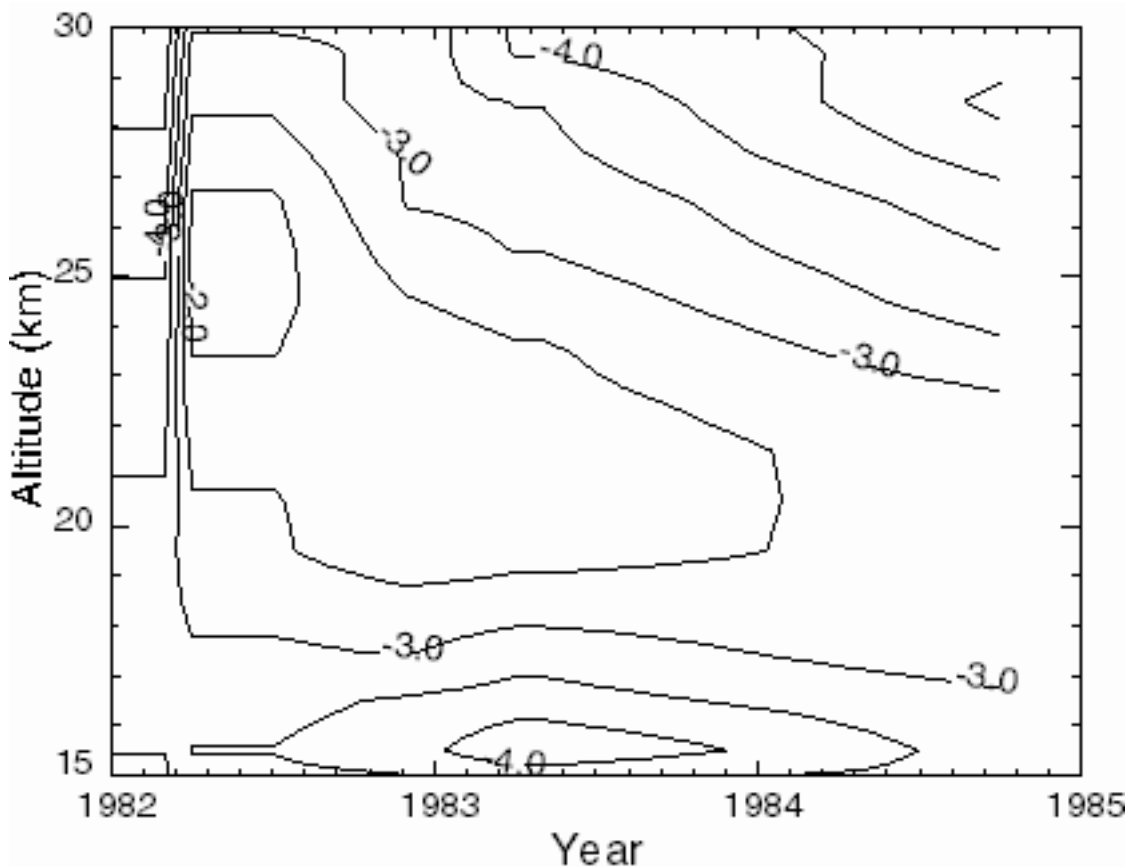


Figure 4.34: Tropical 1000-nm aerosol extinction (shown as \log_{10} of aerosol extinction) spanning the SAGE/SAGE II gap. It includes data from SAGE, SAGE II, and three flights by the NASA Langley Airborne Lidar System (July 1982, November 1982, and May 1983).

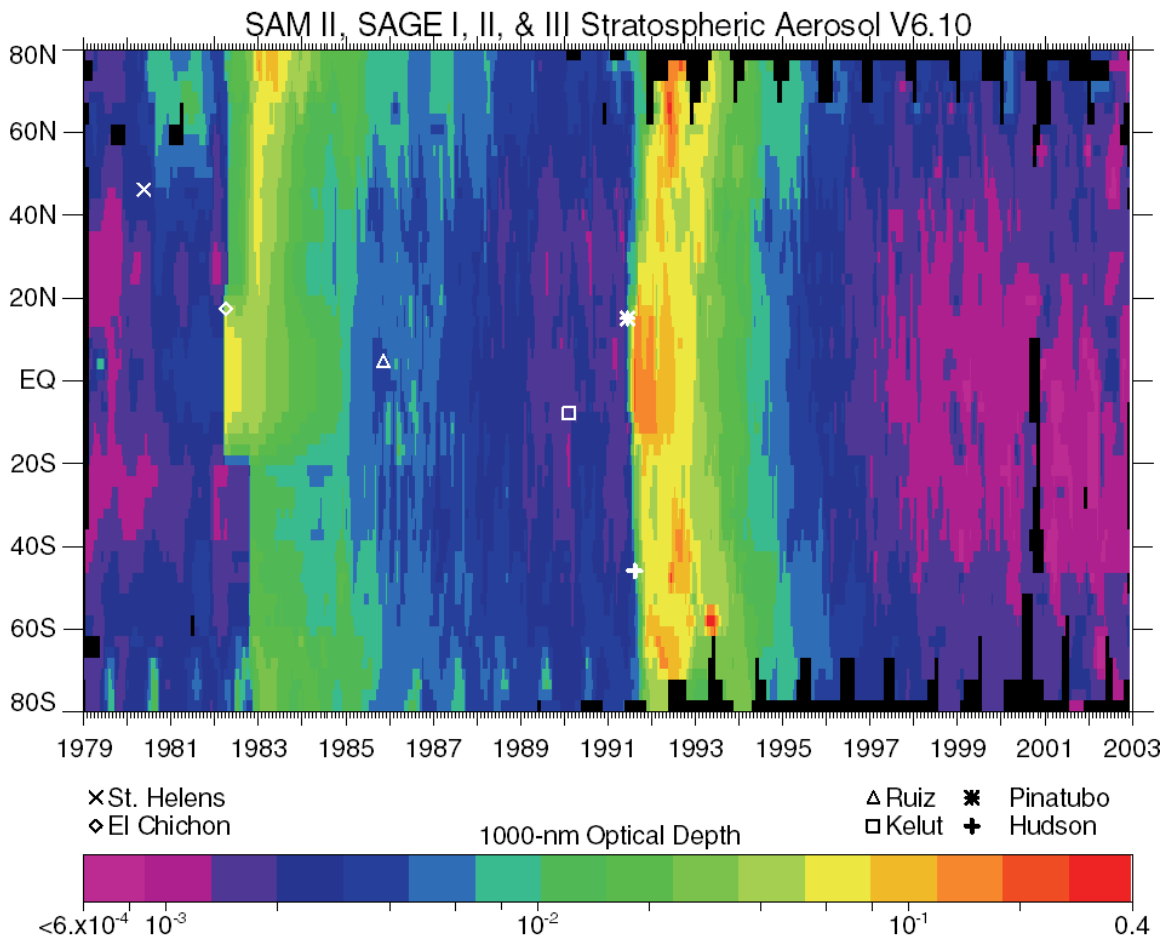


Figure 4.35: A 1000-nm aerosol optical depth record for 1979 through 2002 in which data gaps have been filled (see text).

The work described here has not exhausted available data sources. A more complete use of the airborne lidar data, particularly in the southern hemisphere would be helpful. Other data sets for northern mid-latitudes are also available and could be used to make at least the northern hemisphere depiction more realistic. In addition, the Solar Mesospheric Explorer (SME) used limb scattering to measure ozone, NO_2 and other species and has also produced aerosol measurements that span this period. That data is undergoing a significant revision at this time (Cora Randall, personal communication) and has not been used in this data set.

Extinction Presented in Terms of Equivalent Latitude and Potential Temperature

One frequently presents the SAGE extinction in the usual format of extinction at a given altitude as a function of latitude. This section illustrates a different format for presenting the data which can be considered an aspect of data gap filling since it increases the coverage at high latitudes.

For long-lived atmospheric constituents, the calculation of zonal means can blur steep meridional gradients in constituent concentrations across transport barriers, e.g. the polar vortex edge. This problem becomes particularly acute when the concentration field is far from zonally symmetric. One approach to avoiding this problem is to regrid the data from the native latitude, longitude, altitude and time coordinate system to an equivalent latitude (ϕ_{eq}) [Nash et al., 1996], potential temperature (θ), and time (t) coordinate system before calcu-

lating zonal means. The equivalent latitude is a vortex-aligned coordinate system where 90° latitude is at the center of the vortex, that is, the highest absolute potential vorticity value in that hemisphere. Randel and Wu [1995] and Bodeker et al. [2001] have shown some of the advantages of regriding atmospheric constituent measurements to a (ϕ_{eq}, θ, t) coordinate system.

In Bodeker et al. [2001], version 6.1 SAGE II data (including O_3 , NO_2 , H_2O , aerosol extinction at 386, 452, 525 and 1020 nm, and their respective errors) were analyzed to this coordinate system for isentropic levels of 300, 315, 330, 350, 400, 450, 550 and 650 K, for the period October 1984 to June 2001. Individual solar occultation events (profiles) were extracted from the version 6.1 SAGE II data base. For each of the 8 isentropic levels listed above, the altitude was calculated by linear interpolation within a θ vs. altitude profile. The θ vs. altitude profile for a given occultation event consists of 140 pairs of altitude and θ values. The altitude was read directly from the SAGE II data record and θ was calculated from $T \times (1000./P)^{0.285572}$, where T and P are the NMC temperature and pressure, respectively, provided in the SAGE II data files. For a profile latitude, longitude and potential temperature, the associated PV value was extracted from NCEP/NCAR reanalyses PV fields using bilinear spatial interpolation and linear interpolation in time. The NCEP/NCAR reanalyses are available every 6 hours at $2.5^\circ \times 2.5^\circ$ resolution on each of the 8 isentropic surfaces used here. The equivalent latitude associated with this PV value is calculated from linear interpolation within an equivalent latitude vs. PV profile which in turn was calculated using the method described in Nash et al. [1996]. The equivalent latitude vs. PV profiles were calculated for every 6 hours and the profile closest in time was used. Concentrations for the constituents listed above were then calculated using linear interpolation within a constituent vs. potential temperature profile, which in turn was calculated in a manner identical to the altitude vs. potential temperature profile. An additional constraint that at least one of the levels used in this interpolation was within 10 K of the present isentropic level was imposed.

For ASAP, a similar procedure has been used to produce a complete analysis of SAGE aerosol data products on potential temperature surfaces from 375 to 1300 K in 25 K increments and are available on the ASAP web site. For this analysis, the potential temperature and equivalent latitude information came from auxiliary data files associated with version 6.2 SAGE II data files that were produced by Gloria Manney, JPL. In Figure 4.36a, the results of an analysis of 1020-nm extinction at 550 K is shown while a comparable altitude/latitude analysis (at 22 km) is shown in 4.36b. There are clearly discernable differences between panels (a) and (b), viz.: the data plotted by equivalent latitude extend to higher equivalent latitudes than the data plotted by true latitude, particularly in the Arctic; the data plotted by equivalent latitude show more clearly the exclusion of aerosols from the Antarctic vortex during the winter and spring; further the data plotted by equivalent latitude more clearly show the very low extinctions in the Arctic vortex each winter/spring.

It should be noted however that the transformation into the (ϕ_{eq}, θ, t) coordinate system is not mass conserving and no scaling of the data to conserve total aerosol mass has been made. Care should also be taken in the interpretation of these results at low latitudes. At low latitudes the potential vorticity does not act reliably as a tracer of isentropic transport and it is therefore less likely that contours of long-lived aerosols will be well aligned with those of potential vorticity. For these reasons the regriding to equivalent latitude is most advantageous poleward of $\sim 50^\circ$.

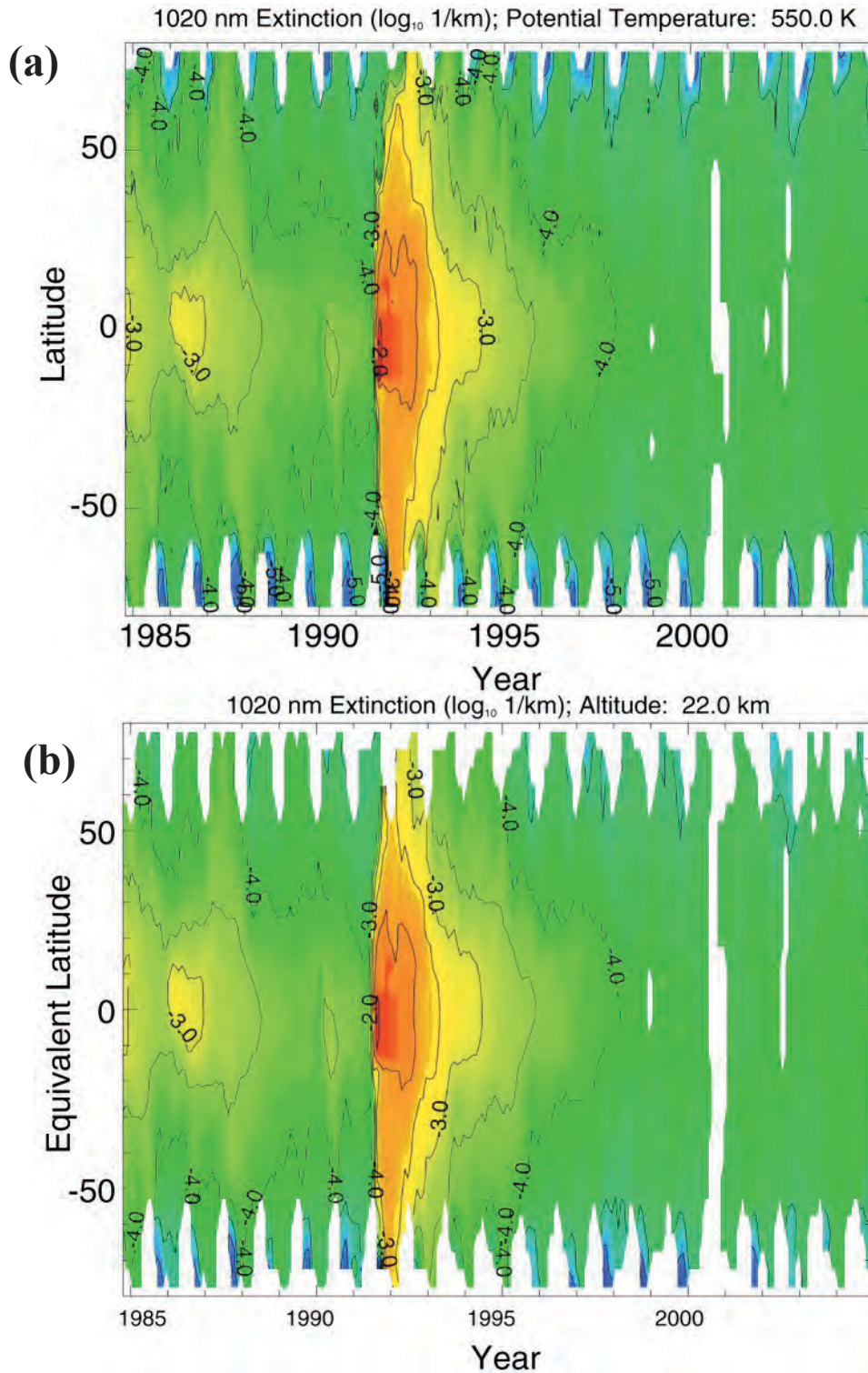


Figure 4.36: SAGE II aerosol extinction at 1020 nm, (a) on the 550 K potential temperature surface as a function of equivalent latitude and (b) at 22 km as a function of latitude.

Retrieved products from HALOE

HALOE measurements of stratospheric sulfate aerosols have been used to retrieve unimodal lognormal size distributions, as described in detail by Hervig *et al.* [1998]. The unimo-

dal lognormal size distribution describes concentration versus radius as a function of the total number concentration (N), distribution width (σ), and median radius (\bar{r}). Although the HALOE extinction spectrum alone cannot be used to reliably infer the aerosol size distribution (except when the aerosol population contains particles larger than about $0.5 \mu\text{m}$), the inverse problem is well-defined when the effective radius is known. Using theoretical relationships derived from *in situ* aerosol measurements, effective radii can be determined from the HALOE $2.45 \mu\text{m}$ extinctions with uncertainties of about $\pm 15\%$. Using extinction ratios with the effective radii determined from the HALOE extinctions, unimodal lognormal size distributions are retrieved from HALOE measurements. The HALOE size distributions are generally unbiased with respect to coincident *in situ* aerosol measurements. Error analysis reveals that uncertainties in the inferred surface areas and volumes are less than 30% and 15%, respectively.

Refractive indices of aqueous sulfuric acid solutions are fundamental to the size distribution retrievals, and the results reported in Hervig et al. [1998] were based on room temperature (300 K) indices [Palmer and Williams, 1975] adjusted to stratospheric temperatures according to the Lorentz-Lorenz relationship using sulfate densities from Luo et al. [1996]. Sulfate indices measured at a lower temperature (215 K) more relevant to the stratosphere were published by Tisdale et al. [1998]. A comparison of the Tisdale et al. indices to the Palmer and Williams room temperature indices, adjusted to 215 K, shows notable differences. Thus, the Tisdale et al. indices were used to recalculate the HALOE aerosol size distributions for this work. Hervig et al. [1998] compared profiles of HALOE unimodal size distributions and surface areas to OPCs over Laramie for 17 coincidences during 1991 to 1996. That work used HALOE size distributions based on the Palmer and Williams [1975] sulfate refractive indices, and showed that the HALOE surface areas were from 10 to 30% higher than the OPC values. HALOE size distributions based on cold temperature refractive indices [Tisdale et al., 1998] result in $\sim 25\%$ less surface area than the previous results. Note that HALOE aerosol size distributions currently available on the HALOE web site are based on the Palmer and Williams refractive indices adjusted to stratospheric temperatures. Aerosol size distributions were only retrieved in the absence of clouds. Cloud identification in HALOE data is described in Section 3.2.2.

The complete record of HALOE aerosol size distributions is available on the internet: http://gwest.gats-inc.com/haloe_aerosols/HALOE_size_distribution_data.html. This archive reports retrievals based on the Tisdale et al. [1998] refractive indices and HALOE V19 extinctions. Examples of aerosol size distribution parameters (concentration, median radius, and distribution width) and size distribution moments (surface area, volume, and effective radius) retrieved from HALOE are shown in Figure 4.37 as time – height cross sections near the equator. The aerosol size distribution is noticeably perturbed when Pinatubo aerosols are present, showing larger median radii and narrower distribution widths. This pattern gives way to broader distributions of smaller particles as time progresses. The aerosol concentration remains fairly stable throughout the time period, at roughly 10 cm^{-3} at altitudes above 19 km. These characteristics are consistent with *in situ* aerosol size distribution measurements from the University of Wyoming. The aerosol surface area and volume are dramatically higher during the Pinatubo period compared to the late 1990s, and suggest that a near steady state was reached after 1997. A complete set of such plots can found on the web site.

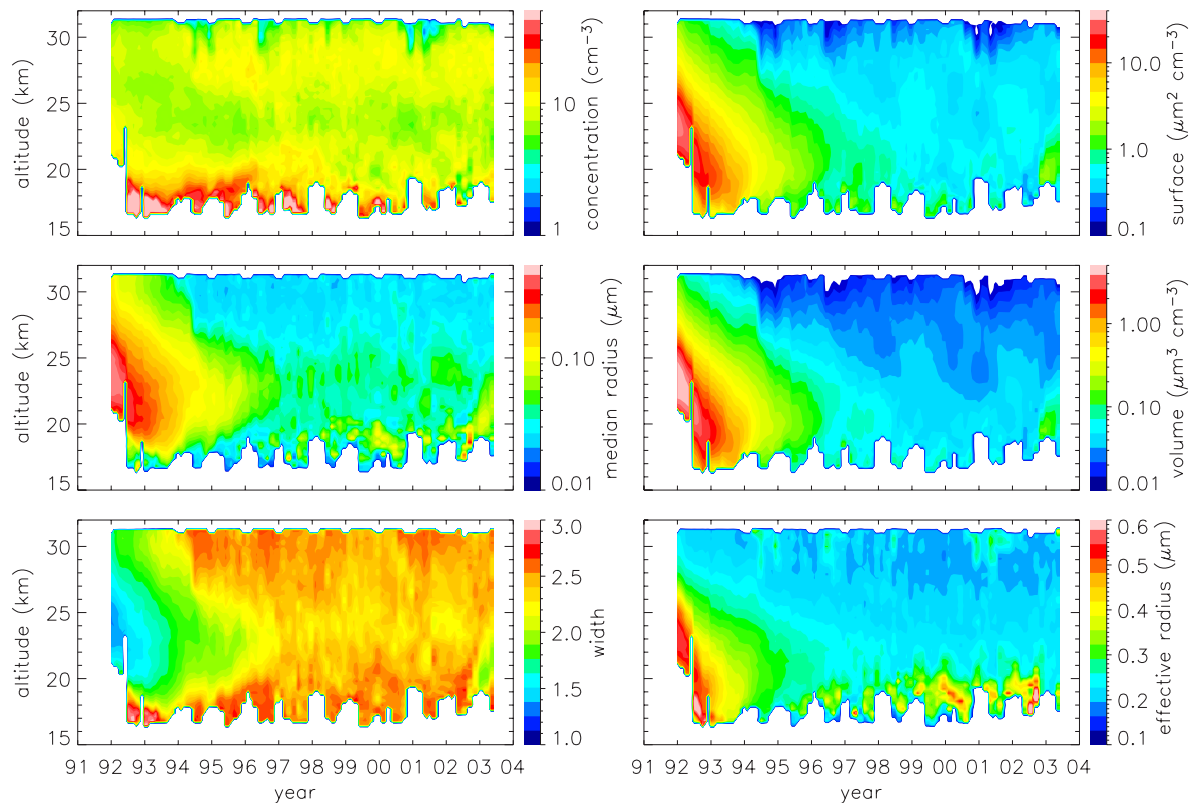


Figure 4.37: Time – height cross sections of aerosol size distribution parameters and size distribution moments retrieved from HALOE. The data are averages for 0° – 5° N latitude and are presented at the native vertical sampling interval of 0.3 km. Data identified as cirrus were removed.

Retrieved products from POAM II, POAM III

Aerosol surface area and volume densities have been calculated (Figures 4.38 and 4.39), from both POAM II and POAM III retrieved aerosol extinction using the principal component analysis (PCA) technique [Steele et al., 1999]. In this approach the aerosol surface area and volume are parameterized as a linear combination of the aerosol extinction in the five POAM aerosol channels. The PCA coefficients, which multiply the aerosol extinction values, are wavelength dependent, but time invariant. The random error in the POAM surface area and volume density retrievals is about 8-15% in the stratosphere for background aerosol conditions [Steele et al., 2003]. To evaluate the bias in the POAM PCA surface area and volume retrievals (as well as that obtained using the same technique with the SAGE II aerosol extinction measurements), Steele et al. [1999] used measurement simulations performed with realistic background aerosol size distributions. The results suggest that POAM surface area and volume retrievals are biased low relative to the true values. The measured aerosol extinction at POAM wavelengths, which is assumed to be due entirely to scattering (not absorption), has low sensitivity to particles with radius $\lesssim 0.1 \mu\text{m}$, although particles in this size range may make a significant contribution especially to the surface area [Randall et al., 2001, Deshler et al., 2003]. The amount of the underestimate is dependent upon the specific size distribution parameters. Average biases were predicted to be around -10% and -5% for surface area and volume densities respectively, with values approaching -40% and -30% for extreme size distributions with the smallest width and mean radius.

Figure 4.38 shows the change in the POAM II aerosol area and volume density from 1994 to 1997 during the decay of the Mt. Pinatubo aerosol. Figure 4.39 shows the seasonal variation of the POAM III area and volume density during the period of 1998-2004, when there was little inter-annual variation.

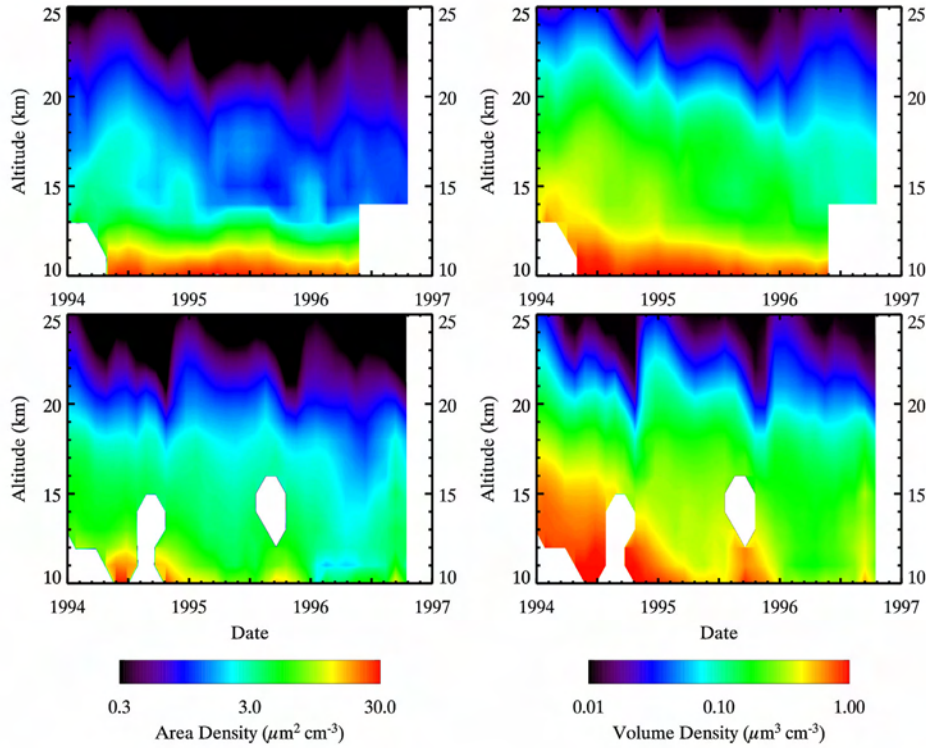


Figure 4.38: Aerosol area and volume density obtained from POAM II measurements at 54-71 N (top row) and at 63-85 S (bottom row) during the period 1994 to 1997.

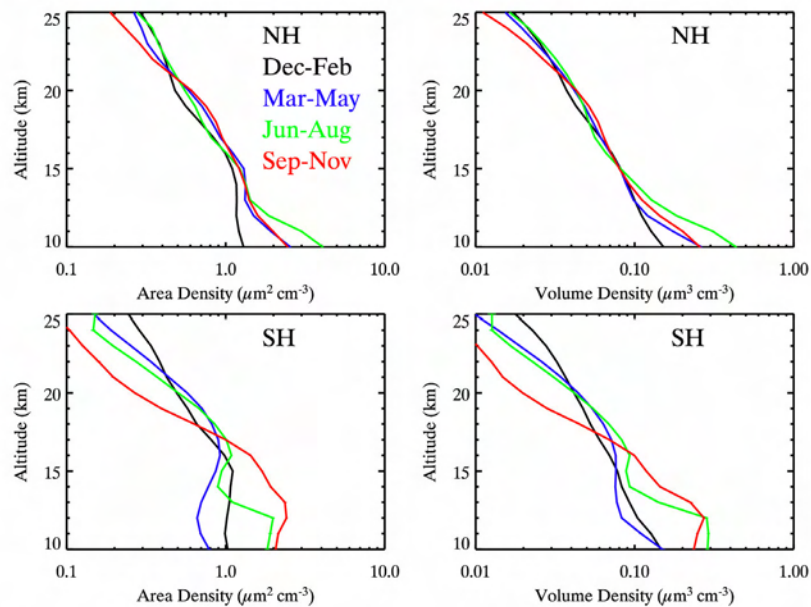


Figure 4.39: Seasonally averaged aerosol area and volume density obtained from the POAM III measurements during 1998 to 2004. Top row shows northern hemisphere results (54-71 N) and bottom row shows southern hemisphere results (63-88 S).

4.3.2 Retrieved Products from Localized Long-term Measurements

Retrieved products from the OPC

To provide functional size distributions representing the cumulative concentration measurements, data are fit with either unimodal or bimodal lognormal size distributions [Jäger and Hofmann, 1991; Hofmann and Deshler, 1991; Deshler et al., 2003]. Thus each measurement of particle concentration at several discrete size bins is fit with a function of the form,

$$N(>r) = \sum_i \int_r^\infty \frac{N_i}{\sqrt{2\pi \ln \sigma_i}} \exp\left(\frac{-\ln^2[a/r_i]}{2\ln^2 \sigma_i}\right) d \ln a, \quad (4.5)$$

where the summation is over either one or two modes of the size distribution. For each mode of the distribution, N_i is total number concentration, r_i median radius, and σ_i distribution width. $N(>r)$ represents the concentration of all particles larger than the lower integration limit, r , and is the quantity measured by the OPCs. The fitting method consists of minimizing the root mean square error = $\sum_k \log^2 [N_m(>r_k) / N(>r_k)]$. The summation is over all measured size channels, r_k . $N_m(>r_k)$, the measured concentration of all particles with $r > r_k$, $N(>r_k)$, is defined by (4.5). The method consists of trying all combinations of measured concentrations to find the set of 5 discrete sizes plus CN concentration giving size distribution parameters which minimize the root mean square difference when all measurements are compared to estimates from the fitted size distribution. Lognormal size distributions are used because: (1) they represent the data well in most cases, (2) they are easy to use - three parameters specify the complete size distribution for each mode included, (3) there are analytical expressions for the distribution moments, and (4) there is some experimental basis to expect aerosol populations to evolve into lognormal size distributions [Granqvist and Buhrman, 1976]. To obtain bimodal distributions requires six estimates of size resolved number concentration. In practice a minimum of five independent measurements are sufficient since the sixth measurement can be inferred to be a low concentration at some size larger than the largest size for which there are measurements. For less than five measurements a unimodal distribution is used.

Monte Carlo simulations were used to assess the impact of measurement uncertainty, due to counting statistics and precision for concentration measurements, and due to pulse width broadening for sizing uncertainties [Deshler et al., 2003]. Results of 750 simulations on four example measurements lead to the conclusion that for lognormal size distributions fitted to the *in situ* measurements, surface areas, volumes and effective radii have uncertainties of $\pm 40\%$, median radii $\pm 30\%$, and distribution widths $\pm 20\%$. The greatest uncertainties were in determining N_2 in periods of low aerosol loading. In these cases standard deviations were over 100%. In contrast, under high aerosol loading N_2 is determined to within 10%. The uncertainty in N_1 is always less than 10%.

Figure 4.40 presents the column integrals of aerosol surface area and volume which can be derived from the size distribution measurements presented in Figure 4.16.

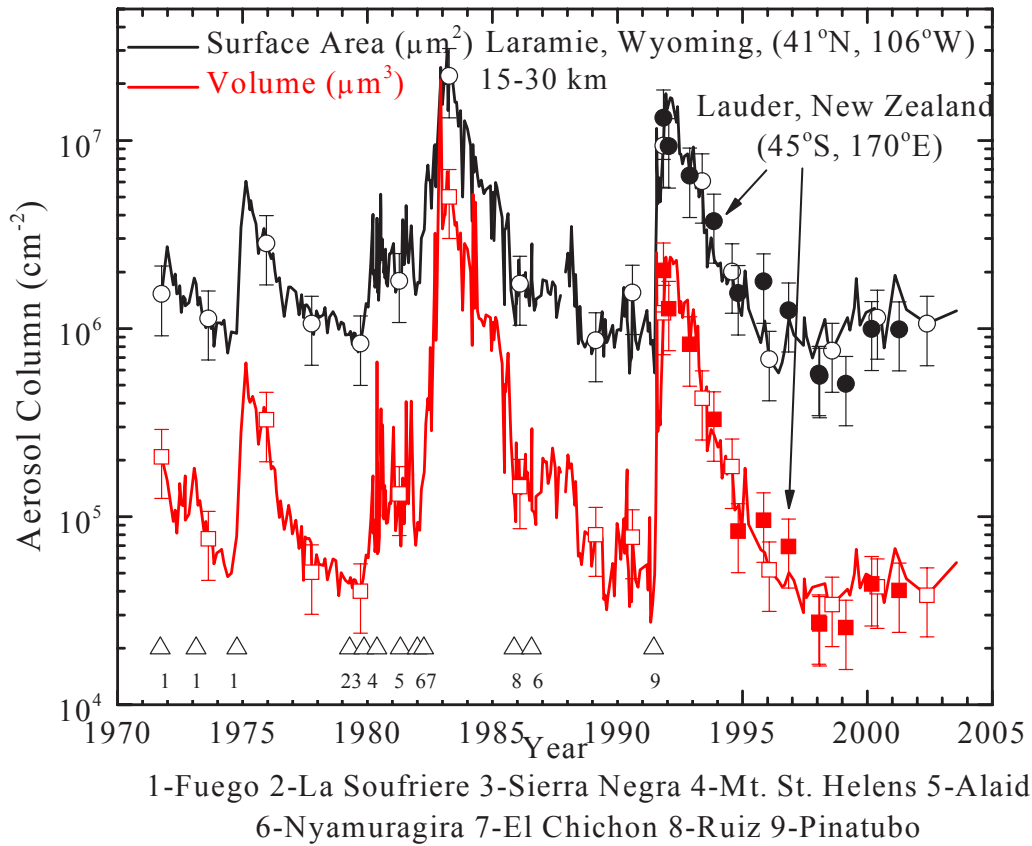


Figure 4.40. History of 15-30 km column integrals, above Laramie, Wyoming, of aerosol surface area (full line) and volume (dotted line). Example error bars are shown on occasional data points. The aerosol surface area and volume are derived from size distributions fit to the in situ measurements. Error bars represent the $\pm 40\%$ error determined for surface area and volume estimates from in situ size distributions. Also included are 12 measurements from Lauder, New Zealand (filled symbols, with error bars) using the same instrumentation. The Laramie measurements represent about 340 individual profiles. Eruption times for the nine stratospherically important volcanic eruptions occurring during the period are indicated.

Retrieved Products from the FSSP-300 and MASP

Figure 4.41 presents the derived quantities obtained from measurements made by the FSSP-300 and MASP as a function of latitude, from December 28, 1988 to March 12, 2000. The top panel shows the effective radius, calculated as the ratio of the third moment of the size distribution to the second moment. The middle panel is the volume density (particle volume per unit volume of air) and the bottom panel is the surface area density. The dashed lines are the maximum values measured in each interval and the vertical bars are the standard deviations about the averages. As in the case of the number concentration, there is a distinct minimum at tropical latitudes with maxima at mid-latitudes, particularly in the north-

ern hemisphere. The decrease in concentration, area and volume in tropical and polar latitudes are a reflection of the shift to smaller particles that are below the detectable size ($0.2 \mu\text{m}$) of either the FSSP or the MASP. In the tropical latitudes, published studies have shown that the large increase in particles less than $0.1 \mu\text{m}$ is a result of new particle formation. In the Arctic regions the shift to smaller particles is a result of the descending air in the Polar vortex.

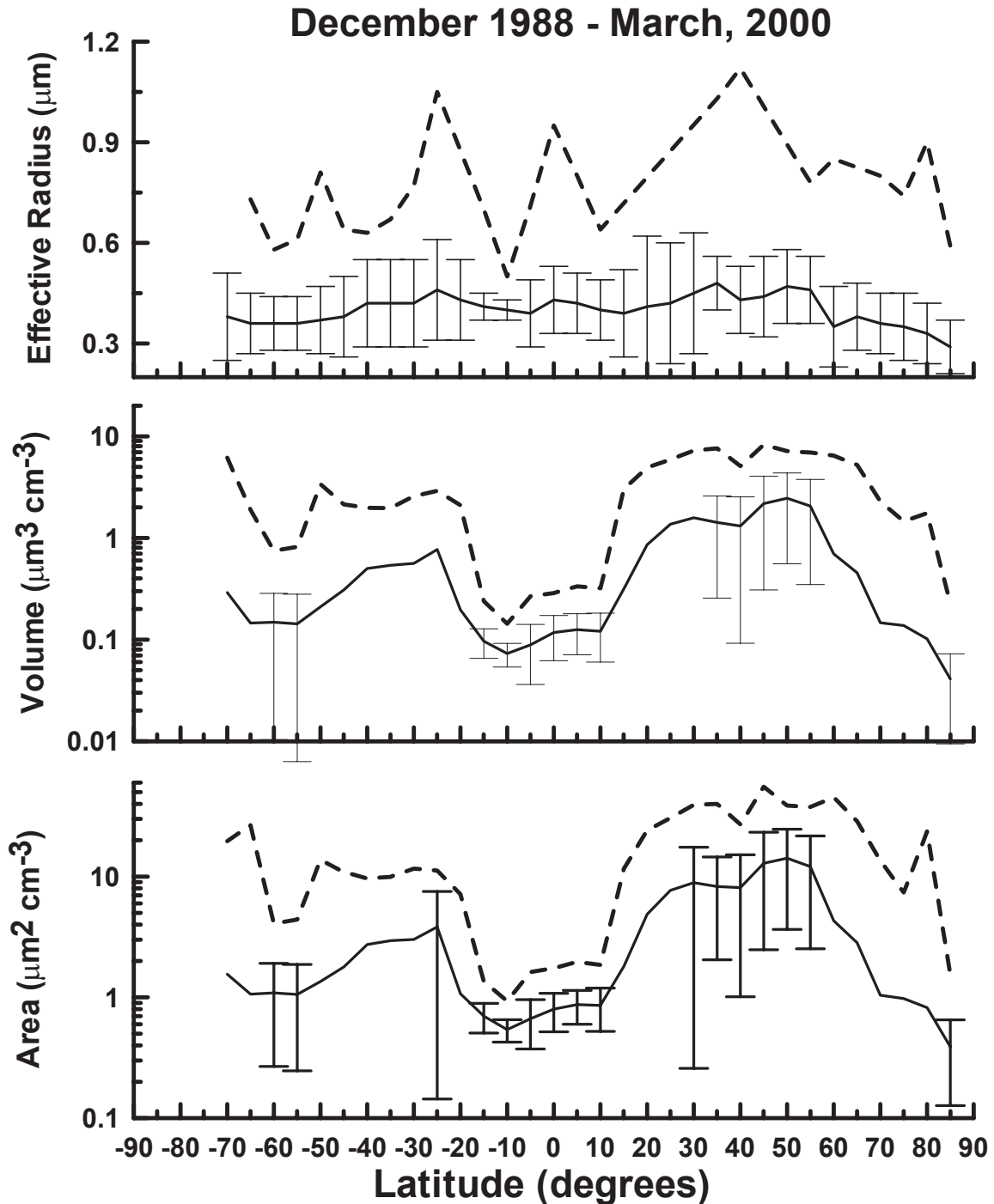


Figure 4.41: Effective radius, volume density and surface area density derived from measurements made with the FSSP-300 and MASP in the altitude range from 17–20 km averaged in 5° intervals of latitude from December, 1988 to March, 2000. The vertical bars are standard deviations about the average (solid line) and the dashed lines are the maxima.

4.4 Relevant Cross-Comparisons Of Averages Or For Coincidences

4.4.1 SAGE/HALOE/OPC Comparisons

Extinction Comparisons

Since aerosol extinction is a strong function of wavelength, comparing measurements made at different wavelengths poses a challenge. Some investigators have dealt with this problem by applying a constant scaling factor to adjust extinctions from visible to IR wavelengths [e.g., Massie et al., 1996; Lu et al., 1997]. While this approach can be valid within the infrared region, bridging the gap between visible and infrared wavelengths is less straightforward. Complications arise because the relationship between visible and infrared extinction is highly dependent on the size distribution and aerosol composition (e.g. sulfuric acid concentration given as wt% H₂SO₄), which determines the refractive index. Since both quantities vary notably with height and time in the stratosphere, a constant scaling factor is generally inadequate. Here aerosol size distributions from the OPCs and from HALOE were used to calculate extinction at the SAGE II wavelengths. For HALOE-SAGE II comparisons this is a robust approach for resolving inherent differences due to measurement wavelength. While the HALOE measurements were manipulated many times (from IR extinctions to size distributions and then to visible extinctions), the SAGE II data set was left in its original state.

Aerosol extinctions at the SAGE II wavelengths were computed from Mie theory using the HALOE and OPC size distributions with refractive indices from Palmer and Williams [1975], which are adequate for visible wavelengths. The refractive index is a function of aerosol composition, and aerosol compositions were determined as a function of temperature, pressure, and water vapor mixing ratio [e.g., Steele and Hamill, 1981]. HALOE water vapor measurements were used for this purpose. Visible sulfate indices are a weak function of composition and potential errors in calculated extinction due to errors in estimated composition are less than 1%. Uncertainties in the calculated extinctions are principally due to uncertainties in the size distributions. Test calculations show that the size distribution errors propagate into extinction uncertainties on the order of 30 to 40%, for HALOE and OPC size distributions.

Time Series Comparisons. Time series were constructed over Laramie (41°N) from the HALOE, SAGE II, and OPC data sets, and over the equator from the HALOE and SAGE II data sets. The time series comparisons did not require coincidence of the respective measurements, and all measurements near a desired location were used. Each data set samples a chosen latitude frequently enough that the average magnitude and trend of extinction should be well represented. The effect of meteorological variability on the aerosol distribution is a factor in comparing non-coincident measurements. However, for the long duration of these comparisons small scale variations become less important than the overall magnitude and trend. An alternative to this approach would be to require time and space coincidence of the measurements. While this approach can work for comparisons of two data sets, three-way coincidences are rare. Additionally, there are no direct coincidences between HALOE and SAGE II at equatorial latitudes.

In Figures 4.42 and 4.43, time series are shown at three representative altitudes over each location for all SAGE II wavelengths. Average tropopause heights are roughly 12 km at middle latitudes and 16 km in the tropics, and the lowest levels chosen were above these

heights to minimize data loss from cloud filtering. SAGE II, HALOE, and OPC measurements over Laramie are compared in Figure 4.42. The appearance and decay of volcanic aerosols are well represented by the three instruments. Aerosol loading due to the eruptions of El Chichón (1982) and Mt. Pinatubo (1991) resulted in similar extinction enhancements during the post-eruption years. These extinctions were observed to decay by roughly two orders of magnitude during a six year period following each eruption. A summary of the comparison differences over Laramie is presented in Table 4.3.

The Laramie comparisons show generally good agreement among the three data sets prior to 1997 at 16 and 22 km, with greater variability and poorer agreement at 28 km at all times. Greater variability at 28 km may be a result of lower aerosol concentrations and smaller sizes at these altitudes. Under these conditions, the extinction measurements are approaching their noise levels, and greater uncertainties are expected for SAGE II and HALOE. Concerning the OPCs, low particle concentrations increase the statistical uncertainty of the measurements due to Poisson counting errors and thus create greater proportionate variability in calculated extinction. The comparisons can be roughly divided into volcanic and background periods, where some clear differences emerge. Volcanic periods were characterized by generally good agreement among the three data sets at all SAGE II wavelengths. During both background periods at 16 and 22 km OPC extinction estimates are lower than the SAGE II extinctions at all wavelengths, with the greatest differences for the 1.02 μm comparison. For example, at 16 km after 1996, the OPC 1.02 μm extinctions are on average a factor of 4 lower than SAGE II, while the 0.386 μm OPC extinctions are a factor of two lower than SAGE II. The SAGE II 1.02 μm measurements should generally have the lowest uncertainties, on the order of 10%, and are roughly 100 times above the detection limit even during background periods. In addition, HALOE extinctions tend to agree with SAGE II values after 1997, except in 1999 when HALOE values can be very low. The extinction differences at the longest SAGE II wavelengths after 1996 indicate problems in deriving longer wavelength extinctions from the OPC measurements in low aerosol loading. This problem is not as severe at the shorter wavelengths during background periods. This difference may arise because of sample volume differences between the OPC and SAGE II. The much larger sample volume of SAGE II would be sensitive to low concentrations of larger particles, which dominate the 1.02 μm Mie kernel (Figure 4.28), while these concentrations may be below the detection limit of the OPC. The shorter wavelength Mie kernels are dominated by smaller more abundant particles. At shorter wavelengths in background periods HALOE extinction estimates are lower than SAGE II extinctions and are closer to OPC estimates.

HALOE and SAGE II measurements were compared over the equator at longitudes from 180°E to 270°E where the occurrence of cirrus is a minimum [e.g., Wang et al., 1996]. These comparisons (Figure 4.43) show less variability at 30 km than over Laramie at 28 km (Figure 4.42). At 25 km HALOE and SAGE II 1.02 μm extinctions are within 25% of each other during the entire comparison period. At shorter wavelengths HALOE and SAGE II agree until the aerosol approaches its background state near 1997. After that time HALOE systematically underestimates SAGE II extinctions for wavelengths < 1.02 μm . The shorter wavelength comparisons at 20 km are similar to those at 25 km. The equatorial differences are similar in direction, if not magnitude, to the HALOE - SAGE II comparisons over Laramie.

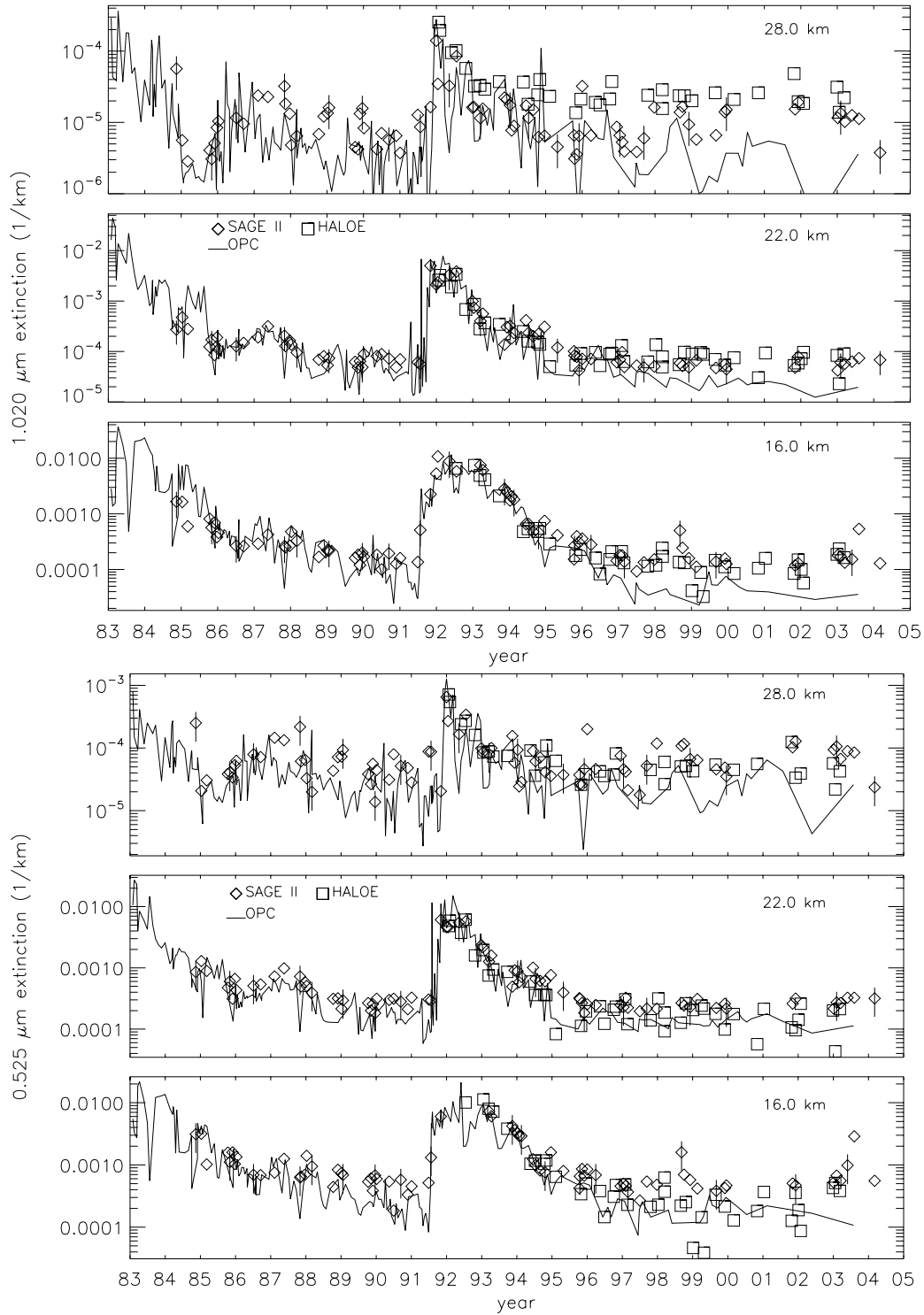


Figure 4.42: Time series at three altitudes over Laramie of aerosol extinction at four SAGE II wavelengths. SAGE II (\diamond) measurements are compared to extinctions calculated from OPC (—) and HALOE (\square) size distributions. HALOE and SAGE II measurements between 41°N and 42°N latitude and 245°E and 265°E longitude were used. Vertical bars on the occasional SAGE II measurement indicate $\pm 50\%$. The SAGE II uncertainties are less than this, and these bars serve only to add perspective. This time series is composed of 81 SAGE II, 202 OPC, and 43 HALOE measurements.

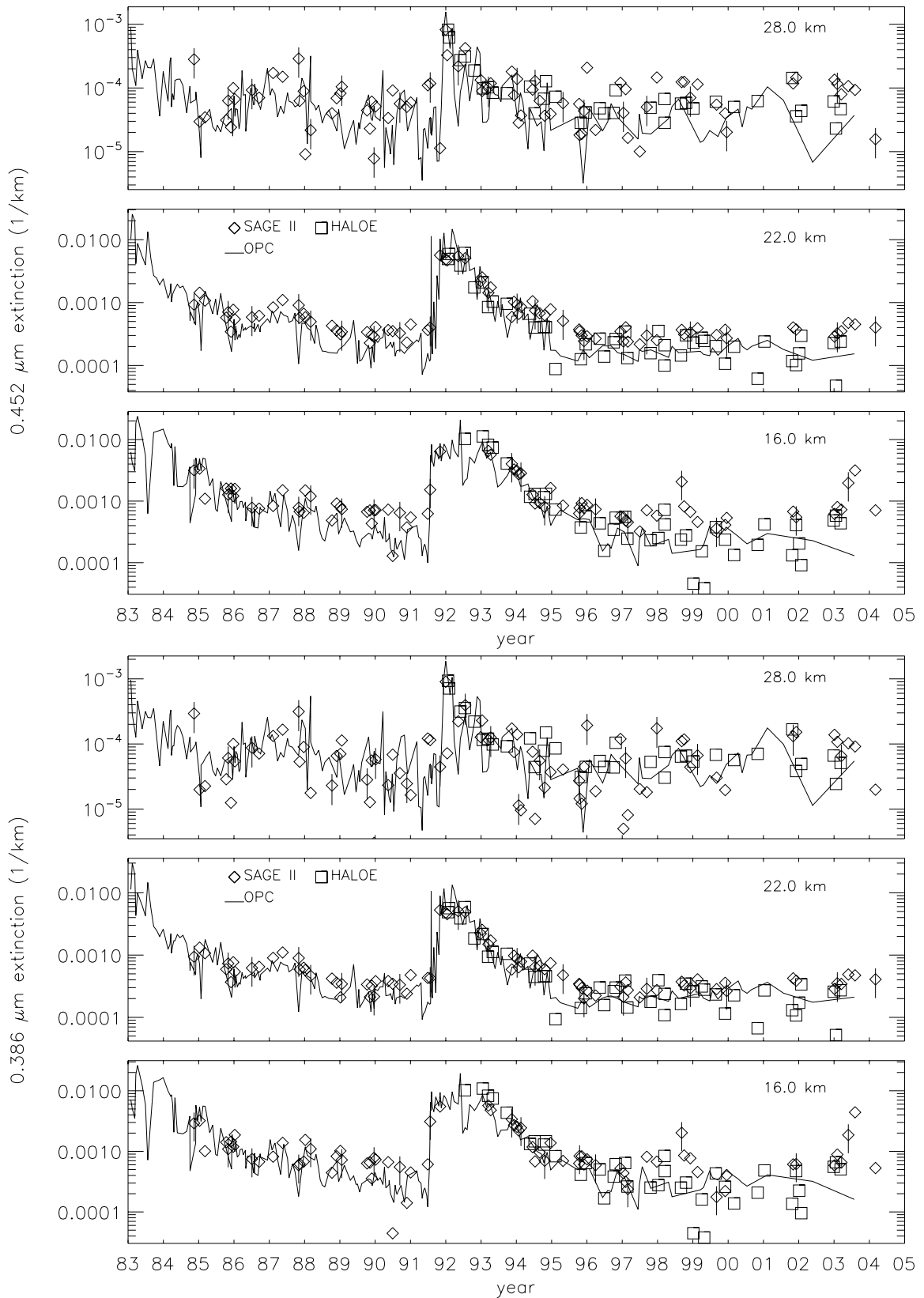


Figure 4.42: Continued.

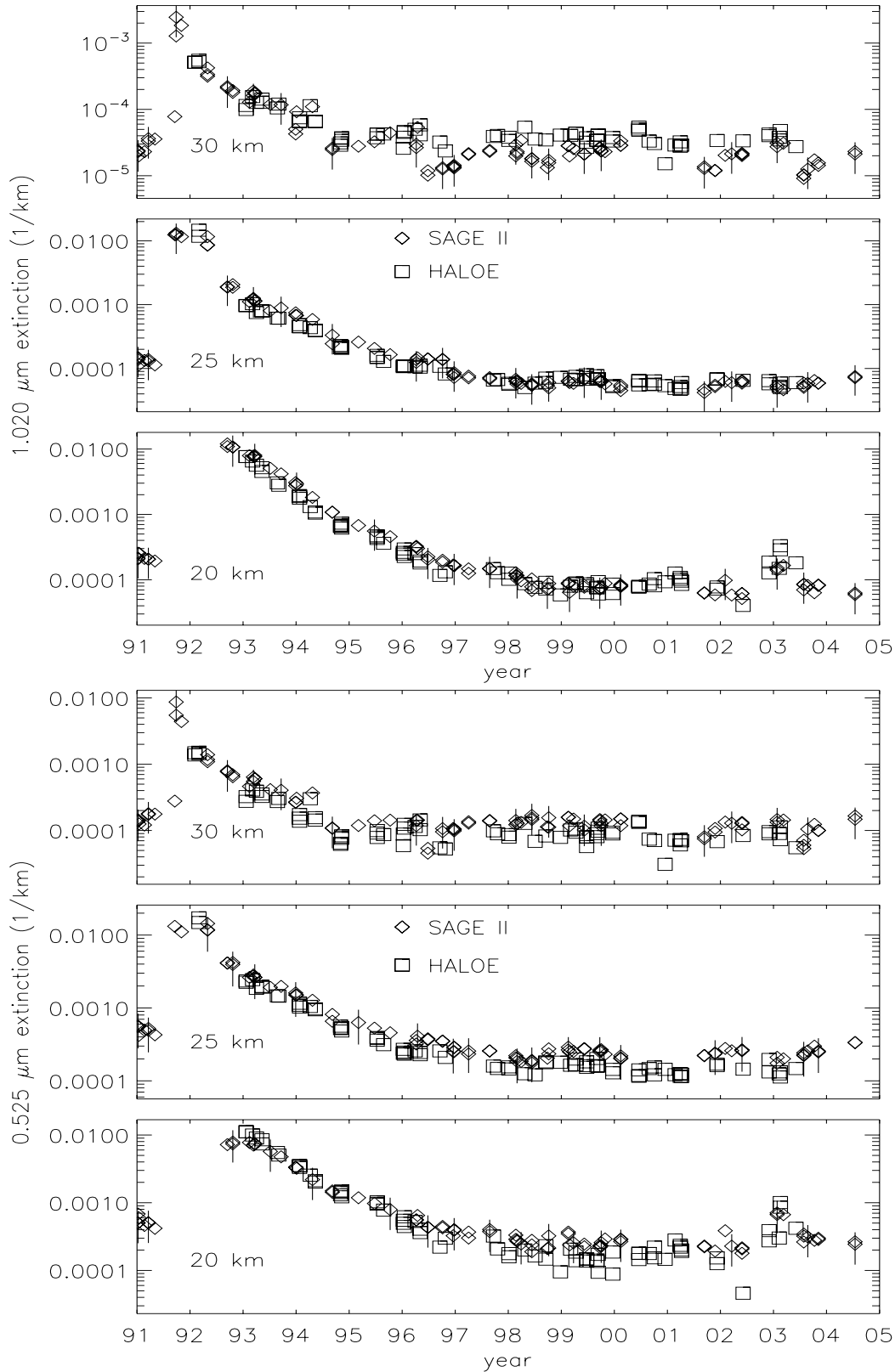


Figure 4.43: Time series at three altitudes of aerosol extinction at four SAGE II wavelengths, from HALOE (\square) and SAGE II (\diamond). Measurements used were between the equator and 1°S latitude and 180°E and 270°E longitude. Vertical bars on the occasional SAGE II measurement indicate $\pm 50\%$. The SAGE II uncertainties are less than this, and these bars serve only to add perspective. This time series is composed of 96 SAGE II and 78 HALOE measurements.

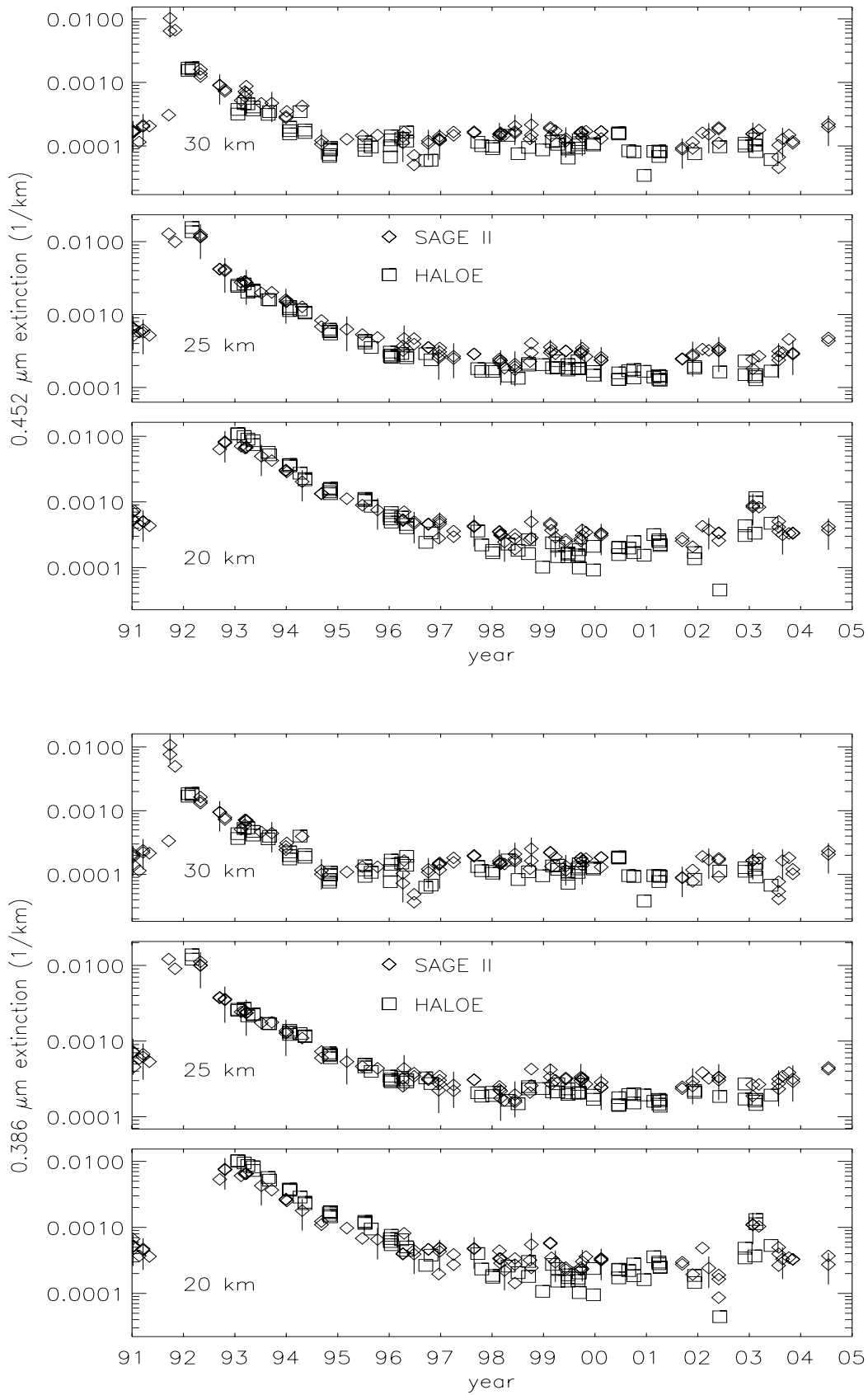


Figure 4.43: Continued

Profile Comparisons. Vertical profiles for coincident measurements between SAGE II and HALOE and SAGE II and the OPCs were compared over the time periods sampled by the instrument pairs. For this purpose, coincident measurements were identified using maximum separations of 24 hours, 2° latitude, and 20° longitude. This led to 353 HALOE-SAGE II comparisons near 41°N and 30 OPC-SAGE II comparisons over Laramie. Coincident profiles were compared for the duration of the data sets and comparison statistics were generated. These are presented as mean profiles, mean differences, and difference standard deviations (random differences). At each altitude, the mean relative difference in percent between SAGE II (S) and the other (O) measurements was computed as

$$\bar{\Delta} = \frac{1}{N} \times \sum_{i=1}^N \Delta_i,$$

where N is the number of coincident measurements and $\Delta_i = 200 \times (O_i - S_i) / (O_i + S_i)$. Standard deviation of the mean relative difference was computed as

$$\sigma_{\bar{\Delta}} = (\sum_{i=1}^N (\Delta_i - \bar{\Delta})^2 / (N - 1))^{1/2}.$$

Separating each comparison into individual years can show varying agreement among the three data sets; however, presenting this analysis is difficult. A hint of such comparisons can be obtained by referring to Figures 4.42 and 4.43 as the composite profile statistics are presented.

Comparison results for coincident HALOE and SAGE II measurements between 38°N and 44°N ($\pm 3^\circ$ latitude of Laramie) are shown in Figure 4.44. These comparisons show a generally constant bias for all wavelengths and altitudes, with HALOE roughly 30% less than SAGE II. The most notable exceptions to this pattern are at 1.02 μm wavelength above 22 km and for the other wavelengths above roughly 30 km. Uncertainties in the mean differences, $(\sigma_{\bar{\Delta}}/N^{1/2})$, are generally less than 5%, indicating that these biases are statistically significant. Comparison statistics for coincident SAGE II and HALOE profiles at southern middle latitudes (not shown) are very similar to comparisons in the northern hemisphere shown in Figure 4.44. There are no direct HALOE-SAGE II coincidences in the tropics and Figure 4.43 serves to document HALOE-SAGE II agreement there.

Comparison results for coincident SAGE II and OPC measurements over Laramie are shown in Figure 4.45. These results indicate clear systematic differences, with the OPC extinctions roughly 30% less than SAGE II at most altitudes and wavelengths. The most notable exception to that statement is at 1.02 μm where differences are larger above 20 km and close to zero below 20 km. While uncertainties in the mean differences can be large (5 to 20%) the reported biases are typically greater than the uncertainties and therefore statistically significant. Larger uncertainties in the OPC-SAGE II mean differences are due to the lower number of coincidences. The results in Figures 4.44 and 4.45 are generally consistent with Figure 4.42, showing greater variability (random differences) at the highest altitudes, and systematic differences that can change with altitude. Because the profile statistics include measurements during volcanic and background periods, certain features in Figures 4.42 and 4.43 are not visible in Figures 4.44 and 4.45.

While the extinction comparisons required manipulation of the HALOE and OPC measurements, the SAGE II measurements were untouched. Thus, these comparisons establish agreement among the instruments at perhaps the most fundamental level possible. While the overall agreement is encouraging, it is clear that the differences change with wavelength, latitude, altitude, and time. As these data sets continue to be used to infer various optical and physical aerosol properties, the extinction comparisons provide a useful

standard to assess the validity of the inferred properties.

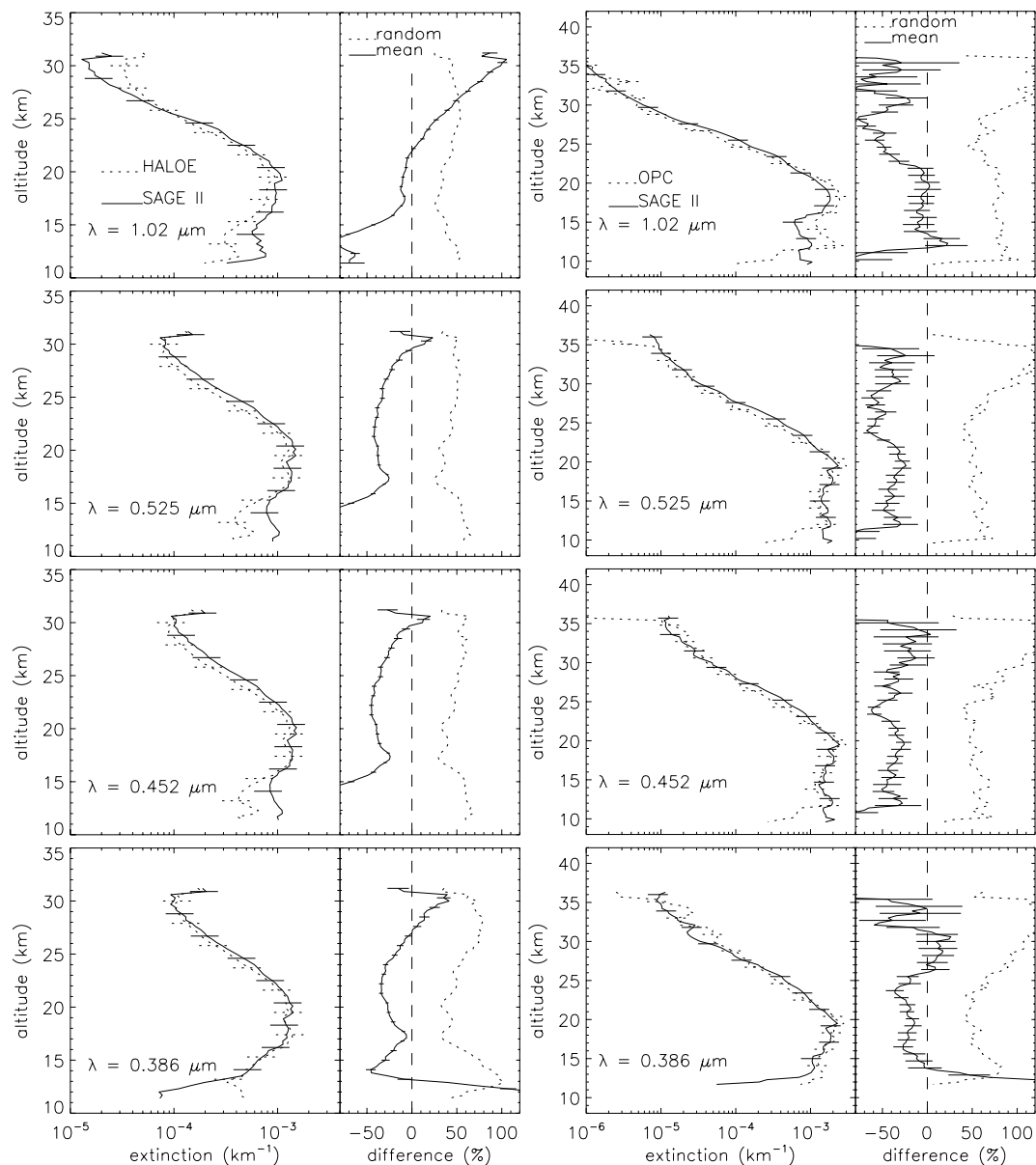


Figure 4.44 (left column): Comparison statistics for 353 coincident HALOE and SAGE II profiles between 38°N and 44°N latitude, from 1991 through 2002. The average profile separations were 11.6 hours, 0.8° latitude, and 7.6° longitude. Statistics are shown as mean profiles, mean differences (HALOE - SAGE II), and difference standard deviations (random differences). See text for details. Error bars on the mean profiles indicate the reported measurement uncertainties, and error bars on the mean differences indicate uncertainties in the mean differences ($\sigma_{\Delta} / N^{1/2}$).

Figure 4.45 (right column): Comparison statistics for 30 coincident OPC and SAGE II profiles over Laramie, from 1984 through 1999. The average profile separations were 12.2 hours, 0.9° latitude, and 6.8° longitude. Statistics are as described in Figure 4.44, except the differences are OPC - SAGE II.

Surface Area Comparisons

This section evaluates aerosol surface area densities (SAD) determined from SAGE II, HALOE, and the OPCs. Thomason et al. [1997b] compared SAGE II aerosol surface areas (derived from V5.96) to the OPCs over Laramie for four years after the Pinatubo eruption. That work showed good agreement for surface areas less than about $15 \mu\text{m}^2 \text{cm}^{-3}$, and systematic differences (SAGE II > OPC) under higher aerosol loading conditions. Hervig et al. [1998] compared HALOE surface areas based on room temperature refractive indices from Palmer and Williams [1975], to OPC results over Laramie. While that work showed that HALOE surface areas were from 10 to 30% higher than the OPC values, the current HALOE surface areas which are based on cold temperature refractive indices from Tisdale et al. [1998] are $\sim 25\%$ lower than the previous results. For the comparisons presented here, SAGE II surface areas were taken from the version 6.2 SAGE II data files. A description of SAGE II SADs is available in section 4.2.1 of this document and in Thomason and Osborn [1992].

Time series of surface area at three altitudes from HALOE, SAGE II, and the OPCs are compared over Laramie in Figure 4.46. A summary of the measurement differences is offered in Table 4.3. SAGE II and the OPCs are in generally good agreement during the entire comparison period at 16 and 22 km. HALOE tends to agree with SAGE II and the OPCs at 16 and 22 km prior to 1998, but is generally lower than SAGE II and the OPCs after 1998. Significant differences exist nearly all the time at 28 km, where SAGE II surface areas are generally lower than HALOE and the OPCs, and at all altitudes after 1998. Steele et al. [1999] noted that surface areas derived from SAGE II using the PCA technique can be biased low when particles are small, which occurs during low aerosol loading, such as at high altitudes or in background periods. This bias can be partly understood from the Mie kernels shown in Figure 4.28. The median radii of these extinction kernels decrease from 0.6 to 0.2 μm for wavelengths from 1.02 to 0.386 μm . In contrast surface area distributions during low aerosol loading have median radii near 0.1 μm . Deshler et al. (2003) present example surface area and extinction distributions illustrating this difference. Thus, during low aerosol loading extinction measurements are not sensitive to a majority of the particles which control surface area. In this case the observed differences in 1.02 μm extinction between the OPCs and SAGE II may be unimportant when comparing surface area density. In general, agreement between SAGE II and the OPC SAD most closely matches the shorter wavelength extinction comparisons. The factor of four bias in the OPC-SAGE II 1.02 μm extinction comparison (Figure 4.42) is not evident in the SAD comparisons shown in Figure 4.46. It might be noted that the quantity plotted in Figure 4.28 is $3Q/4r=dk/dV$. The effect discussed here is more properly related to $dk/dA=3Q/8$ which falls off more steeply than dk/dV for small r .

Time series of aerosol surface area over the equator from HALOE and SAGE II are compared in Figure 4.47. The HALOE-SAGE II surface area comparisons are similar to the equatorial extinction comparisons (Figure 4.43), suggesting that the variability shown is primarily related to the measurements and to atmospheric variability, rather than errors in the conversion to SAD. The HALOE and SAGE II comparisons of extinction and surface area maintain a consistent relationship throughout the comparisons. The OPC and SAGE II comparisons show opposite biases for extinction and surface area (*cf.* Figures 4.42 and 4.46). Although the SAD agreement is fairly reasonable, the OPC extinction is significantly less than SAGE II at all wavelengths, but most notably at 1.02 μm after 1999.

Profile statistics for HALOE-SAGE II surface area comparisons over Laramie are shown in Figure 4.48. These results show that HALOE and SAGE II surface areas match to within the respective error bars, although HALOE is roughly 20% less than SAGE II at altitudes from 19 to 26 km. HALOE-SAGE II surface area comparisons in the southern hemisphere (not shown) are very similar to the northern hemisphere comparisons. Profile statistics for OPC-SAGE II surface area comparisons over Laramie are shown in Figure 4.49. This comparison shows statistically insignificant differences for altitudes from roughly 16 to 25 km, generally covering the peak in aerosol surface area. Below 16 and above 25 km SAGE II underestimates SAD by 30-60% compared with OPC estimates.

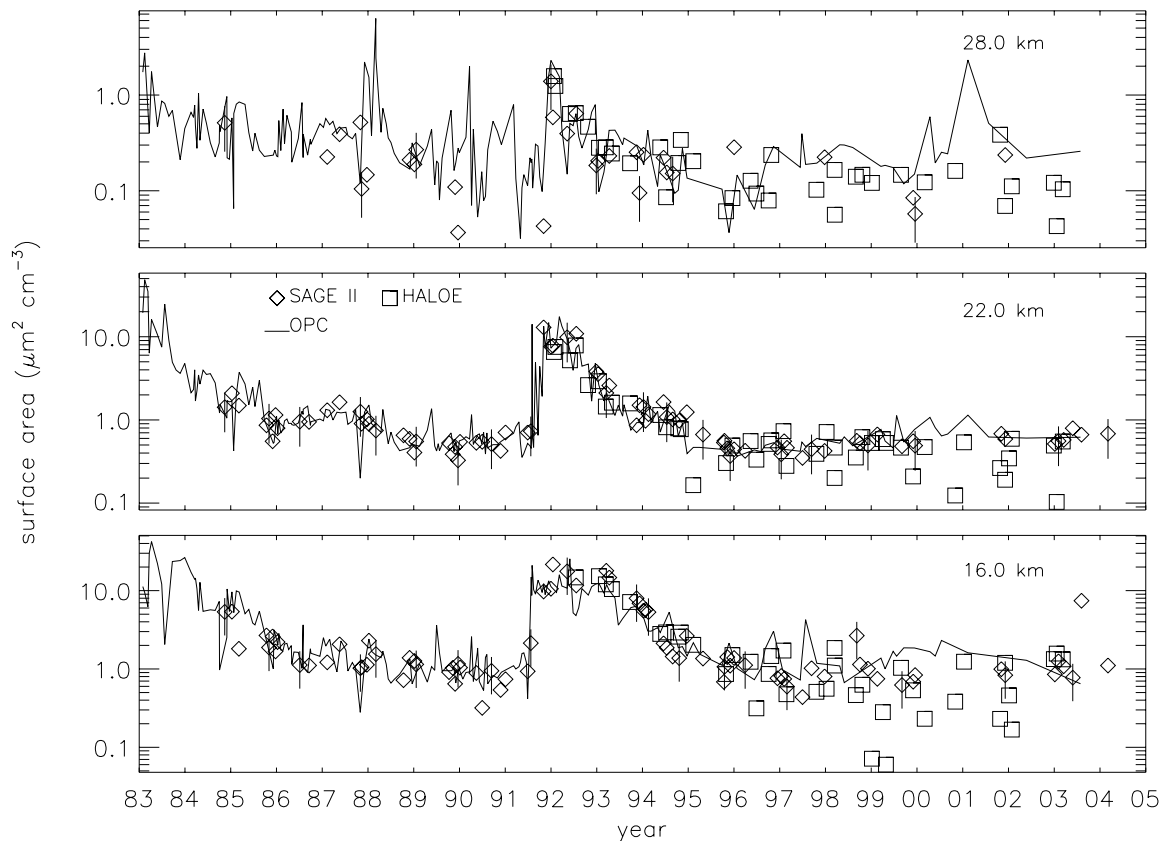


Figure 4.46: Time series of HALOE, OPC, and SAGE II measurements over Laramie as in Figure 4.42, except that aerosol surface area densities are compared.

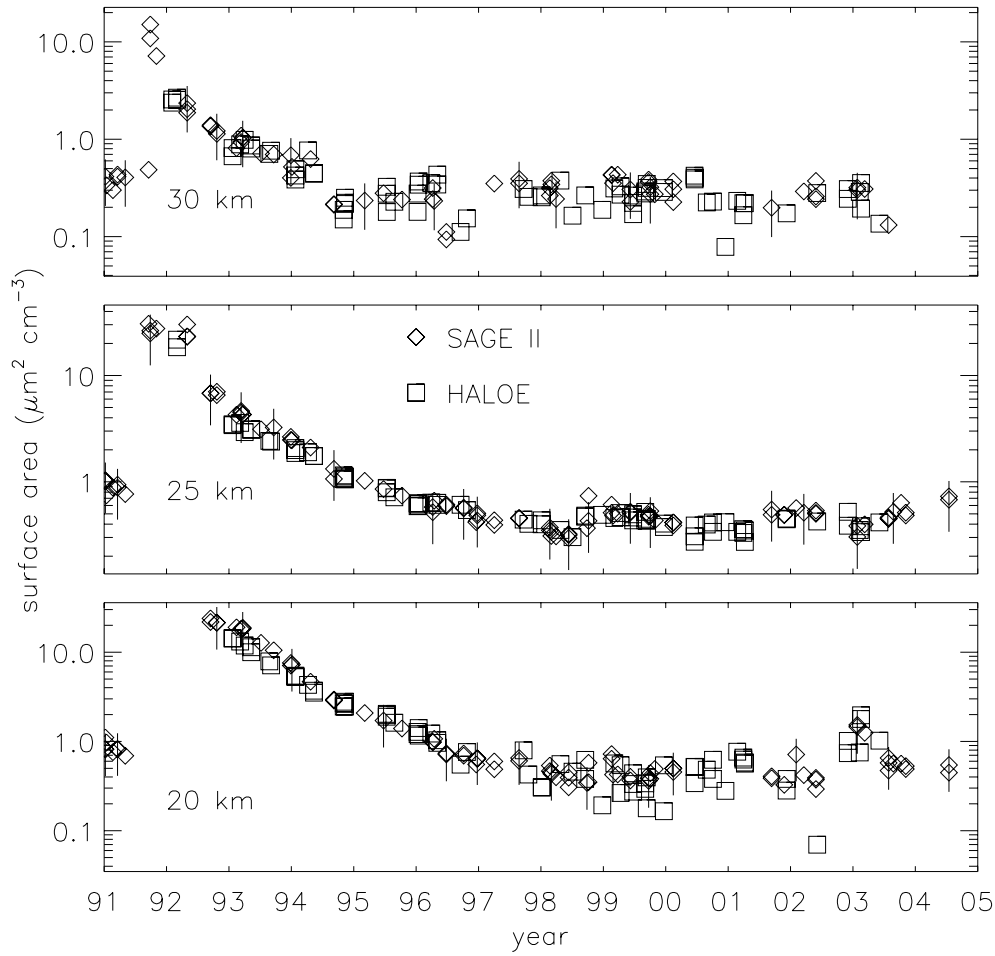


Figure 4.47: Time series of equatorial SAGE II and HALOE measurements as in Figure 4.43, except aerosol surface area densities are compared.

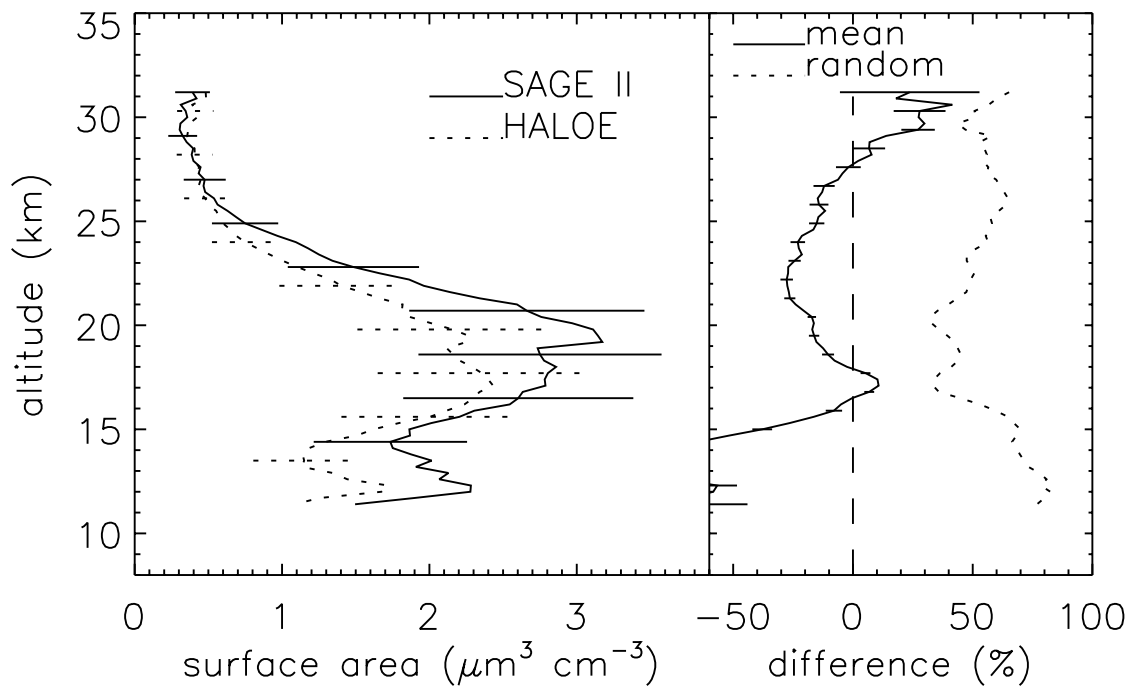


Figure 4.48: Comparison of HALOE and SAGE II measurements over Laramie, as in Figure 4.44 except the results are for surface area density.

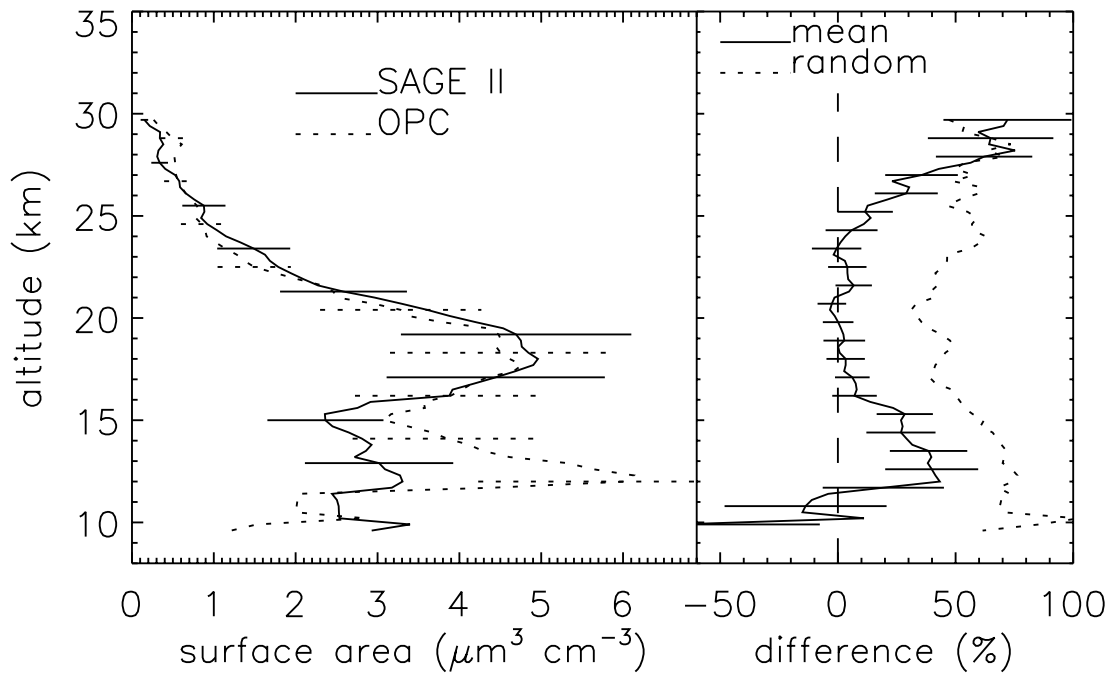


Figure 4.49: Comparison of SAGE II and OPC measurements over Laramie, as in Figure 4.45 except the results are for surface area density.

Summary

Stratospheric aerosol measurements from SAGE II, HALOE, and balloonborne OPCs were compared. These instruments measure different quantities, and a common basis was required to compare the data sets. For this purpose, extinctions at the SAGE II wavelengths were computed from the HALOE and OPC aerosol size distributions for comparison to SAGE II. Aerosol surface areas derived from each data set were compared as well. While the overall impression from these comparisons is encouraging, the agreement can change with latitude, altitude, time, and parameter. The best agreement was generally found when the aerosol extinctions and surface areas were large. For example, the three data sets were in excellent agreement for $1.02 \mu\text{m}$ extinctions greater than roughly $2 \times 10^{-4} \text{ km}^{-1}$. Notable differences can emerge when the aerosol amounts are low, such as background periods at all altitudes, and at altitudes above about 25 km during most years.

Table 4.3 summarizes some of the observed differences near 41°N latitude for a variety of times, altitudes, and parameters. The SAGE II – OPC comparisons are somewhat inconsistent under low aerosol loading when comparing differences for the 1.02 and $0.386 \mu\text{m}$ extinctions and for SAD. The extreme example shown here is the comparison for 1999 – 2000 at 16 km which indicates SAGE II $1.02 \mu\text{m}$ extinctions nearly three times larger than OPC estimates, while SAGE II SADs are 60% lower than the OPC estimates. These inconsistencies persist at higher altitudes, but diminish when shorter wavelength extinctions are compared and when aerosol loading is higher. It should be noted that there were only 3 coincidences during this time period. The inability of the OPCs to properly estimate $1.02 \mu\text{m}$ extinction probably has minimal impact on the SAD comparisons, since the $1.02 \mu\text{m}$ measurements are insensitive to the small particles that control surface area under low aerosol loading. That is, the particle sizes that control the OPC calculation of the $1.02 \mu\text{m}$ extinction and SAD are sufficiently disjoint that the discrepancy in the calculations of $1.02 \mu\text{m}$

extinction does not carry over into the calculation of SAD. Considering the operational algorithm to calculate SAD it is clear that if, say, the OPC underestimates the SAGE II extinctions by roughly the same amount at 1020 and 525 nm, then SAD estimates would agree even if extinction estimates did not. As might be expected, the numerical values presented in the table are altered somewhat when one uses a different set of latitude-longitude-time windows to define coincidences. The small number of coincidences between SAGE II and the OPC make it difficult to put a high degree of confidence in these results. It might also be noted that under very low aerosol loadings the influence of non-sulfate particles will be more significant than under high aerosol loadings. Furthermore, some of the problems associated with the low aerosol loading comparisons are due to the difficulty in identifying the aerosol signal in the measurements.

The SAGE II – HALOE comparisons tend to be internally consistent, with the extinction and SAD comparisons showing similar differences at most times and altitudes. It is not clear that better agreement could be expected, considering the various assumptions made, including the assumptions that the size distribution is log normal and the index of refraction is that for sulfuric acid solutions.

Table 4.3. Summary of HALOE/SAGE II/OPC extinction and surface area density (SAD) differences. Results were divided into three time periods and three altitudes. Differences are indicated as the average ratios of quantities for various instrument combinations. The results are based on coincident measurements near Laramie and the number of coincidences in each time period is indicated. Coincident measurements were identified using maximum separations of 24 hours, 2° latitude and 20° longitude.

<i>Measurement Ratio</i>	<i>Altitude</i>	<i>Quantity</i>	<i>Period</i>		
			<i>1987-1990</i>	<i>1992-1994</i>	<i>1999-2000</i>
SAGE II / OPC	Number of coincidences		8	5	3
	16 km	1.02 μm ext.	1.3 ± 0.8	1.9 ± 1.6	2.6 ± 1.5
		0.386 μm ext.	2.0 ± 1.0	1.3 ± 0.5	1.2 ± 0.1
		SAD	1.1 ± 0.3	1.2 ± 0.4	0.4 ± 0.1
	22 km	1.02 μm ext.	2.1 ± 0.5	2.0 ± 1.4	2.7 ± 1.4
		0.386 μm ext.	1.7 ± 0.6	1.4 ± 0.5	1.8 ± 0.3
		SAD	1.1 ± 0.3	1.6 ± 0.5	0.9 ± 0.1
	28 km	1.02 μm ext.	2.2 ± 0.9	3.1 ± 2.0	3.6 ± 1.4
		0.386 μm ext.	1.4 ± 2.3	1.8 ± 1.7	1.5 ± 1.0
SAD		0.2 ± 0.1	1.4 ± 0.5	N/A	
SAGE II / HALOE	Number of coincidences	N/A	99	53	
	16 km	1.02 μm ext.		1.4 ± 0.3	1.3 ± 0.7
		0.386 μm ext.	N/A	0.9 ± 0.3	3.0 ± 3.5
		SAD		1.0 ± 0.3	2.7 ± 3.4
	22 km	1.02 μm ext.		1.4 ± 0.7	0.9 ± 0.5
		0.386 μm ext.	N/A	1.5 ± 1.5	2.4 ± 3.4
		SAD		1.6 ± 1.5	2.1 ± 3.0
	28 km	1.02 μm ext.		0.7 ± 0.6	0.5 ± 0.2
		0.386 μm ext.	N/A	1.3 ± 1.1	1.6 ± 1.1
SAD			1.1 ± 0.8	1.2 ± 0.6	

4.4.2 SAGE/POAM Comparisons

Since the POAM II-III and SAGE III measurements are taken at very nearly the same wavelengths, they produce aerosol extinction coefficients that can be easily compared. For POAM II and SAGE II the wavelengths are 0.448-0.452 μm and 1.06-1.02 μm , for POAM III and SAGE II they are 0.442-0.452 μm and 1.02-1.02 μm . Coincidence measurements are selected with a distance smaller than 500 km (350 km on average in both hemispheres) and a time interval smaller than 2 hours (20 min on average in NH, 45 min in SH).

For the whole period covering POAM II and for that covering POAM III, the mean of the relative difference (that enables us to show any possible bias) $\bar{\Delta} = N^{-1} \sum_{i=1,N} \Delta_i$ was computed as well as the root mean square difference of the relative differences (which enables us to estimate the mean agreement) $\text{rmsd} = (\sum_{i=1,N} \Delta_i^2 / (N-1))^{1/2}$. Here N is the number of coincident events and $\Delta_i = 200 \times (P_i - S_i) / (P_i + S_i)$ where P stands for POAM and S for SAGE. Results for both hemispheres are shown in Figure 4.50 for POAM II and in Figure 4.51 for POAM III. Below about 12 km and above about 30 km the rmsd is always very large.

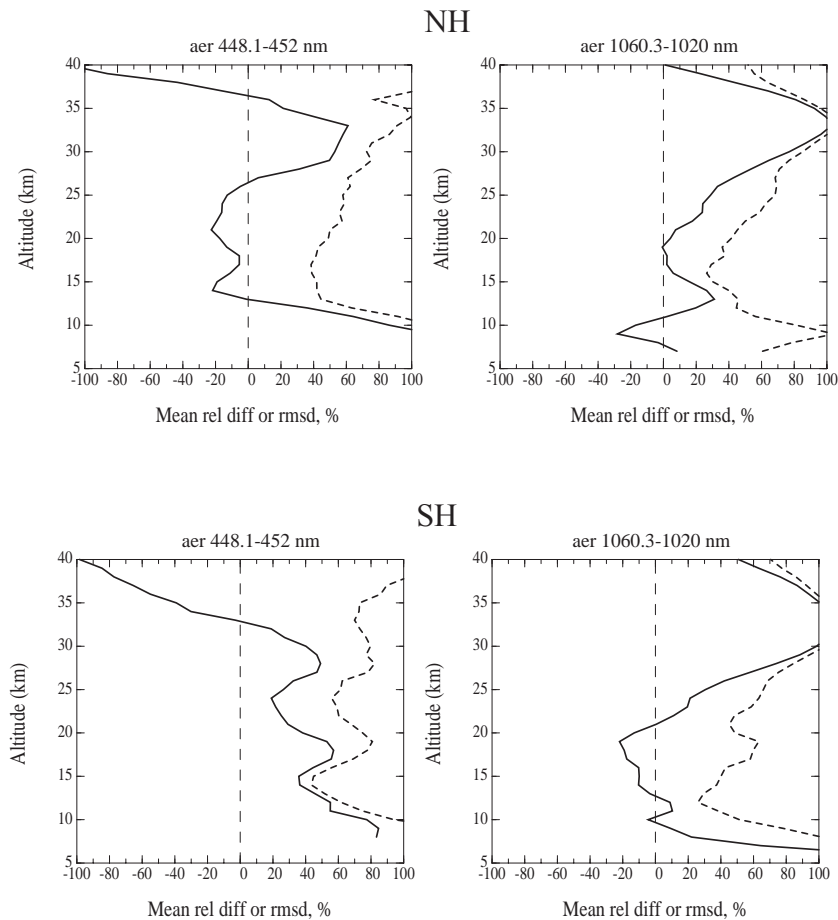


Figure 4.50: Mean relative difference of the extinctions (full line) and root mean square difference (dashed line) for POAM II / SAGE II coincidences. In the northern hemisphere 291 coincidences were identified, and 340 in the southern hemisphere.

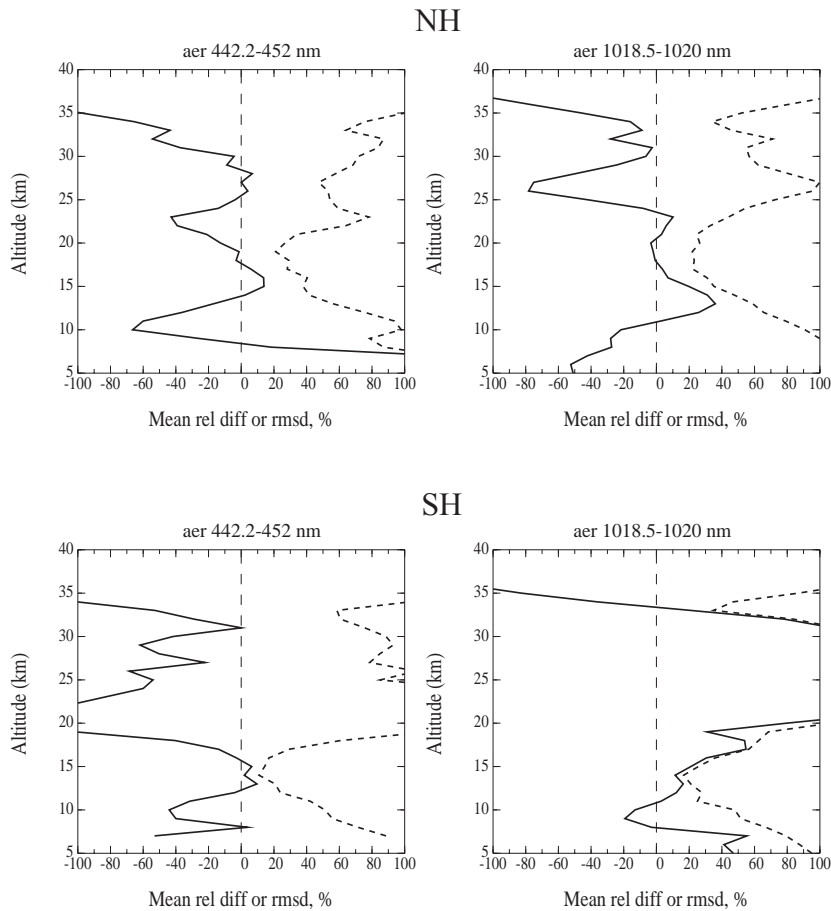


Figure 4.51: Mean relative difference of the extinctions (full line) and root mean square difference (dashed line) for POAM III / SAGE II coincidences. In the northern hemisphere 236 coincidences were identified, and 285 in the southern hemisphere.

For POAM II measurements, the comparison at 448-452 nm shows a small negative bias (POAM<SAGE) in the NH and a large positive bias (POAM>SAGE) in the SH. The mean agreement (rmsd) is worse than 40% in both hemispheres. At 1060-1020 nm there is a positive bias in the 10-15 km range in the NH and a weak bias in the SH. The mean agreement is worse than 30% in both hemispheres. The comparison for POAM III at 442-452 nm exhibits a large negative bias in both hemispheres around 20 km. The mean agreement is worse than 20% in both hemispheres, that is, better than for POAM II. At 1018-1020 nm in the NH there is no bias in the 15-23 km range and a positive bias above 12 km in the SH. The mean agreement is worse than 20% in both hemispheres which is also better than for POAM II.

4.4.3 SAGE/ORA Comparison

A comparison between SAGE and ORA extinction profiles has been carried out previously [Fussen et al., 1998; 2001], making use of 25 coincident events. Figure 4.52 shows a comparison of the 1013 nm ORA channel with the SAGE II 1020 nm from these 25 events. The error bars have been determined as a combination of the experimental error and the statistical variance of the event population. It can be seen that both profiles fit within the error bars.

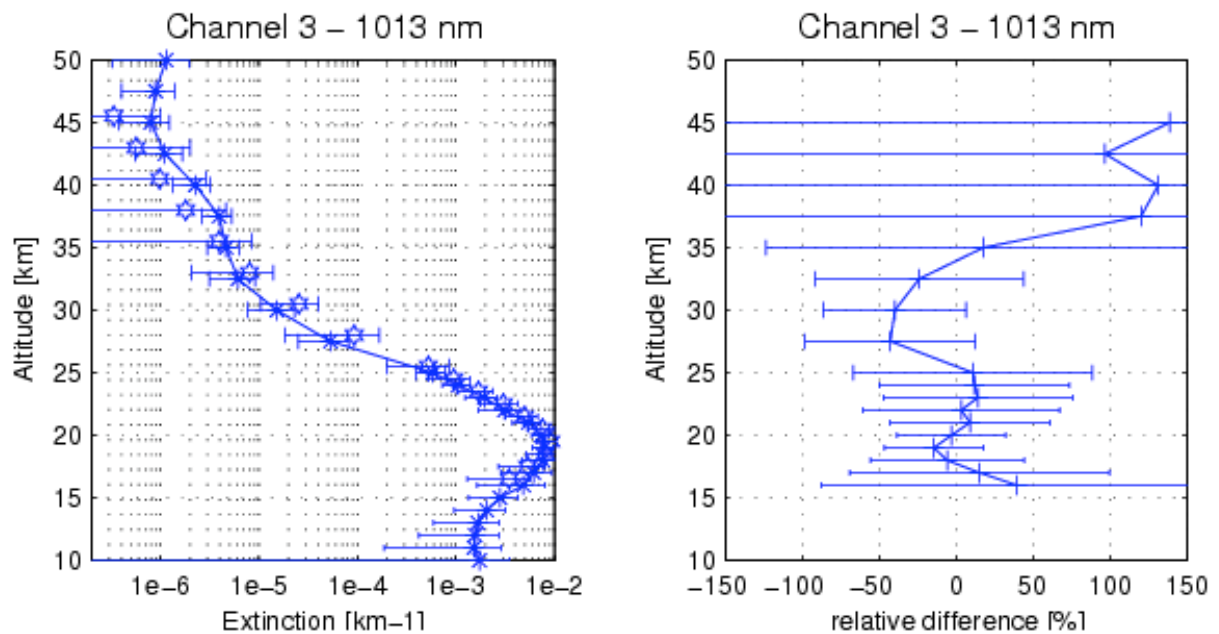


Figure 4.52 (left): Comparison of ORA (asterisks) and SAGE (six-pointed stars) aerosol extinctions at the 1013 nm ORA channel. From Fussen et al. [2001].

Figure 4.53 (right): Relative difference between ORA and SAGE aerosol extinction profiles for the 1013 nm ORA channel. From Fussen et al. [2001].

The relative difference between SAGE II and ORA, calculated as $100 \times (\text{ORA} - \text{SAGE}) / \text{SAGE}$, is reported in Figure 4.53. The difference is found to be lower than 50%, at least for altitudes lower than 35 km. Concerning the other ORA spectral channels, a comparison using data interpolated in altitude and wavelength from available SAGE II extinctions result in relative differences between both data sets which do not exceed 50% in most cases. A detailed description of the comparison can be found in the cited references.

It is worth noting that extinction data are available to ground level in the case of ORA, which constitutes a main advantage of the ORA data set.

4.4.4 Comparisons of SAGE Extinctions with Lidar Backscatter

The use of lidar for validation of the SAGE instruments has been conducted mainly at mid-latitudes and under background aerosol conditions [Russell and McCormick, 1989, Ackerman et al., 1989, Osborn et al., 1989; Oberbeck et al., 1989, Yue et al., 1995, Lu et al., 1997; Lu et al., 2000, Thomason and Osborn, 1992].

Few comparisons between SAGE instruments and lidar aerosol extinction/backscatter profiles measured in the tropics have been reported. Six SAGE I aerosol/molecular extinction ratio profiles at 1.0 μm [McCormick et al., 1979] measured on April 9, 1979 were compared with six lidar aerosol scattering ratio profiles obtained on November 25-26, 1978, measured at 0.694 μm by the Mark II lidar system located at the University of West Indies (18°N, 76.8°W), Kingston, Jamaica [Kent et al., 1971]. The comparison conducted under background conditions showed, on average, lidar aerosol scattering ratios with higher values than SAGE I in the altitude range of 20-25 km [Kent et al., 1982].

Only two comparisons of stratospheric aerosol measurements from SAGE II with a lidar have been reported in the tropics, both qualitative. One of them has been done under stratospheric aerosol background conditions using data from Trivandrum, India (8.6°N, 77°E) for the first months of 1987 [Parameswaran et al., 1991]. The other comparison was conducted at Ahmedabad (23°N, 72.5°E) in April 1992 [Jayaraman et al., 1995], shortly after the Mount Pinatubo eruption.

The comparisons conducted in the tropics, as well as those conducted at midlatitudes, have some common features. They are characterized, in general, by only a few pairs of lidar-SAGE II selected profiles. They are conducted only at one wavelength, mostly under stratospheric aerosol background conditions or only for very few lidar-backscattering profiles measured during at least one and half year after the Mt. Pinatubo eruption. Estimates of the magnitude of the relative percent differences are provided together with visual estimates of the magnitude of the extinction or backscattering differences, obtained from the plots of coincident profiles. However, they lack statistics on the magnitude of such differences. In general all focused on the instrument comparability.

So far, the most extensive post-Pinatubo comparison between SAGE II and lidar aerosol extinction profiles used SAGE II aerosol extinction profiles at 0.525, and 1.020 μm from version 6.0 of the SAGE II data set, provided by the Langley Research Center [Zawodny et al., 2000]. The lidar dataset consists of the vertical profiles of lidar backscattering coefficients at 0.694 or 0.532 μm from five lidar stations (Table 4.4). Two sets of extinction-to-backscattering conversion coefficients were used for converting lidar backscatter profiles at 0.532 and 0.694 μm to SAGE II extinction profiles at 0.525 and 1.020 μm [Thomason and Osborn, 1992] or to the nearby wavelengths at 0.532 μm and 1.064 μm [Jäger and Deshler, 2002]. Absolute and percent differences between SAGE II - measured and lidar - derived aerosol extinction profiles were calculated for the set of coincident profiles at each lidar station. In addition the magnitude of the aerosol extinction variability was determined using both SAGE II sunset/sunrise coincident aerosol extinction profiles as well as lidar derived aerosol extinction profiles from consecutive days. Also the capability of using lidar derived aerosol extinction profiles for filling SAGE II measured aerosol extinction profiles gaps was demonstrated [Antuña et al., 2002; 2003].

Table 4.4: Lidar stations, with wavelength and vertical resolution of lidars, as well as number of coincident profiles.

<i>Station</i>	<i>Latitude</i>	<i>Longitude</i>	<i>λ in μm</i>	<i>Resolution</i>	<i>Coincident Profiles</i>
Mauna Loa	19.5°N	155.6°W	0.694	300 m	49
Camagüey	21.4°N	77.9°W	0.532	300 m	20
Hefei	31.3°N	117.2°E	0.532	600 m	55
Hampton	37.1°N	76.3°W	0.694	150 m	76
Haute Provence	43.9°N	5.7°E	0.532	300 m	178

Figures 4.54 and 4.55 show some SAGE II and lidar coincident profiles for Hampton and Mauna Loa during the first seven months after the Pinatubo eruption. Gaps in SAGE II

(blue profiles) are evident in several panels. Qualitatively, good agreement is obtained if one takes into account the great differences between the principles of measurement and sampling geometry of the two instruments. The preliminary analysis of the differences confirmed the existence of two periods after the eruption, according to the magnitude of the aerosols extinction variability [Chazette et al., 1995]. The quantitative analysis of the differences was conducted for each of those periods separately.

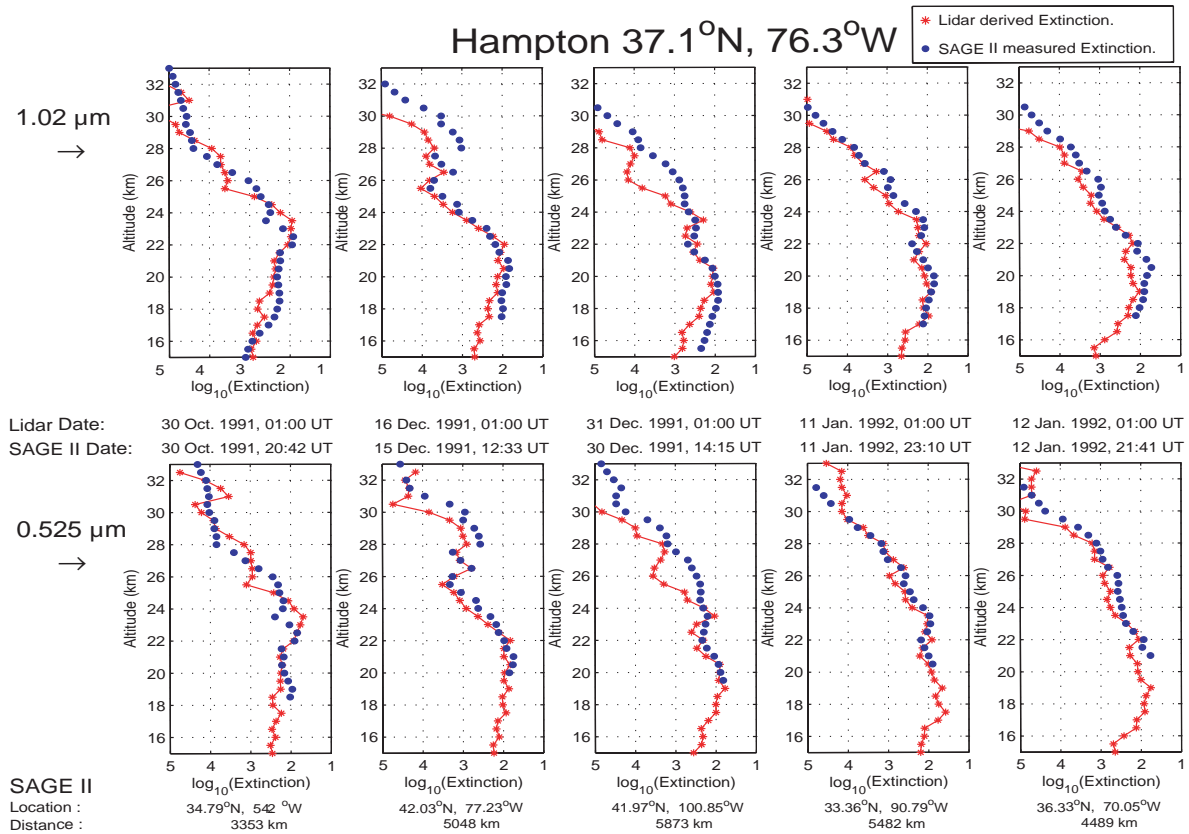


Figure 4.54: SAGE II (blue filled circles) and lidar (red stars) coincident profiles for Hampton during the first seven months after the Pinatubo eruption. Upper panel: 1.020 μm wavelength. Lower panel: 0.525 μm . Coefficients used for converting lidar backscatter profiles at 0.532 and 0.694 μm to SAGE II extinction profiles at 0.525 and 1.020 μm are from Thomason and Osborn [1992].

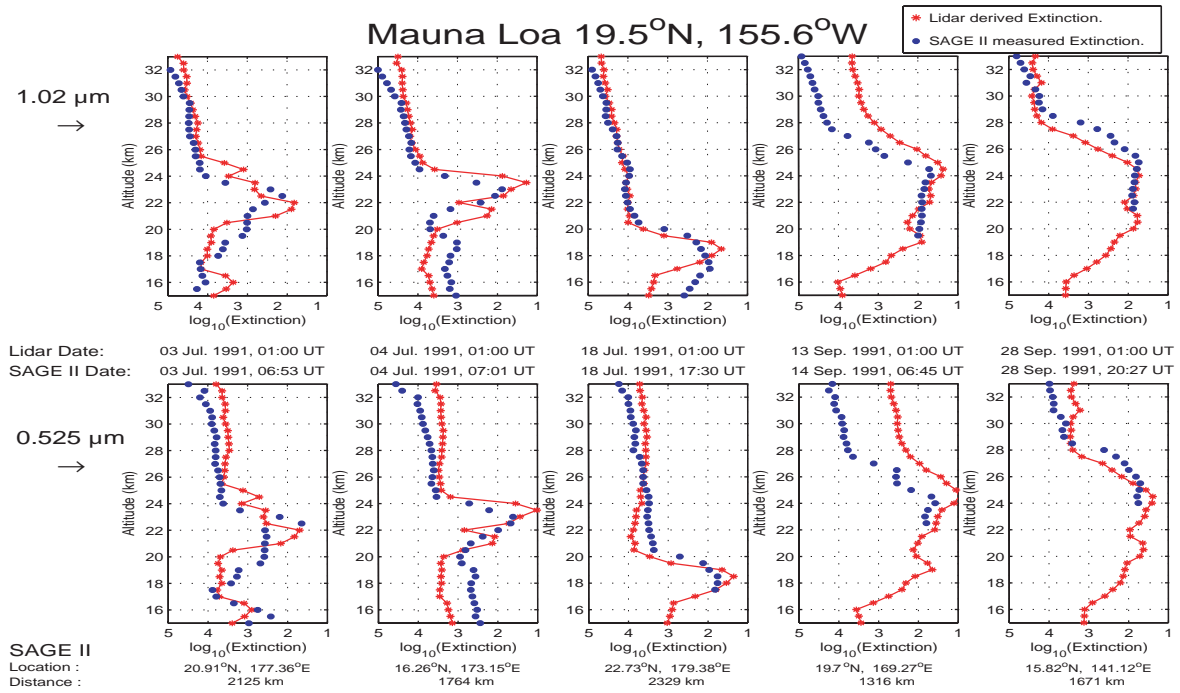


Figure 4.55: SAGE II (blue filled circles) and lidar (red stars) coincident profiles for Mauna Loa during the first seven months after the Pinatubo eruption. Upper panel: 1.020 μm wavelength. Lower panel: 0.525 μm. Coefficients used for converting lidar backscatter profiles at 0.532 and 0.694 μm to SAGE II extinction profiles at 0.525 and 1.020 μm are from Thomason and Osborn [1992].

Magnitudes of the absolute percent extinction differences are shown in Figure 4.56. The first period (Jul 1991 – Jan 1992) is characterized by larger mean percent differences, but they are lower in magnitude at Hampton than at Mauna Loa, because the cloud did not arrive at Hampton until 3 August 1991 [Osborn et al., 1995]. By that time, the initially highly non-homogeneous cloud had become more homogeneous after the settling of the volcanic ash and the mixing effect produced by wind transport. The mean percentage extinction differences do not show a peak in the lower part of the profiles. The vertically averaged mean percentage differences show a decrease of around 15% in the whole column from the first to second period. The second period coincides with significantly smaller peak scattering ratios, with smoother and less layered profiles [Osborn et al., 1995]. The differences are larger at Mauna Loa than at Hampton, because of the higher variability of the stratospheric cloud during its initial stage in low latitudes. As discussed in Antuña et al. [2002], the lidar-derived extinction is higher in general than that measured by SAGE II, except around 20 km. The maximum positive and negative differences are located around 20 and 23 km respectively. From 24 km to around 33 km and between 21 and 22 km the extinction derived from lidar is higher, but the opposite is true below 21 km.

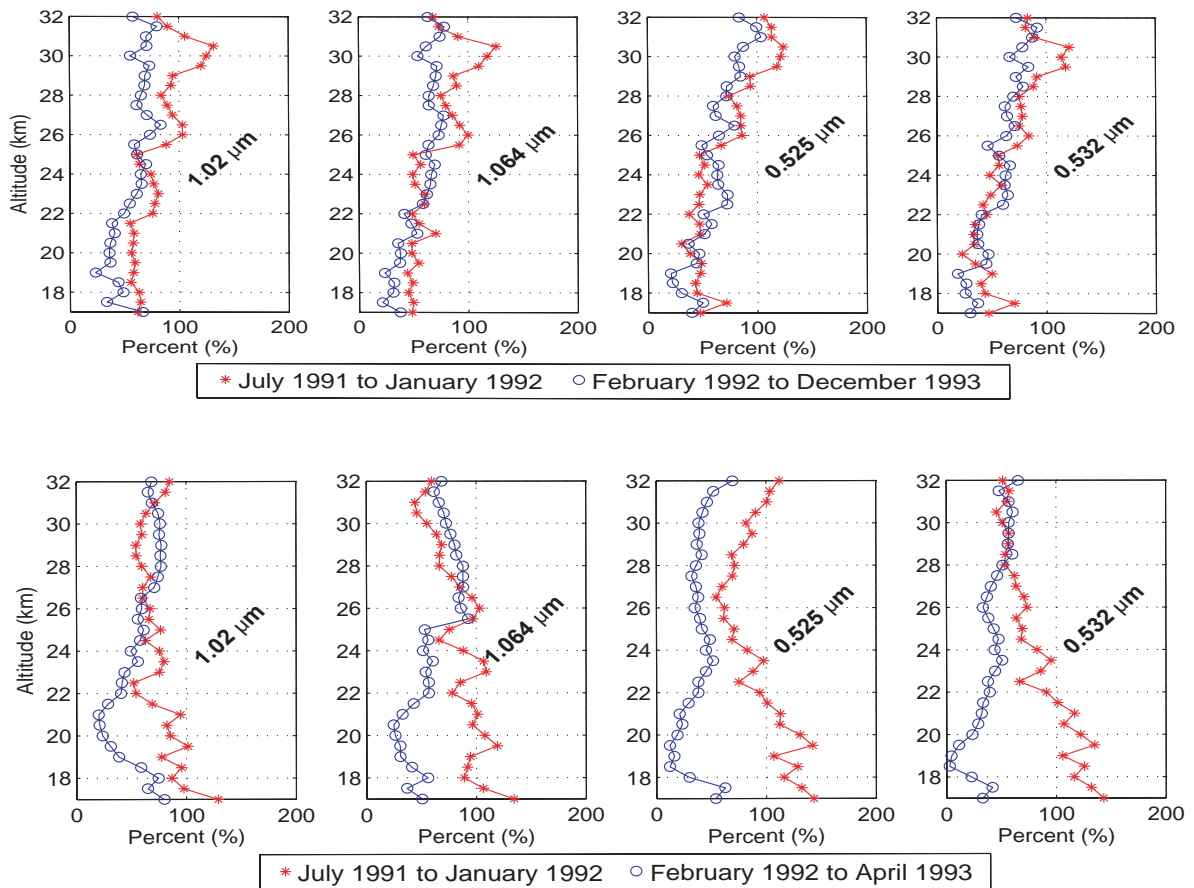


Figure 4.56: Mean absolute differences in % as function of altitude for Hampton (upper row) and Mauna Loa (lower row) between SAGE extinctions and lidar-derived extinctions (time windows indicated in upper right corner). Coefficients used for converting lidar backscatter profiles at 0.532 and 0.694 μm to SAGE II extinction profiles at 0.525 and 1.020 μm are from Thomason and Osborn [1992], those for 0.532 μm and 1.064 μm are from Jäger and Deshler [2002].

By comparing SAGE II sunset/sunrise coincident aerosol extinction profiles as well as one and two day consecutive lidar aerosol backscattering measurements, the magnitude of the time variability of aerosol extinction due to the Mt Pinatubo aerosol cloud has been obtained. That variability reached values between 50 and 150% absolute differences at the core of the cloud for the initial, heterogeneous period, for time lapses of 12 to 48 hours. The degree of agreement between SAGE II extinction profiles and lidar-derived extinction after the eruption is dominated by the magnitude of this variability [Antuña et al., 2003].

The test of the two sets of backscatter-to-extinction coefficients does not reveal appreciable differences since the magnitude of the differences associated with them is lower than the magnitude of the aerosol extinction variability [Antuña et al., 2003]. Before SAGE II - lidar data assimilations are used in stratospheric studies, one should carry out further comparisons between the aerosol extinction profiles measured by SAGE II and lidar derived aerosol extinction profiles, especially under background conditions.

4.5 Conclusions

In this chapter we have presented a fairly complete picture of the stratospheric aerosol. We have not included a number of interesting data sets, nevertheless, we believe that we have generated a representative picture of the stratospheric aerosol. We have included results from eight satellite borne instruments and a large number of other instruments, including both balloon borne and aircraft borne particle counters and ground based and aircraft borne lidar systems.

A significant amount of work was carried out to generate comparisons between the derived products of several instruments. This is difficult to do because the parameters measured by the various instruments differ; even in cases when the same physical quantity is studied, (as for example, extinction) it is usually observed at different wavelengths by different instruments.

The comparisons of the properties of the stratospheric aerosol as determined from the various instruments used in this assessment enable us to draw some general conclusions. First of all, it might be noted that the quality of the agreement is strongly dependent on the altitude and on time. Nevertheless, in general, the aerosol extinctions agree to within 20-60 %. This value depends on whether the comparison is direct (as for SAGE-POAM) or not (as for SAGE-HALOE where the comparison involves modeling and is dependent on the wavelength and assumptions on indices of refraction). Further issues are the coincidence criterion and the comparison methods.

Surface area densities do not agree as well. This is probably due to the differences between the retrieval algorithms and the fact that the various instruments are not sensitive to the same size range of the particles. In general, during periods of high aerosol loading there is agreement in the surface areas calculated from the data obtained from SAGE II, HALOE and the OPC. Disagreements are significantly greater during periods of low aerosol loading, for reasons that have not been clearly determined. It would seem that for periods of high aerosol loading, the calculated aerosol surface areas from any one of the instruments are probably appropriate for use in chemical and radiative studies. Surface areas obtained during periods of low aerosol loading should be treated with care. Finally, it must be noted that, for all measurements, inference of surface area density is carried out assuming a known composition (i.e. known refractive index) for the particles, leading to an additional uncertainty (bias) in the surface area.

In this chapter we have also presented a record of the stratospheric aerosol in which the gaps in the satellite record have been filled in by using lidar and other measurements. The assumptions made in the gap filling procedure have been carefully described. This generates a nearly complete record of the stratospheric aerosol for a period of almost 25 years.

CHAPTER 5

Non-Volcanic Stratospheric Aerosol Trends: 1971 – 2004

Lead Authors:

Terry Deshler
Richard Anderson-Sprecher

Authors:

John Barnes
Barclay Clemesha
Sophie Godin-Beekmann
Roy Grainger
David Hofmann
Horst Jäger
Steven Marsh
Mary Osborn
Dale Simonich

5.1 Introduction

The existence of persistent atmospheric aerosol after volcanic eruptions must have been apparent to careful observers from early times. The reddish diffraction ring around the sun following large volcanic eruptions was first described by Sereno Bishop nine days after the eruption of Krakatoa, in late August 1883, and led to the name Bishop's ring. Less certain is that early observers suspected that aerosol persisted in the stratosphere during volcanically quiescent periods. The first published report suggesting a persistent aerosol layer in the stratosphere used purple twilight observations [Gruner and Kleinert, 1927]. Quantitative observations characterizing the altitudes, sizes, masses, and aerosol compositions involved were first provided by balloonborne impactor measurements in the late 1950s [Junge et al., 1961]. Subsequent measurements by both aircraft- and balloon-borne impactors suggested the global distribution of stratospheric aerosol [Junge and Manson, 1961; Chagnon and Junge, 1961]. On a few occasions, in addition to the impactors which measured particles $> 0.1 \mu\text{m}$, Aitken particle counters were included on the balloon gondola. While the Aitken nuclei concentration decreased through the stratosphere, particles $> 0.1 \mu\text{m}$ had a maximum in concentration near 20 km, suggesting an aerosol source in this region [Junge et al., 1961]. These particles were large enough to create the purple twilight noted by early observers; however, recent work suggests that tropospheric aerosol must also contribute to the purple twilight in cases of a clean stratosphere [Lee and Hernandez-Andres, 2003].

Junge et al.'s measurements were at the end of an extended volcanic-free period [Stothers, 1996], but did not establish a baseline for stratospheric aerosol. Quantifying the global stratospheric aerosol burden, and describing the role of volcanic eruptions, required long term measurements which began in the early 1970s using balloonborne particle counters [Hofmann et al., 1975; Hofmann and Rosen, 1980; Hofmann, 1990]; lidar [Jäger, 2005; Osborn et al., 1995; DeFoor et al., 1992]; and in the late 1970s satellite instruments: SAM (Stratospheric Aerosol Measurements) II (1979-1994) [Pepin et al., 1977; Poole and Pitts, 1994], SAGE (1979-1981) (Stratospheric Aerosol and Gas Experiment) and SAGE II (1984-present) [McCormick et al., 1979, Chu et al., 1989; Thomason et al., 1997]. The impact of sulfur rich volcanic eruptions then became obvious and these have been the dominant source of stratospheric aerosol for the past 30 years. Within the last century the most recent 30-year period has been a relatively active volcanic period. Sato et al. [1993] and Stothers [1996], using solar and stellar extinction data, show that the previous 120 years was dominated by eight major eruptions. Four of these occurred between 1880 and 1910 and four since 1960. The long term measurements which began in the 1970s, have captured the complete cycle for three major eruptions with a global stratospheric impact: Fuego (14°N , October 1974, 3-6 Tg of aerosol), El Chichón (17°N , April 1982, 12 Tg) and Pinatubo (15°N , June 1991, 30 Tg) [McCormick et al., 1995]. Within this record there have been four periods when volcanic influences were at a minimum, 1974, 1978-1980, 1988-1991, and 1997 - present. Table 5.1 summarizes the volcanic activity between 1960 and 2003, including eruptions with stratospheric importance, generally volcano explosivity index (VEI) ≥ 4 [Carn et al., 2003; Newhall and Self, 1982; Simkin and Siebert, 1994; the web pages of the Smithsonian Global Volcanism Network; Schnetzler et al., 1997; Halmer et al., 2002]. Also in Table 5.1 the SO_2 and aerosol loading, if available, are included. Most SO_2 estimates are from Total Ozone Mapping Spectrometer (TOMS) data [Carn et al., 2003]. Missing estimates primarily occur prior to TOMS measurements. Missing estimates since 1979 indicate that information for that volcano was not available.

Table 5.1. Names, locations, dates, Volcano Explosivity Index (VEI) and SO₂ and aerosol loading, when available, for all stratospherically important eruptions 1960 - 2003 [Carn et al., 2003; Simkin and Siebert, 1994; Smithsonian Global Volcanism Network, Schnetzler et al., 1997; Halmer et al., 2002].

<i>Name</i>	<i>Lat</i>	<i>Long</i>	<i>Date</i>	<i>Year</i>	<i>VEI</i>	<i>Aerosol Loading</i>	
						SO ₂ (Mt)	Aerosol (Tg)
Agung	8.3 S	115.. E	Mar 17	1963	5		16-30
			May 16		4		
Shiveluch	56.6 N	161.4 E	Nov 12	1964	4+		
Taal	14.0 N	121.0 E	Sept 28	1965	4		
Kelut	7.9 S	112.3 E	April 26	1966	4		
Awu	3.7 N	125.. E	Aug 12	1966	4		
Fernandino	0.4 S	91.5 W	June 11	1968	4		
Tiatia	44.3 N	146.3 E	Jul 14	1973	4		
Fuego	14.5 N	90.9 W	Oct 14-17	1974	4		3-6
Tobalchik	55.8 N	160.3 E	Jul 6	1975	4+		
Augustine	59.4 N	153.4 W	Jan 22	1976	4		
Soufriere	13.3 N	61.2 W	Apr 14, 17	1979	3		
Sierra Negra	0.8 S	91.2 W	Nov 13	1979	3		
Saint Helens	46.2 N	122.2 W	May 18	1980	5	1.0	
Ulawun	5.0 S	151.3 E	Oct 6 & 7	1980	3		
Alaid	50.9 N	155.6 E	Apr 27-30	1981	4	1.1	
Pagan	18.1 N	145.8 E	May 15	1981	4	0.3	
Nyamuragira	1.4 S	29.2 E	Dec 25	1981	3		
El Chichón	17.0 N	93.2 W	Mar 28	1982	4	8.1	12
			Apr 4		5		
Galunggung	7.3 S	108.0 E	May 17	1982	4		
Colo	0.17 S	121.6 E	Jul 23	1983	4	0.2	
Nevado del Ruiz	4.90 N	75.3 W	Nov 13	1985	3		
Augustine	59.4 N	153.4 W	Mar 27	1986	4?	<0.05	
Nyamuragira	1.4 S	29.2 E	Jul 16	1986	4	0.8	
Chikurachki	50.3 N	155.. E	Nov 20	1986	4?		
Kelut	7.9 S	112.3 E	Feb 10	1990	4	<0.05	
Pinatubo	15.0 N	120.3 E	June 12	1991	6(5+)	17-20	30
Cerro Hudson	45.9 S	73.0 W	Dec 8	1991	5+	3.3	3
Spurr	61.3 N	152.3 W	Jun 27	1992	4	0.2	
Lascar	23.4 S	67.7 W	Apr 19	1993	4	0.4	
Rabaul	4.3 S	152.2 E	Sep 19	1994	4?	0.2	
Kliuchevskoi	56.1 N	160.6 E	Oct 1	1994	4 (3?)	0.1	
Shishaldin	54.8 N	164.0 W	Apr 19	1999	3		
Ulawun	5.05 S	151.3 E	Sep 29	2000	4	<0.05	
Shiveluch	56.6 N	161.4 E	May 22	2001	4?	0	

The VEI, developed by Newhall and Self [1982] to characterize volcanoes, is indicative of the volume of ejecta and the height of the eruption column. The height ranges for a VEI of 3, 4, and 5 are 3-15 km, 10-25 km, and >25 km. VEI alone, however, cannot predict stratospheric impact. Only sulfur rich volcanic eruptions provide the sulfur necessary to form sulfuric acid which then condenses with water into tiny droplets which have stratospheric lifetimes of years. Thus VEI must be coupled with the amount of sulfur ejected from the volcano. For example, Mt. St. Helens, with a VEI of 5.0, contained little sulfur (< 1 Mt), thus the stratosphere was not greatly perturbed by Mt. St. Helens [Robock, 1981], and, if not for El Chichón, stratospheric aerosol would have returned to background within a few years of the

eruption. Schnetzler et al. [1997] and Halmer et al. [2002] have coupled VEI with sulfur emissions to produce a volcanic SO₂ index which is more indicative of the stratospheric impact of a volcano.

The primary emphasis of long term stratospheric aerosol measurements has been on volcanic events. This is partly due to the significant impact large eruptions have on the stratosphere, to the increased signal they provide for instruments, to the dynamic nature of eruptions and their aftermath, to their global distribution, and to the fact that volcanic eruptions have dominated the signal for 20 of the past 30 years [Barnes and Hofmann, 2001; Deshler et al., 2003; Jäger, 2005]. In addition these eruptions are important for analyzing short-term regional and global effects on climate from enhanced stratospheric aerosol loading [Hansen et al., 1992; Dutton and Christy, 1992]. This analysis is important for climate models. Aerosols play an important role in radiative processes, thus influencing the consequences of changing trace gas concentrations in the atmosphere, and altering photolysis rates and the concentrations of trace gases, e.g. ozone, in the atmosphere. The focus here, however, is on long-term non-volcanic variations of stratospheric aerosol levels. Thus the emphasis shall be on levels present during years between major eruptions, rather than on temporary enhancements due to volcanic eruptions. Stratospheric aerosol during non-volcanic periods is referred to as background aerosol. This background aerosol level will be subject to various periodic perturbations, such as seasonal cycles, and long-term secular changes that govern the overall trend in the record. Identifying secular trends in the background aerosol is crucial to predict future aerosol levels.

The background stratospheric aerosol level is defined as that level at which fluctuations in the aerosol loading can no longer be ascribed to specific volcanic injections. It is anticipated that natural and anthropogenic emissions of sulfur, in the form of OCS and SO₂, will then be sufficient to maintain a population of stratospheric aerosol in quasi-steady state. During background periods measurements are expected to remain within variations expected due to measurement error, measurement frequency, and non-volcanic geophysical oscillations, such as induced by season or the quasi-biennial oscillation (QBO). Although serious questions may be raised about the extent to which inter-volcanic periods over the past 30 years have reached background, measurements during these periods provide the only information available to compare stratospheric aerosol in background periods. The best that can be provided is an objective analysis of these measurements. A further complication results from primarily the use of instruments sensitive to bulk aerosol quantities, such as extinction or backscatter, for long term measurements. Thus fine scale changes in aerosol size distribution may be difficult to observe.

The importance of possible changes in background stratospheric aerosol levels led to the analysis of each quiescent period as it appeared in the record. The first of these analyses [Hofmann and Rosen, 1980; Hofmann and Rosen, 1981; Sedlacek et al., 1983] compared the pre-Fuego and pre-El Chichón periods. Comparison of pre-El Chichón measurements with initial measurements of Junge et al. [1961], which were at the end of an extensive volcanic-free period, suggested a possible increase of about a factor of five in aerosol concentration at 20 km during the intervening 20 years leading Hofmann and Rosen [1980] to suggest an increase of 9% yr⁻¹ in aerosol mixing ratio for aerosol > 0.15 μm radius. Sedlacek et al. [1983], comparing globally distributed airborne filter samples during 1974 and 1979, pre-Fuego and pre-El Chichón, suggested a 6% yr⁻¹ increase in background stratospheric sulfur mass. Figure 5.1 presents the long term aerosol measurements from Laramie, Wyoming, initiated by Hofmann et al. [1975], with Junge's initial measurements at nearly the same latitude [Chagnon and Junge, 1961]. Based on instrumental characteristics, Junge et al. [1961]

suggest that their measurements collected particles $> 0.15 \mu\text{m}$ radius with a 55% efficiency. The integrals shown in Figure 5.1 account for this collection efficiency and assume the Wyoming measurements have a 100% collection efficiency, the case which would lead to the minimum difference between measurements, whereas the comparisons shown in Hofmann and Rosen [1980] assume the 55% collection efficiency applied to the Wyoming measurements as well. Applying a collection efficiency of 55% only to Junge et al.'s measurements would have reduced Hofmann and Rosen's [1980] estimate to 6 \% yr^{-1} , instead of 9 \% yr^{-1} . Comparing the average of Junge's measurements shown in Figure 5.1 with the minimum in column integrals observed in 1979 suggests a more conservative increase of 2 \% yr^{-1} , but as apparent from Figure 5.1, would have still suggested a significant increase in background aerosol.

During volcanically quiescent periods the sulfur for stratospheric aerosol arises from the transport of tropospheric OCS, SO_2 , and sulfate aerosol into the stratosphere. The fractional contributions of OCS, SO_2 , and sulfate aerosol to stratospheric aerosol are approximately 35, 25, and 40%, obtained by combining estimates from Weisenstein et al. [1997] and Pitari et al. [2002]. Between 1960 and 1980 anthropogenic emissions of SO_2 increased by over 2 \% yr^{-1} . Assuming that natural sources of SO_2 remained fairly constant at about 30% of total SO_2 emissions [Pitari et al., 2002], this implies an increase of $\sim 1.6 \text{ \% yr}^{-1}$ in SO_2 emissions between 1960 and 1980 [van Ardenne et al., 2001]. During this same period

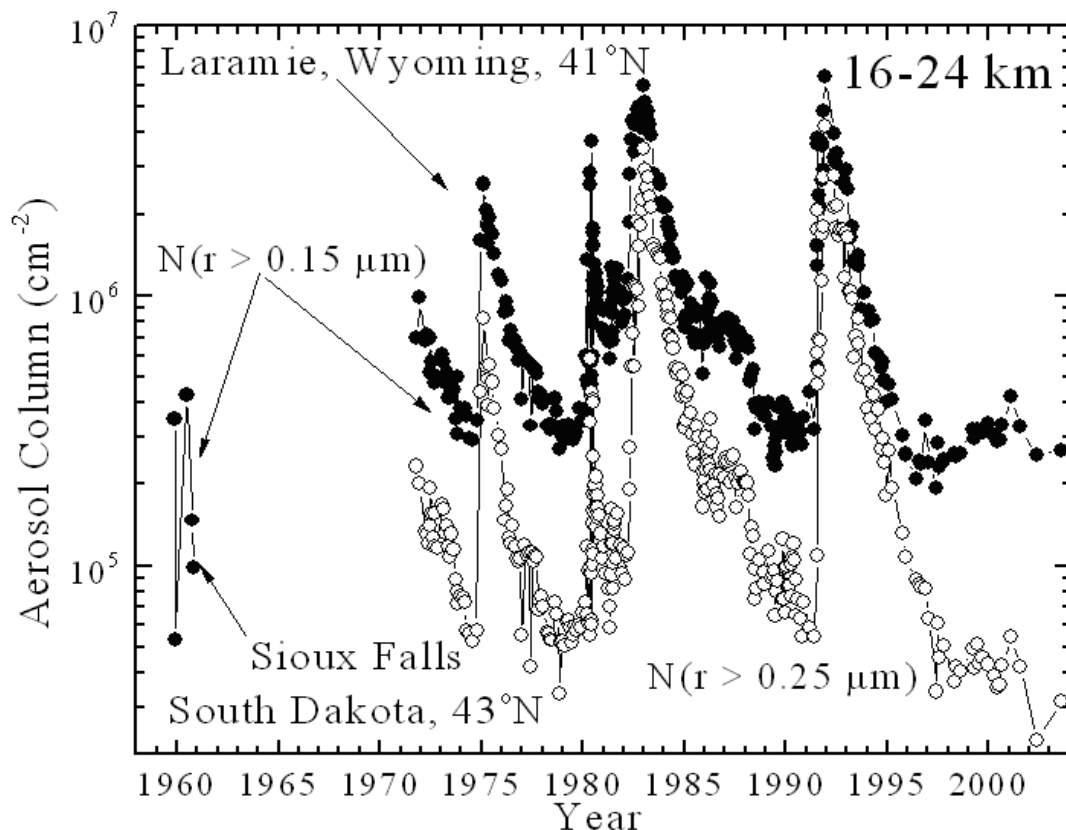


Figure 5.1. Aerosol columns, 16-24 km, for balloonborne in situ measurements of particles with radius $> 0.15 \mu\text{m}$ (filled circles) above Sioux Falls (43°N), 1959-1960 [Chagnon and Junge, 1961], and above Laramie (41°N), 1971-2003. Also included in the Laramie measurements are particles with radius $> 0.25 \mu\text{m}$ (open circles).

OCS increased at a rate of approximately $0.5\% \text{ yr}^{-1}$ [Montzka et al., 2004]. If these increases in SO_2 and OCS are weighted according to their fractional contribution to stratospheric aerosol, assuming that the contribution of sulfate aerosol remains constant, and that stratospheric aerosol responds linearly with respect to source gases, then the increase in stratospheric aerosol can be estimated. These estimates indicate an increase of $\sim 0.6\% \text{ yr}^{-1}$, well below Hoffman and Rosen's [1980] estimate of $9\% \text{ yr}^{-1}$ and even the more conservative estimate of $2\% \text{ yr}^{-1}$ indicated in Figure 5.1. A linear response to changes in source gases is consistent with sensitivity studies to changes in OCS performed with a 2-D model, see Weisenstein et al. [1997] and Chapter 6 of this report.

With the benefit of the present post Pinatubo Wyoming measurements of background aerosol, and considering the scatter in the initial measurements reported by Chagnon and Junge [1961], it appears that the initial measurements of Chagnon and Junge did not fully account for the sampling efficiency of the instrument, or the instrument was sensitive to particles somewhat larger than $0.15 \mu\text{m}$, a possibility considered earlier [Hofmann and Rosen, 1981], but dismissed. In any case it is clear from Figure 5.1 why initial measurements in the 1970 and early 1980 background periods were interpreted as indicating an aerosol increase [Hofmann and Rosen, 1980; 1981]. The aerosol increase observed, however, exceeds what may have been expected based on changes in aerosol source gases.

The question of changes in background stratospheric aerosol was revisited prior to the Pinatubo eruption. Hofmann [1990] compared measurements of aerosol mixing ratio for 0.15 and $0.25 \mu\text{m}$ radius thresholds during volcanically unperturbed periods in 1974, 1979, and 1989. No change was observed in the mixing ratio of $0.15 \mu\text{m}$ particles; however, there was a 50% increase in aerosol mixing ratio for particles $> 0.25 \mu\text{m}$ between 1979 and 1989. Based on this increase Hofmann estimated an increase in aerosol mass on the order of $5\% \text{ yr}^{-1}$ over the decade which is consistent with the earlier estimates of Hofmann and Rosen [1980] and Sedlacek et al. [1983]. A similar increase over the same time period was observed when SAGE I and II measurements were compared; however, Thomason et al. [1997] suggested that 1989 may not have been at true background level, due primarily to Nevado del Ruiz in 1985 and Nyamuragira in 1986. Thus they suggested the elevated aerosol was due to residual volcanic effects. OCS over this period increased by approximately 2% [Montzka et al., 2004] about half of the increase observed by Hofmann [1990].

Resolution of the questions raised by these studies had to wait for the third background period in the modern record, the present post Pinatubo period. Based on long term lidar measurements at Mauna Loa, Hawaii, Barnes and Hofmann [1997] suggest that the decay of aerosol loading following El Chichón and Pinatubo was influenced by the phase of the QBO in tropical stratospheric winds (also evident in the Garmisch lidar data, Jäger [2005]) and that integrated aerosol backscatter in 1995 was below any previous observation at Mauna Loa. Hayashida and Horikawa [2001] used SAGE II extinction measurements to derive Ångström parameters and concluded that the pre-Pinatubo period was still influenced by volcanic eruptions from the mid 1980s and cannot be considered a real background period. Barnes and Hofmann [2001] used the present background period, extending from 1996, to demonstrate variability correlated with the phase of the QBO, with implications for the source of background stratospheric aerosol. Thirty year records of in situ [Deshler et al., 2003] and remote [Jäger, 2005] mid-latitude measurements suggest that stratospheric aerosol in the present, post-Pinatubo period is at or below any previous background period since 1970. These analyses of the post-Pinatubo aerosol suggest, in contrast to studies of earlier background periods, no long term increase in stratospheric background aerosol.

The purpose here is to examine all long term stratospheric aerosol measurements for trends in the background aerosol. This requires records which span at least two of the four volcanically quiescent periods in the modern aerosol record, limiting the data set to the six longest stratospheric aerosol measurement records available. These are: 1) in situ aerosol concentration measurements at 0.15 and 0.25 μm radius from Laramie, Wyoming, USA (1971-2003, 41°N); remote lidar backscatter measurements from: 2) São José dos Campos, Brazil (1972-2003, 23°S), 3) Mauna Loa, Hawaii, USA (1974-2003, 20°N), 4) Hampton, Virginia, USA (1974-2002, 37°N), 5) Garmisch-Partenkirchen, Germany (1976-2002, 48°N); and 6) remote satellite extinction measurements from SAM II (1979-1994), SAGE I (1979-1981) and SAGE II (1984-2003). For each of these measurement platforms the fundamental measurements will be described and then compared during the volcanically quiescent periods, taking into account instrumental or operational changes in the measurements.

5.2 Fundamental measurements

5.2.1 In situ measurements

Stratospheric aerosol measurements at Laramie, Wyoming, began in 1971 using an optical particle counter (OPC) initially developed by Rosen [1964]. The instrument measures the intensity of scattered white light at 25° in the forward direction from single particles passing through the light beam which is larger than the air sample stream. Mie theory is used to determine aerosol size from the amount of scattered light. Initial measurements in the 1970s consisted of measurements of the concentration of particles with radius ≥ 0.15 and $0.25 \mu\text{m}$ at a sample flow rate of 1 liter min^{-1} [Pinnick and Hofmann, 1973; Hofmann et al., 1975]. In 1989, the OPC was modified to make measurements for particles $> 0.4 \mu\text{m}$, to increase the number of sizes measured, and to decrease the minimum concentration measurable [Hofmann and Deshler, 1991]. The scattering angle of the detector axis was increased from 25 to 40° and the air sample flow rate increased from 1 to 10 liters min^{-1} , with appropriate changes in inlet design to maintain roughly isokinetic sampling. This new scattering angle allowed unambiguous detection of particles throughout the size range 0.15 - 10.0 μm . After calibration flights in Laramie to insure that the measurements at 0.15 and 0.25 μm radius are, within measurement limits, the same for counters with scattering angles at 25 and 40°, the new OPC replaced the old OPC for regular flights in Laramie beginning in 1991 [Deshler et al., 1993; Deshler et al., 2003].

A more complete description of the instrument and discussion of error sources is provided in Deshler et al. [2003] and in Chapter 3. Here the primary error sources are summarized. Sizing errors are 10% at 0.15 and 0.25 μm and result primarily from pulse broadening by photo multiplier tubes. Errors in concentrations are controlled by Poisson counting statistics or a precision of $\pm 10\%$ when Poisson counting statistics are not a factor. Poisson uncertainties lead to concentration uncertainties of 85, 25, and 8% for concentrations of 0.01, 0.1, and 1.0 cm^{-3} at a sample rate of 1.0 liter min^{-1} and concentrations of 0.001, 0.01, 0.1 cm^{-3} at 10 liters min^{-1} .

5.2.2 Remote lidar measurements

The first lidar (light detection and ranging) measurements of stratospheric aerosol were completed shortly after Junge et al.'s initial measurements [Fiocco and Grams, 1964]. Lidars provide remote, vertically resolved measurements of atmospheric backscatter at one or more wavelengths. Lidar sites investigating stratospheric aerosols now range in latitude from 90°S

to 80°N, with a number of sites in northern mid latitudes, and a few stations in the sub tropics and southern mid latitudes. The standard measurement from any lidar is backscatter which is the fraction of incident light intensity returned at 180° to the incident light pulse. The backscatter is presented as fraction per steradian per meter of scattering medium. Atmospheric backscatter arises from both molecular (Rayleigh) and aerosol (Mie) scattering. Backscatter also arises from non-spherical particles which do not follow Mie theory (e.g. ice particles, or fresh volcanic ash particles). To obtain aerosol profiles from a lidar requires accounting for three factors which affect the backscattered light received by the lidar telescope: 1) two way light extinction, 2) molecular backscatter, and 3) instrument normalization [e.g. Russell and Hake, 1977]. Molecular backscatter and extinction is typically calculated from pressure/temperature profiles provided by a nearby radiosonde station. In an aerosol free atmosphere, and with a perfectly calibrated lidar, molecular backscatter would coincide with the lidar backscattering measured.

Uncertainties in lidar measurements arise from two-way extinction of the lidar signal, the difficulty of determining an aerosol free region for normalization, signal induced noise, and from detector non-linearity for analog detection systems, or pulse overlapping for photon counting systems. For volcanic conditions there is a large aerosol signal, well above the molecular signal, resulting in small uncertainties. For quiescent conditions aerosol backscatter is less than 5% of molecular scattering, requiring longer integration times. The two-way particle extinction of the lidar signal becomes significant during periods of high aerosol loading but is reduced considerably for measurements during background periods [Simonich and Clemesha, 1989]. The purely instrumental errors from effects such as signal-induced noise can be reduced significantly by careful instrumental design. Long-term calibration problems do not arise because, for each measurement, aerosol back-scatter is determined only after the lidar signal is forced to match that expected from a purely molecular atmosphere at the altitude of normalization. The main source of error is in uncertainties in the molecular profile corresponding to a given lidar profile. The sources of molecular profiles and the estimated precision are given below for each of the lidar series used in this study.

The four lidar records included here are the only multi-decadal lidar records available. They are based at São José dos Campos, Brazil (23.2°S, 45.9°W), Mauna Loa, Hawaii (19.5°N, 155.6°W), Hampton, Virginia (37.1°N, 76.3°W), and Garmisch-Partenkirchen, Germany (47.5°N, 11.1°E). To reduce variations in the measurements due to variations in altitude and thickness of the aerosol layer, the quantity used for long time series comparisons is the vertically integrated backscatter coefficient with units of sr^{-1} . Each lidar will be compared to its own record to assess changes during background periods, but for interest the two tropical/sub tropical and mid latitude lidars are also compared to each other.

The São José dos Campos measurements use the sodium D₂ line at 589 nm and began in 1972. The primary focus of these measurements has been on the atmospheric sodium layer; however, measurements of the stratospheric aerosol content are also available (Clemesha and Simonich, 1978; Simonich and Clemesha, 1997). The wavelength used for the measurements has not changed during the period, although there have been major changes in the laser and improvements in the electronics. Since this site is in the sub tropics, tropopause height fluctuations and variations in the atmospheric density profile are minor. The molecular density profile used is an annual average derived from rawinsonde measurements. An iterative procedure is used to account for aerosol extinction. Ozone absorption is negligible. The measurements presented here represent monthly averages of integrated aerosol backscatter from 17 to 35 km. Error estimates on the integrated profiles are $\pm 5\%$. The number of

measurements per month is dependent on season, more in winter, but averages about 3.7 days per month.

The Mauna Loa, Hawaii, measurements, using a ruby laser, 694 nm, began in 1974 with the main focus on stratospheric aerosol [DeFoor et al., 1992; Barnes and Hofmann, 1997; 2001]. In 1994 a new lidar was built using a Nd:YAG laser measuring backscatter at both the 532-nm harmonic and the 1064-nm fundamental. For data continuity, the 532-nm measurements are converted to 694 nm for easy comparison with the early measurements. There was an overlapping period of about a year (40 observations) during which the ruby lidar backscatter and the Nd:YAG lidar backscatter at both wavelengths were measured. The average absolute backscatter of the ruby lidar agreed to within 2% of the Nd:YAG backscatter interpolated to 694 nm from the measurements at 532 and 1064 nm. The conversion factor obtained from the interpolation is used for the entire 532 nm data set. Errors on the integrated backscatter range from ± 15 to $> \pm 30\%$ for the ruby measurements, depending on aerosol load. These errors are reduced to approximately $\pm 6\%$ for the 532-nm measurements. Since this is another tropical station tropopause fluctuations are minor and the altitude interval for backscatter calculation can be fixed. In this case it is 15.8 to 33 km. Molecular density is obtained from a model for the Ruby lidar analysis and from the nearest radiosonde site (Hilo, Hawaii) for the Nd:YAG lidar.

The Hampton, Virginia, measurements also use a ruby laser, began in 1974, and are focused on stratospheric aerosol [Fuller et al., 1988; Woods et al., 1994; Osborn et al., 1995]. Although there have been incremental improvements in the system, the fundamental operating wavelength and measurement principles have not changed. For this mid latitude station the integration interval is from the tropopause to 30 km. Errors range from 15 - 50% during stratospheric background periods reducing to 5% for measurements following large eruptions. Molecular densities are obtained from a radiosonde station 120 km to the northeast.

The Garmisch-Partenkirchen, Germany, measurements began in 1976 with a ruby laser and are also focused on stratospheric aerosol [Reiter et al., 1979; Jäger, 2005]. There was an interruption in the measurements from May 1990 to March 1991 to convert the lidar to a Nd:YAG system. Measurements beginning in 1991 use the 532-nm harmonic of the Nd:YAG laser, and there was no overlap of the two lidars. As in the case of Mauna Loa, all 532-nm measurements are converted to 694 nm to easily compare with the earlier measurements. The conversion is based on height and time resolved wavelength dependencies which are calculated from particle size distributions applying Mie calculations [Jäger and Deshler, 2002 and 2003]. The size distribution data are derived from monthly measurements with balloonborne optical particle counters at Laramie, Wyoming [Deshler et al., 1993, 2003]. Backscatter integrations cover the altitude range, tropopause + 1 km to profile top. Error estimates range from 10 to 50%, depending on stratospheric aerosol load, for the ruby measurements. These errors are reduced by about half for the 532-nm measurements. Molecular density is obtained from a radiosonde station at Munich, 100 km to the north. Iteration is used to account for aerosol extinction.

5.2.3 Remote satellite measurements

The first satellite based aerosol measurement was completed in 1975 using a photometer pointed at the sun by the astronaut as the earth's limb passed in front of the sun [Pepin et al., 1977]. This led to the first regular satellite measurements of stratospheric aerosol using a single wavelength photometer measuring solar extinction during 15 sunrises and sunsets by the satellite per day, SAM II [McCormick et al., 1979; 1981; Russell et al., 1981]. The

multiwavelength SAGE and SAGE II instruments [Mauldin et al., 1985] followed close behind. These instruments are self calibrating since prior to or after each solar occultation the photometer measures the direct solar transmission without atmospheric extinction. Thus the measured extinction through the atmosphere is truly relative to the exo-atmospheric solar transmission with all instrument artifacts removed.

SAGE II measures solar transmission through the atmosphere with a spectral radiometer. To convert this to aerosol extinction the influence of gas molecules along the tangent line of sight must be removed, as well as gas and aerosol extinction from altitudes above the measurement altitude. The extinction at upper altitudes influences a measurement at the leading and trailing boundaries along the line of sight due to the spherical geometry. Removing these contributions is known as the onion peeling method. The inversion of the SAGE II solar occultation measurements to provide aerosol extinction is described by [Chu et al., 1989]. The effect of subtle changes in the SAGE II instrument are carefully monitored and are routinely evaluated for impact on data products including ozone and aerosol extinction [Thomason and Burton, 2005]. The 1020-nm aerosol extinction exhibits extremely limited sensitivity to changes in instrument characteristics like unobscured solar intensity measurements, dark current, and mirror reflectivity. The 525-nm aerosol channel is slightly more sensitive to such changes, but even there, the possible drift over the lifetime of the instrument is < 1%. Since SAGE II uses National Center for Environmental Protection (NCEP) estimates of molecular density for the computation of the molecular contribution to the line-of-sight transmission, a long-term drift between NCEP temperatures and the real atmosphere could introduce a drift of a few percent over the lifetime of the instrument. There has been a number of SAGE II validation and comparison efforts [Russell et al., 1984; Osborn et al., 1989; Oberbeck et al., 1989; Russell and McCormick, 1989; Hervig and Deshler, 2002]. As the understanding of the instrument performance has evolved a number of revisions of the SAGE II data have been provided; however, for our purposes the revisions are not critical. For any one revision the same data inversion is applied to all past measurements, thus the relative values of extinction over a 20 year period will stay the same even though the absolute values may change from one revision to another.

Of the eleven instruments deployed on satellites in the past 30 years which include stratospheric aerosol measurements, only SAGE II has a record long enough to consider for our purposes. This record can be extended somewhat by SAGE I. SAM II measurements span 12 years, 1979-1991, at high latitudes, 72-83° N/S [Poole and Pitts, 1994]. Although SAM II measurements are not strongly affected by volcanic eruptions, they have a strong annual cycle and wintertime measurements are influenced by polar stratospheric clouds. This coupled with the relatively short record limited our interest in SAM II to a simple inspection of the measurements, which does not show any clear temporal tendency. Only the SAGE II record was considered of sufficient length to be evaluated for trends.

5.3 Measurements

For the quantitative comparison of volcanically quiescent periods, the primary measurement from each instrument will be used. The measurements have been checked to be cloud and tropospheric aerosol free and are at latitudes $\leq 50^\circ$, thus will not be perturbed by polar stratospheric clouds. The screening is done using the local tropopause at each sampling site to determine the base of measurements to be included and relying on individual lidar and in situ investigators to insure no anomalous stratospheric cirrus are included. In fact these are extremely rare. For SAGE II the data selected for analysis were limited to measurements 2 km

above the SAGE II calculated tropopause, and the SAGE II extinctions were checked spectrally for clouds.

For the in situ measurements approximately monthly profiles of aerosol concentration for particles $\geq 0.15, 0.25 \mu\text{m}$ are integrated over altitude columns varying from 5 to 15 km. Typical tropopause heights at Laramie are 10-12 km extending to 15 km in the summer. Column integrals from 15-20 and 20-25 km are presented in Figure 5.2. Global SO_2 emissions since 1970 are shown in Figure 5.2b, the 1970-1990 estimates are from van Ardenne et al. [2001], while the 2000 SO_2 emissions are estimated based on extrapolating the 1990 estimate with a $-2\% \text{ yr}^{-1}$ trend [Hicks et al., 2002]. Model estimates of aerosol during background periods for one year are also shown in Figure 5.2. Each model estimate, covering one year, is shown between 2001 and 2003. The model results are from one 3-D [Timmreck, 2001] and one 2-D [Weisenstein et al., 1997] model. The models, described in detail in Chapter 6, calculate aerosol particle densities in 35 or more bins from 0.001 to $2.58 \mu\text{m}$ as functions of latitude, altitude, and season. For the 20-25 km integral the two model estimates are $\sim 50\%$ above the measurements. The two models disagree on the $0.25 \mu\text{m}$ size. For 15-20 km both models agree, but overestimate the in situ concentration measurements by a factor of 3.

In Figure 5.2, the $0.15 \mu\text{m}$ column integrals reach a plateau between 1.5 and $2.0 \times 10^5 \text{ cm}^{-2}$ at both altitude intervals for the three background periods, while the $0.25 \mu\text{m}$ measurements show a bit more variation, remaining elevated in 1990 - 1991 compared to 1979 and 1997, particularly between 15 and 20 km. The $0.25 \mu\text{m}$ observations prior to Pinatubo were the reason for Hofmann's [1990] estimate of a $5\% \text{ yr}^{-1}$ increase in sulfur mass between 1979 and 1989.

The final measurements in 2002 and 2003 show striking variations, but suffer from a sampling frequency reduced to once per year. The particularly low measurement in 2002, 20-25 km, was checked carefully and was confirmed by two independent simultaneous measurements at $0.25 \mu\text{m}$. Thirty day isentropic back trajectories at 570 and 690 K (~ 24 and 27 km) do not provide any useful insight. At 570 K the air passed through high latitudes, circulated in the central Pacific for ~ 10 days, and then moved eastward, nearly zonally, to Wyoming. At 690 K, the air meandered in the central Pacific, passed zonally to western Kansas, and then, in the final 10 days, circulated anticyclonically southward to New Mexico and northward to Wyoming. The SAGE II data during this period do not show any corroborating areas of clean air, nor are there any significant changes in the variance of the SAGE extinction measurements. Thus there are no simple explanations for this observation of surprisingly low concentrations at $0.25 \mu\text{m}$ between 20 and 25 km.

Histories for the integrated backscatter from the tropical and mid latitude lidars are shown in Figure 5.3. The tropical lidars use an integration beginning at 16-17 km whereas the mid latitude lidars use the tropopause or tropopause + 1 km as a beginning. Integrations extend to above 30 km. Both 2-D and 3-D model estimates of aerosol size distributions were used, along with Mie theory, to estimate integrated backscatter over one year in background conditions. These estimates for the lidar locations and wavelengths are shown between 2003 and 2005 in Figure 5.3.

The extremely low São José measurements prior to 1975 have been compared to northern hemisphere measurements in the same time period [Clemesha and Simonich, 1978]. The São José 20 km aerosol backscatter, β_a , was about half that measured in the northern hemisphere

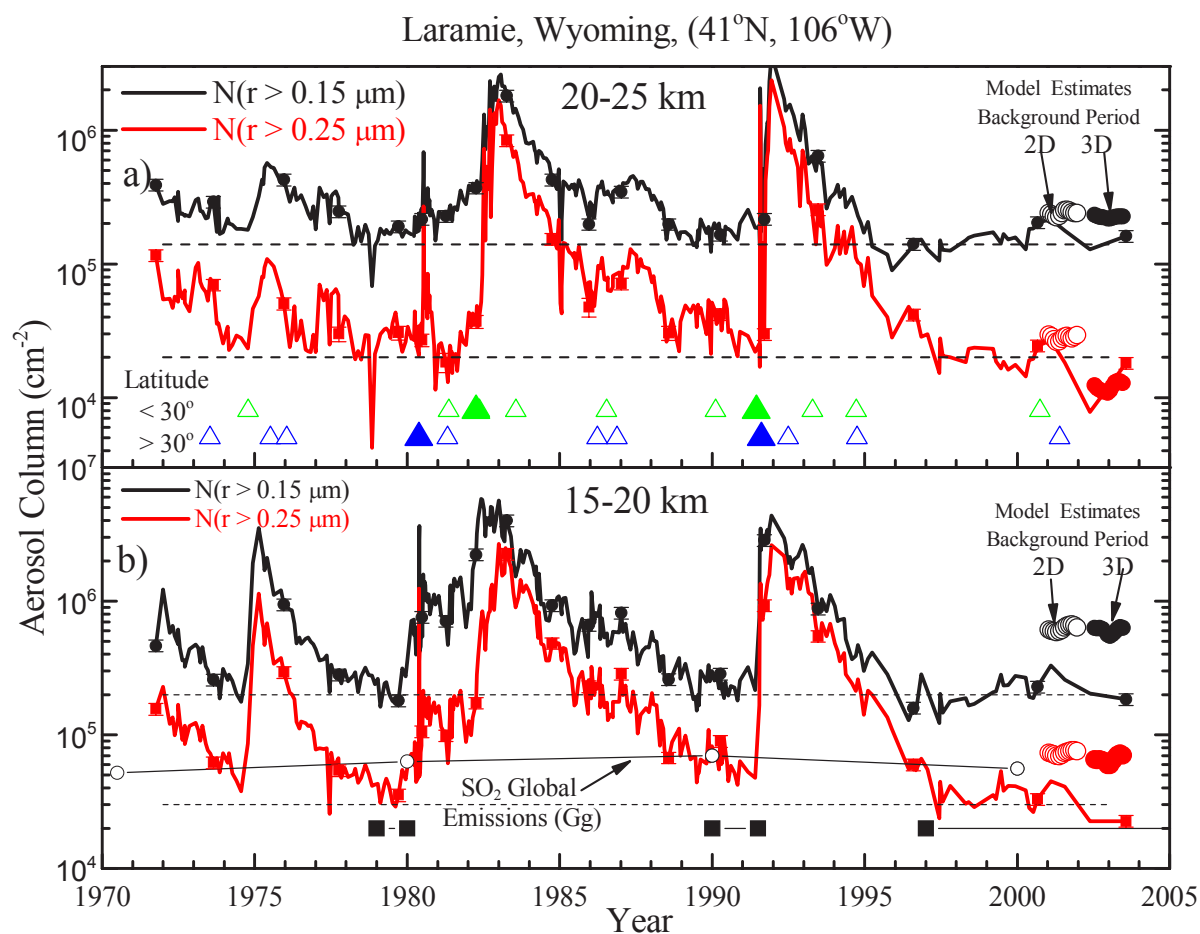


Figure 5.2. History of column integrals of aerosol number for particles with radii > 0.15 and > 0.25 μm from in situ measurements above Laramie, Wyoming, USA. The measurements represent about 340 individual aerosol profiles. The error bars on the occasional measurement represent the counting error of the measurement and rarely exceed the size of the data symbol. a) 20-25 km, b) 15-20 km. The dashed lines are horizontal and are meant only to aid the reader. The times of the most significant volcanic eruptions during the period are indicated with triangles in a), separated into those eruptions at latitudes less (upper symbol) and greater (lower symbol) than 30° . Eruptions with VEI of 5 (large closed symbol) and 4 (small open symbol) are shown. Names of the eruptions are listed in Table 1. Global emissions of SO_2 (Gg of S) are shown in b) for 1970-1990 [van Aardenne et al., 2001]. The scale for aerosol column also applies for Gg of sulfur. The 2000 estimate is based on a 20% decrease since 1990. The regions bounded by boxes in the bottom of a) and b) represent investigator determined background periods. Estimates from a 2-D (open symbols) and 3-D (closed symbols) model of background aerosol levels over one year are shown between 2000 and 2003 in both a) and b).

in 1973 using an airborne lidar operating at nearly the same wavelength [Fernald and Schuster, 1977]. Better agreement was found when β_a from São José was compared with β_a calculated from in situ aerosol measurements at 41°N in the same time period [Pinnick et al., 1976]. Only the Hampton, Virginia, lidar measurements extend into 1974, and these are in general quantitative agreement with the upper range of the early São José measurements. The suggestion from the São José measurements, of the lowest aerosol loading in the record prior to 1975, is not, however, corroborated by similarly low in situ measurements, Figure 5.2. This

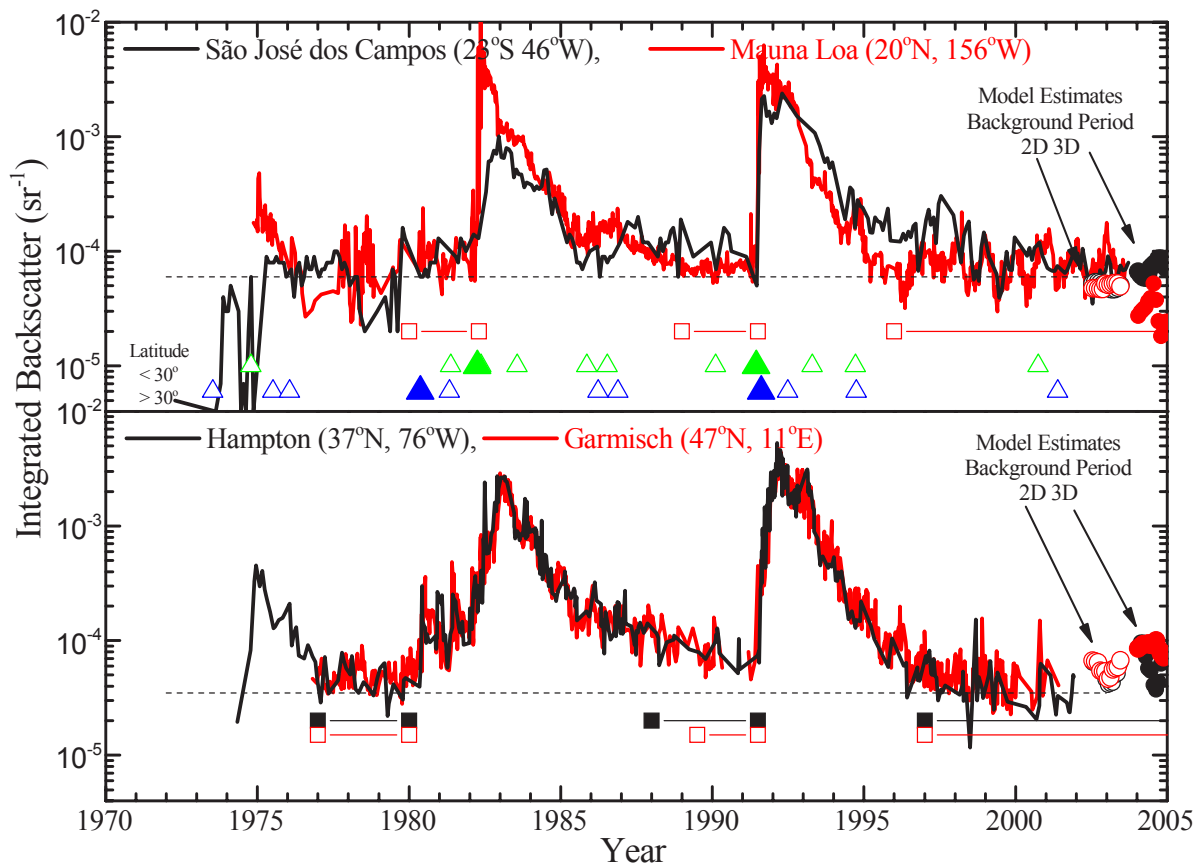


Figure 5.3. History of integrated backscatter from two tropical sites (São José dos Campos and Mauna Loa) and two mid latitude sites (Hampton and Garmisch). The wavelengths for all measurements are 694 nm except for São José which is at 589 nm. Top panel: São José dos Campos, Brazil, integration from 17 - 35 km, and Mauna Loa, Hawaii, USA, integration from 15.8 - 33 km. Bottom panel: Hampton, Virginia, USA, integration from tropopause to 30 km, and Garmisch-Partenkirchen, Germany, integration from tropopause+1 km to layer top. The dashed lines are horizontal and are meant only to aid the reader. The times of the most significant volcanic eruptions during the period are indicated in the top panel with triangles, separated into those eruptions at latitudes less (upper symbol) and greater (lower symbol) than 30°. Eruptions with VEI of 5 (large closed symbol) and 4 (small open symbol) are shown. Names of the eruptions are listed in Table 1. Error estimates range from 5 to 50% and are somewhat dependent on the aerosol load. The regions bounded by squares in the bottom both panels represent investigator determined background periods for Mauna Loa, Hampton, and Garmisch. Results from two model (2-D, open symbols, and 3-D, closed symbols) estimates for integrated backscatter at 694 nm in one year of background conditions are shown between 2003 and 2005 for the lidar locations.

difference may be partly explained if the early São José measurements were biased low due to an undetected problem with the instrument in use at that time, or if there was a hemispheric difference in aerosol loading in 1974. Clemesha and Simonich [1978] suggest the Fuego aerosol did not appear in the southern hemisphere until April 1975 due to the inhibition of eddy transport in 1974 by the meridional circulation in northern winter. Even with this inhibition, there is, however, some suggestion of Fuego aerosol at São José in 1973. Although the early integrated backscattering is below the post-Fuego period, there is an aerosol increase

in late 1973, following the early 1973 Fuego eruption, and again in early 1975, following the late 1974 Fuego eruption, which appears to be the largest of the three eruptions.

The São José measurements in the early 1980s, prior to El Chichón, are in agreement with the Mauna Loa measurements. São José shows a smaller peak and faster decay after El Chichón, but similar peak backscatter and slower decay following Pinatubo. São José measurements are slightly elevated in the background period prior to Pinatubo compared to Mauna Loa measurements and to São José measurements in the period following Pinatubo. The similarity of the fluctuations between São José and Mauna Loa in the 1998 - 2002 period is striking. From the Mauna Loa lidar, the pre- and post-Pinatubo periods are similar, although the variation of the signal in the pre-Pinatubo period is much less than post Pinatubo variability. For the São José measurements the pre- and post-Pinatubo periods are both characterized by significant fluctuations.

The mid latitude lidars are in quite good agreement throughout the record. The peak integrated backscatter following Pinatubo and El Chichón are similar as are the decay rates. The relaxation of the stratosphere following El Chichón is delayed by several minor eruptions. This feature is also apparent in the in situ measurements particularly in the 15-20 km column. Considering the background periods, both lidars agree suggesting that the pre-El Chichón and post-Pinatubo periods are similar, whereas the pre-Pinatubo period is elevated. This again is similar to the in situ measurements particularly for the 0.25 μm measurements between 15 and 20 km. This correspondence between in situ 0.25 μm measurements and integrated lidar backscatter has been noted before [Jäger and Hofmann, 1991; Hofmann et al., 2003].

Comparisons between measurements and models, and between the 2- and 3-D models, are varied. Both model estimates for São José agree with each other and the measurements. For Mauna Loa the 2-D model agrees with measurements while the 3-D model is a factor of two lower. For the mid latitudes the model estimates are self consistent, but between a factor of 1.2 - 1.8 above measurements. This is consistent in direction, if not magnitude, with the model comparisons with in situ measurements. The model simulations in both Figures 5.2 and 5.3 are for a generic background year. The slightly different placements in the two figures are dictated by the space available in the figure.

Optical depths for zonally averaged SAGE and SAGE II aerosol extinctions at 1020 nm over the period 1984 - 2001 are shown in Figure 5.4. The data are zonal averages binned in 10° latitude intervals at the Equator, $\pm 20^\circ$ and $\pm 40^\circ$. The base altitude, 18 km, was chosen to remove any influence of tropospheric aerosol or clouds. These figures show the decaying volcanic signal of El Chichón followed by the strong increase then decay in optical depth following the eruption of Mt. Pinatubo. The optical depth decreases with increasing latitude due to the fact that tropopause height decreases away from the equator, and background aerosol loading decreases with altitude above the tropopause. Thus optical depth for a constant altitude range will decrease with latitude. The difference between the Northern and Southern Hemispheres is within the random uncertainty which is typically $\pm 20\%$. The major exceptions to this are during the Pinatubo peak, for altitudes from 24 to 29 km, when aerosol was still forming, and in 1990 when Kelut is primarily only seen in the southern hemisphere. The difference following Pinatubo is most likely explained by stronger transport into the winter hemisphere from the tropics.

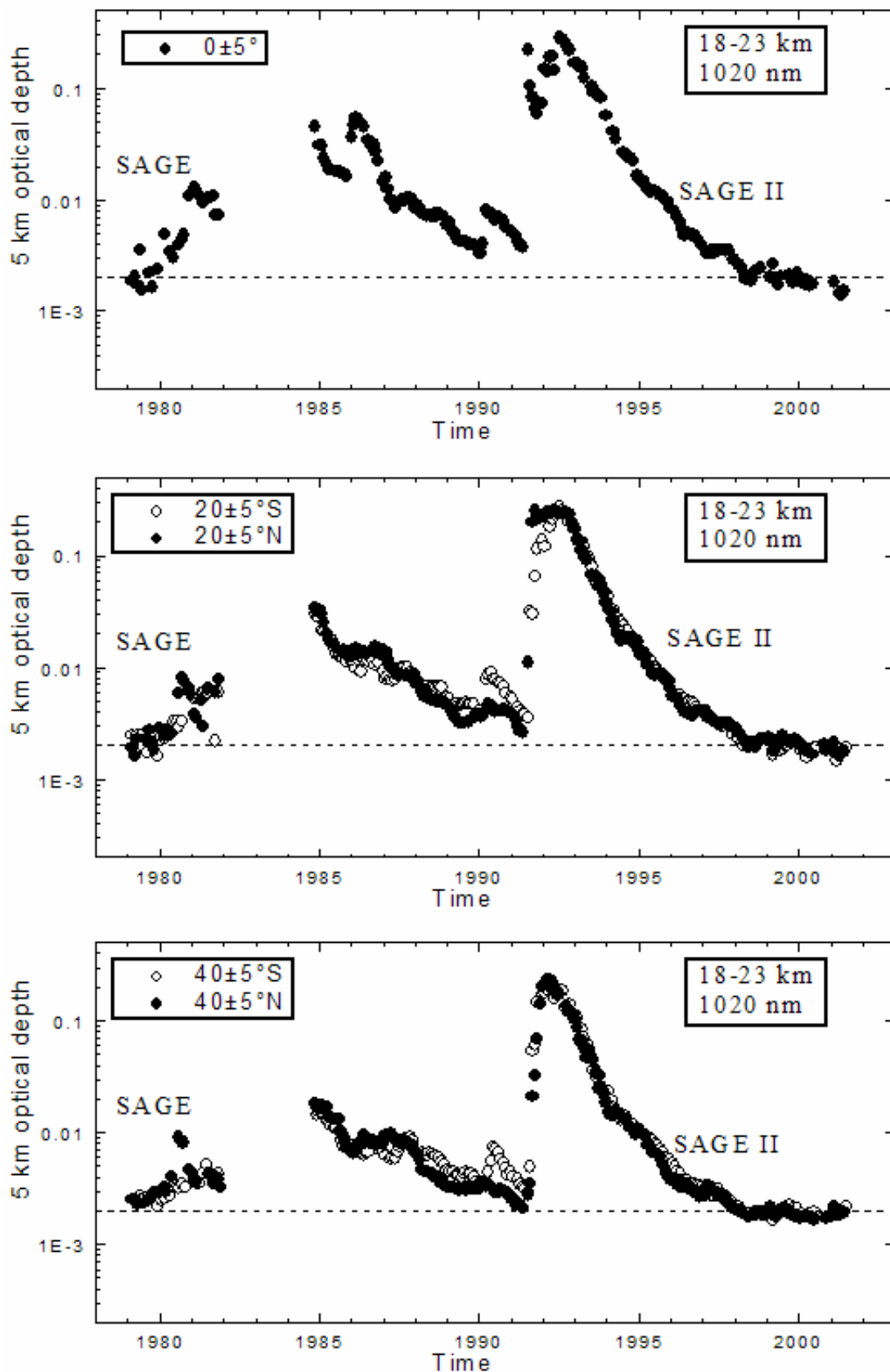


Figure 5.4. Zonal averages, $\pm 5^\circ$, of SAGE and SAGE II 1020 nm optical depths versus time centered at $0, \pm 20$ and $\pm 40^\circ$. Optical depth integrated from 18 to 23 km. Open (closed) symbols are for the Southern (Northern) hemisphere.

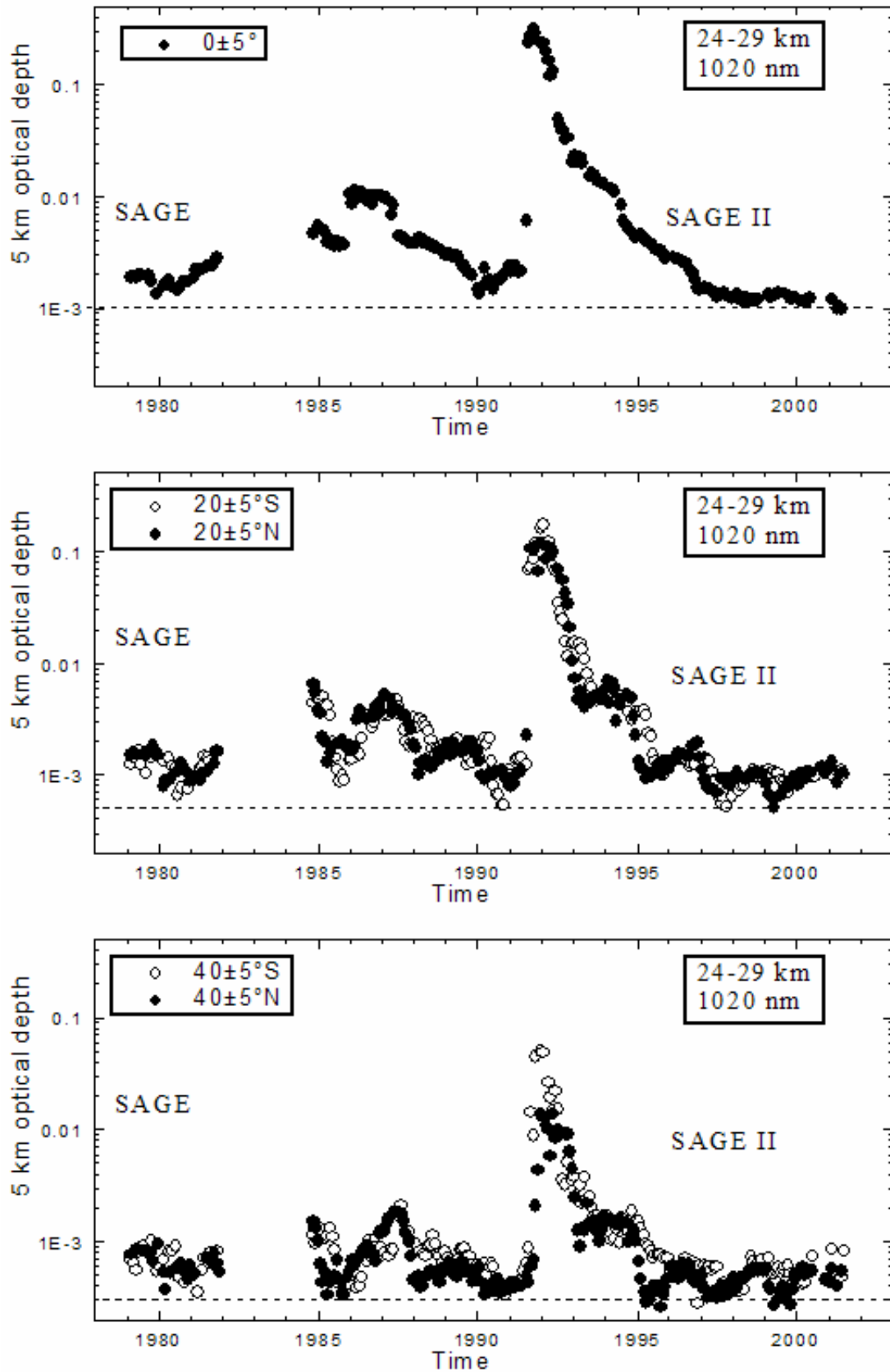


Figure 5.4 (cont.). Zonal averages, $\pm 5^\circ$, of SAGE and SAGE II 1020 nm optical depths versus time centered at $0, \pm 20$ and $\pm 40^\circ$. Optical depth from 24 to 29 km. Open (closed) symbols are for the Southern (Northern) hemisphere.

5.4 Investigation of trends in the long term aerosol measurement records

Previous analyses of long term trends in background stratospheric aerosol have been limited to comparisons of the aerosol record during volcanically quiescent periods. The first of these analyses [Hofmann and Rosen, 1980; Hofmann and Rosen, 1981; Sedlacek et al., 1983] compared measurements in the 1970s with Junge's [1960] initial measurements. The increase that these investigators reported can be seen in Figure 5.1 where Junge's initial 0.15 μm concentration measurements [Chagnon and Junge, 1961] are compared with the long term Laramie record. Figure 5.1 also indicates that in the mid latitudes in the 1970s the periods when stratospheric aerosol may have reached background were short, ~ 1 -2 years.

Table 5.1 lists the time, location, VEI, and aerosol load if available, for all volcanoes with a stratospheric impact, generally $\text{VEI} \geq 4$, since 1960. The 1970s were dominated by one large tropical eruption, Fuego, and no small tropical eruptions. All other eruptions were at high latitudes. In contrast the 1980s were dominated by one large tropical, El Chichón, and several smaller tropical eruptions. The smaller tropical eruptions, particularly Nevado del Ruiz and Nyamuragira, interrupted the decay from El Chichón and led to some controversy about whether stratospheric aerosol had reached background prior to Pinatubo [Hofmann, 1990; Thomason et al., 1997]. This discussion highlights an uncertainty in knowing if and when the lowest background loading is present. In hindsight it now seems clear, based on the volcanically quiescent period following Pinatubo, that background was not reached prior to Pinatubo [Barnes and Hofmann, 2001; Hayashida and Horikawa, 2001], Figures 5.2, 5.3, 5.4.

The statistical analysis here will follow two approaches. The first will follow the lead of previous investigators and compare the 3 volcanically quiescent periods in the 5 long term data sets which capture these. The second will use an empirical model to remove the volcanic signal from the long term records and investigate the residuals for trends. This approach permits the SAGE data to be included. These analyses do not account for the impact of trends in stratospheric water vapor and temperature on aerosol size, but this appears to be minor. The main problems with these approaches are technical. Temporal autocorrelations, present in all data, violate standard statistical independence assumptions. Proper analyses that account for autocorrelation indicate much smaller effective sample sizes, and confidence bounds on estimates are consequently inflated. Also, maximum likelihood estimation with mixed models including autocorrelation parameters is occasionally unstable, and estimation algorithms may fail.

Given sulfuric acid mass, water vapor pressure, and temperature, the composition of stratospheric aerosol can be predicted from thermodynamics [Steele and Hamill, 1981]. Using aerosol composition and assuming a lognormal size distribution with constant width, the mode radius of the aerosol can also be predicted. Since over the record of long term stratospheric aerosol measurements there have been increases in stratospheric water vapor and decreases in stratospheric temperature, both of which would lead to larger particles, the effects of these changes were estimated to see if they were significant. Since the 1950s there has been approximately a $1\% \text{ yr}^{-1}$ increase in stratospheric water vapor [Oltmans and Hofmann, 1995; Kley et al., 2000] and approximately a 0.5 K per decade cooling of the lower to middle stratosphere [Ramaswamy et al., 2001]. These changes in water vapor and temperature were used to estimate the fractional change in particle size and composition. The changes were found to be negligible, less than $10^{-4} \mu\text{m} \text{ decade}^{-1}$ in size and $-0.5\% \text{ decade}^{-1}$ in composition in the lower to middle stratosphere between 70°S and 70°N . These changes of aerosol in volcanically quiescent periods are not observable in the measurements available for

comparison. In addition Nedoluha et al. [2004] suggest the trend in water vapor may not be as high as $1\% \text{ yr}^{-1}$ leading to even less of a change in aerosol size.

5.4.1 Comparison of stratospheric aerosol during non volcanic periods

The results of a comparison of measurements in background periods will depend in large measure on how the periods are specified. While defining background periods is relatively straight forward, specifying background periods can be fraught with difficulty since: a) most stratospheric volcanic aerosol decay processes display an exponential rather than linear character, b) there can be input from minor eruptions between major eruptions, such as after El Chichón, c) recent history has been relatively volcanically active, and d) the time periods for some background periods can be exceedingly short. Between 1971 and 1997 at least 70% of the sampling period was perturbed by volcanic activity.

In spite of these difficulties the in situ, 15-30 km column, and lidar, integrated backscatter, measurements are used to compare the measurements during the three background periods identified for each data set. This analysis is completed because it is straight forward and has been the approach of all preceding analyses of background stratospheric aerosol. The background periods were identified by each investigator based on their individual criteria, Figures 5.2 and 5.3. While a more objective approach would be preferable, the variation in the measurements and the sometimes brief background periods are not amenable to a more objective analysis. The approach followed allows experimentalists, using their understanding of the measurement technique, and characteristics of stratospheric aerosol, to manually inspect the record and select time periods free of volcanic aerosols. Although this method is the most subjective, it benefits from the investigator's experience in recognizing the effects of volcanic activity. The method relies on a subjective assessment of when the characteristic decay of aerosol mixing ratio or integrated backscatter, following a volcanic eruption, no longer influences the record. The background periods identified by the experimentalists at Hampton and Garmisch are equivalent except prior to Pinatubo (Figure 5.3b), adding some credibility to investigator determined background periods. The background periods for Mauna Loa were used also for the São José dos Campos data, except after Pinatubo, then the São José dos Campos background period was begun in 1998.5. Prior to 1997 the background periods identified for the in situ data are quite short. The sensitivity of this analysis to the choice of background periods was tested by changing the background periods selected by $\pm 0.5 \text{ yr}$. These changes did not significantly affect the results.

The comparisons of background periods were completed using analysis of variance with adjustment for autocorrelation to compare the data within each of the three background periods for each data set, and by applying a linear regression model to the log of the aerosol measure versus time to investigate temporal changes in the background periods. Figure 5.5 presents for each data set, the background data, means and 95% confidence intervals for measurements during each background period, and the results from a linear regression model applied to the data.

The analysis of variance tests indicate little difference between the means of the first and third background periods. A statistically significant increase was observed for the middle period, pre-Pinatubo, for the Laramie- $0.25 \mu\text{m}$, Garmisch, and Hampton data. This increase in the background prior to Pinatubo has been discussed by Hofmann [1990] and Thomason et al. [1997] and is clearly evident in the high northern latitude sites in Figure 5.5, except for the

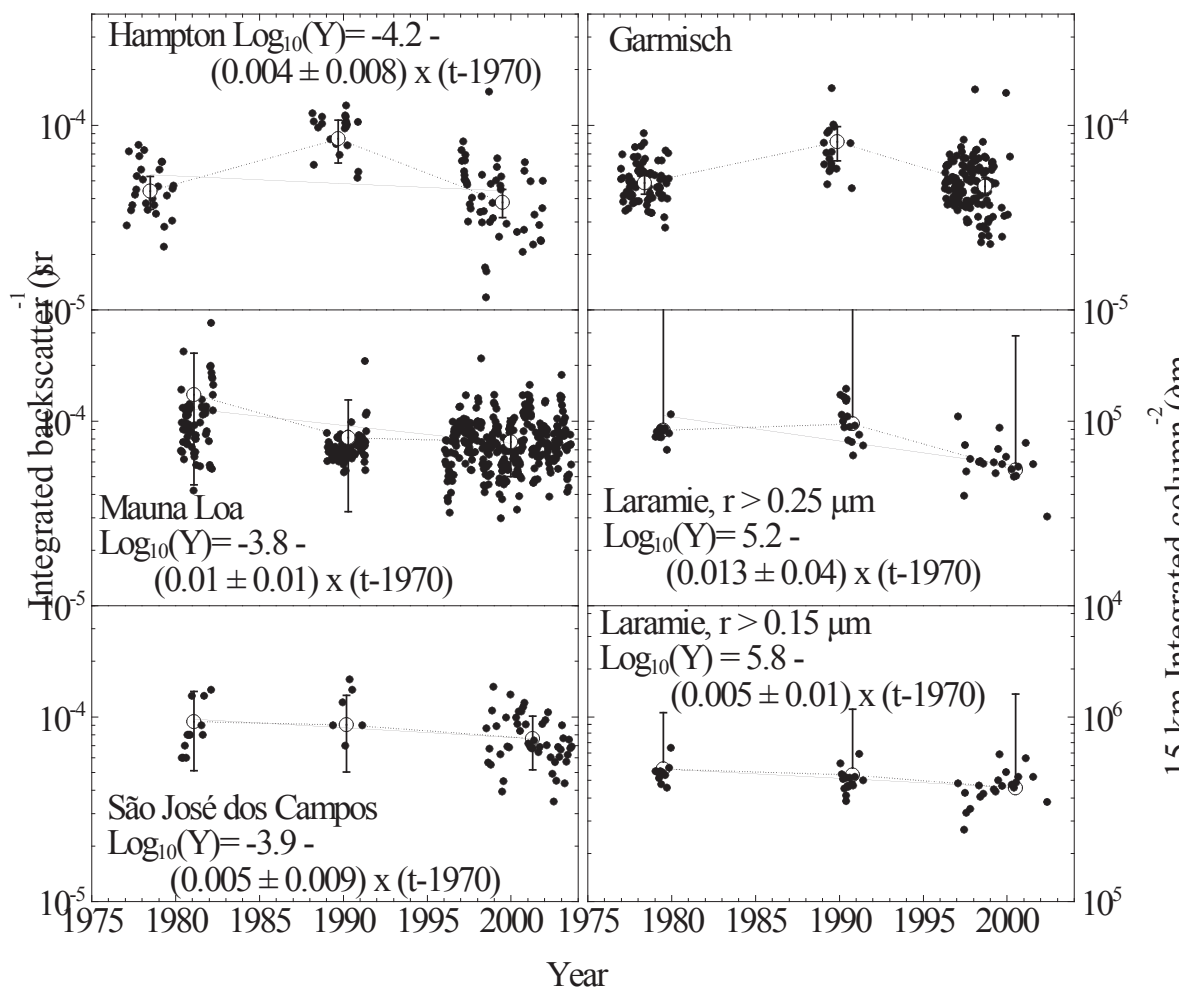


Figure 5.5. Comparison of measurements during three investigator determined background periods for integrated backscatter measured above Garmisch, Hampton, Mauna Loa, and São José dos Campos, and for column integrals, 15-30 km, of aerosol concentration for particles $\geq 0.15, 0.25 \mu\text{m}$ above Laramie. Means and 95% confidence intervals, with adjustments for autocorrelation, for each background period are shown (symbols with error bars connected with a dashed line) along with a linear regression (solid line) when convergence, including autocorrelation, was achieved. This the case for all but Garmisch. The log of the regression equation is shown with 95% confidence intervals for the slope of the equation. The interval on the ordinate for each graph is the same so that even though magnitudes of the aerosol measure differ between the lidar and in situ measurements, the slopes are comparable.

Laramie-0.15 μm data. It now seems clear that this period was still perturbed by residual volcanic activity, either from Kelut in 1990 or remnants from Nyamuragira or Nevado del Ruiz in 1986. The other site to show a non-zero difference with this analysis is Mauna Loa where the data suggest that the first background period is elevated compared to the pre- and post-Pinatubo periods, which show no significant difference. No difference is apparent for any period for the Laramie-0.15 μm and São José dos Campos measurements.

The linear regression for the three background periods analyzed suggests trends and 95% confidence intervals of $-0.5 \pm 1.0 \text{ \% yr}^{-1}$ for the Laramie 0.15 μm , Hampton, and São José dos Campos measurements, $-1 \pm 1.0 \text{ \% yr}^{-1}$ for Mauna Loa measurements, and $-1 \pm 4.0 \text{ \% yr}^{-1}$ for Laramie 0.25 μm measurements. Mixed model linear regression estimation for Garmisch

failed to converge. If autocorrelation is ignored confidence intervals are smaller and these results suggest a negative trend in stratospheric aerosol for the Laramie 0.25 μm and Mauna Loa measurements, which is significant. The data, however, are not independent. Autocorrelations at the scale of one month were estimated between 0.70 and 0.98, values which strongly affect inference. The autocorrelation is high because, on the time frame of one month, and away from large volcanic eruptions, the stratospheric aerosol content changes slowly, and thus a measurement in one month is a good predictor for the following month. Unequal time spacing and the autocorrelations were accommodated by appealing to a one-dimensional spatial model, equivalent to a first-order autoregressive error regression model. The results are compelling in that data which suggest changes in background without accounting for autocorrelations (Laramie-0.25 μm , Mauna Loa, Figure 5.5) do not suggest any trend when autocorrelation is accounted for. Although estimates of growth/decay rates change little, standard errors typically about triple when autocorrelations are included which is the more appropriate model for these data sets.

This analysis follows the lead of the early comparisons of background periods, but concludes that there is no long term trend in background aerosol. This is in agreement with other recent comparisons of background periods using single data sets [Barnes and Hoffman, 1997, 2000, Deshler et al., 2003; Jäger, 2005]. Care, however, must be exercised to limit the confidence in conclusions drawn from comparisons which include just a few epochs containing background data. In particular the conclusion from this analysis is dependent on confidence that stratospheric aerosol had reached background in 1979-1980, prior to Mt. St. Helens. This period is quite short.

5.4.2 Removing the volcanic signal from the long term measurement records

The second approach to analyze for trends in background aerosol seeks to remove the major perturbing signal, the volcanic effects, from the data. The resulting baseline is then analyzed for trend. This approach uses techniques applicable to a wide range of observations and does not require a priori knowledge of the unique behavior of a particular data record. The advantage of this approach is to transform the long term, ~ 30 year, measurement records from ones limited to comparisons of 2-3 time periods, which range from 1 to 5 years, to a record which includes the entire time period of measurements. Considering that the longest satellite record, SAGE II, captures just two non-volcanic periods this is practically the only approach that can take advantage of this global 20 year record. The four lidar records and one in situ record capture three background periods, which comprise $\sim 40\%$ of the measurements at these sites, with the post Pinatubo background period encompassing 20%. Thus, prior to Pinatubo, $\sim 80\%$ of the measurements were completed during volcanically perturbed periods.

The disadvantages of such an effort is that no simple model of volcanic aerosol growth and decay can accurately capture all of the processes involved in the dispersal and removal of volcanic stratospheric aerosol as reflected in each of the various long term measurements. This, however, does not preclude the application of an empirical model to remove the majority of the variance of the aerosol signal produced by volcanic eruptions. Such a model will be inherently tied to each measurement set and can only be applied to that measurement set. Application to a different set of measurements will use the same conceptual model but require a new set of empirical parameters.

The following considerations guided the choice of an empirical model to remove the volcanic influences: (1) The 1-2 order of magnitude changes in aerosol signal from background to volcanic period suggest a log transform of the measurements to avoid excessive weighting of

the volcanic period. (2) The roughly linear decay of any of the aerosol measures plotted in Figures 5.2 and 5.3, on a log scale, suggests a roughly exponential decay of volcanic aerosol. This assumption has some problems as background aerosol levels are approached, but is generally valid and has been used often [Yue et al., 1991; Rosen et al., 1994; Osborn et al., 1995; Deshler et al., 1997]. (3) When modeling the process some attention must be given, at each site, to the time lag between an eruption, the time the initial aerosol pulse arrives and the period of time leading to the peak aerosol signal. The latitude of the observation site with respect to the volcano and the season will influence this, e.g., compare the arrival of El Chichón and Pinatubo aerosol at the four lidar sites shown in Figure 5.3. The transitions are characterized by both a time lag until the aerosols arrive and a buildup period from initial impulse to peak signal. Both the lag and the buildup are extended for more distant sites. 4) Cumulative effects of volcanic inputs and background sources are assumed to be additive. 5) The nature of the data is such that some variation in the measurements is fairly constant (measurement uncertainties), and some increases with scale (local natural variations following large volcanic eruptions). Variation that increases with aerosol signal appears during and following volcanic inputs. Figure 5.6a, displaying the Garmisch lidar measurements on a linear scale, illustrates this point. The variations which increase with integrated backscatter dominate the variance of the signal. Because these effects dominate, it is natural to use a log scale to display data as in Figures 5.1-5.4. 6) It is assumed that there is a non-volcanic, background, component to stratospheric aerosol which would exist in the absence of volcanic eruptions. Based on the data this assumption is reasonable, certainly more reasonable than assuming there is no background aerosol. Explicit inclusion of a term for a baseline in the model is also more consistent with the data than is exclusion of the term. The goal of the modeling exercise is to determine if the background aerosol level has changed, or remained constant, over the course of the measurements. Displays on log scales indicate the data are approximately lognormally distributed. Measurement error and perhaps some of the natural variation, however, exists at a fairly constant level and is approximately normally distributed. The true total “error” in the data is thus probably a convolution of normal and lognormal components, but, overall, the lognormal effects dominate and a simple lognormal model to remove volcanic signals is used.

Based on these considerations the following empirical model is developed for $\log(Y(t))$, where $Y(t)$ is a time dependent aerosol measurement from any of the long term records. Plots of $\log(Y)$ versus time for the aerosol measurements under consideration are shown in Figures 5.2-5.4. The empirical model has the form:

$$\log\{Y(t)\} = \log\{ B \exp(\beta t) + \sum_1^N V_j(t) \} + \text{error}. \quad (5.1)$$

The initial term $B \exp(\beta t)$ allows for an overall trend of the baseline, a value of $\beta = 0$ implies a constant baseline at B , whereas positive and negative values of β represent respectively growth and decline in background levels. The proposed model is thus based on a possibly changing baseline plus a chain of events added together over time. The number of measurable volcanic inputs over the observation period is determined by inspection from the data. Each volcanic input $V_j(t)$ consists of two parts, one for an initial, finite transition period during which aerosols are arriving, and the other for an open-ended period of decay. Exponential decay is assumed to be operative during both periods, although arrival dominates decay during the (usually brief) transition period, and only decay is present for the second period. In the second, more important period, starting at time τ_{jz} , the function is of simple form $P_j \exp(-v_j (t-\tau_{jz}))$ where P_j is the aerosol load at time τ_{jz} and v_j is the volcano dependent

exponential decay rate. The decay parameters v_j are assumed positive, whereas β (the background growth or decay) can be positive or negative.

The first period (transition) is less consequential but more complex. It is assumed that arrival of aerosols follows a positive continuous function $Q_j(t)$. These functions are modeled with three parameters: the time of appearance of volcanic aerosol at a site, τ_{ja} , the time when aerosols cease arriving, τ_{jz} , and the peak level of the wave over this interval, P_j , which may be shown to occur at τ_{jz} . Knowledge of event times puts a lower bound on each τ_{ja} . Assuming that the exact form of the wave is not critical, a truncated quadratic fixed at zero before τ_{ja} and after τ_{jz} , inclusive, is used. For time t between τ_{ja} and τ_{jz} the mean aerosol level is then $\int_{\tau_{ja}}^{\tau_{jz}} Q_j(t) \exp(-v_j(t-\tau_{ja})) dt$. The integral has a closed form that is perhaps unnecessarily

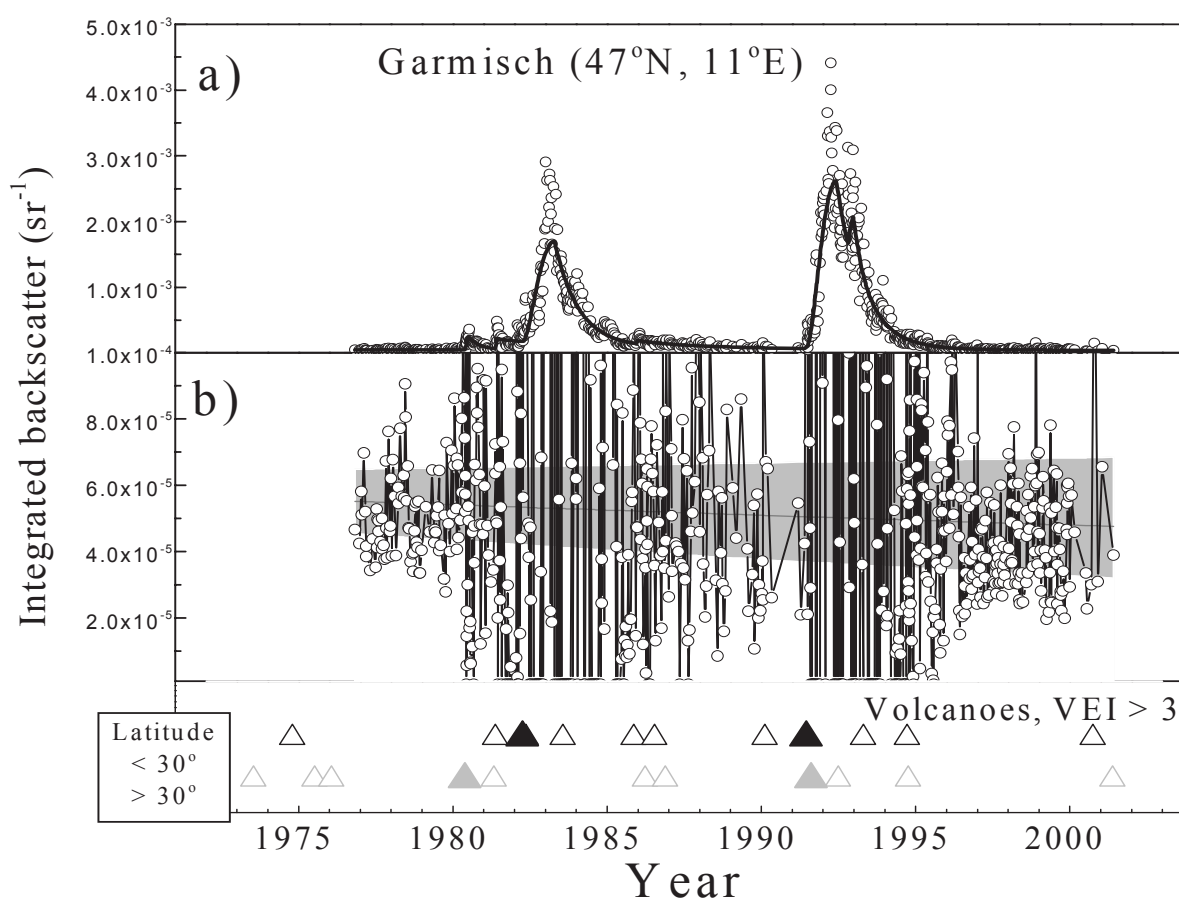


Figure 5.6. (a) Integrated backscatter (data points) from Garmisch, compared with the parametric model (solid line) for Garmisch, plotted on a linear scale. Compare the large variations near the peak of aerosol load for either El Chichón or Pinatubo with the variations of measurements near background. (b) Integrated backscatter for Garmisch with the modeled volcanic effects removed. Values become large and sometimes negative near the eruptions of El Chichón and Pinatubo due to the large natural variations around the volcanic model. Also shown are the mean and $\pm 95\%$ confidence limits for the modeled baseline and its trend.

complex, but it has the virtue of being parsimonious with respect to the parameters required for any one volcano and all parameters have physical interpretations.

For N volcanoes the model has $4N+2$ parameters, four for each volcano and two for the baseline. The chief drawback of this model is not, however, its dimension but rather the fact that conventional fitting is almost impossible to do exactly. The time limits τ_{ja} and τ_{jz} interject breaks in the smoothness of the function, and convergence is not feasible without unconventional optimization methods or else careful monitoring and coaching of the process. For current purposes, a near optimal fit is satisfactory, because the primary purpose of the modeling is to allow volcanic inputs to be removed, leaving a baseline which can be assessed for trend, Figure 5.6b. The residuals are highly autocorrelated over time, and consequently simple linear regression trend analysis is not reliable in terms of inference. The degree of statistical significance is expected to be strongly inflated in these circumstances, so assessment of trend is done using a model that allows for first order autocorrelation. Data are unequally spaced in time, so analysis is performed using a one-dimensional spatial representation instead of a standard time series analysis [Cressie, 1993]. The clustering of points below the baseline and gray area between 1996 and 2000 in Figure 5.6b is somewhat misleading. It is partly an artifact of the linear fit, partly due to the vertical truncation in 5.6b to emphasize the character of the gray area, and partly due to autocorrelation of the data. The vertical truncation masks some influential outliers above the gray area which are carrying a substantial part of the balance. Because of autocorrelation the thick clustering of points recorded between 1996 and 2000 are not as influential as they appear. With unequal time spacing, in particular, counting numbers of points can be deceptive.

The optimization procedure uses a priori estimates for each parameter and then standard squared-error residual minimization to obtain the set of parameters providing the minimum in the residuals. Figure 5.6a presents the results obtained from a fit of the parametric model, Eq. (5.1), to the log of integrated backscatter from Garmisch. In this case 6 volcanic events were included so a 26 parameter model was used. The measurements compared to model estimates on a linear scale are shown in Figure 5.6a, while the aerosol signal with volcanic influences removed is shown in Figure 5.6b along with model estimates of the baseline trend with 95% confidence limits. The results of similar optimized fits to all of the lidar and the in situ measurements are shown in Figure 5.7, on a log scale to display variations during background periods. Also shown are model estimates of the baseline trend with 95% confidence limits (gray shaded area) and the times of volcanic eruptions with $VEI \geq 4$. The boundaries of the shaded area are calculated from $Y(t) = (B \pm \Delta B) \cdot \exp [(\beta \pm \Delta\beta) \cdot (t - t_0)]$. The initial shaded area's finite width is set by ΔB , the uncertainties in B . This area grows because of the uncertainty in the time rate of change of the background, $\Delta\beta$, leading to an increase in uncertainty with time.

The model does a reasonable job of capturing the measurement variations through the volcanic perturbations. However, as apparent from Figure 5.7, not all volcanoes were included in the model for each site. Initially all volcanoes which appeared in the record were included. If convergence of the model was not achieved, then some of the smaller volcanoes were removed for that site and the model rerun. This process was repeated until convergence was achieved. Thus, for example, Nevado del Ruiz and Nyamuragira were not included in the São José dos Campos model, whereas Mt. St. Helens was not included in the Laramie records. Both the Laramie in situ data and Hampton lidar data were highly perturbed by Mt. St. Helens in comparison to other sites. This perturbation created difficulties in establishing a baseline prior to the eruption of El Chichón for the Hampton and Laramie data. Perhaps the proximity

of this volcano and the increased sampling frequency at Laramie and Hampton contributed to these difficulties. For this analysis only elimination of these data from the Laramie record permitted the model to converge at reasonable levels. This extreme step was not taken for the Hampton data, but it is clear from Figure 5.7 that the minimum in the measurements prior to El Chichón, is not modeled correctly for Hampton.

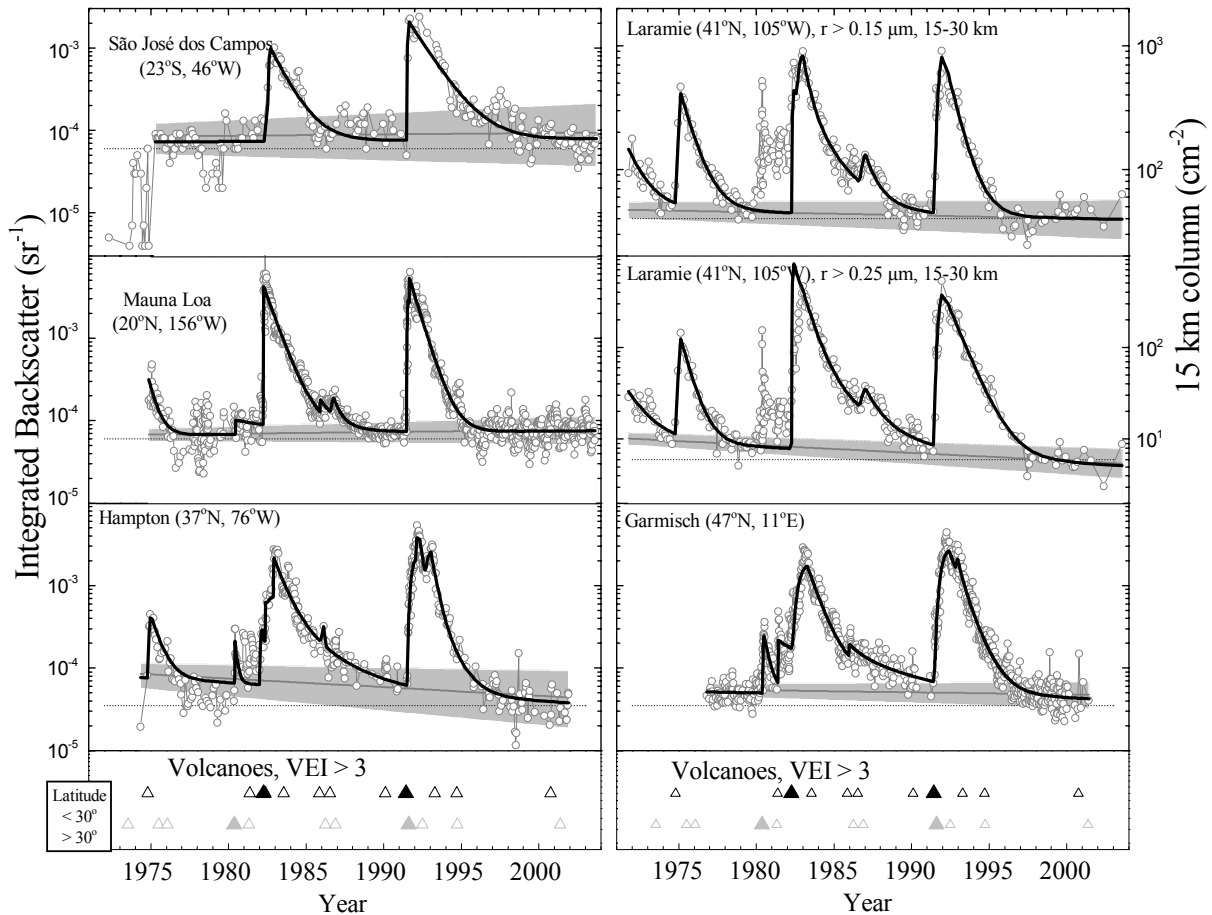


Figure 5.7. Integrated backscatter (data points) from São José dos Campos, Mauna Loa, Hampton and Garmisch lidar measurements, and integrated aerosol column (15-30 km) for particles with radius $\geq 0.15, 0.25 \mu\text{m}$ from Laramie compared with parametric model fits (solid lines) to the log of the measurements. The gray shaded areas provide the estimated background aerosol, with 95% confidence intervals, from the model. The time of volcanic eruptions with VEI ≥ 4 (open triangle) and 5 (closed triangle) are shown at the bottom divided into those eruptions at latitudes less than and greater than 30° of latitude, upper and lower symbols. The model was applied to the São José measurements beginning in 1975, and Mt. St. Helens was not included in the model for Laramie.

Table 5.2 provides the estimates of B , β , P_j and v_j , along with their standard errors for each of the sites. The 95 % confidence limits on any parameter are given approximately by plus and minus two standard errors of the mean. Time parameters τ_{ja} and τ_{jz} are omitted from the table. The measurements with modeled volcanic signal removed for the lidar and two in situ records along with the baseline $\pm 95\%$ confidence interval are shown in Figure 5.8.

Table 5.2. Parameters used in the parametric model used to estimate the measurements from each long term measurement site. The rate parameters have units of yr^{-1} . The standard errors of each parameter are indicated by σ . The 95% confidence intervals are given approximately by parameter $\pm 2\sigma$. Note only the background fit parameters incorporate autocorrelation in the estimates of standard errors. This is not the case for the volcanic fit parameters. When multiple bursts are modeled for a single volcano, parameters for the slowest decay rate are recorded, and the value is marked with an asterisk.

<i>Parameter</i>		<i>Laramie15</i>	<i>Laramie25</i>	<i>São José</i>	<i>MaunaLoa</i>	<i>Hampton</i>	<i>Garmisch</i>
		15-30 km column (cm^{-2})		←	Integrated backscatter $\times 10^4$ (sr^{-1})		→
Back-	B	47	10.0	0.83	0.68	0.85	0.55
Ground	$\sigma(\text{B})$	3.7	0.76	0.15	0.061	0.15	0.049
	β	-0.0056	-0.020	0.0039	0.0045	-0.024	-0.0060
	$\sigma(\beta)$	0.0035	0.0035	0.0080	0.0039	0.0083	0.0042
Fuego	P	360	110	NA	2.9	3.7	NA
	$\sigma(\text{P})$	34	12	NA	0.53	0.78	NA
	ν	1.1	1.5	NA	2.0	2.4	NA
	$\sigma(\nu)$	0.093	0.13	NA	0.34	0.47	NA
El	P	500	840	8.20	41	18	15
Chichón	$\sigma(\text{P})$	110	170	1.50	2.0	4.4	0.70
	ν	2.2	1.4	0.74	1.2	1.9	1.3
	$\sigma(\nu)$	0.76	0.22	0.096	0.037	0.84	0.13
Pinatubo	P	810	390	21	28	17*	26*
	$\sigma(\text{P})$	45	22	4.0	5.4	4.8	1.0
	ν	1.3	0.98	0.70	1.5	1.1*	1.2*
	$\sigma(\nu)$	0.05	0.035	0.072	2.4	0.11	0.035

Based on Figures 5.7, 5.8 and Table 5.2 the change in the baseline, indicated by β , does not differ significantly from zero for the Garmisch, Mauna Loa, São José, and Laramie 0.15 μm records. Slight negative trends, $\sim 2\% \text{ yr}^{-1}$, are determined for the Hampton and Laramie 0.25 μm measurements. These results, suggesting a stable or at most a slightly decreasing, stratospheric background aerosol, are consistent with the simpler analysis of background periods discussed in section 5.4.1. Only the Laramie 0.25 μm measurements result in a slight negative trend for both types of analyses. The simpler analysis of background periods for Hampton data suggests no trend, with perhaps a slight negative trend for Mauna Loa. For the Laramie 0.25 μm measurements the parametric model estimate of background aerosol decreasing at $\sim 2\% \text{ yr}^{-1}$ exceeds the $\sim 1\% \text{ yr}^{-1}$ estimated in section 5.4.1. Errors in the measurements do not allow finer limits to be placed on possible changes.

A similar model was applied to SAGE II satellite data, the only satellite measurements with a history long enough to consider trends in background stratospheric aerosol. For this analysis the SAGE II extinctions were zonally averaged into $\pm 5^\circ$ latitude bins and optical depths calculated in three 5 km altitude intervals, 18-23, 24-29, and 30-35 km. The latitude bins were centered at 0, ± 10 , ± 20 , ± 30 , ± 40 , and $\pm 50^\circ$. This subdivision of the SAGE II measurements provided 33 data sets for each of the four SAGE II extinction measurements. These data are less complex than the lidar and in situ data since the time period covered is only two thirds of the lidar and in situ data and volcanic eruptions were less frequent during this period. The

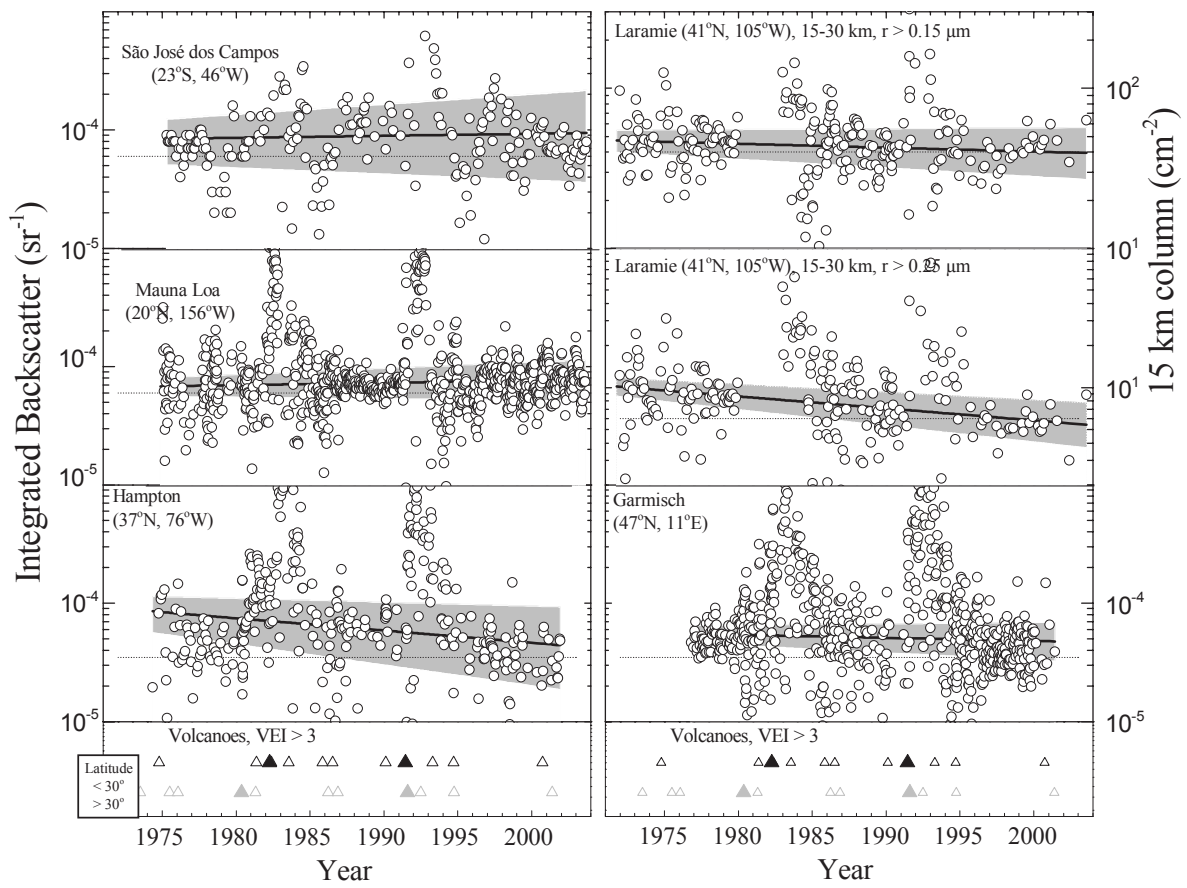


Figure 5.8. Same as Figure 5.7 except the data represent the differences between the measurements and the volcanic portion of the model. The residuals for Laramie in 1980, following Mt. St. Helens, are off scale since Mt. St. Helens was not included in the model for Laramie.

number of volcanic events included in models of the SAGE II measurements varied from 3 to 4 depending on latitude. The tropical eruption of Kelut, a year prior to Pinatubo, did not affect the high latitude measurements. The analysis was completed for all 33 data sets for the 1020 nm extinction measurements since this is the most stable SAGE II aerosol measurement. These results are expected to apply equally as well to some of the other wavelengths; however, care would be required if the shortest wavelength, 385 nm, was used. Time restraints prevented extending the investigation to the other three wavelengths.

Figures 5.9-5.11 present the results of parametric model fits to SAGE II 5 km optical depths for 5 latitude intervals and 3 altitude intervals. Figures 5.12-5.14 provide the SAGE II measurements with the volcanic signal removed compared with the baseline estimates. Figures 5.12-5.14, as Figure 5.8, include the removal of only the volcanic signal. Thus any changes in the background aerosol will appear in Figures 5.8, 5.12-5.14. The results are consistent with the ground-based lidar and balloonborne in situ measurements. The value of the change rate for background aerosol, β , is not, statistically, significantly different from zero for the 20 year SAGE II measurement record. The results shown for SAGE II are indicative of similar analyses at ± 10 , 30 , and 50° . These results highlight the usefulness of

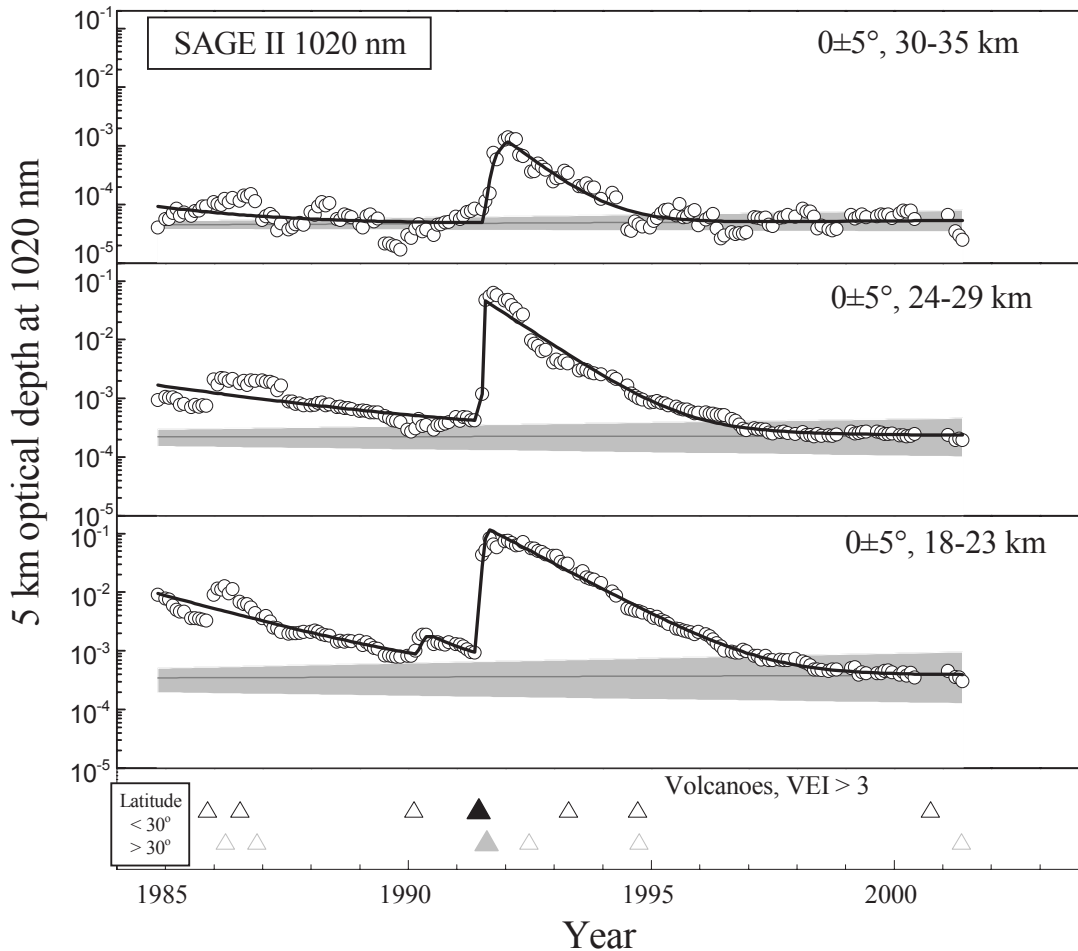


Figure 5.9. Optical depths integrated over three 5-kilometer altitude intervals for zonally averaged ($\pm 5^\circ$) SAGE II 1020 nm extinctions at a latitude of 0° , compared with parametric models fit to the data and with estimates of the baseline and trend for optical depth during background aerosol conditions. The estimated background is shown with $\pm 95\%$ confidence intervals as the gray shaded area. The time of volcanic eruptions with $\text{VEI} \geq 4$ (open triangle) and 5 (closed triangle) are shown at the bottom divided into those eruptions at latitudes less than and greater than 30° of latitude.

this approach for trend analysis of the 20 years of SAGE II measurements. A simple comparison of the volcanically quiescent periods in the SAGE II measurements, Figure 5.4, would preclude such a conclusion. Figure 5.4 suggests either a decline in background stratospheric aerosol or background was not reached at most latitudes prior to the eruption of Pinatubo.

Table 5.3 provides the parameters which were obtained from the non-linear least squares regression applied to the zonally-averaged SAGE II optical depths. Inspection of the fifth and sixth column of the table indicates that the long term trend in the background aerosol is not significantly different from zero. In contrast to the lidar and in situ data the decay rates following El Chichón are significantly different, about a factor of 2 less than the decay rates following Pinatubo. Is this a result of the missing data following El Chichón? To test this, the

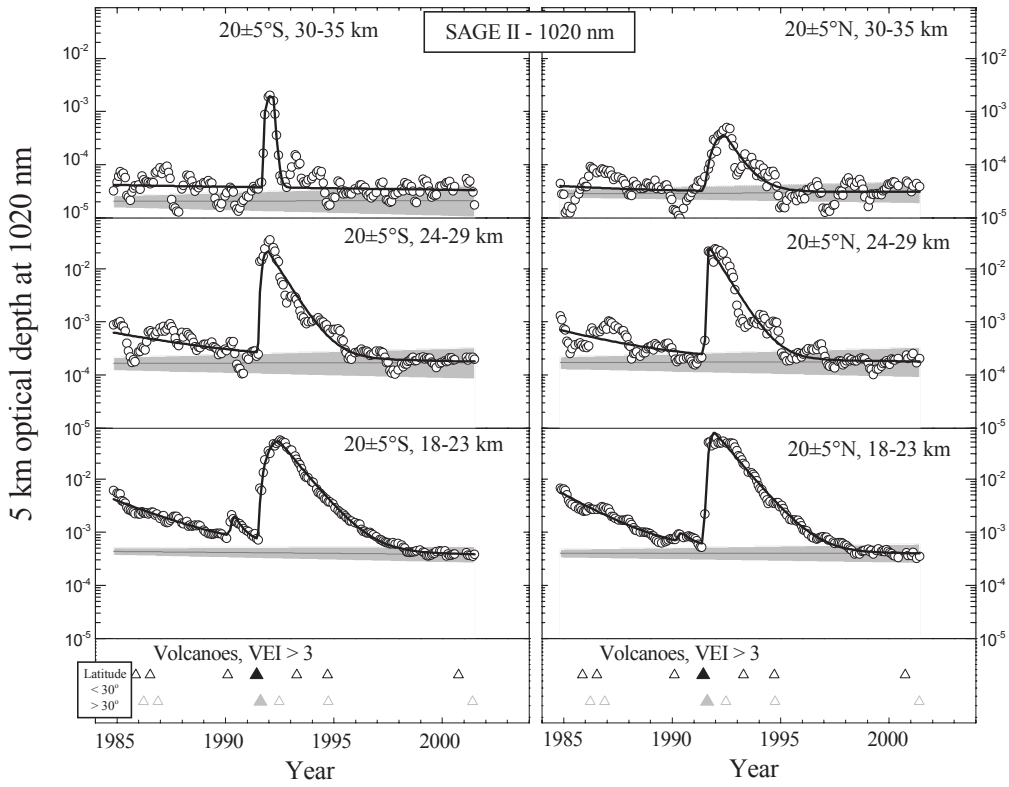


Figure 5.10. Same as Figure 5.9, except for latitudes of ± 20°.

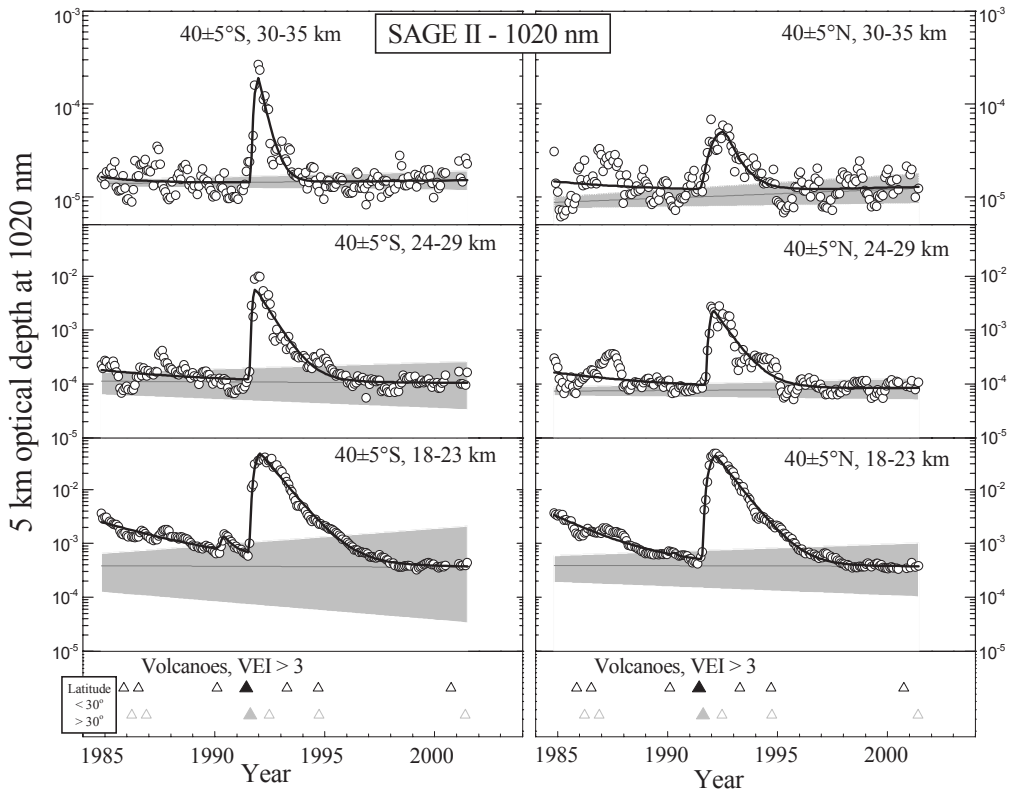


Figure 5.11. Same as Figure 5.9, except for latitudes of ± 40°.

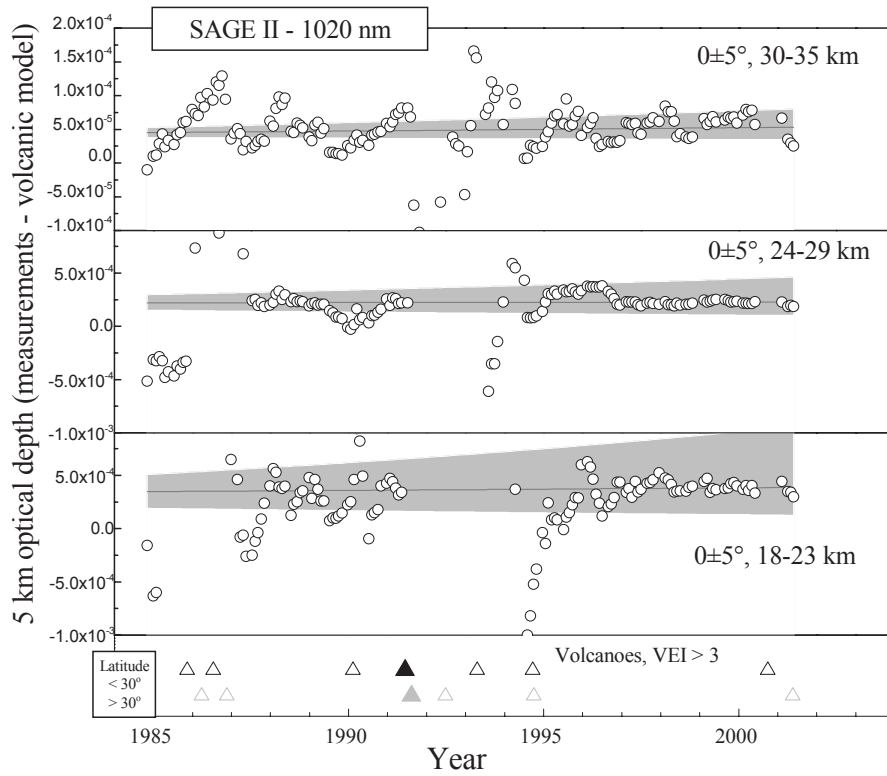


Figure 5.12. Same as Figure 5.9, except the data points are the measurements with the volcanic effect estimated from the model subtracted.

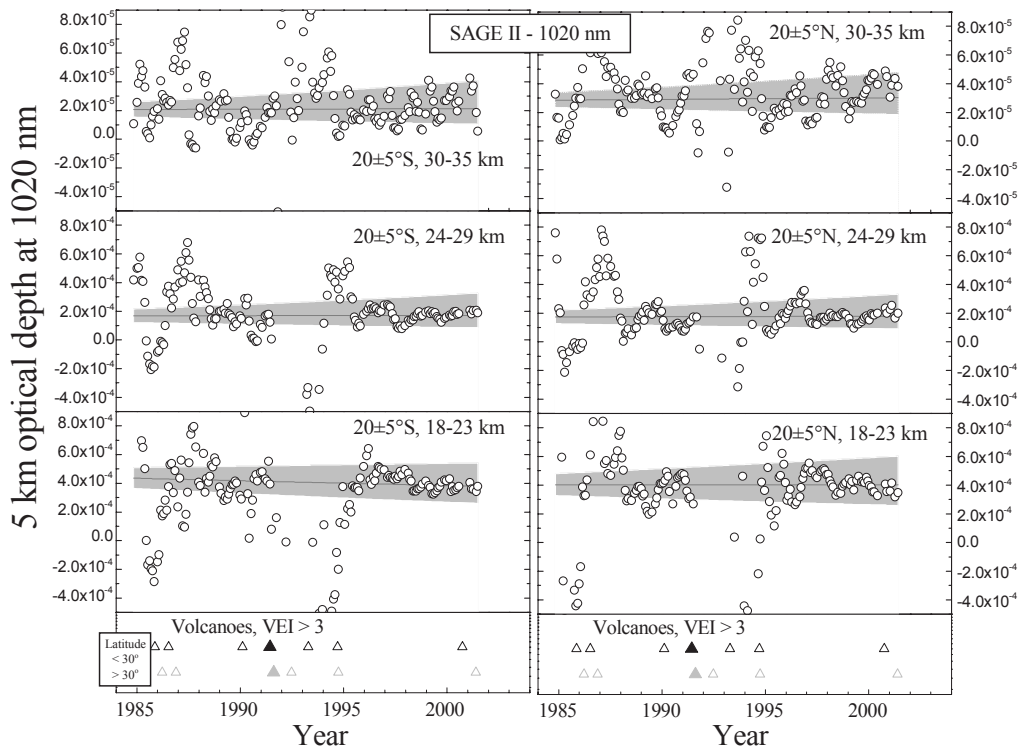


Figure 5.13. Same as Figure 5.10, except the data points are the measurements with the volcanic effect estimated from the model subtracted.

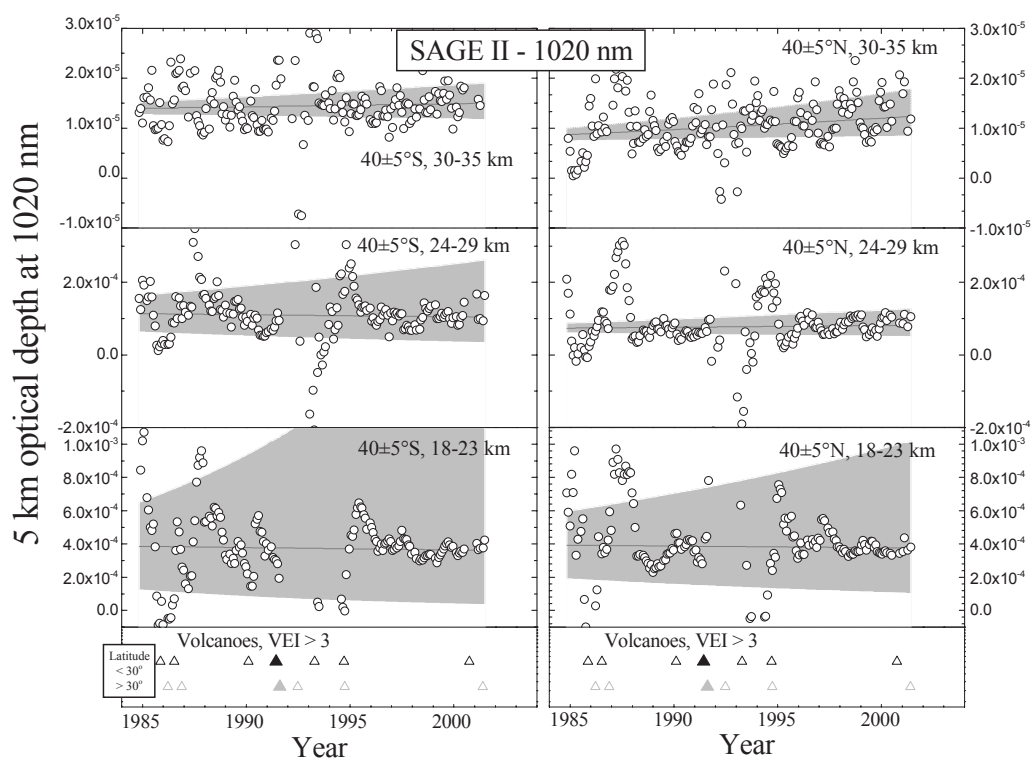


Figure 5.14. Same as Figure 5.11, except the data points are the measurements with the volcanic effect estimated from the model subtracted.

parametric model was rerun for the SAGE II 1020 nm 5 km optical depth at 40°N, but removing data for the two years following Pinatubo. The results did not change significantly. The estimated Pinatubo aerosol decay rate, and background aerosol change rate, changed by less than 1%, while confidence intervals increased by about 10 %.

Figure 5.15 provides the latitude distribution of the background decay term, β (yr^{-1}), with 95% confidence intervals for (1) SAGE II 1020 nm 5 km optical depths at three altitudes, (2) four lidar records and (3) in situ measurements at two sizes. All data records are consistent in providing estimates not significantly different from zero except for the Hampton lidar and Laramie 0.25 μm in situ measurements. As mentioned above, both of these data sets were highly perturbed by Mt. St. Helens, in comparison to other sites, and this perturbation created problems in establishing the baseline prior to El Chichón. Thus, while these two datasets suggest, at a minimum, no long term increase in background aerosol, they do not establish a long term decrease.

5.5 Discussion

The preceding analysis of background stratospheric aerosol suggests that there has been no long term trend in this quantity in the past 30 years. Thus the present long volcanically quiescent period, following Pinatubo, allows us to characterize rather completely stratospheric background aerosol, and provides a test bed for comparison of integral properties of

Table 5.3. Parameters used to model zonal, $\pm 5^\circ$, five kilometer optical depths at 1020 nm from SAGE II. Optical depth ($\times 104$) and exponential change (yr-1) are given for the baseline and the major impacts of El Chichón and Pinatubo along with their standard errors (σ). The 95% confidence intervals are given by parameter $\pm 2 \sigma$.

Alt km	Lat °	Background				El Chichón				Pinatubo			
		B	$\sigma(B)$	β	$\sigma(\beta)$	P	$\sigma(P)$	ν	$\sigma(\nu)$	P	$\sigma(P)$	ν	$\sigma(\nu)$
18-23	-50	3.00	0.15	0.0055	0.003	15.5	0.96	0.27	0.03	369	19.5	1.19	0.03
18-23	-40	3.86	2.32	-0.0039	0.037	21.4	2.12	0.31	0.05	460	22.0	1.15	0.03
18-23	-30	3.87	0.32	-0.0019	0.006	27.8	1.29	0.34	0.02	436	16.0	1.14	0.02
18-23	-20	4.36	0.37	-0.0083	0.006	37.9	1.64	0.40	0.02	512	18.3	1.14	0.02
18-23	-10	3.74	0.50	0.0014	0.009	60.6	3.09	0.44	0.02	1190	52.0	1.05	0.02
18-23	0	3.48	0.80	0.0064	0.016	93.5	7.17	0.53	0.03	1150	74.6	1.10	0.41
18-23	10	3.74	0.60	0.0043	0.011	82.5	5.37	0.56	0.03	1000	58.1	1.05	0.02
18-23	20	4.03	0.38	-0.0003	0.007	53.3	2.85	0.54	0.02	749	34.6	1.11	0.02
18-23	30	4.15	0.30	-0.0015	0.006	39.8	1.89	0.51	0.02	519	19.5	1.19	0.02
18-23	40	3.92	1.01	-0.0027	0.018	30.2	1.56	0.47	0.05	414	17.9	1.21	0.03
18-23	50	2.97	1.13	0.0082	0.025	21.7	1.42	0.41	0.06	287	16.2	1.18	0.04
24-29	-50	0.06	0.00	0.0009	0.009	0.1	0.00	0.00	0.01	2.3	0.4	2.97	0.27
24-29	-40	0.07	0.01	0.0002	0.009	0.1	0.01	0.00	0.01	1.8	0.3	2.75	0.35
24-29	-30	1.27	0.12	0.0008	0.009	1.6	0.30	0.23	0.06	88.0	11.4	1.49	0.10
24-29	-20	1.61	0.23	0.0028	0.011	4.9	0.60	0.24	0.03	235	30.3	1.34	0.07
24-29	-10	2.06	0.31	0.0008	0.012	10.9	0.91	0.25	0.02	484	47.1	1.33	0.05
24-29	0	2.22	0.37	0.0014	0.013	14.7	1.37	0.30	0.03	463	45.2	1.26	0.05
24-29	10	2.01	0.30	0.0043	0.012	11.3	1.14	0.32	0.03	339	37.5	1.36	0.06
24-29	20	1.73	0.24	0.0021	0.011	5.5	0.77	0.30	0.05	248	37.5	1.53	0.08
24-29	30	1.08	0.13	0.0029	0.011	2.1	0.37	0.27	0.06	72.6	10.2	1.44	0.10
24-29	40	0.74	0.07	0.0060	0.008	0.9	0.16	0.22	0.05	22.0	2.9	1.39	0.12
24-29	50	0.45	0.05	0.0043	0.010	0.5	0.06	0.07	0.02	10.1	1.4	1.35	0.14
30-35	-50	0.11	0.01	0.0000	0.005	0.0	0.02	0.56	1.04	1.7	0.2	2.66	0.27
30-35	-40	0.14	0.01	0.0044	0.005	0.0	0.02	0.44	0.39	1.8	0.3	2.68	0.33
30-35	-30	0.11	0.01	0.0005	0.011	0.1	0.01	0.01	0.01	5.0	0.9	12.9	2.98
30-35	-20	0.21	0.03	0.0017	0.013	0.2	0.03	0.03	0.02	19.6	5.6	11.9	2.12
30-35	-10	0.43	0.04	0.0065	0.009	0.4	0.14	0.46	0.18	10.1	1.9	1.62	0.20
30-35	0	0.45	0.04	0.0099	0.008	0.5	0.13	0.45	0.13	11.1	1.6	1.48	0.14
30-35	10	0.38	0.03	0.0054	0.008	0.3	0.08	0.29	0.10	5.2	0.6	1.50	0.20
30-35	20	0.29	0.03	0.0035	0.009	0.1	0.05	0.19	0.12	3.3	0.4	1.58	0.27
30-35	30	0.13	0.01	0.0199	0.009	0.1	0.02	0.15	0.06	1.4	0.2	1.62	0.32
30-35	40	0.09	0.01	0.0212	0.007	0.1	0.01	0.15	0.05	0.4	0.1	1.56	0.23
30-35	50	0.09	0.00	0.0065	0.005	0.0	0.01	0.22	0.36	0.3	0.0	1.69	0.24

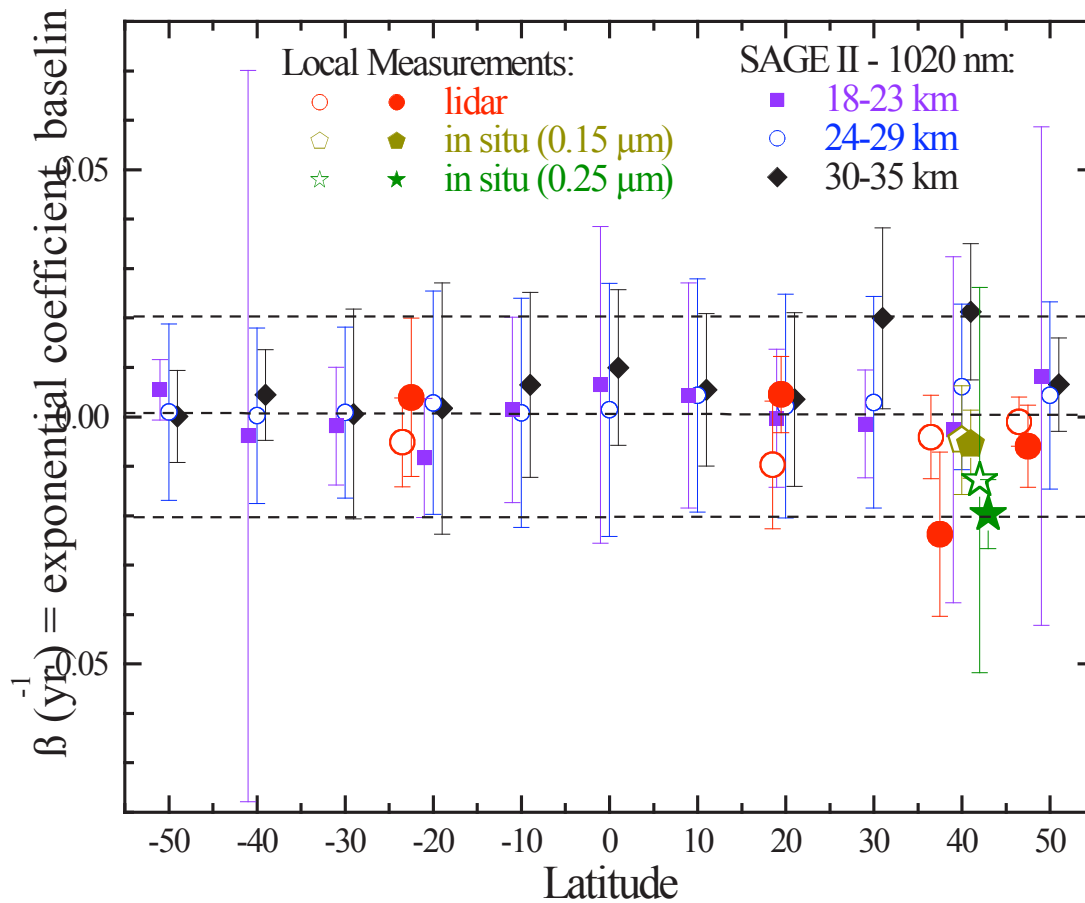


Figure 5.15. Exponential coefficient, β (yr^{-1}) \pm 95% confidence interval, as a function of latitude for $\pm 5^\circ$ zonal averages of 5 km optical depths at 1020 nm from SAGE II for three altitude intervals, for integrated backscatter from São José dos Campos, Mauna Loa, Hampton, and Garmisch, and for 15 - 30 km column integrals of aerosol concentration for particles with radius ≥ 0.15 and $0.25 \mu\text{m}$. For the lidar and in situ data the open symbol represents β based on the analysis of quiescent periods, while the closed symbol represents β obtained from the parametric model. In all cases the values of

stratospheric aerosol, e.g. aerosol surface area and mass, derived from different measurements. Here two such comparisons to address two questions related to background stratospheric aerosol are presented. How well do satellite measurements estimate aerosol surface area under conditions of low aerosol loading when median particle radii for surface area are well below the primary range of sensitivity for satellite extinction measurements at visible wavelengths? What is the global background stratospheric aerosol burden? Although these questions have been considered previously, there is no previous time in the modern aerosol measurement record when stratospheric aerosol have had such an opportunity to relax to a natural state unperturbed by volcanic activity.

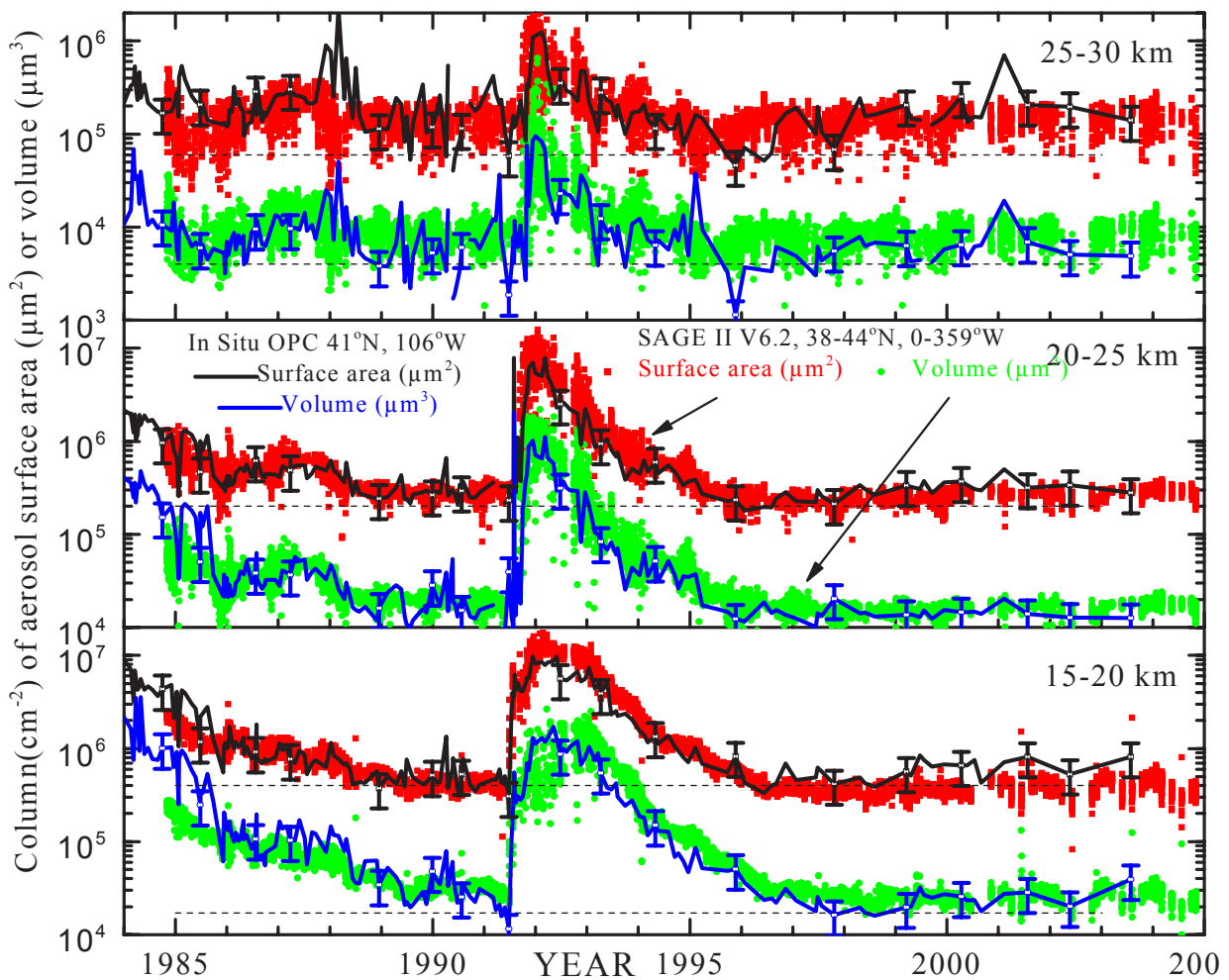


Figure 5.16. History of five kilometer column aerosol surface area and volume in the northern mid latitudes, 1984-2004. The solid lines with intermittent error bars ($\pm 40\%$) are from lognormal size distributions fit to ~ 200 aerosol profiles from balloonborne in situ measurements above Laramie, Wyoming. The symbols are SAGE II V6.2 estimates of surface area and volume from the SAGE II data base for all measurements between 38 and 44°N with no restriction on longitude.

5.5.1 Aerosol surface area: Differences between satellite and in situ measurements

During periods of low stratospheric aerosol loading measurement precision generally decreases as the aerosol signal decreases. Satellite measurements and in situ measurements are perhaps the least impacted. There may, however, be an effect on the retrieval of aerosol surface area from satellite measurements at visible wavelengths [Steele et al., 1999; Randall et al., 2001; Deshler et al. 2003]. Typically surface areas and volumes are calculated from visible wavelength extinction measurements using principal component analysis [Twomey, 1977; Thomason and Poole, 1993; Steele et al., 1999]. Figure 5.16 compares two of the longest records of stratospheric aerosol surface area and volume available [Deshler et al., 2003]. The SAGE II aerosol moments are from the SAGE II data base (V6.2). The SAGE II operational algorithm was described in Chapter 4 and relies heavily on the SAGE II measurements at 525 and 1020 nm. The SAGE II data in Figure 5.16 include all SAGE II measurements between 38 and 44°N. These aerosol moments are similar to moments obtained

by Steele et al. [1999] for high aerosol loading, but are higher than Steele et al. [1999] for background aerosol.

The agreement between the two data sets is well within measurement precision over the record as the stratospheric aerosol transitions from a volcanic to a background state. For this transition the relationship between in situ and satellite volume estimates remains roughly equivalent, with the in situ estimate at the lower range of the satellite estimate. For surface area the relationship between in situ and remote estimates changes, with in situ measurements moving from the lower range to the upper range of the satellite estimates in the transition from volcanic to background.

A physical explanation for the systematic change in the relationship of surface area estimates is offered in Figure 5.17. Differential surface area, volume, and extinction distributions are compared for measurements at two altitudes in 1993, under high aerosol loading, and at two altitudes in 1999, under low aerosol loading. At high aerosol loading there is good overlap between the three differential distributions, Figures 5.17a, b. The median radii of the three distributions, r_s , r_e , r_v , are nearly co-located, particularly at 18 km. At 23 km on 931115 $r_s < r_e$, but there is still excellent overlap of the distributions particularly in the dominant second mode. At low aerosol loading there are significant differences in the median radii and in the sizes covered by the different distributions, Figures 5.17c, d. In low aerosol loading cases, aerosol surface area is controlled by particles between 0.02 and 0.5 μm , $r_s \sim 0.1 \mu\text{m}$, and

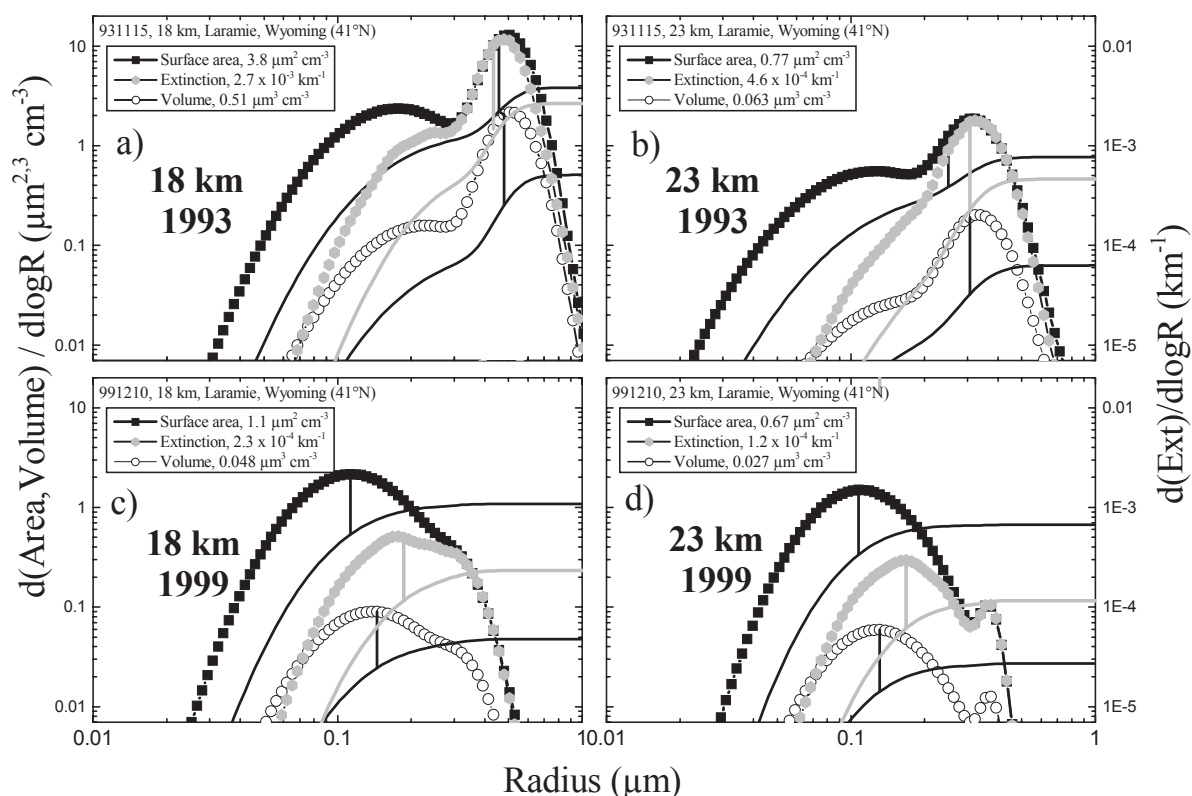


Figure 5.17. Differential (lines and symbols) and cumulative (lines) distributions of aerosol surface area, extinction, and volume at 525 nm for measurements above Laramie, Wyoming, at two altitudes 18 and 23 km for measurements 1.5 years after Pinatubo, 931115, and at low aerosol loading, 991210. The distributions are derived from in situ measurements of aerosol size distribution. The vertical line connecting the differential and cumulative distributions indicates the distribution median radius, i.e. 50% of the cumulative distribution moment is above and below this size. The values of the integrated distribution moments are shown in the legend.

~80% of the total surface area is contributed by particles $< 0.15 \mu\text{m}$. In contrast the extinction distribution is controlled by particles between 0.05 and $0.5 \mu\text{m}$, $r_e \sim 0.2 \mu\text{m}$, and about 25% of the extinction signal is provided by particles less than $0.15 \mu\text{m}$. There is less disparity between extinction and volume distributions. Although $r_v < r_e$, the size range spanned by these two distributions is quite similar in both high and low aerosol loading.

Figure 5.17 suggests that under low aerosol loading the use of extinction measurements to infer aerosol surface area may lead to a systematic underestimation, since aerosol surface area is controlled primarily by particles which contribute minimally to extinction. Accurate measurements of aerosol surface areas under clean stratospheric conditions, even from balloonborne in situ measurements, is also uncertain since the dominant mode of the distribution is captured by just a few measurements: condensation nuclei (CN, $r > 0.01 \mu\text{m}$), and aerosol $> 0.15, 0.25 \mu\text{m}$. The latter measurements only fix the tail of the distribution and are well above r_s . For the in situ measurements the size distribution of particles between 0.01 (CN) and $r > 0.15 \mu\text{m}$ is calculated using unimodal lognormal distributions fit to measurements of the concentration of CN and particles $> 0.15 \mu\text{m}$. The standard method optimizes the fit to the number concentration measurements with size dependent weighting. A fitting method weighted by surface area produced results which were marginally different than the standard method. A comparison using ~450 measurements split between high and low aerosol loading indicated an increase of $12 \pm 36\%$ in surface area for surface area weighted fits to the data compared to no weighting. This result would increase the discrepancy between the in situ and satellite data shown in Figure 5.16; however, 12% is well within the $\pm 40\%$ precision associated with the surface area estimates from the in situ measurements [Deshler et al., 2003].

More accurate measurements of surface area require size resolved concentration measurements between 0.01 and $0.1 \mu\text{m}$. Present aircraft instruments are capable of this with size-resolved measurements for particles $> 0.03 \mu\text{m}$ [Jonsson et al., 1995], but resolution of particle sizes below $0.15 \mu\text{m}$ from balloonborne platforms must await instruments now in the development stage. For a preliminary assessment of the difficulties a lack of size resolution below $0.15 \mu\text{m}$ presents for estimates of surface area from balloonborne in situ measurements, stratospheric aircraft measurements from the Focused Cavity Aerosol Spectrometer (FCAS) [Jonsson et al., 1995] were analyzed. FCAS measurements between 0.03 and $1.67 \mu\text{m}$ radius in 32 size bins were used to simulate measurements from OPCs sensitive to CN, $r > 0.01 \mu\text{m}$, and particles $> 0.15 - 2.0 \mu\text{m}$ in 12 size bins. Bimodal lognormal distributions were then fit to the simulated OPC measurements and estimated aerosol surface areas were compared to surface areas calculated from the discrete size distributions measured by the FCAS. FCAS measurements from 23 September 1997 ($20^\circ\text{N} - 5^\circ\text{S}$, $\theta=380\text{-}500\text{K}$) and 11 March 2000 ($61\text{-}75^\circ\text{N}$, $\theta=400\text{-}470 \text{K}$) were used. The lognormal fits to the simulated measurements reproduced the measured size distributions and surface areas reasonably well, Figure 5.18a; however, there was a systematic overestimation of the surface area by the simulated OPC measurements. Comparisons using ~250 measurements on each day indicated that fits to the simulated OPC data overestimated surface area by $7 \pm 15\%$ on 23 September 1997 and $26 \pm 22\%$ on 11 March 2000. The primary source of error was in fitting distributions to the first mode which were too narrow, resulting in under/over estimates of surface area for particles smaller/larger than the median radii, Figure 5.18b. The overestimation at larger sizes generally overcompensates for under estimation at smaller sizes. For wider first mode distributions, Figure 5.18a, the observations were matched reasonably well and the estimated surface areas were close to the FCAS measurements. Distribution median radii were estimated

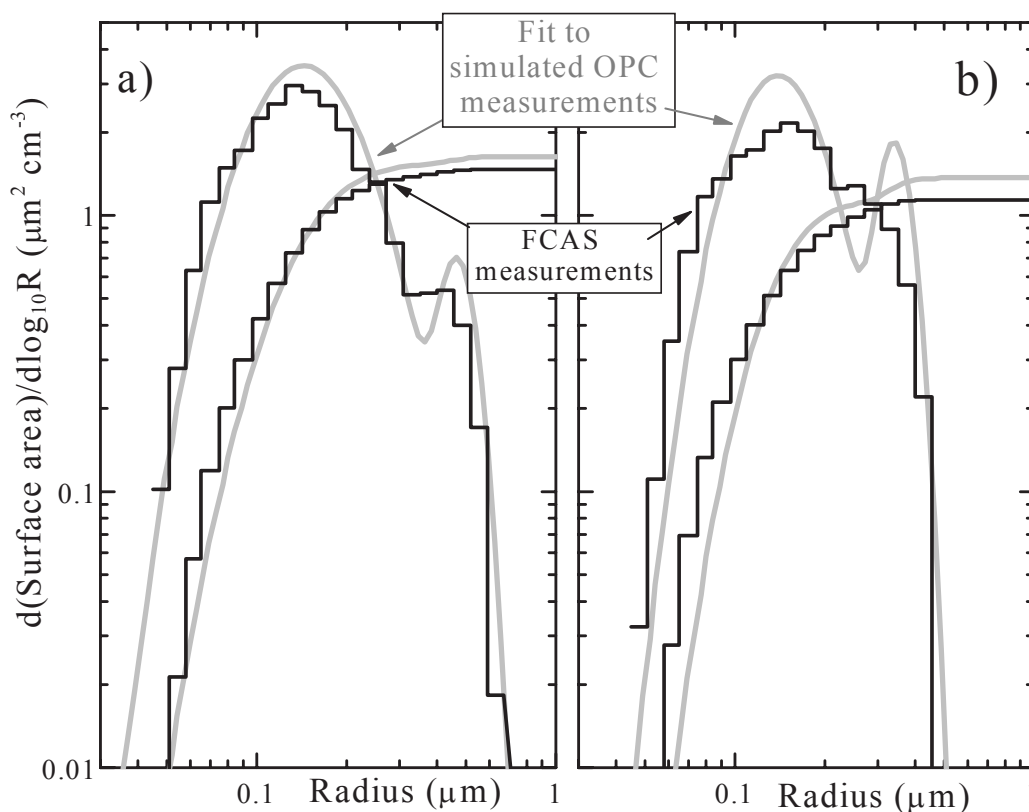


Figure 5.18. Differential and cumulative surface area distributions from discrete FCAS measurements and from bimodal lognormal distributions fit to simulated OPC measurements derived from the FCAS measurements. The two size distributions represent examples of a good fit, left panel, and a poor fit, right panel.

reasonably well even though the median radii of the first mode was always less than $0.1 \mu\text{m}$, well below the first size resolved measurement by the OPC. Thus part of the discrepancy observed in Figure 5.16 may result from overestimates by the OPC; however, this does not fully account for the approximately factor of 2 difference in the worst cases.

5.5.2 Estimates of global stratospheric aerosol burden during background conditions

The source of sulfur for non-volcanic stratospheric aerosol has been discussed since Crutzen's [1976] initial suggestion of OCS. Work in the mid 1990s [Chin and Davis, 1995] suggested that an additional source of sulfur may be required as known emission rates of OCS were insufficient to maintain the background stratospheric aerosol load observed. The measurements discussed here have been compared to the models of Timmrick [2001] and Weisenstein et al. [1997], which use OCS, SO_2 and transport of tropospheric sulfate aerosol into the stratosphere for sulfur sources. These models, if anything, overestimate the background stratospheric aerosol burden when model calculations are compared to aerosol concentrations at specific sizes (Figure 5.2) or integrated backscatter (Figure 5.3). To provide rough estimates of the mass loading which sulfur sources must provide during non-volcanic periods, two single measurement sites are extrapolated to estimate the global stratospheric aerosol load. Although such an extrapolation requires large assumptions, it is believed to provide better than an order of magnitude estimate. The estimates are tied to observations by

normalizing the estimates to 30 Tg of aerosol at the peak of Pinatubo aerosol loading [McCormick et al., 1995].

Extrapolations were made from estimates of integral columns of aerosol volume, from in situ measurements at Laramie, Figure 5.2 and Deshler et al. [2003], but using a 15-30 km column integral, and from aerosol mass inferred from Garmisch integrated backscatter, Figure 5.3 and Jäger [2005]. The integrated backscatter is converted to aerosol mass using Jäger and Deshler [2002, 2003] resulting in estimates provided by Jäger [2005]. Aerosol volumes are converted to aerosol mass using a density of 1.6 g cm^{-3} .

The stratospheric volume containing aerosol was estimated using a simple three cell model with integration limits defined as 18-36 km, 0-30°, 12-33 km, 30-60°, and 10-30 km, 60-90°.

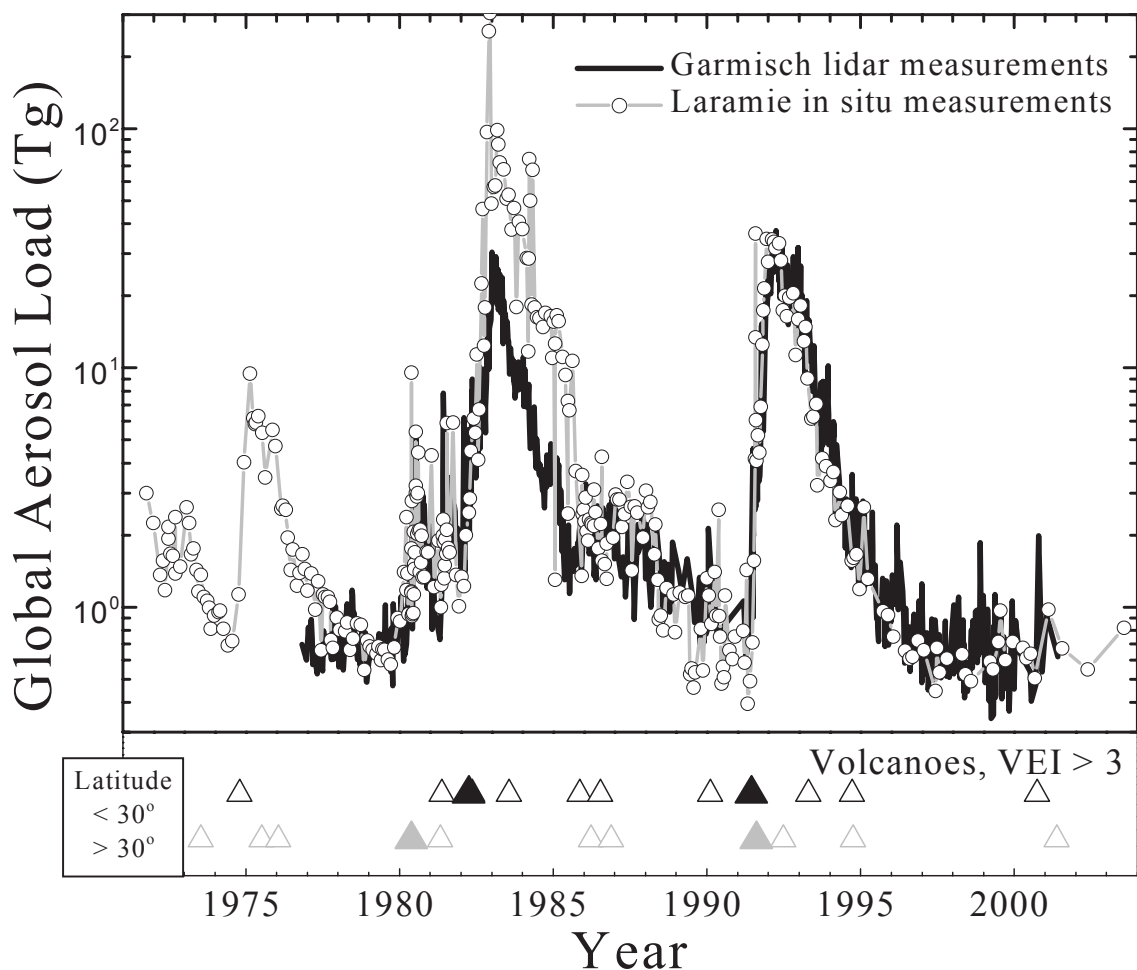


Figure 5.19. Estimates of stratospheric aerosol load based on an extrapolation from in situ profile measurements of aerosol size distribution above Laramie, Wyoming (41°N) and from integrated backscatter measurements above Garmisch (47°N). The in situ measurements use 15-30 km integrated aerosol volume, Figure 5.16, converted to column mass using an aerosol density of 1.6 g cm^{-3} . For backscatter the integrated backscatter columns are converted to mass using Jäger and Deshler [2002, 2003]. The profile measurements are then assumed to apply globally and thus integrated over the stratosphere, with the final result normalized to 30 Tg for Pinatubo. The time of volcanic eruptions with $\text{VEI} \geq 4$ (open triangle) and 5 (closed triangle) are shown at the bottom divided into those eruptions at latitudes less than and greater than 30° of latitude.

The very gross assumption is then made that the aerosol column measured at either Laramie or Garmisch can be used globally for background conditions. The calculations were then normalized to the Pinatubo aerosol load, which has been estimated at 30 Tg of aerosol [McCormick et al., 1995]. The normalization factor for both the in situ and lidar measurements was 0.65, which is surprisingly reasonable given the very large assumptions involved.

Using this simple model the aerosol load extrapolated from the Laramie and Garmisch measurements is shown in Figure 5.19. The usefulness of such a model can be seriously questioned, but it is heartening that the aerosol load shown in Figure 5.19 for Fuego agrees with previous estimates of 3-6 Tg, Table 5.1. The estimates for El Chichón from the in situ measurements are, however, factors of 4-5 too high. This may result from problems resulting from being unable to estimate aerosol concentrations for particles between 0.4 and 1.0 μm resulting from El Chichón compared to direct measurements in this size range following Pinatubo [Deshler et al., 2003]. The Garmisch lidar estimate, using the same model, also normalized to 30 Tg for Pinatubo, gives a maximum of approximately 20 Tg for El Chichón which is above the estimate given in Table 5.1, but closer than the in situ estimate of maximum loading. Based on this rough confirmation of such an extrapolation, the results for background stratospheric aerosol load are approximately 0.6 ± 0.1 (0.7 ± 0.2) Tg for the Laramie in situ (Garmisch lidar) measurements based on averages and population standard deviations for the 1997 - 2003 period. The uncertainties do not account for instrumental uncertainty or uncertainty in the global extrapolation of the measurements. When the in situ data are used to estimate aerosol mass, the elevated 0.25 μm particle concentrations observed in 1990, prior to the eruption of Pinatubo, are not apparent. This is in contrast to Figures 5.2 and 5.5. Instead the measurements in 1990 are similar to the post 1997 measurements.

5.6 Summary and Conclusions

Understanding the non-volcanic fraction of stratospheric aerosol has been one focus of stratospheric aerosol measurements since these measurements began over 40 years ago. Questions such as what are the source gases, how are they transported and transformed in the stratosphere, has there been an impact on natural background levels due to air traffic or other anthropogenic activities, and has the natural background aerosol changed over the course of measurements, have motivated measurements and analyses of background periods. Providing measurements to address these questions, however, has been difficult due to fairly active volcanism over the past 40 years, Table 5.1, with only the post Pinatubo period providing an interval allowing perhaps the first truly non-volcanic aerosol measurements since regular measurements began in the early 1970s. Thus this period provides our best opportunity to observe a stratosphere unperturbed by volcanic activity since long term stratospheric aerosol measurements began.

Junge et al. [1961] initiated stratospheric aerosol measurements in the late 1950s, which was at the end of a volcanically quiescent period. For this reason these measurements provided a baseline against which measurements in the 1970s and 1980s were compared. This provided the basis for early assessments of stratospheric aerosol which concluded that there had been an increase in the background aerosol. Now, with the benefit of minimal volcanism since Pinatubo, a definitive comparison with Junge's initial measurements, Figure 5.1, can be completed. From this comparison, and the stability of measurements following the decay of

Pinatubo volcanic aerosol, it is concluded that Junge's initial in situ measurements underestimated the size range or number concentration, or both, and thus the stratospheric aerosol measurements which can be reliably used to assess trends in the non-volcanic component of stratospheric aerosol began in the early 1970s. Earlier assessments of trends in non-volcanic stratospheric aerosol, which included Junge's initial measurements, 1959 - 1960, were probably premature. This interpretation is predicated on the assumption that the source gases for background stratospheric aerosol were relatively stagnant over this period.

During volcanically quiescent periods the sulfur for stratospheric aerosol arises from the transport of tropospheric OCS, SO₂, and sulfate aerosol into the stratosphere. If the fractional contributions of these source gases (35, 25, 40%) to stratospheric aerosol are coupled with trends in OCS [Montzka et al., 2004] and anthropogenic SO₂ [van Ardenne et al., 2001] a change in background stratospheric aerosol can be estimated for 1960-1990. These estimates indicate an increase of ~0.5% yr⁻¹, well below the earlier estimates of 5-9% yr⁻¹ and even the more conservative estimate of 2% yr⁻¹ indicated in Figure 5.1.

To provide an objective analysis of the stratospheric aerosol record since 1970 the statistical analysis of the six long term stratospheric aerosol records (1 in situ, 4 lidars, 1 satellite) were approached in two ways. First, measurements limited to the three volcanically quiescent periods were compared using standard techniques. Second, an empirical model was developed to remove the volcanic signal from the long term records and to investigate the "de-volcanized" measurements for trend. The data sets used for the analyses are: a) column integrals of in situ concentration measurements from Laramie, Wyoming, at two sizes, 0.15, 0.25 μm; b) integrated backscatter above the tropopause from Garmisch-Partenkirchen, Germany; Hampton, Virginia; Mauna Loa, Hawaii; and São José dos Campos, Brazil; and c) SAGE II extinction. The in situ measurements provide 2 data sets, 15 - 30 km column integrals of aerosol ≥ 0.15, 0.25 μm radius. The lidar records provide 4 data sets. The SAGE II measurements were separated into 33 data sets: zonal (±5°) averages of 5 km optical depths at 1020 nm for 18-23, 24-29, 30-35 km. These data are centered at latitudes of 0, ±10 ... ±50°. SAGE data were included with the SAGE II data for some trial cases, but this did not change conclusions based just on the SAGE II data. The possibility of augmenting these data with SAM measurements was investigated, but there was no latitudinal overlap since the SAGE II data were limited to latitudes ≤ 50° to avoid polar stratospheric clouds. Consideration of SAM II data alone was deemed not helpful once the records were limited to non polar stratospheric cloud periods.

Simple inspection of the long term records suggests that: a) There have been fewer small volcanic eruptions following Pinatubo than during the two previous volcanically quiescent periods. b) The pre-Pinatubo period is elevated compared to the post Pinatubo and pre-El Chichón period. c) The post Pinatubo period and pre-El Chichón period thus control any conclusions regarding long term changes. d) Volcanic aerosol from Pinatubo disappeared from the long term measurement records between 4.5 and 7.5 years following the eruption, dependent on latitude and measurement platform. e) The post Pinatubo period represents our best opportunity to observe a stratosphere unperturbed directly by volcanic activity. f) The current low aerosol levels are believed due to the long period of limited volcanic input. g) Stratospheric aerosol are not expected to fall significantly below current levels, although longer-term variations cannot be ruled out.

Comparison of measurements within the 3 volcanically quiescent periods indicates that only the 1 in situ and 4 lidar records capture the three volcanically quiescent periods, pre El

Chichón, pre Pinatubo and post Pinatubo. SAGE II only captures pre and post Pinatubo and the pre-Pinatubo SAGE II record is not convincingly at background. Investigation of the 5 longer records suggests that the first two periods may also not have reached background, particularly prior to Pinatubo. In 3 of the 4 lidar records (Garmisch, Hampton, São José), and in the 0.25 μm in situ record 15-30 km, the pre-Pinatubo period is elevated compared to the other periods. Simple linear regression over the three periods is controlled by the end points, pre El Chichón, post Pinatubo and indicates either no change (Garmisch, Hampton, São José dos Campos, Laramie-0.15 μm) or a slight decrease in stratospheric aerosol (Mauna Loa, Laramie-0.25 μm). Problems with a simple linear regression arise due to irregular temporal data and the high degree of autocorrelation. Including autocorrelation in the estimates decreases confidence in the estimates (increases standard errors), but does not change the conclusion that the majority of data indicate no trend in background stratospheric aerosol, 1970 - 2005. Two data sets, Mauna Loa and Laramie 0.25 μm , suggest slight negative trends of $-1 \pm 1.0\% \text{ yr}^{-1}$ and $-1 \pm 4\% \text{ yr}^{-1}$, respectively. The results for Mauna Loa are borderline statistically significant when autocorrelation effects are considered. This analysis is dependent on the assumption that stratospheric aerosol in the short 1-2 year period prior to Mt. St. Helens in 1980 was at background.

A time and volcano dependent empirical model was fit to the long term aerosol records to "de-volcanize" the data and thus analyze the entire data set for trend. Working in log space was required to treat errors during cases of high and low aerosol load equally. The empirical model also included a parameter to capture trends in the background aerosol. A standard squared-error residual minimization technique was employed to estimate the optimum parameters for the model for each measurement and each site. This included 4 lidar data sets, 2 in situ data sets (two aerosol sizes) and 33 SAGE II data sets (optical depths at 1020 nm at three altitude and eleven latitude intervals). These analyses allowed for first order autocorrelation and used a one-dimensional spatial representation to account for the temporally disparate sampling intervals. As with the simpler comparison of background periods the autocorrelation increases the standard errors of the trends but does not change the magnitude. For 31 of 33 SAGE II data sets, 3 of 4 lidar records, and in situ measurements at 0.15 μm the analyses suggest no long term trend in stratospheric aerosol. For one lidar site (Hampton) and in situ measurements at 0.25 μm , the results suggest a weak negative trend, on the order of $-2 \pm 0.5\% \text{ yr}^{-1}$. Both these estimates suffer from difficulties introduced by Mt. St. Helens, and a comparison of the model with the data suggests problems in representing properly the measurements prior to El Chichón. In contrast to these two estimates of a negative trend, two SAGE II data sets (30-35 km, 30° and 40°N) suggest a positive trend of the same magnitude, $2\% \text{ yr}^{-1}$.

The overall conclusion from both the simple analysis of quiescent periods and the empirical model fit to the measurements is that background stratospheric aerosol has not displayed a long term trend over the period 1970 - 2005. This conclusion is supported by 94% of the satellite data analyzed, 75% of the lidar data, and 50% of the in situ data. The conclusion from the remaining data is not compelling. In addition to this result from statistical analyses, the long volcanically quiescent period following Pinatubo allows each record to be inspected for trend over a period of 5 to 8 years, and all are consistent in showing no significant change over this latter period.

The statistical analyses were completed on altitude/latitude integrals of the measurements, precluding establishing, or ruling out, long term changes in microphysical properties of background stratospheric aerosol. The focus on integral properties, an inherent limitation of

this investigation, is dictated by the fact that all but the in situ instruments make measurements on ensembles of particles and thus inherently integrate over the size distribution. Thus the in situ record was also integrated to provide a relatively homogenous data set for comparison with the other long term records. Some information concerning the long term tendency of aerosol size distributions is available by comparing altitude integrals of the two sizes, $r > 0.15, 0.25 \mu\text{m}$, measured. The simple comparison here indicates no change in the concentration of particles $> 0.15 \mu\text{m}$ radius with a slight decrease for particles $> 0.25 \mu\text{m}$. This difference is not enough to be apparent in size distribution integrals, e.g. surface area or volume.

Background aerosol present special challenges for inverting surface area from optical extinction measurements. In background conditions median radii of aerosol size distributions are on the order of $0.07 \mu\text{m}$. In these cases extinction at optical wavelengths is determined by less than 50% of the particles which determine surface area. This can lead to underestimates of aerosol surface area during background conditions. The background global stratospheric aerosol load was estimated to be $0.65 \pm 0.2 \text{ Tg}$ based on extrapolating in situ aerosol measurements at Laramie, and lidar measurements at Garmisch, between 1997 and 2003, to encompass the global stratosphere. The uncertainty quoted is the standard deviation of the estimates over the period 1997-2003.

CHAPTER 6

Modeling of Stratospheric Aerosols

Lead Authors:

Debra Weisenstein
Slimane Bekki

Authors:

Michael Mills
Giovanni Pitari
Claudia Timmreck

Contributors:

Mian Chin
Mark Hervig
Fok-Yan Leung
Beiping Luo
Eva Mancini
Joyce Penner
James C. Wilson

6.1 Summary

- Models provide a way to synthesize our knowledge of stratospheric aerosol processes and quantitatively test our understanding against observations. However, model uncertainties, especially transport rates, limit our confidence.
- Sedimentation is a crucial process determining the vertical distribution of aerosol mass and sulfur in the stratosphere. Sedimentation is a strong function of altitude as well as particle size, and reduces sulfur in the upper model stratospheres by over 75%.
- Nucleation of new particles is important near the tropopause, particularly in the tropics, and at polar latitudes in the middle stratosphere in winter. Particle size is determined by nucleation, and subsequently by coagulation, condensation, and evaporation, as well as transport and mixing.
- OCS, SO₂, and particles transported across the tropopause are the primary precursors to stratospheric aerosol. Analysis of sulfur budgets in the models shows that transport of SO₂ and particles, for which SO₂ is the precursor, across the tropical tropopause are potentially large contributors to the stratospheric aerosol burden. Large uncertainties remain in our ability to quantify the relative contributions, but the models show OCS to be the main contributor above 25 km and SO₂ and particles to play a larger role below.
- OCS mixing ratios in the tropics are well represented by the models. However, the models do not all match observations of OCS in mid and high latitudes, reflecting the variability of transport between models. Since this gas represents the main sulfur source in the mid-stratosphere, confidence in the rate of OCS oxidation and aerosol formation in the tropics is gained.
- SO₂ mixing ratios in the tropics show large variability between models. Model differences are probably due to the short lifetime of SO₂ in the tropics along with differences in the OH concentrations and transport differences.
- More SO₂ measurements would be valuable. Better knowledge of SO₂ concentrations in the UT would be required to obtain a correct description of the transport of sulfur into the stratosphere. Knowing SO₂ in the lower-mid stratosphere helps verify the OCS chemical destruction rate and the SO₂ to H₂SO₄ conversion rate, along with transport rates. Above 35 km, observations show an increase in SO₂ which can only be reproduced by models that include a photolytic conversion of gaseous H₂SO₄ into SO₂.
- Comparisons between models and satellite observations of aerosol extinction are generally fairly good at visible wavelengths but are less satisfactory for infrared wavelengths. Aerosol extinction measurements from SAGE II at 0.525 and 1.02 μm can be matched by models above 20-25 km altitude under nonvolcanic conditions. Tropical observations show a sharp vertical gradient in extinction at 17-20 km which varies with season and is not reproduced by the models. Models are less successful at reproducing extinction observations from the HALOE instrument at 3.46 and 5.26 μm.
- Models predict aerosol size distributions which can be approximated by a lognormal function except near regions of nucleation or evaporation. Integrated aerosol quantities such as surface area and effective radius can in principle be calculated without approximation from model size distributions, whereas satellite observations and in situ measurements by optical particle counters used to derive these quantities are either controlled by a priori assumptions regarding the size

distribution or have coarse resolution at the small size bins. Comparisons of these quantities during volcanically quiescent periods are problematic because much of the aerosol density may reside in particles too small to be observed, especially near nucleation regions.

- Simulations of the Mt. Pinatubo period are generally good but dependent on the assumed initial vertical distribution of volcanic sulfur. For instance, model results show very good agreement with column integrated lidar backscatter at both tropical and mid latitude sites, including the magnitude and timing of the aerosol maximum and the rate of decay. Comparisons with SAGE II extinctions show that models may under or over predict extinction at different altitudes depending on the applied model and the assumed vertical distribution of volcanic sulfur at the beginning of the event.
- The modeled rate of recovery from the Pinatubo eruption depends on the quantity considered (extinction, number density, surface area density) and the latitude and altitude of interest. Recovery time constants (e-folding times) show decay rates that lengthen with time past the eruption, consistent observations. Different models exhibit different recovery time constants, however, with a scatter not larger than that of the observations.

6.2 Scope and Rationale

The overall objective of this chapter is to assess whether transport of sulfur compounds (primarily SO₂ and OCS) from the troposphere and known physical processes can explain the distribution and variability of the stratospheric aerosol layer. Since aerosol models synthesize our knowledge about coupled aerosol processes, they, together with observations, are the main tools used here to test our current quantitative understanding of the processes controlling the formation and evolution of the stratospheric aerosol layer. The core of the chapter is devoted to detailed comparisons between global aerosol model simulations and observations. The observations and aerosol products derived from them are presented in Chapter 4. Comparisons are used to evaluate the performances of the models with respect to a range of relevant aerosol quantities and identify gaps in our understanding of aerosol processes or/and deficiencies in their representation in models and, where possible, assess problems in available data sets. It is worth stressing that this up-to-date modeling assessment is not a detailed model intercomparison. The use of different models provides a range of uncertainties in current model simulations, though true uncertainty is likely to be larger than the model spread. The models are described in detail in Section 6.3. They are all well-established global 2-D and 3-D aerosol-chemistry-transport models.

A number of questions which are discussed in the previous chapters are addressed in this up-to-date modeling assessment. The aerosol processes which are discussed in Chapter 1 are illustrated with examples from the models in Section 6.4. Section 6.5 presents direct comparisons between model simulations and measurements of gaseous precursors and aerosols for non-volcanic conditions. This allows us to evaluate the capabilities of global stratospheric aerosol models at the present time, in particular in reproducing the broad features of the non-volcanic aerosol layer. Continuous quiescent volcanic outgassing is considered a 'non-volcanic' source in the chapter as opposed to the intermittent explosive volcanic eruptions whose columns inject sulfur directly into the stratosphere. Sulfur budgets are derived and the respective contributions of OCS, SO₂, and particulate transported from the troposphere to the stratosphere are estimated. Sensitivity studies

designed to highlight model uncertainties and assess the extent to which changes in tropospheric concentrations of gaseous precursors (OCS, SO₂) and aerosols can affect the stratospheric distributions and trends of sulfate aerosols are described in Section 6.6.

Model simulations of a Pinatubo-like stratospheric sulfur injection are described in Section 6.7. They are evaluated against observations focusing on characteristics of the aerosol evolution such as the timing and magnitude of the peak aerosol loading and the aerosol decay rate. These simulations are compared with backscatter observations from lidar stations, satellite extinction measurements, and in situ measurements of particle number density. Finally, the overall results are discussed and summarized in Section 6.8. Model limitations and uncertainties due to the representation of transport and microphysics are discussed, along with limitations of the present observational data. Gaps in our understanding, along with recommendations for future observations and modeling work, are highlighted.

6.3 Model Descriptions

This section is devoted to the descriptions of the aerosol-chemistry-transport models used in the comparisons. Five different modeling groups participated in the comparisons for this chapter. Table 6.1 lists the participating models, investigators, and their institutions. References to each model are also given. Two of the models are three-dimensional (ULAQ, MPI), three are two-dimensional models (AER, UPMC, LASP). Each model represents the global domain from the surface to 30 km (MPI model) or 60 km (AER and UPMC) or higher (ULAQ AND LASP). Grid resolution ranges from 3.75° to 10° in latitude and from 1.2 km to 3.5 km in altitude, as detailed in Table 6.2. Model dynamics (wind fields and temperature) are calculated interactively in the UPMC and LASP 2-D models, but are specified from climatological analyses [Fleming et al., 1999] in the AER model. The MPI aerosol model is fully implemented within the Hamburg climate model ECHAM-4 GCM [Roeckner et al., 1996]. The ULAQ model used dynamical parameters taken from the output of a GCM. Tropospheric processes such as convection and cloud scavenging are included in the 3-D models, with time-dependent rates according to the GCM cloud processes. Two-dimensional models are not designed to simulate tropospheric dynamics or chemistry in detail, since topography, surface properties, and

Table 6.1: Participating Models

Model	Investigator	Institution	References
AER	D. Weisenstein	Atmospheric and Environmental Research, Inc. Lexington, MA, U.S.A.	Weisenstein et al., 1997 Weisenstein et al., 1998
UPMC	S. Bekki	University Pierre et Marie Curie Paris, France	Bekki and Pyle, 1992, 1993 Bekki, 1995
LASP	M. Mills	LASP, University of Colorado Boulder, CO, U.S.A.	Mills et al., 1999 Burkholder et al., 2000
MPI	C. Timmreck	Max-Planck Institut für Meteorologie Hamburg, Germany	Timmreck, 2001
ULAQ	G. Pitari	University L'Aquila Aquila, Italy	Pitari et al., 2002

Table 6.2: Model Domain and Resolution

Model	Type	Domain	Resolution	Dynamics
AER	2D	ground to ~ 60 km	$9.5^\circ \times 1.2$ km	climatology
UPMC	2D	ground to ~ 60 km	$9.5^\circ \times 3.5$ km	interactive
LASP	2D	ground to 112 km	$5^\circ \times 2$ km	interactive
MPI	3D	ground to ~ 30 km	$3.75^\circ(\text{lon.}) \times 3.75^\circ(\text{lat.}) \times 19$ levels	GCM online
ULAQ	3D	ground to ~ 70 km	$22.5^\circ(\text{lon.}) \times 10^\circ(\text{lat.}) \times 26$ levels	GCM offline

localized emissions cannot be included. Therefore our approach in this report is to specify boundary conditions at the tropopause for the 2-D models so that inputs to the stratosphere will be as realistic as possible and independent of 2-D tropospheric dynamics.

Sulfur source gases may include SO₂, OCS, DMS, H₂S, and CS₂, as detailed in Table 6.3, but SO₂ and OCS are the only significant gas species in terms of sulfur input to the stratosphere. DMS, H₂S, and CS₂ have short lifetimes in the troposphere, yielding SO₂ which may be transported to the stratosphere. All models except MPI with an upper boundary at 30 km account for significant recycling of gaseous H₂SO₄ into SO_x (=S+SO+SO₂+SO₃) in the upper stratosphere [Rinsland et al., 1995] via photolysis. The rate of this photolysis reaction has been uncertain and therefore varies among the models, with most assuming photolysis in the UV, though recent work reports photolysis in the visible [Vaida et al., 2004; Mills et al., 2005]. This subject will be discussed further in Section 6.5.2. Most models allow changes in sulfur species to perturb the chemistry of

Table 6.3: Model Chemistry

Model	Source Gases	SO _x Species	H ₂ SO ₄ → SO ₂	Rates from
AER	SO ₂ , OCS, DMS, H ₂ S, CS ₂	SO ₂ , SO ₃ , H ₂ SO ₄	yes	JPL-2000
UPMC	SO ₂ , OCS	S, SO, SO ₂ , SO ₃ , HSO ₃ , H ₂ SO ₄	yes	JPL-2000
LASP	SO ₂ , OCS	SO ₂ , SO ₃ , H ₂ SO ₄	yes	JPL-2000
MPI	SO ₂ , OCS, DMS	S, SO, SO ₂ , SO ₃ , HSO ₃ , H ₂ SO ₄	no	JPL-2000
ULAQ	SO ₂ , OCS, DMS, H ₂ S, CS ₂	SO ₂ , H ₂ SO ₄	yes	JPL-97

OH and ozone, an important feedback during times of massive volcanic eruptions (i.e. larger than Pinatubo) [Bekki, 1995]. However, since OH concentrations are not significantly perturbed by the Pinatubo event, and O₃ concentrations, though perturbed, have a small effect on sulfur gases and aerosols, these feedbacks are not important to the results presented here. The MPI and AER model use pre-calculated values of OH and other oxidants, along with pre-calculated photolysis rates, derived from a model calculation with standard stratospheric chemistry. All the models employ reaction rates from JPL-97 [DeMore et al., 1997] or JPL-2000 [Sander et al., 2000].

The models used in this assessment were developed as stratospheric aerosol models. These models differ from tropospheric aerosol models in that resolving the size distribution of aerosol particles is crucial to predicting the correct sedimentation rate and therefore the lifetime of stratospheric particles. In the troposphere, only particles larger than ~ 1 μm settle appreciably, whereas the thinner air in the stratosphere causes sedimentation rates to be a strong function of both particle radius and air density. Even particles of 0.01 μm have significant sedimentation rates at 30 km. Tropospheric aerosol models typically deal only with total aerosol mass, but may assume a lognormal distribution to resolve the particle sizes. All the models here resolve aerosol sizes into sections, or "bins" (using a geometrical factor between the volumes of consecutive bins), with each bin size transported separately. These types of aerosol schemes are usually referred to as fully size-resolving aerosol schemes. Since the computational cost of resolving an additional dimension (i.e. size space) is very high, size-resolving schemes are only used in two-dimensional models and low-resolution global three-dimensional models.

Tropospheric aerosol models deal with many types of aerosols, including sulfate, dust, sea salt, organics, and black carbon. Stratospheric models typically deal with only sulfate particles (and PSC particles in polar regions), as the other particle types seldom penetrate the lowermost stratosphere. The sulfuric acid aerosols are treated as liquid binary solution droplets (or ternary solution droplets in polar regions). Their exact composition is directly derived from the surrounding temperature and humidity (and nitric acid concentration in polar regions) [Tabazadeh et al., 1997; Carslaw et al., 1995]. It has been suggested [Hunten et al., 1980; Cziczo et al., 2001] that meteoritic material may be contained in a significant fraction of stratospheric aerosols, but none of the models include meteoritic material because of the large uncertainty in its source and stratospheric abundance. The UPMC and ULAQ models include soot particles from surface sources, but find very little soot in the stratosphere due to efficient removal in precipitation. Tropospheric transport, including rapid transport in convective cells, is believed to play an important role in moving sulfur source gases from the boundary layer to the upper troposphere (see Chapter 2). Stratospheric models may not have the spatial resolution in the troposphere to resolve these localized transport features, or the localized nature of some sulfur sources, such as industrial SO₂ emissions. Two-dimensional models in particular have unrealistic tropospheres. This problem is addressed in this assessment by selecting tropopause boundary conditions for the 2-D models which are derived from either observations or 3-D models, so that the input of source gases and aerosols to the stratosphere will be as realistic as possible and less model-dependent.

Microphysical processes (nucleation, condensation/evaporation, coagulation, sedimentation) determine the evolution of the aerosol concentration in each size interval. Table 6.4 gives details of the size range and resolution used by each model. All but the

ULAQ model use volume doubling bin resolution. The ULAQ model uses radius doubling (or a factor of 8 in volume). Some models (UPMC, LASP, and ULAQ) account for different aerosol composition in cold polar regions, where HNO₃ and H₂O condense onto particles forming polar stratospheric clouds (PSCs). Because this report is not intended to be an assessment of PSCs, we have not performed model comparisons with observations when PSCs are present. The presence of PSCs, however, will impact the lifetime of sulfate particles in polar regions.

For details of each model's microphysical scheme, refer to the publications listed in Table 6.1. Here we mention only major similarities and differences. The UPMC model employs heterogeneous nucleation only, the AER, LASP, and MPI models use only homogeneous nucleation, and the ULAQ model uses both homogeneous and heterogeneous nucleation. Nucleation theories and observations often differ by several orders of magnitude, so there is much uncertainty in this calculation. The details of the nucleation scheme are probably less important than correctly predicting regions where nucleation occurs (mainly the tropical tropopause and polar regions). Coagulation will reduce number densities when nucleation rates are large, so large differences in nucleation rates between models do not translate into large differences in predicted size distributions. See Section 6.6.1 for more discussion of this topic.

The processes of condensation and evaporation, coagulation, and sedimentation are treated similarly in all the models though details of the implementations are different. Rainout and washout remove aerosol particles from the troposphere and act as the major sink for stratospheric aerosols in the models. These processes vary with time in the 3-D models but are parameterized more simply in the 2-D models.

Table 6.4: Aerosol Schemes

Model	# bins	Size Range	Resolution	Composition
AER	40	0.00039 to 3.2 μm	volume doubling	H ₂ SO ₄ /H ₂ O
UPMC	25	0.01 to 2.5 μm	volume doubling	H ₂ SO ₄ /H ₂ O/HNO ₃ /soot
LASP	45	0.0005 to 10 μm	volume doubling	H ₂ SO ₄ /H ₂ O/HNO ₃
MPI	35	0.001 to 2.58 μm	volume doubling	H ₂ SO ₄ /H ₂ O
ULAQ	11	0.01 to 10.2 μm	radius doubling	H ₂ SO ₄ /H ₂ O/HNO ₃ /soot

6.4 Model Illustrations of Aerosol Microphysics

In the present section, we illustrate the stratospheric aerosol lifecycle discussed in Chapter 1 with examples from the models. As shown in Figure 6.1, the nucleation process occurs year-round in the tropopause region within the AER model when the Vehkamäki et al. [2002] nucleation parameterization is applied. Between 30°N and 30°S, nucleation occurs from about 10 to 18 km in altitude, though the midlatitude tropopause experiences nucleation to a lesser extent and in a narrower altitude region. The maximum nucleation rate is 2-3 km below the tropopause in the tropics, with 90% of model nucleation

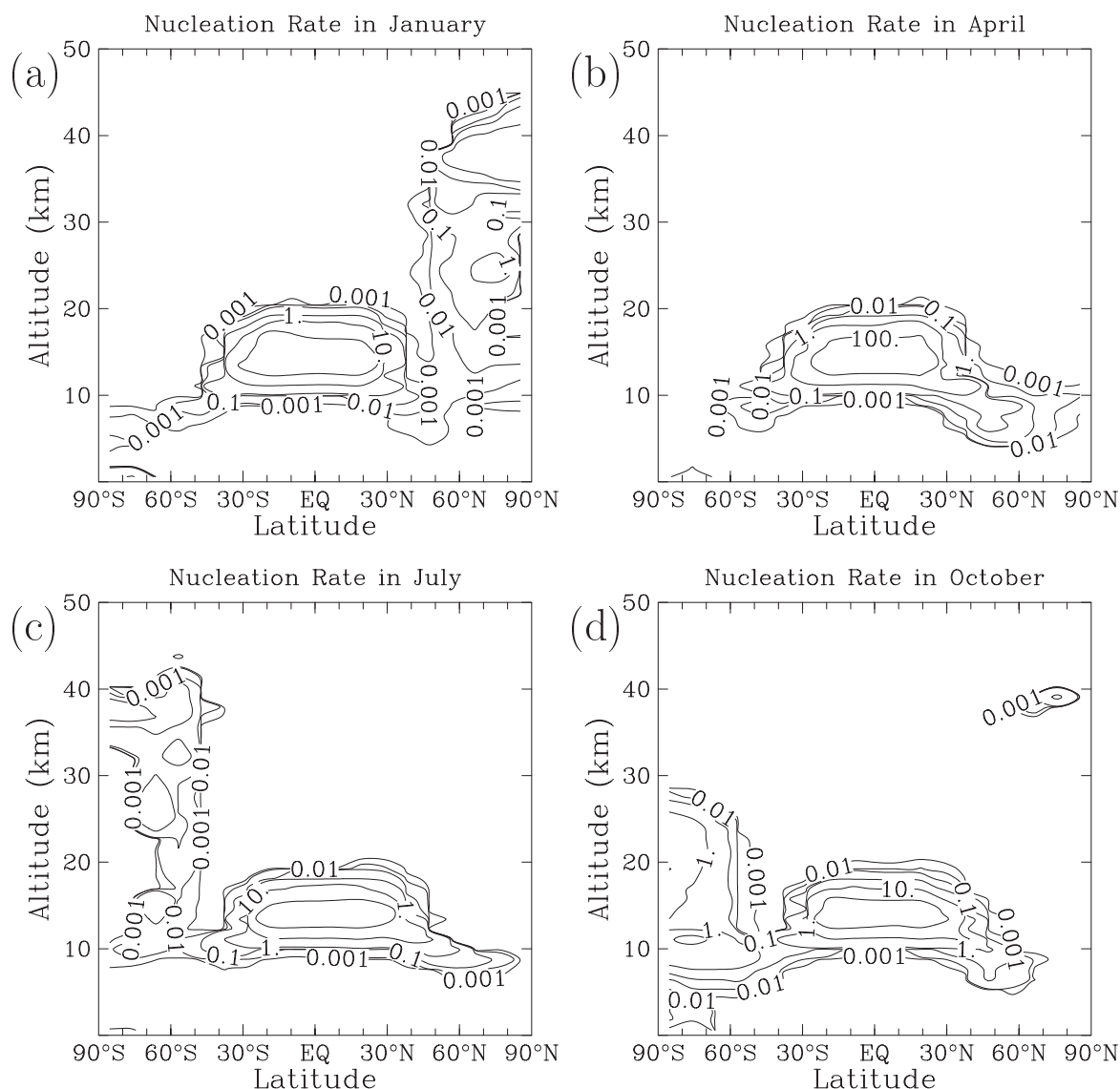


Figure 6.1: Nucleation rate (in 10^{-21} molecules of sulfur per cm^3) for (a) January, (b) April, (c) July, and (d) October as calculated by the AER 2-D model using the Vehkamäki et al. [2002] nucleation scheme. Contours are 0.0001, 0.001, 0.01, 0.1, 1, 10, 100.

occurring in the troposphere. The freshly-nucleated particles are transported into the stratosphere, the imposed primary aerosol merely contributing to the larger size range. The freshly-nucleated particles contribute only a minor amount of aerosol mass to the stratosphere, but are important in determining number density and particle size distribution. The high latitudes experience nucleation in winter (November to March in the Northern Hemisphere, May to November in the Southern Hemisphere) from the tropopause to 30 or even 45 km.

It should be noted that nucleation in the real atmosphere is episodic; occurring in limited geographical regions in short bursts when convection brings high concentrations of gaseous H_2SO_4 into the upper troposphere, or when wave activity depresses local temperatures and causes supersaturation. The models do not include the necessary geographical resolution or convective and wave activity to stimulate nucleation bursts, and therefore tend to calculate nucleation at slower rates continuously over large

geographical areas and time periods. A more accurate representation of nucleation processes within large-scale models would require subgrid scale parameterizations accounting for small-scale fluctuations in key parameters (temperature, sulfuric acid, water vapor, preexisting particles). Because bursts of nucleation would produce extremely high particle concentrations in localized areas, coagulation would be very effective in reducing number concentration within days to weeks. Since coagulation of nanometer-sized particles is self-limiting, it is expected that, for global modeling, simulating the temporal variation of nucleation rate is less important than predicting correctly where and in what seasons nucleation occurs.

Some simple time-dependent microphysical box model calculations will illustrate the processes of nucleation, coagulation, condensation, sedimentation, and evaporation. These calculations with the AER model use 150 bins over the size range from 0.4 nm to 3.2 μm and a time step of 3.6 seconds to deal with rapid aerosol evolution. The AER model's usual time step is 1 hour with 40 bins. Coagulation is active in all simulations, but is generally ineffective when number concentrations are low.

Figure 6.2 shows the evolution of the aerosol particle size distribution over the course of 10 days, assuming no aerosol removal by sedimentation, for typical upper tropospheric conditions (124 mb, 199 K, H_2O mixing ratio of 3.14 ppmv or 14% relative humidity). The calculations are initialized with 40 pptv of H_2SO_4 in the gas phase and no aerosol particles. Condensation is ignored in these calculations so that the effects of nucleation and coagulation are evident. In Figure 6.2a, all the initial gas phase H_2SO_4 is nucleated within the first second, and the distribution subsequently evolves by coagulation. Figure 6.2b represents a case with the same initialization, but including a continuous source of gas phase H_2SO_4 of 40 pptv/day, causing nucleation throughout the integration. The size distributions shown are indicative that an air parcel has seen a recent nucleation event.

The process of heteromolecular condensation is illustrated in Figure 6.3 under lower stratospheric conditions (27.8 mb, 216.5 K, H_2O mixing ratio of 2.76 ppmv or 0.3%

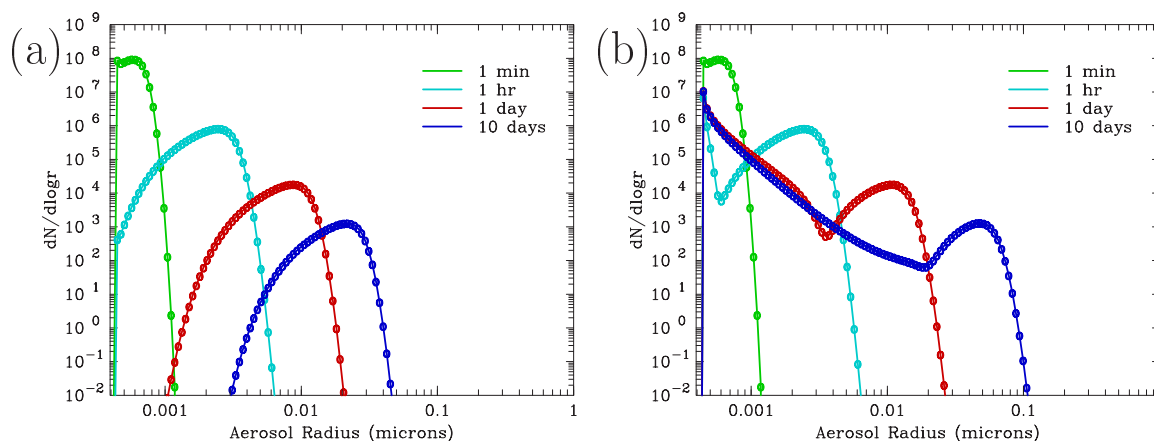


Figure 6.2: Evolution of calculated aerosol size distribution using a microphysical box model for typical upper tropospheric conditions (124 mb, 199 K, H_2O mixing ratio of 3.14 ppmv or 14% relative humidity). Panel A initializes the model with 40 pptv of H_2SO_4 in the gas phase and no aerosol particles. Panel B represents a case with the same initial H_2SO_4 concentration, and a continuous source of gas phase H_2SO_4 of 40 pptv per day. The model uses 150 bins over the size range from 0.4 nm to 3.2 μm and a time step of 3.6 seconds. In this computation, nucleation and coagulation are the only processes responsible for the aerosol evolution, as condensation and sedimentation have been ignored.

relative humidity). The model is initialized with 40 pptv of H_2SO_4 in the gas phase and 40 pptv of H_2SO_4 as aerosol particles with a mode radius of $0.08 \mu\text{m}$ and includes a continuous source of gas phase H_2SO_4 . Figure 6.3a shows a case with nucleation switched off and hence condensation of H_2SO_4 occurs on the preexisting aerosols. Condensation and coagulation strongly reduce the number of small particles while increasing the number of larger particles. As a result, the size distribution narrows. Figure 6.3b shows a case with nucleation included and a continuous source of gas phase H_2SO_4 of 40 pptv/day. The nucleation burst within the first minute provides an additional surface for condensation, and the particles grow rapidly, with most of the condensation occurring on the smaller nucleation-mode particles rather than the initial larger mode. Coagulation is not very effective in case (a) because of the low number densities, but is effective in case (b).

The process of sedimentation is illustrated in Figure 6.4, which shows the evolution over 10 days of a model-calculated aerosol size distribution initialized with a wide lognormal distribution and no gas phase H_2SO_4 . In this case study, aerosol particles are assumed to be lost when they sediment by 100 m ; particles are not replaced by sedimentation from above. Figure 6.4a shows a calculation at 40 mb ($\sim 22 \text{ km}$) and Figure 6.4b a calculation at 6.2 mb ($\sim 35 \text{ km}$). The dependence of sedimentation rate on air density is seen. The larger particles in the distribution are removed at a faster rate at higher altitudes. Even mid-sized particles ($r \sim 0.05 \mu\text{m}$), which have negligible sedimentation velocity in the lower stratosphere, experience substantial sedimentation in the upper stratosphere. The global effect of sedimentation is redistribution of sulfur mass from the middle stratosphere to the lower stratosphere, where subsequent transport of particles into the troposphere leads to removal. This is illustrated in Figure 6.5, which shows calculated vertical profiles of total sulfur ($= \text{OCS} + \text{SO}_2 + \text{gas-phase } \text{H}_2\text{SO}_4 + \text{condensed } \text{H}_2\text{SO}_4$) from the AER model with and without sedimentation at the equator under annual average conditions. Without sedimentation, the vertical profile of total sulfur is, as expected, almost constant with altitude throughout the stratosphere. With sedimentation, the total

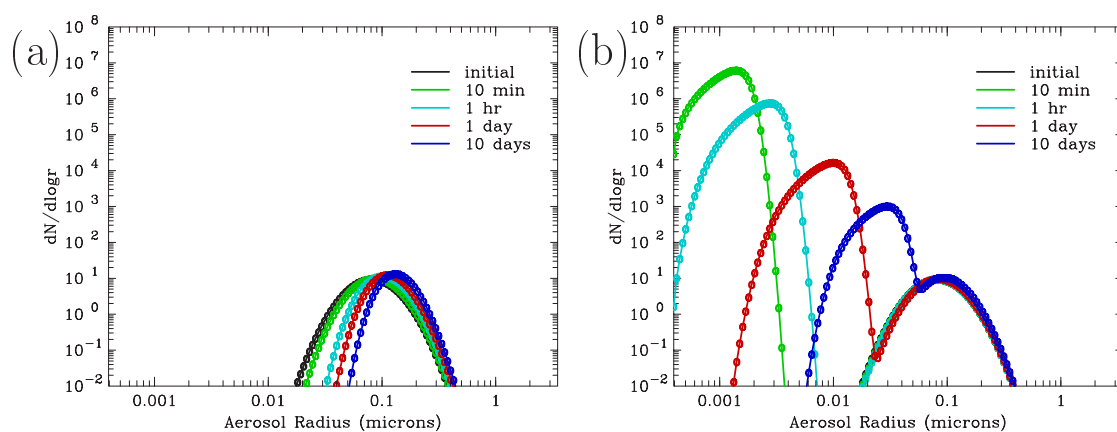


Figure 6.3: Evolution of calculated aerosol size distribution using a microphysical box model for typical lower stratospheric conditions (27.8 mb , 216.5 K , H_2O mixing ratio of 2.76 ppmv or 0.3% relative humidity). The model is initialized with 40 pptv of H_2SO_4 in the gas phase and 40 pptv of H_2SO_4 as aerosol particles with a mode radius of $0.08 \mu\text{m}$ and includes a continuous source of gas phase H_2SO_4 of 40 pptv per day. In Panel A, only condensation onto the preexisting particles is allowed to occur, along with coagulation. In panel B, an initial burst of nucleation creates small particles, which then grow by condensation and coagulation. Sedimentation is disabled. The model uses 150 bins over the size range from 0.4 nm to $3.2 \mu\text{m}$ and a time step of 3.6 seconds.

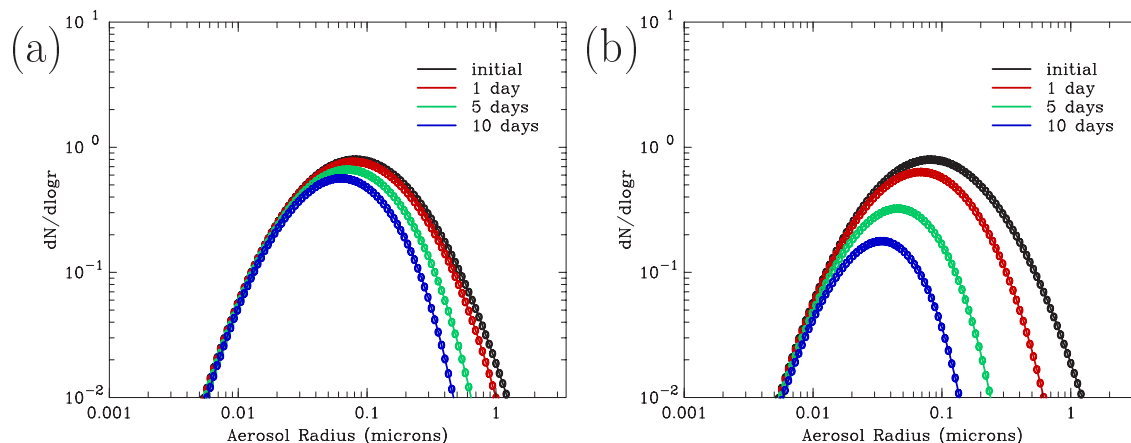


Figure 6.4: Evolution of calculated aerosol size distribution over 10 days using a microphysical box model to illustrate the sedimentation process at (a) 40 mb and (b) 6.2 mb. The model is initialized with no H_2SO_4 in the gas phase and 1.27×10^{15} molecules/ cm^3 of H_2SO_4 as aerosol particles. Sedimentation is assumed to occur when particles fall by 100 m; particles are not replaced by sedimentation from above. The model uses 150 bins over the size range from 0.4 nm to 3.2 μm and a time step of 3.6 seconds.

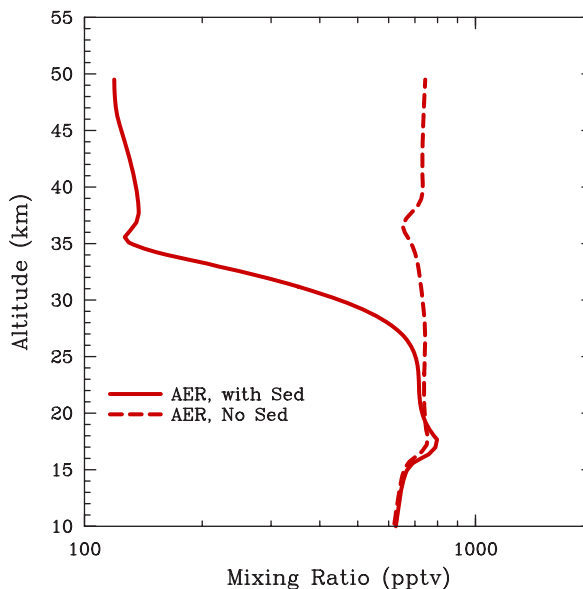


Figure 6.5: Vertical profiles of annual average total sulfur at the equator as calculated by the AER model with (solid line) and without (dashed line) sedimentation.

sulfur decreases with increasing altitude in the lower and middle stratosphere. In the upper stratosphere, where all sulfur is in the gas phase (above the aerosol layer), there is no sedimentation and therefore the profile is constant with altitude. Vertical redistribution of sulfur by sedimentation is very effective. Indeed, the total sulfur above the aerosol layer is less than 150 pptv with sedimentation whereas it is of the order of 700 pptv without sedimentation. Total condensed sulfur in the stratosphere is, however, only 12% less with sedimentation than without.

In the upper stratosphere, particles also experience evaporation. Figure 6.6 illustrates this process at a pressure of 3.2 mb (~ 40 km) and temperature of 255 K. The model is initialized with 90 pptv of H_2SO_4 in the gas phase which remains constant throughout the integration and 150 pptv of H_2SO_4 as aerosol particles, simulating a situation in which an aerosol distribution is moved instantaneously from 35 to 40 km and evaporates, its

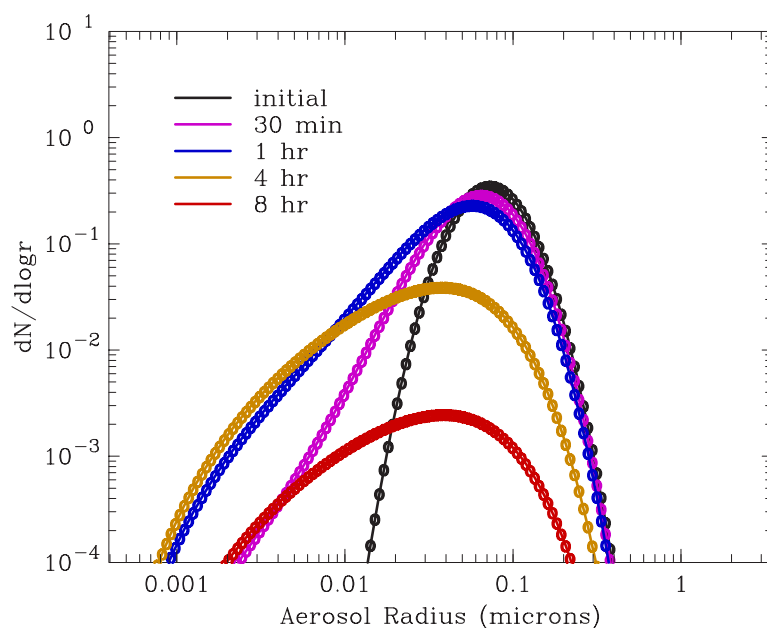


Figure 6.6: Evolution of calculated aerosol size distribution over 8 hours using a microphysical box model to illustrate the evaporation process at 3.2 mb and 255 K. The model is initialized with 90 pptv of H_2SO_4 in the gas phase which remains constant throughout the integration and 150 pptv of H_2SO_4 as aerosol particles. The model uses 150 bins over the size range from 0.4 nm to 3.2 μm and a time step of 3.6 seconds.

evaporation not perturbing ambient conditions. Sedimentation is disabled for clarity. The initial size distribution is lognormal, but as the particles evaporate, particles decrease to smaller sizes than in the initial distribution, and the shape of the distribution changes. In our example, the number of particles does not change for the first hour despite rapid evaporation. All particles are essentially evaporated within one day.

In the atmosphere, particles are transported as they grow by condensation and coagulation, and mixed with particles of different ages. The result is the size distributions produced in a global model. Figure 6.7 shows calculated size distributions from the AER 2-D model at the equator and 47°N in April under nonvolcanic conditions. At the equator, the transport moves particles upward and polewards, though mixing also brings aged particles from higher latitudes into the tropical lowermost stratosphere. In general, particles age as they ascend in the tropics. The peak of small particles ($< 0.001 \mu\text{m}$) at 18 km is a result of nucleation in the tropical upper troposphere and lower stratosphere, whereas the larger particles are those which have resided in the stratosphere for some time. At higher altitudes (23 and 27 km), only the large mode remains with maximum number density at about 0.1 μm , as the small particles have been removed by coagulation. In the upper stratosphere at 32 and 37 km, evaporation has produced particles smaller than 0.01 μm . At 47°N, the 18 km level shows some effects from nucleation near the tropopause. At higher altitudes, the main influence is downward transport from regions where evaporation and sedimentation have depleted the particle densities. Figure 6.8 shows calculated aerosol size distributions at 76°N in February and August. Winter polar conditions lead to nucleation at all altitudes in the middle stratosphere in February. Condensation rates at high latitudes are most pronounced at high altitudes where aerosol-free air flows from above into the polar vortex. In August at 76°N, the size distribution contains a single mode, with peak number density at greater radii at lower altitudes, reflecting the strong downward transport and associated particle aging. The aged size

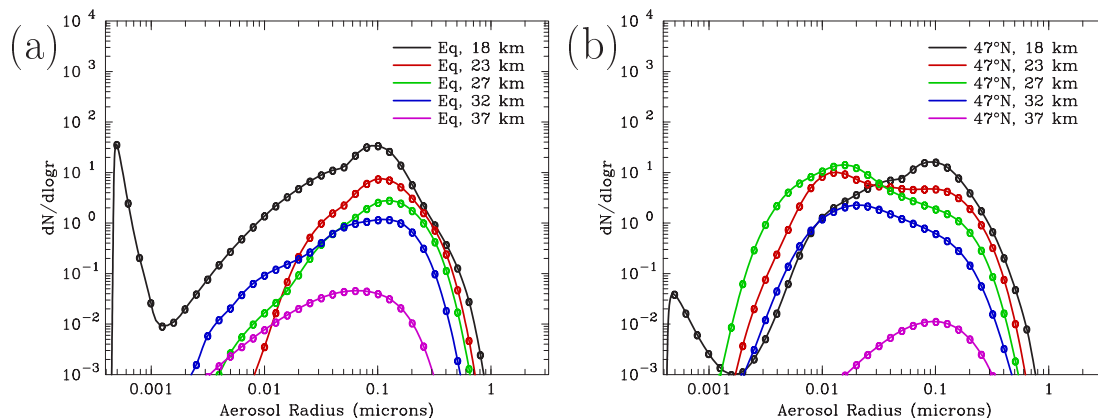


Figure 6.7: Calculated aerosol size distribution from the AER 2-D model in April at (a) the equator and (b) 47°N. The model uses 40 bins over the size range from 0.4 nm to 3.2 μm and a time step of 1 hour.

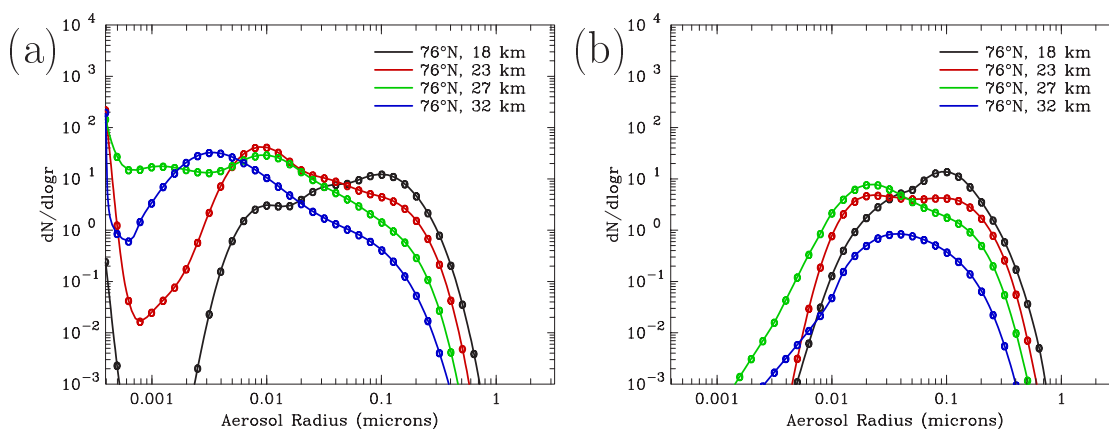


Figure 6.8: Calculated aerosol size distribution from the AER 2-D model at 76°N in (a) February and (b) August. The model uses 40 bins over the size range from 0.4 nm to 3.2 μm and a time step of 1 hour.

distributions resemble a lognormal distribution, which corroborates the use of this functional form for the simplified description of size distributions in Chapters 4 and 5. However, it must be clear that this remains an approximation, limitations of which have been addressed in Chapter 4.

6.5 Model Simulations of Nonvolcanic Conditions

6.5.1 Description of Calculations

The goal of these simulations is to model the stratospheric aerosol layer under nonvolcanic conditions. This will test our understanding of sulfur source gas emissions and transport, and chemical and microphysical processes. Comparisons will be made to observational data taken during volcanically quiescent years. To simplify the comparisons, the models all used identical boundary conditions for OCS and the 2-D models used identical boundary conditions for SO_2 . Each model was run for multiple years until an annually-repeating state was reached.

Details of OCS sources and sinks are discussed in Chapter 2, Section 2.3.1. But because of the long lifetime of OCS, its concentration in the upper troposphere is fairly constant. Therefore we employ constant mixing ratio boundary conditions in the models. The OCS mixing ratio at the surface was specified as 512 pptv with no seasonal or spatial variation,

based on northern hemisphere annual averages reported in Bandy et al. [1992]. The MPI model doesn't calculate OCS but prescribes the mixing ratio with monthly mean values from a 2-D simulation [Grooss et al, 1998]. Seasonal variability of OCS near the tropopause is of order 1% or less in all models. The 3-D models used estimates of SO₂ emission sources from IPCC [Houghton et al., 2001] and allowed model transport by convection and the general circulation to determine SO₂ at the tropical tropopause. Resulting tropopause SO₂ mixing ratios were 25-37 pptv (annual average 30 pptv) in the ULAQ model and 8-13 pptv (annual average 10 pptv) in the MPI model. The two-dimensional models used specified boundary conditions for SO₂ at the tropical tropopause. Since tropopause SO₂ data was not available, we used results from the three-dimensional tropospheric aerosol models which participated in the *IPCC* climate assessment report [Houghton et al., 2001]. The mean annual average value of tropopause SO₂ over the 11 models averaged from 20°S to 20°N was 38.9 pptv [J. Penner, personal communication]. We adopted 40 pptv as the tropical tropopause SO₂ boundary condition, with a range of 0 to 80 pptv for sensitivity studies. The 2-D models, unlike the 3-D models, had no seasonal variation in tropopause SO₂.

The ULAQ 3-D model deals with both tropospheric and stratospheric aerosol particles, including interactions between soot, organics, sea salt, and sulfate particles. The MPI 3-D model treats only sulfate aerosols, and performs microphysical calculations only in the stratosphere and upper troposphere, treating only bulk sulfate mass below. For the 2-D models, we impose a primary aerosol concentration and size distribution at the tropical tropopause, based on aircraft observations made by the University of Denver Aerosol Group (S.-H. Lee, personal communication) using the Focused Cavity Aerosol Spectrometer (FCAS) instrument [Jonsson et al., 1995] between July 1996 and October 1999. This instrument, which is a single particle optical aerosol spectrometer, is discussed in Chapter 3, Section 3.4.3. The 475 size distributions were measured between 18°S latitude and 1.8°N latitude and at potential temperatures between 390 K and 420 K. In 314 cases, the location of the tropopause was known and the distance above the tropopause ranged from -0.43 km to 2.67 km with the mean value being 1.46 km above the tropopause. Only 10 size distributions of the 314 cases were known to be below the tropopause. Thus, the vast majority of the particles sampled for this characterization are believed to consist primarily of sulfate, based on their measurement location [Murphy et al., 1998]. The sizes reported here are those observed at the laser of the FCAS after the particles have undergone heating which removes much of the water from the sulfate. Size distributions were recorded in 32 size channels, with channel mean diameters covering the range from 0.064 μm to 3.12 μm. Each distribution was normalized to a common total sulfate concentration and then the distributions averaged. Figure 6.9 shows the observed distributions and the mean used as the tropopause boundary condition in the 2-D model calculations presented in this chapter. The mean sulfate mass mixing ratio for the 475 measurements was 0.258 ppbv (0.854 ppbm) and the standard deviation of this value was 0.049 ppbv (0.162 ppbm). We adopted the mean value for our tropopause boundary condition, with two standard deviations defining upper and lower limits for sensitivity. As a further sensitivity, we also assume no primary aerosols in the measured size range at the tropopause, allowing the models to generate particles in the upper troposphere which are transported into the stratosphere.

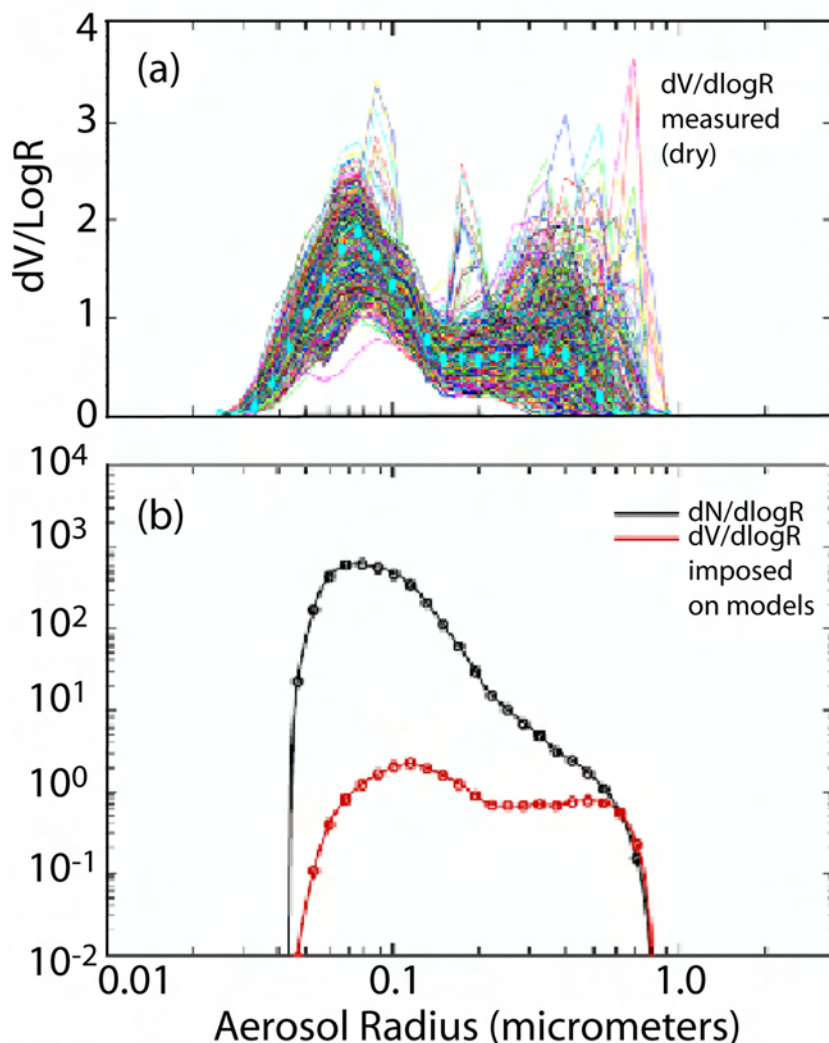


Figure 6.9: Size distribution near the tropical tropopause (a) observed by the FCAS instrument [Jonsson et al., 1995] as a dry volume distribution ($dV/d\log R$) along with the observational mean (heavy line) and (b) number and volume size distribution ($dN/d\log R$, $dV/d\log R$) at the tropical tropopause after hydration used as the tropopause boundary condition in the model calculations. Each observational profile was normalized to the same sulfate mass. Figure (a) provided by J.C. Wilson and S.-H. Lee (private communication).

6.5.2 Comparisons to Precursor Gas Measurements

The model-calculated OCS is compared to observations from the Atmospheric Trace Molecule Spectroscopy (ATMOS) experiment on the space shuttle in 1994 (ATLAS-3) [Gunson et al., 1996; Rinsland et al., 1996] and from the MkIV Fourier transform infrared spectrometer balloon-borne instrument [Leung et al., 2002] between 1992 and 2000. Figure 6.10a shows model-data comparisons with ATMOS at 5°N in November of 1994. The model results are all generally within the error bars of the measurements at 5°N and below 26 km. The ULAQ model has higher OCS concentrations (by 20-30 pptv) in the lower stratosphere than the other models because of OCS production from CS_2 in the mid to upper troposphere, which augments the 512 pptv of OCS specified at ground level. Note that some of the 2-D models also contain this source of OCS, but without effective convection it does not impact the stratosphere as strongly. The good model-measurement agreement in the tropics is reassuring because this region is where tropospheric source gases enter the stratosphere and where the major chemical loss of OCS occurs.

Figure 6.10b shows model comparisons with MkIV observations of OCS at 65°N in July. Additional plots showing comparisons at other latitudes are found in the supplementary material at <http://www.sparc.sunysb.edu>. The models show more variability in mid and high latitudes than in the tropics. This is a result of variations in model transport rates as OCS is transported from low to higher latitudes in the mid stratosphere. All models are generally within the error bars at 35°N. At 65°N in July, the LASP model simulation is sometimes too low and the MPI and ULAQ simulations sometimes too high in comparison with the MkIV limited observations. Correlations between OCS and other long-lived tracers would be most appropriate for testing the rate of chemical destruction of OCS independent of a particular model's transport.

The only available measurement of SO₂ in the stratosphere under nonvolcanic conditions is one ATMOS profile taken in April of 1985 [Rinsland et al., 1995]. Comparison of this

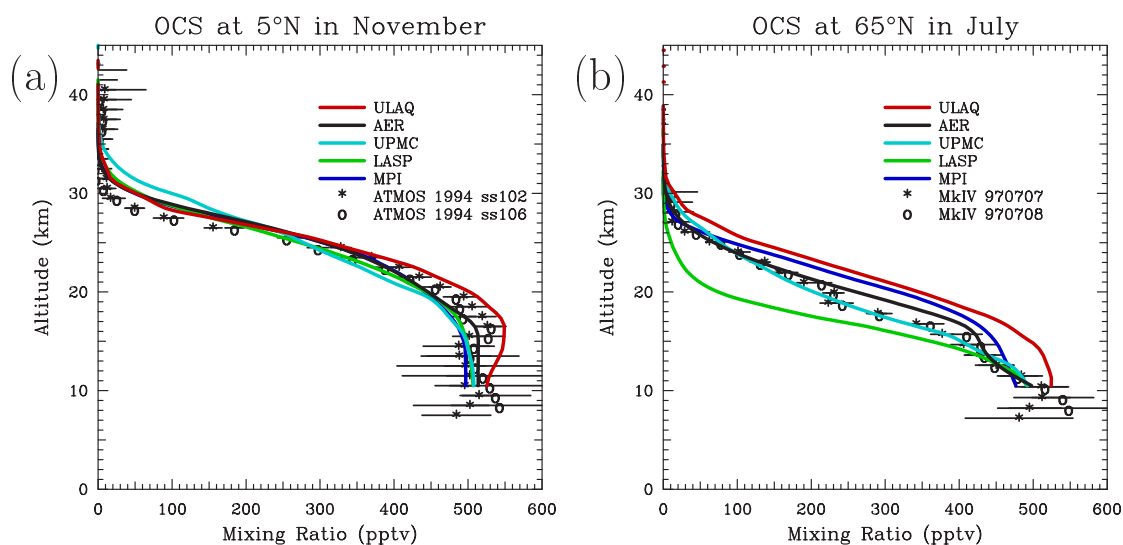


Figure 6.10: OCS calculated mixing ratio profiles at (a) 5°N in November compared to ATMOS observations [Gunson et al., 1996; Rinsland et al., 1996] and (b) 65°N in July compared to MkIV balloon observations [Leung et al., 2002].

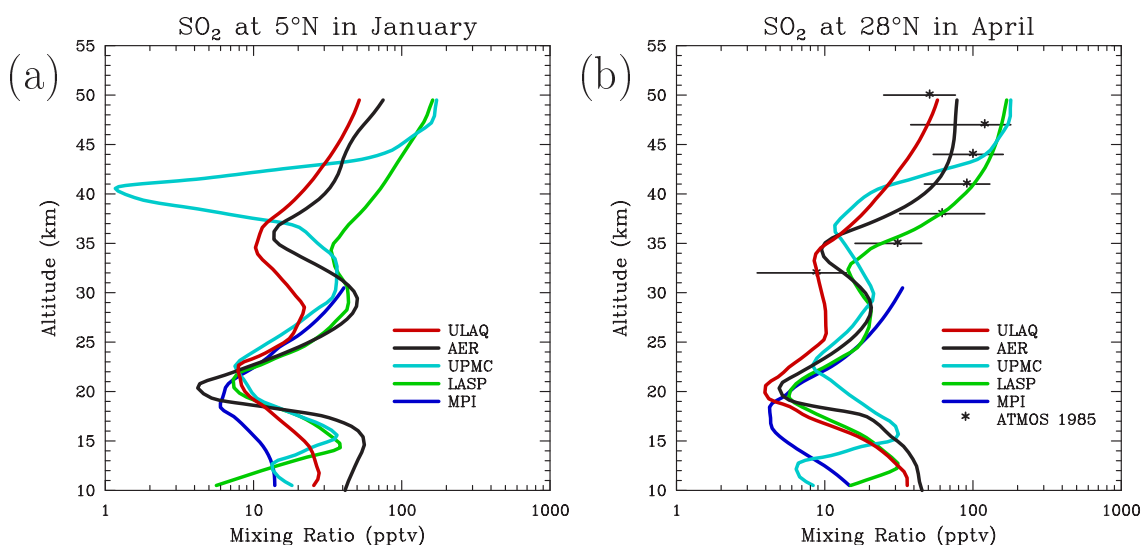


Figure 6.11: Model-calculated SO₂ mixing ratio profile (a) for January at 5°N and (b) at 28°N in April from model calculations and ATMOS observations taken in 1985 [Rinsland et al., 1995].

profile with model results at 28°N is shown in Figure 6.11b. Figure 6.11a shows a similar plot at 5°N in January for model results only. The 2-D models have imposed SO₂ concentrations of 40 pptv at the tropopause (~ 16 km). The 3-D models calculate about 25 pptv (ULAQ) and 10 pptv (MPI) at the tropopause at 5°N in January. Model profiles of SO₂ show falling concentrations from the surface to 20 km due to chemical conversion of surface-emitted SO₂. Photodissociation of OCS causes rising SO₂ concentrations between 20 and 30 km. The sharp rise in SO₂ concentrations above 35 km is a result of aerosol evaporation releasing H₂SO₄ into the gas phase, which is then photolyzed to give back SO₂. The model results do not agree well with each other, varying by factors of 5. Only the LASP model is a close match to the ATMOS observations between 35 and 47 km, with the UPMC model also agreeing with observations between 42 and 47 km. The AER and ULAQ models are lower than observations in most of this altitude range, while the MPI model does not extend high enough for comparison. Additional intercomparisons among the models at 5°N, 45°N, and 45°S for January and July are shown in the supplementary material. As with OCS, model agreement is better in the tropics than at higher latitudes. Intermodel differences in SO₂ in the tropics are much larger than for OCS, a result of the much shorter lifetime of SO₂ and differences in OH concentration.

The sharp rise in SO₂ concentrations above 35 km (Figure 6.11) is a result of aerosol evaporation releasing H₂SO₄ into the gas phase, which is then photolyzed to give back SO₂. The rate of this photolysis reaction has been uncertain until recently and thus varies among the models, with most assuming photolysis in the UV. The UPMC model shows very low SO₂ concentrations at 40 km because the sulfur exists as H₂SO₄ there. A recent paper reports photolysis in the visible [Vaida et al., 2004]. Mills et al. [2005] applied visible H₂SO₄ photolysis in a microphysical model and compared results with observations of H₂SO₄, SO₃, and SO₂ [Arnold et al., 1981; Reiner and Arnold, 1997; Schlager and Arnold, 1987; Viggiano and Arnold, 1981; Rinsland et al., 1995] between 30 and 50 km. They found that an additional upper stratospheric loss mechanism was required to explain vertically decreasing H₂SO₄ and SO₃ vapor above 40 km. Loss of H₂SO₄ by neutralization by metals on meteoritic dust, which acts as a permanent sink for sulfur, was found to be consistent with observations. Photolysis of H₂SO₄ to SO₂ in this region preserves gaseous sulfur in the upper stratosphere. SO₂ is transported downward into the polar regions where it reacts with OH in the presence of sunlight to regenerate H₂SO₄ and then condenses into sulfuric acid aerosols. During polar night, SO₂ will remain in the descending air due to lack of OH. At the return of sunlight in springtime, a descending and growing aerosol layer has been observed [Hofmann et al., 1989], consistent with the model calculations.

6.5.3 Calculated Aerosol Budgets and Burdens

The models can provide detailed descriptions of sulfur species in the stratosphere, their burdens, fluxes across the tropopause, and chemical and microphysical transformation rates. While we cannot specifically validate most of these values against observations, we do gain confidence in them knowing that OCS concentrations reasonably represent observations, and that calculated aerosol extinctions compare favorably with satellite measurements under nonvolcanic conditions. Figure 6.12 diagrams the stratospheric sulfur budget calculated by the AER model. Aerosol accounts for 39% of the total sulfur mass of the stratosphere, with OCS accounting for 58% and SO₂ for 2%. CS₂, DMS, and H₂S have short tropospheric lifetimes and only insignificant amounts of these species are found in the stratosphere. Sulfuric acid gas is continually produced by oxidation of SO₂,

equivalent to the stratospheric sulfate condensation. The lifetime of aerosol in the stratosphere is about 1.4 years according to the AER model. If OCS were the only source of stratospheric sulfur, the aerosol lifetime would be 2.5 years. If SO_2 were the only source of stratospheric sulfur (OCS omitted from model calculation), the lifetime would be 1.2 years. This model-derived budget of stratospheric sulfate indicates that cross-tropopause flux of SO_2 and primary aerosol may be large contributors to the stratospheric aerosol burden, but large uncertainties remain in quantifying that flux. Comparisons with satellite extinction observations will be helpful in reducing this uncertainty.

The morphology of stratospheric aerosols is illustrated in Figure 6.13 which shows annual average fields derived from the AER model between 10 and 40 km altitude. Figure 6.13a shows the calculated mixing ratio of sulfate in aerosol particles, which peaks strongly in the tropics between 20 and 30 km. Stratospheric aerosol mass density in $\mu\text{g}/\text{m}^3$ is shown in Figure 6.13b, includes both sulfate and water. The number density of particles with radii greater than $0.01 \mu\text{m}$ is shown in Figure 6.13c. Highest particle densities are found in the tropical upper troposphere and near the tropopause. At high latitudes in the middle

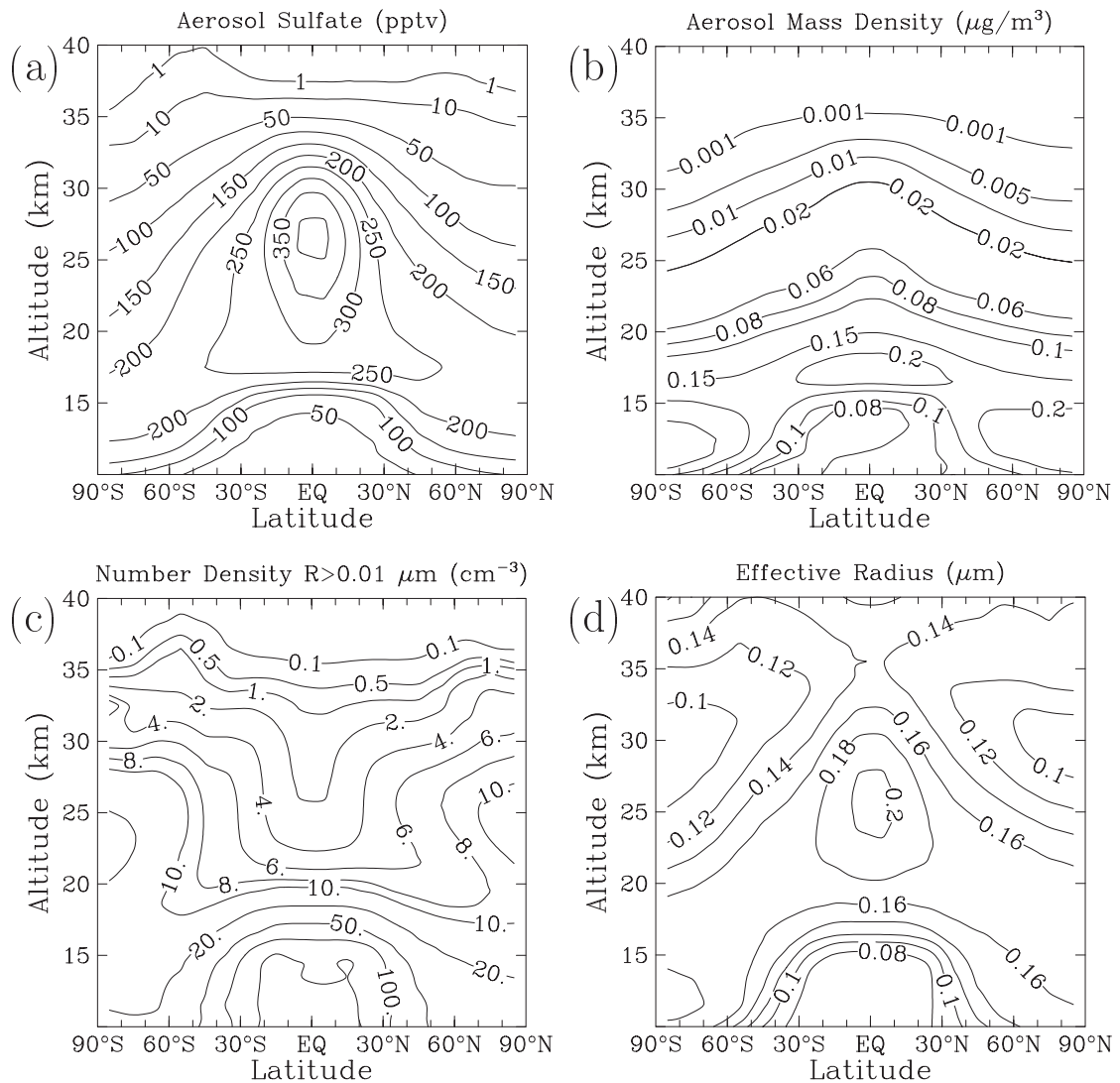


Figure 6.13: Model-calculated annual average morphology of the stratospheric aerosol layer showing (a) mixing ratio of sulfate in aerosol particles (pptv), (b) aerosol mass density ($\mu\text{g}/\text{m}^3$), (c) number density (cm^{-3}) for particles greater than $0.01 \mu\text{m}$ radius, and (d) effective radius (μm) from the AER model between 10 and 40 km.

stratosphere, nucleation takes place in winter and particle densities are greater than at low latitudes. Figure 6.13d shows the effective radius of aerosol particles, which maximizes in the tropical mid stratosphere and the high latitude lower stratosphere, indicating the most aged particles.

6.5.4 Comparisons to Satellite Extinction Measurements

Extinction observations from the SAGE II instrument provide the best spatial and temporal coverage of any stratospheric aerosol dataset. To make the comparisons between model simulations and observations as accurate as possible, Mie scattering codes are used to derive aerosol extinction from the model-calculated aerosol size distributions. Tropical and mid-latitudes profiles of model-calculated and SAGE background aerosol extinction at $0.525 \mu\text{m}$ are shown in Figure 6.14. More profiles can be found at <http://www.sparc.sunysb.edu>. The SAGE data shown are the two-year composite record of 2001 and 2002 representing a nonvolcanic background aerosol field as described in

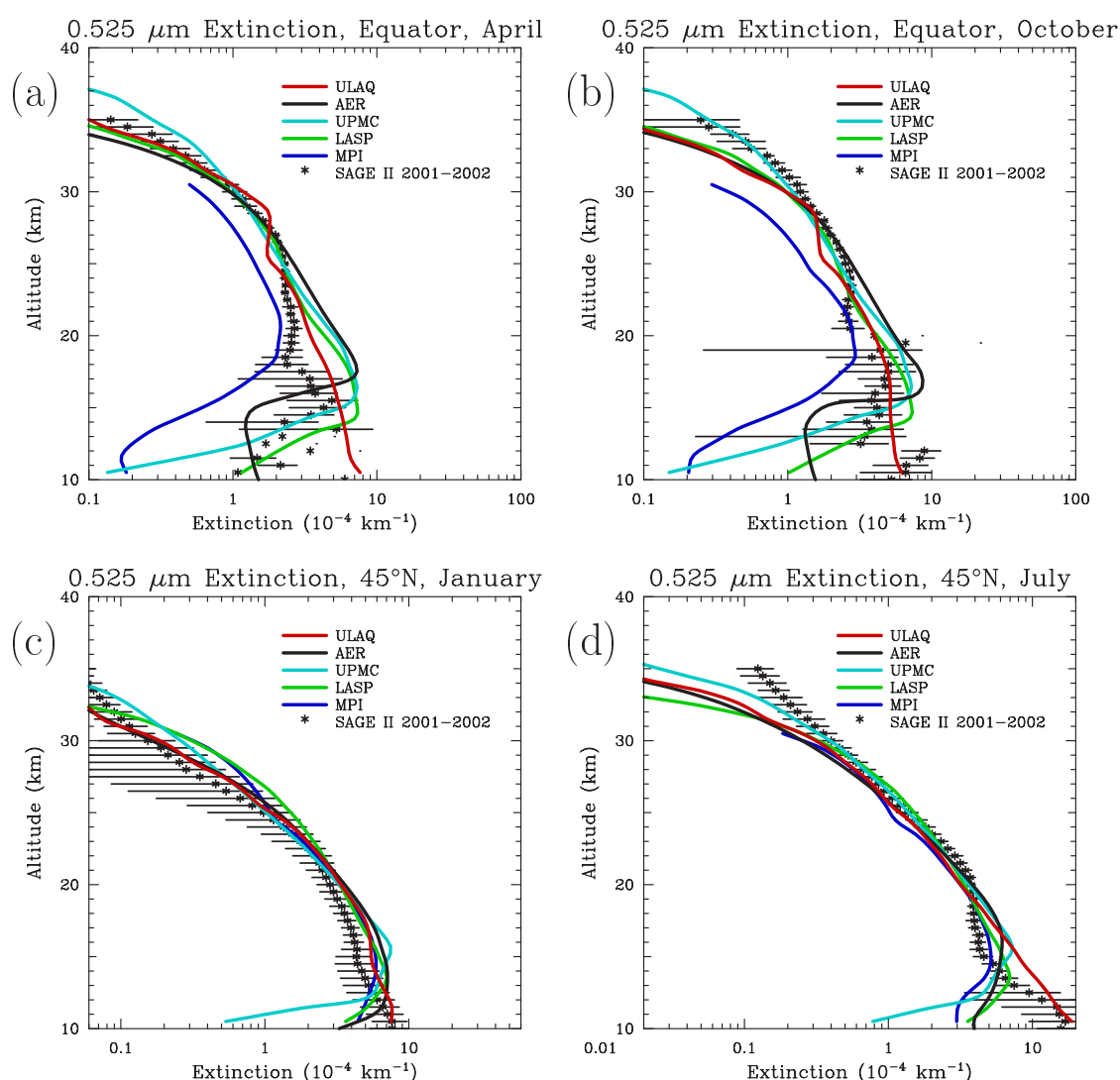


Figure 6.14: Comparison of SAGE II and model-calculated extinctions at $0.525 \mu\text{m}$ in (a) April and (b) October at the equator, (c) January and (d) July at 45°N . SAGE II data are a composite of 2001 and 2002 observations as described in the text.

Chapter 4, Section 4.2.1. Error bars on the SAGE II data are small relative to the plotted symbols between 20 and 30 km, but become larger outside this altitude range. On the log scale shown, the models generally agree with SAGE II observations above the tropopause at 45°N, though over predict somewhat from 12-18 km. At the equator, model results other than MPI match observations above 25 km, but the models often over predict below this altitude. Low extinctions in the MPI model in the tropics may be related to effects of the 30 km upper lid on the general circulation and overestimation of convective scavenging, along with a low value of SO₂ at the tropical tropopause. The observations show a sharp gradient in extinction at about 17 km in April or 20 km in October which the models are unable to reproduce. These gradients in the SAGE II data are unlikely to be due to clouds at the tropical tropopause, as clouds have been eliminated in these data through appropriate filters, though subvisible clouds cannot be fully excluded (see Chapter 4). The extinction in the 2-D models near the tropical tropopause is mainly a function of the imposed aerosol distribution there, whereas the 3-D models simulate the tropospheric sources and transport more accurately without imposed conditions at the tropopause. None of the models are able to reproduce the observed vertical gradients there. The observed aerosol extinction has more seasonal variability than the models. This could be an artifact of the lack of seasonal variability in the models' boundary conditions.

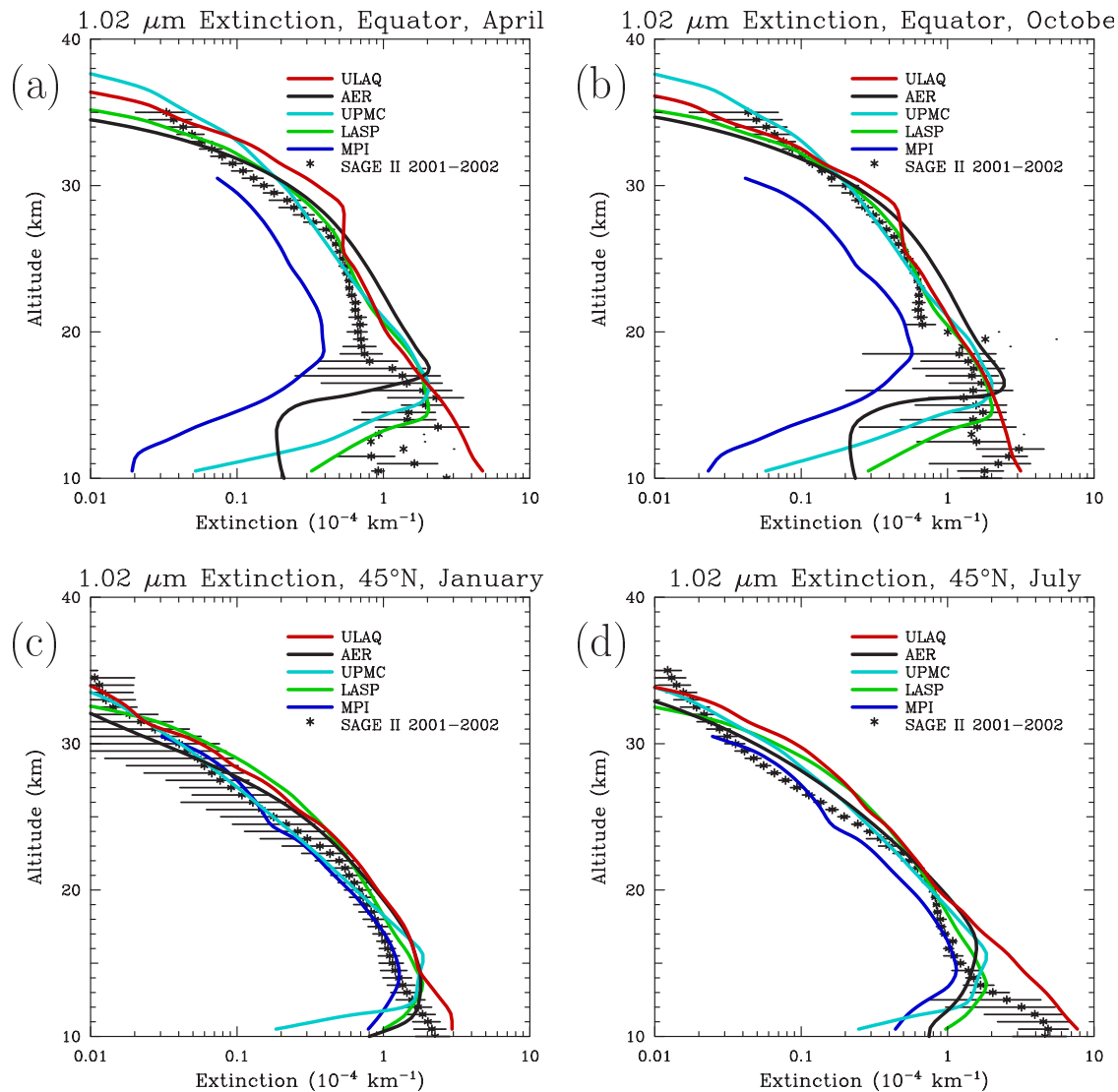


Figure 6.15: Comparison of SAGE II and model-calculated extinctions at 1.02 μm in (a) April and (b) October at the equator, (c) January and (d) July at 45°N. SAGE II data are a composite of 2001 and 2002 observations as described in the text.

Profiles of model-calculated and SAGE background aerosol extinction at $1.02\ \mu\text{m}$ are shown in Figure 6.15. The models tend to overestimate the $1.02\ \mu\text{m}$ extinction somewhat, though the UPMC and LASP models are generally within error bars between 25 and 35 km at the equator. All but the MPI model fall within error bars at the equator between 13 and 17 km in April and between 13 and 20 km in October. The UPMC and MPI models perform well at 45°N in January above 20 km and the other models are within or just above the error bars. In other months (see <http://www.sparc.sunysb.edu>) at 45°N , most of the models overpredict the $1.02\ \mu\text{m}$ extinction at all altitudes, with ULAQ and LASP often higher than the other models. Model results at 45°S (see supplementary material) match observations better than at 45°N for April and October.

Model-calculated extinction profiles at $3.46\ \mu\text{m}$ are shown in Figure 6.16 and compared with extinctions measured by HALOE averaged over the 1999-2004 period. Refractive indices at 3.46 and $5.26\ \mu\text{m}$ are obtained from Tisdale et al. [1998]. Only the AER, UPMC, and MPI models provided $3.46\ \mu\text{m}$ extinctions. AER and UPMC model results

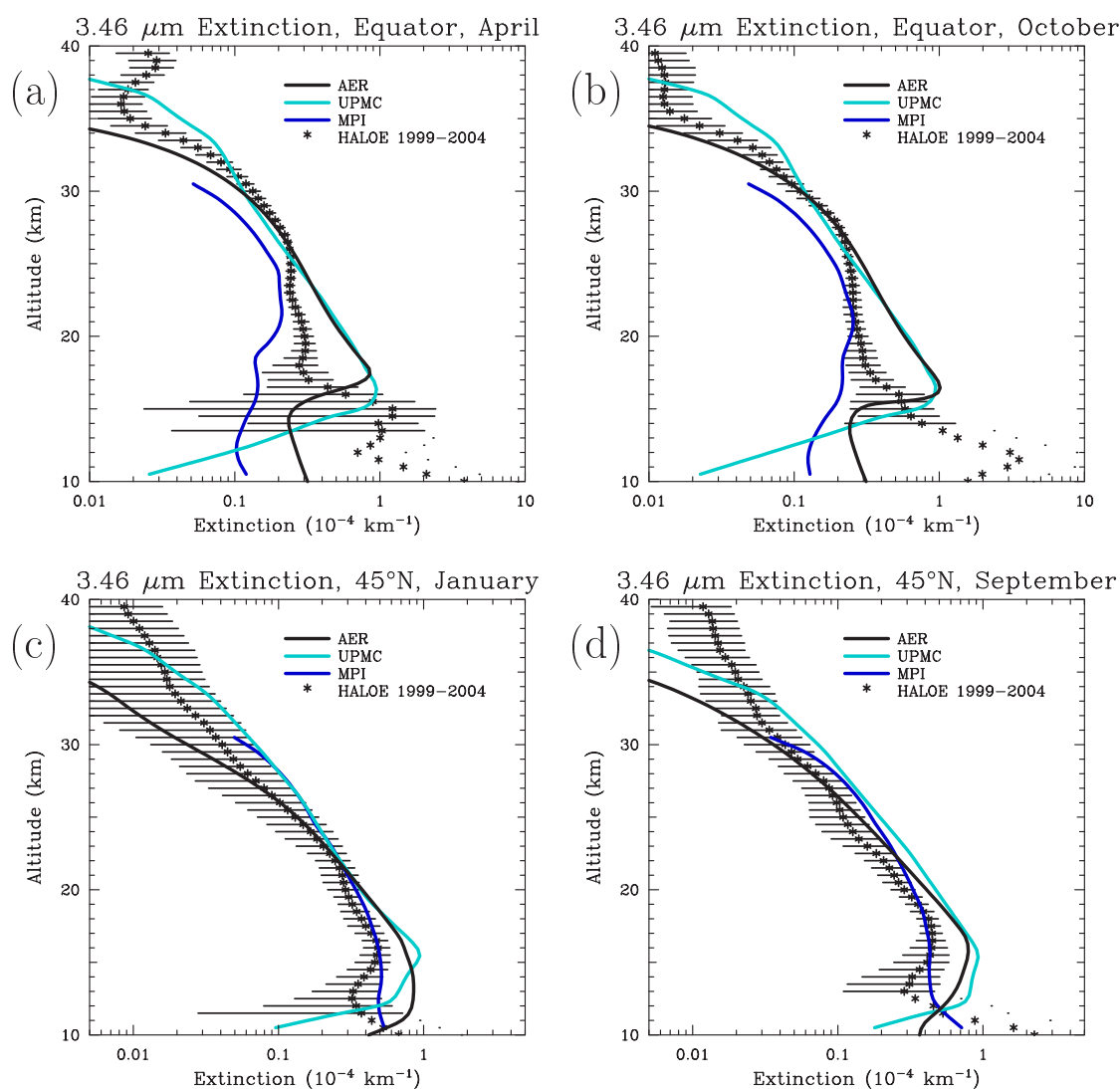


Figure 6.16: Comparison of HALOE and model-calculated extinctions at $3.46\ \mu\text{m}$ in (a) April and (b) October at the equator, (c) January and (d) September at 45°N . HALOE observations are averaged over the 1999-2004 period.

are much higher than observations between 16 and 25 km in the tropics, while the MPI model consistently underpredicts in the tropics at almost all altitudes. The AER and UPMC models match observations between 26 and 30 km, but above 30 km the UPMC model is high and the AER model low. At 45°N the three models all fall within error bars in January above 22 km, but in September the UPMC model falls somewhat above error bars in this altitude range. All models except MPI overpredict below 22 km. Model-calculated extinction profiles at $5.26\ \mu\text{m}$ are compared with HALOE observations in Figure 6.17. The model-calculated values tend to lie well below observations above 23 km in the tropics, though the UPMC model is close to the observations between 32 and 36 km. The ULAQ and UPMC models are near observations in the tropics below 23 km, while the AER model overpredicts there. At 45°N , the UPMC and MPI models are near observations, while the AER and ULAQ models show extinction that decreases too rapidly with altitude.

Overall, the models do a better job of reproducing the $0.525\text{-}\mu\text{m}$ extinction than the $1.02\text{-}\mu\text{m}$ extinction as measured by SAGE II. This may indicate that models have more difficulty reproducing the large end of the aerosol size distribution. Comparisons at 3.46

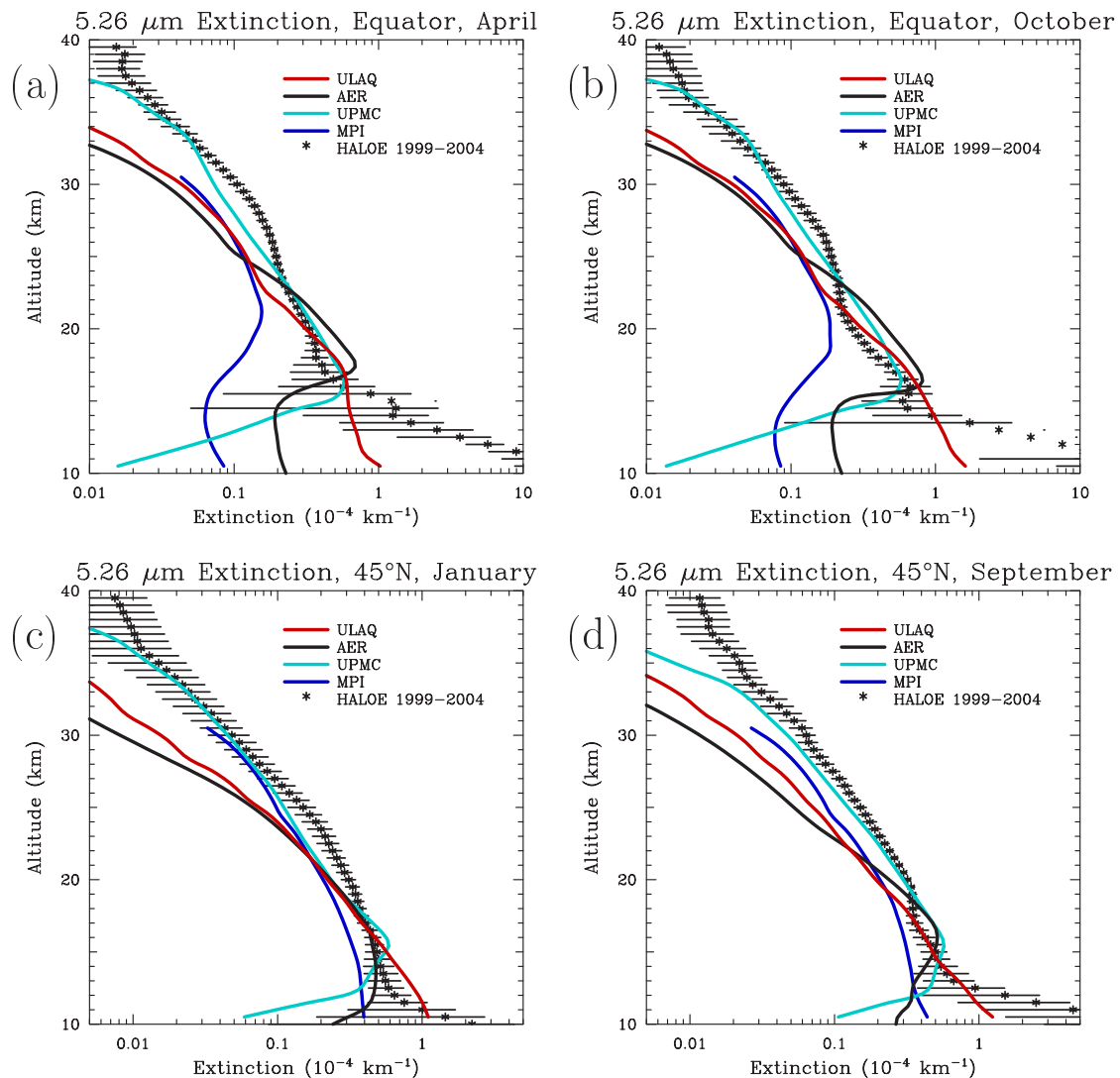


Figure 6.17: Comparison of HALOE and model-calculated extinctions at $5.26\ \mu\text{m}$ in (a) April and (b) October at the equator, (c) January and (d) September at 45°N . HALOE observations are averaged over the 1999-2004 period.

and $5.26 \mu\text{m}$ show a larger spread among the models and significant differences with the HALOE observations. The tropical lower stratosphere proved difficult for any model to reproduce consistently due to strong vertical and seasonal gradients. If we assume that the high extinction values at and just below the tropical tropopause are due to sulfate

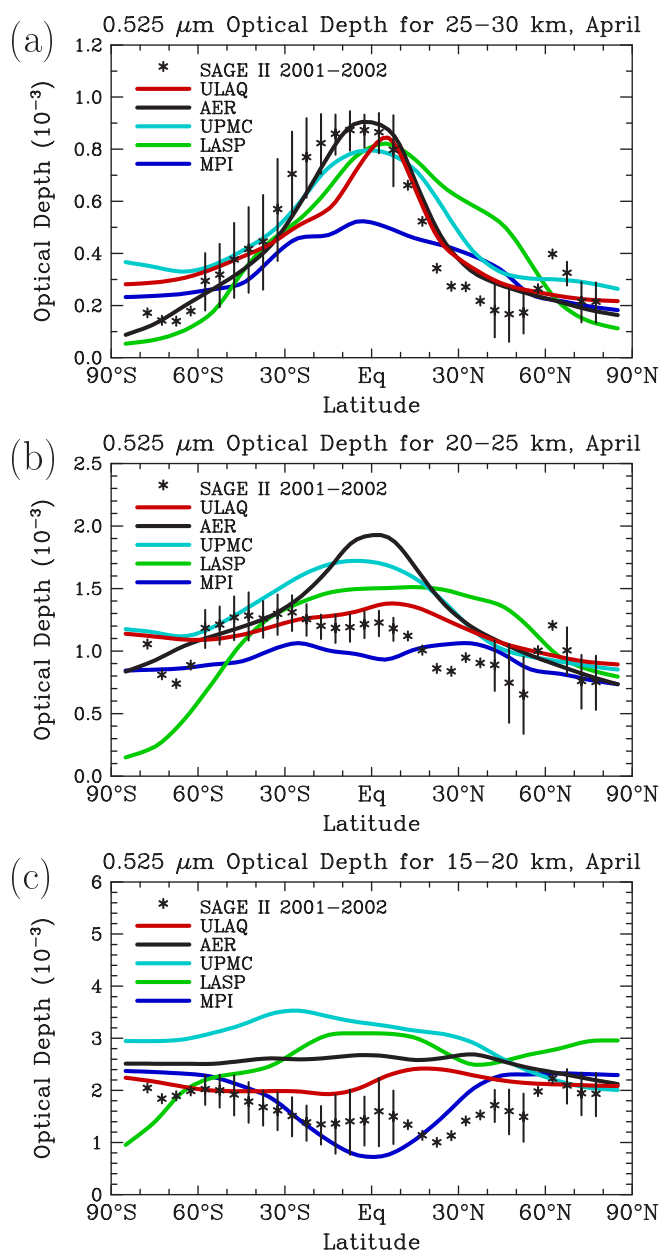


Figure 6.18: Aerosol optical depth at $0.525 \mu\text{m}$ for April of 2000 integrated from (a) 25 to 30 km, (b) 20 to 25 km and (c) 15 to 20 km. SAGE II data from the 2001-2002 composite background period are shown by symbols, model results by colored lines.

Aerosol optical depths at $0.525 \mu\text{m}$ as a function of latitude are shown in Figure 6.18 for April for the 15-20 km layer, the 20-25 km layer, and the 25-30 km layer. SAGE observations using the combined 2001-2002 nonvolcanic average are also indicated on the same plots. One should keep in mind that the lower part of the 15-20 km layer may be at or near the tropopause at tropical latitudes. SAGE observations show a strong latitudinal gradient in $0.525 \mu\text{m}$ optical depth in the 25-30 km layer, with equatorial

aerosols, then the models cannot explain the much lower extinctions a few kilometers above the tropopause, since sulfate aerosols would not evaporate and sedimentation rates are small. The observations have been cleared of clouds, but could potentially be contaminated by subvisible cirrus, or could represent tropospheric aerosols, such as dust, soot from biomass burning, or particles with organic content which do not penetrate the stratosphere. There is indeed evidence that the fraction of sulfate in the aerosol directly below the tropical tropopause is just about 50%, dropping to less than 20% about 2-3 km lower [Murphy et al., 1998]. The models are essentially designed to simulate stratospheric aerosols, not tropospheric aerosols or clouds, and the influence of these aerosol types may be significant to the lowermost stratosphere. Additional years of SAGE data will improve the representativeness of this nonvolcanic observational dataset, which consists of only two years of observations in the current investigation.

optical depths higher than mid and high latitude optical depths by factors of 2-4. The models generally reproduce this gradient and match the absolute value of optical depth well. In the 20-25 km layer, observational gradients are weak, but with high latitude

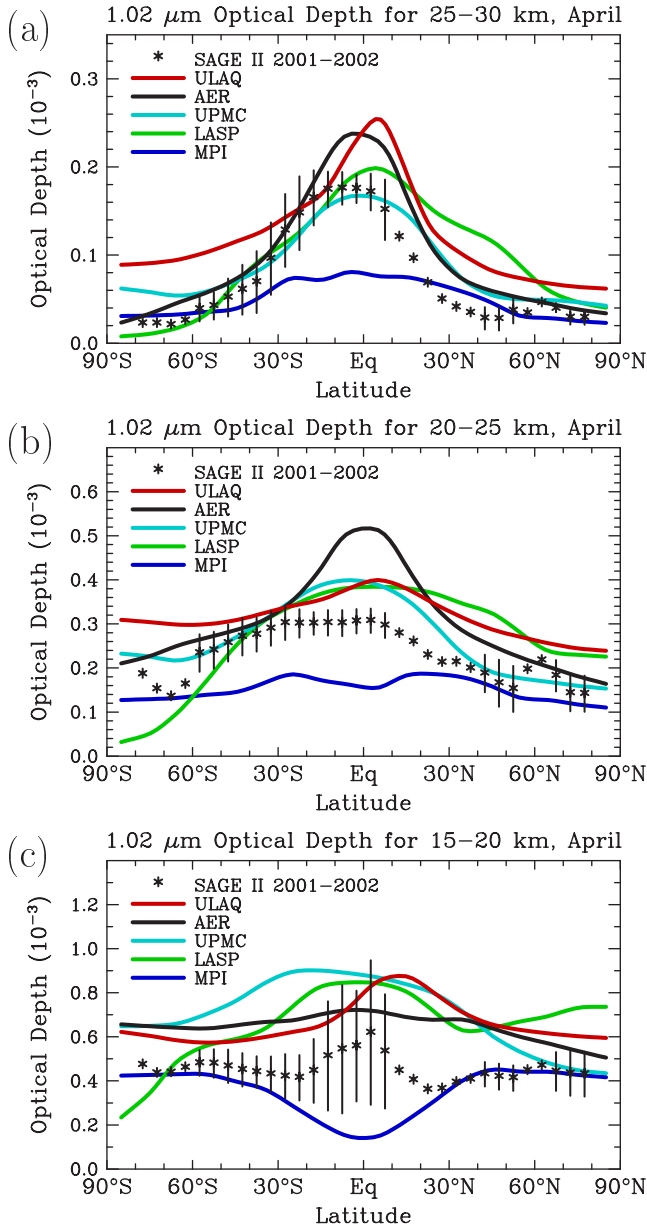


Figure 6.19: Aerosol optical depth at $1.02 \mu\text{m}$ for April of 2000 integrated from (a) 25 to 30 km, (b) 20 to 25 km and (c) 15 to 20 km. SAGE II data from the 2001-2002 composite background period are shown by symbols, model results by colored lines

optical depths generally lower than those at other latitudes. The models vary widely in this layer, with the AER model showing a strong peak in the tropics, the UPMC and LASP model showing weaker gradients which are also higher in low latitudes, and the ULAQ and MPI models showing little latitudinal gradient. The 15-20 km layer shows weak latitudinal gradients in the observations and most of the models, though several of the models predict optical depths that are too high by 50% or more. Similar plots for other months can be found in the supplementary material.

Model-calculated and SAGE optical depths at $1.02 \mu\text{m}$ are shown in Figure 6.19. As found previously, the most pronounced differences between model simulations and SAGE observations are found in the 15-20 km region. Most models also overpredict the $1.02\text{-}\mu\text{m}$ optical depth in the 20-25 km region, but roughly approximate the latitudinal gradient there. In the 25-30 km region, models have significant spread, though the LASP, UPMC, and AER models match the magnitude of the observed optical depth over most of the southern hemisphere in April and much of both hemispheres in January (see supplementary material). The AER and ULAQ models are higher than observations in the tropics in April.

The comparisons between modeled and HALOE optical depths (Figures 6.20 and 6.21) show that most models underestimate optical depths at $5.26 \mu\text{m}$ in the upper and middle stratosphere regions, with the UPMC model performing better than the others. At 25-30 km, observations of 3.46 and $5.26 \mu\text{m}$ optical depth show an equatorial peak. At $5.26 \mu\text{m}$, all models have too weak of a latitudinal gradient at this altitude, though the AER model matches the $3.46 \mu\text{m}$ optical depth quite well here. As with the SAGE wavelengths, observations show weak latitudinal gradients at 15-20 km and 20-25 km,

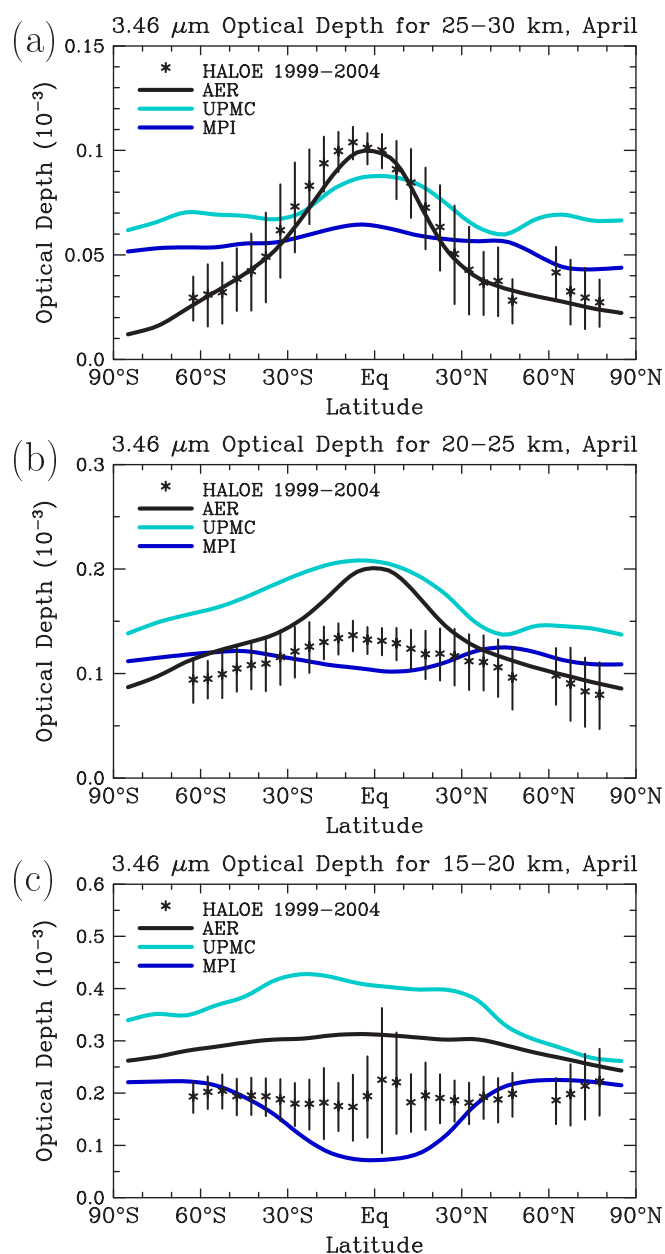


Figure 6.20: Aerosol optical depth at $3.46 \mu\text{m}$ for April of 2000 integrated from (a) 25 to 30 km, (b) 20 to 25 km and (c) 15 to 20 km. HALOE data averaged over the 1999–2004 period are shown by symbols, model results by colored lines.

but the models show a variety of latitudinal gradients in these altitude regions. Only the MPI model approximates the observed optical depths below 25 km at $3.46 \mu\text{m}$, with the AER and UPMC models predicting optical depths too high.

These results are consistent with the previous comparisons of extinction profiles at selected latitudes. Since the models do not match observations at all compared wavelengths, it appears that the models do not accurately predict aerosol size distributions through the full range of particle sizes. The best comparisons are for the $0.525 \mu\text{m}$ wavelength, which is insensitive to particles less than $\sim 0.1 \mu\text{m}$ radius. The $5.26 \mu\text{m}$ extinctions are sensitive to a broader range of particle sizes, and compare very poorly with observations above 25 km for most models. Reasons for this are not clear. Since the main loss process for larger particles is gravitational sedimentation in the middle stratosphere region, it is tempting to attribute the model bias to an inaccurate parameterization of this process in large-scale models. Another possible cause could be numerical diffusion caused by the limited aerosol size resolution used in global models. However, as shown in Section 6.6.1, this does not appear to be a major contributor to model differences with observed extinctions.

6.5.5 Comparisons to Derived Satellite Products

Up to this point, only the primary aerosol properties, extinction and optical depth (integrated extinction), measured by satellite instruments at different wavelengths have been used for the evaluation of the models (see Chapter 4). The equivalents to these primary measurements have been derived from the model-calculated aerosol size

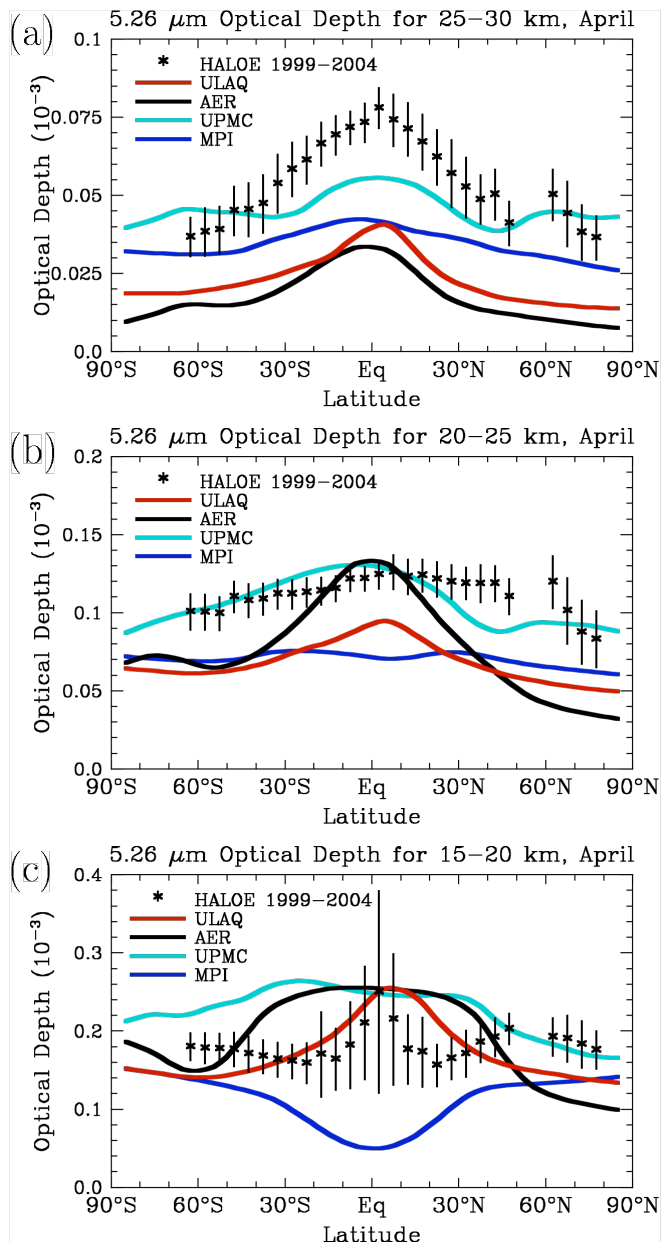


Figure 6.21: Aerosol optical depth at $5.26 \mu\text{m}$ for April of 2000 integrated from (a) 25 to 30 km, (b) 20 to 25 km and (c) 15 to 20 km. HALOE data averaged over the 1999-2004 period are shown by symbols, model results by colored lines.

Only the ULAQ model comes close to SAGE results in this region. In comparison to SAGE surface area, modeled surface area appears to be overestimated by up to a factor 5-10 in some regions.

It is worth noting that while the comparisons with satellite extinctions apply Mie calculations to the modeled aerosol size distributions and therefore in principle capture the extinction of the full distribution for both models and measurements, this is not the case in the comparison with surface area density. In this case, the model result does again show a property of the full distribution, whereas the satellite instrument effectively underestimates the contributions from the smallest particles, and this effect is only partly corrected for by the retrieval algorithm (see Chapter 4). Therefore, the fact that the

distributions and Mie scattering codes. In this section, aerosol bulk properties (surface area density and effective radius) derived from SAGE primary multi-wavelength measurements are used for model evaluation and comparison. A description of the derivations and limitations of these satellite products is provided in Chapter 4, Section 4.2.1. The surface area densities and effective radii from the models are calculated using the entire size distribution available in the models. Surface area density profiles for two seasons at the equator and 45°N are shown in Figure 6.22, with additional latitudes and seasons shown in the supplementary material. These results show greater inter-model variability than was seen for extinction. SAGE II values of surface area density are those derived from the 0.525 and $1.02 \mu\text{m}$ extinction using Equation 4.1 for the 2001-2002 composite year. The models tend to overestimate the surface area density relative to SAGE values, with the ULAQ model being the closest to SAGE surface area and the UPMC or LASP models being the highest. The most pronounced discrepancies between models and SAGE surface area are found in the lower tropical stratosphere.

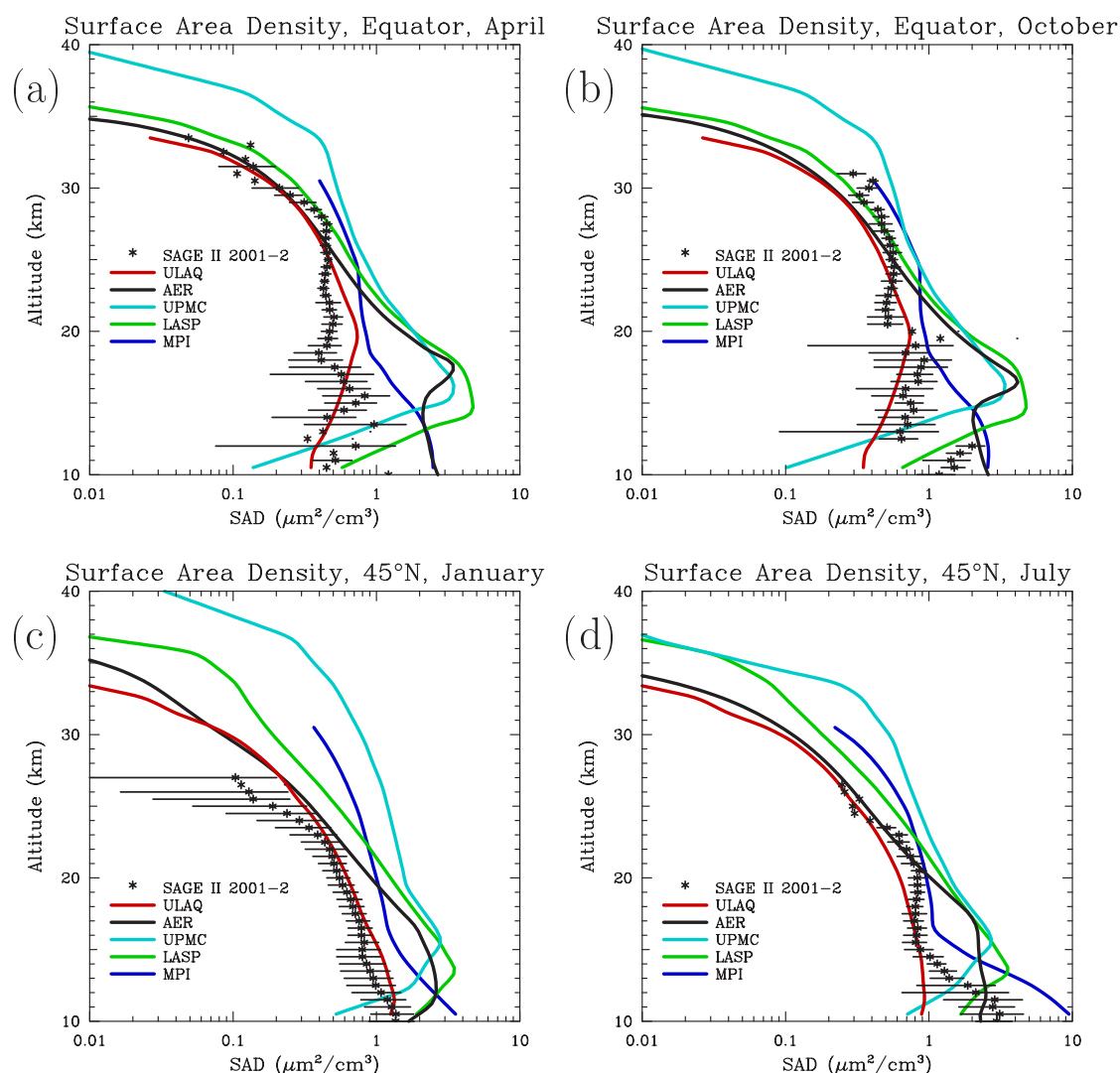


Figure 6.22: Comparison of SAGE II and model-calculated surface area density in (a) April and (b) October at the equator, (c) January and (d) July at 45°N. SAGE II results use Equation 4.1 to obtain surface area from the 2001-2002 composite of 1.02 and 0.525 μm extinction. Model-calculated surface area density is integrated over the model's entire size distribution

measured surface area densities are mostly smaller than the modeled ones is not surprising by itself. SAGE measurements are not very sensitive to particles smaller than 0.1 μm . As a result, the SAGE product underestimates the surface area in regions where the contribution of small particles is significant, such as the tropical tropopause region. This underestimation should be most apparent during background periods when the aerosol loading is low and the average size of the aerosol particles is the smallest.

In order to avoid the difference in particle size sensitivity between the satellite-derived surface area and the model-derived surface area, we have calculated surface area densities from the models using extinctions in the same manner as the SAGE II data product obtains surface area density (i.e. using the SAGE algorithm given in Equation 4.1). These extinction-derived surface area densities, shown in Figure 6.23, are considerably smaller than the corresponding integrated surface area densities for all models, except for the AER model above 25 km and the ULAQ model at some altitudes. Note that the ULAQ model is 3-D and includes tropospheric aerosol particles and more realistic tropospheric transport, which the 2-D models do not, but has the coarsest size resolution. The

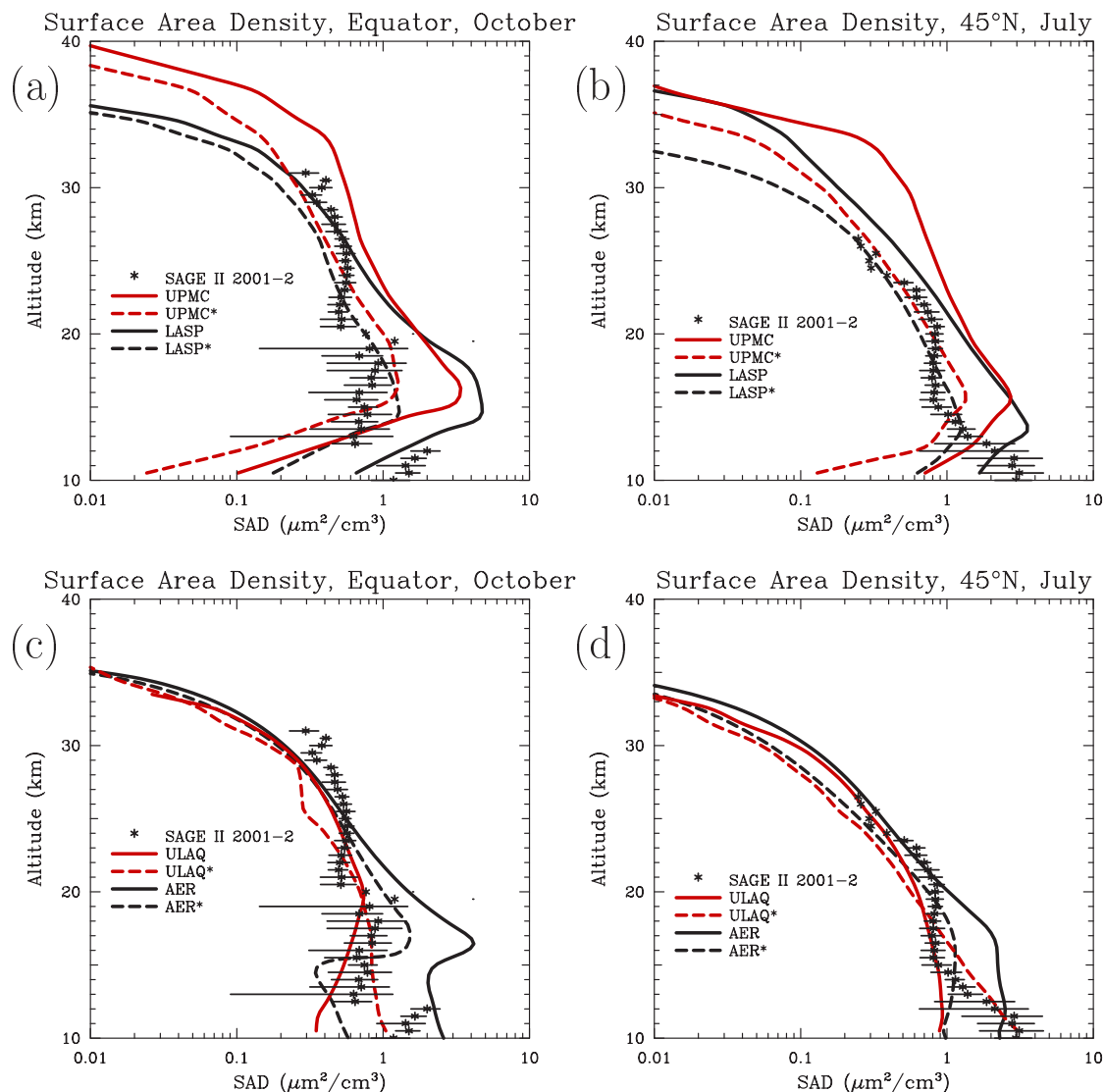


Figure 6.23: Comparison of surface area density derived from SAGE II observations (same as in Figure 6.22) and that calculated by the models at the equator in October (left panels) or 45°N in July (right panels). Dashed lines (labeled with a * after the model name) represent model surface area density derived from the 1.02 and 0.525 μm extinctions using Equation 4.1, while solid lines represent surface area density as integrated over the model's entire size distribution.

extinction-derived model results are often considerably closer to the SAGE-derived surface area densities.

We have calculated surface area density from the models employing lower limits on the particle size in the surface area integration. Figure 6.24 shows these results from the AER model, integrating over particles larger than 0.05 μm , particles larger than 0.1 μm , and particle larger than 0.15 μm . Integrals over particles greater than 0.05 or 0.1 μm differ from the full size distribution integration only below 25 km in the tropics or 20 km at midlatitudes, indicating that the particles smaller than 0.1 μm are only a significant contributor to the surface area density in the lower stratosphere. The integration over particles greater than 0.15 μm differs from the full integration at all altitudes. Integrating over particles larger than 0.1 μm yields a higher surface area than obtained by the extinction method, while integrating over particles larger than 0.15 μm yields a lower

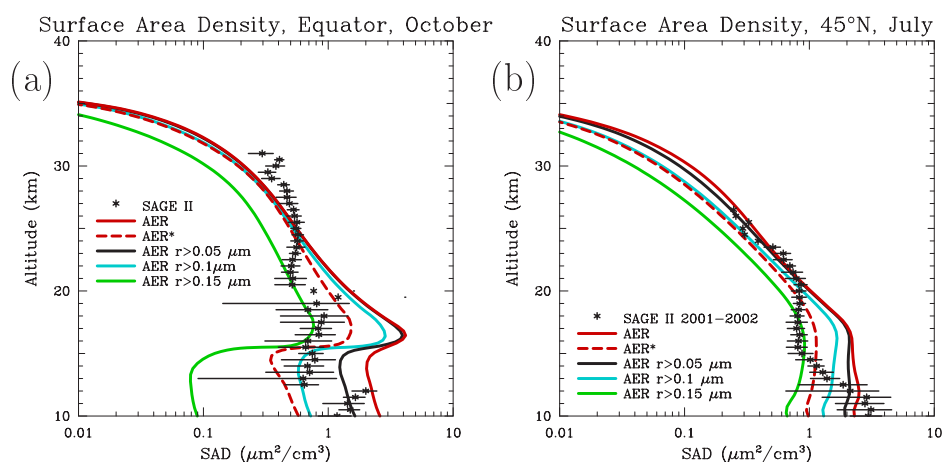


Figure 6.24: Comparison of surface area density derived from SAGE II observations (same as in Figure 6.22) and that calculated by the AER model at (a) the equator in October, and (b) 45°N in July. Dashed lines (AER*) represent model surface area density derived from the 1.02 and 0.525 μm extinctions using Equation 4.1, while solid lines represent surface area density as integrated over the model's aerosol size distribution with a lower radius cutoff as specified.

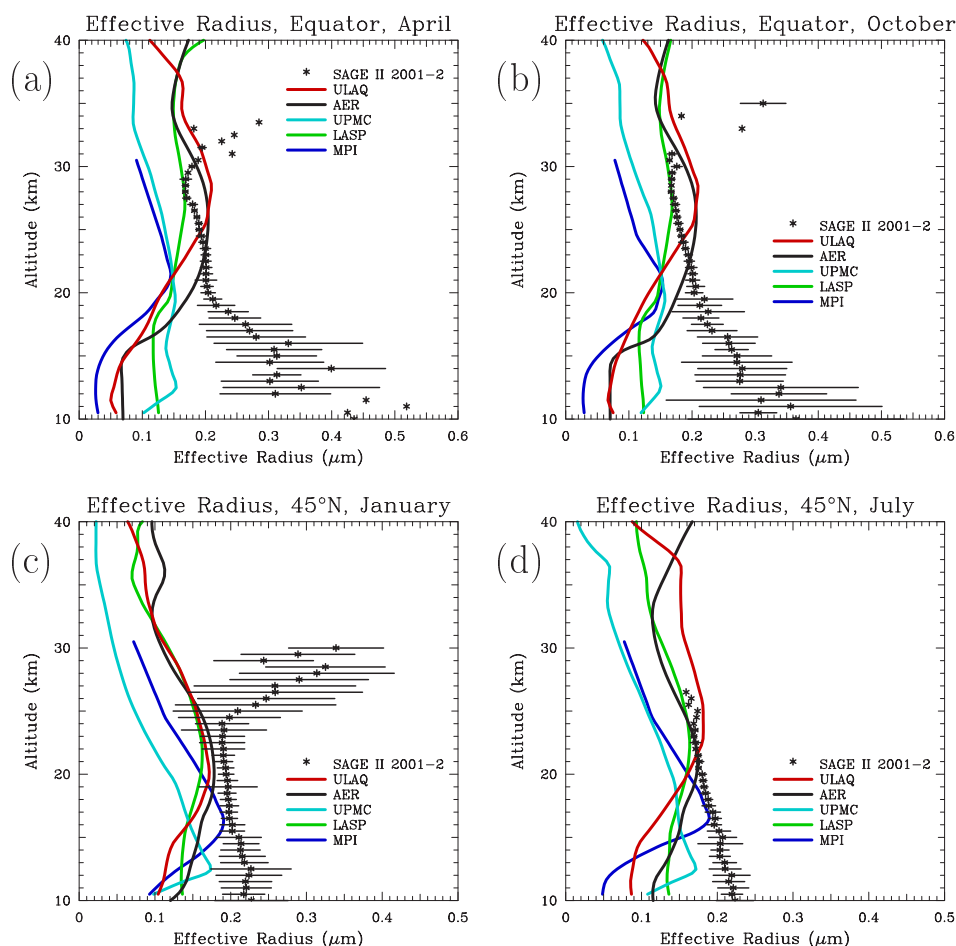


Figure 6.25: Comparison of SAGE II and model-calculated effective radius (a) April and (b) October at the equator, (c) January and (d) July at 45°N. SAGE II results use Equation 4.4 to obtain effective radius from the 2001-2002 composite of 1.02 μm extinction.

surface area which is within the range of SAGE II derived surface area density between 15 and 20 km but otherwise below it. Using a fixed size cutoff as we have done here is

not an accurate comparison with SAGE II derived surface area since extinctions show a range of sensitivity to aerosol particle size, not an abrupt cutoff. Yet it illustrates the inherent difficulty of comparing size distributions obtained from extinction measurements with model calculations. The lack of sensitivity of SAGE primary measurements to small particles probably explains much of the differences in the model-derived surface area density and the SAGE II derived surface area density. This explains why the differences between models and SAGE 0.525 μm extinction are very small compared to the differences in terms of surface area.

Aerosol effective radius is shown in Figure 6.25 for April and October at the equator and January and July at 45°N. SAGE II effective radius is derived from the 1.02 μm extinctions using Equation 4.4 for the 2001-2004 composite year. The models tend to produce lower effective radii than those inferred from the SAGE II instrument for the same reason that surface area densities tend to be higher, the lack of SAGE sensitivity to small particles. Models match SAGE II effective radii most closely between 20 and 30 km in the tropics, 15-25 km at 45°N, though the MPI and UPMC model generate smaller effective radii than SAGE II or the other models above 25 km. The model spread in effective radius ranges from 0.1 μm to 0.2 μm at 25 km at the equator, indicating that models differ substantially in the predicted size distributions.

6.6 Sensitivity Studies and Analyses

6.6.1 Sensitivity to model formulation

In this section we attempt to quantify the sensitivity of our results to the way in which the model represents the aerosol size distribution and to the formulation of some of the aerosol processes modeled. Where we can identify such differences, we can gain some understanding of the differences among the models used in this report. However, we make no attempt to diagnose intermodel differences or compare process formulations from model to model. Each model is a complex combination of many parameterizations and formulations and uses its own transport fields, so such an intercomparison is beyond the scope of this report. As a consequence, it cannot be shown here that models which use more precise representations of physical processes produce results more consistent with observations.

Sensitivity to bin resolution

Any aerosol formulation using fixed bin sizes suffers from numerical diffusion in size space, which may cause an increase in the width of the size distribution and may shift aerosol from small to larger bins too rapidly. The latter could result in excess sedimentation in the middle stratosphere and artificially lower the stratospheric aerosol burden. Global models, 3-D models in particular, must balance computational cost against accuracy. The AER 2-D model is capable of using a variety of aerosol bin resolutions, specified by the parameter V_{rat} , the volume ratio between consecutive bins, and the radius of the smallest bin R_{min} . We have made four sensitivity calculations using the AER model with different values of V_{rat} and R_{min} to test this sensitivity in a global model. Values of V_{rat} used include 1.2, 2.0, and 8.0. The AER, UPMC, LASP, and MPI models all employ V_{rat} values of 2.0. The ULAQ model uses a V_{rat} value of 8.0. Sensitivity studies used values of R_{min} of 0.39 nm and 10 nm at both $V_{\text{rat}}=2.0$ and $V_{\text{rat}}=8.0$. Of the models used in

this report, AER, LASP, and MPI use R_{\min} values between 0.39 and 1 nm while the UPMC and ULAQ models use $R_{\min}=10$ nm.

The calculations with different bin resolutions in the AER model show decreasing stratospheric aerosol mass density with increasing bin spacing (i.e. increasing V_{rat}). The effect on aerosol mass density of using $V_{\text{rat}}=2.0$ vs $V_{\text{rat}}=1.2$ is a few percent in the lower stratosphere at high latitudes, and up to 10% at 30 km. Using $V_{\text{rat}}=8$ relative to $V_{\text{rat}}=2$ leads to aerosol mass density decreases of 10-15% in the high latitude lower stratosphere and 25-30% at 30 km. Global stratospheric aerosol mass is lowered by $\sim 10\%$ in this case. Calculated size distributions are broadened with larger values of V_{rat} , producing more particles of both large and small size and fewer particles near $0.1 \mu\text{m}$. Figure 6.26 shows profiles of aerosol extinction at 0.525 and $1.02 \mu\text{m}$ at the equator in October and 45°N in July from models with three different values of V_{rat} . The largest differences in extinction occur below the tropopause where nucleation occurs. Because the AER model considers only sulfate aerosols and has poor transport in the troposphere, the comparison with SAGE II data below the tropopause should not be used to validate the aerosol bin

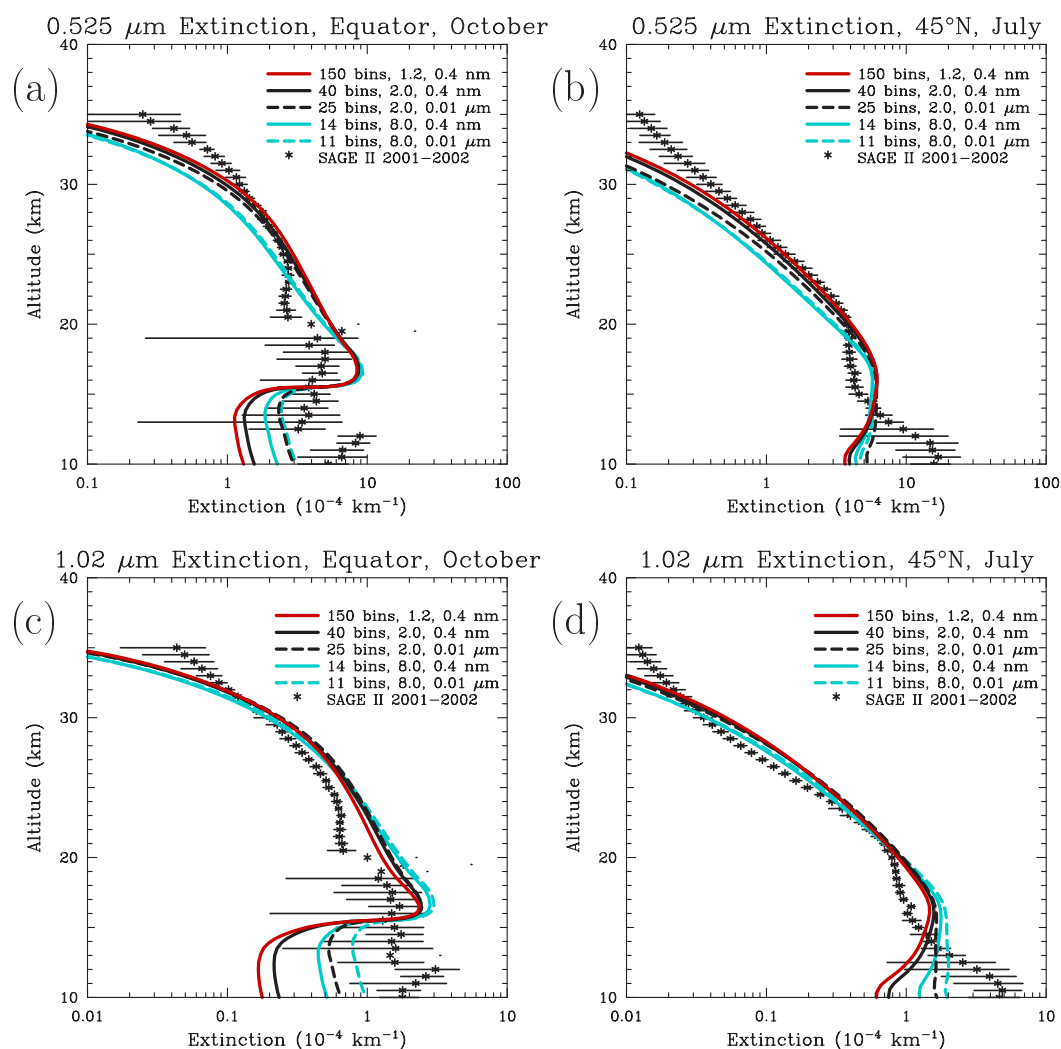


Figure 6.26: Comparison of SAGE II and calculated extinctions from the AER model at $1.02 \mu\text{m}$ at (a) the equator in October and (b) 45°N in July with different size resolutions. The numbers specified in the figure legend are number of size bins, volume ratio between adjacent bins (V_{rat}), and radius of smallest size bin (R_{\min}).

resolution. Above the tropopause, larger values of V_{rat} lead to lower extinction values at $0.525 \mu\text{m}$ and higher extinction values at $1.02 \mu\text{m}$.

The effect of increasing the smallest radius considered from 0.4 nm (the size of several molecules) to 10 nm changes the aerosol mass density only above $20\text{--}25 \text{ km}$, and modifies the global stratospheric aerosol mass by only 2% . Using a minimum radius of 10 nm forces the nucleated sulfuric acid mass into particles of this size, bypassing the coagulation process that would otherwise be required to achieve particles in this size range. This may in fact be preferable for global models, since their spatial resolution doesn't allow for localized nucleation, which would result in very high number densities and very high coagulation rates. The calculated size distributions are not greatly affected by the lack of small particles except in nucleation regions and evaporation regions. Figure 6.26 also shows the differences in extinction between models which are identical except for the value of R_{min} (compare solid and dashed lines of the same color). Below $15\text{--}18 \text{ km}$, the extinction is larger with larger R_{min} . Otherwise extinction differences due to R_{min} are small. Errors due to numerical diffusion caused by limited size resolution are found to be unlikely to explain most of the discrepancies between observed and modeled aerosol extinctions. Differences between models are not likely to be explained significantly by differences in bin resolution either, as other factors such as transport differences are probably more important.

Sensitivity to nucleation rate

Despite many years of experimental and theoretical research regarding nucleation of binary $\text{H}_2\text{O}\text{--}\text{H}_2\text{SO}_4$ aerosols, there is still an uncertainty of several orders of magnitude in nucleation rates of atmospheric aerosols [Hale et al., 2000]. While theories of classical binary homogeneous nucleation are well known, calculations from these theories do not always match observations. These theories have been modified by considering hydrated sulfate clusters and ternary nucleation involving ammonia [Kulmala et al., 2000] or nucleation on organics [O'Dowd et al., 2002] or chemiions [Yu and Turco, 2000; Lovejoy et al., 2004]. In addition, nucleation likely occurs in the atmosphere in the vicinity of deep convective events and where gravity waves induce temperature fluctuation, situations not spatially resolved in global models. Nucleation processes are discussed in Chapter 1, Section 1.5.1 of this report. Here we investigate the sensitivity of our model results to a standard nucleation parameterization and to the thermodynamic upper limit of nucleation. The upper limit is obtained by assuming that the collision of any two sulfur molecules at their thermal speed results in a new particle, with the appropriate water fraction condensing instantaneously.

The AER model was run with the Vehkamäki et al. [2002] nucleation scheme and the thermodynamic upper limit. Total atmospheric nucleation was larger by over two orders of magnitude when using the upper limit. This results in more particles of smaller mean size. Surface area density increases by up to 80% in the tropical upper troposphere with increased nucleation, but only by $5\text{--}20\%$ in most of the stratosphere. Aerosol mass density does not change below 20 km , but increases by $5\text{--}15\%$ above 20 km and up to 30% at 30 km . This indicates the lessening of the effect of gravitational settling on the slightly smaller particles, once they have sufficiently long travel times in the middle stratosphere. Global aerosol mass remains almost unchanged. Changes in stratospheric aerosol extinction are small (less than 10% at $1.02 \mu\text{m}$). Coagulation acts as a self-limiting

process to limit the sensitivity of stratospheric aerosol to nucleation, which occurs mostly in the upper tropical troposphere.

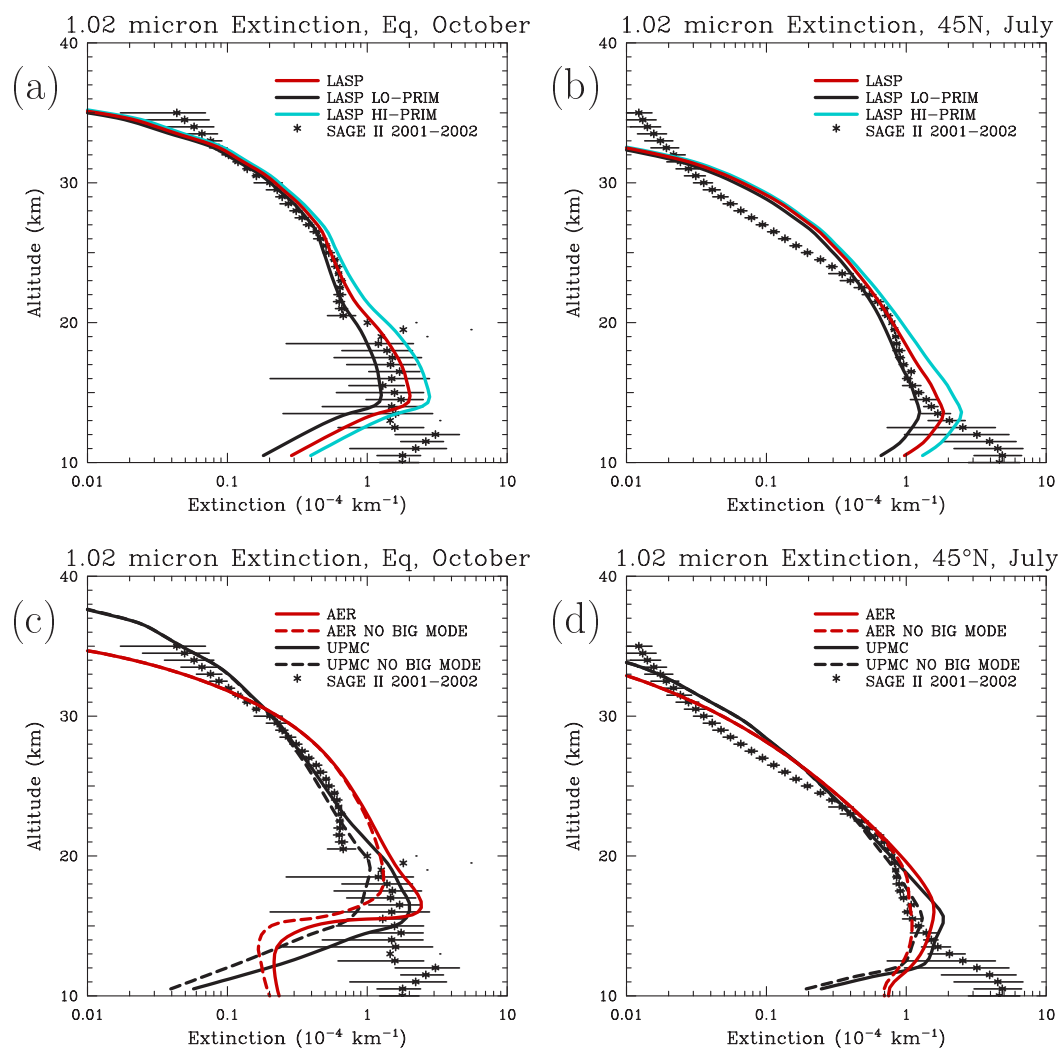


Figure 6.27: Comparison of SAGE II and model-calculated extinctions at 1.02 μm in October at the equator (left panels) and 45°N in July (right panels) from the LASP, AER, and UPMC 2-D models using different tropopause boundary conditions for primary primary aerosol. LO-PRIM has primary aerosol concentration reduced by two standard deviations (to 160 pptv), HI-PRIM has primary aerosol concentration increased by two standard deviation (to 356 pptv), and NO BIG MODE has removed the particles greater than 0.3 μm from the primary aerosol distribution.

6.6.2 Primary aerosol sensitivity

While the ULAQ 3-D model used in this report has its own tropospheric aerosol scheme, the 2-D models (LASP, AER, and UPMC) need to prescribe the amount of condensible material and aerosol at the tropical tropopause. To test the sensitivity of our results to the assumed aerosol concentration and size distribution at the tropical tropopause, we have performed sensitivity studies with the LASP, AER, and UPMC models. These sensitivity studies provide not only model sensitivity to this parameter, but an indication of the importance of particles transported across the tropical tropopause to the stratospheric aerosol budget.

The LASP model performed calculations to vary the tropopause aerosol input concentration over the two standard deviation (37%) range reported by S.-H. Lee (Figure 6.9) while maintaining the same size distribution. Figures 6.27a and 6.27b show profiles of $1.02\ \mu\text{m}$ extinction from the LASP model at the equator in October and at 45°N in July. Additional months, as well as $0.525\ \mu\text{m}$ extinctions, are shown in the supplementary material. Aerosol extinctions above 25 km are insensitive to aerosol crossing the tropopause, being primarily related to sulfur derived from OCS. Results labeled "LO-PRIM" used 160 pptv of tropopause primary aerosol and results labeled "HI-PRIM" used 356 pptv of tropopause primary aerosol. The standard tropopause aerosol produces the best fit to observations at the equator in October in the 14-20 km region in the LASP model, with results from model calculations with tropopause aerosol reduced or enhanced by two standard deviation also within the error bars of the SAGE II observations. At 45°N in July, the LASP model results at the lower limit of tropopause aerosol fit the observations better between 14 and 20 km.

Figures 6.27c and 6.27d show profiles of $1.02\ \mu\text{m}$ extinction from the AER and UPMC models with the larger mode ($0.3\text{-}0.8\ \mu\text{m}$ radius) of the primary aerosol eliminated. This decreases the input sulfur mass at the tropical tropopause by 25%. If the large aerosol mode reported by S.-H. Lee were not pure sulfate, but rather tropospheric particles of a different composition, or solid particles coated with sulfate, then those particles would contribute to the extinction near the tropopause but not to the sulfur burden of the stratosphere. The large primary aerosol mode has a big effect on extinction between 15 and 20 km in the tropics and a more modest affect at 45°N . Comparisons with observations in the tropics show that results with and without the large mode of primary aerosols are all within the observational error bars in the tropics below 18 km, though results without the large mode are a better fit between 18 and 22 km. At 45°N in July, model results without the large mode are a better match to observations. Aerosol mass is unchanged above 20 km with or without the large mode primary particles, confirming that these particles do not penetrate into the middle stratosphere in our model simulations.

Shown in Figure 6.12, the AER model's sulfur budget changes with tropopause aerosol input. The primary aerosol input to the stratosphere varies from 50 to 82 kilotons of sulfur per year over the one sigma range discussed here. This results in a range of the stratospheric aerosol burden from 170 to 204 kilotons of sulfur. The change in primary aerosol of $\pm 19\%$ (one sigma range) leads to an aerosol mass mixing ratio change of -8 to +10%. In the case with the large particles removed from the primary aerosol distribution, the influx of primary aerosol to the stratosphere is 43 kilotons of sulfur per year and the stratospheric burden 174 kilotons of sulfur.

6.6.3 Tropopause SO_2 sensitivity

The AER and LASP models performed sensitivity studies to the imposed SO_2 concentration at the tropopause. The standard simulation used 40 pptv of SO_2 and 258 pptv of primary aerosol at the tropopause. Measured SO_2 concentrations in the upper troposphere vary widely, up to 200 pptv [Thornton et al., 1999], and we have chosen upper and lower limits of 0 and 80 pptv of tropopause SO_2 for our sensitivity tests. The SO_2 concentrations near the tropopause do not have an immediate direct effect on local aerosol because reaction with OH and then gas-to-particle transformation are required. Changes in tropopause SO_2 concentration will lead to changes in aerosol number through nucleation, and will affect particle size through condensation. We find the sensitivity of

extinction at 1.02 or 0.525 μm to tropopause SO_2 to be quite small when primary aerosol is included in the simulations from both the AER and LASP models. This is because the SO_2 range tested (± 40 pptv) is small compared to the imposed primary aerosol sulfur concentration (258 pptv) and because the impact of additional SO_2 on the large particle sizes which scatter visible light is small.

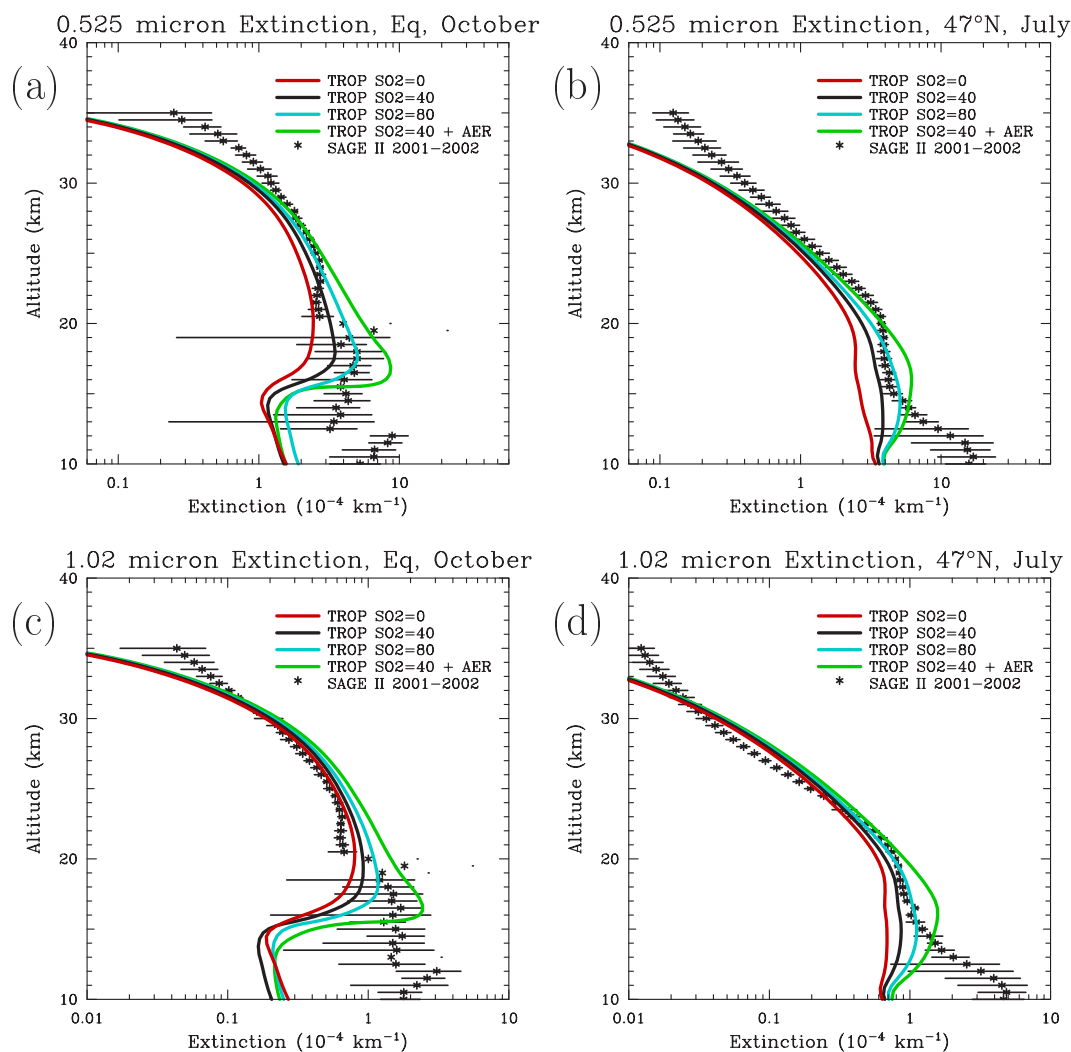


Figure 6.28: Comparison of SAGE II and model-calculated extinctions at 0.525 μm (top panels) and 1.02 μm (bottom panels) in October at the equator (left panels) and 45°N in July (right panels) from the AER 2-D model using different tropopause boundary conditions for SO_2 (0, 40, and 80 pptv) without primary aerosol and for SO_2 of 40 pptv with primary aerosol.

The AER model was used for simulations without primary aerosol but with tropopause SO_2 of 0, 40, and 80 pptv. Extinctions at 0.525 and 1.02 μm are shown in Figure 6.28 for these simulations. A calculation with primary aerosol and 40 pptv of tropopause SO_2 is also shown for comparison. There is strong sensitivity of extinction to tropopause SO_2 over the range modeled, with the 0.525 μm extinction showing more sensitivity than the 1.02 μm extinction. Tropopause SO_2 impacts stratospheric aerosol extinction as high as 30 km, at greater altitudes than those showing sensitivity to tropopause primary aerosol in the AER model. In the 15-25 km altitude range, the simulation with no primary aerosol and tropopause SO_2 of 80 pptv produces less extinction than with the lower limit (160 pptv) of primary aerosol. In the tropics in October, the simulation with 80 pptv of

SO₂ matches SAGE II 0.525 μm observations between 15 and 20 km. At the same time and latitude, the 1.02 μm SAGE II extinction between 20 and 30 km is matched best by the simulation with no tropopause SO₂. Among the simulations with modified primary aerosol and tropopause SO₂ amounts, none are a universally good match for SAGE II observations from 1999-2000. The vertical and latitudinal variations observed in SAGE II extinctions are not reproduced well by the models.

6.6.4 OCS sensitivity

Observations of OCS mixing ratios discussed in Chapter 2 indicate considerable variability on seasonal time scales and as functions of latitude, longitude, and altitude. Observations at the Jungfraujoch, Lauder, and Wollongong indicate long-term trends of -5%/decade, -6.9%/decade, and -3.5%/decade (see Section 2.3.1 for details). These trends, while small but statistically significant, may have had implications for stratospheric aerosol levels. We have investigated the sensitivity of model-calculated aerosol loading to changes in tropospheric OCS by decreasing the surface mixing ratio of OCS by 10% in the AER model. This results in a decrease of only 3% in the global stratospheric aerosol mass burden, and local decreases in mass density and surface area density of up to 6% and 5%, respectively above 25 km. As discussed in Section 6.5.3, OCS forms the primary aerosol source above 25 km, while SO₂ and particles transported from the troposphere are more important below. Extinctions at 0.525 and 1.02 μm decrease by 7% and 9%, respectively, above 20-25 km when OCS is reduced by 10%.

6.7 Model Simulations of Volcanic Conditions

6.7.1 Description of Calculations

The models have performed a simulation of the evolution of the stratospheric aerosol following the Mt. Pinatubo volcanic eruption in the Philippines on June 15, 1991. Models were initialized with 20 megatons of SO₂ [Bluth et al., 1992; McCormick et al., 1995] in the 16-30 km altitude region [Read et al., 1993] over the tropical site. Each model makes somewhat different assumptions concerning the vertical and horizontal distribution of the volcanic SO₂, with the ULAQ model injecting no SO₂ below 21 km. Subsequently the SO₂ is converted to H₂SO₄ via reaction with OH. OH fields are either calculated or prescribed in the models, yielding an e-folding time for SO₂ chemical loss of approximately 30 day. Nucleation rates are enhanced over background conditions for the first few months following the eruption. However, the majority of the volcanic sulfur is converted to aerosol by condensation onto preexisting particles, resulting in larger stratospheric aerosol particle sizes for several years. In agreement with observations, the models calculate that the perturbation decays with e-folding times of about 1 year, with near-background levels reached again in the late 1990s.

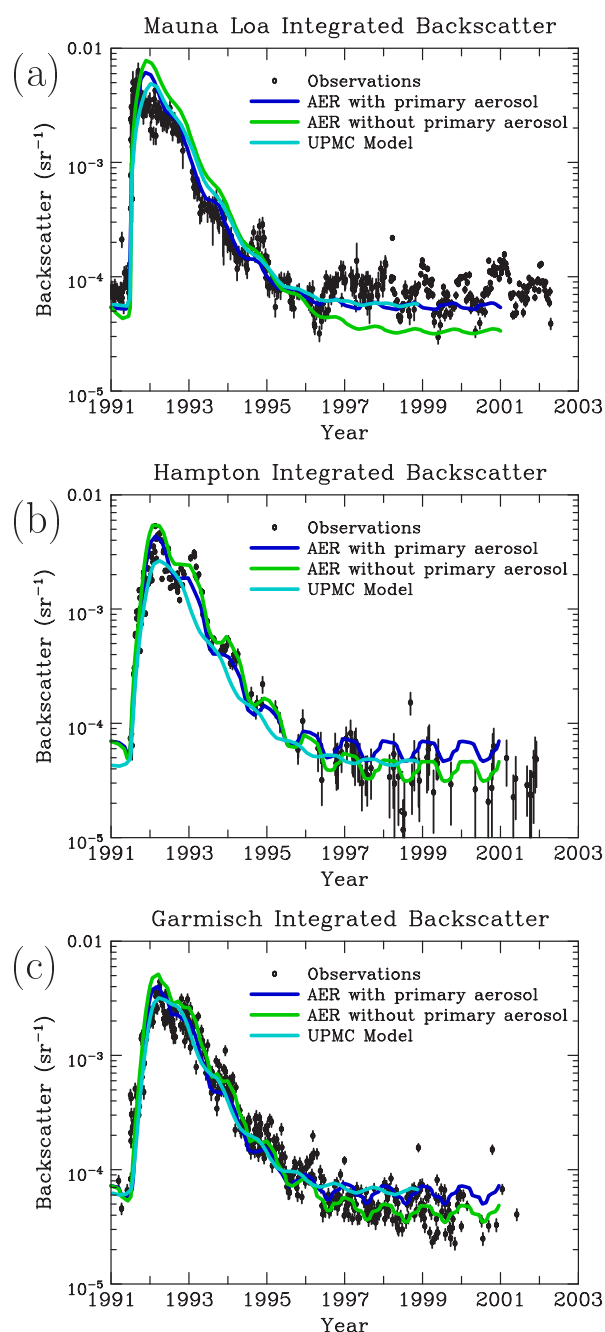


Figure 6.29: Integrated lidar backscatter at 694 nm at (a) Mauna Loa (19°N , 15.8-33 km) (b) Hampton, VA, (37°N , tropopause to 30 km) and (c) Garmisch-Partenkirchen (47°N , tropopause + 1 km to top) for the post-Pinatubo period. Observations are shown by black dots with error bars, model results by solid lines. AER model results are shown both with and without assumed primary aerosol entering the stratosphere at the tropical tropopause.

toward background values. Mauna Loa observations may reflect the volcanic eruption of Rabaul on September 14, 1994 which the models did not simulate. AER model results with and without prescribed primary aerosol entering the stratosphere at the tropical tropopause are shown, the difference being small except after 1996. The simulation with

6.7.2 Comparisons with Lidar Backscatter Measurements

The evolution of Mt. Pinatubo volcanic aerosols has been monitored at several lidar measurement stations. Model-calculated backscatter columns (i.e. backscatter integrated vertically) are compared to observations at a tropical site (Mauna Loa at 19°N) and two midlatitude sites (Hampton at 37°N and Garmisch-Partenkirchen at 47°N) in Figure 6.29. The lidar instruments, which operate at about $0.67\ \mu\text{m}$, are discussed in Chapter 3, Section 3.3.2, and the lidar data in Chapter 4, Section 4.1.3. Column integrals at Mauna Loa include 15.8 to 33 km, at Hampton from the tropopause to 30 km, and at Garmisch from 1 km above the tropopause to the top of the aerosol layer. The evolution of the backscatter column can be decomposed into three phases: a very steep increase, a maximum, and a slow decay toward background levels. The steep increase in backscatter column is reproduced by the models (AER, UPMC). The lidar data show that the backscatter column peaks earlier at Mauna Loa (about 3-6 months) compared to the midlatitude sites (8 or 9 months); this is also the case in the models but the difference between the sites is not as pronounced. The magnitude and timing of the maximum observed at midlatitude stations is reproduced by the models. However, the maximum at Mauna Loa occurs later in the models.

Overall, the model-calculated values appear to match rather well the lidar measurements during the slow decay

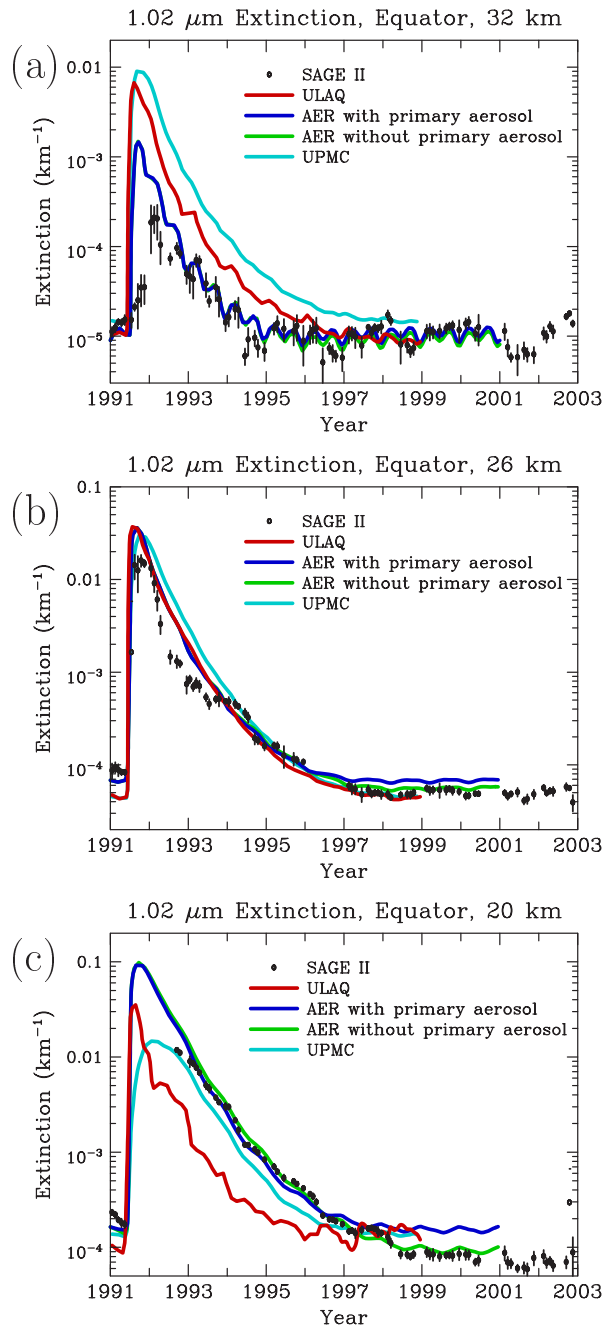


Figure 6.30: Aerosol extinction at $1.02 \mu\text{m}$ for 1991 to 2002 at the (a) equator and 32 km, (b) equator and 26 km, and (c) equator and 20 km. SAGE II data are shown by black symbols with error bars, model results by colored lines.

of the backscatter column to the background level not before 1997.

Lidars are not sensitive to small aerosol particles. Therefore, the backscatter column is mainly a measure of medium to large aerosol particles (typically particles greater than a tenth of a micron). As most of the aerosol mass is contained in this size range, the backscatter also provides an estimate of the aerosol mass loading. The ability of the models to reproduce the broad features of the evolution of the backscatter column indicates that the evolution of the aerosol mass loading is adequately simulated in the

primary aerosol appears to match the Mauna Loa observations best, while the simulation without primary aerosol matches best at Hampton. The variability in the Garmisch data is as large as the difference in the two AER simulations. The pronounced annual cycle in the model calculated integrated backscatter at midlatitudes is due mostly to the shifting tropopause height. As expected, the lidar data exhibit much more variability than the model simulations which represent a zonal average. The observations show variability on short-term and inter-annual timescales. This variability is of dynamical origin and is vastly underestimated in the models. The variability makes it difficult to define exactly background aerosol levels in the lidar data. As a result, the timing of the return to a background state can only be defined as a return to within this background variability. The higher the background variability of an aerosol parameter is compared to the volcanic perturbation, the quicker the return to the background level appears to be. For example, the variability in the measured backscatter column at Mauna Loa is very high, giving the impression that the return to background levels occurred in 1995, several years earlier than at midlatitude sites. In contrast, there is little variability in the model-calculated integrated backscatter. Consequently, the background backscatter level is relatively well defined. The models predict a return

models, with an overall sufficiently accurate description of particle nucleation, growth, coagulation, evaporation, sedimentation, and dynamical transport.

6.7.3 Comparisons with SAGE II Observations

The evolution of $1.02 \mu\text{m}$ extinction at the equator (Figure 6.30) over the 1991 to 2002 period shows that the aerosol extinction starts increasing immediately after the Pinatubo eruption. The model-simulated extinctions increase at approximately the correct rate at 26 km, but much too rapidly at 32 km, with model simulations of 32 km extinction rising almost as rapidly as the 26 km extinction. There were no SAGE II data available at 20 km shortly after the eruption because of the large optical thickness of the aerosol cloud.

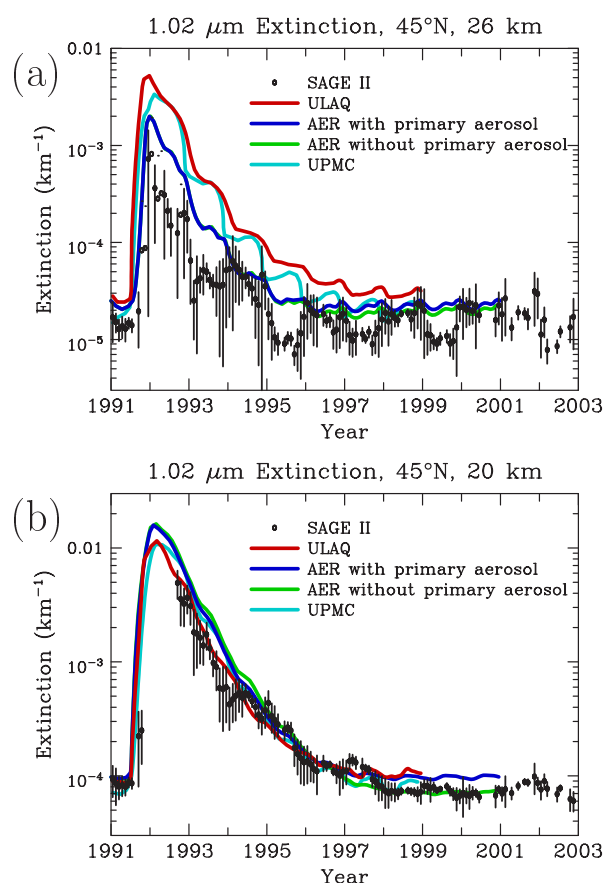


Figure 6.31: Aerosol extinction at $1.02 \mu\text{m}$ for 1991 to 2002 at (a) 45°N and 26 km and (b) 45°N and 20 km. SAGE II data are shown by symbols with error bars, model results by colored lines.

At 26 km, all three models (ULAQ, AER, UPMC) do a reasonable job at simulating the $1.02 \mu\text{m}$ extinction over the entire period except in 1992 and 1993, when model calculations are too high compared to SAGE observations. At 20 km, the AER and UPMC models match the SAGE II extinctions fairly well, while the ULAQ modeled values are too low. AER model simulations both with and without imposed primary aerosols at the tropical tropopause are shown; they differ at 20 km in the tropics, but not significantly at the other altitudes. The AER simulation without primary aerosol drops to lower levels after 1997, matching better the SAGE 20 km extinctions. At 32 km, the AER model simulations are close to the observations after 1992, while ULAQ and UPMC modeled values are too high. This would indicate that either the upward transport in the ULAQ and UPMC models is too strong in the tropics or that the volcanic SO_2 cloud was placed too high initially.

At 45°N (Figure 6.31), all the models do a good job at simulating the extinction at 20 km, but they all overestimate extinctions at 26 km compared to SAGE data. Like for the lidar data, there are significant fluctuations from one year to another in the SAGE time series. The fluctuations are visible, not only close to the background level, but also during the decay. In contrast, there is again little variability in the model-calculated extinctions, though some models obtain seasonal fluctuations at the higher altitudes which only superficially resemble observed fluctuations. Comparisons of model simulations with SAGE aerosol extinctions at $0.525 \mu\text{m}$ can be found in the supplementary material, providing a very similar overall picture.

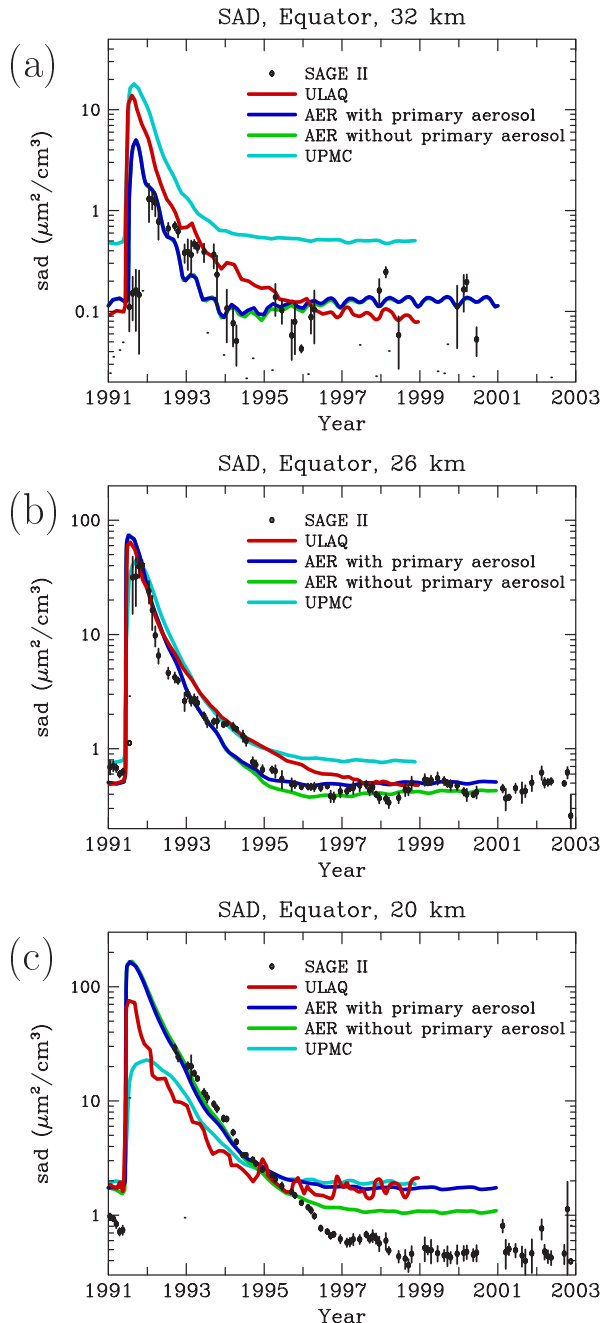


Figure 6.32: Surface area density ($\mu\text{m}^2/\text{cm}^3$) for 1991 to 2002 at the (a) equator and 32 km, (b) equator and 26 km, and (c) equator and 20 km. SAGE II results derived using Equation 4.1 are shown by symbols, model results by colored lines.

Section 3.3.1, and its observations in Chapter 4, Section 4.1.3. The results are shown in Figure 6.33 at three altitudes at 41°N for particles greater than $0.15 \mu\text{m}$. A similar comparison for particles greater than $0.25 \mu\text{m}$ can be found in the supplementary material. The UPMC and AER models do a good job of reproducing the peak number density of particles greater than $0.15 \mu\text{m}$ at 22 and 26 km, but only the UPMC model accurately captures the peak at 18 km, with the AER peak being 50% too high. The number concentration of large particles seems to return to background values by about 1995, several years earlier than for the $1.02 \mu\text{m}$ aerosol extinction.

Surface area densities calculated by the models for the Pinatubo period are shown in Figure 6.32 for 20, 26, and 32 km at the equator. Model simulations follow fairly closely the surface area densities derived from SAGE II data at 26 km for the entire time period, but at 20 km they match the observations only before 1996. As seen in the surface area density comparison for background conditions, models predict surface area densities substantially higher than SAGE in the tropical lower stratosphere during periods of low aerosol loadings. This is not surprising. Small particles are abundant in this region and visible wavelength aerosol extinction is weakly sensitive to small particles. During the period of highly enhanced aerosol loading following Pinatubo, particle effective radius increases from ~ 0.15 to $\sim 0.5 \mu\text{m}$ with a strongly reduced contribution from small particles to the surface area density. As a result, models and SAGE-derived surface area densities agree fairly well before 1996.

6.7.4 Comparisons with OPC Data

Model-calculated particle number concentrations are compared to measurements made with a balloon-borne optical particle counter (OPC) by Terry Deshler at the University of Wyoming [Deshler et al., 2003] between 1991 and 2003. The instrument is described in Chapter 3,

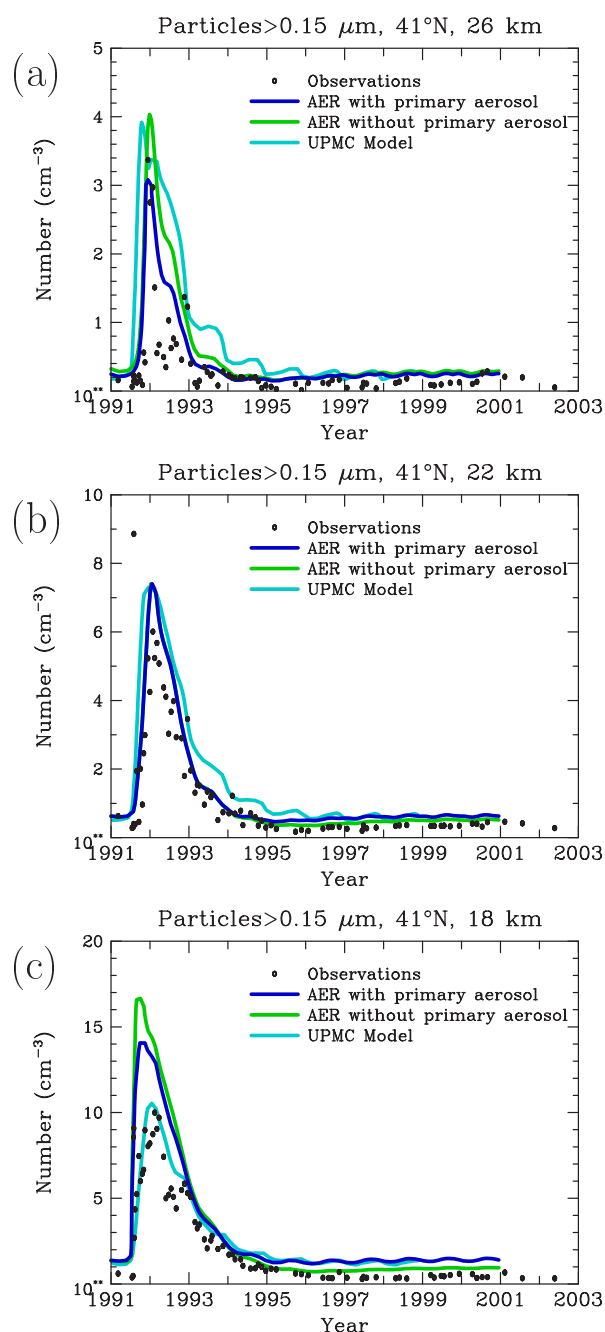


Figure 6.33: Number densities of particles with radius greater than $0.15 \mu\text{m}$ for 1991 to 2002 at (a) 26 km, (b) 22 km and (c) 18 km in Wyoming. Observations taken by balloon-borne OPC instruments [Deshler et al., 2003] at the University of Wyoming are shown by symbols, model results by colored lines.

used for quantifying the loss rate of an atmospheric constituent with respect to a specific process (e.g., chemical, dynamical, or physical process).

Apart from the long-term decay, the most obvious variations are seasonal, with an annual cycle that appears most clearly toward the end of the decay period, close to the background state (see Figures 6.29 to 6.33). There is also a substantial amount of fluctuation on inter-annual timescales in the observational time series (lidar, SAGE). As

6.7.5 Aerosol Decay Rates

E-folding Decay Timescale

This section is devoted to a detailed study of the decay of the stratospheric aerosol layer toward its background state after the volcanic eruption of Mount Pinatubo. In a sense, it is a compliment to Chapter 5 which is devoted to identifying and analyzing the background component of the stratospheric aerosol. Identifying background periods unambiguously from the observations has proven difficult, but is more straight-forward with model simulations. Models lack most sources of short-term variability, and can effectively isolate the effects of a single volcanic eruption. We focus our attention on the evolution of aerosol levels a month after the backscatter peak in order to consider the decay only. Model simulations and observations of several aerosol quantities (backscatter column, extinction, surface area density, particle number density) are shown in Figures 6.29 to 6.33. The decay of model-calculated or measured aerosol quantities toward background values tends to follow an exponential rather than linear law. For this reason, we have quantified the decay rate with an e-folding timescale, which is the time taken for an aerosol quantity to decay to $1/e$ of its initial value. The e-folding timescale is commonly

we are only interested in the long term decay, it would be valuable to remove the scatter originating from the short-term variability in the time series. However, it is difficult to remove accurately the short-term fluctuations (such as seasonal variations) without affecting at all the long term decay in the time series because the seasonal variations are embedded into a strongly varying decay. In order to avoid any possible spurious effects from smoothing or the assumptions required for curve-fitting, we simply derive the e-folding timescale from the raw time series using the variation of the aerosol quantity monthly mean from one year to another. The e-folding decay timescale τ_{decay} is given by

$$\tau_{decay} = \frac{1}{\log[\beta(month_{(i+6)}) / \beta(month_{(i-6)})]} \quad (6.1)$$

where $\beta(month_{(i)})$ is the monthly mean of an aerosol quantity in month i . This relationship does not provide the decay timescale over the entire time series; indeed, the timescale can only be calculated over the period of the time series truncated by 6 months at both ends. By using data points 12 months apart, Equation 6.1 removes the regular seasonal variations found in the models. Model-calculated and observational time series are processed in exactly the same way.

Decay Timescales Derived from Backscatter Column

In Figure 6.34 the e-folding decay timescale τ_{decay} is plotted as a function of time for the three lidar stations. In the figure, model results are shown by colored lines; observational data are shown with black dots. While model-calculated e-folding timescales vary relatively smoothly during the post-Pinatubo period, observational data show large variability from month to month that defies identification of a return to background on this basis. As expected, the backscatter variability is accentuated in the temporal derivative. The background variability in the lidar time series is such that the timescale, as defined by Equation 6.1, starts becoming negative from time to time in the last phase of the long-term decay. For example, negative values start appearing in 1995 at Mauna Loa. It is this short-term variance which prevents the decay timescales from tending toward high values during the last phase of the decay, after 1995-1996. This indicates that the variance from the short-term variability outweighs the variance from the long-term decay. Therefore, any timescales derived from the lidar data after about 1995 cannot provide any reliable information on the last phase of the decay and should be discarded from the analysis.

The evolution of model-calculated and lidar-based timescales show clearly that the volcanic aerosol backscatter perturbation does not decay with a constant e-folding timescale. There is, first, a short phase (about a year following the peak) during which the time scale decreases to a minimum of about 5-10 months, with general agreement between models and observations during this period. Then the decay timescale starts increasing rapidly. The evolution is very similar at the three sites in the model simulations, with the UPMC model and the AER primary aerosol model yielding almost identical e-folding times, while the AER model without primary aerosol has shorter e-folding times. Model-calculated e-folding timescales of about 1 year are reached in mid-1994 (3 years after the eruption), values of 6 years mid-1996, and a value of about 100 years mid-1998. A similar evolution is seen until 1995 in the lidar-based timescales with values reaching very approximately 1 year in mid-1994 and up to 3 years in mid-1995. After 1995, negative values of decay timescale appear. The variability in the lidar times

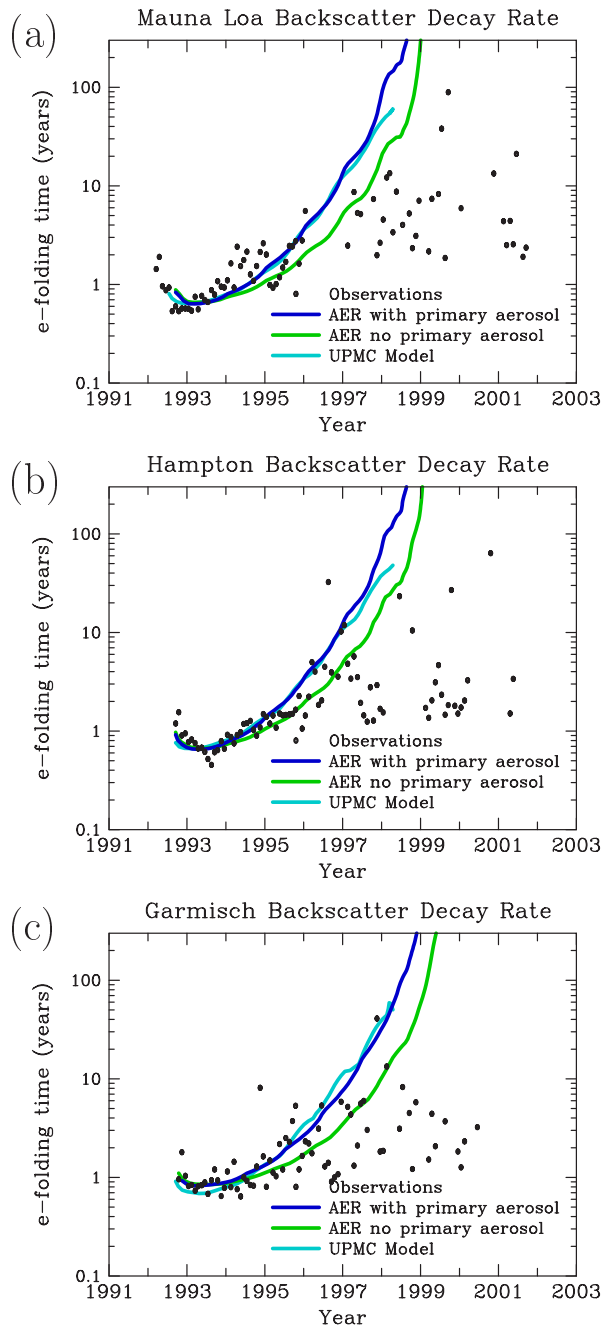


Figure 6.34: E-folding time (years) of integrated lidar backscatter at 694 nm at (a) Mauna Loa (19°N) (b) Hampton, VA, (37°N) and (c) Garmisch-Partenkirchen (47°N) for the post-Pinatubo period. Equation 6.1 applied to observations, shown by black dots, or model results, shown by colored lines, to obtain decay timescales.

2.5% per year) giving a return of model-calculated backscatters to the background level about 6.5 years after the eruption (i.e. the end of 1997 for the UPMC and AER models with primary aerosol). The AER model without primary aerosol gives slightly longer times for the return to the background level. The choice of the threshold value appears rather arbitrary. But, this does not affect much the timing of the return to the background state. Indeed, a threshold timescale value of 20 years (corresponding to a change of 5%

series is such that no conclusions can be drawn out of the last phase of the decay. This agreement between measurements and model-simulations confirms that global models are able to simulate realistically the aerosol decay following the Mount Pinatubo eruption.

The sharp increase in the decay timescale from about 1993 originates from the drop in the mean size of the aerosol particles. Indeed, the main removal process for the aerosol particles is gravitational sedimentation. This process is highly selective with respect to the size of the aerosol particles; it is very efficient for large volcanic aerosols but has a negligible effect on the small particles. As a result, the large particles are removed very rapidly in the first phase of the decay. This is accompanied by a drop in the mean aerosol size and hence a rapidly decreasing efficiency of sedimentation during the decay.

In theory, the aerosol layer reaches the background state when the decay e-folding timescale is infinity. If the decay rate follows an exponential law, the time taken for a volcanic perturbation to vanish completely should in principle be infinity. In practice, one can choose a threshold value of the e-folding timescale beyond which aerosol changes can be neglected for the purpose of the problem considered. We choose a value of 40 years (which corresponds to a change of

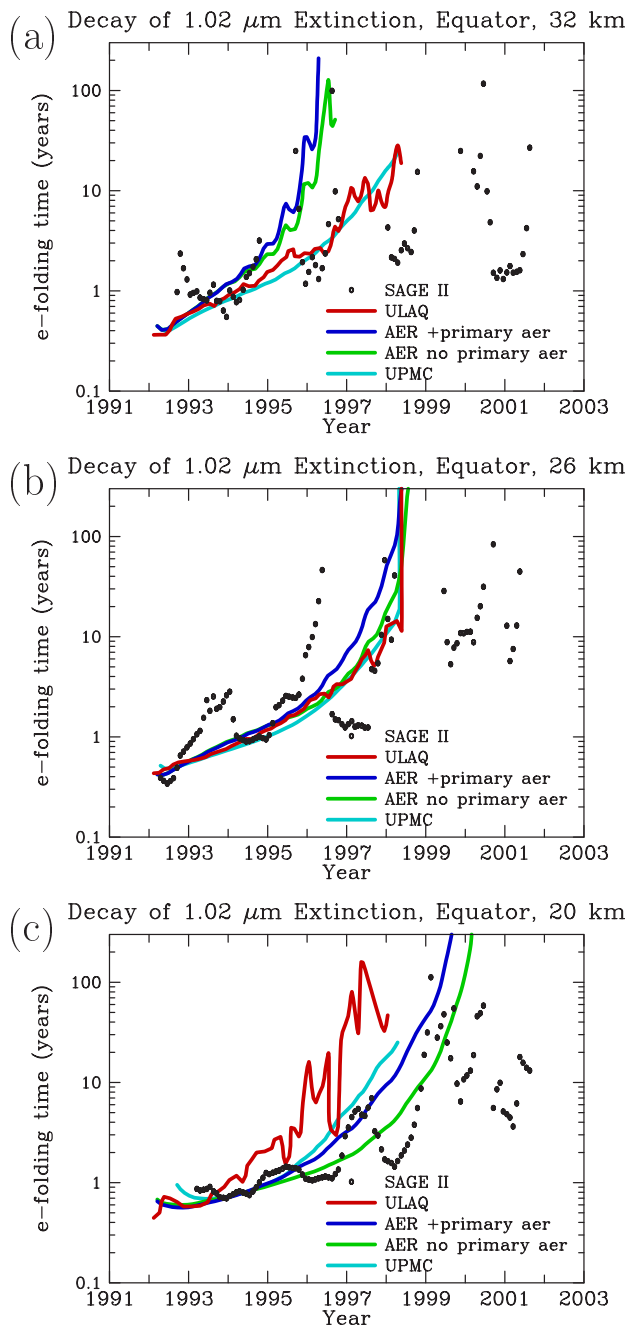


Figure 6.35: E-folding time (years) of aerosol extinction at $1.02 \mu\text{m}$ for 1991 to 2002 at the (a) equator and 32 km, (b) equator and 26 km, and (c) equator and 20 km. Equation 6.1 applied to observations, shown by black dots, or model results, shown by colored lines, to obtain decay timescales.

to a change of 2.5% per year), the return to the background state occurs at the beginning of 1998 in the model simulations. At 32 km, the ULAQ and UPMC models predict a similar evolution of the e-folding timescale, while the AER model predicts a much quicker return to the background state. Assuming again a threshold value of 40 years for the timescale, the return of the $1.02 \mu\text{m}$ extinctions to background values occurs by the beginning of 1996 in the AER simulations whereas it has not occurred yet by the

per year) gives a return to the background state 6 years after the eruption (i.e. mid-1997) whereas a threshold value of 80 years (corresponding to a change of 1.25% per year) gives a return to the background state 7 years after the eruption (i.e. mid-1998). It is worth pointing out that the return to the background state is sometimes established from comparisons with background levels defined a priori, for example, the aerosol levels before the volcanic eruption. The approach used here is based on the evolution of the decay timescale and does not require identifying background levels a priori.

Decay Timescales Derived from Extinction and Number Density

E-folding timescales of $1.02 \mu\text{m}$ extinction at the equator and 20, 26, and 32 km are shown in Figure 6.35. As expected, there are more differences between the model simulations for height-resolved aerosol quantities than for vertically integrated quantities such as backscatter. At the equator and 20 km, the ULAQ model predicts a more rapid increase of the timescales than the AER and UPMC models. Decay rates derived from SAGE II data tend to agree more with the AER and UPMC model simulations at this altitude. At the equator and 26 km, all models predict very similar e-folding timescales. If one assumes that the background aerosol state is reached when the extinction-based decay timescale exceeds a threshold value of 40 years (which corresponds

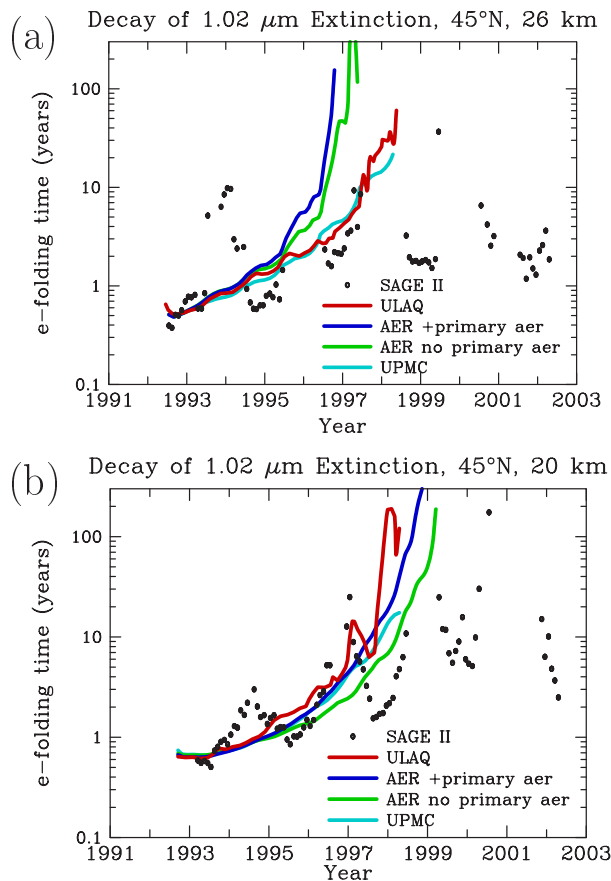


Figure 6.36: E-folding time (years) of aerosol extinction at 1.02 μm for 1991 to 2002 at (a) 45°N and 26 km and (b) 45°N and 20 km. Equation 6.1 applied to observations, shown by black dots, or model results, shown by colored lines, to obtain decay timescales.

26 km. In the model simulations, background number density levels are reached as early as 1995 and by 1997 at the latest (assuming a threshold timescale value of 40 years). The fact that the large particle number density decays more rapidly than the integrated backscatter or the 1.02 μm extinction is not totally unexpected. Particles greater than 0.15 μm are strongly affected by sedimentation. Therefore, their number density should decay more rapidly than the 1.02 μm extinction which is sensitive to particles down to 0.1 μm . The 0.67 μm backscatter is sensitive to even smaller particles. There is a very strong scatter in the OPC-derived timescales at high altitudes. At 18 km, where there is much less scatter, the agreement with the AER and UPMC model simulations is satisfactory until 1995. After 1995, the large scatter precludes any meaningful comparisons.

beginning of 1998 in the ULAQ and UPMC simulations. Similar plots at 45°N are shown in Figure 6.36. The models tend to agree at 20 km but the AER model disagrees with the other two models at 26 km.

The overall evolution of the timescales derived from SAGE extinctions at the equator and at 45°N is similar to what is predicted by the models, with an increase from the minimum occurring at about 1992-1993. However, large inter-annual fluctuations are superimposed on the overall temporal increase in the SAGE-derived timescales. For example, the timescale at 26 km and 45°N varies between 1 and 10 years in 1993-1994. The variability is such at high altitudes that no clear trend can be established after 1993-1994. At low altitudes (i.e. 20 km), the SAGE-derived timescale broadly match the evolution of the model-calculated timescale until 1997.

Figure 6.37 displays the decay rates of number density of particles greater than 0.15 μm radius at the Wyoming balloon site (41°N) at 18, 22, and

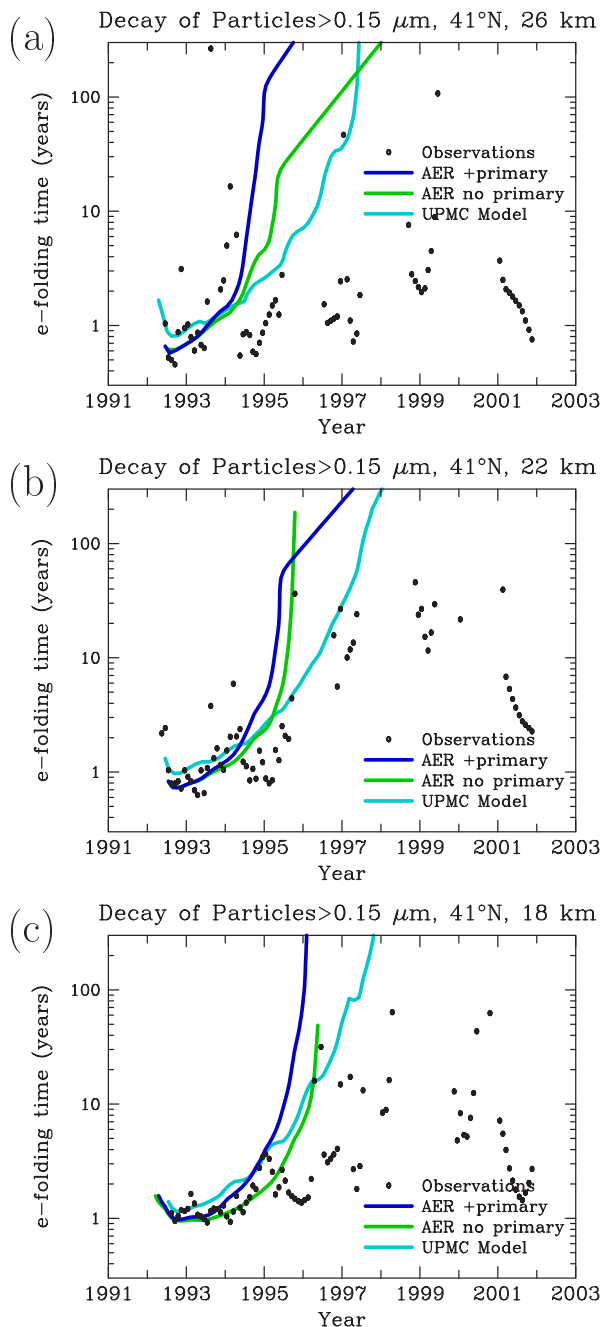


Figure 6.37: E-folding time (years) of number densities of particles with radius greater than $0.15 \mu\text{m}$ for 1991 to 2002 at (a) 26 km, (b) 22 km and (c) 18 km in Wyoming. Equation 6.1 applied to observations taken by balloon-borne OPC instruments [Deshler et al., 2003] at the University of Wyoming, shown by black dots, or model results, shown by colored lines, to obtain decay timescales.

models perform well under volcanic conditions. This confirms that the growth of aerosols to volcanic sizes and their subsequent removal is reproduced in a realistic way in the models. Model uncertainties are related to geographical and height resolution as well as particle size resolution. Further uncertainties stem from the implementation of gas phase and heterogeneous chemistry, microphysics, and transport. Transport is likely to be one of the largest sources of uncertainty.

6.8 Discussion

6.8.1 Uncertainties

Detailed comparisons of model calculations against a range of observations have been performed in this chapter. Overall, models appear to be able to reproduce most of the broad features of the distribution of stratospheric aerosols and their key precursors (OCS, SO_2). The results provide some validation of our knowledge of stratospheric sulfur sources and chemistry, and of our understanding of stratospheric aerosol processes and model parameterizations. However, the validation can only be viewed as partial for stratospheric aerosols. Indeed, the global properties of the aerosol layer are the result of complex interactions between microphysical, physicochemical and transport processes. It is very difficult to test our quantitative understanding of individual aerosol processes from comparisons against measurements of aerosol quantities that are determined by multiple processes. It is often not possible to identify unambiguously the specific cause of model discrepancies with observations or differences between model simulations.

The sensitivity studies in Section 6.6 have shown how sensitive the modeling of the background aerosol layer is to uncertainties in sulfur sources and sulfur transport to the stratosphere. Comparisons of the Mt. Pinatubo simulations with observations have shown that the

In this study, we employ both 2-D and 3-D models. 2-D models are limited by their lack of an adequate tropospheric representation. The non-zonal nature of the source and sink regions of OCS and SO₂ has an impact on the transport of these gases to the stratosphere [Pitari et al., 2002; Notholt et al., 2005]. The structure of the tropical tropopause region itself is highly non-zonal in temperature, dynamics, chemistry, and cloud processing. While we have attempted to impose reasonable boundary conditions at the tropical tropopause in the 2-D models, the physics of actual stratosphere-troposphere exchange is not properly parameterized. The limited resolution of 3-D models results in inadequacies in this regard as well. Small-scale transport features such as convective cells, outflow regions, and slowly rising air parcels traveling large distances close to the local tropopause are not properly resolved in global models although they are important to the entry of tropospheric gases into the stratosphere. The effects of cloud processing on trace gases and aerosols in the upper troposphere are not well understood. Heterogeneous conversion of SO₂ to H₂SO₄ to aerosol sulfate occurs on cloud droplets and is the most important sulfate source in the troposphere. However, the small fraction of sulfate left in the atmosphere rather than removed by rain has not been observationally estimated on a global basis.

Much of our understanding of precursor gas chemistry and aerosol microphysics is based on theory and laboratory studies rather than atmospheric observations. While there is evidence that, in terms of aerosol total mass, only sulfuric acid and water (and nitric acid in cold polar regions) are important aerosol components in the stratosphere, tropospheric aerosols also contain dust, soot, organics, ammonia, and sea salt. These components are present in upper tropospheric aerosol and in trace amounts also in lower stratospheric aerosol [Murphy et al., 1998]. They influence aerosol properties and size distributions in the lower stratosphere. Interactions between sulfate aerosols and cirrus ice particles may also be important in the TTL region. Size distributions are determined by a combination of nucleation rates, coagulation rates, condensation rates, local water vapor concentrations, transport, and sedimentation. Size distributions have not been observationally verified in most of the stratosphere. Observations in the lowermost stratosphere are limited to coarse size resolution of particles greater than 5 nm in radius. One surrogate for size resolution observations is the ratios of extinctions at different wavelengths. The models do not accurately match the vertical profile of extinction ratios. Model sensitivity to bin resolution or nucleation rate does not explain this deficiency.

Transport is a major cause of uncertainty in global modeling. This is evident in comparisons between models and comparisons between models and observations. The two 3-D models use circulation parameters calculated by a GCM, with aerosol microphysics implemented within the GCM for the MPI model, the UPMC and LASP model use self-consistent 2-D transport calculated interactively, and the AER model uses a 2-D climatology of transport derived from observations. Interannual variability is not present in most of these models. Intermodel transport variability is most clearly seen in the comparison of OCS profiles in Figure 6.10. While OCS profiles at the equator vary little between models, the same profiles at 65°N show considerable variability. The transport time from the tropical tropopause to the tropical lower stratosphere is short (months) and the local lifetime of OCS long (years), and therefore little intermodel variability is evident in OCS in the tropics, whereas longer transport times and greater variability are evident at 65°N. The shorter chemical lifetime of SO₂ and the variability of OH concentrations between models result in large intermodel variability in SO₂ even in the tropics. Transport variability between model-calculated aerosol extinctions is clearly

shown in the optical depth plotted on a linear scale (Figures 6.18-6.21). No model consistently reproduced the observed latitudinal variability of optical depth for a range of altitudes. We can consider this variability between models as a proxy for the uncertainty in model transport, since each model uses an independently-derived transport circulation. The true uncertainty is unknown and probably larger than intermodel differences, given that most models predict shorter mean ages of stratospheric air than observations indicate [Waugh and Hall, 2002].

In summary, a large fraction of the uncertainties in the description of the stratospheric aerosol layer may be traced back to the modeling of transport in the lower stratosphere and in the tropopause region. While 3-D models represent this transport much more realistically than 2-D models, even they have difficulties resolving mesoscale processes close to the tropical tropopause. This might be related to the single largest uncertainty highlighted in this chapter, the large scatter of the models under volcanically quiescent conditions in the tropical upper troposphere/lower stratosphere region (e.g., Figure 6.14). This uncertainty is further complicated by the observational difficulty of safely excluding subvisible clouds from the satellite data and by the limited temporal coverage of near-background conditions in the SAGE II record. Conversely, both 2-D and 3-D models in general do a commendable job in describing the aerosol layer in the free stratosphere, at tropical as well as extra-tropical latitudes.

6.8.2 Future Trends of Stratospheric Sulfate Aerosols

Future changes in the distribution and global amount of stratospheric sulfate aerosols may be produced by increasing or decreasing emissions of precursor gases (OCS, SO₂), changes in the emission pattern of these gases, and circulation changes associated with changing climate conditions. Changes in stratospheric aerosol would, in turn, modify stratospheric ozone concentrations through heterogeneous chemistry. Changes in both ozone and aerosols would alter patterns of stratospheric heating and in turn modify stratospheric temperatures and circulation patterns.

Tropospheric SO₂ originates from both natural (volcanoes, oceans, biomass burning) and anthropogenic (fossil fuel) sources, and its distribution shows a strong geographical dependence. Anthropogenic emissions represent approximately 65-75% of the total amount [Spiro et al., 1992; Houghton et al., 2001]. Deep convective uplift is the primary mixing mechanism for tropospheric SO₂ and is particularly efficient in the tropics and over mid-latitude continental regions during summertime. For these reasons, future trends of anthropogenic sulfur released in the tropics may affect the amount of upper tropospheric SO₂ available for upward transport in the stratospheric tropical pipe and perturb the lower stratospheric budget of sulfate aerosols. According to Notholt et al. [2005] the emissions from tropical and subtropical Asia including China and India may already have started to influence the amount of sulfur-containing gases reaching the stratosphere through the "stratospheric fountain" region over the Maritime Continent and Western Pacific. OCS in the tropical upper troposphere may be enhanced by increases in biomass burning [Notholt et al., 2003].

Pitari et al. [2002] have used the ULAQ climate-chemistry coupled model to study the sensitivity of stratospheric aerosols to changing anthropogenic emissions of SO₂. They have found a global stratospheric mass density increase in 2030 with respect to 2000 of 35% and 7%, for IPCC-SRES scenarios A2 and B1 [Nakicenovic et al., 2001], respectively. In the latter case, the amount of stratospheric aerosols is found to increase,

even though the global anthropogenic sulfur flux decreases from 69 Tg-S/yr in 2000 to 53.5 Tg-S/yr in 2030. The reason lies in regional changes of sulfur emissions. Pollution regulation in mid-latitude western industrialized countries is decreasing the amount of SO₂ released, while the opposite is taking place in developing countries, mostly located at tropical latitudes (India, China, Middle East, Africa, Central and South America). The study of Pitari et al. [2002] indicates that these increasing tropical emissions of anthropogenic sulfur may be responsible for significant changes in stratospheric sulfate aerosol mass and surface area density through efficient convective uplift of surface SO₂ to the tropical tropopause, where the middle atmosphere is fed through the stratospheric tropical pipe. Surface area and mass density are predicted to increase in the Northern Hemisphere 100-200 mb layer by about 0.5 μm²/cm³ and 50 ng/m³, respectively. This potential future increase of aerosol surface area density may be important for the lower stratospheric ozone photochemistry, via heterogeneous chemical reactions involving NO_x and chlorine and bromine oxides.

Besides changes in the emission patterns, changes in atmospheric circulation may also affect the future stratospheric aerosol layer. Little is known about this. Butchart and Scaife [2001] suggested that the mean meridional circulation might accelerate in a future greenhouse climate. Using a global climate model they predicted that, in response to the projected changes in greenhouse gas concentrations during the first half of the twenty-first century, the rate of mass exchange will increase by 3% per decade. This increase is due to more vigorous extratropical planetary waves emanating from the troposphere. All other things kept constant, if this acceleration actually happened, the resulting faster resupply of sulfur would make the role of particle sedimentation relatively less important, leading to higher total sulfur mixing ratio (falling in between the two lines in Figure 6.5) and consequently a larger optical depth of the stratospheric aerosol layer. Pitari et al. [2002] simulated the effect of changing climate in 2030 on the future sulfate layer. Changes in greenhouse gases produced a warmer troposphere, cooler stratosphere, and increased the residual mean vertical velocities in the tropical stratosphere. Compared with an atmosphere in which dynamics and temperature remained unchanged from 2000, the 2030 atmosphere produced a slightly smaller stratospheric burden of both SO₂ and aerosol. The expected increase in aerosol burden due to increased circulation strength may have been overwhelmed by other factors, such as changes in H₂O, OH, temperature, or convection.

Changes in aerosol may impact atmospheric temperature and circulation due to absorption or scattering of sunlight, or changes in cloud properties which could change atmospheric reflectivity. Indeed, changes in aerosol amount due to the Mt. Pinatubo eruption have been found to increase the tropical lower stratospheric temperatures [Labitzke, 1994] and to decrease the tropical ozone column [Schoeberl et al., 1993]. Changes in stratospheric circulation due to the Pinatubo eruption have been found in model experiments [Pitari and Mancini, 2002]. Long-term trends in aerosol could have similar but more modest effects.

6.8.3 Conclusions

The models are successful in reproducing observed concentrations of OCS in the tropics. Because OCS is the primary sulfur source above 25 km, and its chemical loss is primarily tropical, this provides confidence in the simulated total sulfur mass in the middle stratosphere. We have less confidence in model predictions of sulfur in the lower stratosphere. SO₂ measurements for the tropical lower stratosphere under nonvolcanic

conditions are not yet possible from satellite instruments. Such measurements of SO₂ in the tropics between 12 and 30 km over several seasons will be necessary to quantify the importance of transported tropospheric SO₂ to the stratospheric sulfur budget. Uncertainty also remains regarding the importance of primary aerosol from the troposphere.

Models reproduce observed extinction from satellite instruments with mixed success. Observed extinctions under nonvolcanic conditions in the tropics above 25 km and at midlatitudes above 20 km are within the SAGE II error bars at 0.525 and 1.02 μm for most models, but only the UPMC model comes close to reproducing the 5.26 μm extinctions measured by the HALOE instrument. Extinctions are not reproduced well in the tropical lower stratosphere. It appears that the primary aerosol distribution imposed at the tropopause may need to be refined to match extinction measurements at the SAGE II wavelengths under background conditions. The FCAS measurements used to obtain the tropopause aerosol distribution (S.-H. Lee, private communication) were an average over observations taken between 1996 and 1999 and therefore likely contain some residual effects of the Pinatubo eruption, whereas the model comparisons employ a composite of SAGE II observations over the 2000-2001 period, when volcanic influence is absent. Further observations of aerosol size and composition in the tropics up to 23 km are needed to determine the cause of the model discrepancy.

Model comparisons with lidar column observations at three sites have verified that models correctly reproduce the rise and decay of integrated aerosol backscatter and mass under volcanic conditions. Comparisons with SAGE II data during the Pinatubo period also show good agreement with models, though not consistently at all altitudes. We have shown that volcanic aerosol decays with a non-constant e-folding time which lengthens as aerosol effective radius drops. Because the models used here lack significant interannual variability in transport, model decay rates can be analyzed more easily than observations. We find e-folding rates of less than one year before mid 1994, reaching values of 40 years between 1997 and 1999. This methodology allows us to determine when volcanic aerosols have decayed to background levels with no a priori information on background levels. Observational data exhibit too much scatter to gain useful information from this method beyond 1995. A more comprehensive treatment of this issue is given in Chapter 5.

Future modeling studies should strive to include a more complete representation of upper tropospheric aerosols and relevant gas phase and heterogeneous chemistry in this region. The lower stratospheric aerosol layer is shown in our sensitivity studies to depend on input from the tropical upper troposphere. Aerosols in the upper troposphere are not purely of H₂SO₄-H₂O composition but include organics (often more than 50% by mass), mineral dust, soot, and other compounds. Organic matter in aerosols is largely absent 1-2 km above the tropopause [Murphy et al., 1998]. Vertical profiles of extinction observed by SAGE II fall sharply from high upper tropospheric values to much lower stratospheric values in only a few kilometers. This sharp gradient cannot be reproduced by any of the present models, but may be explained by a volatile component such as organics in upper tropospheric aerosols. An adequate 3-D representation of transport processes and cloud processing will be required to match aerosol observations in the troposphere-stratosphere transition region. Meteoritic material may be important to the morphology of stratospheric aerosols in polar air descending from the mesosphere, and thus should be included in future modeling studies. Reproducing the seasonal variability of aerosols remains a challenge for current models. New observations of SO₂ in the upper

troposphere and lower stratosphere, H_2SO_4 and SO_2 in the middle and upper stratosphere, and aerosol size distributions throughout the stratosphere will help to refine our understanding of stratospheric aerosols.

References

- Ackerman, M., C. Brogniez, B. S. Diallo, G. Fiocco, P. Gobbi, M. Herman, H. Jäger, J. Lenoble, C. Lippens, G. Mégie, J. Pelon, R. Reiter and R. Santer, European validation of SAGE II aerosol profiles, *J. Geophys. Res.*, *94*, 8399-8411, 1989.
- Adams, P. J. and J. H. Seinfeld, Predicting global aerosol size distributions in general circulation models, *J. Geophys. Res.-Atmos.*, *107* (D19), art. no.-4370, 2002.
- Adriani, A., T. Deshler, G. Di Donfrancesco, G. P. Gobbi, Polar stratospheric clouds and volcanic aerosol during spring 1992 over McMurdo Station, Antarctica: Lidar and particle counter comparisons, *J. Geophys. Res.*, *100*, 25877-25897, 1995.
- Adriani A., P. Massoli, G. Di Donfrancesco, F. Cairo, M. L. Moriconi, M. Snels, Climatology of polar stratospheric clouds based on lidar observations from 1993 to 2001 over McMurdo Station, Antarctica, *J. Geophys. Res.*, *109*, D24211, doi:10.1029/2004JD004800, 2004.
- Anderson, B. E., W. R. Cofer, J. W. Barrick, D. R. Bagwell and C. H. Hudgins, Airborne observations of aircraft aerosol emissions II: Factors controlling volatile particle production, *Geophys. Res. Lett.*, *25*, 1693-1696, 1998.
- Anderson, T. R., S. A. Spall, A. Yool, P. Cipollini, P. G. Challenor and M. J. R. Fasham, Global fields of sea surface dimethylsulfide predicted from chlorophyll, nutrients and light, *J. Marine Syst.*, *30*, 1-20, 2001.
- Andreae, M. O., and H. Raemdonck, Dimethyl sulfide in the surface ocean and the marine atmosphere: a global view, *Science*, *221*, 744-747, 1983.
- Andreae, M. O. and T. W. Andreae, The cycle of biogenic sulfur compounds over the Amazon basin 1. Dry season, *J. Geophys. Res.*, *93* (D2), 1487-1497, 1988.
- Andreae, M. O., H. Berresheim, H. Bingemer, D. J. Jacob, B. L. Lewis, S.-M. Li and R. W. Talbot, The atmospheric sulfur cycle over the Amazon basin 2. wet season, *J. Geophys. Res.*, *95* (D10), 16813-16824, 1990.
- Andreae, T. W., G. A. Cutter, N. Hussain, J. Radford-Knoery and M. O. Andreae, Hydrogen sulfide and radon in and over the western North Atlantic Ocean, *J. Geophys. Res.*, *96*, 18753-18760, 1991.
- Andreae, M. O., W. Elbert, R. Gabriel, D. W. Johnson, S. Osborne and R. Wood, Soluble ion chemistry of the atmospheric aerosol and SO₂ concentrations over the eastern North Atlantic during ACE-2, *Tellus*, *52B*, 1066-1087, 2000.
- Andreae, M. O., R. J. Ferek, F. Bermond, K. P. Byrd, R. T. Engstrom, S. Hardin, P. D. Houmere, F. LeMarrec, H. Raemdonck and R. B. Chatfield, Dimethyl sulfide in the marine atmosphere, *J. Geophys. Res.*, *90* (D7), 12891-12900, 1985.
- Andreae, T. W., M. O. Andreae, H. G. Bingemer and C. Leck, Measurements of dimethyl sulfide and H₂S over the western North Atlantic and the tropical Atlantic, *J. Geophys. Res.*, *98* (D12), 23389-23396, 1993.
- Angell, J. K., Comparisons of stratospheric warming following Agung, El Chichón and Pinatubo volcanic eruptions, *Geophys. Res. Lett.*, *20*, 715-718, 1993.
- Angell, J. K., J. Korshover and W. G. Planet, Ground-based and satellite evidence for a pronounced total-ozone minimum in early 1983 and responsible atmospheric layers, *Mon. Weather Rev.*, *113*, 641-646, 1985.
- Antuña, J. C., A. Robock, G. Stenchikov, J. Zhou, C. David, J. Barnes and L. Thomason, Spatial and temporal variability of the stratospheric aerosol cloud produced by the 1991 Mount Pinatubo eruption, *J. Geophys. Res.*, *108*, 4624-4635, doi:10.1029/2003JD003722, 2003.
- Antuña, J. C., A. Robock, G. L. Stenchikov, L. W. Thomason and J. E. Barnes, Lidar validation of SAGE II aerosol measurements after the 1991 Mount Pinatubo eruption. *J. Geophys. Res.*, *107* (D14), 4194, doi:10.1029/2001JD001441, 2002.

- Arijs, E., D. Nevejans, D. Fussen, P. Frederick, E. Van Ransbeek, F. W. Taylor, S. B. Calcutt, S. T. Werrett, C. L. Hepplewhite and T. M. Pritchard, The ORA occultation radiometer on EURECA; Instrument description and preliminary results, *Adv. Spa. Res.*, *16*, 833-836, 1995.
- Arnold, F., V. Bürger, B. Droste-Franke, F. Grimm, A. Krieger, J. Schneider and T. Stimp, Acetone in the upper troposphere and lower stratosphere: Impact on trace gases and aerosols, *Geophys. Res. Lett.*, *24*, 3017-3020, 1997.
- Arnold, F., R. Fabian and W. Joos, Measurements of the height variation of sulfuric-acid vapor concentrations in the stratosphere, *Geophys. Res. Lett.*, *8*, 293-296, 1981.
- Arnold, F., J. Schneider, K. Gollinger, H. Schlager, P. Schulte, D. E. Hagen, P. D. Whitefield and P. van Velthoven, Observations of upper tropospheric sulfur dioxide- and acetone-pollution: Potential implications for hydroxyl radical and aerosol formation, *Geophys. Res. Lett.*, *24*, 57-60, 1997.
- Arsene, C., I. Barnes, K. H. Becker and R. Mocanu, FT-IR product study on the photo-oxidation of dimethyl sulphide in the presence of NO_x - Temperature dependence, *Atmos. Env.*, *35*, 3769-3780, 2001.
- Atkinson, R., D. L. Baulch, R. A. Cox, J. N. Crowley, R. F. Hampson, R. G. Hynes, M. E. Jenkin, M. J. Rossi and J. Troe, Evaluated kinetic and photochemical data for atmospheric chemistry: Volume I – gas-phase reactions of O_x, HO_x, NO_x and SO_x species, *Atmos. Chem. Phys.*, *4*, 1461-1738, 2004.
- Aumont, O., S. Belviso and P. Monfray, Dimethylsulfoniopropionate (DMSP) and dimethylsulfide (DMS) sea surface distributions simulated from a global three-dimensional ocean carbon cycle model, *J. Geophys. Res.*, *107*, 10.1027/1999JC000111, 2002.
- Aydin, M., W. J. De Bruyn and E. S. Saltzman, Preindustrial atmospheric carbonyl sulfide (OCS) from an Antarctic ice core, *Geophys. Res. Lett.*, *29*, 10.1029/2002GL014796, 2002.
- Ayers, G. P., S. T. Bentley, J. P. Ivey and B. W. Forgan, Dimethylsulfide in marine air at Cape Grim, 41°S, *J. Geophys. Res.*, *100*, 21013-21021, 1995.
- Bandy, A. R., D. C. Thornton, B. W. Blomquist, S. Chen, T. P. Wade, J. C. Ianni, G. M. Mitchell and W. Nadler, Chemistry of dimethyl sulfide in the equatorial Pacific atmosphere, *Geophys. Res. Lett.*, *23*, 741-744, 1996.
- Bandy, A. R., D. C. Thornton and J. E. Johnson, Carbon disulfide measurements in the atmosphere of the Western North Atlantic and the Northwestern South Atlantic Oceans, *J. Geophys. Res.*, *98*, 23449-23457, 1993.
- Bandy, A. R., D. C. Thornton, D. L. Scott, M. Lalevic, E. E. Lewin and A. R. Driedger III, A time series for carbonyl sulfide in the northern hemisphere, *J. Atmos. Chem.*, *14*, 527-534, 1992.
- Banic, C. M., W. R. Leitch, G. A. Isaac, L. I. Kleinman, S. R. Springston and J. I. MacPherson, Transport of ozone and sulfur to the North Atlantic atmosphere during the North Atlantic Regional Experiment, *J. Geophys. Res.*, *101* (D22), 29091-29104, 1996.
- Barnes, I., K. H. Becker and I. Patroescu, The tropospheric oxidation of dimethyl sulfide: A new source of carbonyl sulfide, *Geophys. Res. Lett.*, *21*, 2389-2392, 1994.
- Barnes, I., K. H. Becker and I. Patroescu, FTIR product study of the OH initiated oxidation of dimethyl sulphide: Observations of carbonyl sulphide and dimethyl sulphoxide, *Atmos. Env.*, *30*, 1805-1814, 1996.
- Barnes, J. E., and D. J. Hofmann, Lidar measurements of stratospheric aerosol over Mauna Loa, *Geophys. Res. Lett.*, *24*, 1923-1926, 1997.
- Barnes, J. E., and D. J. Hofmann, Variability in the stratospheric background aerosol over Mauna Loa observatory, *Geophys. Res. Lett.*, *28*, 2895-2898, 2001.
- Bates, T. S., J. D. Cline, R. H. Gammons and S. R. Kelly-Hansen, Regional and seasonal variations in the flux of oceanic dimethylsulfide to the atmosphere, *J. Geophys. Res.*, *92*, 2930-2938, 1987.

- Bates, T. S., B. K. Lamb, A. Guenther, J. Dignon and R. E. Stoiber, Sulfur emissions to the atmosphere from natural sources, *J. Atmos. Chem.*, *14*, 315-337, 1992.
- Bauman, J. J., Stratospheric aerosol climatology derived from satellite solar occultation and infrared emission measurements, Ph.D. dissertation, 237 pp, State Univ. of New York, Stony Brook, 2000.
- Bauman, J. J., P. B. Russell, M. A. Geller and P. Hamill, A stratospheric aerosol climatology from SAGE II and CLAES measurements: 1. Methodology, *J. Geophys. Res.*, *108*, 4832, doi:10.1029/2002JD002882, 2003a.
- Bauman, J. J., P. B. Russell, M. A. Geller and P. Hamill, A stratospheric aerosol climatology from SAGE II and CLAES measurements: 2. Results and comparisons, 1984-1999, *J. Geophys. Res.*, *108* (D13), 4383, doi:10.1029/2002JD002993, 2003b.
- Baumgardner, D., J. E. Dye, B. Gandrud, K. Barr, K. Kelly, K. R. Chan, Refractive indices of aerosols in the upper troposphere and lower stratosphere, *Geophys. Res. Lett.*, *23*, 749-752, 1996.
- Baumgardner, D., J. E. Dye, B. Gandrud, R. G. Knollenberg, The multiangle aerosol spectrometer probe: A new instrument for airborne particle research, *AMS 9th Symp. Met. Obs. and Instr.*, March 27-31, 1995, Charlotte, N.C., 1995.
- Baumgardner, D., J. E. Dye, R. G. Knollenberg and B. W. Gandrud, Interpretation of measurements made by the FSSP-300X during the Airborne Arctic Stratospheric Expedition, *J. Geophys. Res.*, *97*, 8035-8046, 1992.
- Bekki, S., Oxidation of volcanic SO₂: A sink for stratospheric OH and H₂O, *Geophys. Res. Lett.*, *22*, 913-916, 1995.
- Bekki, S., and J. A. Pyle, 2-D assessment of the impact of aircraft sulphur emissions on the stratospheric sulphate aerosol layer, *J. Geophys. Res.*, *97*, 15839-15847, 1992.
- Bekki, S., and J. A. Pyle, Potential impact of combined NO_x and SO_x emissions from future high speed civil transport aircraft on stratospheric aerosol and ozone, *Geophys. Res. Lett.*, *20*, 723-726, 1993.
- Benkovitz, C. M., M. T. Scholtz, J. Pacyna, L. Tarrasón, J. Dignon, E. C. Voldner, P. A. Spiro, J. A. Logan and T. E. Graedel, Global gridded inventories of anthropogenic emissions of sulfur and nitrogen, *J. Geophys. Res.*, *101*, 29239-29253, 1996.
- Berresheim, H., M. O. Andreae, R. L. Iverson and S. M. Li, Seasonal variations of dimethylsulfide emissions and atmospheric sulfur and nitrogen species over the western north Atlantic Ocean, *Tellus*, *43B*, 353-372, 1991.
- Berresheim, H., P. H. Wine and D. D. Davis, Sulfur in the atmosphere, in: *Composition, Chemistry, and Climate of the Atmosphere*, H. B. Singh (Ed.), vol., pp. 251-307, Van Nostrand Reinhold, New York, 1995.
- Bevilacqua, R. M., Introduction to the special section: Polar Ozone and Aerosol Measurement (POAM II), *J. Geophys. Res.*, *102*, 23591-23592, 1997.
- Bevilacqua, R. M., M. D. Fromm, J. M. Alfred, J. S. Hornstein, G. E. Nedoluha, K. W. Hopfel, J. D. Lumpe, C. E. Randall and E. P. Shettle, Observations and analysis of PSCs detected by POAM III during the 1999/2000 northern hemisphere winter, *J. Geophys. Res.*, *107* (D20), 8281, doi:10.1029/2001JD000477, 2002.
- Beyerle, G., R. Neuber, O. Schrems, F. Wittrock and B. Knudsen, Multiwavelength lidar measurements of stratospheric aerosols above Spitsbergen during winter 1992/1993, *Geophys. Res. Lett.*, *21*, 57-60, 1994.
- Biele, J., R. Neuber, J. Warming, I. Beninga, P. von der Gathen, J. Notholt, K. Stebel and O. Schrems, The evolution of stratospheric clouds over Spitsbergen, *J. Aerosol. Sci.*, *28*, Suppl. 1, 423-424, 1997.
- Biele, J., A. Tsias, B. P. Luo, K. S. Carslaw, R. Neuber, G. Beyerle and T. Peter, Nonequilibrium coexistence of solid and liquid particles in Arctic stratospheric clouds, *J. Geophys. Res.*, *106*, D19, 22992-23007, 2001.

- Bigg, E. K., A mechanism for the formation of new particles in the atmosphere, *Atmos. Res.*, *43*, 129-137, 1997.
- Bingemer, H. G., M. O. Andreae, T. W. Andreae, P. Artaxo, G. Helas, D. J. Jacob, N. Mihalopoulos and B. C. Nguyen, Sulfur gases and aerosols in and above the Equatorial African rain forest, *J. Geophys. Res.*, *97* (D6), 6207-6217, 1992.
- Bingemer, H. G., S. Bürgermeister, R. L. Zimmerman and H.-W. Georgii, Atmospheric OCS: Evidence for a contribution of anthropogenic sources?, *J. Geophys. Res.*, *95*, 20617-20622, 1990.
- Bingen, C., D. Fussen and F. Vanhellemont, A global climatology of stratospheric aerosol size distribution parameters derived from SAGE II data over the period 1984-2000: 1. Methodology and climatological observations, *J. Geophys. Res.*, *109*, D06201, doi:10.1029/2003JD003518, 2004a.
- Bingen, C., D. Fussen and F. Vanhellemont, A global climatology of stratospheric aerosol size distribution parameters derived from SAGE II data over the period 1984-2000: 2. Reference data, *J. Geophys. Res.*, *109*, D06202, doi:10.1029/2003JD003511, 2004b.
- Bingen, C., F. Vanhellemont and D. Fussen, A new regularized inversion method for the retrieval of stratospheric aerosol size distribution applied to 16 years SAGE II data (1984-2000): method, results and validation, *Ann. Geophys.*, *21* (3), 797-804, 2003.
- Blake, N. J., D. G. Streets, J.-H. Woo, I. J. Simpson, J. Green, S. Meinardi, K. Kita, E. Atlas, H. E. Fuelberg, G. Sachse, M. A. Avery, S. Vay, R. W. Talbot, J. E. Dibb, A. R. Bandy, D. C. Thornton, F. S. Rowland and D. R. Blake, Carbonyl sulfide and carbon disulfide : Large scale distributions over the western Pacific from Asia during TRACE-P, *J. Geophys. Res.*, *109*, D15S05, doi: 10.1029/2003JD004259, 2004.
- Bland, P. A., T. B. Smith, A. J. T. Jull, F. J. Berry, A. W. R. Bevan, S. Cloudt, C. T. Pillinger, The flux of meteorites to the earth over the last 50000 years, *Mon. Not. R. Astron. Soc.*, *283*, 551-565, 1996.
- Blomquist, B. W., A. R. Bandy and D. C. Thornton, Sulfur gas measurements in the eastern North Atlantic Ocean during the Atlantic Stratocumulus Transition Experiment / Marine Gas Exchange Experiment, *J. Geophys. Res.*, *101*, 4377-4392, 1996.
- Bluth, G. J. S., S. D. Doiron, C. C. Schnetzler, A. J. Krueger and L. S. Walter, Global tracking of the SO₂ clouds from the June 1991 Mount Pinatubo eruptions, *Geophys. Res. Lett.*, *19*, 151-154, 1992.
- Bluth, G. J. S., C. C. Schnetzler, A. J. Krueger and L. S. Walter, The contribution of explosive volcanism to global atmospheric sulphur dioxide concentrations, *Nature*, *366*, 327-329, 1993.
- Bodeker, G. E., J. C. Scott, K. Kreher and R. L. McKenzie, Global ozone trends in potential vorticity coordinates using TOMS and GOME intercompared against the Dobson network: 1978-1998, *J. Geophys. Res.*, *106* (D19), 23029-23042, 2001.
- Borrmann, S., J. E. Dye, D., Baumgardner, J. C. Wilson, H. H. Jonsson, C. A. Brock, M. Loewenstein, J. R. Podolske, G. V. Ferry and K. S. Barr, In-situ measurements of changes in stratospheric aerosol and the N₂O-aerosol relationship inside and outside of the polar vortex, *Geophys. Res. Lett.*, *20* (22), 2559-2562, 1993.
- Borrmann S., A. Thomas, V. Rudakov, V. Yushkov, B. Lepuchov, T. Deshler, N. Vinnichenko, V. Khattatov, L. Stefanutti, Stratospheric aerosol measurements in the Arctic winter of 1996/1997 with the M-55 Geophysika high-altitude research aircraft, *Tellus B*, *52* (4), 1088-1103, 2000.
- Brasseur, G., and S. Solomon, *Aeronomy of the Middle Atmosphere*, 452 pp., D. Reidel, Dordrecht, Holland, 1984.
- Brasseur, G. P., J. J. Orlando and G. S. Tyndall (Eds.), *Atmospheric Chemistry and Global Change*, pp., Oxford University Press, New York, 1999.

- Bregman, B., P.-H. Wang and J. Lelieveld, Chemical ozone loss in the tropopause region on subvisible clouds calculated with a chemistry-transport model, *J. Geophys. Res.*, 107 (D3), 4032, doi:10.1029/2001JD000761, 2002.
- Brewer, A. M., Evidence for a world circulation provided by the measurements of helium and water vapor, *Quart. J. Roy. Meteor. Soc.*, 75, 351-363, 1949.
- Brock, C. A., P. Hamill, J. C. Wilson, H. H. Jonsson and K. R. Chan, Particle formation in the upper tropical troposphere: A source of nuclei for the stratospheric aerosol, *Science* 270, 1650-1653, 1995.
- Brock, C. A., B. Kaercher, A. Petzold, R. Busen and M. Fiebig, Ultrafine particle size distributions measured in aircraft exhaust plumes, *J. Geophys. Res.*, 105, 26555-26567, 2000.
- Brogniez, C., L. Cazier, R. Ramanahérisoa, J. Lenoble, Climatology of stratospheric aerosols from SAGE II and POAM II satellite measurements: Evaluation of their impact on radiative forcing, *Proc. of the ALPS99 International Conference, Meribel, France, 18-22 January 1999*, WK1, 22, 1999.
- Brogniez, C., J. Lenoble, R. Ramanahérisoa, K. H. Fricke, E. P. Shettle, K. W. Hoppel, R. M. Bevilacqua, J. Hornstein, J. Lumpe, M. D. Fromm and S. S. Krigman, Second European Stratospheric Arctic and Midlatitude Experiment campaign: Correlative measurements of aerosol in the northern polar atmosphere, *J. Geophys. Res.*, 102 (D1), 1489-1494, 1997.
- Burkholder, J. B., and S. McKeen, UV absorption cross sections for SO₃, *Geophys. Res. Lett.*, 24, 3201-3204, 1997.
- Burkholder, J. B., M. Mills and S. McKeen, Upper limit for the UV absorption cross sections of H₂SO₄, *Geophys. Res. Lett.*, 27 (16), 2493-2496, 2000.
- Burton, S. P., L. W. Thomason, Y. Sasano and S. Hayashida, Comparison of Aerosol Extinction Measurements by ILAS and SAGE II, *Geophys. Res. Lett.*, 26, 1719-1722, 1999.
- Butchart, N., and A. A. Scaife, Removal of chlorofluorocarbons by increased mass exchange between the stratosphere and troposphere in a changing climate, *Nature*, 410, 799-802, 2001.
- Carmichael, G., D. Streets, G. Calori, M. Amann, M. Z. Jacobson, J. Hansen and H. Ueda, Changing trends in sulfur emissions in Asia: Implications for acid deposition, air pollution, and climate, *Env. Sci. Technol.*, 36, (22), 2002.
- Carn, S. A., A. J. Krueger, G. J. S. Bluth, S. J. Schaefer, N. A. Krotkov, I. M. Watson and S. Datta, Volcanic eruption detection by the Total Ozone Mapping Spectrometer (TOMS) instruments: a 22-year record of sulfur dioxide and ash emissions. In: *Volcanic Degassing* (eds. C. Oppenheimer, D. M. Pyle and J. Barclay), Geological Society, London, Special Publications, 213, 177-202, 2003.
- Carroll, M. A., Measurements of OCS and CS₂ in the free troposphere, *J. Geophys. Res.*, 90, 10483-10486, 1985.
- Carslaw, K. S., B. P. Luo, S. L. Clegg, T. Peter, P. Brimblecombe, P. J. Crutzen, Stratospheric aerosol growth and HNO₃ gas-phase depletion from coupled HNO₃ and water-uptake by liquid particles, *Geophys. Res. Lett.*, 21, 2479-2482, 1994.
- Carslaw, K. S., B. Luo and Th. Peter, An analytic expression for the composition of aqueous HNO₃-H₂SO₄ stratospheric aerosol including gas phase removal of HNO₃, *Geophys. Res. Lett.*, 22, 1877-1880, 1995.
- Carslaw, K. S., T. Peter and S. L. Clegg, Modeling the composition of liquid stratospheric aerosols, *Rev. Geophys.*, 35, 125-154, 1997.
- Castleman, J. A. W., H. R. Munkelwitz and B. Manowitz, Isotopic studies of the sulfur component of the stratospheric aerosol layer, *Tellus*, 26, 222-234, 1974.
- Chagnon, C. W., and C. E. Junge, The vertical distribution of sub-micron particles in the stratosphere, *J. Meteor.*, 18, 746-752, 1961.

- Chatfield, R. B., and P. J. Crutzen, Sulfur dioxide in the remote oceanic air: Cloud transport of reactive precursors, *J. Geophys. Res.*, *89*, 7111-7132, 1984.
- Chazette, P., C. David, J. Lefrère, S. Godin, J. Pelon and G. Mégie, Comparative lidar study of the optical, geometrical, and dynamical properties of stratospheric post-volcanic aerosols, following the eruptions of El Chichón and Mount-Pinatubo, *J. Geophys. Res.*, *100*, 23195-23207, 1995.
- Chin, M., and D. D. Davis, Global sources and sinks of OCS and CS₂ and their distributions, *Glob. Biogeochem. Cycles*, *7*, 321-337, 1993.
- Chin, M., and D. D. Davis, A reanalysis of carbonyl sulfide as a source of stratospheric background sulfur aerosol, *J. Geophys. Res.*, *100*, 8993-9005, 1995.
- Chu, W., and M. P. McCormick, Inversion of stratospheric aerosol and gaseous constituents from spacecraft solar extinction data in the 0.38-1.0 micron wavelength region, *Appl. Opt.*, *18*, 1404-1414, 1979.
- Chu, W. P., M. P. McCormick, J. Lenoble, C. Brogniez and P. Pruvost, SAGE II inversion algorithm, *J. Geophys. Res.*, *94*, 8339-8351, 1989.
- Clarke, A. D., and V. N. Kapustin, A Pacific aerosol survey. Part I: A decade of data on particle production, transport, evolution, and mixing in the troposphere, *J. Atmos. Sci.* *59*, 363-382, 2002.
- Clarke, A. D., V. N. Kapustin, F. L. Eisele, R. J. Weber and P. H. McMurry, Particle production near marine clouds: Sulfuric acid and predictions from classical binary nucleation, *Geophys. Res. Lett.*, *26*, 2425-2428, 1999.
- Clement, C. F., and I. J. Ford, Gas-to-particle conversion in the atmosphere: II. Analytical models of nucleation bursts, *Atmos. Env.*, *33*, 489-499, 1999.
- Clemesha, B. R. and D. M. Simonich, Stratospheric dust measurements 1970-1977, *J. Geophys. Res.*, *83*, 2403-2408, 1978.
- Colberg, C. A., B. P. Luo, H. Wernli, T. Koop and T. Peter, A novel model to predict the physical state of atmospheric H₂SO₄/NH₃/H₂O aerosol particles, *Atmos. Chem. Phys.*, *3*, 909-924, 2003.
- Cooper, D. J., and E. S. Saltzman, Measurements of atmospheric dimethylsulfide, hydrogen sulfide, and carbon disulfide during GTE/CITE 3, *J. Geophys. Res.*, *98* (D12), 23397-23409, 1993.
- Cressie, N. A. C, *Statistics for Spatial Data*, John Wiley & Sons, New York, 1993.
- Crutzen, P. J., The influence of nitrogen oxide on the atmospheric ozone content, *Q. J. R. Meteorol. Soc.*, *96*, 320-327, 1970.
- Crutzen, P. J., The possible importance of CSO for the sulfate layer of the stratosphere, *Geophys. Res. Lett.*, *3*, 73-76, 1976.
- Cubukcu, N., T. N. Krishnamurti and R. C. Dougherty, Chemical composition in convective and nonconvective regions during PEM-Tropics B, *J. Geophys. Res.*, *108* (D2), 8231, doi:10.1029/2001JD000346, 2003.
- Curtius, J., B. Sierau, F. Arnold, M. de Rreus, J. Ström, H. A. Scheren and J. Lelieveld, Measurement of aerosol sulfuric acid 2. Pronounced layering in the free troposphere during the second Aerosol Characterizing Experiment (ACE-2), *J. Geophys. Res.*, *106*, 31975-31990, 2001.
- Cziczo, D. J., P. J. DeMott, C. Brock, P. K. Hudson, B. Jesse, S. M. Kreidenweis, A. J. Prenni, J. Schreiner, D. S. Thomson and D. M. Murphy, A method for single particle mass spectrometry of ice nuclei, *Aerosol Sci. Technol.*, *37* (5), 460-470, 2003.
- Cziczo, D. J., D. S. Thomson and D. M. Murphy, Ablation, flux and atmospheric implications of meteors inferred from stratospheric aerosol, *Science*, *291*, 1772-1775, 2001.
- Danilin, M. J., D. W. Fahey, U. Schumann, M. J. Prather, J. E. Penner, M. K. W. Ko, D. K. Weisenstein, C. H. Jackman, G. Pitari, I. Kohler, R. Sausen, C. J. Weaver, A. R. Douglass, P. S. Connell, D. E. Kinnison, F. J. Dentener, E. L. Fleming, T. K. Berntsen, I. S. A. Isak-

- sen, J. M. Haywood, B. Kaercher, Aviation fuel tracer simulations: Model intercomparison and implications, *Geophys. Res. Lett.*, *25*, (21), 3947-3950, 1998.
- Danilin, M. Y., R.-L. Shia, M. K. W. Ko, D. K. Weisenstein, N. D. Sze, J. J. Lamb, T. W. Smith, P. D. Lohn and M. J. Prather, Global stratospheric effects of the alumina emissions by solid-fueled rocket motors, *J. Geophys. Res.*, *106*, 12727-12738, 2001.
- David C., S. Bekki, S. Godin, G. Megie and M. P. Chipperfield, Polar Stratospheric Cloud climatology over Dumont d'Urville between 1989 and 1993 and the influence of volcanic aerosols on their formation. *J. Geophys. Res.*, *103*, 22163-22180, 1998.
- Davis, D. D., G. Chen, A. Bandy, D. Thornton, F. Eisele, L. Mauldin, D. Tanner, D. Lenschow, H. Fuelberg, B. Hubert, J. Heath, A. Clarke and D. Blake, Dimethyl sulfide oxidation in the equatorial Pacific: Comparison of model simulations with field observations for DMS, SO₂, H₂SO₄(g), MSA(g), MS, and NSS, *J. Geophys. Res.*, *104* (D5), 5765-5784, 1999.
- de Reus, M., J. Ström, J. Curtius, L. Pirjola, E. Vignati, F. Arnold, H. C. Hansson, M. Kulmala, J. Lelieveld and F. Raes, Aerosol production and growth in the upper free troposphere, *J. Geophys. Res.*, *105*, 24751-24762, 2000.
- de Reus, M., J. Ström, P. Hoor, J. Lelieveld and C. Schiller, Particle production in the lowermost stratosphere by convective lifting of the tropopause, *J. Geophys. Res.*, *104*, 23935-23949, 1999.
- de Reus, M., J. Ström, M. Kulmala, L. Pirjola, J. Lelieveld, C. Schiller and M. Zöger, Airborne measurements in the tropopause region and the dependence of new particle formation on preexisting particle number concentration, *J. Geophys. Res.*, *103*, 31255-31263, 1998.
- DeFoor, T., and E. Robinson, Stratospheric lidar profiles from Mauna Loa Observatory during winter 1985-1986, *Geophys. Res. Lett.*, *14*, 618-621, 1987.
- DeFoor, J. E., E. Robinson and S. Ryan, Early lidar measurements of the June 1991 Pinatubo eruption plume at Manua Loa Observatory, Hawaii, *Geophys. Res. Lett.*, *19*, 187-190, 1992
- Delmas, R. and J. Servant, Atmospheric balance of sulphur above an equatorial forest, *Tellus*, *35B*, 110-120, 1983.
- DeMore, W. B., S. P. Sander, D. M. Golden, R. F. Hampson, M. J. Kurylo, C. J. Howard, A. R. Ravishankara, C. E. Kolb and M. J. Molina, *Chemical kinetics and photochemical data for use in stratospheric modeling*, Evaluation number 12, JPL Publication 97-4, Jet Propulsion Laboratory, NASA, 1997.
- DeMott, P. J., D. J. Cziczo, A. J. Prenni, D. M. Murphy, S. M. Kreidenweis, D. S. Thomson, R. Borys and D. C. Rogers, Measurements of the concentration and composition of nuclei for cirrus formation, *Proc. Natl. Acad. Sci.*, *100*, 14655-14660, 2003b.
- DeMott, P. J., K. Sassen, M. R. Poellot, D. Baumgardner, D. C. Rogers, S. D. Brooks, A. J. Prenni and S. M. Kreidenweis, African dust aerosols as atmospheric ice nuclei, *Geophys. Res. Lett.*, *30* (14), art. no.-1732, doi: 10.1029/2003GL017410, 2003a.
- Deshler, T., M. E. Hervig, D. J. Hofmann, J. M. Rosen and J. B. Liley, Thirty years of in situ stratospheric aerosol size distribution measurements from Laramie, Wyoming (41°N) using balloon-borne instruments, *J. Geophys. Res.*, *108*, 4167, doi:10.1029/2002JD002514, 2003.
- Deshler, T., B. J. Johnson and W. R. Rozier, Balloonborne measurements of Pinatubo aerosol during 1991 and 1992 at 41°N, vertical profiles, size distribution and volatility, *Geophys. Res. Lett.*, *20*, 1435-1438, 1993.
- Deshler, T., B. J. Johnson, D. J. Hofmann and B. Nardi, Correlations between ozone loss and volcanic aerosol at latitudes below 14 km over McMurdo Station, Antarctica, *Geophys. Res. Lett.* *23*, 2931-2934, 1996.
- Deshler, T., J. B. Liley, G. Bodeker, W. A. Matthews and D. J. Hofmann, Stratospheric aerosol following Pinatubo, comparison of the north and south mid latitudes using *in situ* measurements, *Adv. Space Res.*, *20*, 2057-2061, 1997.

- di Sarra, A., L. Bernardini, M. Cacciani, G. Fiocco and D. Fua, Stratospheric aerosols observed by lidar over northern Greenland in the aftermath of the Pinatubo eruption, *J. Geophys. Res.*, *103*, 13873-13891, 1998.
- Dibb, J. E., R. W. Talbot and E. M. Scheuer, Composition and distribution of aerosols over the North Atlantic during the Subsonic Assessment Ozone and Nitrogen Oxide Experiment (SONEX), *J. Geophys. Res.*, *105*, 3709-3717, 2000.
- Drdla, K., M. R. Schoeberl and E. V. Browell, Microphysical modeling of the 1999-2000 Arctic winter: 1. Polar stratospheric clouds, denitrification and dehydration, *J. Geophys. Res.*, *108*, art. no. 8312, doi:10.1029/2001JD000782, 2002.
- Dutton, E. G., and J. R. Christy, Solar radiative forcing at selected locations and evidence for global lower tropospheric cooling following the eruptions of El Chichón and Pinatubo, *Geophys. Res. Lett.*, *19*, 2313-2316, 1992.
- Dutton, G. S., S. A. Montzka, B. D. Hall, T. M. Thompson and J. W. Elkins, In situ measurements of carbonyl sulfide and methyl chloride, *Eos Trans. AGU*, *82*(47), Fall Meeting Suppl., A51F-0134, 2001.
- Easter, R. C., and L. K. Peters, Binary homogeneous nucleation: Temperature and relative humidity fluctuations, nonlinearity, and aspects of new particle production in the atmosphere, *J. Appl. Meteorol.*, *33*, 775-784, 1994.
- Eckhardt, S., A. Stohl, H. Wernli, P. James, C. Forster and N. Spichtinger, A 15-year climatology of warm conveyor belts, *J. Clim.*, *17* (1), 218-237, 2004.
- Loevblad, G., L. Tarrasón, K. Torseth and S. Dutchak (Eds.), EMEP Assessment Part I, European Perspective, EMEP Co-operative programme for monitoring and evaluation of the long-range transmission of air pollutants in Europe, 180 p., Oslo, 2004.
- EPA, *Air Trends Sulfur Dioxide*, U.S. Environmental Protection Agency, www.epa.gov/airtrends/sulfur/html, 2003.
- Eparvier, F. G., D. W. Rusch, R. T. Clancy and G. E. Thomas, Solar Mesosphere Explorer satellite measurements of El Chichon stratospheric aerosols, 2. Aerosol mass and size parameters, *J. Geophys. Res.*, *99*, 20533-20544, 1994.
- European Commission (EC), *European research in the stratosphere 1996-2000*, Scientific assessment, Directorate-General for Research, EUR 19867, 378p., 2001.
- Fahey, D. W., R. S. Gao, K. S. Carslaw, J. Kettleborough, P. J. Popp, M. J. Northway, J. C. Holecek, S. C. Ciciora, R. J. McLaughlin, T. L. Thompson, R. H. Winkler, D. G. Baumgardner, B. Gandrud, P. O. Wennberg, S. Dhaniyala, K. McKinney, T. Peter, R. J. Salawitch, T. P. Bui, J. W. Elkins, C. R. Webster, E. L. Atlas, H. Jost, J. C. Wilson, R. L. Herman, A. Kleinbohl and M. von Konig, The detection of large HNO₃-containing particles in the winter arctic stratosphere, *Science*, *291* (5506), 1026-1031, 2001.
- Fenn, M. A., E. V. Browell, C. F. Butler, W. B. Grant, S. A. Kooi, M. B. Clayton, G. L. Gregory, R. E. Newell, Y. Zhu, J. E. Dibb, H. E. Fuelberg, B. E. Anderson, A. R. Bandy, D. R. Blake, J. D. Bradshaw, B. G. Heikes, G. W. Sachse, S. T. Sandholm, H. B. Singh, R. W. Talbot, D. C. Thornton, Ozone and aerosol distributions and air mass characteristics over the South Pacific during the burning season, *J. Geophys. Res.*, *104* (D13), 16197-16212, 1999.
- Ferek, R. J., and D. A. Hegg, Measurements of dimethyl sulfide and SO₂ during GTE/CITE 3, *J. Geophys. Res.*, *98* (D12), 23435-23442, 1993.
- Fernald, F. G., and B. G. Schuster, Wintertime 1973 airborne lidar measurements of stratospheric aerosols, *J. Geophys. Res.*, *82*, 433-437, 1977.
- Ferrare, R. A., S. H. Melfi, D. N. Whiteman, K. D. Evans and R. Leifer, Raman lidar measurements of aerosol extinction and backscattering. 1. Methods and comparisons, *J. Geophys. Res.*, *103* (D16) 19663-19672, 1998.
- Finnlayson-Pitts, B. J., and J. N. Pitts, *Atmospheric Chemistry*, J. Wiley & Sons, New York, 1986.

- Fiocco, G., and G. Grams, Observations of the aerosol layer at 20 km by optical radar, *J. Atmos. Sci.*, 21, 323-324, 1964.
- Fiocco, G., and L. D. Smullin, Detection of scattering layers in the upper atmosphere (60-140 km) by optical radar, *Nature*, 199, 1275-1276, 1963.
- Fleming, E. L., C. H. Jackman, R. S. Stolarski and D. B. Considine, Simulation of stratospheric tracers using an improved empirically-based two-dimensional model transport formulation, *J. Geophys. Res.*, 104, 23911-23934, 1999.
- Flentje H. and C. Kiemle, Erosion and mixing of filaments in the arctic lower stratosphere revealed by airborne lidar measurements, *J. Geophys. Res.*, 108 (D8), 4332, doi: 10.1029/2002JD002168, 2003.
- Folkens, I., P. O. Wennberg, T. F. Hanisco, J. G. Anderson and R. J. Salawitch, OH, HO₂ and NO in two biomass burning plumes: Sources of HO_x and implications for ozone production, *Geophys. Res. Lett.*, 24, 24, 3185-3188, 1997.
- Fromm, M., J. Alfred and M. Pitts, A unified, long-term, high-latitude stratospheric aerosol and cloud database using SAM II, SAGE II, and POAM II/III data: algorithm description, database definition, and climatology, *J. Geophys. Res.*, 108, art. no. 4366, doi: 10.1029/2002JD002772, 2003.
- Fromm, M., J. Alfred, K. Hoppel, J. Hornstein, R. Bevilacqua, E. Shettle, R. Servranckx, Z. Li and B. Stocks, Observations of boreal forest fire smoke in the stratosphere by POAM III, SAGE II, and lidar in 1998, *Geophys. Res. Lett.*, 27, 1407-1410, 2000.
- Fromm, M. D., R. M. Bevilacqua, J. Hornstein, E. Shettle, K. Hoppel, J. D. Lumpe, Observations of Antarctic polar stratospheric clouds by POAM II: 1994-1996. An analysis of Polar Ozone and Aerosol Measurement (POAM) II Arctic polar stratospheric cloud observations, 1993-1996, *J. Geophys. Res.*, 104 (D20), 24341-24358, doi: 10.1029/1999JD900273, 1999.
- Fromm, M. D., J. D. Lumpe, R. M. Bevilacqua, E. Shettle, J. Hornstein, S. T. Massie, K. H. Fricke, Observations of Antarctic polar stratospheric clouds by POAM II: 1994-1996, *J. Geophys. Res.*, 102 (D19), 23659-23673, 1997.
- Fuller, W. H. Jr., M. T. Osborn and W. H. Hunt, 48-inch lidar aerosol measurements taken at the Langley Research Center: May 1974 to December 1987, *NASA RP 1209*, October, 1988.
- Fussen, D., E. Arijs, D. Nevejans and F. Leclere, Tomography of the Earth's atmosphere by the space-borne Ora radiometer: Spatial inversion algorithm, *J. Geophys. Res.*, 102, 4357-4365, 1997.
- Fussen, D., E. Arijs, F. Vanhellemont, C. Brogniez and J. Lenoble, Validation of the ORA spatial inversion algorithm with respect to the Stratospheric Aerosol and Gas Experiment II data, *Appl. Opt.*, 37, 3121-3127, 1998.
- Fussen, D., F. Vanhellemont and C. Bingen, Remote sensing of the Earth's atmosphere by the spaceborne occultation radiometer ORA: Final inversion algorithm, *Appl. Opt.*, 40, 941-948, 2001a.
- Fussen, D., F. Vanhellemont and C. Bingen, Evolution of stratospheric aerosols in the post-Pinatubo period measured by the occultation radiometer experiment ORA, *Atmos. Env.*, 35, 5067-5078, 2001b.
- Fussen, D., F. Vanhellemont and C. Bingen, Evidence of transport, sedimentation and coagulation mechanisms in the relaxation of post-volcanic stratospheric aerosols, *Ann. Geophys.*, 19, 1157-1162, 2001c.
- Fussen, D., F. Vanhellemont, C. Bingen and S. Chabrilat, Ozone profiles from 30 to 100 km measured by the Occultation Radiometer instrument during the period Aug 1992-Apr 1993, *Geophys. Res. Lett.*, 27, 3449-3452, 2000.
- Gabric, A., N. Murray, L. Stone and M. Kohl, Modelling the production of dimethylsulfide during a phytoplankton bloom, *J. Geophys. Res.*, 98, 22805-22816, 1993.

- Galloway, J. N., W. C. Keene, A. A. P. Pszenny, D. W. Whelpdale, H. Sievering, J. T. Merrill and J. F. Boatman, Sulfur in the Western North Atlantic Ocean Atmosphere: Results from a summer 1988 ship/aircraft experiment, *Glob. Biogeochem. Cycles*, 4, No.4, 349-365, 1990.
- Gottelman, A., and P. M. d. F. Forster, Definition and climatology of the tropical tropopause layer, *J. Met. Soc. Japan*, 80, 4B, 911-924, 2002.
- Gottelman, A., M. L. Salby and F. Sassi, Distribution and influence of convection in the tropical tropopause region, *J. Geophys. Res.*, 107, 10.1029/2001JD001048, 2002b.
- Gottelman, A., W. J. Randel, F. Wu and S. T. Massie, Transport of water vapor in the tropical tropopause layer, *Geophys. Res. Letts.*, 29, 10.1029/2001GL013818, 2002a.
- Glaccum, W., R. Lucke, R. M. Bevilacqua, E. P. Shettle, J. S. Hornstein, D. T. Chen, J. D. Lumpe, S. S. Krigman, D. J. Debrestian, M. D. Fromm, F. Dalaudier, E. Chassefiere, C. Deniel, C. E. Randall, D. W. Rusch, J. J. Olivero, C. Brogniez, J. Lenoble and R. Kremer, The Polar Ozone and Aerosol Measurement (POAM II) Instrument, *J. Geophys. Res.*, 101, 14479-14487, 1996.
- Gleason, J. F., P. K. Bhartia, J. R. Herman, R. McPeters, P. Newman, R. S. Stolarski, L. Flynn, G. Labow, D. Larko, C. Seftor, C. Wellemeyer, W. D. Komhyr, A. J. Miller and W. Planet, Record low global ozone in 1992, *Science*, 260, 523-526, 1993.
- Goldman, A., M. T. Coffey, T. M. Stephen, C. P. Rinsland, W. G. Mankin and J. W. Hannigan, Isotopic OCS from high-resolution balloon-borne and ground-based infrared absorption spectra, *J. Quant. Spectrosc. Radiat. Transf.*, 67, 447-455, 2000.
- Goodman, J., K. G. Snetsinger, G. V. Ferry, N. H. Farlow, H. Y. Lem and D. M. Hayes, Altitude variations in stratospheric aerosols of a tropical region, *Geophys. Res. Lett.*, 9, 609-612, 1982.
- Graf, H.-F., J. Feichter and B. Langmann, Volcanic sulfur emissions: Estimates of source strength and its Contribution to the global sulfate distribution, *J. Geophys. Res.*, 102, 10727-10738, 1997.
- Graf, H.-F., B. Langmann and J. Feichter, The contribution of Earth degassing to the atmospheric sulfur budget, *Chem. Geol.*, 147, 131-145, 1998.
- Granqvist, C. G., and R. A. Buhrman, Log-normal size distributions of ultrafine metal particles, *Solid State Comm.*, 18, 123-126, 1976.
- Gregory, G. L., A. S. Bachmeier, D. R. Blake, B. G. Heikes, D. C. Thornton, A. R. Bandy, J. D. Bradshaw and Y. Kondo, Chemical signatures of aged Pacific marine air: Mixed layer and free troposphere as measured during PEM-West A, *J. Geophys. Res.*, 101 (D1), 1727-1742, 1996.
- Griffith, D. W. T., N. B. Jones and W. A. Matthews, Interhemispheric ratios and annual cycle of carbonyl sulfide (OCS) total column from ground-based solar FTIR spectra, *J. Geophys. Res.*, 103, 8447-8454, 1998.
- Grooss, J. U., C. Brühl and T. Peter, Impact of aircraft emissions on tropospheric and stratospheric ozone, Part I: Chemistry and 2-D model results, *Atmos. Env.*, 32, 3173-3184, 1998.
- Gruner, P., and H. Kleinert, Die Dämmerungserscheinungen, *Probl. Kosm. Phys.*, 10, 1-113, 1927.
- Gunson, M. R., M. M. Abbas, M. C. Abrams, M. Allen, L. R. Brown, T. L. Brown, A. Y. Chang, A. Goldman, F. W. Irion, L. L. Lowes, E. Mahieu, G. L. Manney, H. A. Michelsen, M. J. Newchurch, C. P. Rinsland, R. J. Salawitch, G. P. Stiller, G. C. Toon, Y. L. Yung and R. Zander, The Atmospheric Trace Molecule Spectroscopy (ATMOS) experiment: Deployment on the ATLAS Space Shuttle missions, *Geophys. Res. Lett.*, 23, 2333-2336, 1996.
- Haag, W., and B. Kärcher, The impact of aerosols and gravity waves on cirrus clouds at mid-latitudes, *J. Geophys. Res.*, 109, D12202, doi:10.1029/2004JD004579, 2004.
- Hale, B. N., and M. Kulmala, Eds., *Nucleation and Atmospheric Aerosols 2000*, American Institute of Physics, Melville, New York, pp. 335, 2000.

- Halmer, M. M., H.-U. Schmincke and H.-F. Graf, The annual volcanic gas input into the atmosphere, in particular into the stratosphere: a global data set for the past 100 years, *J. Volcanol. Geotherm. Res.*, *115*, 511-528, 2002.
- Hamill, P., E. J. Jensen, P. B. Russell and J. J. Bauman, The life cycle of stratospheric aerosol particles, *Bull. Am. Meteorol. Soc.*, *78*, 1395-1410, 1997.
- Hamill, P., O. B. Toon and R. P. Turco, Aerosol nucleation in the winter arctic and Antarctic stratospheres, *Geophys. Res. Lett.*, *17*, 417-420 Suppl. S, 1990.
- Hansen, J., A. Lacis, R. Ruedy and K. Sato, Potential climate impact of Mount Pinatubo eruption, *Geophys. Res. Lett.*, *19*, 215-218, 1992.
- Hansen, J., M. Sato, L. Nazarenko, R. Ruedy, A. Lacis, D. Koch, I. Tegen, T. Hall, D. Shindell, B. Santer, P. Stone, T. Novakov, L. Thomason, R. Wang, Y. Wang, D. Jacob, S. Hollandsworth, L. Bishop, J. Logan, A. Thompson, R. Stolarski, J. Lean, R. Wilson, S. Levitus, J. Antonov, N. Rayner, D. Parker and J. Cristy, Climate forcings in the Goddard Institute for Space Studies SI2000 simulations, *J. Geophys. Res.*, *107* (D18), 4347, doi:10.1029/2001JD001143, 2002.
- Hanson, D., and K. Mauersberger, Laboratory Studies of the Nitric-Acid Trihydrate - Implications for the South Polar Stratosphere, *Geophys. Res. Lett.*, *15* (8), 855-858, 1988.
- Hanson, D. R., and F. L. Eisele, Measurement of prenucleation molecular clusters in the NH₃, H₂SO₄, H₂O system, *J. Geophys. Res.-Atmos.*, *107* (D12), art. no. 4158, doi: 10.1029/2001JD001100, 2002.
- Hartmann, D. L., *Global Physical Climatology*, Academic Press, pp. 408, 1994.
- Hartmann, D. L., J. R. Holton and Q. Fu, The heat balance of the tropical tropopause, cirrus, and stratospheric dehydration, *Geophys. Res. Lett.*, *28*, 1969-1972, 2001.
- Hatsushika, H. and Yamazaki, K., Stratospheric drain over Indonesia and dehydration within the tropical tropopause layer diagnosed by air parcel trajectories, *J. Geophys. Res.*, *108*, doi: 10.1029/2002JD002986, 2003.
- Hayashida, S., and M. Horikawa, Anti-correlation between stratospheric aerosol extinction and the Ångström parameter from multiple wavelength measurements with SAGE II - a characteristic of the decay period following major volcanic eruptions, *Geophys. Res. Lett.*, *19*, 4063-4066, 2001.
- Heath, D. F., E. Hilsenrath and S. Janz, Characterization of a hardened ultrastable UV linear variable filter and recent results on the radiometric stability of narrow band interference filters subjected to temperature/humidity, thermal/vacuum, and ionizing radiation environments, *J. Soc. Photo Opt. Instrum. Eng.*, *3501*, 401-411, 1998.
- Heath, D. F., Z. Wei and, E. Hilsenrath, Calibration and characterization of remote sensing instruments using ultra stable interference filters, *J. Soc. Photo Opt. Instrum. Eng.*, *3221*, 300-308, 1997.
- Hendricks, J., B. Kärcher, A. Doppelheuer, J. Feichter, U. Lohmann and D. Baumgardner, Simulating the global atmospheric black carbon cycle: a revisit to the contribution of aircraft emissions, *Atmos. Chem. Phys.*, *4*, 2521-2541, 2004.
- Hendricks, J., B. Kärcher, U. Lohmann and M. Ponater, Do aircraft black carbon emissions affect cirrus clouds on the global scale?, *Geophys. Res. Lett.*, *32*, L12814, doi:10.1029/2005GL022740, 2005.
- Hermann, M., J. Heintzenberg, A. Wiedensohler, A. Zahn, G. Heinrich, C. A. M. Brenninkmeijer, Meridional distributions of aerosol particle number concentrations in the upper troposphere and lower stratosphere obtained by Civil Aircraft for Regular Investigation of the Atmosphere Based on an Instrument Container (CARIBIC) flights, *J. Geophys. Res.*, *108*, 4114, doi:10.1029/2001JD001077, 2003.
- Hervig, M. E., and T. Deshler, Evaluation of aerosol measurements from SAGE II, HALOE, and balloonborne optical particle counters, *J. Geophys. Res.*, *107* (D3), 10.1029/2001JD000703, 2002.

- Hervig, M., and M. McHugh, Cirrus detection using HALOE measurements, *Geophys. Res. Lett.*, 26, 719-722, 1999.
- Hervig, M. E., T. Deshler and J. M. Russell III, Aerosol size distributions obtained from HALOE spectral extinction measurements, *J. Geophys. Res.*, 103, 1573-1583, 1998.
- Hervig, M. E., J. M. Russell III, L. L. Gordley, J. Daniels, S. R. Drayson, J. H. Park, Aerosol effects and corrections in the Halogen Occultation Experiment, *J. Geophys. Res.*, 100, 1067-1079, 1995.
- Hervig, M. E., J. M. Russell III, L. L. Gordley, J. Daniels, J. H. Park, S. R. Drayson and T. Deshler, Validation of aerosol measurements made by the Halogen Occultation Experiment, *J. Geophys. Res.*, 101, 10267-10275, 1996.
- Hicks, B. B., R. S. Artz, T. P. Meyers and R. P. Hosker Jr., Trends in eastern U.S. sulfur air quality from the Atmospheric Integrated Research Monitoring Network, *J. Geophys. Res.*, 107 (D12), 10.1029/2000JD000165, 2002.
- Highwood, E. J. and B. J. Hoskins, The tropical tropopause, *Quart. J. Roy. Meteor. Soc.*, 124, 1579-1604, 1998.
- Hintze, P. E., H. G. Kjaergaard, V. Vaida and J. B. Burkholder, Vibrational and electronic spectroscopy of sulfuric acid vapor, *J. Phys. Chem. A*, 107, 1112-1118, 2003.
- Hitchman, M. H., M. McKay and C. R. Trepte, A climatology of stratospheric aerosol, *J. Geophys. Res.*, 99 (D10), 20689-20700, 1994.
- Hobbs, P. V., An overview of the University of Washington airborne measurements and results from the Tropospheric Aerosol Radiative Forcing Observational Experiment (TARFOX), *J. Geophys. Res.*, 104, 2233-2238, 1999.
- Hobbs, P. V., Sulfur dioxide data from aircraft measurements along the U.S. East coast during project TARFOX, private communication of Prof. P.V. Hobbs, University of Washington, Dept. of Atmospheric Sciences, Seattle, WA, U.S., 2002.
- Hofmann, D. J., Increase in the stratospheric background sulfuric acid aerosol mass in the past 10 years, *Science*, 248, 996-1000, 1990.
- Hofmann, D. J., Aircraft sulfur emissions, *Nature*, 349, 651, 1991.
- Hofmann, D. J., Twenty years of balloon-borne tropospheric aerosol measurements at Laramie, Wyoming, *J. Geophys. Res.*, 98, 12753-12766, 1993.
- Hofmann, D. J., and T. Deshler, Stratospheric cloud observations during formation of the Antarctic ozone hole in 1989, *J. Geophys. Res.*, 96, 2897-2912, 1991.
- Hofmann, D. J., and J. M. Rosen, Stratospheric sulfuric acid layer: Evidence for an anthropogenic component, *Science*, 208, 1368-1370, 1980.
- Hofmann, D. J., and J. M. Rosen, On the background stratospheric aerosol layer, *J. Atmos. Sci.*, 38, 168-181, 1981.
- Hofmann, D. J., and J. M. Rosen, Antarctic observations of stratospheric aerosol and high altitude condensation nuclei following the El Chichon eruption, *Geophys. Res. Lett.*, 12, 13-16, 1985.
- Hofmann, D. J., and S. Solomon, Ozone destruction through heterogeneous chemistry following the eruption of El Chichón, *J. Geophys. Res.*, 94, 5029-5041, 1989.
- Hofmann, D. J., J. Barnes, E. Dutton, T. Deshler, H. Jäger, R. Keen and M. Osborn, Surface-based observations of volcanic emissions to the stratosphere, in *Volcanism and the Earth's Atmosphere*, Geophysical Monograph Series, Volume 139, A. Robock and C. Rodgers (Eds.), AGU, Washington, DC, 2004.
- Hofmann, D. J., J. M. Rosen, J. W. Harder and J. V. Hereford, Balloon-borne measurements of aerosol, condensation nuclei, and cloud particles in the stratosphere at McMurdo Station, Antarctica, during the spring of 1987, *J. Geophys. Res.*, 94, 11253-11269, 1989.
- Hofmann, D. J., J. M. Rosen, T. J. Pepin and R. G. Pinnick, Stratospheric aerosol measurements, I, Time variations at northern midlatitudes, *J. Atmos. Sci.*, 32, 1446-1456, 1975.

- Hofmann, D. J., R. Stone, M. Wood, T. Deshler and J. Harris, An analysis of 25 years of balloon-borne aerosol data in search of a signature of the subsonic commercial aircraft fleet, *Geophys. Res. Lett.*, *25*, 2433-2436, 1998.
- Holton, J. R., and A. Gettelman, Horizontal transport and the dehydration of the stratosphere, *Geophys. Res. Lett.*, *28*, 2799-2802, 2001.
- Holton, J. R., P. H. Haynes, M. E. McIntyre, A. R. Douglass, R. B. Rood and L. Pfister, Stratosphere-troposphere exchange, *Rev. Geophys.*, *33*, 403-439, 1995.
- Houghton, J. T., Y. Ding, D. J. Griggs, M. Noguer, P. J. van der Linden and D. Xiaosu (Eds.), *Climate Change 2001: The Scientific Basis*, Cambridge University Press, 944 pp., 2001.
- Huebert, B. J., B. W. Blomquist, J. E. Hare, C. W. Fairall, J. E. Johnson and T. S. Bates, Measurement of the sea-air DMS flux and transfer velocity using eddy correlation, *Geophys. Res. Lett.*, *31*, L23113, doi:10.1029/2004GL021567, 2004.
- Hughes, D. W., Meteors, in: *Cosmic Dust*, J. McDonnell (Ed.), Chap. 3, John Wiley, N.Y., 1978.
- Hunten, D. M., R. P. Turco and O. B. Toon, Smoke and dust particles of meteoric origin in the mesosphere and stratosphere, *J. Atm. Sciences*, *37*, 1342-1357, 1980.
- Hynes, A. J., P. H. Wine and J. M. Nicovich, Kinetics and mechanism of the reaction of OH with CS₂ under atmospheric conditions, *J. Phys. Chem.*, *92*, 3846, 1988.
- Intergovernmental Panel on Climate Change (IPCC), *Aviation and the Global Atmosphere*, J. E. Penner, D. H. Lister, D. J. Griggs, D. J. Dokken and M. McFarland (Eds.), Cambridge Univ. Press, 373 pp., 1999.
- Irion F. W., M. R. Gunson, G. C. Toon, A. Y. Chang, A. Eldering, E. Mahieu, G. L. Manney, H. A. Michelsen, E. J. Moyer, M. J. Newchurch, G. B. Osterman, C. P. Rinsland, R. J. Salawitch, B. Sen, Y. L. Yung and R. Zander, Atmospheric Trace Molecule Spectroscopy (ATMOS) experiment version 3 data retrievals, *Appl. Opt.*, *41* (33), 6968-6979, 2002.
- Jacobson, M. C., H.-C. Hansson, K. J. Noone and R. J. Charlson, Organic atmospheric aerosols: Review and state of science, *Rev. Geophys.*, *38*, 267-294, 2000.
- Jaeglé, L., HO_x chemistry in the upper troposphere: Where do we stand? *IGAC Newsletter*, *19*, <http://www.igac.noaa.gov/newsletter/index.php>, 2001.
- Jaeglé, L., D. J. Jacob, W. H. Brune and P. O. Wennberg, Chemistry of HO_x radicals in the upper troposphere, *Atm. Environ.* *35*, 469-489, 2001.
- Jaeglé, L., D. J. Jacob, P. O. Wennberg, C. M. Spivakovsky, T. F. Hanisco, E. J. Lanzendorf, E. J. Hintsa, D. W. Fahey, E. R. Keim, M. H. Proffitt, E. L. Atlas, F. Flocke, S. Schauffler, C. T. McElroy, C. Midwinter, L. Pfister and J. C. Wilson, Observed OH and HO₂ in the upper troposphere suggest a major source from convective injection of peroxides, *Geophys. Res. Lett.*, *24*, 3181-3184, 1997.
- Jaeschke, W., T. S. Salkowski, J. P. Dierssen, J. v. Trümbach, U. Krischke and A. Günther, Measurements of trace substances in the Arctic troposphere as potential precursors and constituents of Arctic Haze, *J. Atmos. Chem.*, *34*, 291-319, 1999.
- Jäger, H., Stratospheric aerosols: Observations, trends, and effects, *J. Aerosol Sci.*, *22*, Suppl. 1, S517-S520, 1991.
- Jäger, H., Long-term record of lidar observations of the stratospheric aerosol layer at Garmisch-Partenkirchen, *J. Geophys. Res.*, *110*, D08106, doi:10.1029/2004JD005506, 2005.
- Jäger, H., and T. Deshler, Lidar backscatter to extinction, mass and area conversions based on midlatitude balloonborne measurements of stratospheric aerosols, *Geophys. Res. Lett.*, *29*(19), 2919, doi:10.1029/2002GL015609, 2002.
- Jäger, H., and T. Deshler, Correction to Lidar backscatter to extinction, mass and area conversions for stratospheric aerosols based on midlatitude balloonborne size distribution measurements, *Geophys. Res. Lett.*, *30*(7), 1382, doi:10.1029/2003GL017189, 2003.

- Jäger, H., and D. Hofmann, Midlatitude lidar backscatter to mass, area, and extinction conversion model based on in situ aerosol measurements from 1980 to 1987, *Appl. Opt.*, *30*, 127-138, 1991.
- Jäger, H., and K. Wege, Stratospheric ozone depletion at northern midlatitudes after major volcanic eruptions, *J. Atmos. Chem.*, *10*, 273-287, 1990.
- Jayaraman, A., S. Ramachandran, Y. B. Acharya and B. H. Subbaraya, Pinatubo volcanic aerosols layer decay observed at Ahmedabad (23°N), India, using ND:YAG backscatter lidar, *J. Geophys. Res.*, *100*, 23209-23214, 1995.
- Jensen, E., and K. Drdla, Nitric acid concentrations near the tropical tropopause: Implications for the properties of tropical nitric acid trihydrate clouds, *Geophys. Res. Lett.*, *29*, art. no. 2001, doi:10.1029/2002GL015190, 2002.
- Johnson, J. E., and T. S. Bates, Atmospheric measurements of carbonyl sulfide, dimethyl sulfide, and carbon disulfide using the electron capture sulfur detector, *J. Geophys. Res.*, *98* (D12), 23411-23421, 1993.
- Johnston, P. V., and R. L. McKenzie, NO₂ observations at 45°S during the decreasing phase of solar cycle 21, from 1980 to 1987, *J. Geophys. Res.*, *94*, 3473-3486, 1989.
- Johnson, J. E., A. R. Bandy, D. C. Thornton and T. S. Bates, Measurements of atmospheric carbonyl sulfide during the NASA chemical instrumentation test and evaluation project: Implications for the global COS budget, *J. Geophys. Res.*, *98*, 23442-23448, 1993.
- Johnston, P. V., R. L. McKenzie, J. G. Keys and W. A. Matthews, Observations of depleted stratospheric NO₂ following the Pinatubo volcanic eruption., *Geophys. Res. Lett.*, *19*, 211-213, 1992.
- Jonsson, H. H., J. C. Wilson, C. A. Brock, R. G. Knollenberg, R. Newton, J. E. Dye, D. Baumgardner, S. Borrmann, G. V. Ferry, R. Pueschel, D. C. Woods and M. C. Pitts, Performance of a focused cavity aerosol spectrometer for measurements in the stratosphere of particle size in the 0.06-2.0 μm diameter range, *J. Atmos. Oceanic Technol.*, *12*, 115-129, 1995.
- Junge, C. E., and J. E. Manson, Stratospheric aerosol studies, *J. Geophys. Res.*, *66*, 3975, 1961.
- Junge, C. E., C. W. Changnon and J. E. Manson, Stratospheric aerosols, *J. Meteor.*, *18*, 81-108, 1961.
- Kärcher, B., Aircraft-generated aerosols and visible contrails, *Geophys. Res. Lett.*, *23*, 1933-1936, 1996.
- Kärcher, B., Properties of subvisible cirrus clouds formed by homogeneous freezing, *Atmos. Chem. Phys.*, *2*, 161-170, 2002.
- Kärcher, B., and S.K. Meilinger, Perturbation of the aerosol layer by aviation-produced aerosols: A parameterization of plume processes, *Geophys. Res. Lett.*, *25*, 4465-4468, 1998.
- Kärcher, B., and S. Solomon, On the composition and optical extinction of particles in the tropopause region, *J. Geophys. Res.*, *104*, 27441-27459, 1999.
- Kärcher, B., and J. Ström, The roles of dynamical variability and aerosols in cirrus cloud formation, *Atmos. Chem. Phys.*, *3*, 823-838, 2003.
- Kärcher, B., W. Haag, C. Voigt and A. Lauer, EQUIL4 – A Model to calculate the equilibrium partitioning between the gas phase, liquid NH₃/H₂SO₄/HNO₃/H₂O aerosols, and ice crystals, *Deutsches Zentrum für Luft- und Raumfahrt (DLR), Research Report*, DLR FB 2004-22, 28pp, 2004.
- Kärcher, B., R. P. Turco, F. Yu, M. Y. Danilin, D. K. Weisenstein, R. C. Miake-Lye and R. Busen, A unified model for ultrafine aircraft particle emissions, *J. Geophys. Res.*, *105*, 29379-29386, 2000.
- Kärcher, B., F. Yu, F.P. Schröder and R. P. Turco, Ultrafine aerosol particles in aircraft plumes: Analysis of growth mechanisms, *Geophys. Res. Lett.*, *25*, 2793-2796, 1998.

- Karsten, U., C. Wiencke and G. O. Kirst, Dimethylsulphiopropionate (DMSP) accumulation in green macroalgae from polar to temperate regions: Interactive effects of light versus salinity and light versus temperature, *Pol. Biol.*, *12*, 603-607, 1992.
- Keckhut, P., M. L. Chanin and A. Hauchecorne, Stratosphere temperature measurement using Raman lidar, *Appl. Opt.*, *29*, 5182-5186, 1990.
- Keil, K., Meteorite composition, in: Wedepohl, H. (Ed.), *Handbook of Geochemistry*, vol. 1, Springer, pp. 116-133, 1969.
- Kent, G. S., M. P. McCormick and M. T. Philip, Comparison of low latitude lidar and Sage satellite measurements, *11th Int. Laser Radar Conf., NASA CP-2228*, 8-12, 1982.
- Kent, G. S., P. Sandland and R. W. H. Wright, A second-generation laser radar., *J. Appl. Met.*, *10*, 443-452, 1971.
- Kent, G. S., P.-H. Wang and K. M. Skeens, Discrimination of cloud and aerosol in the Stratospheric Aerosol and Gas Experiment (SAGE III) occultation data, *Appl. Opt.*, *33*, 8639-8649, 1997a.
- Kent, G. S., D. M. Winker, M. A. Vaughan, P.-H. Wang and K. M. Skeens, Simulation of SAGE II cloud measurements using airborne lidar data, *J. Geophys. Res.*, *102*, 21795-21807, 1997b.
- Kettle, A. J., *Extrapolation of the oceanic flux of DMS, CO, COS, and CS₂*, Ph.D. Thesis, York University, Toronto, 2000.
- Kettle, A. J., and M. O. Andreae, Flux of dimethylsulfide from the oceans: A comparison of updated data sets and flux models, *J. Geophys. Res.*, *105*, 26793-26808, 2000.
- Kettle A. J., M. O. Andreae, D. Amouroux, T. W. Andreae, T. S. Bates, H. Berresheim, H. Bingemer, R. Boniforti, M. A. J. Curran, G. R. DiTullio, G. Helas, G. B. Jones, M. D. Keller, R. P. Kiene, C. Leck, M. Lévassieur, G. Malin, M. Maspero, P. Matrai, A. R. McTaggart, N. Mihalopoulos, B. C. Nguyen, A. Novo, J. P. Putaud, S. Rapsomanikis, G. Roberts, G. Schebeske, S. Sharma, R. Simo, R. Staubes, S. Turner and G. Uher, A global database of sea surface dimethylsulfide (DMS) measurements and a procedure to predict sea surface DMS as a function of latitude, longitude, and month, *Glob. Biogeochem. Cycles*, *13*, 399-444, 1999.
- Kettle, A. J., U. Kuhn, M. von Hobe, J. Kesselmeier, M. O. Andreae, The global budget of atmospheric carbonyl sulfide: Temporal and spatial variations of the dominant sources and sinks, *J. Geophys. Res.*, *107* (D22), 4658, doi:10.1029/2002JD002187, 2002a.
- Kettle, A. J., U. Kuhn, M. von Hobe, J. Kesselmeier, P. S. Liss and M.O. Andreae, Comparing forward and inverse models to estimate the seasonal variation of hemisphere-integrated fluxes of carbonyl sulfide, *Atmos. Chem. Phys.*, *2*, 343-361, 2002b.
- Kettle, A. J., T. S. Rhee, M. von Hobe, A. Poulton, J. Aiken and M. O. Andreae, Assessing the flux of different volatile sulfur gases from the ocean to the atmosphere, *J. Geophys. Res.*, *106*, 12193-12209, 2001.
- Kiendler, A., and F. Arnold, Unambiguous identification and measurement of sulphuric acid cluster chemiions in aircraft jet engine exhaust, *Atmos. Env.*, *36*, 1757-1761, 2002.
- Kim, K. H., and M. O. Andreae, Determination of carbon disulfide in natural waters by adsorbent preconcentration and gas chromatography with flame photometric detection, *Analyt. Chem.*, *59*, 2670-2673, 1987.
- Kinne, S., O. B. Toon and M. J. Prather, Buffering of stratospheric circulation by changing amounts of tropical ozone--a Pinatubo case study, *Geophys. Res. Lett.*, *19*, 1927-1930, 1992.
- Kirst, G. O., C. Thiel, H. Wolff, J. Nothnagel, M. Wanzek and R. Ulmke, Dimethylsulfonio-propionate (DMSP) in ice-algae and its possible biological role, *Mar. Chem.*, *35*, 381-388, 1991.
- Kjellström, E., A three-dimensional global model study of carbonyl sulfide in the troposphere and lower stratosphere, *J. Atmos. Chem.*, *29*, 151-177, 1998.

- Kjellström, E., J. Feichter, R. Sausen and R. Hein, The contribution of aircraft emissions to the atmospheric sulfur budget, *Atmos. Env.*, 33, 3455-3465, 1999.
- Klett, J. D., Stable analytical inversion solution for processing lidar returns, *Appl. Opt.*, 20, 211-220, 1981.
- Klett, J. D., Lidar inversion with variable backscatter/extinction ratios, *Appl. Opt.*, 24, 1638-1643, 1985.
- Kley, D., J. M. Russell III and C. Phillips, SPARC Assessment of Upper Tropospheric and Stratospheric Water Vapor, *SPARC Report No. 2*, 2000.
- Korhonen, P., M. Kulmala, A. Laaksonen, Y. Viisanen R. McGraw and J. H. Seinfeld, Ternary nucleation of H₂SO₄, NH₃, and H₂O in the atmosphere, *J. Geophys. Res.*, 104, 26349-26353, 1999.
- Koziol, A. S., and J. Pudykiewicz, High-resolution modeling of size-resolved stratospheric aerosol, *J. Atmos. Sci.*, 55, 3127-3147, 1998.
- Krouse, H. R., and V. A. Grinenko (Eds.), Stable Isotopes: Natural and Anthropogenic sulphur in the Environment, Scope 43, 400 pp., John Wiley Publishing, New York, 1991.
- Kulmala, M., U. Pirjola and J. M. Makela, Stable sulphate clusters as a source of new atmospheric particles, *Nature*, 404, 66-69, 2000.
- Kulmala, M., H. Vehkamäki, T. Petäjä, M. Dal Maso, A. Lauri, V. M. Kerminen, W. Birmili and P. H. McMurry, Formation and growth rates of ultrafine atmospheric particles: a review of observations, *J. Aerosol. Sci.*, 35 (2), 143-176, 2004.
- Kumer, J. B., J. L. Mergenthaler, A. E. Roche, R. W. Nightingale, G. A. Ely, W. G. Uplinger, J. C. Gille, S. T. Massie, P. L. Bailey, M. R. Gunson, M. C. Abrams, G. C. Toon, B. Sen, J.-F. Blavier, R. A. Stachnik, C. R. Webster, R. D. May, D. G. Murcray, F. J. Murcray, A. Goldman, W. A. Traub, K. W. Jucks and D. G. Johnson, Comparison of correlative data with nitric acid data, version7, from the cryogenic limb array etalon spectrometer (CLAES) deployed on the NASA Upper Atmosphere Research Satellite, *J. Geophys. Res.*, 101, 9621-9656, 1996.
- Laaksonen, A., L. Pirjola, M. Kulmala, K.-H. Wohlfrom, F. Arnold and F. Raes, Upper tropospheric SO₂ conversion into sulfuric acid aerosols and cloud condensation nuclei, *J. Geophys. Res.*, 105, 1459-1469, 2000.
- Labitzke, K., Stratospheric temperature changes after the Pinatubo eruption, *J. Atmos. Terr. Phys.*, 56, 1027-1034, 1994.
- Labitzke, K., and M. P. McCormick, Stratospheric temperature increases due to Pinatubo aerosols, *Geophys. Res. Lett.*, 19, 207-210, 1992.
- Lal, D., and B. Peters, Cosmic ray produced radioactivity on the earth, *Handbuch der Physik*, pp. 551-612, Springer, New York, 1967.
- Lambert, A., R. G. Grainger, J. J. Remedios, C. D. Rodgers, M. Corney and F. W. Taylor, Measurements of the evolution of the Mount Pinatubo aerosol clouds by ISAMS, *Geophys. Res. Lett.*, 20, 1287-1290, 1993.
- Larsen, N., B. M. Knudsen, J. M. Rosen, N. T. Kjøme and E. Kyro, Balloon borne backscatter observations of type 1 PSC formation: inference about physical state from trajectory analysis, *Geophys. Res. Lett.*, vol 23, 1091-1094, 1996.
- Lee, C. C.-W., and M. H. Thiemens, The $\delta^{17}\text{O}$ and $\delta^{18}\text{O}$ measurements of atmospheric sulfate from a coastal and high alpine region: A mass-independent isotopic anomaly, *J. Geophys. Res.*, 106, 17359-17373, 2001.
- Lee, D. S., P. E. Clare, J. Haywood, B. Kärcher, R. W. Lunn, I. Pilling, A. Slingo and J. R. Tilston, Identifying the uncertainties in radiative forcing of climate from aviation contrails and aviation-induced cirrus, *Report DERA/AS/PTD/CR000103*, 69 p., 2000.
- Lee, R. L., and J. Hernandez-Andres, Measuring and modeling twilight's purple light, *Appl. Opt.*, 42, 445-457, 2003.

- Lefèvre, M., A. Vézina, M. Levasseur and J. W. H. Dacey, A model of dimethylsulfide dynamics for the subtropical North Atlantic, *Deep Sea Res. I*, 49, 2221-2239, 2002.
- J. Lelieveld, P. J. Crutzen, V. Ramanathan, M. O. Andreae, C. A. M. Brenninkmeijer, T. Campos, G. R. Cass, R. R. Dickerson, H. Fischer, J. A. de Gouw, A. Hansel, A. Jefferson, D. Kley, A. T. J. de Laat, S. Lal, M. G. Lawrence, J. M. Lobert, O. L. Mayol-Bracero, A. P. Mitra, T. Novakov, S. J. Oltmans, K. A. Prather, T. Reiner, H. Rodhe, H. A. Scheeren, D. Sikka and J. Williams, The Indian Ocean experiment, Widespread air pollution from south and south-east Asia, *Science*, 291, 1031-1036, 2001.
- Leung, F.-Y. T., A. J. Colussi, M. R. Hoffmann and G. C. Toon, Isotopic fractionation of carbonyl sulfide in the atmosphere: Implications for the source of background stratospheric sulfate aerosol, *Geophys. Res. Lett.*, 29, 10.1029/2001GL013955, 2002.
- Lin, N.-H., and V. K. Saxena, Changes in Antarctic stratospheric aerosol characteristics due to Mount Pinatubo eruption as monitored by SAGE II satellite, *J. Geophys. Res.*, 97, 7635-7649, 1992.
- Liu, S. C., and G. C. Reid, Sodium and other minor constituents of meteoric origin in the atmosphere, *Geophys. Res. Letters*, 6, 283-286, 1979.
- Love, S. G., and D. E. Brownlee, A direct measurement of the terrestrial mass accretion rate of cosmic dust, *Science*, 262, 550-553, 1993.
- Lovejoy, E. R., J. Curtius and K. D. Froyd, Atmospheric ion-induced nucleation of sulfuric acid and water, *J. Geophys. Res.-Atmos.*, 109 (D8), art. no. D08204, doi: 10.1029/2003JD004460, 2004.
- Lovelock, J. E., R. J. Maggs and R. A. Rasmussen, Atmospheric dimethyl sulfide and the natural sulphur cycle, *Nature*, 237, 452-453, 1972.
- Lu, C.-H., G. K. Yue, G. L. Manney, H. Jäger and V. A. Mohnen, Lagrangian approach for Stratospheric Aerosol and Gas Experiment (SAGE) II profile intercomparisons, *J. Geophys. Res.*, 105, 4563-4572, 2000.
- Lu, J., V. A. Mohnen, G. K. Yue and H. Jäger, Intercomparison of multiplatform stratospheric aerosol and ozone observations, *J. Geophys. Res.*, 102, 16127-16136, 1997.
- Lucke, R. L. D. Korwan, R. M. Bevilacqua, J. S. Hornstein, E. P. Shettle, D. T. Chen, M. Daehler, J. D. Lumpe, M. D. Fromm, D. Debrestian, B. Neff, M. Squire, G. König-Langlo and J. Davies, The Polar Ozone and Aerosol Measurement (POAM) III instrument and early results, *J. Geophys. Res.*, 104, 18755-18799, 1999.
- Lumpe, J. D., R. M. Bevilacqua, K. W. Hoppel, S. S. Krigman, D. L. Kriebel, C. E. Randall, D. W. Rusch, C. Brogniez, R. Ramanananaherosa, E. P. Shettle, J. J. Olivero, J. Lenoble and P. Pruvost, POAM II retrieval algorithm and error analysis, *J. Geophys. Res.*, 102, 23593-23614, 1997.
- Lumpe, J. D., R. M. Bevilacqua, K. W. Hoppel and C. E. Randall, POAM III retrieval algorithm and error analysis, *J. Geophys. Res.*, 107 (D21), 4575, doi:10.1029/2002JD002137, 2002.
- Luo, B. P., U. K. Krieger and T. Peter, Densities and refractive indices of H₂SO₄/HNO₃/H₂O solutions to stratospheric temperatures, *Geophys. Res. Lett.*, 23, 3707-3710, 1996.
- Mahieu, E., C. P. Rinsland, R. Zander, P. Duchatelet, C. Servais and M. De Mazière, Tropospheric and stratospheric carbonyl sulfide (OCS): long-term trends and seasonal cycles above the Jungfraujoch station, *Proceedings of the "Sixth European Symposium on Stratospheric Ozone"*, Göteborg, Sweden, September 2-6, 2002, EUR 20650, ISBN 92-894-5484-9, pp. 309-312, 2003.
- Mahieu E., R. Zander, L. Delbouille, P. Demoulin, G. Roland and C. Servais, Observed Trends in Total Vertical Column Abundances of Atmospheric Gases from IR Solar Spectra Recorded at the Jungfraujoch, *J. Atmos. Chem.*, 28, 227-243, 1997.
- Manabe, S. and R. T. Wetherald, Thermal equilibrium of the atmosphere with a given distribution of relative humidity, *J. Atmos. Sci.*, 24, 241-, 1967.

- Mari, C., K. Suhre, T. S. Bates, J. E. Johnson, R. Rosset, A. R. Bandy, F. L. Eisele, R. L. Mauldin III and D. C. Thornton, Physico-chemical modeling of the First Aerosol Characterization Experiment (ACE 1) Lagrangian B 2. DMS emission, transport and oxidation at the mesoscale, *J. Geophys. Res.*, *103*, 16457-16473, 1998.
- Markowski, G. R., Improving the Twomey algorithm for inversion of aerosol measurements data, *Aerosol Sci. Technol.*, *7*, 127-141, 1988.
- Maroulis, P. J., A. L. Torres, A. B. Goldberg and A. R. Bandy, Atmospheric SO₂ measurements on Project GAMETAG, *J. Geophys. Res.*, *85*, 7345-7349, 1980.
- Massie, S. T., J. C. Gille, D. P. Edwards, P. L. Bailey, L. V. Lyjak, C. A. Craig, C. P. Cavanaugh, J. L. Mergenthaler, A. E. Roche, J. B. Kumer, A. Lambert, R. G. Grainger, C. D. Rodgers, F. W. Taylor, J. M. Russell III, J. H. Park, T. Deshler, M. E. Hervig, E. F. Fishbein, J. W. Waters and W. A. Lahoz, Validation studies using multiwavelength Cryogenic Limb Array Etalon Spectrometer (CLAES) observations of stratospheric aerosols, *J. Geophys. Res.*, *101*, 9757-9773, 1996.
- Mauldin, L. E., N. H. Zaun, M. P. McCormick, J. H. Guy and W. R. Vaughn, Stratospheric Aerosol and Gas Experiment II instrument: A functional description, *Opt. Eng.*, *24*, 307-312, 1985.
- McCormick, M. P., and M. T. Osborn, Airborne lidar measurements of El Chichón stratospheric aerosols: October 1982 to November 1982, *NASA RP 1136*, 1985a.
- McCormick, M. P., and M. T. Osborn, Airborne lidar measurements of El Chichón stratospheric aerosols: January 1983 to February 1983, *NASA RP 1148*, 1985b.
- McCormick, M. P., and M. T. Osborn, Airborne lidar measurements of El Chichón stratospheric aerosols: July 1982, *NASA RP 1166*, 1986a.
- McCormick, M. P., and M. T. Osborn, Airborne lidar measurements of El Chichón stratospheric aerosols: May 1983, *NASA RP 1172*, 1986b.
- McCormick, M. P., and M. T. Osborn, Airborne lidar measurements of El Chichón stratospheric aerosols: January 1984, *NASA RP 1175*, 1987.
- McCormick, M. P., W. P. Chu, G. W. Grams, P. Hamill, B. M. Herman, L. R. McMaster, T. J. Pepin, P. B. Russell, H. M. Steele and T. J. Swissler, High-latitude stratospheric aerosols measured by the SAM II satellite system in 1978 and 1979, *Science*, *214*, 328-331, 1981.
- McCormick, M. P., P. Hamill, T. J. Pepin, W. P. Chu, T. J. Swissler and L. R. McMaster, Satellite studies of the stratospheric aerosol, *Bull. Am. Meteor. Soc.*, *60*, 1038-1046, 1979.
- McCormick, M. P., S. K. Poultney, V. van Wijk, C. O. Alley, R. T. Bettinger and J. A. Perschy, Backscattering from the upper atmosphere (75-160 km) detected by optical radar, *Nature*, *209*, 798-799, 1966.
- McCormick, M. P., T. J. Swissler, W. H. Fuller, W. H. Hunt and M. T. Osborn, Airborne and ground-based lidar measurements of the El Chichón stratospheric aerosol from 90°N to 56°S, *Geofisica Internat.*, *23*, 187-222, 1984.
- McCormick, M. P., L. W. Thomason and C. R. Trepte, Atmospheric effects of the Mt. Pinatubo eruption, *Nature*, *373*, 399-404, 1995.
- McKenzie, R. L., J. M. Rosen, N. T. Kjöme, T. J. McGee, M. R. Gross, U. N. Singh, R. F. Ferrare, P. Kimvilakani, O. Uchino and T. Nagai, Multi-wavelength profiles of aerosol backscatter over Lauder, New Zealand, 24 November 1992, *Geophys. Res. Lett.*, *21*, 789-792, 1994.
- Measures, R. M. (Ed.), *Laser remote sensing, Fundamentals and Applications*, Wiley, Interscience, 1984.
- Meilinger, S. K., B. Kärcher, R. von Kuhlmann and Th. Peter, On the impact of heterogeneous chemistry on ozone in the tropopause region, *Geophys. Res. Lett.*, *28* (3), 515-518, 2001.
- Meixner, F. X., The vertical sulfur dioxide distribution at the tropopause level, *J. Atmos. Chem.*, 175-189, 1984.

- Meixner, F. X., H.-W. Georgii, G. Ockelmann, H. Jäger and R. Reiter, The arrival of the Mt. St. Helens eruption cloud over Europe, *Geophys. Res. Lett.*, *8*, 163-166, 1981.
- Mergenthaler, J. L., A. E. Roche, J. B. Kumer and G. A. Ely, Cryogenic limb array etalon spectrometer observations of tropical cirrus, *J. Geophys. Res.*, *104*, 22183-22194, 1999.
- Metzger, S., F. Dentener, M. Krol, A. Jeuken and J. Lelieveld, Gas/aerosol partitioning - 2. Global modeling results, *J. Geophys. Res.-Atmos.*, *107* (D16), art. no.-4313, doi: 10.1029/2001JD001103, 2002.
- Miao, Q., *An analysis of errors associated with the measurement of aerosol concentration in situ with optical particle counters*, M.S. Thesis, University of Wyoming, 71 pp, 2001.
- Mie, G., Beiträge zur Optik trüber Medien speziell kolloidaler Metallösungen. *Ann. Phys.*, *25*, 377-445, 1908.
- Miles, G. M., R. G. Grainger and E. J. Highwood, The significance of volcanic eruption strength and frequency for climate, *Q. J. R. Meteorol. Soc.*, *130*, 2361-2376, 2004.
- Milhalopoulos, N., J. P. Putaud, B. C. Nguyen and S. Belviso, Annual variation of atmospheric carbonyl sulfide in the marine atmosphere in the southern Indian Ocean, *J. Atmos. Chem.*, *13*, 73-82, 1991.
- Miller, T. M., J. O. Ballenthin, A. A. Viggiano, B. E. Anderson and C. C. Wey, Mass distribution and concentrations of negative chemiions in th exhaust of a jet engine: Sulfuric acid concentrations and observation of particle growth, *Atmos. Env.* *39*, 3069-3079, 2005.
- Mills, M. J., O. B. Toon and S. Solomon, S., A two-dimensional microphysical model of the polar stratospheric CN layer, *Geophys. Res. Lett.*, *26*, 1133-1136, 1999.
- Mills M. J., O. B. Toon, V. Vaida, P. E. Hintze, H. G. Kjaergaard, D. P. Schofield and T. W. Robinson, Photolysis of sulfuric acid vapor by visible light as a source of the polar stratospheric CN layer, *J. Geophys. Res.*, *110*, D08201, doi:10.1029/2004JD005519, 2005.
- Minikin, A., A. Petzold, J. Strom, R. Krejci, M. Seifert, P. van Velthoven, H. Schlager and U. Schumann, Aircraft observations of the upper tropospheric fine particle aerosol in the Northern and Southern Hemispheres at midlatitudes, *Geophys. Res. Lett.*, *30* (10), art. no.-1503, doi: 10.1029/2002GL016458, 2003.
- Minnis, P., E. F. Harrison, L. L. Stowe, G. G. Gibson, F. M. Denn, D. R. Doelling and W. L. Smith Jr., Radiative Climate Forcing by the Mt. Pinatubo Eruption, *Science*, *259*, 1411-1415, 1993.
- Möhler, O. and F. Arnold, Gaseous sulfuric acid and sulfur dioxide measurements in the arctic troposphere and lower stratosphere: implications for hydroxyl radical abundances, *Geophys. Res. Lett.*, *19*, 1763-1766, 1992.
- Montzka, S. A., M. Aydin, M. Battle, J. H. Butler, E. S. Saltzman, B. D. Hall, A. D. Clarke, D. Mondeel and J. W. Elkins, A 350-year atmospheric history for carbonyl sulfide inferred from Antarctic firn air and air trapped in ice, *J. Geophys. Res.*, *109*, D22302, doi:10.1029/2004JD004686, 2004.
- Montzka, S. A., J. A. Lind, G. S. Dutton, B. D. Hall, D. J. Mondeel, J. H. Butler and J. W. Elkins, Recent global measurements of atmospheric COS and historic trends inferred from firn air at the South Pole, *Eos Trans. AGU*, *82*(47), Fall Meet. Suppl., A51F-0144, 2001.
- Mozurkiewicz, M., and J. G. Calvert, Reaction probability of N₂O₅ on aqueous aerosols, *J. Geophys. Res.*, *93*, 15889-15896, 1988.
- Murphy, D. M., D. S. Thomson and M. J. Mahoney, In situ measurements of organics, meteoritic material, mercury and other elements in aerosols at 5 to 19 kilometers, *Science*, *282*, 1664-1668, 1998.
- Nakicenovic, N., and R. Swart, *IPCC Special Report on Emission Scenarios*, Cambridge University Press, 599 pp., 2001.
- Napari, I., M. Kulmala and H. Vehkamäki, Ternary nucleation of inorganic acids, ammonia, and water, *J. Chem. Phys.*, *117*, (18), 8418-8425, 2002.

- Nash, E. R., P. A. Newman, J. E. Rosenfield and M. R. Schoeberl, An objective determination of the polar vortex using Ertel's potential vorticity, *J. Geophys. Res.*, *101* (D5), 9471-9478, 1996.
- Nedoluha, G. E., R. M. Bevilacqua, R. M. Gomez, B. C. Hicks, D. E. Siskind and J. M. Russell III, Long-term variations in water vapor and their effect on ozone, *Proceedings Quadrennial Ozone Symposium*, Kos, Greece, 2004.
- Nedoluha, G. E., R. M. Bevilacqua, K. W. Hoppel, J. D. Lumpe and H. Smit, Polar Ozone and Aerosol Measurement III measurements of water vapor in the upper troposphere and lowermost stratosphere, *J. Geophys. Res.*, *107* (D10) doi: 10.1029/2001JD000793, 2002.
- Newell, R. E., W. Hu, Z. X. Wu, Y. Zhu, H. Akimoto, B. E. Anderson, E. V. Browell, G. L. Gregory, G. W. Sachse, M. C. Shipham, A. S. Bachmeier, A. R. Bandy, D. C. Thornton, D. R. Blake, F. S. Rowland, J. D. Bradshaw, J. H. Crawford, D. D. Davis, S. T. Sandholm, W. Brockett, L. DeGreef, D. Lewis, D. McCormick, E. Monitz, J. E. Collins, B. G. Heikes, J. T. Merrill, K. K. Kelly, S. C. Liu, Y. Kondo, M. Koike, C.M. Liu, F. Sakamaki, H. B. Singh, J. E. Dibb and R. W. Talbot, Atmospheric sampling of Supertyphoon Mireille with NASA DC-8 aircraft on September 27, 1991, during PEM-West A, *J. Geophys. Res.*, *101* (D1), 1853-1871, 1996.
- Newhall, C. G., and S. Self, The Volcanic Explosivity Index (VEI): An estimate of Explosive Magnitude for Historical Volcanism, *J. Geophys. Res.*, *87*, 1231-1238, 1982.
- Nguyen, B. C., N. Mihalopoulos and S. Belviso, Seasonal variation of atmospheric dimethylsulfide at Amsterdam Island in the southern Indian Ocean, *J. Atmos. Chem.*, *11*, 123-141, 1990.
- Nielsen, H., J. Pilot, L. N. Grinenko, V. A. Grinenko, A. Lein, A. Yu., J. W. Smith and R. G. Pankina, Chapter 4: Lithospheric sources of sulfur, in: H.R. Krouse and V.A. Grinenko (Eds.), *Stable Isotopes, Natural and Anthropogenic Sulphur in the Environment*, SCOPE 43, J. Wiley & Sons, 1991.
- Nilsson, E. D., and M. Kulmala, The potential for atmospheric mixing processes to enhance the binary nucleation rate, *J. Geophys. Res.*, *103*, 1381-1389, 1998.
- Nilsson, E. D., L. Pirjola and M. Kulmala, The effect of atmospheric waves on aerosol nucleation and size distribution, *J. Geophys. Res.*, *105*, 19917-19926, 2000.
- Notholt, J., Z. Kuang, C. P. Rinsland, G. C. Toon, M. Rex, N. Jones, T. Albrecht, H. Deckelmann, J. Krieg, C. Weinzierl, H. Bingemer, R. Weller and O. Schrems, Enhanced Upper Tropical Tropospheric COS: Impact on the Stratospheric Aerosol Layer, *Science*, *300*, 307-310, 2003.
- Notholt J., B. P. Luo, S. Fueglistaler, D. Weisenstein, M. Rex, M.G. Lawrence, H. Bingemer, I. Wohltmann, T. Corti, T. Warneke, R. von Kuhlmann and T. Peter, Influence of tropospheric SO₂ emissions on particle formation and the stratospheric humidity, *Geophys. Res. Lett.*, *32*, L07810, doi:10.1029/2004GL022159, 2005.
- Notholt, J., G. C. Toon, C. P. Rinsland, N. S. Pougatchev, N. B. Jones, B. J. Connor, R. Weller, M. Gautrois and O. Schrems, Latitudinal variations of trace gas concentration in the free troposphere measured by solar absorption spectroscopy during a ship cruise, *J. Geophys. Res.*, *105* (D1), 1337-1349, 2000.
- Nowak, J. B., D. D. Davis, G. Chen, F. L. Eisele, R. L. Mauldin III, D. J. Tanner, C. Cantrell, E. Kosciuch, A. Bandy, D. Thornton and A. Clarke, Airborne observations of DMSO, DMS, and OH at marine tropical latitudes, *Geophys. Res. Lett.*, *28*, 2201-2204, 2001.
- Oberbeck, V. R., J. M. Livingston, P. B. Russell, R. F. Pueschel, J. M. Rosen, M. T. Osborn, M. A. Kritz, K. G. Snetsinger and G. V. Ferry, SAGE II aerosol validation: Selected altitude measurements, including particle micromerements, *J. Geophys. Res.*, *94*, 8367-8380, 1989.
- Ockelmann, G. E. F., and H.-W. Georgii, Grossraeumige Verteilung des atmosphaerischen Schwefeldioxids in der freien Atmosphaere, *Meteorol. Rdsch.*, *41*, 136-146, 1989.

- O'Dowd, C. D., P. Aaltok K. Hameri, M. Kulmala and T. Hoffman, Aerosol formation - Atmospheric particles from organic vapours, *Nature*, 416, 497-498, 2002.
- Oltmans, S. J., and D. J. Hofmann, Increases in lower-stratospheric water vapor at a mid-latitude northern hemisphere site from 1981 to 1994, *Nature*, 374, 146-149, 1995.
- Osborn, M. T., R. J. DeCoursey, C. R. Trepte, D. M. Winder and D. C. Woods, Evolution of the Pinatubo volcanic cloud over Hampton, Virginia, *Geophys. Res. Lett.*, 22, 1101-1104, 1995.
- Osborn, M. T., J. M. Rosen, M. P. McCormick, P.-H. Wang, J. M. Livingston and T. J. Swissler, SAGE II aerosol correlative observations: profile measurement, *J. Geophys. Res.*, 94, 8353-8366, 1989.
- Palmer, K. F., and D. Williams, Optical constants of sulfuric acid: Application to the clouds of Venus?, *Appl. Opt.*, 14, 208-219, 1975.
- Parameswaran, K., K. O. Rose, B. V. Krishna Murthy, M. T. Osborn and L. R. McMaster, Comparison of aerosol extinction profiles from lidar and SAGE II data at a tropical station, *J. Geophys. Res.*, 96, 10861-10866, 1991.
- Penner, J. E., M. Andreae, H. Annegarn, L. Barrie, J. Feichter, D. Hegg, A. Jayaraman, R. Leaitch, D. Murphy, J. Nganga and G. Pitari, Aerosols, their direct and indirect effects, In: *Climate change 2001: The scientific basis*, J.T. Houghton et al. (eds), Cambridge University Press, Cambridge, U.K. and New York, N.Y., USA, 881 pp, 2001.
- Pepin, T. J., M. P. McCormick, W. P. Chu, F. Simon, T. J. Swissler, R. R. Adams, K. R. Crumbly and W. H. Fuller Jr., Stratospheric aerosol measurements, *NASA SP-421*, 127-136, 1977.
- Perry, K. D., and P. V. Hobbs, Further evidence for particle nucleation in clear air adjacent to marine cumulus clouds, *J. Geophys. Res.*, 99, 22803-22818, 1994.
- Peter, Th., C. Brühl and P. J. Crutzen, PSC-formation probability caused by high-flying aircraft, *Geophys. Res. Lett.*, 18, 1465-1468, 1991.
- Petzold, A., A. Döpelheuer, C. A. Brock and F. Schröder, In situ observations and model calculations of black carbon emissions by aircraft at cruise altitude, *J. Geophys. Res.*, 104, 22171-22181, 1999.
- Petzold, A., C. Hoell, B. Kärcher, J. Beuermann, C. Schiller, H. Ziereis and H. Schlager, In situ observations of aerosol properties above ice saturation in the polar tropopause region, *J. Geophys. Res.*, 105, 29387-29395, 2000.
- Pinnick, R. G., and D. J. Hofmann, Efficiency of light-scattering aerosol particle counters, *Appl. Optics*, 12, 2593-2597, 1973.
- Pinnick, R. G., J. M. Rosen and D. J. Hofmann, Measured light scattering properties of individual aerosol particles compared to Mie scattering theory, *Appl. Optics*, 12, 37-41, 1973.
- Pinnick, R. G., J. M. Rosen and D. J. Hofmann, Stratospheric aerosol measurements III: Optical model calculations. *J. Atmos. Sci.*, 33, 304-314, 1976.
- Pinto, J. P., R. P. Turco and O. B. Toon, Self-limiting physical and chemical effects in volcanic eruption clouds, *J. Geophys. Res.*, 94, 11165-11174, 1989.
- Pitari, G., and E. Mancini, Short-term climatic impact of the 1991 volcanic eruption of Mt. Pinatubo and effects on atmospheric tracers, *Nat. Hazards Earth Syst. Sci.*, 2, 91-108, 2002.
- Pitari, G., E. Mancini and A. Bregman, Climate forcing of subsonic aviation: Indirect role of sulfate particles via heterogeneous chemistry, *Geophys. Res. Lett.*, 29, 2057, doi: 10.1029/2002GL015705, 2002.
- Pitari, G., E. Mancini and V. Grewe, Deep convective transport in a two-dimensional model: Effects on lower stratospheric aerosols and ozone, *Meteorol. Z.*, 11, 187-196, 2002.
- Pitari, G., E. Mancini, V. Rizi and D. T. Shindell, Impact of future climate and emission changes on stratospheric aerosols and ozone, *J. Atmos. Sci.*, 59, 414-440, 2002.

- Pitts, M. C., and L. W. Thomason, The impact of the eruptions of Mount Pinatubo and Cerro Hudson on Antarctic aerosol levels during the 1991 austral spring, *Geophys. Res. Lett.*, *20*, 2451, 1993.
- Plumb, R. A., A "tropical pipe" model of stratospheric transport, *J. Geophys. Res.-Atmos.*, *101* (D2), 3957-3972, 1996.
- Pollack, J. B., Toon, O. B. C. Sagan, A. Summers, B. Baldwin and W. V. Camp, Volcanic explosions and climate change: A theoretical assessment, *J. Geophys. Res.*, *81*, 1071-1083, 1976.
- Poole, L. R., and M. C. Pitts, Polar stratospheric cloud climatology based on Stratospheric Aerosol Measurement II observations from 1978 to 1989, *J. Geophys. Res.*, *99*, 13083-13089, 1994.
- Prados, A. I., G. E. Nedoluha, R. M. Bevilacqua, D. R. Allen, K. W. Hoppel, POAM III ozone in the upper troposphere and lowermost stratosphere: Seasonal variability and comparisons to aircraft observations, *J. Geophys. Res.*, *108* (D7), doi: 10.1029/2002JD002819, 2003.
- Prather, M. J., Catastrophic loss of stratospheric ozone in dense volcanic clouds, *J. Geophys. Res.*, *97*, 10187-10191, 1992.
- Prather, M. J., and D. J. Jacob, A persistent imbalance in HO_x and NO_x photochemistry of the upper troposphere driven by deep tropical convection, *Geophys. Res. Lett.*, *24*, 3189-3192, 1997.
- Prospero, J. M., D. L. Savoie and R. Arimoto, Long-term record of nss-sulfate and nitrate in aerosols on Midway Island, 1981-2000: Evidence of increased (now decreasing?) anthropogenic emissions from Asia, *J. Geophys. Res.*, *108* (D1), 4019, doi:10.1029/2001JD001524, 2003.
- Pueschel, R. F., K. A. Boering, S. Verma, S. D. Howard, G. V. Ferry, J. Goodman, D. A. Allen and P. Hamill, Soot aerosol in the lower stratosphere: Pole-to-pole variability and contributions by aircraft, *J. Geophys. Res.*, *102*, 13113-13118, 1997.
- Pueschel, R. F., S. Verma and H. Rohatschek, Vertical transport of anthropogenic soot aerosol into the middle atmosphere, *J. Geophys. Res.*, *105*, 3727-3736, 2000.
- Rahmes, T. F., A. H. Omar and D. J. Wuebbles, Atmospheric distribution of soot particles by current and future aircraft fleets and resulting radiative forcing of climate, *J. Geophys. Res.*, *103*, 31657-31667, 1998.
- Ramaswamy, V., M.-L. Chanin, J. Angell, J. Barnett, D. Gaffen, M. Gelman, P. Keckhut, Y. Koshelkov, K. Labitzke, J.-J.R. Lin, A. O'Neill, J. Nash, W. Randel, R. Rood, K. Shine, M. Shiotani and R. Swinbank, Stratospheric temperature trends: observations and model simulations. *Rev. Geophysics*, *39*, 71-122, 2001.
- Randall, C. E., R. M. Bevilacqua, J. D. Lumpe and K. W. Hoppel, Validation of POAM III aerosols: comparison to SAGE II and HALOE, *J. Geophys. Res.*, *106*, 27525-27536, 2001.
- Randall, C. E., R. M. Bevilacqua, J. D. Lumpe, K. W. Hoppel, D. W. Rusch and E. P. Shettle, Comparison of polar ozone and aerosol measurement (POAM) II and stratospheric aerosol and gas experiment (SAGE) II aerosol extinction measurements from 1994 to 1996, *J. Geophys. Res.*, *105*, 3929-3942, 2000.
- Randall, C. E., D. W. Rusch, J. J. Olivero, R. M. Bevilacqua, L. R. Poole, J. D. Lumpe, M. D. Fromm, K. W. Hoppel, J. S. Hornstein and E. P. Shettle, An Overview of POAM II Aerosol Measurements at 1.06 um, *Geophys. Res. Lett.*, *23*, 3195-3198, 1996.
- Randel, W. J., and F. Wu, TOMS total ozone trends in potential vorticity coordinates, *Geophys. Res. Lett.*, *22* (6), 683-686, 1995.
- Read, W. G., L. Froidevaux and J. W. Waters, Microwave limb sounder measurements of stratospheric SO₂ from the Mt. Pinatubo volcano, *Geophys. Res. Lett.*, *20*, 1299-1302, 1993.
- Reiner, T., and F. Arnold, Stratospheric SO₃: Upper limits inferred from ion composition measurements - Implications for H₂SO₄ and aerosol formation, *Geophys. Res. Lett.*, *24*, 1751-1754, 1997.

- Reiner, T., O. Moehler and F. Arnold, Improved atmospheric trace gas measurements with an aircraft-based tandem mass spectrometer: Ion identification by mass-selected fragmentation studies, *J. Geophys. Res.*, *103* (D23), 31309-31320, 1998.
- Reiner, T., D. Sprung, C. Jost, R. Gabriel, O. L. Mayol-Bracero and M. O. Andreae, Chemical characterization of pollution layers over the tropical Indian Ocean: signatures of emissions from biomass and fossil fuel burning, *J. Geophys. Res.*, *106* (D22), 28497-28510, 2001.
- Reiter, R., H. Jäger, W. Carnuth and W. Funk, The stratospheric aerosol layer observed by lidar since October 1976. A contribution to the problem of hemispheric climate, *Arch. Met. Geoph. Biokl., Ser. B*, *27*, 121-149, 1979.
- Rinsland, C. P., A. Goldman, E. Mahieu, R. Zander, J. Notholt, N. B. Jones, D. W. T. Griffith, T. M. Stephen and L. S. Liou, Ground-based infrared spectroscopic measurements of carbonyl sulfide: free tropospheric trends from a 24-year time series of solar absorption measurements, *J. Geophys. Res.*, *107* (D22), 4657, doi:10.1029/2002JD002522, 2002.
- Rinsland, C. P., M. R. Gunson, M. K. W. Ko, D. K. Weisenstein, R. Zander, M. C. Abrams, A. Goldman, N. D. Sze and G. K. Yue, H₂SO₄ photolysis: A source of sulfur dioxide in the upper stratosphere, *Geophys. Res. Lett.*, *22*, 1109-1112, 1995.
- Rinsland, C. P., E. Mahieu, R. Zander, M. R. Gunson, R. J. Salawitch, A. Y. Chang, A. Goldman, M. C. Abrams, M. M. Abbas, M. J. Newchurch and F. W. Irion, Trends of OCS, HCN, SF₆, CHClF₂ (HCFC-22) in the lower stratosphere from 1985 to 1994 Atmospheric Trace Molecule Spectroscopy experiment measurements near 30°N latitude, *Geophys. Res. Lett.*, *23*, 2349-2352, 1996.
- Rinsland, C. P., R. Zander, E. Mahieu, P. Demoulin, A. Goldman, D. H. Ehhalt and J. Rudolph, Ground-based infrared measurements of carbonyl sulfide total column abundances: Long-term trends and variability, *J. Geophys. Res.*, *97*, 5995-6002, 1992.
- Rizzi, V., F. Masci, G. Redaelli, P. Di Carlo, M. Iarlori, G. Visconti and L. W. Thomason, Lidar and SAGE II observations of Shishaldin volcano aerosols and lower stratospheric transport, *Geophys. Res. Lett.*, *27*, 3445-3449, 2000.
- Robock, A., The Mount St. Helens volcanic eruption of 18 May 1980: Minimal climatic effect, *Science*, *212*, 1383-1384, 1981
- Roche, A. E., J. B. Kumer, J. L. Mergenthaler, G. A. Ely, W. G. Uplinger, J. F. Potter, T. C. James and L. W. Sterritt, The cryogenic limb array etalon spectrometer (CLAES) on UARS: Experiment description and performance, *J. Geophys. Res.*, *98*, 10763-10775, 1993.
- Rodgers, C. D., Retrieval of atmospheric temperature and composition from remote measurements of thermal radiation, *Rev. Geophys.*, *14*, 609-624, 1976.
- Rodhe, H., Human impact on the atmospheric sulfur balance, *Tellus*, *51* A-B, 110-122, 1999.
- Roeckner, E., K. Arpe, L. Bengtsson, M. Christoph, M. Claussen, L. Dümenil, M. Esch, M. Giorgetta, U. Schlese and U. Schulzweida, The atmospheric general circulation model ECHAM-4: Model description and simulation of present-day climate, *Rep. 218, Max-Planck Inst. für Meteorol.*, Hamburg, Germany, 1996.
- Romakkaniemi, S., H. Kokkola, A. Petzold and A. Laaksonen, Growth of upper tropospheric aerosols due to uptake of HNO₃, *Atmos. Chem. Phys.*, *4*, 549-556, 2004.
- Rosen, J. M., The vertical distribution of dust to 30 km, *J. Geophys. Res.*, *69*, 4673-4676, 1964.
- Rosen, J. M., *Calibration of the University of Wyoming Backscattersonde 1999*, Copy available on request, December 2000.
- Rosen, J. M., and D. J. Hofmann, Unusual behavior in the condensation nuclei concentration at 30 km, *J. Geophys. Res.*, *88*, 3725-3731, 1983.
- Rosen, J. M., and D. J. Hofmann, Optical modeling of stratospheric aerosols - present status, *Appl. Opt.*, *25*, 410-419, 1986.
- Rosen, J. M., and N. T. Kjome, The Backscattersonde: a new instrument for atmospheric aerosol research, *Appl. Opt.*, *30*, 1552-1561, 1991b.

- Rosen, J. M., N. T. Kjome, R. L. McKenzie and J. B. Liley, Decay of Mount Pinatubo aerosol at midlatitudes in the northern and southern hemispheres, *J. Geophys. Res.*, *99*, 25733-25739, 1994.
- Rosen, J. M., N. T. Kjome, H. Fast, V. U. Khattatov and V. V. Rudakov, Penetration of Mt. Pinatubo aerosols into the north polar vortex, *Geophys. Res. Lett.*, *19*, 1751-1754, 1992.
- Rosen, J. M., N. T. Kjome and J. B. Liley, Tropospheric aerosol backscatter at a midlatitude site in the northern and southern hemispheres, *J. Geophys. Res.*, *102*, 21329-21339, 1997.
- Rosen, J. M., N. T. Kjome, H. Fast and N. Larsen, Volcanic aerosol and polar stratospheric clouds in the winter 1992/93 north polar vortex, *Geophys. Res. Lett.*, *21*, 61-64, 1994a.
- Rosen, J. M., N. T. Kjome, R. L. McKenzie and J. B. Liley, Decay of Mt. Pinatubo aerosol at midlatitudes in the northern and southern hemispheres, *J. Geophys. Res.*, *99*, 25733-25739, 1994b.
- Rosen, J. M., N. T. Kjome and S. J. Oltmans, Balloon borne observations of backscatter, frost point and ozone in polar stratospheric clouds at the South Pole, *Geophys. Res. Lett.*, *18*, 171-174, 1991a.
- Rosen, J. M., N. T. Kjome and S. J. Oltmans, Simultaneous ozone and polar stratospheric cloud observations at South Pole Station during winter and spring 1991, *J. Geophys. Res.*, *98*, 12741-12751, 1993.
- Rosen, J. M., R. M. Morales, N. T. Kjome, V. W. J. H. Kirchhoff and F. R. da Silva, Equatorial aerosol-ozone structure and variations as observed by balloon-borne backscatter sondes since 1995 at Natal, Brazil (6°S), *J. Geophys. Res.*, *109*, D03201, doi:10.1029/2003JD003715, 2004.
- Rosen, J. M., S. J. Oltmans and W. F. Evans, Balloon borne observations of PSCs, frost point, ozone and nitric acid in the north polar vortex, *Geophys. Res. Lett.*, *16*, 791-794, 1989.
- Rosen, J. M., S. Young, J. Laby, N. Kjome, J. Gras, Springtime aerosol layers in the free troposphere over Australia: Mildura Aerosol Tropospheric Experiment (MATE 98), *J. Geophys. Res.*, *105*, 17833-17842, 2000.
- Rosenlof, K. H., and J. R. Holton, Estimates of the stratospheric residual circulation using the downward control principle, *J. Geophys. Res.*, *98*, 10465-10479, 1993.
- Rowland, F. S., H. Sato, H. Khwaja and S. M. Elliott, The hydrolysis of chlorine nitrate and its possible atmospheric significance, *J. Phys. Chem.*, *90*, 1985-1988, 1986.
- Rusch, D. W., R. T. Clancy, F. G. Eparvier and G. E. Thomas, Solar Mesosphere Explorer satellite measurements of El Chichon stratospheric aerosols 1. Cloud morphology, *J. Geophys. Res.*, *99*, 20525-20532, 1994.
- Russell, J. M. III, L. L. Gordley, J. H. Park, S. R. Drayson, D. H. Hesketh, R. J. Cicerone, A. F. Tuck, J. E. Frederick, J. E. Harries and P. J. Crutzen, The Halogen Occultation Experiment, *J. Geophys. Res.*, *98*, 10777-10797, 1993.
- Russell, L. M., D. H. Lenschow, K. K. Laursen, P. B. Krummel, S. T. Siems, A. R. Bandy, D. C. Thornton and T. S. Bates, Bidirectional mixing in an ACE 1 boundary layer overlain by a second turbulent layer, *J. Geophys. Res.*, *103*, 16411-16432, 1998.
- Russell, P. B., and D. Hake Jr., The post-Fuego stratospheric aerosol: lidar measurements, with radiative and thermal implications, *J. Atmos. Sci.*, *34*, 163-177, 1977.
- Russell, P. B., and P. Hamill, Spatial variation of stratospheric aerosol acidity and model refractive index: Implications of recent results, *J. Atmos. Sci.*, *41*, 1781-1790, 1984.
- Russell, P. B., and M. P. McCormick, SAGE II aerosol data validation and initial data use: An introduction and overview, *J. Geophys. Res.*, *94*, 8335-8338, 1989.
- Russell, P. B., J. M. Livingston, E. G. Dutton, R. F. Pueschel, J. A. Reagan, T. E. DeFoor, M. A. Box, D. Allen, P. Pilewskie, B. M. Herman, S. A. Kinne and D. J. Hofmann, Pinatubo and pre-Pinatubo optical-depth spectra: Mauna Loa measurements, comparisons, inferred particle size distributions, radiative effects, and relationship to lidar data, *J. Geophys. Res.*, *98*, 22969-22985, 1993.

- Russell, P. B., M. P. McCormick, T. J. Swissler, W. P. Chu, J. M. Livingston, W. H. Fuller, J. M. Rosen, D. J. Hofmann, L. R. McMaster, D. C. Woods and T. J. Pepin, Satellite and correlative measurements of the stratospheric aerosol. II: Comparison of measurements made by SAM II, dustsondes, and an airborne lidar, *J. Atmos. Sci.*, *38*, 1296-1312, 1981.
- Russell, P. B., M. P. McCormick, T. J. Swissler, J. M. Rosen, D. J. Hofmann and L. R. McMaster, Satellite and correlative measurements of the stratospheric aerosol. III: Comparison of measurements made by SAM II, SAGE, dustsondes, filters, impactors, and lidar, *J. Atmos. Sci.*, *41*, 1792-1800, 1984.
- Russell, P. B., T. J. Swissler and M. P. McCormick, Methodology for error analysis and simulation of lidar aerosol measurements, *Appl. Opt.*, *18*, 3783-3797, 1979.
- Saltzman, E. S., and D. J. Cooper, Shipboard measurements of atmospheric dimethylsulfide and hydrogen-sulfide in the Caribbean and Gulf of Mexico, *J. Atmos. Chem.*, *7*, 191-209, 1988.
- Sander, S. P., R. R. Friedl, W. B. DeMore, A. R. Ravishankara, D. M. Golden, C. E. Kolb, M. J. Kurylo, R. F. Hampson, R. E. Huie, M. J. Molina and G. K. Moortgat, *Chemical kinetics and photochemical data for use in stratospheric modeling, Supplement to evaluation 12: Update of key reactions*, Evaluation Number 13 JPL Publication 00-3, Jet Propulsion Laboratory, NASA, 2000.
- Sander, S. P., R. R. Friedl, D. M. Golden, M. J. Kurylo, R. E. Huie, V. L. Orkin, G. K. Moortgat, A. R. Ravishankara, C. E. Kolb, M. J. Molina and B. J. Finlayson-Pitts, *Chemical kinetics and photochemical data for use in atmospheric studies*, Evaluation number 14, JPL Publications, 02-25, 1-334, 2003.
- Sasano, Y., Preface, *J. Geophys. Res.*, *107*, D24, 8204, 10.1029/2002JD002155, 2002.
- Sato, M., J. E. Hansen, M. P. McCormick and J. B. Pollack, Stratospheric aerosol optical depths, 1850-1990, *J. Geophys. Res.*, *98*, 22987-22994, 1993.
- Schlager, H., and F. Arnold, Balloon-borne composition measurements of stratospheric negative-ions and inferred sulfuric-acid vapor abundances during the Map-Globus 1983 campaign, *Planet. Space Sci.*, *35*, 693-701, 1987.
- Schneider, M., *Continuous observations of atmospheric trace gases by ground-based FTIR spectroscopy at Izaña observatory, Tenerife Island*, Dissertation, University of Karlsruhe, Karlsruhe, 2002.
- Schnetzler, C. C., G. J. S. Bluth, A. J. Krueger and L. S. Walter, A proposed volcanic sulfur dioxide index (VSI), *J. Geophys. Res.*, *102* (B9), 20087-20092, 1997.
- Schoeberl, M. R., P. K. Bhartia and E. Hilsenrath, Tropical ozone loss following the eruption of Mt. Pinatubo, *Geophys. Res. Lett.*, *20*, 29-32, 1993.
- Schröder, F. P. and J. Ström, Aircraft measurements of submicrometer aerosol particles (>7 nm) in the mid-latitude free troposphere and tropopause region, *Atmos. Res.*, *44*, 333-356, 1997.
- Schröder, F. P., B. Kärcher, M. Fiebig and A. Petzold, Aerosol states in the free troposphere at northern midlatitudes, *J. Geophys. Res.*, *107*, 8126, doi:10.1029/2000JD000194, 2002.
- Schröder, F. P., B. Kärcher, A. Petzold, R. Baumann, R. Busen, C. Hoell and U. Schumann, Ultrafine aerosol particles in aircraft plumes: In situ observations, *Geophys. Res. Lett.*, *25*, 2789-2792, 1998.
- Schumann, U., F. Arnold, R. Busen, J. Curtius, B. Kärcher, A. Kiendler, A. Petzold, H. Schlager, F. Schröder and K.-H. Wohlfrom, Influence of fuel sulfur on the composition of aircraft exhaust plumes: The experiments SULFUR1-7, *J. Geophys. Res.*, *107*, 4247, doi: 10.1029/2001JD000813, 2002.
- Schumann, U., H. Schlager, F. Arnold, J. Ovarlez, H. Kelder, O. Hov, G. Hayman, I. S. A. Isaksen, J. Staehlin and P. D. Whitefield, Pollution from aircraft emissions in the North Atlantic flight corridor: Overview on the POLINAT projects, *J. Geophys. Res.*, *105*, 3605-3631, 2000.

- Sciare, J., N. Mihalopoulos and F. J. Dentener, Interannual variability of atmospheric dimethylsulfide in the southern Indian Ocean, *J. Geophys. Res.*, *105*, 26369-26377, 2000.
- Sedlacek, W.A., E.J. Mroz, A.I. Lazrus and B.W. Gandrud, A decade of stratospheric sulfate measurements compared with observations of volcanic eruptions, *J. Geophys. Res.*, *88*, 3741-3776, 1983.
- Sherwood, S. C., and A. E. Dessler, Convective Mixing near the Tropical Tropopause: Insights from Seasonal Variations, *J. Atm. Sci.*, *60*, 2674-2685, 2003.
- Shipley, S. T., D. H. Tracy, E. W. Eloranta, J. T. Trauger, J. T. Sroga, F. L. Roesler and J. A. Weinman, A High Spectral Resolution Lidar to measure optical scattering properties of atmospheric aerosols, Part I: Instrumentation and theory, *Appl. Opt.*, *23*, 3716-3, 1983
- Shooter, D., Sources and sinks of oceanic hydrogen sulfide – an overview, *Atmos. Env.*, *33*, 3467-3472, 1999.
- Simkin, T., and L. Siebert, *Volcanoes of the World: a Regional Directory, Gazetteer, and Chronology of Volcanism during the last 10,000 Years*, Geoscience Press, 349 pp., 1994.
- Simó, R., and J. Dachs, Global ocean emission of dimethylsulfide predicted from biogeochemical data, *Glob. Biogeochem. Cycles*, *16*, 1078, doi: 10.1029/2001GB001829, 2002.
- Simonich, D. M., and B. R. Clemesha, A History of aerosol measurements at São José dos Campos, Brazil (23 S, 46 W) from 1972 to 1995, *Advances in Atmospheric Remote Sensing with Lidar - Selected papers of the 18th International Laser Radar Conference*, Springer-Verlag, Berlin, Germany, 481-484, 1997.
- Singh, H. B., A. M. Thompson and H. Schlager, SONEX airborne mission and coordinated POLINAT-2 activity: overview and accomplishments, *Geophys. Res. Lett.*, *26*, 3053-3056, 1999.
- Slatt, B. J., D. F. S. Natusch, J. M. Prospero and D. L. Savoie, Hydrogen sulfide in the atmosphere of the northern equatorial Atlantic Ocean and its relation to the global sulfur cycle, *Atmos. Env.*, *12*, 981-991, 1978.
- Solomon, S., Stratospheric ozone depletion: A review of concepts and theory, *Rev. Geophys.*, *37*, 275-316, 1999.
- Solomon, S., R. R. Garcia, F. S. Rowland and D. J. Wuebbles, On the depletion of Antarctic ozone, *Nature*, *321*, 755-758, 1986.
- Solomon, S., R. W. Portman, R. R. Garcia, L. W. Thomason, L. R. Poole and M. P. McCormick, The role of aerosol variability in anthropogenic ozone depletion at northern mid-latitudes, *J. Geophys. Res.*, *101*, 6713-6727, 1996.
- Solomons, T. W. G., *Organic Chemistry*, John Wiley Inc., New York, 1996.
- Sorokin, A., and P. Mirabel, Ion recombination in aircraft exhaust plumes, *Geophys. Res. Lett.*, *28*, 955-958, 2001.
- Sorokin, A., X. Vancassel and P. Mirabel, Emission of ions and charged soot particles by aircraft engines, *Atmos. Chem. Phys.*, *3*, 325-334, 2003.
- SPARC Assessment of Upper Tropospheric and Stratospheric Water Vapor, D. Kley, J. M. Russell III and C. Phillips (Eds.), WCRP 113, WMO/TD – No. 1043, *SPARC Report No. 2*, 2000.
- SPARC/IOC/GAW Assessment of Trends in the Vertical Distribution of Ozone, N. Harris, R. Hudson and C. Phillips (Eds.), *SPARC Report No.1, WMO-Ozone research and Monitoring Project Report No. 43*, 1998.
- Spiro, P. A., D. J. Jacob and J. A. Logan, Global inventory of sulfur emissions with 1° x 1° resolution, *J. Geophys. Res.*, *97*, 6023-6036, 1992.
- Spivakovsky, C. M., J. A. Logan, S. A. Montzka, Y. J. Balkanski, M. Foreman-Fowler, D. B. A. Jones, L. W. Horowitz, A. C. Fusco, C. A. M. Brenninkmeijer, M. J. Prather, S. C. Wofsy and M. B. McElroy, Three-dimensional climatological distribution of tropospheric HO: Update and evaluation, *J. Geophys. Res.*, *105*, 8931-8980, 2000.

- Steele, H. M., and P. Hamill, Effects of temperature and humidity on the growth and optical properties of sulfuric acid-water droplets in the stratosphere, *J. Aerosol Sci.*, *12*, 517-528, 1981.
- Steele, H. M., and R. P. Turco, Retrieval of aerosol size distributions from satellite extinction spectra using constrained linear inversion, *J. Geophys. Res.*, *102*, 16737-16747, 1997.
- Steele, H. M., J. D. Lumpe, C. E. Randall and R. M. Bevilacqua, The climatology of the polar aerosol from POAM instruments, *Phys. Geograph.*, *26*, (1), 2005.
- Steele, H. M., J. D. Lumpe, R. P. Turco, R. M. Bevilacqua and S. T. Massie, Retrieval of aerosol surface area and volume densities from extinction measurements: Application to POAM II and SAGE II, *J. Geophys. Res.*, *104*, 9325-9336, 1999.
- Stefanutti, L., L. Sokolov, S. Balestri, A. R. MacKenzie and V. Khatatov, The M-55 geophysics as a platform for the airborne polar experiment, *J. Atmos. Oceanic Technol.*, *16*(10), 1303-1312, 1999.
- Stenchikov, G., I. Kirchner, A. Robock, H.-F. Graf, J. Antuna, R. Grainger, A. Lambert and L. Thomason, Radiative forcing from the 1991 Mount Pinatubo volcanic eruption, *J. Geophys. Res.*, *103*, 13827-13826, 1998.
- Stern, D. I., *Global sulfur emissions in the 1990s*, Rensselaer Working Papers in Economics No. 0311, Rensselaer Polytechnic Institute, Troy, N.Y., U.S.A., 33 pp, 2003.
- Stevens, B., D. H. Lenschow, G. Vali, H. Gerber, A. Bandy, B. Blomquist, J.-L. Brenguier, C. S. Bretherton, F. Burnet, T. Campos, S. Chai, I. Faloon, D. Friesen, S. Haimov, K. Laursen, D. K. Lilly, S. M. Loehrer, S. P. Malinowsky, B. Morley, M. D. Petters, D. C. Rogers, L. Russell, V. Savic-Jovic, J. R. Snider, D. Straub, M. J. Szumowski, H. Takagi, D. C. Thornton, M. Tschudi, C. Twohy, M. Wetzell and M. C. van Zanten, Dynamics and chemistry of marine stratocumulus – DYCOMS-II, *Bull. Am. Meteorol. Soc.*, *84*, 579-593, 2003a.
- Stevens, B., D. H. Lenschow, I. Falcona, C.-H. Moeng, D. K. Lilly, B. Blomquist, G. Vali, A. Bandy, T. Campos, H. Gerber, S. Haimov, B. Morley and D. Thornton, On entrainment rates in nocturnal marine stratocumulus, *Q. J. R. Meteorol. Soc.*, *129*, 3469-3493, 2003b.
- Stoiber, R. E., S. N. Williams and B. Huebert, Annual contribution of sulfur dioxide to the atmosphere by volcanoes, *J. Volcanol. Geotherm. Res.*, *33*, 1-8, 1987.
- Stothers, R. B., The great Tambora eruption in 1815 and its aftermath, *Science*, *224*, 1191-1198, 1984.
- Stothers, R. B., Major optical depth perturbations to the stratosphere from volcanic eruptions: Pyrheliometric period, 1881-1960, *J. Geophys. Res.*, *101*, 3901-3920, 1996.
- Strawa, A. W., K. Drdla, G. V. Ferry, S. Verma, R. F. Pueschel, M. Yasuda, R. J. Salawitch, R. S. Gao, S. D. Howard, P. T. Bui, M. Loewenstein, J. W. Elkins, K. K. Perkins and R. Cohen, Carbonaceous aerosol (Soot) measured in the lower stratosphere during POLARIS and its role in stratospheric photochemistry, *J. Geophys. Res.*, *104*, 26753-26766, 1999.
- Streets, D. G., N. Y. Tsai, H. Akimoto and K. Oka, Sulfur dioxide emissions in Asia in the period 1985 – 1997, *Atmos. Env.*, *34*, 4413-4424, 2000.
- Sturges, W. T., S. A. Penkett, J. M. Barnola, J. Chappellaz, E. Atlas and V. Stroud, A long-term measurement record of carbonyl sulfide (COS) in two hemispheres from firm air measurements, *Geophys. Res. Lett.*, *28*, 4095-4098, 2001.
- Sunda, W., D. J. Kieber, R. P. Kiene and S. Huntsman, An antioxidant function for DMSP and DMS in marine algae, *Nature*, *418*, 317-320, 2002.
- Tabazadeh, A., O. B. Toon, S. L. Clegg and P. Hamill, A new parameterization of H₂SO₄/H₂O aerosol composition: Atmospheric implications, *Geophys. Res. Lett.*, *24*, 1931-1934, 1997.
- Tabazadeh, A., R. P. Turco and M. Z. Jacobson, A model for studying the composition and chemical effects of stratospheric aerosols, *J. Geophys. Res.*, *99*, 12897-12914, 1994.
- Talbot R. W., J. E. Dibb, B. L. Lefer, J. D. Bradshaw, S. T. Sandholm, D. R. Blake, N. J. Blake, G. W. Sachse, J. E. Collins, B. G. Heikes, J. T. Merrill, G. L. Gregory, B. E. Ander-

- son, H. B. Singh, D. C. Thornton, A. R. Bandy and R. R. Pueschel, Chemical characteristics of continental outflow from Asia to the troposphere over the western Pacific Ocean during February – March 1994: Results from PEM-West B, *J. Geophys. Res.*, *102* (D23), 28255-28274, 1997.
- Talbot, R. W., J. E. Dibb, K. I. Klemm, J. D. Bradshaw, S. T. Sandholm, D. R. Blake, G. W. Sachse, J. Collins, B. G. Heikes, G. L. Gregory, B. E. Anderson, H. B. Singh, D. C. Thornton and J. T. Merrill, Chemical characteristics of continental outflow from Asia during September-October 1991: Results from PEM-West A, *J. Geophys. Res.*, *101*, 1713-1725, 1996.
- Talbot, R. W., J. E. Dibb and M. B. Loomis, Influences of vertical transport on free tropospheric aerosols over the central USA in springtime, *Geophys. Res. Lett.*, *25*, 1367-13770, 1998.
- Tanaka, N., and K. K. Turekian, Use of cosmogenic ^{35}S to determine the rates of removal of atmospheric SO_2 , *Nature*, *352*, 226-228, 1991.
- Thomason, L. W., and S. P. Burton, SAGE II Stratospheric Aerosol Extinction Measurements in the Lower Tropical Stratosphere at Near Non-Volcanic Levels, *Atmos. Chem. Physics. Disc.*, 2005.
- Thomason, L. W., and G. Taha, SAGE III Aerosol Extinction Measurements: Initial Results, *Geophys. Res. Lett.*, *30*, 1631, doi: 10.1029/2003GL017317, 2003.
- Thomason, L. W., and M. T. Osborn, Lidar conversion parameters derived from SAGE II extinction measurements, *Geophys. Res. Lett.*, *19*, 1655-1658, 1992.
- Thomason, L. W., and L. R. Poole, Use of stratospheric aerosol properties as diagnostics of Antarctic vortex processes, *J. Geophys. Res.*, *98*, 23003-23012, 1993.
- Thomason, L. W., S. P. Burton, J. M. Zawodny and N. Iyer, *Species separations and error analysis in SAGE II Version 6.0 data products*, Quadrennial Ozone Symposium, Sapporo, Japan, July 3-8, 2000.
- Thomason, L. W., G. S. Kent, C. R. Trepte and L. R. Poole, A comparison of the stratospheric aerosol background periods of 1979 and 1989-1991, *J. Geophys. Res.*, *102*, 3611-3616, 1997a.
- Thomason, L. W., L. R. Poole and T. R. Deshler, A global climatology of stratospheric aerosol surface area density as deduced from SAGE II: 1984-1994, *J. Geophys. Res.*, *102*, 8967-8976, 1997b.
- Thomason, L. W., J. M. Zawodny, S. P. Burton and N. Iyer, *The SAGE II algorithm: Version 6.0 and on-going developments*, 8th Scientific Assembly of International Association of Meteorology and Atmospheric Sciences, Innsbruck Austria, July 10-18, 2001.
- Thornton, D. C., and A. R. Bandy, Sulfur dioxide and dimethyl sulfide in the Central Pacific troposphere, *J. Atmos. Chem.*, *17*, 1-13, 1993.
- Thornton, D. C., A. R. Bandy, N. Beltz, A. R. Driedger and R. Ferek, Advection of sulfur dioxide over the western Atlantic ocean during CITE 3, *J. Geophys. Res.*, *98*, 23459-23467, 1993.
- Thornton, D. C., A. R. Bandy, B. W. Blomquist and B. E. Anderson, Impact of anthropogenic and biogenic sources and sinks on carbonyl sulfide in the North Pacific troposphere, *J. Geophys. Res.*, *101*, 1873-1881, 1996.
- Thornton, D. C., A. R. Bandy, B. W. Blomquist, A. R. Driedger and T. P. Wade, Sulfur dioxide distributed over the Pacific Ocean 1991-1996, *J. Geophys. Res.*, *104*, 5845-5854, 1999.
- Thornton, D. C., A. R. Bandy, B. W. Blomquist, J. D. Bradshaw and D. R. Blake, Vertical transport of sulfur dioxide and dimethyl sulfide in deep convection and its role in new particle formation, *J. Geophys. Res.*, *102*, 28501-28509, 1997.
- Thornton, D. C., A. R. Bandy and A. R. Driedger III, Sulfur dioxide over the western Atlantic ocean, *Glob. Biogeochem. Cycles*, *1*, 317-328, 1987.
- Thornton, D. C., A. R. Bandy and A. R. Driedger III, Sulfur dioxide in the North American Arctic, *J. Atmos. Chem.*, *9*, 331-346, 1989.

- Thornton, D. C., A. R. Bandy, F. H. Tu, B. W. Blomquist, G. L. Mitchell, W. Nadler and D. H. Lenschow, Fast airborne sulfur dioxide measurements by Atmospheric Pressure Ionization Mass Spectrometry (APIMS), *J. Geophys. Res.*, *107*, 4632, doi:10.1029/2002JD002289, 2002.
- Thuburn, J., and G. C. Craig, On the temperature structure of the tropical stratosphere, *J. Geophys. Res.*, *107* (D2), 10.1029/2001JD000448, 2002.
- Tie, X., X. Lin and G. Brasseur, Two-dimensional coupled dynamical/chemical/microphysical simulation of global distribution of El Chichon volcanic aerosol, *J. Geophys. Res.*, *99*, 16779-16792, 1994.
- Timmreck, C., Three-dimensional simulation of stratospheric background aerosol: First results of a multiannual general circulation model simulation, *J. Geophys. Res.*, *106*, 28313-28332, 2001.
- Timmreck, C., and H.-F. Graf, A microphysical model for simulation of stratospheric aerosol in a climate model, *Meteorol. Z.*, *9*, 263-282, 2000.
- Tisdale, R. T., D. L. Glandorf, M. A. Tolbert and O. B. Toon, Infrared optical constants of low-temperature H₂SO₄ solutions representative of stratospheric sulfate aerosols, *J. Geophys. Res.*, *103*, 25353-25370, 10.1029/98JD02457, 1998.
- Tolbert, M. A., M. J. Rossi and D. M. Golden, Heterogeneous interactions of chlorine nitrate hydrogen chloride and nitric acid with sulfuric acid surfaces at stratospheric temperatures, *Geophys. Res. Lett.*, *15*, 847-850, 1988.
- Torres, A. L., P. J. Maroulis, A. B. Goldberg and A. R. Bandy, Atmospheric OCS measurements on project Gametag, *J. Geophys. Res.*, *85*, 7357-7360, 1980.
- Trepte, C. R., and M. H. Hitchman, Tropical stratospheric circulation deduced from satellite aerosol data, *Nature*, *355*, 626-628, 1992.
- Tu, F. H., D. C. Thornton, A. R. Bandy, G. R. Carmichael, Y. Tang, K. L. Thornhill, G. W. Sachse and D. R. Blake, Long-range transport of sulfur dioxide in the central Pacific, *J. Geophys. Res.*, *109*, D15S08, doi:10.1029/2003JD004309, 2004.
- Tu, F. H., D. C. Thornton, A. R. Bandy, M.-S. Kim, G. Carmichael, Y. Tang, L. Thornhill and G. Sachse, Dynamics and transport of sulfur dioxide over the Yellow Sea during TRACE-P, *J. Geophys. Res.*, *108*, D20, 8790, doi:10.1029/2002JD003227, 2003.
- Tucker, B. J., P. J. Maroulis and A. R. Bandy, Free tropospheric measurements of CS₂ over a 45°N to 45°S latitude range, *Geophys. Res. Lett.*, *12*, 9-11, 1985.
- Turco, R. P., O. B. Toon, P. Hamill and R. C. Whitten, Effects of meteoric debris on stratospheric aerosols and gases, *J. Geophys. Res.*, *86*, 1113-1128, 1981.
- Turco, R. P., R. C. Whitten, O. B. Toon, J. B. Pollac and P. Hamill, OCS, stratospheric aerosols and climate, *Nature*, *283*, 283-286, 1980.
- Turco, R. P., J.-X. Zhao and F. Yu, A new source of tropospheric aerosols: Ion-ion recombination, *Geophys. Res. Lett.*, *25*, 635-638, 1998.
- Turner, S. M., G. Malin, P. D. Nightingale and P. S. Liss, Seasonal variation of dimethyl sulphide in the North Sea and an assessment of fluxes to the atmosphere, *Mar. Chem.*, *54*, 245-262, 1996.
- Turner, S. M., P. D. Nightingale, W. Broadgate and P. S. Liss, The distribution of dimethyl sulphide and dimethylsulfoniopropionate in Antarctic waters and sea ice, *Deep Sea Res., Part II*, *42*, 1059-1080, 1995.
- Twohy, C. H., C. F. Clement, B. W. Gandrud, A. J. Weinheimer, T. L. Campos, D. Baumgardner, W. H. Brune, I. Faloona, G. W. Sachse, S. A. Vay and D. Tan, Deep convection as a source of new particles in the midlatitude upper troposphere, *J. Geophys. Res.-Atmos.*, *107* (D21), art. no.-4560, doi: 10.1029/2001JD000323, 2002.
- Twomey, S. A., *Introduction to the mathematics of inversion in remote sensing indirect measurements*, 243 pp., Elsevier Sci., New York, 1977.
- U.S. Standard Atmosphere, *U.S. Government Printing Office, Washington, D.C.*, 1976.

- Ulshöfer, V. S., G. Uher and M. O. Andreae, Evidence for a winter sink of atmospheric carbonyl sulfide in the northeast Atlantic Ocean, *Geophys. Res. Lett.*, *22*, 2602-2604, 1995.
- Vaida, V., H. G. Kjaergaard, P. E. Hintze and D. J. Donaldson, Photolysis of sulfuric acid vapor by visible solar radiation, *Science*, *299*, 1566-1568, 2003.
- van Aardenne, J. A., F. J. Dentener, J. G. J. Olivier, C. G. M. Klein Goldewijk and J. Lelieveld, A 1° x 1° resolution data set of historical anthropogenic trace gas emissions for the period 1890 - 1990, *Glob. Biogeochem. Cycles*, *15*, 909-928, 2001.
- Van den Berg, A. J., S. M. Turner, F. C. van Duyl and P. Ruardij, Model structure and analysis of dimethylsulfide (DMS) production in the southern North Sea, considering phytoplankton dimethylsulphoniopropionate- (DMSP) lyase and eutrophication effects, *Mar. Ecol. Progr. Ser.*, *145*, 233-244, 1996.
- Vanhellemont F., D. Fussen and C. Bingen, Temporal and spatial distribution of the stratospheric aerosol optical thickness at 1013 nm derived from the ORA experiment after the Pinatubo eruption, *Geophys. Res. Lett.*, *27*, 1647-1649, 2000.
- Vehkamäki, H., M. Kulmala, I. Napari, K. E. J. Lehtinen, C. Timmreck, M. Noppel and A. Laaksonen, An improved parameterization for sulfuric acid/water nucleation rates for tropospheric and stratospheric conditions, *J. Geophys. Res.*, *107*, doi:10.1029/2002JD002184, 2002.
- Viggiano, A. A., and F. Arnold, Extended sulfuric acid vapor concentration measurements in the stratosphere, *Geophys. Res. Lett.*, *8*, 583-586, 1981.
- Voigt, C., H. Schlager, B. P. Luo, A. D. Dornbrack, A. Roiger, P. Stock, J. Curtius, H. Vossing, S. Borrmann, S. Davies, P. Konopka, C. Schiller, G. Shur and T. Peter, Nitric Acid Trihydrate (NAT) formation at low NAT supersaturation in Polar Stratospheric Clouds (PSCs), *Atmos. Chem. Phys.*, *5*, 1371-1380, 2005.
- Wang, P. K., A cloud model interpretation of jumping cirrus above storm top, *Geophys. Res. Lett.*, *31* (18), Art. No. L18106, doi: 10.1029/2004GL020787, 2004.
- Wang, P. H., M. P. McCormick, L. R. McMaster, W. P. Chu, T. J. Swissler, M. T. Osborn, P. B. Russell, V. R. Oberbeck, J. Livingston, J. M. Rosen, D. J. Hofmann, G. W. Grams, W. H. Fuller and G. K. Yue, SAGE II aerosol data validation based on retrieved aerosol model size distribution from SAGE II aerosol measurements, *J. Geophys. Res.*, *94*, 8381-8393, 1989.
- Wang, P. H., P. Minnis, M. P. McCormick, G. S. Kent and K. M. Skeens, A 6-year climatology of cloud occurrence frequency from stratospheric aerosol and gas experiment II observations (1985-1990), *J. Geophys. Res.*, *101*, 29407-29429, 1996.
- Watts, S. F., The mass budgets of carbonyl sulfide, dimethyl sulfide, carbon disulfide and hydrogen sulfide, *Atmos. Env.*, *34*, 761-779, 2000.
- Waugh, D. W., and T. M. Hall, Age of stratospheric air: Theory, observations, and models, *Rev. Geophys.*, *40*, doi:10.1029/2000RG000101, 2002.
- Weisenstein, D. K., M. K. W. Ko, I. G. Dyominov, G. Pitari, L. Ricciardulli, G. Visconti and S. Bekki, The effects of sulfur emissions from HSCT aircraft: A 2-D model intercomparison, *J. Geophys. Res.*, *103*, 1527-1547, 1998.
- Weisenstein, D. K., G. K. Yue, M. K. W. Ko, N. D. Sze, J. M. Rodriguez and C. J. Scott, A two-dimensional model of sulfur species and aerosol, *J. Geophys. Res.*, *102*, 13019-13035, 1997.
- Weiss, P. S., J. E. Johnson, R. H. Gammon and T. A. Bates, Reevaluation of the open ocean source of carbonyl sulfide to the atmosphere, *J. Geophys. Res.*, *100*, 23083-23092, 1995.
- Weisser, C., K. Mauersberger, J. Schreiner, N. Larsen, F. Cairo, A. Adriani, J. Ovarlez and T. Deshler, Composition analysis of liquid particles in the Arctic stratosphere, *Atmos. Chem. Phys. Disc.*, *4*, 2513-2531, 2004.
- Wennberg, P. O., R. C. Cohen, R. M. Stimpfle, J. P. Koplów, J. G. Anderson, R. J. Salawitch, D. W. Fahey, E. L. Woodbridge, E. R. Keim, R. S. Gao, C. R. Webster, R. D. May, D. W. Toohey, L. M. Avallone, M. H. Proffitt, M. Loewenstein, J. R. Podolske, K. R. Chan and S.

- C. Wofsy, Removal of stratospheric O₃ by radicals: In situ measurements, of OH, HO₂, NO, NO₂, ClO, and BrO, *Science*, 266, 398-404, 1994.
- Wilson J. C., E. D. Blackshear and J. H. Hyun, The function and response of an improved stratospheric condensation nucleus counter, *J. Geophys. Res. (Oceans and Atmospheres)*, 88, 6781-6785, 1983.
- Wilson, J. C., M. R. Stolzenburg, W. E. Clark, M. Loewenstein, G. V. Ferry, K. R. Chan and K. K. Kelly, Stratospheric sulfate aerosol in and near the northern-hemisphere polar vortex - the morphology of the sulfate layer, multimodal size distributions, and the effect of denitri-fication, *J. Geophys. Res.*, 97 (D8), 7997-8013, 1992.
- WMO (World Meteorological Organization), *Scientific Assessment of Ozone Depletion: 2002*, Global Ozone Research and Monitoring Project—Report No. 47, 498 pp., Geneva, 2003.
- Wohlfrom, K.-H., S. Eichkorn, F. Arnold and P. Schulte, Massive positive and negative ions in the wake of a jet aircraft: Detection by a novel aircraft-based large ion mass spectrometer, *Geophys. Res. Lett.*, 27, 3853-3856, 2000.
- Wolz, G., and H.-W. Georgii, Large scale distribution of sulfur dioxide results from the TRO-POZ II flights, *Idojaras*, 100, 23-41, 1996.
- Woods, D. C., M. T. Osborn, D. M. Winker, R. J. DeCoursey and O. Youngbluth, 48-inch lidar aerosol measurements taken at the Langley Research Center: July 1991 to December 1992, *NASA RP 1334*, July 1994.
- Wrenn, S. J., L. J. Butler, G. A. Rowland, C. J. H. Knox and L. F. Phillips, The necessity for multiphoton processes in the 193-nm photochemistry of sulphuric acid aerosols, *J. Photoch. Photobio. A.*, 129, 101-104, 1999.
- Xie, H., R. M. Moore and W. L. Miller, Photochemical production of carbon disulphide in seawater, *J. Geophys. Res.*, 103, 5635-5644, 1998.
- Xu, X., H. G. Bingemer, H.-W. Georgii and U. Schmidt, Measurements of carbonyl sulfide (COS) in surface seawater and marine air, and estimates of the air-sea flux from observa-tions during two Atlantic cruises, *J. Geophys. Res.*, 106, 3491-3502, 2001.
- Xu, X., *Investigations into the tropospheric cycle of COS: Atmospheric distribution, air-sea and air-vegetation exchanges*, Dissertation, University of Frankfurt, Frankfurt am Main, 2001.
- Yin, Y., K. S. Carslaw and D. J. Parker, Redistribution of trace gases by convective clouds – mixed phase processes, *Atmos. Chem. Phys.*, 3, 293-306, 2002.
- Yu, F. Q., and R. P. Turco, Ultrafine aerosol formation via ion-mediated nucleation, *Geophys. Res. Lett.*, 27, 883-886, 2000.
- Yu, F. Q., and R. P. Turco, Evolution of aircraft-generated volatile particles in the far wake regime: Potential contributions to ambient CCN IN, *Geophys. Res. Lett.*, 26, 1703-1706, 1999.
- Yue, G. K., A new approach to retrieval of aerosol size distributions and integral properties from SAGE II aerosol extinction spectra, *J. Geophys. Res.*, 104, 27491-27506, 1999.
- Yue, G. K., and A. Deepak, Latitudinal and altitudinal variation of size distribution of strato-spheric aerosols inferred from sage aerosol extinction coefficient measurements at 2 wave-lengths, *Geophys. Res. Lett.*, 11, 999-1002, 1984.
- Yue, G. K., M. P. McCormick and E.-W. Chiou, Stratospheric aerosol optical depth observed by the SAGE II experiment: Decay of the El Chichon and Ruiz volcanic perturbations., *J. Geophys. Res.*, 96, 5209-5219, 1991.
- Yue, G. K., L. R. Poole, M. P. McCormick, R. E. Veiga, P.-H. Wang, V. Rizi, F. Masci, A. D’Altorio and G. Visconti, Comparing simultaneous stratospheric aerosols and ozone lidar measurements with SAGE II data after the Mount Pinatubo eruption, *Geophys. Res. Lett.*, 22, 1881-1884, 1995.

- Yue, G. K., R. E. Veiga and P.-H. Wang, SAGE II observations of a previously unreported stratospheric volcanic aerosol cloud in the northern polar summer of 1990, *Geophys. Res. Lett.*, *21*, 429-432, 1994.
- Yvon, S. A., D. J. Cooper, V. Koropalov and E. S. Saltzman, Atmospheric hydrogen sulfide over the equatorial Pacific (SAGA 3), *J. Geophys. Res.*, *98*, 16979-16983, 1993.
- Zander, R., C. P. Rinsland, C. B. Farmer, J. Namkung, R. H. Norton and J. M. Russell III, Concentrations of carbonyl sulfide and hydrogen cyanide in the free upper troposphere and lower stratosphere deduced from ATMOS/Spacelab 3 infrared solar occultation spectra, *J. Geophys. Res.*, *93*, 1663-1678, 1988.
- Zawodny, J. M., L. W. Thomason, N. Iyer and S. P. Burton, Version 6.0 Refinements to the SAGE II transmission profiles, in: *Proc. Quadrennial Ozone Symposium, July 3-8, 2000, Sapporo, Japan*, 2000.
- Zemmelink, H. J., W. W. C. Gieskes, W. Kleessen, H. W. de Groot, H. J. W. de Baar, J. W. H. Dacey, E. J. Hintsa and W. R. McGillis, Simultaneous use of relaxed eddy accumulation and gradient flux techniques for the measurement of sea-to-air exchange of dimethyl sulphide, *Atmos. Env.*, *36*, 5709-5717, 2002.
- Zhao, J., O. B. Toon and R. P. Turco, Origin of condensation nuclei in the springtime polar stratosphere, *J. Geophys. Res.*, *100*, 5215-5227, 1995a.
- Zhao, J., R. P. Turco and O. B. Toon, A model simulation of Pinatubo volcanic aerosols in the stratosphere, *J. Geophys. Res.*, *100*, 7315-7328, 1995b.
- Zhao, R., *Laboratory measurements of the response of optical particle counters to particles of different shape and refractive index*, M.S. Thesis, University of Wyoming, 57 pp, 1996.

Appendix I

WCRP Reports

- WCRP-1 VALIDATION OF SATELLITE PRECIPITATION MEASUREMENTS FOR THE GLOBAL PRECIPITATION CLIMATOLOGY PROJECT (Report of an International Workshop, Washington, D.C., 17-21 November 1986) (WMO/TD-No. 203) (out of print)
- WCRP-2 WOCE CORE PROJECT 1 PLANNING MEETING ON THE GLOBAL DESCRIPTION (Washington, D.C., 10-14 November 1986) (WMO/TD-No. 205) (out of print)
- WCRP-3 INTERNATIONAL SATELLITE CLOUD CLIMATOLOGY PROJECT (ISCCP) WORKING GROUP ON DATA MANAGEMENT (Report of the Sixth Session, Fort Collins, U.S.A., 16-18 June 1987) (WMO/TD-No. 210) (out of print)
- WCRP-4 JSC/CCCO TOGA NUMERICAL EXPERIMENTATION GROUP (Report of the First Session, Unesco, Paris, France, 25-26 June 1987) (WMO/TD-No. 204) (out of print)
- WCRP-5 CONCEPT OF THE GLOBAL ENERGY AND WATER CYCLE EXPERIMENT (Report of the JSC Study Group on GEWEX, Montreal, Canada, 8-12 June 1987 and Pasadena, U.S.A., 5-9 January 1988) (WMO/TD-No. 215) (out of print)
- WCRP-6 INTERNATIONAL WORKING GROUP ON DATA MANAGEMENT FOR THE GLOBAL PRECIPITATION CLIMATOLOGY PROJECT (Report of the Second Session, Madison, U.S.A., 9-11 September 1988) (WMO/TD-No. 221) (out of print)
- WCRP-7 CAS GROUP OF RAPPORTEURS ON CLIMATE (Leningrad, U.S.S.R., 28 October-1 November 1985) (WMO/TD-No. 226) (out of print)
- WCRP-8 JSC WORKING GROUP ON LAND SURFACE PROCESSES AND CLIMATE (Report of the Third Session, Manhattan, U.S.A., 29 June-3 July 1987) (WMO/TD-No. 232) (out of print)
- WCRP-9 AEROSOLS, CLOUDS AND OTHER CLIMATICALLY IMPORTANT PARAMETERS: LIDAR APPLICATIONS AND NETWORKS (Report of a Meeting of Experts, Geneva, Switzerland, 10-12 December 1985) (WMO/TD-No. 233) (out of print)
- WCRP-10 RADIATION AND CLIMATE (Report of the First Session, JSC Working Group on Radiative Fluxes, Greenbelt, U.S.A., 14-17 December 1987) (WMO/TD-No. 235) (out of print)
- WCRP-11 WORLD OCEAN CIRCULATION EXPERIMENT - IMPLEMENTATION PLAN - DETAILED REQUIREMENTS (Volume I) (WMO/TD-No. 242) (out of print)

- WCRP-12 WORLD OCEAN CIRCULATION EXPERIMENT - IMPLEMENTATION PLAN - SCIENTIFIC BACKGROUND (Volume II) (WMO/TD-No. 243) (out of print)
- WCRP-13 RADIATION AND CLIMATE (Report of the Seventh Session of the International Satellite Cloud Climatology Project (ISCCP) Working Group on Data Management, Banff, Canada, 6-8 July 1988) (WMO/TD-No. 252) (out of print)
- WCRP-14 AN EXPERIMENTAL CLOUD LIDAR PILOT STUDY (ECLIPS) (Report of the WCRP/CSIRO Workshop on Cloud Base Measurement, CSIRO, Mordialloc, Victoria, Australia, 29 February-3 March 1988) (WMO/TD-No. 251) (out of print)
- WCRP-15 MODELLING THE SENSITIVITY AND VARIATIONS OF THE OCEAN-ATMOSPHERE SYSTEM (Report of a Workshop at the European Centre for Medium Range Weather Forecasts, 11-13 May 1988) (WMO/TD-No. 254) (out of print)
- WCRP-16 GLOBAL DATA ASSIMILATION PROGRAMME FOR AIR-SEA FLUXES (Report of the JSC/CCCO Working Group on Air-Sea Fluxes, October 1988) (WMO/TD-No. 257) (out of print)
- WCRP-17 JSC/CCCO TOGA SCIENTIFIC STEERING GROUP (Report of the Seventh Session, Cairns, Queensland, Australia, 11-15 July 1988) (WMO/TD-No. 259) (out of print)
- WCRP-18 SEA ICE AND CLIMATE (Report of the Third Session of the Working Group on Sea Ice and Climate, Oslo, 31 May-3 June 1988) (WMO/TD-No. 272) (out of print)
- WCRP-19 THE GLOBAL PRECIPITATION CLIMATOLOGY PROJECT (Report of the third Session of the International Working Group on Data Management, Darmstadt, FRG, 13-15 July 1988) (WMO/TD-No. 274) (out of print)
- WCRP-20 RADIATION AND CLIMATE (Report of the Second Session of the WCRP Working Group on Radiative Fluxes, Geneva, Switzerland, 19-21 October 1988) (WMO/TD-No. 291) (out of print)
- WCRP-21 INTERNATIONAL WOCE SCIENTIFIC CONFERENCE (Report of the International WOCE Scientific Conference, Unesco, Paris, 28 November-2 December 1988) (WMO/TD-No. 295) (out of print)
- WCRP-22 THE GLOBAL WATER RUNOFF DATA PROJECT (Workshop on the Global Runoff Data Set and Grid estimation, Koblenz, FRG, 10-15 November 1988) (WMO/TD-No. 302) (out of print)
- WCRP-23 WOCE SURFACE FLUX DETERMINATIONS - A STRATEGY FOR IN SITU MEASUREMENTS (Report of the Working Group on In Situ Measurements for Fluxes, La Jolla, California, U.S.A., 27 February-3 March 1989) (WMO/TD-No. 304) (out of print)
- WCRP-24 JSC/CCCO TOGA NUMERICAL EXPERIMENTATION GROUP (Report of the Second Session, Royal Society, London, U.K., 15-16 December 1988) (WMO/TD-No. 307) (out of print)

-
- WCRP-25 GLOBAL ENERGY AND WATER CYCLE EXPERIMENT (GEWEX) (Report of the First Session of the JSC Scientific Steering Group for GEWEX, Pasadena, U.S.A., 7-10 February 1989) (WMO/TD-No. 321) (out of print)
- WCRP-26 WOCE GLOBAL SURFACE VELOCITY PROGRAMME (SVP) (Workshop Report of WOCE/SVP Planning Committee and TOGA Pan-Pacific Surface Current Study, Miami, Florida, U.S.A., 25-26 April 1988) (WMO/TD-No. 323) (out of print)
- WCRP-27 DIAGNOSTICS OF THE GLOBAL ATMOSPHERIC CIRCULATION (Based on ECMWF analyses 1979-1989, Department of Meteorology, University of Reading, Compiled as part of the U.K. Universities Global Atmospheric Modelling Project) (WMO/TD-No. 326) (out of print)
- WCRP-28 INVERSION OF OCEAN GENERAL CIRCULATION MODELS (Report of the CCCO/WOCE Workshop, London, 10-12 July 1989) (WMO/TD-No. 331) (out of print)
- WCRP-29 CAS WORKING GROUP ON CLIMATE RESEARCH (Report of Session, Geneva, 22-26 May 1989) (WMO/TD-No. 333) (out of print)
- WCRP-30 WOCE - FLOW STATISTICS FROM LONG-TERM CURRENT METER MOORINGS: THE GLOBAL DATA SET IN JANUARY 1989 (Report prepared by Robert R. Dickinson, Eddy Statistics Scientific Panel) (WMO/TD-No. 337) (out of print)
- WCRP-31 JSC/CCCO TOGA SCIENTIFIC STEERING GROUP (Report of the Eighth Session, Hamburg, FRG, 18-22 September 1989) (WMO/TD-No. 338) (out of print)
- WCRP-32 JSC/CCCO TOGA NUMERICAL EXPERIMENTATION GROUP (Report of the Third Session, Hamburg, FRG, 18-20 September 1989) (WMO/TD-No. 339) (out of print)
- WCRP-33 TOGA MONSOON CLIMATE RESEARCH (Report of the First Session of the Monsoon Numerical Experimentation Group, Hamburg, FRG, 21-22 September 1989) (WMO/TD-No. 349) (out of print)
- WCRP-34 THE GLOBAL PRECIPITATION CLIMATOLOGY PROJECT (Report of the Fourth Session of the International Working Group on Data Management, Bristol, U.K., 26-28 July 1989) (WMO/TD-No. 356) (out of print)
- WCRP-35 RADIATION AND CLIMATE (Report of the Third Session of the WCRP Working Group on Radiative Fluxes, Fort Lauderdale, U.S.A., 12-15 December 1989) (WMO/TD-No. 364) (out of print)
- WCRP-36 LAND-SURFACE PHYSICAL AND BIOLOGICAL PROCESSES (Report of an ad-hoc Joint Meeting of the IGBP Co-ordinating Panel No. 3 and WCRP Experts, Paris, France, 24-26 October 1989) (WMO/TD-No. 368) (out of print)
- WCRP-37 GLOBAL ENERGY AND WATER CYCLE EXPERIMENT (Report of the Workshop to Evaluate the Need for a Rain Radar in Polar Orbit for GEWEX, Greenbelt, U.S.A., 25-26 October 1989) (WMO/TD-No. 369) (out of print)
- WCRP-38 GLOBAL ENERGY AND WATER CYCLE EXPERIMENT (Report of the First Session of the WCRP-GEWEX/IGBP-CP3 Joint Working Group on Land-

- Surface Experiments, Wallingford, U.K., 25-26 January 1990) (WMO/TD-No. 370) (out of print)
- WCRP-39 RADIATION AND CLIMATE (Intercomparison of Radiation Codes in Climate Models, Report of Workshop, Paris, France, 15-17 August 1988) (WMO/TD-No. 371) (out of print)
- WCRP-40 GLOBAL ENERGY AND WATER CYCLE EXPERIMENT (Scientific Plan), August 1990 (WMO/TD-No. 376) (out of print)
- WCRP-41 SEA-ICE AND CLIMATE (Report of the Fourth Session of the Working Group, Rome, Italy, 20-23 November 1989) (WMO/TD-No. 377) (out of print)
- WCRP-42 PLANETARY BOUNDARY LAYER (Model Evaluation Workshop, Reading, U.K., 14-15 August 1989) (WMO/TD-No. 378) (out of print)
- WCRP-43 INTERNATIONAL TOGA SCIENTIFIC CONFERENCE PROCEEDINGS (Honolulu, U.S.A., 16-20 July 1990) (WMO/TD-No. 379) (out of print)
- WCRP-44 GLOBAL ENERGY AND WATER CYCLE EXPERIMENT (Report of the 2nd Session of the JSC Scientific Steering Group, Paris, France, 15-19 January 1990) (WMO/TD-No. 383) (out of print)
- WCRP-45 SEA ICE NUMERICAL EXPERIMENTATION GROUP (SINEG) (Report of the First Session, Washington, D.C., 23-25 May 1989) (WMO/TD-No. 384) (out of print)
- WCRP-46 EARTH OBSERVING SYSTEM FOR CLIMATE RESEARCH (Report of a WCRP Planning Meeting, Reading, U.K., 2-3 July 1990) (WMO/TD-No. 388) (out of print)
- WCRP-47 JSC/CCCO TOGA SCIENTIFIC STEERING GROUP (Report of the Ninth Session, Kona, Hawaii, U.S.A., 23-25 July 1990) (WMO/TD-No. 387) (out of print)
- WCRP-48 SPACE OBSERVATIONS OF TROPOSPHERIC AEROSOLS AND COMPLEMENTARY MEASUREMENTS (Report of experts meeting at Science and Technology Corporation, Hampton, Virginia, U.S.A., 15-18 November 1989) (WMO/TD-No. 389) (out of print)
- WCRP-49 TOGA MONSOON CLIMATE RESEARCH (Report of the Second Session of the Monsoon Numerical Experimentation Group, Kona, Hawaii, U.S.A., 26-27 July 1990) (WMO/TD-No. 392) (out of print)
- WCRP-50 TOGA NUMERICAL EXPERIMENTATION GROUP (Report of the Fourth Session, Palisades, New York, U.S.A., 13-14 June 1990) (WMO/TD-No. 393) (out of print)
- WCRP-51 RADIATION AND CLIMATE (Report of the First Session, International Working Group on Data Management for WCRP Radiation Projects, New York City, U.S.A., 21-23 May 1990) (WMO/TD-No. 398) (out of print)
- WCRP-52 THE RADIATIVE EFFECTS OF CLOUDS AND THEIR IMPACT ON CLIMATE (Review prepared by Dr. A. Arking at request of IAMAP Radiation Commission) (WMO/TD-No. 399) (out of print)

-
- WCRP-53 CAS/JSC WORKING GROUP ON NUMERICAL EXPERIMENTATION (Report of the Sixth Session, Melbourne, Australia, 24-28 September 1990) (WMO/TD-No. 405) (out of print)
- WCRP-54 RADIATION AND CLIMATE (Workshop on Implementation of the Baseline Surface Radiation Network, Washington, D.C., 3-5 December 1990) (WMO/TD-No. 406) (out of print)
- WCRP-55 GLOBAL CLIMATE MODELLING (Report of First Session of WCRP Steering Group on Global Climate Modelling, Geneva, Switzerland, 5-8 November 1990) (WMO/TD-No. 411) (out of print)
- WCRP-56 THE GLOBAL CLIMATE OBSERVING SYSTEM (Report of a meeting convened by the Chairman of the Joint Scientific Committee for the WCRP, Winchester, U.K., 14-15 January 1991) (WMO/TD-No. 412) (out of print)
- WCRP-57 GLOBAL ENERGY AND WATER CYCLE EXPERIMENT (Report of the 3rd Session of the JSC Scientific Steering Group, Hamilton, Bermuda, 21-25 January 1991) (WMO/TD-No. 424) (out of print)
- WCRP-58 INTERCOMPARISON OF CLIMATES SIMULATED BY 14 ATMOSPHERIC GENERAL CIRCULATION MODELS (CAS/JSC Working Group on Numerical Experimentation, prepared by Dr. G.J. Boer et al) (WMO/TD-No. 425) (out of print)
- WCRP-59 INTERACTION BETWEEN AEROSOLS AND CLOUDS (Report of Experts Meeting, Hampton, Virginia, U.S.A., 5-7 February 1991) (WMO/TD-No. 423) (out of print)
- WCRP-60 THE GLOBAL PRECIPITATION CLIMATOLOGY PROJECT (Report of the Fifth Session of the International Working Group on Data Management, Laurel, Maryland, U.S.A., 20-21 May 1991) (WMO/TD-No. 436)
- WCRP-61 GLOBAL ENERGY AND WATER CYCLE EXPERIMENT (Report of the Second Session of the WCRP-GEWEX/IGBP Core Project on BAHC Joint Working Group on Land-Surface Experiments, Greenbelt, Maryland, U.S.A., 3-4 June 1991) (WMO/TD-No. 437)
- WCRP-62 SEA-ICE AND CLIMATE (Report of a Workshop on Polar Radiation Fluxes and Sea-Ice Modelling, Bremerhaven, Germany, 5-8 November 1990) (WMO/TD-No. 442)
- WCRP-63 JSC/CCCO TOGA SCIENTIFIC STEERING GROUP (Report of the Tenth Session, Gmunden, Austria, 26-29 August 1991) (WMO/TD-No. 441)
- WCRP-64 RADIATION AND CLIMATE (Second Workshop on Implementation of the Baseline Surface Radiation Network, Davos, Switzerland, 6-9 August 1991) (WMO/TD-No. 453)
- WCRP-65 SEA-ICE AND CLIMATE (Report of the Fifth Session of the Working Group, Bremerhaven, Germany, 13-15 June 1991) (WMO/TD-No. 459)
- WCRP-66 GLOBAL ENERGY AND WATER CYCLE EXPERIMENT (Report of the First GEWEX Temperature/Humidity Retrieval Workshop, Greenbelt, U.S.A., 23-26 October 1990) (WMO/TD-No. 460) (out of print)
- WCRP-67 GEWEX CONTINENTAL SCALE INTERNATIONAL PROJECT (Scientific Plan, December 1991) (WMO/TD-No. 461) (out of print)

- WCRP-68 SIMULATION OF INTERANNUAL AND INTRASEASONAL MONSOON VARIABILITY (Report of Workshop, Boulder, CO, U.S.A., 21-24 October 1991) (WMO/TD-No. 470)
- WCRP-69 RADIATION AND CLIMATE (Report of Fourth Session of the WCRP Working Group on Radiative Fluxes, Palm Springs, U.S.A., 24-27 September 1991) (WMO/TD-No. 471)
- WCRP-70 CAS/JSC WORKING GROUP ON NUMERICAL EXPERIMENTATION (Report of the Seventh Session, Boulder, CO, U.S.A., 24-29 October 1991) (WMO/TD-No. 477)
- WCRP-71 GLOBAL CLIMATE MODELLING (Report of Second Session of WCRP Steering Group on Global Climate Modelling, Bristol, U.K., 18-20 November 1991) (WMO/TD-No. 482)
- WCRP-72 SCIENTIFIC CONCEPT OF THE ARCTIC CLIMATE SYSTEM STUDY (ACSYS) (Report of the JSC Study Group on ACSYS, Bremerhaven, Germany, 10-12 June 1991 and London, U.K., 18-19 November 1991) (WMO/TD-No. 486) (out of print)
- WCRP-73 TOGA NUMERICAL EXPERIMENTATION GROUP (Report of the Fifth Session, San Francisco, California, U.S.A., 9-11 December 1991) (WMO/TD-No. 487)
- WCRP-74 GLOBAL ENERGY AND WATER CYCLE EXPERIMENT (Report of the Fourth Session of the JSC Scientific Steering Group for GEWEX, Tokyo, Japan, 27-31 January 1992) (WMO/TD-No. 490)
- WCRP-75 HYDROLOGY AND SURFACE RADIATION IN ATMOSPHERIC MODELS (Report of a GEWEX Workshop, European Centre for Medium-range Weather Forecasts, Reading, U.K., 28 October-1 November 1991) (WMO/TD-No. 492) (out of print)
- WCRP-76 REVIEWS OF MODERN CLIMATE DIAGNOSTIC TECHNIQUES - Satellite data in climate diagnostics, (A. Gruber and P.A. Arkin, November 1992) (WMO/TD-No. 519) (out of print)
- WCRP-77 INTERNATIONAL SATELLITE CLOUD CLIMATOLOGY PROJECT (Radiance Calibration Report, December 1992) (WMO/TD-No. 520) (out of print)
- WCRP-78 GLOBAL OBSERVATIONS, ANALYSES AND SIMULATION OF PRECIPITATION (Report of Workshop, National Meteorological Center, Camp Springs, Maryland, U.S.A., 27-30 October 1992) (WMO/TD-No. 544) (out of print)
- WCRP-79 INTERCOMPARISON OF TROPICAL OCEAN GCMS (TOGA Numerical Experimentation Group, prepared by T. Stockdale et al., April 1993) (WMO/TD-No. 545)
- WCRP-80 SIMULATION AND PREDICTION OF MONSOONS - RECENT RESULTS (TOGA/WGNE Monsoon Numerical Experimentation Group, New Delhi, India, 12-14 January 1993) (WMO/TD-No. 546)

-
- WCRP-81 ANALYSIS METHODS OF PRECIPITATION ON A GLOBAL SCALE (Report of a GEWEX Workshop, Koblenz, Germany, 14-17 September 1992) (WMO/TD-No. 558) (Out of print)
- WCRP-82 INTERCOMPARISON OF SELECTED FEATURES OF THE CONTROL CLIMATES SIMULATED BY COUPLED OCEAN-ATMOSPHERE GENERAL CIRCULATION MODELS (Steering Group on Global Climate Modelling, September 1993) (WMO/TD-No. 574)
- WCRP-83 STRATOSPHERIC PROCESSES AND THEIR ROLE IN CLIMATE (SPARC): INITIAL REVIEW OF OBJECTIVES AND SCIENTIFIC ISSUES (SPARC Scientific Steering Group, December 1993) (WMO/TD-No. 582) (out of print)
- WCRP-84 PROCEEDINGS OF THE INTERNATIONAL CONFERENCE ON MONSOON VARIABILITY AND PREDICTION (Trieste, Italy, 9-13 May 1994) (WMO/TD-No. 619) (Out of print)
- WCRP-85 INITIAL IMPLEMENTATION PLAN FOR THE ARCTIC CLIMATE SYSTEM STUDY (ACSYS) (September 1994) (WMO/TD-No. 627) (out of print)
- WCRP-86 CLOUD-RADIATION INTERACTIONS AND THEIR PARAMETERIZATION IN CLIMATE MODELS (Report of international workshop, Camp Springs, Maryland, U.S.A., 18-20 October 1993) (WMO/TD-No. 648)
- WCRP-87 PROCEEDINGS OF THE WORKSHOP ON GLOBAL COUPLED GENERAL CIRCULATION MODELS (La Jolla, California, USA, 10-12 October 1994) (WMO/TD-No. 655)
- WCRP-88 INTRASEASONAL OSCILLATIONS IN 15 ATMOSPHERIC GENERAL CIRCULATION MODELS (Results from an AMIP diagnostic subproject) (WMO/TD-No. 661)
- WCRP-89 CLIMATE VARIABILITY AND PREDICTABILITY (CLIVAR) Science Plan (August 1995) (WMO/TD-No. 690) (out of print)
- WCRP-90 WORKSHOP ON CLOUD MICROPHYSICS PARAMETERIZATIONS IN GLOBAL ATMOSPHERIC CIRCULATION MODELS (Kananaskis, Alberta, Canada, 23-25 May 1995) (WMO/TD-No. 713)
- WCRP-91 PROCEEDINGS OF THE INTERNATIONAL SCIENTIFIC CONFERENCE ON TOGA (Melbourne, Australia, 2-7 April 1995) (WMO/TD-No. 717)
- WCRP-92 PROCEEDINGS OF THE FIRST INTERNATIONAL AMIP SCIENTIFIC CONFERENCE (Monterey, California, USA, 15-19 May 1995) (WMO/TD-No. 732)
- WCRP-93 PROCEEDINGS OF THE WORKSHOP ON ACSYS SOLID PRECIPITATION CLIMATOLOGY PROJECT (Reston, VA, USA, 15-15 September 1995) (WMO/TD-No. 739) (out of print)
- WCRP-94 PROCEEDINGS OF THE ACSYS CONFERENCE ON THE DYNAMICS OF THE ARCTIC CLIMATE SYSTEM (Göteborg, Sweden, 7-10 November 1994) (WMO/TD-No. 760) (out of print)

- WCRP-95 WCRP WORKSHOP ON AIR-SEA FLUX FIELDS FOR FORCING OCEAN MODELS AND VALIDATING GCMS (Reading, UK, 24-27 October 1995) (WMO/TD-No. 762) (out of print)
- WCRP-96 NORTHERN HEMISPHERE ATMOSPHERIC BLOCKING AS SIMULATED BY 15 ATMOSPHERIC GENERAL CIRCULATION MODELS IN THE PERIOD 1979-1988 (Results from an AMIP Diagnostic subproject) (WMO/TD-No. 784) (out of print)
- WCRP-97 INTERNATIONAL WORKSHOP ON RESEARCH USES OF ISCCP DATASETS (NASA Goddard Institute for Space Studies, New York, NY, USA, 15-18 April 1996) (WMO/TD-No. 790) (out of print)
- WCRP-98 PROCEEDINGS OF THE WORKSHOP ON THE IMPLEMENTATION OF THE ARCTIC PRECIPITATION DATA ARCHIVE (APDA) AT THE GLOBAL PRECIPITATION CLIMATOLOGY CENTRE (GPCC), (Offenbach, Germany, 10-12 July 1996) (WMO/TD-804)
- WCRP-99 PROCEEDINGS OF THE FIRST SPARC GENERAL ASSEMBLY (Melbourne, Australia, 2-6 December 1996) (WMO/TD-No. 814) (2 volumes)
- WCRP-100 MONSOON PRECIPITATION IN AMIP RUNS (Results from an AMIP diagnostic subproject) (WMO/TD-No. 837)
- WCRP-101 CLIVAR - A RESEARCH PROGRAMME ON CLIMATE VARIABILITY AND PREDICTABILITY FOR THE 21ST CENTURY, 1997 (WMO/TD-No. 853)
- WCRP-102 ORGANIZATION OF INTERNATIONALLY CO-ORDINATED RESEARCH INTO CRYOSPHERE AND CLIMATE (Proceedings of a meeting of experts on cryosphere and climate) (WMO/TD-No. 867)
- WCRP-103 CLIVAR INITIAL IMPLEMENTATION PLAN (WMO/TD-No.869)
- WCRP-104 PROCEEDINGS OF THE FIRST WCRP INTERNATIONAL CONFERENCE ON REANALYSES (Silver Spring, Maryland, USA, 27-31 October 1997) (WMO/TD-No. 876)
- WCRP-105 SPARC IMPLEMENTATION PLAN (WMO/TD-No. 914)
- WCRP-106 PROCEEDINGS OF THE ACSYS CONFERENCE ON POLAR PROCESSES AND GLOBAL CLIMATE (Rosario, Orcas Island, WA, USA, 3-6 November 1997) (WMO/TD-No. 908)
- WCRP-107 COARE-98: PROCEEDINGS OF A CONFERENCE ON THE TOGA COUPLED OCEAN-ATMOSPHERE RESPONSE EXPERIMENT (COARE) (Boulder, CO, USA, 7-14 July 1998) (WMO/TD-No. 940)
- WCRP-108 PROCEEDINGS OF THE INTERNATIONAL CLIVAR CONFERENCE(Paris, France, 2-4 December 1998) (WMO/TD No. 954)
- WCRP-109 PROCEEDINGS OF THE SECOND WCRP INTERNATIONAL CONFERENCE ON REANALYSES (Wokefield Park, nr Reading, UK, 23-27 August 1999) (WMO/TD-No. 985)
- WCRP-110 WORKSHOP ON CLOUD PROCESSES AND CLOUD FEEDBACKS IN LARGE-SCALE MODELS (ECMWF, Reading, Berkshire, UK, 9-13 November 1999) (WMO/TD-No. 993)

-
- WCRP-111 PALEOCLIMATE MODELLING INTERCOMPARISON PROJECT (PMIP) (Proceedings of workshop, La Huardière, Canada, 4-8 October 1999) (WMO/TD-NO. 1007)
- WCRP-112 INTERCOMPARISON AND VALIDATION OF OCEAN-ATMOSPHERE ENERGY FLUX FIELDS (Final report of the Joint WCRP/SCOR Working Group on Air-Sea Fluxes) (November 2000) (WMO/TD-No. 1036)
- WCRP-113 SPARC ASSESSMENT OF UPPER TROPOSPHERIC AND STRATOSPHERIC WATER VAPOUR (WMO/TD-No. 1043) (limited distribution only)
- WCRP-114 CLIMATE AND CRYOSPHERE (CLIC) PROJECT, SCIENCE AND CO-ORDINATION PLAN – VERSION 1 (WMO/TDNo. 1053)
- WCRP-115 WCRP/SCOR WORKSHOP ON INTERCOMPARISON AND VALIDATION OF OCEAN ATMOSPHERE FLUX FIELDS (BOLGER CENTER, POTOMAC, MD, USA, 21-24 MAY 2001) (WMO/TD-No. 1083)
- WCRP-116 SPARC INTERCOMPARISON OF MIDDLE ATMOSPHERE CLIMATOLOGIES (WMO/TD-No. 1142) (limited distribution only)

Appendix II

List of Acronyms

AAOE	Airborne Antarctic Ozone Experiment
AASE	Airborne Arctic Stratospheric Expedition
ABLE-2A	Amazon Boundary Layer Experiment 2A
ABLE-2B	Amazon Boundary Layer Experiment 2B
ACCENT	Atmospheric Composition Change, the European Network of Excellence
ACE-2	Second Aerosol Characterization Experiment
ADC	Analog-to-Digital Converter
AER	Atmospheric and Environmental Research, Inc.
APE	Airborne Polar Experiment
APE-POLECAT	APE-Polar Ozone, Leewaves, Chemistry and Transport
APE-THESEO	APE-Third European Stratospheric Experiment on Ozone
AROTAL	Airborne Raman Ozone, Temperature and Aerosol Lidar
ASAP	Assessment of Stratospheric Aerosol Processes
ASHOE/MAESA	Airborne Southern Hemisphere Ozone Experiment / Measurements for Assessing the Effects of Stratospheric Aircraft
ASTEX	Atlantic Stratocumulus Transition Experiment
ATLAS	Applications Laboratory for Application and Science
ATLAS-3	Atmospheric Laboratory for Applications and Science 3
ATMOS	Atmospheric Trace Molecule Spectroscopy
BC	Black carbon
CCD	Charge Coupled Device
CCN	Cloud Condensation Nuclei
CFC	ChloroFluoroCarbons
CIMS	Chemical Ionization Mass Spectrometer
CITE-3	Chemical Instrument Test and Evaluation 3
CLAES	Cryogenic Limb Array Etalon Spectrometer
CN	Condensation nuclei
CNC	Condensation Nucleus Counter
CRYSTALF	Cirrus Regional Study of Tropical Anvils and Cirrus Layers - Florida Area Cirrus Experiment
CTM	Chemistry Transport Model
DAAC	Distributed Active Archive Center
DLR	Deutschen Zentrum für Luft- und Raumfahrt
EC	European Commission
ECD	Electron Capture Detector
EMEP	Co-operative Programme for Monitoring and Evaluation of the Long-range Transmission of Air pollutants in Europe
EMEX	Equatorial Mesoscale Experiment
ER-2	NASA High-altitude Science Aircraft
ERBS	Earth Radiation Budget Satellite
ESPO	NASA's Earth Science Project Office
EUPLEX/Envisat	European Union Polar Stratospheric Cloud and Lee-Wave Experiment / Environmental Satellite
FCAS	Focused Cavity Aerosol Spectrometer
FOV	Field-of-View

FPD	Flame Photometric Detector
FSSP	Forward Scattering Spectrometer Probe
FT	Free Troposphere
FTIR	Fourier Transform Infrared
GAMETAG	Global Atmospheric Measurements Experiment of Tropospheric Aerosols and Gases
GC	Gas Chromatography
GC/MS/ILS	Samples Gas Chromatography Mass Spectrometry with Isotopically Labeled Standards
GCM	Global Climate Model
GOME	Global Ozone Monitoring Experiment
GOME	Global Ozone Monitoring Experiment
GRAM	Global Reference Atmosphere Model
HALOE	Halogen Occultation Experiment
HSRL	High Spectral Resolution Lidar
IHR	Inter-hemispheric Ratio
INDOEX	Indian Ocean Experiment
IPCC	Intergovernmental Panel on Climate Change
IPCC-SRES	IPCC Special Reports on Emission Scenarios
IR	Infra Red
JPL	NASA Jet Propulsion Laboratory
LaRC	Langley Research Center
LASP	Laboratory for Atmospheric and Space Physics
Lidar	LIght Detection And Ranging
LS	Lower Stratosphere
LTA	Liquid Ternary Aerosol
MASP	Multiangle Aerosol Spectrometer Probe
MkIV	Mark IV Fourier Transform InfraRed Interferometer
MPI	Max Planck Institute
MS	Mass Spectrometer
NARE	North Atlantic Regional Experiment
NASA	National Aeronautics and Space Administration
NASA-PEM	NASA-Pacific Exploratory Mission
NCAR	National Center for Atmospheric Research
NCEP	National Center for Environmental Prediction
Nd:YAG	Neodymium-Doped Yttrium Aluminum Garnet
NDSC	Network for the Detection of Stratospheric Change
NH	Northern Hemisphere
NMASS	Nuclei-Mode Aerosol Size Spectrometer
NOAA	National Oceanic & Atmospheric Administration
OHP	Observatoire de Haute-Provence
OLEX	Ozone Lidar Experiment
OPC	Optical Particle Counter
ORA	Occultation Radiometer
PCA	Principal Component Analysis
PEM	Pacific Exploratory Mission
PEM-Tropics	Pacific Exploratory Mission Tropics
PEM-West	Pacific Exploratory Mission West
PMC	Polar Mesospheric Cloud
PMT	Photomultiplier Tube

POAM	Polar Ozone and Aerosol Measurement
POLARIS	Photochemistry of Ozone Loss in the Arctic Region in Summer
POLINAT	Pollution from Aircraft Emissions in the North Atlantic Flight Corridor
ppt	Parts per Trillion
Pre-AVE	Pre-Aura Validation Experiment
PSC	Polar Stratospheric Cloud
PSL	Polystyrene Latex
PV	Potential Vorticity
PVU	Potential Vorticity Unit
QBO	Quasi-Biennial Oscillation
SAD	Surface Area Density
SAGE	Stratospheric Aerosol and Gas Experiment
SAM	Stratospheric Aerosol Measurement
SH	Southern Hemisphere
SME	Solar Mesospheric Explorer
SOLVE	SAGE III Ozone Loss and Validation Experiment
SONEX	Subsonic Assessment Ozone and NO _x Experiment
SPADE	Stratospheric Photochemistry And Dynamics Experiment
SPARC	Stratospheric Processes And their Role in Climate
SPOT	Satellite Pour l'Observation de la Terre
SSA	Stratospheric Sulfate Aerosol
STRAT	Stratospheric Tracers of Atmospheric Transport
STRATOZ III	Stratospheric Ozone Campaign
SVC	Subvisible Cirrus
TARFOX	Tropospheric Aerosol Radiative Forcing Observational Experiment
TOMS	Total Ozone Mapping Spectrometer
TP	Tropopause
TRACE-P	Transport and Chemical Evolution over the Pacific mission of NASA
TROPOZ II	Tropospheric Ozone Campaign
TTL	Tropical Tropopause Layer
UARS	Upper Atmosphere Research Satellite
UKMO	United Kingdom Met Office
ULAQ	University of L'Aquila Global Climate Model
UNEP	United Nations Environmental Programme
UPMC	Université Pierre et Marie Curie
UT	Upper Troposphere
UTLS	Upper Troposphere/Lower Stratosphere
UV	UltraViolet
VEI	Volcanic Explosivity Index
Vintersol	Validation of International Satellites and Study of Ozone Loss
VMR	Volume Mixing Ratio
WAM	WB57F Aerosol Mission
WATOX	Western Atlantic Ocean Experiment

Appendix III

List of Authors and Contributors

The editors express their gratitude to the following colleagues who contributed text, figures, and most of all their time to one or more of the report chapters:

Richard Anderson-Sprecher
University of Wyoming
Laramie, WY, USA

Juan-Carlos Antuña
Camaguey Meteorological Station
Camaguey, Cuba

John Barnes
NOAA
Hilo, HI, USA

Darrel Baumgardner
NCAR
Boulder, CO, USA

Slimane Bekki
Service d'Aéronomie/IPSL
CNRS
Paris, France

Harald Berresheim
Brandenburg Technological University
Brandenburg, Germany

Richard Bevilacqua
Naval Research Laboratory
Washington, DC, USA

Christine Bingen
IASB
Brussels, Belgium

Nicola Blake
University of California, Irvine
Irvine, CA, USA

Heinz Bingemer
University of Frankfurt
Frankfurt, Germany

Colette Brogniez
University of Lille
Lille, France

Charles A. Brock
NOAA
Boulder, CO, USA

Sharon Burton
SAIC
Hampton, VA, USA

Mian Chin
NASA
Greenbelt, MD, USA

Barclay Clemesha
INPE
Sao Jose dos Campos, Brazil

Christine David
Service d'Aéronomie du CNRS
Paris, France

Nicholas Deutscher
University of Wollongong
Wollongong, NSW, Australia

Terry Deshler
University of Wyoming
Laramie, USA

Didier Fussen
IASB
Brussels, Belgium

Michael Fromm
NRL
Washington, DC, USA

Appendices

Roy Grainger
Univeristy of Oxford
Oxford, UK

Sophie Godin-Beekmann
CNRS
Paris France

David Griffith
University of Wollongong
Wollongong, NSW, Australia

David Griffith
University of Wollongong
Wollongong, NSW, Australia

Mark Hervig
GATS, Inc.
Newport News, VA, USA

Patrick Hamill
San Jose State University
San Jose, California

David Hofmann
NOAA
Boulder, CO, USA

Peter Hobbs
University of Washington
Seattle, WA, USA

Chris Hostettler
NASA
Hampton, VA, USA

James Holton
University of Washington
Seattle, WA, USA

Horst Jäger
IFU
Garmisch-Partenkirchen,
Germany
S.-H. Lee
Denver University
Denver, CO, USA

Nina Iyer
SAIC
Hampton, VA, USA

Anthony Kettle
University of East Anglia
Norwich, UK

Beiping Luo
ETH
Zurich, Switzerland

Fok-Yan Leung
Harvard University
Cambridge, MA, USA

Eva Mancini
University of L'Aquila
L'Aquila, Italy

Emmanuel Mahieu
University of Liege
Liege, Belgium

John Mergenthaler
Lockheed-Martin, Inc.
Menlo Park, CA, USA

Steven Marsh
University of Oxford
Oxford, UK

Stephen Montzka
NOAA
Boulder, CO, USA

Michael Mills
University of Colorado
Boulder, CO, USA

Mary T. Osborn
SAIC
Hampton, VA, USA

Justus Notholt
Univeristy of Bremen
Bremen, Germany

Thomas Peter
ETH
Zurich, Switzerland

Joyce Penner
University of Michigan
Ann Arbor, MI, USA

Giovanni Pitari
Universita' L'Aquila
L'Aquila, Italy

Giovanni Pitari
Universita' L'Aquila
L'Aquila, Italy

J. Michael Reeves
Denver University
Denver, CO, USA

Graciela B. Raga
Centro de Ciencias de la Atmósfera,
UNAM
Mexico City, Mexico

Claudia Timmreck
MPI
Hamburg, Germany

James Rosen
University of Wyoming
Laramie, WY, USA

James C. Wilson
Denver University
Denver, CO, USA

Debra Weisenstein
AER
Lexington, MA, USA

